

Sound Field Synthesis for Line Source Array Applications in Large-Scale Sound Reinforcement

Der Fakultät für Informatik und Elektrotechnik der
Universität Rostock
zur Erlangung des akademischen Grades eines
Dr.-Ing.

vorgelegte Dissertation

von
Frank Schultz
geboren am 17.05.1979 in Leipzig

Current Version = Official Release 2016-06-13

This work is licensed under CC BY-SA 4.0

Als Dissertation genehmigt von
der Fakultät für Informatik und Elektrotechnik
der Universität Rostock

Datum der Einreichung 15.12.2015
Datum der Annahme 07.03.2016
Datum der Verteidigung 29.04.2016
Datum der Endversion 13.06.2016

Gutachter Prof. Dr.-Ing. Sascha Spors
Forschungsgruppe Signalverarbeitung und virtuelle Akustik, Universität Rostock

Prof. Dr.-Ing. habil. Rudolf Rabenstein
Lehrstuhl für Multimediakommunikation und Signalverarbeitung, FAU Erlangen-Nürnberg

Prof. Dr. phil. Stefan Weinzierl
Fachgebiet Audiokommunikation, TU Berlin

Thank you, Bruce !

Acknowledgments

I deeply thank my dissertation advisor Sascha Spors for his continuous inspiration, faith, endless support, dedication and encouragement, which allowed to finalize this thesis under the most magnificent working conditions I have ever experienced.

Sincere thanks goes to Stefan Weinzierl who initially brought me to the research business, became an inspiring and confident mentor when working at TU Berlin and rendered an expert opinion for this thesis.

I highly appreciate Rudolf Rabenstein's effort rendering a further expert opinion for this thesis and making me inspired over the last years. Thank you.

Many thanks to Jens Ahrens, Filippo M. Fazi, Anselm Goertz, Christian Heil, Michael Makarski, Evert W. Start, Ambrose Thompson and Franz Zotter for long term inspiration.

I am very grateful that Günter Krauss and Franz Lermer introduced me to the industrial business and that they became trustful mentors when I started R&D in Audio DSP at Dynacord.

Many thanks to Ralf Baumgartner, Jakob Bergner, Gergely Firtha, Stephan Kruppa, Bob McCarthy, Mauricio Ramirez, Thorsten Schulze, Elena Shabalina, Florian Straube and Hagen Wierstorf for fruitful and inspiring discussions.

I deeply appreciate the collaboration with Matthias Geier, Nara Hahn, Till Rettberg and Fiete Winter at the institute in Rostock, thanks for the very relaxed teamwork climate.

Special thanks to Florian, Jens, Nara, Sascha and Till for proofreading.

Contents

List of Figures	xi
List of Tables	xxi
1 Introduction	1
1.1 History of Large-Scale Sound Reinforcement	2
1.2 Research Motivation	16
1.3 Objective of this Thesis	18
2 Fundamentals of Sound Field Synthesis	19
2.1 Differential Notation of the Wave Equation	19
2.2 Integral Notation of the Wave Equation	21
2.2.1 Helmholtz Integral Equation (HIE)	21
2.2.2 High Frequency Boundary Element Method	24
2.2.3 Rayleigh Diffraction Integrals	28
2.2.4 Rayleigh-Sommerfeld Diffraction Integrals	36
2.2.5 Fresnel-Kirchhoff Diffraction Integral	39
2.2.6 Fresnel and Fraunhofer Approximation	40
2.2.7 Single Layer Potential	43
2.3 SFS of a Spherical Wave	46
2.4 SFS of a Plane Wave	55
2.5 Prefilter FIR-Design for 2.5D SFS	64
2.6 Summary	70
3 Discussion of WST	73
3.1 Baseband Sampling	75
3.2 WST Driving Functions	85

3.2.1	Infinite, Continuous SSD	85
3.2.2	Spatial Discretization	88
3.2.3	Spatial Truncation	93
3.2.4	Spatial Truncation and Discretization	107
3.2.5	Delay-and-Sum Beamforming	122
3.3	Ideal WST-Postfilter	130
3.4	WST Criteria	134
3.4.1	WST#1 Criterion	138
3.4.2	WST#2 Criterion	157
3.4.3	WST#3 Criterion	161
3.5	Summary	169
4	Wavefront Shaping	173
4.1	Arc Array vs. Straight Array	174
4.1.1	Array Morphing	179
4.1.2	Beamwidth and Grating Lobes for Arc Arrays	183
4.2	Line Source Array Control and Prediction	196
4.2.1	LSA Prediction Kernel	196
4.2.2	Venue Model	202
4.2.3	LSA Model	202
4.2.4	LSA Control	203
4.3	Visualization and Quality Measures	207
4.4	Simulations	209
4.5	Summary	250
5	Conclusion	251
5.1	Novelty Aspects	252
5.2	Outlook	255
A	Abbreviations and Acronyms	257
B	Coordinate Systems	259
C	Fourier Transform Conventions	261

D Piston Diffraction Theory	265
D.1 Circular Piston	265
D.1.1 On-Axis Pressure	265
D.1.2 Fraunhofer Approximation	270
D.1.3 Fresnel-/Fraunhofer Transition Distance	277
D.2 Line Piston	279
D.2.1 On-Axis Pressure	279
D.2.2 Fraunhofer Approximation	288
D.2.3 Fresnel-/Fraunhofer Transition Distance	288
Bibliography	317
Curriculum Vitae	319
Statement of Authorship	323
Abstract / Zusammenfassung	324
Theses	325

List of Figures

1.1	Array types for large-scale sound reinforcement.	7
2.1	Geometry for the Helmholtz-Integral Equation (HIE) according to (2.15). Exemplarily shown is a virtual (primary) spherical monopole at position $\mathbf{x}_{\mathbf{PS}}$ that is to be synthesized within V by the secondary source distribution (SSD) on ∂V	22
2.2	Geometry for the Rayleigh-Sommerfeld and the Fresnel-Kirchhoff diffraction using a point source at $\mathbf{x}_{\mathbf{PS}}$ that illuminates an aperture \mathcal{A} in an otherwise infinite opaque screen \mathcal{B} . The region \mathcal{B}^+ is assumed to be dark in the evaluation volume V	36
2.3	Geometry to estimate the shortest distance $\Delta r_{\mathbf{PS}}$ from a point source at $\mathbf{x}_{\mathbf{PS}}$ to a linear SSD. The vectors $\mathbf{x}_0 - \mathbf{x}_{\mathbf{PS}}$, $\mathbf{x} - \mathbf{x}_0$, \mathbf{n} and $\mathbf{n}_{\mathbf{SSD}}$ must be coplanar for 2.5D SFS.	49
2.4	Ideal WFS prefilter impulse response according to (2.193) and (2.195).	67
2.5	Ideal WFS prefilter impulse response according to (2.198).	68
2.6	Windowed FIR-design for (2.198) using a Kaiser-Bessel window.	69
2.7	Sound fields of 2.5D WFS for a spherical or a plane wave using a circular or linear SSD with indicated WFS driving functions, $c = 343 \text{ m/s}$, $f = 686 \text{ Hz} \rightarrow \lambda = 0.5 \text{ m}$ for 1 Pa amplitude at reference line or point.	72
3.1	Signal processing model for SFS using a linear, spatially discretized and truncated SSD. Representation in temporal (top) and spatio-temporal spectrum domain (bottom), cf. [Sta97, Fig. 5.7], [Sta97, Fig. 5.13]. Linear convolution w.r.t. y, k_y is denoted by \otimes , multiplication w.r.t. y, k_y by \odot	74

3.2	Time domain baseband sampling model.	75
3.3	$20 \log_{10}(G_0(x, k_y, z, \omega))$ in dB (2.162) for $x = 1$ m and $z = 0$ m. Levels > -12 dB clipped to white, levels < -60 dB clipped to black, $k = \frac{\omega}{c}$	77
3.4	Sampling strategies for SFS applications with qualitative representations of the spatio-temporal spectra.	82
3.5	Spatial sampling of a purely propagating driving function.	83
3.6	Spatial sampling of a purely evanescent driving function.	84
3.7	Signal flow of the single layer potential for a linear, infinite, continuous SSD located on the y -axis.	85
3.8	Spatio-temporal spectra of WST driving functions.	87
3.9	Sound field synthesis for an infinite, continuous linear array.	87
3.10	Signal flow of the single layer potential for a linear, infinite, discretized SSD located on the y -axis.	88
3.11	Side view of the discretized SSD setup. The infinite SSD is located on the y -axis. SFS is considered within the xy -plane ($x > 0$). The SSD becomes continuous for a secondary source spacing $\Delta y \rightarrow 0$	89
3.12	$ G_0(x, k_y, \omega) $ in dB (2.162) for $x = 1$ m. Sampled driving function $D_S(k_y, \omega)$ (3.30) for a full-band cylindrical wave into x -direction schematically indicated with a white line. The white dot indicates the contribution for $f = 3430$ Hz. Spectral repetitions indicated with red lines. The red markers \blacktriangle indicate propagating spatial postaliasing for $f = 3430$ Hz, whereas these marked with \blacktriangledown indicate evanescent spatial postaliasing.	90
3.13	Infinite, discretized SSD with $\Delta y = \frac{2\pi}{25}$ m. Synthesized sound fields for $f = 3430$ Hz, i.e. $\lambda = 0.1$ m. Fig. 3.13a shows the intended wavefront, Fig. 3.13b all propagating spatial postaliasing contributions, Fig. 3.13d evanescent spatial postaliasing contributions, Fig. 3.13f the resulting sound field due to superposition (3.32).	91
3.14	Signal flow of the single layer potential for a linear, finite length, continuous SSD located on the y -axis.	94

3.15	Relation between spatio-temporal spectra of WST driving functions with same BW_{NN} and corresponding farfield radiation patterns for a chosen temporal frequency.	94
3.16	Simplified radiation characteristics on x -axis for a rectangular windowed, continuous LSA under constant volume acceleration, cf. Fig. D.8.	98
3.17	Level of sound field $ P(x, y, \omega) $ in dB_{rel} computed by numerical evaluation of (3.58). Continuous, finite length LSA driven with $D_w(k_y, \omega)$ (3.38) for $L = 5.5$ m and $L/\lambda = 8$, $\lambda = 0.6875$ m $\rightarrow f \approx 500$ Hz.	102
3.18	On-axis level for Fig. 3.17.	103
3.19	On-axis Fresnel/Fraunhofer transition: (3.60) vs. (D.59) (subscript 'CS'). $L = 5.5$ m and $L/\lambda = 8$, $\lambda = 0.6875$ m $\rightarrow f \approx 500$ Hz, cf. Fig. 3.18.	106
3.20	Signal flow of the single layer potential for a linear, finite length, discretized SSD located on the y -axis.	107
3.21	Examples of the driving functions (3.69) vs. (3.38).	109
3.22	Spatial postaliasing types for $D_{w,S}(k_y, \omega)$	112
3.23	Unit gain normalized driving function (3.69) in different spaces for $N = 11$, $\frac{\omega}{c} = 20$ rad/m, $\Delta y = 2\pi/10$ m, thus $\Delta y/\lambda = 2$, cf. [Van02, Fig. 2.18].	114
3.24	Level of sound fields with a discretized, finite length array for $L = 5.5$ m and $L/\lambda = 8$, $\lambda = 0.6875$ m $\rightarrow f \approx 500$ Hz using $D_{w,S}(k_y, \omega)$ (3.69) with $N = 5$, $\Delta y = 1.1$ m, cf. Fig. 3.15c and Fig. 3.15d that depict $D_{w,S}(k_y, \omega)$ for the same parameterization.	116
3.25	$ P(x, y, \omega) \Delta y $ in dB_{rel} for LSA driven with $D_{w,S}(k_y, \omega)$ (3.69) using $L = \Delta y N = 5.5$ m = const for different discretization steps and $L/\lambda = 8 \rightarrow \lambda = 0.6875$ m $\rightarrow f \approx 500$ Hz.	118
3.26	On-axis level for $ P_{\text{main}}(x, y = 0, \omega) \Delta y $, $ P_{\text{side}}(x, y = 0, \omega) \Delta y $ and $ P(x, y = 0, \omega) \Delta y $ in dB_{rel} for LSA driven with $D_{w,S}(k_y, \omega)$ (3.69) using $L = \Delta y N = 5.5$ m = const for different discretization steps and $L/\lambda = 8 \rightarrow \lambda = 0.6875$ m $\rightarrow f \approx 500$ Hz.	119

3.27	On-axis level $ P(x, y = 0, \omega) \Delta y $ in dB_{rel} for LSA driven with $D_{w,S}(k_y, \omega)$ (3.69) using $L = \Delta y N = 5.5 \text{ m} = \text{const}$ for different discretization steps and temporal frequencies Fig. 3.27a, Fig. 3.27c: 1 kHz, Fig. 3.27b, Fig. 3.27d: 2 kHz.	120
3.28	$ P(x, y = 0, \omega) \Delta y \diamond, G_{0,2D,\text{Far}}(x, \omega) \circ, \text{Mod}(\Delta y, N, x, \omega) \Delta y \square$ (3.89) in dB_{rel} for LSA driven with $D_{w,S}(k_y, \omega)$ (3.69) using $L = \Delta y N = 5.5 \text{ m} = \text{const}$ and different discretization steps. $\frac{L}{\lambda} = 8$	123
3.29	Supersonic DSB: unit gain normalized driving function (3.107) in different spaces for $N = 15$, $\frac{\omega}{c} = 10 \text{ rad/m}$, $\Delta y = 2\pi/20 \text{ m}$, thus $\frac{\Delta y}{\lambda} = \frac{1}{2}$ and $\varphi_{\text{Steer}} = -60^\circ$, $k_{y,\text{Steer}} = -8.66 \text{ rad/m}$, $\tau = 0.7932 \text{ ms}$, $c_{\text{Steer}} = 396.06 \text{ m/s}$	127
3.30	Subsonic DSB: unit gain normalized driving function (3.107) in different spaces for $N = 11$, $\frac{\omega}{c} = 10 \text{ rad/m}$, $\Delta y = 2\pi/15 \text{ m}$, thus $\frac{\Delta y}{\lambda} = \frac{2}{3}$ and $k_{y,\text{Steer}} = -15 \text{ rad/m}$, $\tau = 1.8318 \text{ ms}$, $c_{\text{Steer}} = 228.\bar{6} \text{ m/s}$	128
3.31	Aliasing frequency over steering angle (3.112).	130
3.32	Signal flow of the single layer potential for a linear, infinite, discretized SSD located on the y -axis using a reconstruction filter.	130
3.33	Spatial sampling and reconstruction: continuous WST driving function $D(y_0, \omega)$, sampled driving function $D_S(y_0, \omega)$ and reconstructed driving function $D_{S,\text{Rect}}(y_0, \omega)$ with the rect-function used as the postfilter.	131
3.34	WST signal processing model in temporal (top) and spatio-temporal spectrum domain (bottom). Linear convolution w.r.t. y , k_y is denoted by \circledast , multiplication w.r.t. y , k_y by \odot . This is equivalent to Fig. 3.1 except for the omitted prefilter.	134
3.35	Side view of the discussed setup with LSA length L . The LSA is either built from line pistons of length l on the y -axis or circular pistons of diameter $2r_0$ located within the yz -plane and centered on y -axis. The distance between the centers of two adjacent pistons is indicated as the spatial discretization step Δy . Wave propagation within the xy -plane for $\mathbf{x} = (x > 0, y, z = 0)^T$ is considered. The wave propagation angle $-\frac{\pi}{2} \leq \varphi \leq +\frac{\pi}{2}$ holds.	135

3.36	Grating lobe level vs. q for (a) a line piston LSA and (b) a circular piston LSA. Relative grating lobe levels for $k_y = \mu \frac{2\pi}{\Delta y}$, $1 \leq \mu \leq 5$ are given. Only for a large number N of pistons this level corresponds to the actual local maxima/minima of (3.137) and (3.143).	139
3.37	Comparison of $l = 3''$ line piston (left) and $2r_0 = 3''$ circular piston (right) postfilter characteristics. Top: $q = 1$ (no gaps between adjacent pistons), bottom: WST#1 compliant according to (3.142), (3.149)	144
3.38	LSA with line piston using (3.132), (3.128), (3.129), (3.133), (3.58) and $f = 1.6$ kHz, $\lambda = 0.214$ m, $L = 4.953$ m, $L/\lambda = 23.1044$, $N = 13$, $\Delta y = 0.3930179$ m, $\Delta k_y = 15.9870214$ rad/m, $q = 0.6024800$, $l = 0.2367854$ m.	146
3.39	Example III: \bigcirc : main lobe level decay on x -axis ($\varphi = 0^\circ$), \square : grating lobe level decay on y -axis ($\varphi = +90^\circ$)	148
3.40	Example I: $f = 1.600$ kHz, $\lambda = 0.214$ m, $L = 4.9530000$ m, $N = 13$, $\Delta y = 0.3810000$ m, $\Delta k_y = 16.4913000$ rad/m, $q = 1.0000000$, $r_0 = 0.1905000$ m	150
3.41	Example I: $f = 1.600$ kHz, $\lambda = 0.214$ m, $L = 4.9530000$ m, $N = 11$, $\Delta y = 0.4592320$ m, $\Delta k_y = 13.6819413$ rad/m, $q = 0.7853982$, $l = 0.3606800$ m	151
3.42	Example II: $f = 1.600$ kHz, $\lambda = 0.214$ m, $L = 5.0685173$ m, $N = 11$, $\Delta y = 0.4687517$ m, $\Delta k_y = 13.4040792$ rad/m, $q = 0.8127970$, $l = 0.3810000$ m	152
3.43	Example II: $f = 1.600$ kHz, $\lambda = 0.214$ m, $L = 5.0685173$ m, $N = 21$, $\Delta y = 0.2435289$ m, $\Delta k_y = 25.8005749$ rad/m, $q = 0.8127970$, $l = 0.1979395$ m	153
3.44	Example III: $f = 1.463$ kHz, $\lambda = 0.234$ m, $L = 5.0685173$ m, $N = 11$, $\Delta y = 0.4687517$ m, $\Delta k_y = 13.4040792$ rad/m, $q = 0.8127970$, $l = 0.3810000$ m	154
3.45	Example IV: $f = 1.600$ kHz, $\lambda = 0.214$ m, $L = 4.9530000$ m, $N = 13$, $\Delta y = 0.3810000$ m, $\Delta k_y = 16.4913000$ rad/m, $q = 1.0000000$, $l = 0.3810000$ m	155

3.46	Example V: $f = 1.600$ kHz, $\lambda = 0.214$ m, $L = 4.9530000$ m, $N = 13$, $\Delta y = 0.3930179$ m, $\Delta k_y = 15.9870214$ rad/m, $q = 0.6024800$, $l = 0.2367854$ m	156
3.47	Aliasing frequency $f_{\max} = \frac{c}{\lambda_{\min}}$ over steering angle (3.112).	158
3.48	DSB with $D_{w,S,\text{Steered}}(k_y, \omega)$ (3.107) for $\varphi_{\text{Steer}} = -16^\circ$. Line piston LSAs with $q = \text{ARF} = 1$, $L = 4.953$ m (3.136). Left: $l = 3$ ", right: $l = 15$ ".	159
3.49	Geometry for WFC model, cf. [Urb03, Fig. 8], [Ure04, Fig. 38].	162
3.50	Diffracted sound field $\Re\{P(\mathbf{x}, \omega)\}$ of a virtual point source synthesized by a baffled line piston with $l = 0.343$ m for $f = 5$ kHz using a WFC $\alpha = 1/2$, i.e. $x_{\text{PS}} = 0.4116$ m, $\theta = 22.62^\circ$, $x_{\text{ref}} = 100$ m, $c = 343$ m/s. Normalized to $\Re\{P(\mathbf{x} = (\frac{\lambda}{2}, 0, 0)^T, \omega)\} = -1/2$	164
3.51	Uniformly driven LSA with line pistons that exhibit a specified WFC. The array factor $D_{w,S}(\varphi)$ (3.82), the postfilter $H_{\text{Post}}(\varphi) = H_{\text{WFC}}(\varphi)$ (3.160) and the resulting final array factor $D_{w,S,H}(\varphi) = D_{w,S}(\varphi) \cdot H_{\text{Post}}(\varphi)$ for $f = 5$ kHz, $l = 0.343$ m, $c = 343$ m/s are visualized.	165
3.52	Schematic sketch of an LSA built from $N_B = 3$ cabinets of physical length L_B spaced by Δy_B . Each cabinet has $N_l = 3$ line pistons of length l spaced by Δy_l . The total physical length of the LSA is L_{LSA} . N_B and N_l are assumed to be odd-numbered.	166
3.53	Array factors $D_{w,S,B}(\phi)$, $D_{w,S,l}(\phi)$ and the final array factor $D_{w,S,H}(\phi)$ (3.163) using $H_{\text{WFC}}(\phi)$ for $f = 16$ kHz, $c = 343$ m/s are visualized. Fig. a) and b): 3×5.3 " waveguides per LSA cabinet, α is varied. Fig. c) and d): $9 \times 1.7\bar{6}$ " waveguides per LSA cabinet, q_B is varied. $q_l=1$, $N_C = 11$ for all cases.	167
4.1	Geometry for an arc array with arc length L , cf. [Ure04, Fig. 14], [Ure04, Fig. 16].	175
4.2	Fractional order differentiators/integrators (4.13), (4.14), (4.18) and (4.17) using $\omega_c = 2\pi 2000$ rad/s evaluated for $0 \leq \mu \leq 5$	179
4.3	On-axis frequency responses for variations of array size, windowing, curving and distance doubling. Array driven with (4.9) and synthesized with (4.1), $x_{\text{Ref}} = 16$ m, $f_c = 515$ Hz = const.	180

4.4	Continuous arc array, rectangular window. Left: on-axis pressure for distance doublings starting from $x = 1$ m. Right: FRP for $r = 2^{17}$ m.	188
4.5	Continuous arc array, Kaiser-Bessel window. Left: on-axis pressure for distance doublings starting from $x = 1$ m. Right: FRP for $r = 2^{17}$ m.	189
4.6	Discrete arc array, rectangular window. Left: on-axis pressure for distance doublings starting from $x = 1$ m. Right: FRP for $r = 2^{17}$ m.	190
4.7	Discrete arc array, Kaiser-Bessel window. Left: on-axis pressure for distance doublings starting from $x = 1$ m. Right: FRP for $r = 2^{17}$ m.	191
4.8	Discrete arc array, rectangular window. Left: on-axis pressure for distance doublings starting from $x = 1$ m. Right: FRP for $r = 2^{17}$ m.	192
4.9	Discrete arc array, Kaiser-Bessel window. Left: on-axis pressure for distance doublings starting from $x = 1$ m. Right: FRP for $r = 2^{17}$ m.	193
4.10	Discrete arc array, rectangular window. Left: on-axis pressure for distance doublings starting from $x = 1$ m. Right: FRP for $r = 2^{17}$ m.	194
4.11	Discrete arc array, Kaiser-Bessel window. Left: on-axis pressure for distance doublings starting from $x = 1$ m. Right: FRP for $r = 2^{17}$ m.	195
4.12	Geometry and variables for the LSA setup, cf. [Str15a, Fig. 1].	196
4.13	Example of a farfield radiation pattern for a virtual, directed non-focused point source, cf. [Gun03c, Fig. 15].	205
4.14	LSA_K1_Design1: Setup.	216
4.15	LSA_K1_Design1: Driving functions.	217
4.16	LSA_K1_Design1: Frequency response.	218
4.17	LSA_K1_Design1: SPL distribution in xy -plane with the same colormap as Fig. 4.16b and 6 dB isobars w.r.t. 116 dB _{SPL}	219
4.18	LSA_K1_Design2: Setup.	220
4.19	LSA_K1_Design2: Driving functions.	221

4.20	LSA_K1_Design2: Frequency response.	222
4.21	LSA_K1_Design2: SPL distribution in xy -plane with the same colormap as Fig. 4.20b and 6 dB isobars w.r.t. 106 dB _{SPL}	223
4.22	LSA_K1_Design3: Setup.	224
4.23	LSA_K1_Design3: Driving functions.	225
4.24	LSA_K1_Design3: Frequency response.	226
4.25	LSA_K1_Design3: SPL distribution in xy -plane with the same colormap as Fig. 4.24b and 6 dB isobars w.r.t. 108 dB _{SPL}	227
4.26	LSA_K1_Design4: Setup.	228
4.27	LSA_K1_Design4: Driving functions.	229
4.28	LSA_K1_Design4: Frequency response.	230
4.29	LSA_K1_Design4: SPL distribution in xy -plane with the same colormap as Fig. 4.28b and 6 dB isobars w.r.t. 108 dB _{SPL}	231
4.30	LSA_K1_Design5: Setup and virtual source.	232
4.31	LSA_K1_Design5: Driving functions.	233
4.32	LSA_K1_Design5: Frequency response.	234
4.33	LSA_K1_Design5: SPL distribution in xy -plane with the same colormap as Fig. 4.32b and 6 dB isobars w.r.t. 108 dB _{SPL}	235
4.34	LSA_K1_Design6: Setup and virtual source.	236
4.35	LSA_K1_Design6: Driving functions.	237
4.36	LSA_K1_Design6: Frequency response.	238
4.37	LSA_K1_Design6: SPL distribution in xy -plane with the same colormap as Fig. 4.36b and 6 dB isobars w.r.t. 110 dB _{SPL}	239
4.38	LSA_K1_Design7: Setup and virtual source.	240
4.39	LSA_K1_Design7: Driving functions.	241
4.40	LSA_K1_Design7: Frequency response.	242
4.41	LSA_K1_Design7: SPL distribution in xy -plane with the same colormap as Fig. 4.40b and 6 dB isobars w.r.t. 106 dB _{SPL}	243
4.42	LSA_K1_Design8: Setup and virtual source.	244
4.43	LSA_K1_Design8: Driving functions.	245
4.44	LSA_K1_Design8: Frequency response.	246
4.45	LSA_K1_Design8: SPL distribution in xy -plane with the same colormap as Fig. 4.44b and 6 dB isobars w.r.t. 106 dB _{SPL}	247
4.46	LSA_K1_Design8: $D_{w,s}(k_y, \omega)$, cf. Table 3.1.	248

4.47 LSA_K1_Design8: $D_{w,S,H}(k_y, \omega)$, cf. Table 3.1.	249
D.1 Baffled circular piston with constant volume acceleration on main axis (D.2). Diameter $d_0 = 0.5$ m, $c = 343$ m/s.	269
D.2 Dispersion relation for propagating waves using Ewald sphere, $k_r = \sqrt{k_x^2 + k_y^2}$, $k_x = k_r \cos \varphi$, $k_y = k_r \sin \varphi$, $k_z = \frac{\omega}{c} \cos \vartheta$, $k_r = \frac{\omega}{c} \sin \vartheta$, $\frac{\omega}{c} = \sqrt{k_r^2 + k_z^2}$. Example for: $\varphi = 30^\circ$, $\vartheta = 60^\circ$, $\frac{\omega}{c} = 1$ rad/m.	273
D.3 Jinc function for circular piston, sinc function for line piston. . .	274
D.4 Farfield radiation pattern of circular pistons with $\frac{\omega}{c} = 1$ rad/m (for convenient Ewald sphere visualization, cf. Fig. D.2) and different radii, $c = 343$ m/s, cf. [Kin00, Fig. 7.4.5], [Bor06, Tbl. 8.2].	275
D.5 Fresnel-/Fraunhofer distance x_B of a circular piston within yz - plane with radius r_0 using the half angle opening φ_N , cf. [Hei92b, Fig. 6].	277
D.6 Radiation of a baffled circular piston within yz -plane with (2.85), $\frac{\omega}{c} r_0 = 7$, $d_0 = 10''$, $c = 343$ m/s, $\varphi_N = 33.2^\circ$, $x_B = 0.194$ m, 0 dB at $\mathbf{x} = (2, 0, 0)^T$	278
D.7 left: Fresnel integrals (D.57), right: Cornu's spiral in complex plane	282
D.8 Line piston on-axis characteristics, cf. [Lip86], [Ure02], [Ure04] .	287
D.9 Fresnel-/Fraunhofer distance x_B of a line piston with length l using the half angle opening φ_N , cf. [Hei92b, Fig. 12].	289
D.10 Circular piston on axis, cf. [Hei92b, Fig. 13]. Evaluation of (D.2) normalized to 0 dB at $x = 2r_0$ and $f = 20$ Hz. Fres- nel/Fraunhofer transition distance x_B (D.44) indicated as line. .	290
D.11 Line piston on axis, cf. [Hei92b, Fig. 13]. Numerical evaluation of the integral (D.48) normalized to 0 dB at $x = l$ and $f = 20$ Hz. Fresnel/Fraunhofer transition distance x_B (D.79) indicated as line.	291

List of Tables

2.1	Discussed WFS and SDM driving functions and their connections for a virtual (non-focused) spherical and plane wave. . . .	70
3.1	Implications for the LSA setup according to Fig. 3.1 when being driven with the specified spatio-temporal spectra. References to the WST driving function equations are given.	74
3.2	Propagating pre- and postaliasing due to propagating D and propagating G , cf. Fig. 3.5.	80
3.3	Evanescent postaliasing due to propagating D and evanescent G , cf. Fig. 3.5. Evanescent prealiasing is not occurring due to bounded D	80
3.4	Propagating pre- and postaliasing due to evanescent D and propagating G , cf. Fig. 3.6.	80
3.5	Evanescent pre- and postaliasing due to evanescent D and evanescent G , cf. Fig. 3.6.	80
3.6	Side lobe characteristics (3.75) for odd N	110
4.1	Geometric and acoustic parameters for the LSA setup in Fig. 4.12.199	
4.2	Electro-acoustic parameters for the LSA setup in Fig. 4.12. . . .	200
4.3	Parameters that are held constant for the given simulations of different LSA design studies.	201

Chapter 1

Introduction

Large-scale sound reinforcement (LS-SR) [Ols36, Wol36, Sch50, Ear04] is an engineering discipline for engineering and setting up electric devices (power amplifiers, signal processors) and electro-acoustic devices (loudspeakers, microphones) in order to transmit audio signals as sound waves to be received by a large audience in a large venue, contrary to rather small-sized home entertainment. Another established term for LS-SR is public address (PA), that is typically only used when considering electro-acoustic transmission of speech signals. However, *PA system* is a common term for sound reinforcement systems of any description.

In search of optimized LS-SR using loudspeaker arrays, especially for improved concert sound, this thesis is concerned with uniting two technologies that found their first practical implementations in acoustics in the early 1990s. These approaches are known as Wave Field Synthesis (WFS) [Ber88, Ber92b] and Wavefront Sculpture Technology (WST)¹ [Hei92b, Urb03]. From the vantage point of the present it is interesting that the publications [Ber92b, Hei92b] – presented at the *92nd Convention of the Audio Engineering Society* in 1992 – essentially determined much of the audio engineering research and development for the following decades. WFS constitutes a holographic method to synthesize wavefronts based on the Helmholtz integral equation and several approximations of it. WST was introduced for further improvement of LS-SR by reducing disturbing interferences between multiple loudspeakers that build

¹Wavefront Sculpture Technology[®] is a registered trademark of L-ACOUSTICS US, LLC. The explicit labeling is omitted in the remainder of the thesis and only the relevant research results are discussed.

an array and is based on fundamental array processing. In principle, WFS and WST follow the same idea being based on the same acoustic signal processing framework to produce homogeneous sound fields – or rather coherent wavefronts – for large audiences. These links shall be elaborated in detail throughout this work.

1.1 History of Large-Scale Sound Reinforcement

After the advent of electro-acoustics in the late 19th century, engineers became concerned with LS-SR for large audiences in the beginning of the 20th century. In the first instance, PA was used for large demonstrations and rallies, for which some thousand listeners being at the same location could be addressed for the first time [Gre23, Ear04]. With the advent of electrically amplified music performances in the mid 20th century, concerts demanded the usage of LS-SR, which – nowadays termed as *concert sound* or *touring sound* – constitutes an essential part of the entertainment industry.

Since LS-SR cannot be realized with a single loudspeaker for large audiences and large venues due to power limitations, rather many of them must be deployed – as line or clustered loudspeaker arrays – to ensure appropriate audience coverage. Several hundred loudspeaker cabinets are typically utilized for large stadium concerts [Esk86, p.138], [Kü15, p.26]. Hence, interference of waves emanated from multiple sources becomes a problem that LS-SR has to deal with. In acoustics, this is especially demanding, since a large signal bandwidth of about 8 octaves (40 Hz - 10 kHz) is to be reproduced. For LS-SR, the loudspeaker array dimension is smaller, equally sized or larger than radiated wave lengths; the loudspeaker spacing may be larger than the radiated wave length; the dimension of the audience area is typically much larger than the size of the used loudspeaker arrays; the number of attendees (receivers) is much larger than the number of used loudspeakers (transmitters) and the audience may be situated in the nearfield of the array. This initial situation is in contrast to optics and electromagnetics, where e.g. the considered signal bandwidth is typically narrow, the transceivers are typically larger than the considered wave lengths and mostly farfield conditions can be assumed. For this reason, LS-SR research and development is still after the best compromise for required applications.

However, the "...chief factors which are a measure of the performance of loud speakers or combinations of loud speakers..." being:

1. Frequency range.
2. Uniformity [sic] of response.
3. Directional characteristics.
4. Efficiency.
5. Power handling capacity." [Wol30, p.201] remain today as in the past.

Stenzel and Wolff/Malter

Two outstanding articles [Ste27, Ste29] were published in the 1920s by Stenzel. Later on, a monograph [Ste58] revisits and collects several findings in acoustic array processing. Although Stenzel was not concerned with PA or LS-SR, but rather dealt with acoustic and electromagnetic signal transmission and reception for ship transport, the articles provide important fundamentals on array processing that later became well known textbook knowledge [Ols40, Sku54, Ber54]. The articles discuss the radiation characteristics of continuous and discretized linear arrays built from spherical monopoles – a result that is already well known in antenna design that time e.g. [Fos26] – and also of baffled circular and rectangular pistons using the Neumann Rayleigh integral. The two *product theorems* of array processing [Van02, Ch. 2.8] are introduced. Electronic beam steering for single frequencies, i.e. the *phased array* approach is described. The anti-aliasing condition ("Eindeutigkeit" in [Ste27, Ch. 2c]), i.e. the avoidance of propagating grating lobes is given for the uniformly driven ("natürliche Charakteristik" *ibid.*) and phased driven ("künstliche Charakteristik", *ibid.*) linear array. This is a remarkable result since it anticipates the sampling condition – firstly given and proved for time signal sampling and reconstruction by Kotelnikov in 1933 [Kot33] (English reprint e.g. [Kot06]) – by some years. Although, the interpolation/reconstruction process constitutes a different problem in time signal baseband sampling and sound radiation from discretized linear arrays, the equivalent sampling conditions

$$f_{\max} < \frac{f_s}{2} \quad \text{temporal sampling theorem} \quad (1.1)$$

$$\lambda_{\min} > 2 d_s \quad \text{spatial sampling theorem, general} \quad (1.2)$$

to avoid prealiasing (and in acoustics propagating postaliasing) hold, where f_{\max} is the maximum allowed frequency in a temporal baseband signal, to be sampled with sampling frequency f_s and λ_{\min} the smallest wave length allowing grating lobe free sound fields using an linear array of spherical monopoles with sampling distance d_s .

In 1930 the yet cited fundamental article [Wol30] revisited the results of Stenzel amongst others, with own enhancements on non-uniformly driven arrays and curved line sources. The authors realized that curving a linear array reduces the level of lobes and broadens the lobes for wave lengths smaller than the array size. Furthermore, they discussed the influence of directed horn speakers that can be used for shaping and smoothing (i.e. reducing grating lobes) the arrays farfield directivity to a desired characteristic.

Actually, all important fundamentals on the interaction of acoustic sources were theoretically known by the end of the 1930s. They were of course refined by improved mathematical treatments and in the following decades different lines for realizing LS-SR were pursued that came along with the technological progress.

Line Arrays for Public Address

Rather short line arrays were early adopted for pure speech-based LS-SR, i.e. PA. The problems of a uniformly driven line array (ULA) (strongly frequency dependent directivity, large side lobe level, frequency response variation both on and off-axis, strong frequency dependent near- to farfield transition) were circumvented by curving, by simple frequency independent tapering (i.e. spatial windowing), by frequency dependent tapering (gain shading) and/or so called nested arrays or logarithmically spaced transducers [Dav52, Pri53, Paw61, Kle63, Tay64, Aug70, Hix70, Smi71, Sal72, vdW96]. In his dissertation [Hil51], Hills introduces a concise mathematical framework for the synthesis of farfield radiation patterns using linear arrays. Similar to [Sch43] the link of the array weights and its spatial z - and Fourier transform is given and discussed for different normalized wave number variables. Design methods for farfield radiation patterns with equal minor lobes and maximum directivity are introduced, that resemble the Dolph-Chebyshev and Slepian windows.

Ideally, all approaches above try to keep the ratio of radiated wave length and array length constant to obtain a frequency independent, constant farfield

directivity and thereby a frequency independent near- to farfield transition. In other words: with increasing the frequency the effective length of the line array is to be decreased (however also the maximum achievable SPL decreases), and ultimately this should be a continuous function. With the first digital delay units available [Ble71] digitally beam steered line arrays could be realized [Wor77, Kid79].

Frequency independent farfield characteristics, i.e. line arrays with constant beamwidth are also achieved with so called allpass arrays, introduced to acoustics in e.g. [Kut78, Kut82, Mö88, Goo93, Aar00, Goo05b, Goo06, Goo08]. The well known Bessel array [Fra83, Kit83, Kee90] constitutes a special case of an allpass array as was revisited by [Aar00, Goo08]. Allpass array designs are based on the fact that the discrete-space Fourier transform of the array weights constitutes the farfield radiation pattern of the linear array. Hence, a constant magnitude of the Fourier spectrum (i.e. the autocorrelation of the weights constitutes a weighted Dirac impulse) is the ideal design goal, giving the approach its designation.

Another approach known as constant beamwidth transducer (CBT) initially derived for a spherical cap array [Rog78, Van83] is based on the observation that the frequency independent farfield beam pattern with a desired main lobe beamwidth and very low side lobe level is equal to the normal particle velocity when deploying Legendre polynomials as array weights. In [Kee00] this was realized for acoustic arc arrays and later extended to work with linear arrays by applying digital delays [Kee02, Kee03, Fin08]. The temporal characteristics of a CBT array was discussed in [Kee15]. A multiple CBT array using overlapped directivities to obtain the final desired directivity is discussed in [Fen15].

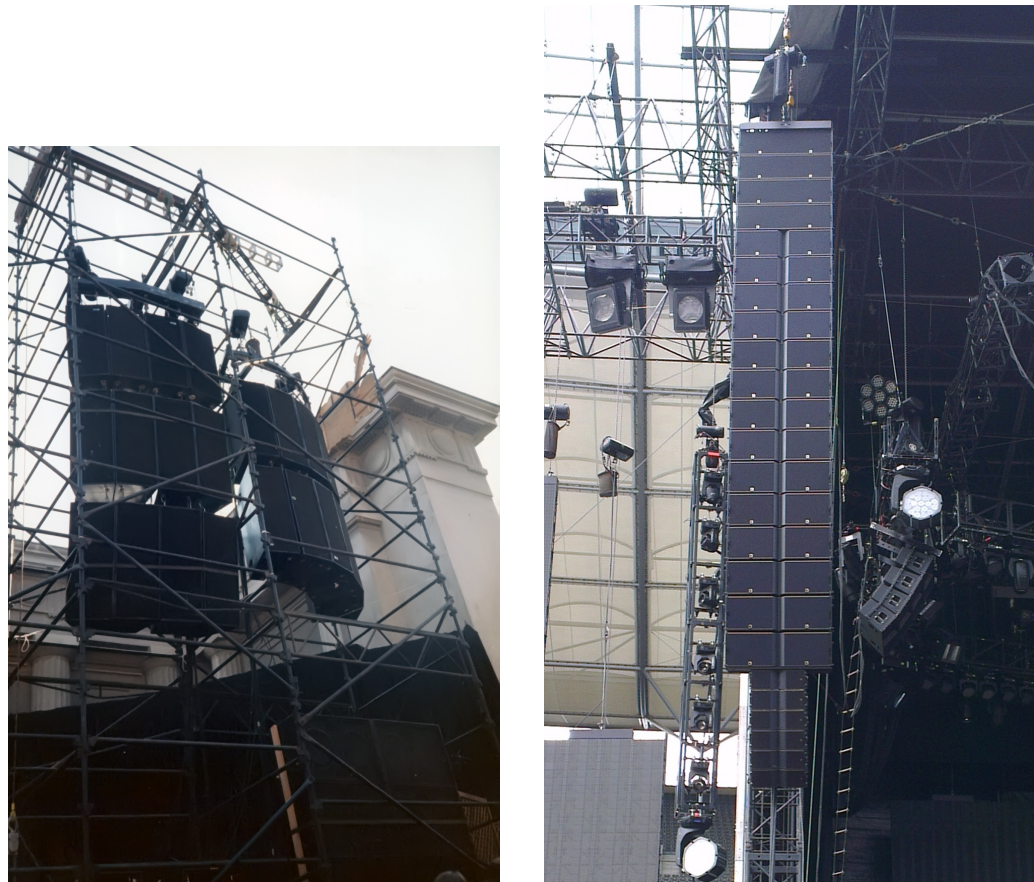
In the 1990s digitally controlled line arrays for speech reinforcement were further developed, above all [Sch92]. In [vdW94] a large column speaker for speech PA in highly reverberant environments is discussed using frequency dependent tapering and beam tilting/steering by digital delays. This was taken up by [dV94b] with a developed digital array control unit and led to what the company *Duran Audio* introduced as *Digital Directivity Control* (DDC), a term that was already used in [Mey85b, Mey85a] for a similar approach of beam steering. A comparable treatment based on digital infinite impulse response

(IIR) filters and delays was given in [Lee98]. The design of a logarithmically spaced linear array is discussed in [vdW96], which is a special version of a nested array and ensures frequency independent directivity. This concept was used e.g. by *Duran Audio* for line columns that aim at speech-based PA. The company later introduced *Digital Directivity Synthesis* (DDS) [vB00, Sta01] for beam shaping using finite impulse response (FIR) filters. This technique solves an optimization problem numerically for a desired sound field towards the loudspeaker filters.

Line and Cluster Arrays for Concert Sound

All the approaches above rely on fulfilling the spatial sampling condition (1.2) to work well behaved, i.e. avoid grating lobes. For the limited bandwidth of speech signals this may be easier accomplished than for the whole audio spectrum, that is typically required for concert sound. Thus, the latter was rather realized with clustered arrays deploying directed horn loudspeakers [Ear04], cf. Fig. 1.1a for a typical setup of a cluster array. The 'point and shoot'-principle, mostly performed by overlapping splayed horns at their -6 dB coverage angles within the audience space, was dominantly used until the end of the 1990s, due to the high SPL and full audio bandwidth requirements, by concurrently accepting spatial aliasing and grating lobes that corrupt the sound field. The radiation characteristics of clustered horn arrays were studied by means of measurements and theoretical predictions in many publications such as [Sin78, Fid89, Gan90, Mey90b, Ure94, Smi95, Ure95b, Ure95a, Ure96, Ahn96, Smi97]. Virtually all conclude that horn driven arrays suffer from grating lobes. Furthermore it is observed that array curving broadens the lobes, while simultaneously the achievable sound pressure level (SPL) decreases. This yields smoother farfield radiation patterns except for the case when grating lobes smear into the main lobe. The limited capability of electronic beam steering and/or wavefront shaping using digital delays is observed, therefore pursuing array curving towards proper audience coverage.

A touring sound system used for the band Grateful Dead – also known as *wall of sound* – is a notable application of line arrays in concert sound reinforcement [Dav75]. The system consisted of several line, planar and arc arrays and was setup onto the stage behind the band. Hence, the system worked as the PA for the audience and simultaneously as a monitor system for the band.



(a) Cluster array, image courtesy of Clayton Call and Bob McCarthy.

(b) Line source array, own picture, taken on 2012-05-30 in Berlin Olympic Stadium.

Figure 1.1: Array types for large-scale sound reinforcement.

One of the specialties of this approach was the individual PA of the different instruments, i.e. each source had its own dedicated cluster or line array section.

A method termed *Phased Point Source Technology* (PPST) is introduced in [Gun98], that led to the development of the *EAW KF900* system [EAW98]. The papers discuss several issues for large LS-SR. Individual cabinets (different types for long/mid/short throw and nearfills) with a well defined wide horizontal and narrow vertical farfield directivity are considered for setting up a clustered-type array in the horizontal and a line-type array in the vertical dimension. The horizontal directivity of the whole array is shaped by geometrical means, while the vertical one is electronically controlled via frequency dependent shading and beam steering [Gun03a, Gun03b, Gun03c]. A strategy

of 'manually' measuring acoustic transfer functions (ATFs) from individual array sources to desired audience/evaluation points is proposed. Based on these ATFs, filters (i.e. magnitude, phase and delay) for an optimum superposition of all sources can be derived that should provide a homogeneous audience coverage. Although the *KF900* system was rarely used for the touring business, but rather for fixed LS-SR installations due to its sophisticated and demanding setup process, its development forms the basis for *EAWs* most recent line source arrays *Anyra* [But14] and *Anna*.

Different approaches for the prediction of sound fields by superimposed ATFs of single sources are discussed in [Jac90], such as a simple spherical monopole superposition, and the piston source – as a reasonable approximation of actual measurements already anticipated by [Mey84a] – as well the phasor sum technique. The so called hybrid technique considers measured farfield radiation pattern balloons of loudspeakers for prediction. The approach is nowadays used by many sound field prediction software, such as *MAPP Online Pro*, *MAPP XT*, *EASE* and *EASE Focus*, cf. [Ahn00, Bai01, Mey03, Fei05a, Fei05b, Fei07a, Fei07b]. The latter publications introduced the Generic Loudspeaker Library (GLL) format. The requirements and practical limitations for GLL based simulation of LSAs were then discussed in [Fei09a, Fei09b, Goe10, Fei14]. The measurement of full 3D loudspeaker directivities was also concerned in [Gun90]. In [Gun99, Gun00b, Gun00c] an improved method for the prediction of horn radiating loudspeakers is introduced with a tessellation model. A comparable approach is [Glo03]. [Sei96] is a follow up research of [Mey90b] by Meyer Sound, concerning the angular resolution of measured loudspeaker balloons, similar to [Gun90]. They conclude, that even 2° resolution may not be sufficient for exact sound field prediction of loudspeaker arrays. Based upon this research, the decision for data resolution of 1/48th octave and 1° in *MAPP Online* – released in the beginning of the 2000s – was presumably made. An interesting contribution regarding the measurement of loudspeaker balloons is found in [Ang98]. The ATFs are decomposed into eigenvalues of the spherical surface functions using spherical Nearfield Acoustic Holography (NAH) [Wu08]. The topic was reissued by [Faz08, Bel15] recently.

The transient radiation of ideally baffled pistons is given in [Ste71] based

on the Rayleigh integral's formulation in the time domain. This is taken up in [Lee94] where the transient fields of baffled rectangular and circular pistons are addressed. The approach is based on the efficient numerical evaluation of the time-domain representation of the Neumann Rayleigh integral and can be used for arbitrarily shaped radiators for given limits. [Har75] discusses the on-axis pressure characteristic and nearfield behavior of line arrays (i.e. the Fresnel/Fraunhofer transition) and addresses the high frequency attenuation in air. Other thorough treatments of the radiation of line sources are given in [Lip86, Lip90, Lip95]. [Och89] discusses the directivity and on-axis pressure of baffled rectangular sources. An efficient numerical evaluation method by splitting the Neumann Rayleigh integral into small individual rectangular pistons and using their farfield directivities is given. The approach is very related to the piston source method of [Mey84a, Jac90].

David G. Meyer

In the 1980s, David G. Meyer published several proceedings and articles that include fundamental ideas being used nowadays. Retrospectively, these pioneering contributions were much ahead of time, since the presented approaches were only commercially realized or reinvented some years or even decades later.

In [Mey82, Mey84a] proposes a model and introduces a software for the numerical prediction of sound fields and polar plots from multi-source arrays of arbitrary shape. This model introduces the approach of the later referred sound field prediction (1.3) and already includes loudspeaker farfield directivities, although due to memory limitations only vertical and horizontal farfield radiation patterns were measured and stored, from which the three-dimensional directivity is obtained by extrapolation. A very important observation is made upon the validity of the model: assuming that the spatial evaluation point is in the farfield of all individual sources, the near- and the farfield of the array can be predicted accurately.

The follow-up contributions [Mey83, Mey84b] discuss the full digital control of a planar loudspeaker array (9x5 drivers), which deploys a combination of tapering, frequency dependent tapering and allpass array techniques. Band-pass filter banks and tapped delay lines were realized to control the driving function (i.e. the magnitude, the phase and the group delay per filter bank) of the array by means of digital signal processing (DSP). The term *Digital Direc-*

tivity Control (DDC) is established, for which Meyer consequently presented an VLSI DSP-design in [Mey85a, Mey85b].

In [Mey89, Mey90a] he further proceeds with a multiple line array setup, that is digitally controlled for short-, mid- and long-throw beam tilting. The array was setup into the ceiling. A discussion of steering angle resolution vs. sampling frequency for integer sample delay steps is given. The coverage of the array is discussed with ASCII-character visualized sound maps, indicating homogeneous PA by usage of Hamming window tapering. This is followed up by [Sch92], where the DFT/DTFT based design of optimum frequency dependent tapering is discussed. The usage of the Slepian window, that can be approximated by the Kaiser-Bessel window is proposed. It is also suggested to tilt the individual loudspeakers into direction of the beam steering angle to avoid or minimize grating lobes.

In conclusion, Meyer gave a lot of ideas for solving the forward problem of sound reinforcement using optimized beam steering and -forming. Just to indicate the coincidence, [Sch92] was also presented at the *92nd Convention of the Audio Engineering Society* such as the initial paper [Hei92b] on WST and one of the very first publications on WFS [Ber92b].

First Generation of Line Source Arrays in Concert Sound

By the end of the 1980s and beginning of the 1990s researchers reconsidered further improving LS-SR, since clustered arrays with horn speakers suffer from high grating lobe levels. Furthermore, the setup of these clustered arrays is very time consuming. This appears not feasible for a fast-paced working environment such as touring sound.

[Hei92b] addresses the problem of avoiding or at least reducing grating lobes when arraying loudspeakers. Grating lobe free sound fields in general require a very small speaker spacing for the highest audio frequencies according to (1.2), which was not considered feasible by the time of publication. Instead of deploying conventional horns, the usage of waveguides – i.e. specially designed horns, where the horn exit resembles a very thin rectangular slot that ideally emanates an equal-phase cylindrical like wave front [Hei92a] and can be modeled as an ideal line source – is motivated. From this originates the terminology *line source array* (LSA) contrary to the *line array* (LA), that refers to a linear array built from conventional (e.g. point or horn) sources [LA01].

By ideally allowing no gaps between the individual ideal waveguides, grating lobes are completely suppressed for a uniformly driven LSA, which trivially models a quasi-continuous linear array. With the *Active Radiating Factor* (ARF) theorem the grating lobe level in the farfield radiation pattern can be linked and predicted w.r.t. the gap size of adjacent waveguides. This is initially setup in order that grating lobes should not exceed the largest sidelobe level of a uniformly driven LSA. The ARF theorem was recently readdressed in [Fen14] and is rigorously treated in the spatio-temporal spectrum domain in this thesis in Ch. 3. Since the waveguide's height is rather large for the first practically designed systems, there is very limited capability for grating lobe free electronic beam steering [Mey02]. Thus, directivity control has to be realized by geometrically shaping the array and pure gain shading. The approach is designated as *Wavefront Sculpture Technology* (WST), for which [Urb01, Urb03] define five criteria for proper LSA operation. One of them is the sampling condition (1.2), another one the ARF theorem, both initially derived in [Hei92b]. The other criteria define a maximum allowed wavefront curvature at the waveguide's exit, the maximum allowed splaying angle between the LSA cabinets for a given waveguide height and an optimal array curvature to provide a homogeneous and frequency independent SPL loss over the audience [Urb01, Urb03]. The latter is also addressed as divergence shading in [Gun00a] and a similar approach was simulated and measured in [Sta04]. The introduced *Array Morphing* [LA13] – basically a prefilter equally applied to all LSA cabinets – is of great help to shape the overall skewness of the ATFs.

The WST criteria were confirmed in [Ure01b], following a discussion of on-axis pressure responses and the near/farfield transition of geometrically shaped arrays [Ure02]. Feasible geometric shapes for LS-SR, such as the arc, J-shaped and spiral array were initially discussed in [Ure01a] in terms of their farfield directivities for continuous sources. These approaches were differently patented, e.g. [Leh00, Eng09]. In [Kee10] a performance comparison for straight and curved line arrays is given including J-shaped, spirally shaped and CBT curved and driven arrays. These arrays are modeled as continuous radiators. Hence, no statements on their grating lobe characteristics can be made. The collected results of Ureda are published as a journal article

[Ure04] and can be seen as one of the fundamental works besides [Urb03]. The contributions were accompanied by further JBL-based research such as [Eng01, Sch02, But02, Bai03] that discusses practical aspects of LSA designs. The problem of front/rear hinge splaying vs. grating lobe level, the impact of insufficient wavefront curvature for large splay angles and HF absorption compensation by band-zoning [Tho11] are discussed in [Web03].

After introducing the first WST-compliant LSA (*L-ACOUSTICS V-DOSC*) in 1992, virtually all large loudspeaker companies designed their first WST-alike LSAs within the next ten years. Thus, by beginning of the 2000s, large companies like *Adamson*, *Alcons*, *Clair Brothers*, *d&b audiotechnik*, *EAW*, *Electro-Voice*, *JBL*, *Martin Audio*, *Meyer Sound* and *Nexo* had products to compete with. A fundamental change of approaching LS-SR – the transition from using LSAs instead of clustered arrays – was observable.

LSA designs that rely only on curving and limited gain shading to obtain a homogeneous audience coverage could be assigned to the *first generation of line source arrays* used for LS-SR, cf. Fig. 1.1b for a typical LSA setup. Optimized curving for an intended audience coverage was developed [Glo02, Tho06].

Second Generation of Line Source Arrays in Concert Sound

Duran Audio released an LSA family termed *AXYS Target* also in the early 2000s [Dur07]. The most innovative part of this design that time is the active amplification and an internal DSP controller per LSA cabinet, that enabled the control of all individual drivers with IIR and/or FIR filters. These filters could be obtained by the previously introduced and already mentioned technologies *Digital Directivity Control* (DDC) [vB00] and *Digital Directivity Synthesis* (DDS) [vB00, Sta01]. DDS is a numerical optimization scheme, that solves the inverse problem, i.e. finding optimized FIR filters for each LSA driver from a desired pre-definable target sound field. Although, *AXYS* seemed to be not competitive against other products, it established what could be termed the *second generation of line source arrays*. These LSAs rely not only on curving but also on full electronic control of the individual LSA drivers.

The optimization approach (cf. [vB00, Fig. 17] vs. [Tho09, Fig. 1]) was – amongst others [Glo02, Ter10] – taken up by *Martin Audio* [Tho08, Tho09, Tho11, Tho13] resulting in the *Multi-cellular Loudspeaker Array* (MLA) and the *OmniLine* array. The *MLA* is controlled with FIR filters and uses three

individually controllable HF drivers per LSA cabinet. The *OmniLine* system uses IIR filters and exhibits a 21 mm driver spacing for the high audio frequencies, not following the waveguide paradigm. Similar optimization algorithms [Fei13] are realized with *AFMG's FIRmaker* software for LSA designs that can handle FIR filters. *FIRmaker* can also be utilized with first generation LSAs, albeit with limited optimization success due to the limited capability for electronic beam steering using delays.

While the mentioned *Martin Audio* LSAs still deploy curving, the first LSA that is exclusively straightly fixed was introduced by *EAW* with the *Anyra* system [But14], utilizing 14 individually controllable high frequency drivers mounted to horns with 1 inch exit size per LSA cabinet. According to (1.2) and assuming no gaps between the waveguides this allows grating lobe free beam steering up to 6.7 kHz for all possible beam angles and up to 10 kHz, if only angles $< \pm 20^\circ$ are allowed.

Mid of 2015 *d&b audiotechnik* introduced so called *array processing* to their large LSAs. Above the spatial aliasing frequency these LSAs are controlled by optimized frequency dependent gain shading rather than using delays and gains. This approach still requires an optimum array curving towards the audience in favor of using a coarser spatial sampling of individual controllable waveguides.

Line Source Array Related Research

Researchers became concerned with optimal designs of waveguides for vertical as well as horizontal directivity [Col01, Sch06b, Sch06a, Col09, Hay12, Hay13, Niz13, Lec13, Hug15, Lec15, Mus16]. The acoustic transfer functions and impulse responses for a straight array modeled with line pistons are given in [Jia04, She07a, She07b]. [An09] shows the reduction of grating lobes with a staggered waveguides, which effectively increases the ARF. A rigorous treatment of the radiation characteristics of linear arrays modeled with line and circular pistons can be found in [Bei02]. With so called digital and geometric radiation controlled (DGRC) arrays [Mey06], also introduced as a so called mixed mechanical/digital approach [Per10a] and further developed to an LSA in [Col15], the initial ideas of [Sch92] are reconsidered.

A treatise on the history of LS-SR was recently given in [Sch15a, Sch15b].

Wave Field Synthesis

In the 1990s Audio-DSP technology became affordable to practically synthesize virtual acoustic fields for the first time. In 1988 Berkhout proposed the usage of holography for acoustic signals using loudspeaker arrays [Ber88]. This technique was introduced as *Wave Field Synthesis* (WFS) [Ber92b], temporarily also designated as *Wave Front Synthesis* [Ber92a]. Initially developed and realized at the Delft University of Technology for more than one decade [Ber93, Vog93, dV94b, Boo95, Sta95, dV96, Sta97, Ver97, Son00, Hul04], the publications [dV94a, Sta96, vB00, vB01, Sta01] of their researchers address the LS-SR community directly with the invention of DDC and DDS, as well as utilizing curved, electronically controlled loudspeaker arrays, and thus pioneering the second generation of touring sound LSAs.

The first Delft dissertation on WFS [Vog93] is a comprehensive collection of the early state of research, while at the same time authors became interested in numerical optimization schemes to synthesize desired sound fields [Kir93, Kir96]. Two important WFS contributions [Sta95, Sta96] for LSA applications were published by Evert W. Start. In [Sta95] the signal processing framework of sound field synthesis using planar and linear arrays is introduced, that is also capable to explain radiation synthesis with straight LSAs. The concept of spatial filtering and the physical meaning and role of the required spatial anti-aliasing and reconstruction filters is explained. This was later on readdressed in [Ahr10c, Fir12]. In [Sta96] the advantages of curved arrays for improved audience coverage and reduced grating lobe level is discussed. [Ver97] continues the research on the signal processing framework and especially discusses the involved loudspeakers, that act as spatial reconstruction filters.

In [dV09] the WFS research state so far is documented including a comprehensive bibliography on the topic. Besides optimizing and adapting driving functions for different applications [Ape04, Cor06, Mel08, Kol09, Sal10, Per10b, Vö11, Lee12, Lee13], WFS with directed virtual sources was studied [Jac05, Cor07, Baa08, Rom08, Per08, Fra12, Rom15].

Initiated by revisiting the WFS theory [Rab06, Rab08, Spo08b] and considering WFS as a single layer potential method for SFS, spatial aliasing artifacts [Spo06b, Spo09] and nearfield effects [Spo07b] were discussed that extend the

initial derivations from Delft. At about that time researchers were also strongly concerned with the connections of sound field synthesis approaches in different array geometries [Nic99, Spo08c, Ahr10a, Faz10a, Koy13]. Typically, geometries are chosen for which an orthogonal/orthonormal basis function expansion of the wave equation is well known, such as planar/linear, cylindrical and spherical/circular arrays. For that the simple source formulation, the single layer potential and the equivalent scattering approach yield the same analytic solutions for the unknown driving function, which was firstly shown in [Faz07a, Faz07c, Faz07b, Faz09, Faz13] for *Ambisonics*, a so called SFS method that is restricted to spherical/circular arrays. Solving the inverse problem of the single layer potential from a virtual plane wave sound field towards the driving functions by means of an analytic deconvolution was performed for planar/linear and spherical/circular arrays in [Ahr08c, Ahr08b]. The first method – both methods are not restricted to virtual plane waves – became well known as *Spectral Division Method* [Ahr10d], whereas the latter one constitutes a mathematical formulation of what is known as *Nearfield-Compensated Higher-Order Ambisonics* (NFC-HOA) [Dan03, Pol05, Ahr08a, Zot09, Faz12]. Both approaches are explicit solutions of the SFS problem in appropriately chosen coordinate systems [Ahr10b, Ahr12b], whereas WFS constitutes the implicit solution.

By introducing the so called secondary source selection criterion [Nic99, Spo07a, Spo08b] WFS could be adapted to also work with spherical/circular arrays. This consequently allowed a comparison of WFS and NFC-HOA in terms of spatial aliasing, modal bandwidth and their temporal and temporal spectrum characteristics [Spo06c, Spo08a, Ahr09, Ahr10e]. It could be concluded that WFS – as a spatially fullband synthesis – is a high-frequency / farfield approximation of Nearfield-Compensated *Infinite-Order Ambisonics* [Ahr12a, p.135], thus linking the explicit and implicit SFS solution.

The SDM solution for a virtual point source [Spo10] reveals that WFS – using a linear array – is a high-frequency / farfield approximation of spatially fullband SDM, again linking the explicit and implicit SFS solution in the coordinate system under discussion. Furthermore, the equivalence of SDM and the Neumann Rayleigh integral was observed in [Ahr10d]. WFS was recently linked to the so called high frequency boundary element method [Zot13], which

is strongly linked to well known diffraction principles. These aspects are further formalized in the present thesis.

[Spo11, Spo13, Wie14] are extensive reviews of the recent state of research on analytic SFS and its perception.

Numerical Solutions for Sound Field Synthesis

The numerical solution of the spatially discretized inverse SFS problem using regularization [Nel01, Kim04, Bai13a] and optimization with different cost functions is discussed in e.g. [Kir93, Kir96, Nel01, War01, Cho02, Pol05, Wu09, Kam10, Ell10, Lil10, Shi10, Bet12, Ell12, Rad13, Rob13, Zha13, Bai14, Cai14, Col14a, Col14b, Oka14, G14, G15] and is extensively studied for so called personal audio systems or multi-zone SFS at the moment. It aims at synthesizing independently (rather small) spatial regions for individual sound reinforcement using (rather small) loudspeaker arrays.

1.2 Research Motivation

Whenever multiple acoustic sources interact interference phenomena are observable. Whether and how these interferences can be exploited for a homogeneous coverage of an large audience is the key question of LS-SR in general [McC10] and also of this thesis. Naturally, optimized LS-SR must deal with compromises and no all-round solution exists. In essence, dealing with LSAs for LS-SR is not fundamentally different than using other array types. The approaches merely lead to different interference phenomena and differ in the capabilities of exploiting them for improved audience coverage.

Setting up and controlling LSAs towards appropriate LS-SR was originally seen as a radiation synthesis problem, i.e. controlling the farfield radiation pattern of the LSA. With the introduction of the WST the mindset changed towards adapting the radiated wavefront for the audience. In its initial form this was controlled with geometrically curved LSAs and nowadays either by exclusive electronic control of straight LSAs or by combining geometric and electronic control.

It is elaborated in this thesis and could be understood as the key message, that the LS-SR problem can be also interpreted as the sound field synthesis of a virtual source rather than a radiation synthesis problem. This alternative viewpoint of course does not change the underlying physics but might be more

convenient explaining and interpreting occurring phenomena. Incidentally, the strong connections of WST and WFS can be revealed.

A well known approach for numerical sound field prediction of a finite LSA is based on the complex summation of N driven LSA cabinets at the positions $\mathbf{x}_0[n]$ [Mey84a, (52)], [Mey03, (2)], [Fei09b, (11)]

$$P(\mathbf{x}, \omega) = \sum_{n=1}^N D(\mathbf{x}_0[n], \omega) \cdot \underbrace{H_n(\mathbf{x}, \mathbf{x}_0[n], \omega)}_{H_{\text{CDPS}}(\mathbf{x}, \mathbf{x}_0[n], \omega)} \frac{e^{-j \frac{\omega}{c} |\mathbf{x} - \mathbf{x}_0[n]|}}{4 \pi |\mathbf{x} - \mathbf{x}_0[n]|} \quad (1.3)$$

using the so called complex-directivity point source (CDPS) model [Fei09b]. This models the LSA cabinets by their individual farfield radiation patterns $H_n(\mathbf{x}, \mathbf{x}_0[n], \omega) \leftrightarrow H_n(\varphi, \vartheta, \omega)$. Each LSA cabinet is filtered with a driving function $D(\mathbf{x}_0[n], \omega)$.

The key goal of homogeneous LS-SR does not differ from electric transmission technology. The acoustic impulse response (AIR) of the transmission path from the LSA to an evaluation point should resemble a Dirac delta function as close as possible. This is synonymous with requiring a flat temporal magnitude spectrum for the acoustic transfer function (ATF). This should ideally hold for the whole audience to be covered. Due to the wave propagation time and the SPL loss over distance – which can be highly varied using LSAs – the AIRs/ATFs include an additional delay τ and amplitude loss term $A_l(\mathbf{x})$. Then, ideally follows

$$p_{\text{AIR}}(\mathbf{x}, t) \propto A(\mathbf{x}) \frac{\delta(t - \tau(\mathbf{x}))}{A_l(\mathbf{x})}, \quad P_{\text{ATF}}(\mathbf{x}, \omega) \propto A(\mathbf{x}) \frac{e^{-j\omega\tau(\mathbf{x})}}{A_l(\mathbf{x})}. \quad (1.4)$$

With the additional amplitude $A(\mathbf{x})$ audience and non-audience zones (such as room boundaries that should be avoided to cover) can be differently weighted. Ideally, $\tau(\mathbf{x})$, $A_l(\mathbf{x})$ and $A(\mathbf{x})$ should be smooth functions of space. From (1.3) it can be seen that the ATF is obtained by superposition of weighted sources. Thus, interferences between these source must be controlled such that the AIRs in the audience approach the ideal $p_{\text{AIR}}(\mathbf{x}, t)$. How well this works is a matter of (i) the LSA design and curving, which assigns $H_{\text{CDPS}}(\mathbf{x}, \mathbf{x}_0[n], \omega)$ and of (ii) the electronic control, which assigns $D(\mathbf{x}_0[n], \omega)$. This is discussed in detail throughout the thesis.

1.3 Objective of this Thesis

As mentioned above it is the aim of this thesis approaching optimized LS-SR as a forward sound field synthesis problem and to unite WFS and WST. This requires careful revision of WFS and WST in the first instance before merging them. Hence, the thesis is organized as follows:

In Ch. 2 WFS is revisited. For that (1.3) is recast towards a continuous problem formulation using ideal point sources. The chapter follows the structure of [Sta97, Ch. 2&3] and provides an in-depth discussion on the high-frequency boundary element method, that is linked to well known diffraction principles and to WFS as shown. The implicit and explicit solutions of the sound field synthesis problem for a virtual plane wave and a spherical one are collected, providing missing links in existing literature.

In Ch. 3 WST is revisited for straight arrays. For that the continuous SFS problem formulation is discretized by consequent application of the acoustic signal processing framework and explaining radiation phenomena within the spatio-temporal Fourier spectrum domain and with its inverse spatial Fourier transform, here termed angular spectrum synthesis. This chapter roughly follows the structure of [Sta97, Ch. 4&5] here as a matter of priority discussing a special case of wave propagation perpendicular to the array, i.e. a broadband array. It is extensively discussed how the addressed WST criteria are embedded within the fundamentals of sound field synthesis and array processing. The WST criteria that are related to linear arrays can be consistently classified and reinterpreted with the proposed framework. Two approaches for the interpretation of diffraction and spatial aliasing effects give new insights into the radiation characteristics of straight line arrays modeled with directed speakers.

In Ch. 4 the problem of optimum audience coverage as a forward sound field synthesis problem is treated. At first the difference between a straight and arc array is discussed in terms of their farfield radiation patterns and on-axis characteristics. The chapter then introduces an approach for WFS of a virtual, directed source. This yields audience adapted wavefront shaping and thus optimum audience coverage. The approach is compared to other forward solutions, such as the CBT-like array or pure geometric WST-like control.

Chapter 2

Fundamentals of Sound Field Synthesis

This chapter¹ reconsiders the fundamentals of sound field synthesis (SFS) and diffraction theory. Since the multi-dimensional acoustic signal processing is treated with different conventions in the literature, it appears meaningful to give a consistent review of the most important concepts and equations.

In general, linear acoustics in a dissipationless medium with a constant speed of sound c and a constant density of air ϱ_0 is considered, assuming free-field conditions besides the radiating sources under discussion. The Fourier transform conventions for the temporal and spatial domain of App. C are used.

2.1 Differential Notation of the Wave Equation

Linear acoustics phenomena are described by the partial differential wave equation. The linearized, inhomogeneous wave equation for a three-dimensional sound pressure field using the Laplace operator Δ reads [Bla00, (10.D-10)]

$$\left(\Delta - \frac{1}{c^2} \frac{\partial^2}{\partial t^2} \right) p(\mathbf{x}, t) = -q(\mathbf{x}, t), \quad (2.1)$$

¹[Sch14c, Sch16] is partly reissued herein.

for which a Fourier transform with respect to time (C.2) yields [Mor86, (7.1.16)]

$$\left(\Delta + \left(\frac{\omega}{c}\right)^2\right) P(\mathbf{x}, \omega) = -Q(\mathbf{x}, \omega). \quad (2.2)$$

Using the Dirac delta function $\delta(\cdot)$ and imaginary unit j , the three-dimensional free-field Green's function [DeS92, Ch.2], [Wat15, Ch.2]

$$g_{0,3D}(\mathbf{x}, \mathbf{x}_0, t) = \frac{\delta\left(t - \frac{|\mathbf{x} - \mathbf{x}_0|}{c}\right)}{4\pi |\mathbf{x} - \mathbf{x}_0|} \quad \text{for } ct > |\mathbf{x} - \mathbf{x}_0|, \quad (2.3)$$

$$G_{0,3D}(\mathbf{x}, \mathbf{x}_0, \omega) = \frac{e^{-j\frac{\omega}{c}|\mathbf{x} - \mathbf{x}_0|}}{4\pi |\mathbf{x} - \mathbf{x}_0|} \quad (2.4)$$

solves the three-dimensional wave equation to a Dirac inhomogeneity

$$\left(\Delta - \frac{1}{c^2} \frac{\partial^2}{\partial t^2}\right) g_{0,3D}(\mathbf{x}, \mathbf{x}_0, t) = -\delta(\mathbf{x} - \mathbf{x}_0) \delta(t) \quad (2.5)$$

$$\left(\Delta + \left(\frac{\omega}{c}\right)^2\right) G_{0,3D}(\mathbf{x}, \mathbf{x}_0, \omega) = -\delta(\mathbf{x} - \mathbf{x}_0). \quad (2.6)$$

The two-dimensional free-field Green's function [DeS92, Ch.2], [Wat15, Ch.2]

$$g_{0,2D}(\mathbf{x}, \mathbf{x}_0, t) = \begin{cases} 0 & ct < |\mathbf{x} - \mathbf{x}_0| \\ \frac{c}{2\pi \sqrt{(ct)^2 - |\mathbf{x} - \mathbf{x}_0|^2}} & ct > |\mathbf{x} - \mathbf{x}_0|. \end{cases} \quad (2.7)$$

$$G_{0,2D}(\mathbf{x}, \mathbf{x}_0, \omega) = -\frac{j}{4} H_0^{(2)}\left(\frac{\omega}{c} |\mathbf{x} - \mathbf{x}_0|\right) \quad (2.8)$$

solves the two-dimensional wave equation to a Dirac inhomogeneity

$$\left(\Delta - \frac{1}{c^2} \frac{\partial^2}{\partial t^2}\right) g_{0,2D}(\mathbf{x}, \mathbf{x}_0, t) = -\delta(\mathbf{x} - \mathbf{x}_0) \delta(t) \quad (2.9)$$

$$\left(\Delta + \left(\frac{\omega}{c}\right)^2\right) G_{0,2D}(\mathbf{x}, \mathbf{x}_0, \omega) = -\delta(\mathbf{x} - \mathbf{x}_0). \quad (2.10)$$

The linearized, homogeneous wave equation for a three-dimensional pressure field reads [Mor86, (6.2.8)]

$$\left(\Delta - \frac{1}{c^2} \frac{\partial^2}{\partial t^2}\right) p(\mathbf{x}, t) = 0, \quad (2.11)$$

for which a Fourier transform with respect to time (C.2) yields the Helmholtz equation

$$\left(\Delta + \left(\frac{\omega}{c}\right)^2\right) P(\mathbf{x}, \omega) = 0. \quad (2.12)$$

2.2 Integral Notation of the Wave Equation

With the closed volume V , its smooth surface $A = \partial V$, the vector $\mathbf{x}_0 \in \partial V$, the position vector $\mathbf{x} \in \partial V \cup V$, the inward unit normal vector \mathbf{n} and the 3D freefield Green's function $G_{0,3D}(\mathbf{x}, \mathbf{x}_0, \omega)$ (2.4), the integral representation of (2.2) is with the normal derivative $\frac{\partial(\cdot)}{\partial n}$ given as [Wun96, (2.82d)]

$$P(\mathbf{x}, \omega) = \iiint_V Q(\mathbf{x}_0, \omega) G_{0,3D}(\mathbf{x}, \mathbf{x}_0, \omega) dV + \oint_{\partial V} \left[-\frac{\partial P(\mathbf{x}_0, \omega)}{\partial n} G_{0,3D}(\mathbf{x}, \mathbf{x}_0, \omega) + \frac{\partial G_{0,3D}(\mathbf{x}, \mathbf{x}_0, \omega)}{\partial n} P(\mathbf{x}_0, \omega) \right] dA(\mathbf{x}_0), \quad (2.13)$$

originating from the 4th Green's identity for scalar fields [Wun96, 2.2.3]. For homogeneous boundary conditions the surface integral vanishes, thus obtaining

$$P(\mathbf{x}, \omega) = \iiint_V Q(\mathbf{x}_0, \omega) G_{0,3D}(\mathbf{x}, \mathbf{x}_0, \omega) dV. \quad (2.14)$$

2.2.1 Helmholtz Integral Equation (HIE)

For $Q(\mathbf{x}_0, \omega) = 0$ (i.e. the Helmholtz equation), however imposing inhomogeneous boundary conditions (2.13) reduces to [Col13, (2.5)], [Wil99, (8.15)]

$$\oint_{\partial V} \left[-\frac{\partial P(\mathbf{x}_0, \omega)}{\partial n} G_{0,3D}(\mathbf{x}, \mathbf{x}_0, \omega) + \frac{\partial G_{0,3D}(\mathbf{x}, \mathbf{x}_0, \omega)}{\partial n} P(\mathbf{x}_0, \omega) \right] dA(\mathbf{x}_0) \quad (2.15)$$

$$= \begin{cases} +P(\mathbf{x}, \omega) & \forall \mathbf{x} \in V \\ +1/2 P(\mathbf{x}, \omega) & \forall \mathbf{x} \in \partial V \\ 0 & \forall \mathbf{x} \notin V \end{cases}$$

under the assumption that $P(\mathbf{x}, \omega)$ is continuously differentiable at $\mathbf{x} = \mathbf{x}_0$. See Fig. 2.1 for a sketch of the geometry. The surface integral (2.15) is referred to

as the *Helmholtz-Integral Equation* (HIE) and in German to as the *Kirchhoff-Helmholtz Integral* (KHI).

The normal derivative $\frac{\partial P(\mathbf{x}_0, \omega)}{\partial n}$ takes the gradient of $P(\mathbf{x}, \omega)$ with respect to the field variable \mathbf{x} , evaluates it at $\mathbf{x} = \mathbf{x}_0$ and specifies the dot product $\langle \cdot, \cdot \rangle$ of the resulting vector and the inward unit normal \mathbf{n} at the respective position \mathbf{x}_0 , hence can be written as

$$\frac{\partial P(\mathbf{x}_0, \omega)}{\partial n} = \langle \text{grad}_{\mathbf{x}} P(\mathbf{x}, \omega) \Big|_{\mathbf{x}=\mathbf{x}_0}, \mathbf{n}(\mathbf{x}_0) \rangle. \quad (2.16)$$

The term $\frac{\partial G_{0,3D}(\mathbf{x}, \mathbf{x}_0, \omega)}{\partial n}$ in (2.15) takes the gradient of $G_{0,3D}(\mathbf{x}, \mathbf{x}_0, \omega)$ with respect to the variable \mathbf{x}_0 and determines the dot product with \mathbf{n} at the relevant position \mathbf{x}_0 , written as

$$\frac{\partial G_{0,3D}(\mathbf{x}, \mathbf{x}_0, \omega)}{\partial n} = \langle \text{grad}_{\mathbf{x}_0} G_{0,3D}(\mathbf{x}, \mathbf{x}_0, \omega), \mathbf{n}(\mathbf{x}_0) \rangle. \quad (2.17)$$

The normal derivative with $r = |\mathbf{x} - \mathbf{x}_0|$ is given as

$$\frac{\partial G_{0,3D}(\mathbf{x}, \mathbf{x}_0, \omega)}{\partial n} = +\frac{1}{r} \left(1 + j \frac{\omega}{c} r \right) \cos \varphi_r G_{0,3D}(\mathbf{x}, \mathbf{x}_0, \omega), \quad (2.18)$$

$$\frac{\partial G_{0,3D}(\mathbf{x}, \mathbf{x}_0, \omega)}{\partial n} \approx +j \frac{\omega}{c} \cos \varphi_r G_{0,3D}(\mathbf{x}, \mathbf{x}_0, \omega) \quad \text{for } \frac{\omega}{c} r \gg 1, \quad (2.19)$$

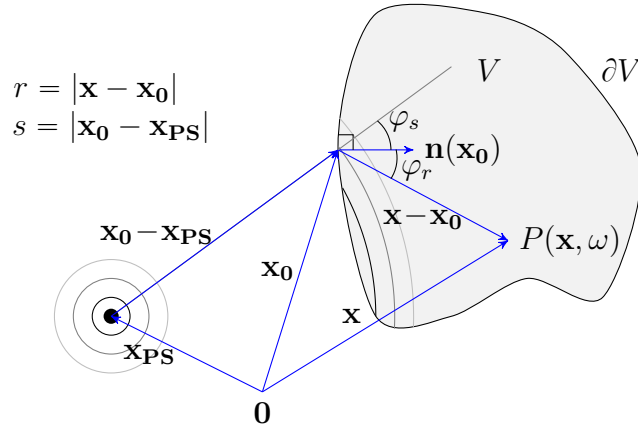


Figure 2.1: Geometry for the Helmholtz-Integral Equation (HIE) according to (2.15). Exemplarily shown is a virtual (primary) spherical monopole at position \mathbf{x}_{PS} that is to be synthesized within V by the secondary source distribution (SSD) on ∂V .

where φ_r is the angle between $\mathbf{n}(\mathbf{x}_0)$ and $\mathbf{x} - \mathbf{x}_0$ and thus [Olv10, (1.6.2)]

$$\cos \varphi_r = \frac{\langle \mathbf{x} - \mathbf{x}_0, \mathbf{n}(\mathbf{x}_0) \rangle}{|\mathbf{x} - \mathbf{x}_0|}. \quad (2.20)$$

$\frac{\partial G_{0,3D}(\mathbf{x}, \mathbf{x}_0, \omega)}{\partial n}$ exhibits ideal spherical dipole characteristic in the farfield, whereas $G_{0,3D}(\mathbf{x}, \mathbf{x}_0, \omega)$ is an ideal spherical monopole source. The HIE thus postulates the superposition of a single and a double layer potential and is the fundamental solution of the SFS problem for a source-free volume. Ideally, SFS treated as an interior problem aims at reproducing the pressure field $S(\mathbf{x}, \omega)$ of a virtual, so called primary source located outside of V for which $\frac{\partial S(\mathbf{x}_0, \omega)}{\partial n}$ and $S(\mathbf{x}_0, \omega)$ have to be known in order to physically realize the HIE, that is $P(\mathbf{x}, \omega) = S(\mathbf{x}, \omega) \forall \mathbf{x} \in V$ and $P(\mathbf{x}, \omega) = 0 \forall \mathbf{x} \notin V$. Analytic solutions may not exist for a given problem or may not be feasible. Therefore, very often only the single layer potential (SLP) using a secondary source distribution (SSD) of monopoles

$$P(\mathbf{x}, \omega) = \oint_{\partial V} D(\mathbf{x}_0, \omega) G_{0,3D}(\mathbf{x}, \mathbf{x}_0, \omega) dA(\mathbf{x}_0) \quad (2.21)$$

is considered for SFS aiming at synthesizing only $P(\mathbf{x}) = S(\mathbf{x})$ for $\mathbf{x} \in V$, i.e. only V is controllable. In practice the SLP is approximated with densely packed loudspeaker arrays by exploiting the fact that the radiation characteristics of many real loudspeakers for low audio frequencies are similar to that of a spherical monopole. It appears useful to give a consistent review and provide links of SFS approaches and different diffraction theories. For that two simple primary sources are considered next.

Point Source

For a point source at position $\mathbf{x}_{PS} \notin V$ and the temporal spectrum $P(\omega)$

$$P_{PS}(\mathbf{x}, \omega) = P(\omega) \frac{e^{-j \frac{\omega}{c} |\mathbf{x} - \mathbf{x}_{PS}|}}{4 \pi |\mathbf{x} - \mathbf{x}_{PS}|} \quad (2.22)$$

the normal derivative (2.16) with $s = |\mathbf{x}_0 - \mathbf{x}_{PS}|$ and

$$\cos \varphi_s = \frac{\langle \mathbf{x}_0 - \mathbf{x}_{PS}, \mathbf{n}(\mathbf{x}_0) \rangle}{|\mathbf{x}_0 - \mathbf{x}_{PS}|} \quad (2.23)$$

is given as

$$\frac{\partial P_{\text{PS}}(\mathbf{x}_0, \omega)}{\partial n} = -\frac{1}{s} \left(1 + j \frac{\omega}{c} s\right) \cos \varphi_s P_{\text{PS}}(\mathbf{x}_0, \omega), \quad (2.24)$$

$$\frac{\partial P_{\text{PS}}(\mathbf{x}_0, \omega)}{\partial n} \approx -j \frac{\omega}{c} \cos \varphi_s P_{\text{PS}}(\mathbf{x}_0, \omega) \quad \text{for } \frac{\omega}{c} s \gg 1. \quad (2.25)$$

Plane Wave

For a plane wave with propagating direction indicated by the unit vector \mathbf{n}_{PW}

$$P_{\text{PW}}(\mathbf{x}, \omega) = P(\omega) e^{-j \frac{\omega}{c} \langle \mathbf{n}_{\text{PW}}, \mathbf{x} \rangle} \quad (2.26)$$

the normal derivative (2.16) is given as

$$\frac{\partial P_{\text{PW}}(\mathbf{x}_0, \omega)}{\partial n} = -j \frac{\omega}{c} \cos \varphi_p P_{\text{PW}}(\mathbf{x}_0, \omega) \quad (2.27)$$

using the angle φ_p between the vectors \mathbf{n}_{PW} and $\mathbf{n}(\mathbf{x}_0)$ and thus

$$\cos \varphi_p = \langle \mathbf{n}_{\text{PW}}, \mathbf{n}(\mathbf{x}_0) \rangle. \quad (2.28)$$

2.2.2 High Frequency Boundary Element Method

Different approximations, known as High Frequency Boundary Element Method (HF-BEM) are given in literature to reduce the complexity of the HIE. It is shown here that these approaches are related to Fresnel-Kirchhoff and Rayleigh-Sommerfeld diffraction, that are typically given for point source wave propagation in more detail. As a first step, (2.18) inserted into (2.15) leads to

$$P(\mathbf{x}, \omega) = \oint_{\partial V} \left[-\frac{\partial P(\mathbf{x}_0, \omega)}{\partial n} + \frac{1}{r} \left(1 + j \frac{\omega}{c} r\right) \cos \varphi_r P(\mathbf{x}_0, \omega) \right] G_{0,3\text{D}}(\mathbf{x}, \mathbf{x}_0, \omega) dA(\mathbf{x}_0) \quad (2.29)$$

for $\mathbf{x} \in V$.

(i) *HF-BEM Kernel*: The assumption that the impedance of the boundary surface is approximately equivalent to the medium's impedance, i.e. $Z_0 = \rho_0 c$ is made. This holds for virtual sources that are sufficiently far away in order

that at the boundary

$$Z_0 = \varrho_0 c = \frac{P(\mathbf{x}_0, \omega)}{V_n(\mathbf{x}_0, \omega)} \rightarrow P(\mathbf{x}_0, \omega) = \varrho_0 c V_n(\mathbf{x}_0, \omega) \quad (2.30)$$

can be written. Furthermore, the normal derivative $\frac{\partial P(\mathbf{x}_0, \omega)}{\partial n}$ corresponds to the temporal Fourier spectrum of the normal velocity $V_n(\mathbf{x}_0, \omega)$ by the Euler equation [Sku71, Ch. 13.5]

$$\frac{\partial P(\mathbf{x}_0, \omega)}{\partial n} = -j\omega \varrho_0 V_n(\mathbf{x}_0, \omega). \quad (2.31)$$

Inserting $\frac{\partial P(\mathbf{x}_0, \omega)}{\partial n}$ (2.31) and $P(\mathbf{x}_0, \omega)$ (2.30) into (2.29) leads to [Her03, (11)]

$$P(\mathbf{x}, \omega) = \oint_{\partial V} j\omega \varrho_0 V_n(\mathbf{x}_0, \omega) \left(1 + \cos \varphi_r \left(1 + \frac{1}{j \frac{\omega}{c} r} \right) \right) G_{0,3D}(\mathbf{x}, \mathbf{x}_0, \omega) dA(\mathbf{x}_0), \quad (2.32)$$

which is known as the kernel of the HF-BEM [Her03]. Under the assumption $\frac{\omega}{c} r \gg 1$ (2.19), the kernel reduces to

$$P(\mathbf{x}, \omega) = \oint_{\partial V} j\omega \varrho_0 V_n(\mathbf{x}_0, \omega) (1 + \cos \varphi_r) G_{0,3D}(\mathbf{x}, \mathbf{x}_0, \omega) dA(\mathbf{x}_0). \quad (2.33)$$

This equation is used in [Hei92b, (1)] for the prediction of sound fields that are radiated from straight and curved loudspeaker arrays. The equation holds only if the wave length is much smaller than the dimension of the secondary source distribution (SSD).

(ii) *WFS as HF-BEM*: A differently written HF-BEM equation in context of a Wave Field Synthesis (WFS) derivation was introduced in [Zot13]. Again, under the assumption that $\frac{\omega}{c} r \gg 1$, (2.29) reduces to

$$P(\mathbf{x}, \omega) = \oint_{\partial V} \left[-\frac{\partial P(\mathbf{x}_0, \omega)}{\partial n} + j \frac{\omega}{c} \cos \varphi_r P(\mathbf{x}_0, \omega) \right] G_{0,3D}(\mathbf{x}, \mathbf{x}_0, \omega) dA(\mathbf{x}_0). \quad (2.34)$$

By furthermore assuming that all evaluation points \mathbf{x} are similarly very far away from all \mathbf{x}_0 , i.e. $\varphi_r \approx 0$ and thus $\cos \varphi_r \approx 1$ holds. With that (2.34)

reduces to the SLP [Zot13, (19)]

$$P(\mathbf{x}, \omega) = \oint_{\partial V} \left[-\frac{\partial P(\mathbf{x}_0, \omega)}{\partial n} + j \frac{\omega}{c} P(\mathbf{x}_0, \omega) \right] G_{0,3D}(\mathbf{x}, \mathbf{x}_0, \omega) dA(\mathbf{x}_0), \quad (2.35)$$

from which a WFS driving function for a point source is derived in [Zot13, Sec. 6], as will be revisited below.

HF-BEM for a Point Source

For a virtual point source (2.22) the HF-BEM kernel (2.32) and the WFS HF-BEM kernel (2.35) are given in further detail.

(i) *HF-BEM Kernel*: At first, inserting (2.4), (2.18), (2.22) and (2.24) into the HIE (2.15) yields for $\mathbf{x} \in V$

$$P(\mathbf{x}, \omega) = \oint_{\partial V} \left[\frac{1 + j \frac{\omega}{c} s}{s} \cos \varphi_s + \frac{1 + j \frac{\omega}{c} r}{r} \cos \varphi_r \right] P_{PS}(\mathbf{x}_0, \omega) G_{0,3D}(\mathbf{x}, \mathbf{x}_0, \omega) dA(\mathbf{x}_0). \quad (2.36)$$

Under the usual HF-BEM assumptions $\frac{\omega}{c} r \gg 1$ (2.19) and $\frac{\omega}{c} s \gg 1$ (2.25) the HIE for a point source approximates to

$$P(\mathbf{x}, \omega) = \oint_{\partial V} j \frac{\omega}{c} (\cos \varphi_s + \cos \varphi_r) P_{PS}(\mathbf{x}_0, \omega) G_{0,3D}(\mathbf{x}, \mathbf{x}_0, \omega) dA(\mathbf{x}_0). \quad (2.37)$$

This equation is similar to the later referred Fresnel-Kirchhoff diffraction formula (2.91). By introducing the source velocity under the assumption (2.30)

$$P(\mathbf{x}, \omega) = \oint_{\partial V} j \frac{\omega}{c} \varrho_0 c (\cos \varphi_s + \cos \varphi_r) V_{PS,n}(\mathbf{x}_0, \omega) G_{0,3D}(\mathbf{x}, \mathbf{x}_0, \omega) dA(\mathbf{x}_0), \quad (2.38)$$

(2.33) is recovered for a virtual point source

$$P(\mathbf{x}, \omega) = \oint_{\partial V} j \omega \varrho_0 (1 + \cos \varphi_r) V_{PS,n}(\mathbf{x}_0, \omega) G_{0,3D}(\mathbf{x}, \mathbf{x}_0, \omega) dA(\mathbf{x}_0) \quad (2.39)$$

if $\cos \varphi_s = 1$ holds.

(ii) *WFS as HF-BEM*: Inserting (2.22) and (2.24) into the SLP (2.35)

$$P(\mathbf{x}, \omega) = \oint_{\partial V} \left[\frac{1 + j \frac{\omega}{c} s}{s} \cos \varphi_s + j \frac{\omega}{c} \right] P_{\text{PS}}(\mathbf{x}_0, \omega) G_{0,3\text{D}}(\mathbf{x}, \mathbf{x}_0, \omega) dA(\mathbf{x}_0). \quad (2.40)$$

Again, assuming $\frac{\omega}{c} s \gg 1$ (2.25) yields

$$P(\mathbf{x}, \omega) = \oint_{\partial V} j \frac{\omega}{c} (1 + \cos \varphi_s) P_{\text{PS}}(\mathbf{x}_0, \omega) G_{0,3\text{D}}(\mathbf{x}, \mathbf{x}_0, \omega) dA(\mathbf{x}_0). \quad (2.41)$$

Only secondary sources on the surface A that can directly 'see' the point source should contribute to the integral in order to obtain a more accurate result [Her03]. This holds for $\cos \varphi_s > 0$. [Zot13] reformulated the required secondary source selection criterion of [Spo07a, (8, 12)], cf. (2.115) – in HF-BEM known as determining the visible elements [Her03] – to

$$1 + \cos \varphi_s \approx 2 \max\{\cos \varphi_s, 0\}. \quad (2.42)$$

The 3D WFS driving function is then with (2.22) and (2.23) given as

$$D(\mathbf{x}_0, \omega) = \begin{cases} 2j \frac{\omega}{c} \cos \varphi_s P_{\text{PS}}(\mathbf{x}_0, \omega) & \text{for } \cos \varphi_s > 0 \\ 0 & \text{else} \end{cases}. \quad (2.43)$$

This result is identical with (2.88), i.e. the Sommerfeld-Rayleigh diffraction under the Neumann Green' function boundary condition, which actually holds for planar secondary source distributions in its initial derivation. Here the assumption is made that a potentially curved surface is locally plane, cf. [Ahr12a, p.96].

HF-BEM for a Plane Wave

A similar HF-BEM based 3D WFS driving function can be derived for a virtual plane wave. Inserting (2.27) and (2.26) into (2.35) yields the SLP

$$P(\mathbf{x}, \omega) = \oint_{\partial V} j \frac{\omega}{c} (1 + \cos \varphi_p) P_{\text{PW}}(\mathbf{x}_0, \omega) G_{0,3\text{D}}(\mathbf{x}, \mathbf{x}_0, \omega) dA(\mathbf{x}_0), \quad (2.44)$$

and reveals the driving function

$$D(\mathbf{x}_0, \omega) = j \frac{\omega}{c} (1 + \cos \varphi_p) P_{\text{PW}}(\mathbf{x}_0, \omega). \quad (2.45)$$

The secondary source selection criterion is again formulated as

$$1 + \cos \varphi_p \approx 2 \max\{\cos \varphi_p, 0\}. \quad (2.46)$$

The 3D WFS driving function is then with (2.26), (2.28) given as

$$D(\mathbf{x}_0, \omega) = \begin{cases} 2j \frac{\omega}{c} \cos \varphi_p P_{\text{PW}}(\mathbf{x}_0, \omega) & \text{for } \cos \varphi_p > 0 \\ 0 & \text{else} \end{cases} \quad (2.47)$$

and thus equivalent to the later derived 3D Neumann Rayleigh integral driving function (2.148).

2.2.3 Rayleigh Diffraction Integrals

The HIE can be exactly simplified by imposing homogeneous boundary conditions on the Green's function to be fulfilled at \mathbf{x}_0 , i.e. the Neumann

$$\frac{\partial G_{\text{N}}(\mathbf{x}, \mathbf{x}_0, \omega)}{\partial n} = 0 \quad (2.48)$$

and Dirichlet boundary condition

$$G_{\text{D}}(\mathbf{x}, \mathbf{x}_0, \omega) = 0. \quad (2.49)$$

However, only for simple geometries these required Green's functions are analytically known, e.g. for planar, spherical [Wil99, Ch. 6.7.5] and cylindrical [Wil99, Ch. 4.5] shaped surfaces, yielding the Rayleigh and Rayleigh-like integrals. The Rayleigh integrals for planar and linear arrays are of importance here and deserve advanced summary. Their first textbook appearance is observed in [rBR96, p. 104 ff.].

By considering an infinite plane \mathcal{A}_∞ centered at the origin and a hemisphere \mathcal{C} with radius $r \rightarrow \infty$ to enclose the volume V and \mathbf{n} pointing into V , the HIE

consists of integration over two boundaries

$$\left[\iint_{\mathcal{A}_\infty} + \iint_{\mathcal{C}} \right] \left\{ -\frac{\partial P(\mathbf{x}_0, \omega)}{\partial n} G_{0,3D}(\mathbf{x}, \mathbf{x}_0, \omega) + \frac{\partial G_{0,3D}(\mathbf{x}, \mathbf{x}_0, \omega)}{\partial n} P(\mathbf{x}_0, \omega) \right\} dA = P(\mathbf{x}, \omega) \quad (2.50)$$

to describe the sound pressure within V . The integral over \mathcal{C} vanishes if the Sommerfeld radiation condition [Sku71, Ch. 23.2.3], [Wil99, (8.28)]

$$\lim_{|\mathbf{x}_0| \rightarrow \infty} |\mathbf{x}_0| \left(-\frac{\partial P(\mathbf{x}_0, \omega)}{\partial n} + j \frac{\omega}{c} P(\mathbf{x}_0, \omega) \right) = 0 \quad (2.51)$$

is fulfilled.

Implicit Derivation

For an infinite plane – here the yz -plane $\mathbf{x}_0 = (0, y_0, z_0)^T$ with $\mathbf{n} = (1, 0, 0)^T$ is considered without loss of generality – the homogeneous Neumann boundary condition (2.48) leads to the simplification of the HIE (2.15) with the image source method [Mor86, Ch. 7.4], [Wil99, Ch. 8.8.3]

$$P_{\text{NG},\infty}(\mathbf{x}, \omega) = \iint_{-\infty}^{+\infty} -\frac{\partial P(\mathbf{x}_0, \omega)}{\partial n} \underbrace{2 G_{0,3D}(\mathbf{x}, \mathbf{x}_0, \omega)}_{G_{\text{N}}(\mathbf{x}, \mathbf{x}_0, \omega)} dy_0 dz_0, \quad (2.52)$$

by requiring only the integration over \mathcal{A}_∞ and assuming that the Sommerfeld radiation condition is fulfilled. This implies that the considered V is the infinitely large hemisphere for $x > 0$, which is called target half-space $\mathbf{x} = (x > 0, y, z)^T$. As a consequence of the reduction, the other half-space cannot be controlled to $P(\mathbf{x}, \omega) = 0$ but rather is $P(-x, y, z, \omega) = P(+x, y, z, \omega)$ for the planar source [Bor06, Ch. 8.11.1]. For the here chosen geometry the normal derivative reduces to

$$\frac{\partial P(\mathbf{x}_0, \omega)}{\partial n} = \frac{\partial P(\mathbf{x}, \omega)}{\partial x} \Big|_{\mathbf{x}=\mathbf{x}_0} = \frac{\partial P(\mathbf{x}, \omega)}{\partial x} \Big|_{y=y_0, z=z_0}. \quad (2.53)$$

The homogeneous Dirichlet boundary condition (2.49) leads to the simpli-

fication of the HIE (2.15)

$$P_{\text{DG},\infty}(\mathbf{x}, \omega) = \iint_{-\infty}^{+\infty} \frac{\partial}{\partial n} \left[\underbrace{2 G_{0,3\text{D}}(\mathbf{x}, \mathbf{x}_0, \omega)}_{G_{\text{D}}(\mathbf{x}, \mathbf{x}_0, \omega)} \right] P(\mathbf{x}_0, \omega) dy_0 dz_0, \quad (2.54)$$

following the same assumptions. With $r = |\mathbf{x} - \mathbf{x}_0| = \sqrt{x^2 + (y - y_0)^2 + (z - z_0)^2}$ the normal derivative reduces to, cf. (2.18), (2.20)

$$\begin{aligned} \frac{\partial G_{0,3\text{D}}(\mathbf{x}, \mathbf{x}_0, \omega)}{\partial n} &= \frac{1}{r} \left(1 + j \frac{\omega}{c} r\right) \cos \varphi_r G_{0,3\text{D}}(\mathbf{x}, \mathbf{x}_0, \omega) = \\ \frac{\partial G_{0,3\text{D}}(\mathbf{x}, \mathbf{x}_0, \omega)}{\partial x_0} &= \frac{1}{r} \left(1 + j \frac{\omega}{c} r\right) \frac{x}{r} G_{0,3\text{D}}(\mathbf{x}, \mathbf{x}_0, \omega). \end{aligned} \quad (2.55)$$

The integrals are very well known as Rayleigh diffraction integrals, often referred to as first and second one, although this numbering differs in literature on optics and acoustics, cf. [Bor72, Goo05a, NV06] vs. [Vog93, Wil99]. It is recommended to state the deployed boundary condition explicitly, rather than referring to an inconsistent numbering.

It is worth realizing that this Rayleigh diffraction integrals provide a unique solution to the SFS problem in three dimensions for the imposed boundary conditions on the Green's function. No assumptions, other than the Sommerfeld radiation condition, have been made.

The initial derivation of 3D Wave Field Synthesis originated from the Dirichlet Rayleigh integral (2.54), cf. [Ber88, (7a)], [Ber92a, (1)] by taking (2.19), (2.20) into account, requiring a plane of dipole loudspeakers and using the pressure as the driving function for the secondary sources. Another formulation of 3D WFS originated from the Neumann Rayleigh integral (2.52), cf. [Vog93, Sta97, Ver97, Rab06, Spo08b] requiring a plane of monopole loudspeakers and using the pressure gradient as the driving function. Thus, WFS can be seen as an implicit solution of SFS. The latter 3D WFS approach is equivalent to the spatio-temporal spectrum representation of the Neumann Rayleigh integral, that leads to Spectral Division Method in three-dimensions as an explicit deconvolution solution for a planar SSD, cf. [Ahr10d, Sch14c]. Typically, analytic solutions for SFS in Cartesian coordinates are derived by the assumption of an infinite linear or planar SSD, cf. Ch. 2.3, Ch. 2.4.

Spatio-Temporal Spectrum Derivation

In the 1960s the connection between the Rayleigh integrals and their spatio-temporal Fourier spectrum representations due to the convolution/multiplication duality was observed [Wol64, She67a, She67b, Lal68b, Lal68a, Sch68], which is nowadays covered in textbooks [Wil99, Ch. 2.10], [NV06, Ch. 6.5], [Mö09, Ch. 13.5.4]. Without loss of generality, let's assume planes parallel to the yz -plane with $x > x_0$ and $\mathbf{x} = (x = \text{const}, y, z)^T$ and $\mathbf{x}_0 = (x_0 = \text{const}, y_0, z_0)^T$. Let's furthermore assume that the spatial Fourier transform of the pressure for the plane at x_0

$$P(x_0, k_y, k_z, \omega) = \iint_{-\infty}^{+\infty} P(x_0, y_0, z_0, \omega) e^{+j(k_y y_0 + k_z z_0)} dy_0 dz_0 \quad (2.56)$$

and the spatial Fourier transform of the normal velocity w.r.t. x -direction for the plane at x_0

$$V_n(x_0, k_y, k_z, \omega) = \iint_{-\infty}^{+\infty} V_n(x_0, y_0, z_0, \omega) e^{+j(k_y y_0 + k_z z_0)} dy_0 dz_0 \quad (2.57)$$

exist. The dispersion relation $(\frac{\omega}{c})^2 = k_x^2 + k_y^2 + k_z^2$ requires physical valid wave numbers for propagating and decaying evanescent waves by taking [NV06, Ch. 2.2], [Wil99, Ch. 2.6]

$$k_x = \begin{cases} +\sqrt{(\frac{\omega}{c})^2 - (k_y^2 + k_z^2)} & \text{for } (\frac{\omega}{c})^2 > (k_y^2 + k_z^2) \\ -j\sqrt{(k_y^2 + k_z^2) - (\frac{\omega}{c})^2} & \text{for } (k_y^2 + k_z^2) > (\frac{\omega}{c})^2 \end{cases} \quad (2.58)$$

into account.

Furthermore, the link of the 3D freefield Green's function (2.4) with its spatio-temporal spectrum – this expansion is well known as Weyl representation [DeS92, (2.9.10)] or Weyl integral [Lal68b, (B2)], [Wil99, (2.64)] – reads

$$G_{0,3D}(\mathbf{x}, \mathbf{x}_0, \omega) = \frac{1}{4\pi^2} \iint_{-\infty}^{+\infty} \frac{e^{-j k_x |x-x_0|}}{2j k_x} e^{+j(k_y y_0 + k_z z_0)} e^{-j(k_y y + k_z z)} dk_y dk_z. \quad (2.59)$$

The Rayleigh integrals are convolution integrals (here w.r.t. y and z)

$$P(\mathbf{x}, \omega) = f(x_0, y, z) *_y *_z h(x - x_0, y, z), \quad (2.60)$$

where $f(x_0, y_0, z_0)$ is defined as a function of the pressure or the pressure gradient on the plane at x_0 and $h(x - x_0, y, z)$ a wavefield propagator function that extrapolates towards the SFS sound pressure at the plane at x . It can be shown that the convolution/multiplication of the Fourier transform duality leads to

$$\begin{aligned} P(\mathbf{x}, \omega) &= \iint_{-\infty}^{+\infty} f(x_0, y_0, z_0) h(x - x_0, y - y_0, z - z_0) dy_0 dz_0 \quad (2.61) \\ &= \underbrace{\mathcal{F}_y^{-1} \mathcal{F}_z^{-1} \{j \varrho_0 \omega V_n(x_0, k_y, k_z, \omega)\}}_{f(x_0, y, z)} *_y *_z \underbrace{\mathcal{F}_y^{-1} \mathcal{F}_z^{-1} \left\{ \frac{e^{-j k_x (x - x_0)}}{j k_x} \right\}}_{h(x - x_0, y, z)}, \end{aligned}$$

$$P(x, k_y, k_z, \omega) = [j \varrho_0 \omega V_n(x_0, k_y, k_z, \omega)] \cdot \left[2 \frac{e^{-j k_x (x - x_0)}}{2 j k_x} \right] \quad (2.62)$$

for extrapolation of the pressure gradient function

$$f(x_0, y_0, z_0) = - \left. \frac{P(\mathbf{x}, \omega)}{\partial x} \right|_{\mathbf{x}=\mathbf{x}_0}, \quad (2.63)$$

that is linked to the normal velocity by the Euler equation (2.31). Comparing the spatio-temporal spectrum of $h(x - x_0, y, z)$ – or rather $h(x - x_0, y - y_0, z - z_0)$ using the shift theorem – with (2.59) yields

$$h(x - x_0, y - y_0, z - z_0) = 2 G_{0,3D}(\mathbf{x}, \mathbf{x}_0, \omega), \quad (2.64)$$

revealing the equivalence with the Neumann Rayleigh integral (2.52) for the chosen geometry. Eq. (2.62) can also be given as

$$P(x, k_y, k_z, \omega) = V_n(x_0, k_y, k_z, \omega) \cdot \left[j \varrho_0 \omega \frac{e^{-j k_x (x - x_0)}}{j k_x} \right], \quad (2.65)$$

for which [Mö09, (13.96)], [Wil99, (2.70)]

$$h_v(x - x_0, y, z) = \mathcal{F}_y^{-1} \mathcal{F}_z^{-1} \left\{ j \varrho_0 \omega \frac{e^{-j k_x (x - x_0)}}{j k_x} \right\} \quad (2.66)$$

maybe be termed the *velocity based forward wavefield propagator* function, i.e. [Mö09, (13.100)], [Wil99, (2.74)]

$$h_v(x - x_0, y - y_0, z - z_0) = 2j \varrho_0 \omega G_{0,3D}(\mathbf{x}, \mathbf{x}_0, \omega) \quad (2.67)$$

that extrapolates the normal velocity of the plane at x_0

$$f(x_0, y_0, z_0) = V_n(\mathbf{x}_0, \omega) \quad (2.68)$$

to the pressure $P(\mathbf{x}, \omega)$ at a plane $x > x_0$. Hence, the Neumann Rayleigh integral (2.52) is written as

$$P_{\text{NG},\infty}(\mathbf{x}, \omega) = \iint_{-\infty}^{+\infty} +2j \varrho_0 \omega V_n(\mathbf{x}_0, \omega) G_{0,3D}(\mathbf{x}, \mathbf{x}_0, \omega) dy_0 dz_0. \quad (2.69)$$

With the convolution/multiplication duality of the Fourier transform

$$P(\mathbf{x}, \omega) = \iint_{-\infty}^{+\infty} f(x_0, y_0, z_0) h_p(x - x_0, y - y_0, z - z_0) dy_0 dz_0 \quad (2.70)$$

$$= \underbrace{\mathcal{F}_y^{-1} \mathcal{F}_z^{-1} \{P(x_0, k_y, k_z, \omega)\}}_{f(x_0, y, z)} *_{y,z} \underbrace{\mathcal{F}_y^{-1} \mathcal{F}_z^{-1} \{e^{-j k_x (x - x_0)}\}}_{h_p(x - x_0, y, z)},$$

$$P(x, k_y, k_z, \omega) = [P(x_0, k_y, k_z, \omega)] \cdot [e^{-j k_x (x - x_0)}] \quad (2.71)$$

the *pressure based forward wavefield propagator* can be extracted to

$$h_p(x - x_0, y - y_0, z - z_0) = 2 \frac{\partial G_{0,3D}(\mathbf{x}, \mathbf{x}_0, \omega)}{\partial x_0} \quad (2.72)$$

for the pressure function $f(x_0, y_0, z_0) = P(\mathbf{x}_0, \omega)$, revealing the identity with the Dirichlet Rayleigh integral (2.54).

Fourier-NAH / Inverse Diffraction

Eq. (2.71), (2.62) and (2.65) constitute the basis for so called Planar Fourier Transform-Based Near-Field Acoustical Holography (Fourier-NAH) [Ste82], [Wil99, Ch. 3], [Wu08], [Bai13b, Ch. 5], also known as inverse diffraction in optics [NV06, Ch. 9]. It aims at solving the inverse problem, i.e. performing a deconvolution. Still considering $x > x_0$ and a half-space problem (imposing the Neumann or Dirichlet boundary condition on the wavefield propagator), (i) either the pressure of the (measurement) plane at x towards the pressure on the plane at x_0 can be extrapolated with the *pressure based inverse wavefield propagator*

$$P(x_0, k_y, k_z, \omega) = P(x, k_y, k_z, \omega) \cdot e^{+j k_x (x-x_0)}, \quad (2.73)$$

(ii) or the pressure of the (measurement) plane at x towards the normal velocity on the plane at x_0 can be extrapolated by (cf. (2.62), (2.65))

$$j \varrho_0 \omega V_n(x_0, k_y, k_z, \omega) = P(x, k_y, k_z, \omega) \cdot j k_x e^{+j k_x (x-x_0)} \quad (2.74)$$

$$V_n(x_0, k_y, k_z, \omega) = P(x, k_y, k_z, \omega) \cdot \frac{j k_x e^{+j k_x (x-x_0)}}{j \varrho_0 \omega}, \quad (2.75)$$

referring (2.75) to as the *velocity based inverse wavefield propagator*. Hence, for infinite planes or finite planar sources that are ideally baffled

$$P(\mathbf{x}_0) = \mathcal{F}_y^{-1} \mathcal{F}_z^{-1} \left\{ \mathcal{F}_y \mathcal{F}_z \{P(\mathbf{x}, \omega)\} \cdot e^{+j k_x (x-x_0)} \right\} \quad (2.76)$$

$$V_n(\mathbf{x}_0) = \mathcal{F}_y^{-1} \mathcal{F}_z^{-1} \left\{ \mathcal{F}_y \mathcal{F}_z \{P(\mathbf{x}, \omega)\} \cdot \frac{k_x}{\varrho_0 \omega} e^{+j k_x (x-x_0)} \right\} \quad (2.77)$$

constitute the fundamentals of planar NAH [Wu08, Table I].

The initial derivation of the so called Spectral Division Method (SDM) [Ahr08c, Ahr10d] as an SFS deconvolution solution for planar and linear loud-speaker arrays is performed without any boundary condition imposed on the Green's function, therefore deploying the single layer potential

$$P(\mathbf{x}, \omega) = \iint_{-\infty}^{+\infty} D(\mathbf{x}_0, \omega) G_{0,3D}(\mathbf{x}, \mathbf{x}_0, \omega) dy_0 dz_0. \quad (2.78)$$

In terms of a planar NAH-like notation follows the deconvolution, i.e. the inverse problem solution for the driving function (cf. (2.59))

$$D(\mathbf{x}_0) = \mathcal{F}_y^{-1} \mathcal{F}_z^{-1} \{ \mathcal{F}_y \mathcal{F}_z \{ P(\mathbf{x}, \omega) \} \cdot 2j k_x e^{+j k_x (x-x_0)} \} \quad (2.79)$$

with $D(\mathbf{x}_0) = \mathcal{F}_y^{-1} \mathcal{F}_z^{-1} \{ D(x_0, k_y, k_z) \}$ by observing from (2.74)

$$\underbrace{2j \varrho_0 \omega V_n(x_0, k_y, k_z, \omega)}_{D(x_0, k_y, k_z)} = P(x, k_y, k_z, \omega) \cdot 2j k_x e^{+j k_x (x-x_0)}. \quad (2.80)$$

This proves the identity of 3D SDM as an explicit SFS solution and 3D WFS with the Neumann Rayleigh integral as an implicit SFS solution. For model based wave types (for which propagating and evanescent 'modes' could be extrapolated analytically exact) and an infinite SSD plane, the spatio-temporal spectrum of the pressure at plane $x > x_0$ can be used to find the explicit solution for the driving function's spatio-temporal spectrum [Sch14c, (50)]

$$D(x_0, k_y, k_z) = \underbrace{\check{P}(k_y, k_z, \omega) e^{-j k_x x}}_{P(x, k_y, k_z, \omega)} \cdot 2j k_x e^{+j k_x (x-x_0)} \quad (2.81)$$

$$= \check{P}(k_y, k_z, \omega) \cdot 2j k_x e^{-j k_x x_0}, \quad (2.82)$$

with $\check{P}(k_y, k_z, \omega)$ denoting the so called angular spectrum [Ahr12a, Ch. 2.2.7]. Note, that this is identical with the proposed approach termed wave field reconstruction (WFR) [Koy13, Ch. 5]. It is very important realizing that Fourier-NAH (such as for planar, cylindrical and spherical geometries) is based on the Rayleigh/Rayleigh-like integrals. Since the Neumann and Dirichlet Green's functions for planar problems are trivially connected to the freefield Green's function by factor 2 the deconvolution of the SLP, i.e. SDM can only be connected to a Fourier-NAH-like approach for planar (and linear) geometries. The deconvolution of the SLP for SFS with a spherical/cylindrical geometry differs from their Fourier-NAH counterparts. However, the link for solving the inverse problem in spherical coordinates was given in [Faz10b] and termed Near-Field Acoustical Holography.

2.2.4 Rayleigh-Sommerfeld Diffraction Integrals

The Rayleigh integrals are only valid for an infinite plane, however then they are an exact solution of the Helmholtz equation (2.12) in the half-space $x > x_0$ [Pri04]. In optics the wave radiation through a finite, non-reflecting aperture \mathcal{A} enclosed by an opaque screen \mathcal{B} is a well formulated problem, that also can be deployed to acoustic problems. The opaque screen \mathcal{B} is then interpreted either as a sound-hard/rigid or as a sound-soft boundary surface and the aperture \mathcal{A} constitutes the secondary source distribution using either monopoles or dipoles.

The HIE must now be evaluated for three surfaces, i.e. the planar aperture \mathcal{A} , the planar opaque screen, i.e. the non-illuminated side of the screen \mathcal{B}^+ and the semi-sphere \mathcal{C}

$$\left[\iint_{\mathcal{A}} + \iint_{\mathcal{B}^+} + \iint_{\mathcal{C}} \right] \left\{ -\frac{\partial P(\mathbf{x}_0, \omega)}{\partial n} G_{0,3D}(\mathbf{x}, \mathbf{x}_0, \omega) + \frac{\partial G_{0,3D}(\mathbf{x}, \mathbf{x}_0, \omega)}{\partial n} P(\mathbf{x}_0, \omega) \right\} dA = P(\mathbf{x}, \omega) \quad (2.83)$$

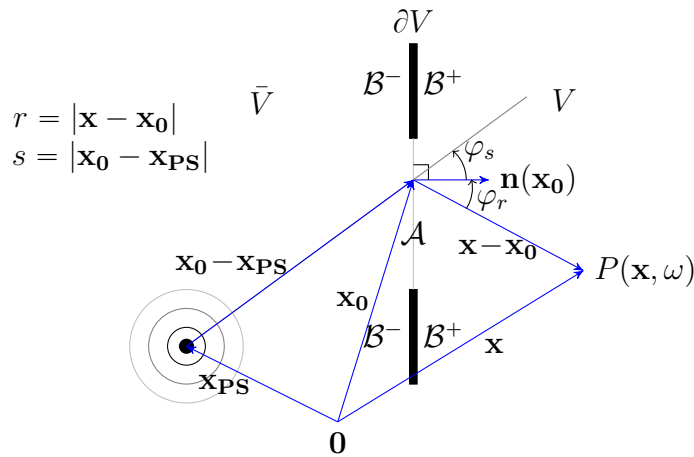


Figure 2.2: Geometry for the Rayleigh-Sommerfeld and the Fresnel-Kirchhoff diffraction using a point source at \mathbf{x}_{PS} that illuminates an aperture \mathcal{A} in an otherwise infinite opaque screen \mathcal{B} . The region \mathcal{B}^+ is assumed to be dark in the evaluation volume V .

to describe the sound pressure within V . The initial Kirchhoff boundary conditions [Bor06, (8.3.15)], [Som54, p.198], [Goo05a, p.44]

$$\begin{aligned} \text{on } \mathcal{A} : P(\mathbf{x}_0, \omega) &= P(\mathbf{x}, \omega) ; & \frac{\partial P(\mathbf{x}_0, \omega)}{\partial n} &= \frac{\partial P(\mathbf{x}, \omega)}{\partial n} \\ \text{on } \mathcal{B}^+ : P(\mathbf{x}_0, \omega) &= 0 ; & \frac{\partial P(\mathbf{x}_0, \omega)}{\partial n} &= 0 \end{aligned} \quad (2.84)$$

and the Sommerfeld radiation condition (2.51) reduce the integration over the finite aperture \mathcal{A} , cf. Fig. 2.2 for a sketch of the geometry under discussion.

The Kirchhoff boundary conditions were initially established by Kirchhoff in order to simplify the HIE for arbitrarily shaped surfaces. It is assumed that the sound field $P(\mathbf{x}_0, \omega)$ and its normal derivative within the aperture is the same either with or without the opaque screen around it. Secondly, it is assumed that – in terms of acoustics – the pressure and the velocity are zero in the vicinity of the dark side \mathcal{B}^+ . Obviously, these conditions do not represent the physical reality in general. For the case of a planar screen, however only two of the Kirchhoff boundary conditions have to be fulfilled, since the Neumann or Dirichlet boundary condition imposed on the Green's function already hold with physical validity. Thus, only the boundary condition imposed on $\frac{\partial P(\mathbf{x}_0)}{\partial n}$ is required to simplify (2.52) to

$$P_{\text{NG},\mathcal{A}}(\mathbf{x}, \omega) = \iint_{\mathcal{A}} - \frac{\partial P(\mathbf{x}_0, \omega)}{\partial n} [2 G_{0,3\text{D}}(\mathbf{x}, \mathbf{x}_0, \omega)] dy_0 dz_0, \quad (2.85)$$

taking no assumptions on $P(\mathbf{x}_0, \omega)$. In contrast, only the boundary condition on $P(\mathbf{x}_0, \omega)$ is required to reformulate (2.54) to

$$P_{\text{DG},\mathcal{A}}(\mathbf{x}, \omega) = \iint_{\mathcal{A}} +P(\mathbf{x}_0, \omega) \left[2 \frac{\partial G_{0,3\text{D}}(\mathbf{x}, \mathbf{x}_0, \omega)}{\partial n} \right] dy_0 dz_0, \quad (2.86)$$

taking no assumptions on $\frac{\partial P(\mathbf{x}_0)}{\partial n}$. These integrals are referred to as the Rayleigh-Sommerfeld diffraction integrals [Bor06, Ch. 8.11.2]. They hold only if (i) the boundary surface/opaque screen is of infinite dimension, modeling a rigid infinite baffle \mathcal{B} for (2.85) and a sound-soft infinite baffle \mathcal{B} for (2.86), respectively. For practical reasons of finite sized baffles acting in otherwise free field conditions the following requirements must hold to approximately match the real

occurring diffraction: (i) the aperture dimension \mathcal{A} is much larger than the considered radiated wave length λ , and (ii) the wave length is much smaller than the evaluation distance $r = |\mathbf{x} - \mathbf{x}_0|$.

The integrals are frequently used in SFS for modeling planar, linear and rectangular and circular secondary source distributions of finite extent, although analytic driving functions are derived for infinite linear and planar secondary source distributions. Thus, for low audio frequencies and comparable small apertures acting in free-field conditions, SFS will not be correct, since the diffraction effects are not compensated for.

The Rayleigh-Sommerfeld integrals are typically given in more detail for screen diffraction of a spherical monopole source. Reconsidering the approaches from HF-BEM Ch. 2.2.2 by using (2.4), (2.22) and their respective farfield/high-frequency approximations of the normal derivative (2.19), (2.25), on the one hand yields the Neumann Rayleigh-Sommerfeld diffraction integral [NV06, (6.43)], [Goo05a, (3.44)]

$$\begin{aligned} P_{\text{NG},\mathcal{A},\text{Monopole}}(\mathbf{x}, \omega) &= \iint_{\mathcal{A}} \left[\frac{j}{\lambda} \cos \varphi_s P_{\text{PS}}(\mathbf{x}_0, \omega) \right] \frac{e^{-j \frac{\omega}{c} r}}{r} dy_0 dz_0 & (2.87) \\ &= \iint_{\mathcal{A}} \left[2j \frac{\omega}{c} \cos \varphi_s P_{\text{PS}}(\mathbf{x}_0, \omega) \right] G_{0,3\text{D}}(\mathbf{x}, \mathbf{x}_0, \omega) dy_0 dz_0 \end{aligned}$$

according to the assumed validity conditions above. The term within the brackets of (2.88) is recognized as the far-field/high frequency approximated driving function for 3D Neumann-WFS of a virtual spherical monopole [Zot13] as discussed above in Ch. 2.2.2, cf. (2.43). Inserting (2.19) into (2.86) on the other hand yields the Dirichlet Rayleigh-Sommerfeld diffraction integral [NV06, (6.42)], [Goo05a, (3.43)]

$$\begin{aligned} P_{\text{DG},\mathcal{A},\text{Monopole}}(\mathbf{x}, \omega) &= \iint_{\mathcal{A}} \left[\frac{j}{\lambda} P_{\text{PS}}(\mathbf{x}_0, \omega) \right] \cos \varphi_r \frac{e^{-j \frac{\omega}{c} r}}{r} dy_0 dz_0 & (2.88) \\ &= \iint_{\mathcal{A}} \left[2j \frac{\omega}{c} P_{\text{PS}}(\mathbf{x}_0, \omega) \right] \cos \varphi_r G_{0,3\text{D}}(\mathbf{x}, \mathbf{x}_0, \omega) dy_0 dz_0. \end{aligned}$$

This is identical with the initial 3D Dirichlet-WFS formulation [Ber92a, (2b)], [Ber92b, (2b)], that actually requires secondary dipole sources.

2.2.5 Fresnel-Kirchhoff Diffraction Integral

For a planar screen the Rayleigh-Sommerfeld diffraction is less demanding w.r.t. the boundary conditions than the Fresnel-Kirchhoff diffraction, that considers an arbitrarily shaped aperture \mathcal{A} of finite extent. Equations (2.83), (2.84), (2.51) and $\mathbf{x} \in V$ yield the integral

$$P_{\text{FK}}(\mathbf{x}, \omega) = \iint_{\mathcal{A}} \left[-\frac{\partial P(\mathbf{x}_0, \omega)}{\partial n} G_{0,3\text{D}}(\mathbf{x}, \mathbf{x}_0, \omega) + \frac{\partial G_{0,3\text{D}}(\mathbf{x}, \mathbf{x}_0, \omega)}{\partial n} P(\mathbf{x}_0, \omega) \right] dA(\mathbf{x}_0). \quad (2.89)$$

In this case the evaluated sound field $P_{\text{FK}}(\mathbf{x}, \omega)$ is only correct if all Kirchhoff boundary conditions (2.84) are fulfilled. They are approximately fulfilled if the aperture dimension is much larger than the considered wave length λ , and if the wave length is much smaller than the evaluation distance $r = |\mathbf{x} - \mathbf{x}_0|$ as well as the point source distance $s = |\mathbf{x}_0 - \mathbf{x}_{\text{PS}}|$. It is well known that the general Fresnel-Kirchhoff diffraction equation (2.89) is the arithmetic average of both Rayleigh-Sommerfeld diffraction equations (2.85), (2.86), cf. [Wol64], [Bor06, (8.11.23)], [NV06, (6.22)] for point source diffraction

$$P_{\text{FK}}(\mathbf{x}, \omega) = \frac{P_{\text{NG},\mathcal{A}}(\mathbf{x}, \omega) + P_{\text{DG},\mathcal{A}}(\mathbf{x}, \omega)}{2}. \quad (2.90)$$

Again inserting the point source field (2.22) and the Green's function (2.4) and their respective farfield/high-frequency approximations of the normal derivative (2.25) and (2.19) into (2.89) yields the Fresnel-Kirchhoff diffraction integral of a point source [Bak50, (Ch.2, 1.34)], [Bor06, (8.3.17)], [Goo05a, (3-27)], [NV06, (6.41)]

$$\begin{aligned} P_{\text{FK,Monopole}}(\mathbf{x}, \omega) &= \iint_{\mathcal{A}} \left[\frac{j}{\lambda} \frac{\cos \varphi_s + \cos \varphi_r}{2} P_{\text{PS}}(\mathbf{x}_0, \omega) \right] \frac{e^{-j\frac{\omega}{c}r}}{r} dA(\mathbf{x}_0), \\ P_{\text{FK,Monopole}}(\mathbf{x}, \omega) &= \iint_{\mathcal{A}} \left[j \frac{\omega}{c} (\cos \varphi_s + \cos \varphi_r) P_{\text{PS}}(\mathbf{x}_0, \omega) \right] G_{0,3\text{D}}(\mathbf{x}, \mathbf{x}_0, \omega) dA(\mathbf{x}_0), \end{aligned} \quad (2.91)$$

which is identical to HF-BEM as already discussed in Ch. 2.2.2. It is worth noting, that the Fresnel-Kirchhoff-Diffraction and the Rayleigh-Sommerfeld

diffraction equations predict about the same diffracted sound field

$$P_{\text{FK,Monopole}}(\mathbf{x}, \omega) \approx P_{\text{NG,A,Monopole}}(\mathbf{x}, \omega) \approx P_{\text{DG,A,Monopole}}(\mathbf{x}, \omega) \quad (2.92)$$

for the case of $\cos \varphi_s \approx 1$ (small angles of source incidence, i.e. a point source far away from ∂V) and $\cos \varphi_r \approx 1$ (small evaluation angle), cf. [Wol64], [Bor06, Ch. 8.11.2]. This explains the similarity of differently derived WFS approaches (Neumann [Sta97, Ch. 3.1] vs. Dirichlet [Sta97, Ch. 3.2]), when considering the farfield/high-frequency approximation both for the virtual source position as well as for the evaluation position.

2.2.6 Fresnel and Fraunhofer Approximation

The Fresnel and Fraunhofer approximations are useful simplifications of the diffraction integrals to obtain an analytic description of the diffraction effects of baffled sources in different evaluation regions, referred to as the Fresnel and the Fraunhofer region in front of apertures.

Due to its importance for SFS and radiation synthesis of linear arrays, the Neumann Rayleigh-Sommerfeld integral is discussed for the different approximations, cf. [Dub99, Pri04, Mas07], [Mö09, Ch. 3.5], [NV06, Ch. 6.7ff], [Goo05a, Ch. 4.2ff]. Let's define a vector set

$$\mathbf{x}' = (y, z)^T, \mathbf{x} = (x, \mathbf{x}')^T, \mathbf{x}'_0 = (y_0, z_0)^T, \mathbf{x}_0 = (x_0, \mathbf{x}'_0)^T, \mathbf{r} = (x - x_0, \mathbf{x}' - \mathbf{x}'_0)^T \quad (2.93)$$

for which $x_0 = 0$ is chosen according to the preceding sections. With

$$r = |\mathbf{x} - \mathbf{x}_0| = \sqrt{x^2 + (y - y_0)^2 + (z - z_0)^2}, \quad (2.94)$$

$$R = |\mathbf{x} - \mathbf{0}| = \sqrt{x^2 + y^2 + z^2}, \quad (2.95)$$

the Neumann Rayleigh-Sommerfeld diffraction integral (2.85) is written as

$$P_{\text{NG,A}}(\mathbf{x}, \omega) = \iint_{\mathcal{A}} -\frac{\partial P(\mathbf{x}_0, \omega)}{\partial n} \frac{e^{-j\frac{\omega}{c}r}}{2\pi r} dy_0 dz_0. \quad (2.96)$$

In literature typically the Taylor series of (2.94) is given as

$$r = |\mathbf{x} - \mathbf{x}_0| \approx R - \frac{\langle \mathbf{x}', \mathbf{x}'_0 \rangle}{R} + \frac{|\mathbf{x}'_0|^2}{2R} + \dots, \quad (2.97)$$

which however ignores the fact that for $\mathbf{x} - \mathbf{x}_0$ actually a multi-dimensional variable Taylor series must be given. Applying (2.97) in the exponential function of (2.96) and replacing $r = |\mathbf{x} - \mathbf{x}_0|$ with R in the denominator *ibid.* yields a Fresnel approximation known in literature [NV06, (6.52)], [Mas07, (5)]

$$P_{\text{Fresnel,NG,A}}(\mathbf{x}, \omega) = \frac{e^{-j\frac{\omega}{c}R}}{2\pi R} \iint_{\mathcal{A}} -\frac{\partial P(\mathbf{x}_0, \omega)}{\partial n} e^{-j\frac{\omega}{c}[\frac{|\mathbf{x}'_0|^2}{2R} - \frac{\langle \mathbf{x}', \mathbf{x}'_0 \rangle}{R}]} dy_0 dz_0, \quad (2.98)$$

which is valid if

$$\frac{\omega}{c} \frac{(|\mathbf{x}'_0|^2 - 2\langle \mathbf{x}', \mathbf{x}'_0 \rangle)^2}{8R^3} \ll 1. \quad (2.99)$$

This Fresnel approximation (2.98) represents the case of a diffracted spherically spreading wave, cf. [Mas07, (5)].

Another possible Fresnel approximation is derived when a further Taylor series

$$R = \sqrt{x^2 + y^2 + z^2} = x \sqrt{1 + \frac{y^2 + z^2}{x^2}} \approx x \left(1 + \frac{y^2 + z^2}{2x^2}\right) \quad (2.100)$$

is applied, assuming that $x^2 \gg y^2 + z^2$, i.e. assuming small evaluation angles. The integral then takes the form [NV06, (6.56)], cf. [Goo05a, (4-14)], [Pri04, (4)]

$$P_{\text{Fresnel,NG,A}}(\mathbf{x}, \omega) = \frac{e^{-j\frac{\omega}{c}x}}{4\pi x} \iint_{\mathcal{A}} -2 \frac{\partial P(\mathbf{x}_0, \omega)}{\partial n} e^{-j\frac{\omega}{c} \frac{|\mathbf{x}' - \mathbf{x}'_0|^2}{2x}} dy_0 dz_0, \quad (2.101)$$

which is valid if

$$\frac{\omega}{c} \frac{|\mathbf{x}' - \mathbf{x}'_0|^4}{8x^3} \ll 1 \quad \leftrightarrow \quad \frac{\pi}{4\lambda} [(y - y_0)^2 + (z - z_0)^2]^2 \ll x^3. \quad (2.102)$$

This Fresnel approximation (2.101) represents the case of a diffracted plane wave, cf. [Mas07, (4)]. This case becomes useful when evaluating the on-axis diffraction of uniformly driven pistons or line arrays, as discussed for the

circular and line piston in Ch. 3 and App. D.

If only the first order terms are considered in the Taylor series (2.97)

$$r = |\mathbf{x} - \mathbf{x}_0| \approx R - \frac{\langle \mathbf{x}', \mathbf{x}'_0 \rangle}{R} + \dots, \quad (2.103)$$

(2.96) takes the form of the Fraunhofer approximation

$$P_{\text{Fraunhofer,NG,A}}(\mathbf{x}, \omega) = \frac{e^{-j\frac{\omega}{c}R}}{4\pi R} \iint_{\mathcal{A}} -2 \frac{\partial P(\mathbf{x}_0, \omega)}{\partial n} e^{+j\frac{\omega}{c} \frac{\langle \mathbf{x}', \mathbf{x}'_0 \rangle}{R}} dy_0 dz_0, \quad (2.104)$$

which is valid if

$$\frac{\omega}{c} \frac{|\mathbf{x}'_0|^2}{2R} \ll 1. \quad (2.105)$$

For a linear array on y -axis with length L and an allowed maximum phase error of $\frac{\pi}{4}$

$$\frac{\omega}{c} \frac{|\mathbf{x}'_{0\text{max}}|^2}{2R} < \frac{\pi}{4} \rightarrow \frac{2\pi}{\lambda} \frac{(L/2)^2}{2R} < \frac{\pi}{4} \rightarrow \frac{R}{L} \gg \frac{L}{\lambda} \quad (2.106)$$

yields one well known farfield condition [Mö09, Ch. 3.6], besides $R \gg \lambda$ and $R \gg L$ that originate from the Rayleigh-Sommerfeld diffraction's conditions.

A very important and fundamental property of the Fraunhofer region is revealed when casting

$$\frac{y}{R} = \sin \varphi \sin \vartheta \rightarrow \frac{\omega}{c} \sin \varphi \sin \vartheta = k_y \quad (2.107)$$

$$\frac{z}{R} = \cos \vartheta \rightarrow \frac{\omega}{c} \cos \vartheta = k_z \quad (2.108)$$

to the real valued wave numbers k_y and k_z (i.e. propagating waves) using

$$\mathbf{x} = (x, y, z)^T = R \cdot (\cos \varphi \sin \vartheta, \sin \varphi \sin \vartheta, \cos \vartheta)^T \quad (2.109)$$

and $-\frac{\pi}{2} \leq \varphi \leq +\frac{\pi}{2}$, $0 \leq \vartheta \leq \pi$.

With (2.31) the Fraunhofer approximation (2.104) then can be rewritten as

$$P_{\text{Fraunhofer,NG},\mathcal{A}}(\mathbf{x}, \omega) = j \varrho_0 \omega \frac{e^{-j\frac{\omega}{c}R}}{2\pi R} \iint_{\mathcal{A}} V_n(\mathbf{x}_0, \omega) e^{+jk_y y_0 + jk_z z_0} dy_0 dz_0, \quad (2.110)$$

using the normal velocity of the source located in \mathcal{A} . If the source is rigidly baffled, the normal velocity on \mathcal{B}^+ is zero and the integration range can be formulated more generally to [Hec77]

$$P_{\text{Fraunhofer,NG},\mathcal{A}}(\mathbf{x}, \omega) = j \varrho_0 \omega \frac{e^{-j\frac{\omega}{c}R}}{2\pi R} \iint_{-\infty}^{+\infty} V_n(\mathbf{x}_0, \omega) e^{+jk_y y_0 + jk_z z_0} dy_0 dz_0. \quad (2.111)$$

The integral resembles a spatial Fourier transform. Thus, the spatio-temporal spectrum $V_n(k_y, k_z, \omega)$ of the normal source velocity evaluated for $k_y^2 + k_z^2 < (\frac{\omega}{c})^2$, i.e. only for propagating wave radiation yields the frequency dependent farfield radiation pattern $V_n(\varphi, \vartheta, \omega)$ of the source w.r.t. the radiating angles φ, ϑ . This well understood fact becomes very important for describing sound fields radiated by LSAs later on in this thesis, cf. pg. 95.

Henceforth, the temporal spectrum $D(\mathbf{x}_0, \omega)$ of the secondary source excitation signal, typically termed driving function in SFS is considered to be proportional to the normal velocity as

$$D(\mathbf{x}_0, \omega) \propto j \varrho_0 \omega V_n(\mathbf{x}_0, \omega). \quad (2.112)$$

2.2.7 Single Layer Potential

To approach SFS with the SLP, different approaches exist to derive the unknown driving function analytically for simple model based wave types.

The so called explicit solution can be found by means of mode matching (i.e. the deconvolution performed as a division in an appropriate orthogonal/orthonormal function space) [Faz10a, Ahr12a, Sch14c], for which SDM and Nearfield Compensated Higher Order Ambisonics (NFC-HOA) are well known concepts for planar, linear and spherical, circular SSDs, respectively.

The implicit solution can be derived by diffraction theory, which initially was performed for planar and linear arrays deploying the Rayleigh integrals.

The initial derivation of WFS as the implicit solution is based on the Rayleigh integral under Dirichlet boundary condition imposed on the Green's function (2.54) for the synthesis of a virtual spherical monopole source by a planar and linear SSD consisting of spherical dipoles [Ber88, Ber92b, Ber92a]. [Ber93] –as a summary of [Ber92b, Ber92a] – additionally gives a detailed treatment on the stationary phase approximation (SPA) for the reduction of the 3D Rayleigh integral towards 2.5D for usage of a linear array that consists of dipoles. These approaches are based on the Dirichlet Rayleigh integral (2.54), thus the approach should be termed Dirichlet-WFS here.

In [Vog93, dV94a] the synthesis operator, i.e. the driving function is adapted to work with a linear array that consists of monopoles. Later on [dV96] derives driving functions that compensate for the farfield directivity of the used loudspeakers. The derivation of WFS using the SPA from the 3D (2.52) towards the 2.5D Neumann Rayleigh operator for a virtual point source was further formalized in [Sta96, Sta97, Ver97] and became embedded into an acoustic signal processing framework. These approaches – sometimes referred to as *traditional WFS theory* and here termed Neumann-WFS – consider linear SSDs built from ideal point sources and ensure amplitude correct synthesis along a reference line parallel to the SSD.

In case of a (i) planar or (ii) linear SSD the SLP is direct proportional to the Neumann (i) 3D or (ii) 2.5D Rayleigh integral. For the 3D case SDM and Neumann-WFS are identical [Sch14c]. For the 2.5D case SDM constitutes the exact SFS solution, whereas WFS is a high-frequency/farfield approximated SDM solution [Spo10].

For closed SSDs, in practice very often circular or rectangular shapes, the Neumann Rayleigh-Sommerfeld diffraction is deployed with a secondary source selection criterion by activating only the visible elements, cf. HF-BEM in Ch. 2.2.2. This is realized with an additional spatial window applied to the driving function as

$$w(\mathbf{x}_0) \cdot D(\mathbf{x}_0, \omega) \rightarrow D(\mathbf{x}_0, \omega). \quad (2.113)$$

For a plane wave this window may be defined as [Spo08b, (13)]

$$w(\mathbf{x}_0) = \begin{cases} 1 & \text{if } \cos \varphi_p = \langle \mathbf{n}_{\mathbf{P}\mathbf{W}}, \mathbf{n}(\mathbf{x}_0) \rangle > 0 \quad (2.28) \\ 0 & \text{else} \end{cases}, \quad (2.114)$$

and for point sources as [Spo07a, (8&12)]

$$w(\mathbf{x}_0) = \begin{cases} 1 & \text{if } \cos \varphi_s = \frac{\langle \mathbf{x}_0 - \mathbf{x}_{\mathbf{P}\mathbf{S}}, \mathbf{n}(\mathbf{x}_0) \rangle}{|\mathbf{x}_0 - \mathbf{x}_{\mathbf{P}\mathbf{S}}|} > 0 \quad (2.23) \\ 0 & \text{else} \end{cases}. \quad (2.115)$$

The following subsections give a review on SDM and Neumann-WFS for the SFS of a spherical and plane wave. The SDM solutions are only valid for planar and linear SSDs, whereas all WFS solutions given in general vector notation can be used for convex shaped SSDs. When referring to as correct SFS in the following, it is assumed that (i) the aperture is much larger than the considered wave length in order that the diffraction model holds and (ii) the assumptions that lead to the different farfield/high-frequency approximations hold as well as (iii) no spatial aliasing occurs.

Since planar and spherical SSDs are expensively to be realized, many SFS approaches use loudspeakers along a line contour (mostly linear, rectangular and circular) that are setup in the horizontal plane at height of the listener's ears. The following sections consistently consider the following geometry setups:

- planar SSD yz -plane $\mathbf{x}_0 = (0, y_0, z_0)^T$, 3D SFS half space $\mathbf{x} = (x > 0, y, z)^T$, $\mathbf{n} = (1, 0, 0)^T$, Neumann Rayleigh
- linear SSD y -axis $\mathbf{x}_0 = (0, y_0, 0)^T$, 2.5D SFS half plane $\mathbf{x} = (x > 0, y, 0)^T$, $\mathbf{n} = (1, 0, 0)^T$, Neumann Rayleigh
- spherical SSD centered around origin with $\mathbf{x}_0 = (x_0, y_0, z_0)^T$, radius $r_0 = |\mathbf{x}_0| = \text{const}$, 3D SFS space $\mathbf{x} = (x, y, z)^T$ for $|\mathbf{x}| < r_0$, $\mathbf{n}(\mathbf{x}_0) = -\mathbf{x}_0/r_0$, Neumann Rayleigh diffraction using additional $w(\mathbf{x}_0)$ in $D(\mathbf{x}_0, \omega)$
- circular SSD centered around origin within xy -plane with $\mathbf{x}_0 = (x_0, y_0, 0)^T$, radius $r_0 = |\mathbf{x}_0| = \text{const}$, 2.5D SFS plane $\mathbf{x} = (x, y, 0)^T$ for $|\mathbf{x}| < r_0$, $\mathbf{n}(\mathbf{x}_0) = -\mathbf{x}_0/r_0$, Neumann Rayleigh diffraction using using additional $w(\mathbf{x}_0)$ in $D(\mathbf{x}_0, \omega)$

For 2.5D SFS the reference line is located parallel to the y -axis at $x_{\text{Ref}} > 0$. For the reference point \mathbf{x}_{Ref} within the listener region usually the origin of the circular SSD is chosen. No focused point sources are considered in this thesis, therefore requiring $\mathbf{x}_{\text{PS}} \notin V$. For the plane wave propagating direction using planar and linear SSDs, $\cos \varphi_p > 0$ is required for radiation into the considered listener region.

2.3 SFS of a Spherical Wave

The SFS of a point source (2.22) with position $\mathbf{x}_{\text{PS}} \notin V$, i.e. not within the considered synthesis space shall be shortly revisited, giving comments on different approaches and revealing slight misconceptions in literature.

3D Neumann-WFS

3D Neumann-WFS for a planar SSD is straightforward using (2.52)

$$D(\mathbf{x}_0, \omega) = -2 \frac{\partial P(\mathbf{x}_0, \omega)}{\partial n}. \quad (2.116)$$

With the normal derivative (2.24) and (2.23) the driving function reads [Spo08b, (19)]

$$D(\mathbf{x}_0, \omega) = \frac{2}{s} \left(1 + j \frac{\omega}{c} s\right) \cos \varphi_s P_{\text{PS}}(\mathbf{x}_0, \omega) \quad (2.117)$$

and under the assumption $\frac{\omega}{c} s \gg 1$ this approximates to

$$D(\mathbf{x}_0, \omega) = 2j \frac{\omega}{c} \cos \varphi_s P_{\text{PS}}(\mathbf{x}_0, \omega), \quad (2.118)$$

which was already given for the Neumann Sommerfeld-Rayleigh diffraction (2.88) and in context of HF-BEM (2.43).

3D SDM

For the SDM solution of a point source some remarks were given in [Sch14c], that are shortly revisited here. Consider the point source at $\mathbf{x}_{\text{PS}} = (x_{\text{PS}} < 0, y_{\text{PS}}, z_{\text{PS}})^{\text{T}}$, the SSD in the yz -plane $\mathbf{x}_0 = (0, y_0, z_0)^{\text{T}}$, the synthesis half space $\mathbf{x} = (x > 0, y, z)^{\text{T}}$ with $\mathbf{n} = (1, 0, 0)^{\text{T}}$. For the explicit solution of (2.21) towards the driving function the expansions of the Green's function and the

point source have to be known. With the Weyl representation (2.59)

$$\frac{e^{-j\frac{\omega}{c}|\mathbf{x}-\mathbf{x}_0|}}{4\pi|\mathbf{x}-\mathbf{x}_0|} = \frac{1}{4\pi^2} \iint_{-\infty}^{+\infty} \frac{e^{-jk_x(x-x_0)}}{2jk_x} e^{+j(k_y y_0 + k_z z_0)} e^{-j(k_y y + k_z z)} dk_y dk_z$$

using the definitions for k_x (2.58) for propagating and evanescent wave propagation, $x > x_0$ and $\mathbf{x} \neq \mathbf{x}_0$, the decomposition of (2.78) w.r.t. k_y and k_z is given as (cf. (2.81), [Sch14c, (49)])

$$\underbrace{\check{P}(k_y, k_z, \omega) e^{-jk_x x}}_{P(x, k_y, k_z, \omega)} = D(x, k_y, k_z, \omega) \cdot \left[\frac{e^{-jk_x(x-x_0)}}{2jk_x} \right] \quad (2.119)$$

using the eigen-'modes' $\frac{e^{-jk_x(x-x_0)}}{2jk_x}$ of the acoustic transfer function (ATF). From (2.59) also the expansion of the point source $x_{\text{PS}} < x_0$ and $x_0 < x < \infty$ can be extracted to

$$P(x, k_y, k_z, \omega) = P(\omega) \frac{1}{2jk_x} e^{+j\langle \mathbf{k}, \mathbf{x}_{\text{PS}} \rangle} e^{-jk_x x}. \quad (2.120)$$

Solving (2.119) for $D(x, k_y, k_z, \omega)$ yields (cf. sign corrected [Sch14c, (A10,A11)])

$$D(x, k_y, k_z, \omega) = P(\omega) \frac{\frac{1}{2jk_x} e^{+j\langle \mathbf{k}, \mathbf{x}_{\text{PS}} \rangle} e^{-jk_x x}}{\frac{e^{-jk_x(x-x_0)}}{2jk_x}}. \quad (2.121)$$

By circumpassing the singularity $k_x = 0$ in the integration path or requiring $k_x \neq 0$ the terms $\frac{1}{2jk_x}$ and $e^{-jk_x x}$ cancel out, which is valid for all $x_0 < x < \infty$. The driving function then can be obtained by inverse spatial Fourier transform

$$D(\mathbf{x}_0, \omega) = P(\omega) \frac{1}{4\pi^2} \iint_{-\infty}^{+\infty} e^{-j\langle \mathbf{k}, \mathbf{x}_0 - \mathbf{x}_{\text{PS}} \rangle} dk_y dk_z. \quad (2.122)$$

A solution for this integral could not be found in literature and derived by the author so far.

2.5D SDM (Spors)

An SDM deconvolution solution of the 2.5D SFS problem was given in [Spo10] for the point source. For the linear SSD on the y -axis with $\mathbf{x}_0 = (0, y_0, 0)^T$,

the virtual point source (2.22) located at $\mathbf{x}_{\text{PS}} = (x_{\text{PS}} < 0, y_{\text{PS}}, 0)^{\text{T}}$ and the synthesis region $\mathbf{x} = (x > 0, y, 0)^{\text{T}}$ with $\mathbf{n} = (1, 0, 0)^{\text{T}}$, the driving function's spatio-temporal spectrum reads [Spo10, (21)]

$$D(k_y, \omega) = P(\omega) e^{+j k_y y_{\text{PS}}} \times \begin{cases} \frac{H_0^{(2)}(\sqrt{(\frac{\omega}{c})^2 - k_y^2} \cdot (x_{\text{Ref}} - x_{\text{PS}}))}{H_0^{(2)}(\sqrt{(\frac{\omega}{c})^2 - k_y^2} \cdot x_{\text{Ref}})} & \text{for } k_y^2 < (\frac{\omega}{c})^2 \\ \frac{K_0(\sqrt{(\frac{\omega}{c})^2 - k_y^2} \cdot (x_{\text{Ref}} - x_{\text{PS}}))}{K_0(\sqrt{(\frac{\omega}{c})^2 - k_y^2} \cdot x_{\text{Ref}})} & \text{for } k_y^2 > (\frac{\omega}{c})^2 \end{cases} \quad (2.123)$$

for correct SFS along a **reference line** parallel to the y -axis at $x_{\text{Ref}} > 0$. With the assumptions [Spo10, (23a, 23b)]

$$\sqrt{|\left(\frac{\omega}{c}\right)^2 - k_y^2|} \cdot x_{\text{Ref}} \gg 1 \quad \sqrt{|\left(\frac{\omega}{c}\right)^2 - k_y^2|} \cdot (x_{\text{Ref}} - x_{\text{PS}}) \gg 1 \quad (2.124)$$

the spectrum can be simplified with the large argument approximations of the Hankel and modified Bessel functions to [Spo10, (22)]

$$D(k_y, \omega) = P(\omega) e^{+j k_y y_{\text{PS}}} \sqrt{\frac{x_{\text{Ref}}}{x_{\text{Ref}} - x_{\text{PS}}}} \cdot \begin{cases} e^{+j \sqrt{(\frac{\omega}{c})^2 - k_y^2} \cdot x_{\text{PS}}} & \text{for } k_y^2 < (\frac{\omega}{c})^2 \\ e^{+\sqrt{k_y^2 - (\frac{\omega}{c})^2} \cdot x_{\text{PS}}} & \text{for } k_y^2 > (\frac{\omega}{c})^2. \end{cases} \quad (2.125)$$

The point source is allowed to be very close to the SSD as long as the above assumptions are valid. The inverse spatial Fourier transform leads to

$$D(x_{\text{Ref}}, y_0, \omega) = P(\omega) j \frac{\omega}{c} \frac{1}{2} \sqrt{\frac{x_{\text{Ref}}}{x_{\text{Ref}} - x_{\text{PS}}}} \frac{x_{\text{PS}}}{s} H_1^{(2)}\left(\frac{\omega}{c} s\right). \quad (2.126)$$

The transform is not straightforward. The solution in [Spo10] is derived in the way that the correction factor together with the Neumann normal derivative of an ideal line source is considered

$$D(x_{\text{Ref}}, y_0, \omega) = P(\omega) \sqrt{\frac{x_{\text{Ref}}}{x_{\text{Ref}} - x_{\text{PS}}}} \cdot -2 \frac{\partial}{\partial x} \left[-\frac{j}{4} H_0^{(2)}\left(\frac{\omega}{c} |\mathbf{x} - \mathbf{x}_{\text{PS}}|\right) \right] \Big|_{\mathbf{x}=\mathbf{x}_0}, \quad (2.127)$$

for which a forward spatial Fourier transform w.r.t. $y \rightarrow k_y$ is performed for the bracket term using [Gra07, (6.677.3)], [Gra07, (6.677.4)] and calculating the normal derivative $\frac{\partial}{\partial x}(\cdot)|_{\mathbf{x}=\mathbf{x}_0}$ in the spatio-temporal spectrum domain. It

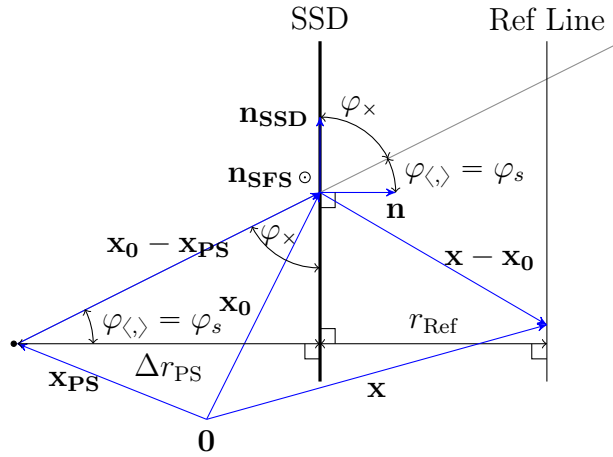


Figure 2.3: Geometry to estimate the shortest distance Δr_{PS} from a point source at \mathbf{x}_{PS} to a linear SSD. The vectors $\mathbf{x}_0 - \mathbf{x}_{PS}$, $\mathbf{x} - \mathbf{x}_0$, \mathbf{n} and \mathbf{n}_{SSD} must be coplanar for 2.5D SFS.

is interesting that the Neumann boundary condition of the Green's function was utilized to derive the Fourier transform pair (2.125) $\circ \bullet$ (2.126), thus to solve the deconvolution problem as SDM. This provides a further link between Neumann-WFS and SDM for linear/planar arrays. For $\frac{\omega}{c} s \gg 1$, (2.126) can be further approximated to [Spo10, (25)]

$$D(x_{Ref}, y_0, \omega) = P(\omega) \sqrt{\frac{j \frac{\omega}{c}}{2\pi}} \sqrt{\frac{x_{Ref} - x_{PS}}{x_{Ref} - x_{PS}} \frac{-x_{PS}}{s} \frac{e^{-j \frac{\omega}{c} s}}{\sqrt{s}}}, \quad (2.128)$$

which then not anymore allows point sources very close to the SSD, except when $\frac{\omega}{c} \gg 1$ holds. As pointed out in [Spo10], (2.128) is precisely identical to the 2.5D Neumann-WFS driving function derived by the two stationary phase approximations (2.141), [Vog93, (3.5.15)], [dV94a, (3)], [dV96, Sec. 4], [Sta97, (3.16&3.17)], [Ver97, (2.27)].

2.5D Neumann-WFS with a linear SSD is therefore a farfield/high frequency approximation of the exact 2.5D SDM solution (2.123). This statement holds in general for arbitrary primary sources, cf. [Fir16].

Eq. (2.128) should be given for arbitrarily located linear SSDs in general vector notation for convenience. At first, realize that

$$\frac{-x_{PS}}{s} = \cos \varphi_s = \frac{\langle \mathbf{x}_0 - \mathbf{x}_{PS}, \mathbf{n}(\mathbf{x}_0) \rangle}{|\mathbf{x}_0 - \mathbf{x}_{PS}|}. \quad (2.129)$$

Furthermore, with one of the two possible unit normals \mathbf{n}_{SFS} of the SFS half plane under consideration, the distance of the SSD to the point source reads

$$\Delta r_{\text{PS}} = |(\mathbf{x}_0 - \mathbf{x}_{\text{PS}}) \times \overbrace{\frac{\mathbf{n}_{\text{SFS}} \times \mathbf{n}}{|\mathbf{n}_{\text{SFS}} \times \mathbf{n}|}}^{\mathbf{n}_{\text{SSD}}}| = \langle \mathbf{x}_0 - \mathbf{x}_{\text{PS}}, \mathbf{n} \rangle, \quad (2.130)$$

due to $\Delta r_{\text{PS}} = \langle \mathbf{s}, \mathbf{n} \rangle = |\mathbf{s}| |\mathbf{n}| \cos \varphi_{\langle, \rangle}$ and $\Delta r_{\text{PS}} = |\mathbf{s} \times \mathbf{n}_{\text{SSD}}| = |\mathbf{s}| |\mathbf{n}_{\text{SSD}}| \sin \varphi_{\times}$, cf. Fig. 2.3. This then yields the driving function in general vector notation, i.e. [Sta97, (3.16&3.17)]

$$D(\mathbf{x}_0, r_{\text{Ref}}, \omega) = P(\omega) \sqrt{\frac{j\frac{\omega}{c}}{2\pi}} \sqrt{\frac{r_{\text{Ref}}}{r_{\text{Ref}} + \Delta r_{\text{PS}}}} \frac{\langle \mathbf{x}_0 - \mathbf{x}_{\text{PS}}, \mathbf{n}(\mathbf{x}_0) \rangle}{|\mathbf{x}_0 - \mathbf{x}_{\text{PS}}|} \frac{e^{-j\frac{\omega}{c}|\mathbf{x}_0 - \mathbf{x}_{\text{PS}}|}}{\sqrt{|\mathbf{x}_0 - \mathbf{x}_{\text{PS}}|}}, \quad (2.131)$$

under the assumption that (i) the vectors $\mathbf{x}_0 - \mathbf{x}_{\text{PS}}$, $\mathbf{x} - \mathbf{x}_0$, \mathbf{n} and \mathbf{n}_{SSD} are coplanar, i.e. located in the same plane that is considered for SFS and that (ii) the point source position fulfills $\cos \varphi_s > 0$. r_{Ref} denotes the distance of the **reference line** parallel to the SSD. Inverse temporal Fourier transform yields the driving filter

$$d(\mathbf{x}_0, r_{\text{Ref}}, t) = \sqrt{\frac{r_{\text{Ref}}}{r_{\text{Ref}} + \Delta r_{\text{PS}}}} \frac{\langle \mathbf{x}_0 - \mathbf{x}_{\text{PS}}, \mathbf{n}(\mathbf{x}_0) \rangle}{|\mathbf{x}_0 - \mathbf{x}_{\text{PS}}|} \frac{1}{\sqrt{|\mathbf{x}_0 - \mathbf{x}_{\text{PS}}|}} \frac{1}{\sqrt{2\pi}} \cdot \left(\mathcal{F}^{-1} \left(\sqrt{j\frac{\omega}{c}} * p(t) * \delta(t - \frac{|\mathbf{x}_0 - \mathbf{x}_{\text{PS}}|}{c}) \right) \right). \quad (2.132)$$

In Fig. 2.7c and Fig. 2.7d the synthesis of a virtual point source with the driving function (2.131) and a linear SSD within the xy -plane is visualized.

2.5D Neumann-WFS from 3D to 2.5D (Delft, Start)

2.5D Neumann-WFS was initially derived by a stationary phase approximation of the 3D Neumann Rayleigh integral [Sta96]. With the SSD in the yz -plane using $\mathbf{x}'_0 = (0, y_0, z_0)^T$, the point source (2.22) located at $\mathbf{x}_{\text{PS}} = (x_{\text{PS}} < 0, y_{\text{PS}}, 0)^T$ and the SFS region $\mathbf{x} = (x > 0, y, 0)^T$ with $\mathbf{n} = (1, 0, 0)^T$ the 3D Neumann Rayleigh integral (2.52) for the farfield/high frequency approximated normal

derivative (2.25) reads with $\cos \varphi'_s = \frac{\langle \mathbf{x}'_0 - \mathbf{x}_{\text{PS}}, \mathbf{n}(\mathbf{x}'_0) \rangle}{|\mathbf{x}'_0 - \mathbf{x}_{\text{PS}}|}$

$$P(\mathbf{x}, \omega) = \int_{-\infty}^{+\infty} \left[\int_{-\infty}^{+\infty} P(\omega) \frac{e^{-j\frac{\omega}{c}|\mathbf{x}'_0 - \mathbf{x}_{\text{PS}}|}}{2\pi|\mathbf{x}'_0 - \mathbf{x}_{\text{PS}}|} j\frac{\omega}{c} \cos \varphi'_s G_{0,3\text{D}}(\mathbf{x}, \mathbf{x}'_0, \omega) dz_0 \right] dy_0. \quad (2.133)$$

First stationary phase approximation

The inner integral can be treated with a first stationary phase approximation w.r.t. z_0 [Arf05, (7.113)] under the assumption $|\frac{\omega}{c}(|\mathbf{x}'_0 - \mathbf{x}_{\text{PS}}| + |\mathbf{x} - \mathbf{x}'_0|)| \gg 1$. With $\mathbf{x}_0 = (0, y_0, 0)^T$ and the usual conventions used throughout this chapter

$$\cos \varphi_s = \frac{\langle \mathbf{x}_0 - \mathbf{x}_{\text{PS}}, \mathbf{n}(\mathbf{x}_0) \rangle}{|\mathbf{x}_0 - \mathbf{x}_{\text{PS}}|} \quad s = |\mathbf{x}_0 - \mathbf{x}_{\text{PS}}| \quad r = |\mathbf{x} - \mathbf{x}_0| \quad (2.134)$$

this results in [Sta97, (3.10&3.11)], [Ver97, (2.21)], [Spo10, (10)]

$$P(\mathbf{x}, \omega) = \int_{-\infty}^{+\infty} P(\omega) \sqrt{\frac{j\frac{\omega}{c}}{2\pi}} \sqrt{\frac{r}{s+r}} \cos \varphi_s \frac{e^{-j\frac{\omega}{c}s}}{\sqrt{s}} G_{0,3\text{D}}(\mathbf{x}, \mathbf{x}_0, \omega) dy_0, \quad (2.135)$$

reducing the planar to a linear SSD located on the y -axis. The driving function for the SLP thus reads

$$D(y_0, \omega) = P(\omega) \sqrt{\frac{j\frac{\omega}{c}}{2\pi}} \sqrt{\frac{r}{s+r}} \cos \varphi_s \frac{e^{-j\frac{\omega}{c}s}}{\sqrt{s}}. \quad (2.136)$$

Its gain factor $g = \sqrt{\frac{r}{s+r}}$ depends on the receiver position, which is usually not desired. However, for a circular SSD centered at \mathbf{x}_{Ref} this driving function may be deployed using $r_0 = |\mathbf{x}_{\text{Ref}} - \mathbf{x}_0|$ and the secondary source selection criterion $D(\mathbf{x}_0, \omega) = 0$ if $\cos \varphi_s < 0$. This results in the correct 2.5D SFS, where the amplitude is correctly synthesized at the **reference point** \mathbf{x}_{Ref} as long as the made approximations are valid:

$$D(\mathbf{x}_0, \mathbf{x}_{\text{Ref}}, \omega) = P(\omega) \sqrt{\frac{j\frac{\omega}{c}}{2\pi}} \sqrt{\frac{|\mathbf{x}_{\text{Ref}} - \mathbf{x}_0|}{|\mathbf{x}_0 - \mathbf{x}_{\text{PS}}| + |\mathbf{x}_{\text{Ref}} - \mathbf{x}_0|}} \frac{\langle \mathbf{x}_0 - \mathbf{x}_{\text{PS}}, \mathbf{n}(\mathbf{x}_0) \rangle}{|\mathbf{x}_0 - \mathbf{x}_{\text{PS}}|} \frac{e^{-j\frac{\omega}{c}|\mathbf{x}_0 - \mathbf{x}_{\text{PS}}|}}{\sqrt{|\mathbf{x}_0 - \mathbf{x}_{\text{PS}}|}} \quad (2.137)$$

Eq. (2.137) requires coplanarity of the involved vectors $\mathbf{x}_0 - \mathbf{x}_{\text{PS}}$, $\mathbf{x} - \mathbf{x}_0$, $\mathbf{x}_{\text{Ref}} - \mathbf{x}_0$, $\mathbf{n}(\mathbf{x}_0)$. Inverse temporal Fourier transform yields the driving filter

$$d(\mathbf{x}_0, \mathbf{x}_{\text{Ref}}, t) = \sqrt{\frac{|\mathbf{x}_{\text{Ref}} - \mathbf{x}_0|}{|\mathbf{x}_0 - \mathbf{x}_{\text{PS}}| + |\mathbf{x}_{\text{Ref}} - \mathbf{x}_0|}} \frac{\langle \mathbf{x}_0 - \mathbf{x}_{\text{PS}}, \mathbf{n}(\mathbf{x}_0) \rangle}{|\mathbf{x}_0 - \mathbf{x}_{\text{PS}}|} \frac{1}{\sqrt{|\mathbf{x}_0 - \mathbf{x}_{\text{PS}}|}} \frac{1}{\sqrt{2\pi}} \cdot \left(\mathcal{F}^{-1} \left(\sqrt{j \frac{\omega}{c}} \right) * p(t) * \delta \left(t - \frac{|\mathbf{x}_0 - \mathbf{x}_{\text{PS}}|}{c} \right) \right). \quad (2.138)$$

In Fig. 2.7a and Fig. 2.7b at the end of this chapter the synthesis of a virtual point source with the driving function (2.137) and a circular SSD within the xy -plane is visualized.

Second stationary phase approximation

In order that the driving function holds for more than one receiver point for a linear SSD – or rather for another parametric curve where amplitude correct SFS occurs [Fir16] – a second stationary phase approximation is performed w.r.t. y_0 to obtain a new gain factor g that replaces the one used in (2.136). Under the assumption that $|\frac{\omega}{c} (|\mathbf{x}_0 - \mathbf{x}_{\text{PS}}| + |\mathbf{x} - \mathbf{x}_0|)| \gg 1$ and by usage of the intercept theorem the condition [Sta97, (3.14 , corrected)]

$$\frac{r}{s} = \frac{x}{-x_{\text{PS}}} \quad (2.139)$$

is obtained, when finding that the stationary point is located at the position where the vector from the point source to the evaluation point intersects the SSD, cf. [Sta96, Fig. 5]. The gain factor then becomes

$$g = \sqrt{\frac{r}{s+r}} = \sqrt{\frac{\frac{r}{s}}{1 + \frac{r}{s}}} = \sqrt{\frac{x}{x - x_{\text{PS}}}}. \quad (2.140)$$

The driving function for the SLP thus reads [Sta97, (3.16&3.17)], [Ver97, (2.27)], [Spo10, (12)] – identical to the twice applied high frequency/farfield approximated SDM solution (2.128) w.r.t. (2.129) –

$$D(x_{\text{Ref}}, y_0, \omega) = P(\omega) \sqrt{\frac{j \frac{\omega}{c}}{2\pi}} \sqrt{\frac{x_{\text{Ref}}}{x_{\text{Ref}} - x_{\text{PS}}}} \cos \varphi_s \frac{e^{-j \frac{\omega}{c} s}}{\sqrt{s}} \quad (2.141)$$

and synthesizes the sound field correctly along a line parallel to the SSD, for which typically a certain **reference line** at $x = x_{\text{Ref}}$ is chosen. For $x_0 < x <$

x_{Ref} the amplitude is then typically too high and for $x > x_{\text{Ref}}$ too low, but the desired wave front is synthesized as desired.

2.5D Neumann-WFS from 2D to 2.5D (Spors)

A solution for 2.5D Neumann-WFS starting from the 2D Neumann Rayleigh integral

$$P(\mathbf{x}, \omega) = \int_{-\infty}^{+\infty} \underbrace{-2 \frac{\partial P_{\text{PS}}(\mathbf{x}_0, \omega)}{\partial n}}_{D_{2\text{D},\text{WFS}}(\mathbf{x}_0, \omega)} G_{0,2\text{D}}(\mathbf{x}, \mathbf{x}_0, \omega) dy_0 \quad (2.142)$$

was proposed in [Rab06, Spo08b]. Consider a linear SSD along the y -axis denoted with $\mathbf{x}_0 = (0, y_0, 0)^T$, the point source (2.22) located at $\mathbf{x}_{\text{PS}} = (x_{\text{PS}} < 0, y_{\text{PS}}, 0)^T$ and the synthesis region $\mathbf{x} = (x > 0, y, 0)^T$ with $\mathbf{n} = (1, 0, 0)^T$. The large argument approximation $\frac{\omega}{c} r \gg 1$ of the Hankel function [Olv10, 10.2.6] – that inherently is a stationary phase approximation [Arf05, Ex. 7.3.1, p.493] – can be used to derive [Rab06, (13.31)], [Spo08b, (24)]

$$G_{0,2\text{D}}(\mathbf{x}, \mathbf{x}_0, \omega) = -\frac{j}{4} H_0^{(2)}\left(\frac{\omega}{c} r\right) \approx \sqrt{\frac{2\pi r}{j\frac{\omega}{c}}} \underbrace{\frac{e^{-j\frac{\omega}{c} r}}{4\pi r}}_{G_{0,3\text{D}}(\mathbf{x}, \mathbf{x}_0, \omega)}, \quad (2.143)$$

from which (2.142) can be reformulated towards a SLP representation

$$P(\mathbf{x}, \omega) = \int_{-\infty}^{+\infty} \underbrace{D_{2\text{D},\text{WFS}}(\mathbf{x}_0, \omega)}_{D_{2.5\text{D},\text{WFS}}(\mathbf{x}, \mathbf{x}_0, \omega)} \sqrt{\frac{2\pi r}{j\frac{\omega}{c}}} G_{0,3\text{D}}(\mathbf{x}, \mathbf{x}_0, \omega) dy_0. \quad (2.144)$$

Inserting (2.117) – note here the dimensionality mismatch using a normal derivative of a 3D pressure field within a 2D problem – to $D_{2.5\text{D},\text{WFS}}(\mathbf{x}, \mathbf{x}_0, \omega)$ yields [Spo08b, (29)]

$$D(\mathbf{x}_0, \mathbf{x}_{\text{Ref}}, \omega) = P(\omega) \sqrt{\frac{|\mathbf{x}_{\text{Ref}} - \mathbf{x}_0|}{2\pi}} \cos \varphi_s \left(\frac{1}{\sqrt{j\frac{\omega}{c} s}} + \sqrt{j\frac{\omega}{c}} \right) \frac{e^{-j\frac{\omega}{c} s}}{s}, \quad (2.145)$$

for SFS w.r.t. a **reference point** $\mathbf{x}_{\text{Ref}} = (x > 0, y, 0)^T$. For a farfield/high frequency approximation $\frac{\omega}{c} s \gg 1$ in (2.117) the driving function approximates to [Spo08b, (37)]

$$D(\mathbf{x}_0, \mathbf{x}_{\text{Ref}}, \omega) = P(\omega) \sqrt{\frac{j \frac{\omega}{c}}{2\pi}} \sqrt{|\mathbf{x}_{\text{Ref}} - \mathbf{x}_0|} \cos \varphi_s \frac{e^{-j \frac{\omega}{c} s}}{s}. \quad (2.146)$$

The proposed approach leads to wrong amplitudes at the reference point. This is due to the fact that deploying the stationary phase approximation to the Hankel function only ignores the influence of the 3D spherical wave primary field along the secondary source line monopole in z -direction. By reducing the line monopole to the spherical monopole independently from a 3D primary field, only the normal derivative of the sound field directly on the linear SSD (at $z = 0$) is used to derive the driving function, which turns out to be inaccurate. This effect is known as virtual source dimensional mismatch [Fir16]. In [Vö12] an intuitive technique was proposed to compensate this amplitude error for a single receiver point. However, the exact location of amplitude correct synthesis is only investigated in detail in [Fir16].

By rewriting the result of the driving that originates from the correct first stationary phase approximation (2.137) to (cf. [Spo08b, (35)])

$$D(\mathbf{x}_0, \mathbf{x}_{\text{Ref}}, \omega) = P(\omega) \sqrt{\frac{j \frac{\omega}{c}}{2\pi}} \sqrt{\frac{s \cdot |\mathbf{x}_{\text{Ref}} - \mathbf{x}_0|}{s + |\mathbf{x}_{\text{Ref}} - \mathbf{x}_0|}} \cos \varphi_s \frac{e^{-j \frac{\omega}{c} s}}{s} \quad (2.147)$$

it becomes obvious that (2.146) is only correct if $s \gg |\mathbf{x}_{\text{Ref}} - \mathbf{x}_0|$ holds. This implies that the point source must be farther away from the SSD than the reference point from the SSD. For meaningful reference point distances this condition implies that the synthesized wavefront curvature is then almost planar. Since a planar wavefront curvature within the plane under discussion constitutes a 2D sound field the initial incomplete phase approximation (2.143) for 3D sound fields becomes correct in terms of 2D sound fields. Hence, although the approach here leads to an incorrect driving function for point sources, it is a useful derivation for 2.5D Neumann-WFS of plane waves as revisited later.

2.4 SFS of a Plane Wave

The SFS of a plane wave (2.26) with propagating direction \mathbf{n}_{PW} shall also be shortly revisited, giving comments on different approaches and revealing slight misconceptions in literature.

3D Neumann-WFS

3D Neumann-WFS for a planar SSD is again straightforward using (2.116). With the normal derivative (2.27) the driving function reads [Spo08b, (17)]

$$D(\mathbf{x}_0, \omega) = 2j \frac{\omega}{c} \cos \varphi_p P_{\text{PW}}(\mathbf{x}_0, \omega), \quad (2.148)$$

which was already given in context of HF-BEM (2.47). Note that only plane wave propagating directions are allowed that fulfill $\cos \varphi_p > 0$. For the customized geometry under discussion – a planar SSD within the yz -plane $\mathbf{x}_0 = (0, y_0, z_0)^T$ as well SFS in the target half-space $\mathbf{x} = (x > 0, y, z)^T$ with $\mathbf{n}(\mathbf{x}_0) = (1, 0, 0)^T$ – the driving function can be rewritten

$$D(\mathbf{x}_0, \omega) = P(\omega) \cdot 2j k_{x,\text{PW}} \cdot e^{-j k_{y,\text{PW}} y_0} e^{-j k_{z,\text{PW}} z_0} \quad (2.149)$$

in terms of the temporal angular frequency ω and temporal frequency independent radiation direction \mathbf{n}_{PW} that is linked as

$$\mathbf{n}_{\text{PW}} = \begin{pmatrix} \cos \varphi_{\text{PW}} \sin \vartheta_{\text{PW}} \\ \sin \varphi_{\text{PW}} \sin \vartheta_{\text{PW}} \\ \cos \vartheta_{\text{PW}} \end{pmatrix}, \quad \mathbf{k}_{\text{PW}} = \begin{pmatrix} k_{x,\text{PW}} \\ k_{y,\text{PW}} \\ k_{z,\text{PW}} \end{pmatrix} = \frac{\omega}{c} \cdot \mathbf{n}_{\text{PW}}. \quad (2.150)$$

3D SDM (Ahrens)

Considering the same customized geometry as for 3D Neumann-WFS, the SLP (2.78) can be rewritten as a convolution integral (here w.r.t. y and z)

$$P(\mathbf{x}, \omega) = \iint_{-\infty}^{+\infty} D(\mathbf{x}_0, \omega) G_{0,3\text{D}}(\mathbf{x}, \mathbf{x}_0, \omega) dy_0 dz_0 = D(\mathbf{x}, \omega) *_y *_z G_{0,3\text{D}}(\mathbf{x}, \mathbf{0}, \omega). \quad (2.151)$$

The explicit solution, i.e. deconvolution for $D(\mathbf{x}_0, \omega)$ for a plane wave was derived in e.g. [Faz10a, (4.83)], [Ahr08c], [Ahr10d, (5)], [Ahr12a, (3.65)], [Ahr12b, (10)], revisited in [Sch14c, Sec. 6.1]. These solutions are equal to the planar NAH-like approach discussed above on p.34. Note that a strict proof of the convergence of the involved integrals is not provided by any of these derivations and also not here. With (2.82) ($x_0 = 0$) follows

$$D(\mathbf{x}_0, \omega) = \frac{1}{4\pi^2} \iint_{-\infty}^{+\infty} \frac{\check{P}(k_y, k_z, \omega)}{\frac{1}{2jk_x}} e^{-j(k_y y_0 + k_z z_0)} dk_y dk_z. \quad (2.152)$$

Recall the allowed wave numbers w.r.t. the x -dimension (2.58)

$$k_x = \begin{cases} +\sqrt{\left(\frac{\omega}{c}\right)^2 - (k_y^2 + k_z^2)} & \text{for } \left(\frac{\omega}{c}\right)^2 > (k_y^2 + k_z^2) \\ -j\sqrt{(k_y^2 + k_z^2) - \left(\frac{\omega}{c}\right)^2} & \text{for } (k_y^2 + k_z^2) > \left(\frac{\omega}{c}\right)^2 \end{cases}. \quad (2.153)$$

The angular spectrum of the plane wave is given as

$$\check{P}(k_y, k_z, \omega) = P(\omega) \cdot 4\pi^2 \delta(k_y - k_{y,\text{PW}}) \delta(k_z - k_{z,\text{PW}}). \quad (2.154)$$

Inserting (2.154) to (2.152) and performing the inverse spatial Fourier transform with the sifting property of the Dirac function yields [Ahr10d, (7)]

$$D(\mathbf{x}_0, \omega) = P(\omega) \cdot 2jk_{x,\text{PW}} \cdot e^{-jk_{y,\text{PW}}y_0} e^{-jk_{z,\text{PW}}z_0}. \quad (2.155)$$

The same solution like 3D Neumann-WFS (2.149) is obtained. This was expected since 3D Neumann-WFS as the implicit solution and 3D SDM as the explicit solution are equivalent approaches for the 3D SFS problem using planar SSDs [Sch14c].

2.5D SDM (Ahrens)

The SDM solution is again the explicit solution for the 2.5D SFS problem using a linear SSD on the y -axis here for discussion. The synthesized sound

field $P(\mathbf{x}, \omega)$ is described similar to (2.78) by

$$P(\mathbf{x}, \omega) = \int_{-\infty}^{+\infty} D(\mathbf{x}_0, \omega) G_{0,3D}(\mathbf{x}, \mathbf{x}_0, \omega) dy_0 \quad (2.156)$$

using $\mathbf{x} = (x > 0, y, 0)^T$ and $\mathbf{x}_0 = (0, y_0, 0)^T$. The infinite linear SSD is incapable of radiating three dimensional plane waves due to the dimension reduction. The possible wave radiation directions also underlie a reduced set of wave numbers, i.e. k_x , k_y and k_z cannot be controlled independently. The wave number k_y describes the wave propagation along the SSD orientation. The radial wave number k_r describes the radiation direction of conical wavefronts. For a plane wave radiation direction ϑ_{PW} , φ_{PW}

$$\left(\frac{\omega}{c}\right)^2 - k_{y,PW}^2 = \underbrace{\left(\frac{\omega}{c}\right)^2 (\cos^2 \varphi_{PW} \sin^2 \vartheta_{PW} + \cos^2 \vartheta_{PW})}_{k_{r,PW}^2 = k_{x,PW}^2 + k_{z,PW}^2} \quad (2.157)$$

holds. For a desired temporal angular frequency ω and chosen $k_{y,PW}$ along the SSD [Ahr12a, (3.76)]

$$\left(\frac{\omega}{c}\right)^2 - k_{y,PW}^2 = \text{const} = k_{r,PW}^2 \quad (2.158)$$

follows, and either ϑ_{PW} or φ_{PW} can be controlled. Following the SDM approach of [Ahr12a, Ch. 3.7], [Ahr10d, Sec. IIB], the convolution along the y -axis in (2.156) can be transferred to a spatio-temporal spectrum multiplication w.r.t. k_y

$$P(x, k_y, z, \omega) = D(x, k_y, z, \omega) \cdot G_0(x, k_y, z, \omega). \quad (2.159)$$

This holds again under the assumption that the SSD characteristic is uniform, i.e. the Green's function is shift-invariant. Explicitly solving for $D(x, k_y, z, \omega)$ yields

$$D(x, k_y, z, \omega) = \frac{P(x, k_y, z, \omega)}{G_0(x, k_y, z, \omega)} \quad (2.160)$$

and the inverse spatial Fourier transform (C.3) leads to the unknown driving function as an explicit solution

$$D_{2.5D,SDM}(\mathbf{x}_0, \omega) = \frac{1}{2\pi} \int_{-\infty}^{+\infty} \frac{P(x, k_y, z, \omega)}{G_0(x, k_y, z, \omega)} e^{-j k_y \cdot y_0} dk_y, \quad (2.161)$$

provided that the integral converges and $G_0(x, k_y, z, \omega) \neq 0$.

The spatio-temporal spectrum of $G_{0,3D}(\mathbf{x}, \mathbf{0}, \omega)$ located in the origin w.r.t. k_y is given as [Ahr12a, (C.10)], [Ahr10d, (52)]

$$G_0(x, k_y, z, \omega) = \begin{cases} -\frac{j}{4} H_0^{(2)} \left(\sqrt{\left(\frac{\omega}{c}\right)^2 - k_y^2} \cdot \sqrt{x^2 + z^2} \right) & \text{for } k_y^2 < \left(\frac{\omega}{c}\right)^2 \\ \frac{1}{2\pi} K_0 \left(\sqrt{k_y^2 - \left(\frac{\omega}{c}\right)^2} \cdot \sqrt{x^2 + z^2} \right) & \text{for } k_y^2 > \left(\frac{\omega}{c}\right)^2, \end{cases} \quad (2.162)$$

where $H_0^{(2)}(\cdot)$ denotes the cylindrical Hankel function of 0th order of 2nd kind and $K_0(\cdot)$ the modified Bessel function of 0th order of 2nd kind [Olv10, §10.1]. The 1st case in (2.162) describes propagating waves, the 2nd case corresponds to evanescent waves. The spatio-temporal spectrum of the desired plane wave is given as

$$P(x, k_y, z, \omega) = P(\omega) \cdot e^{-j k_{x,PW} \cdot x} e^{-j k_{z,PW} \cdot z} 2\pi \delta(k_y - k_{y,PW}). \quad (2.163)$$

and from (2.160) follows [Ahr12b, (3.74)], [Ahr10d, (13)]

$$D(x, k_y, z, \omega) = \frac{P(\omega) \cdot e^{-j k_{x,PW} \cdot x} e^{-j k_{z,PW} \cdot z} \cdot 2\pi \delta(k_y - k_{y,PW})}{-\frac{j}{4} H_0^{(2)} \left(\sqrt{\left(\frac{\omega}{c}\right)^2 - k_{y,PW}^2} \cdot \sqrt{x^2 + z^2} \right)} \quad (2.164)$$

for propagating wave radiation. Note the application of the Delta function sifting property again. The numerator exhibits a three-dimensional problem, while the denominator's problem is a two-dimensional one describable in cylindrical coordinates. This geometrical mismatch is conveniently merged when the sound field within only the half xy -plane and only wave propagation angles for this plane are considered, i.e. $z = 0$, $k_z = 0$ and $x > 0$. Then a pure axial

and radial wave number set

$$k_{y,\text{PW}}^2 = \left(\frac{\omega}{c} \sin \varphi_{\text{PW}}\right)^2 \quad k_{r,\text{PW}}^2 = \left(\frac{\omega}{c} \cos \varphi_{\text{PW}}\right)^2 \quad (2.165)$$

follows for $\vartheta_{\text{PW}} = \frac{\pi}{2}$. The driving functions's spatio-temporal spectrum is reformulated to [Ahr12a, (3.78)], [Ahr10d, (16)]

$$D(x, k_y, \omega) = \frac{P(\omega) \cdot e^{-j k_{r,\text{PW}} \cdot x}}{-\frac{j}{4} H_0^{(2)}(k_{r,\text{PW}} \cdot x)} 2 \pi \delta(k_y - k_{y,\text{PW}}) \quad (2.166)$$

and still depends on the distance x from the SSD. The sound field is therefore only correctly synthesized at a chosen parallel reference line $x = x_{\text{Ref}} > 0$. The inverse spatial Fourier transform (C.3) of (2.166) yields [Ahr10d, (17)]

$$D(x_{\text{Ref}}, y_0, \omega) = \frac{P(\omega) \cdot e^{-j \frac{\omega}{c} \cos \varphi_{\text{PW}} \cdot x_{\text{Ref}}}}{-\frac{j}{4} H_0^{(2)}\left(\frac{\omega}{c} \cos \varphi_{\text{PW}} \cdot x_{\text{Ref}}\right)} e^{-j \frac{\omega}{c} \sin \varphi_{\text{PW}} \cdot y_0}. \quad (2.167)$$

It can be shown that the driving function does not reproduce a desired plane wave using a linear SSD. The sound field rather exhibits an amplitude decay proportional to $\frac{1}{\sqrt{x}}$ in the farfield which is typical for a cylindrical wave amplitude decay [Ahr12a, (3.38)], [Ahr10d, (20)].

For $k_{r,\text{PW}} \cdot x_{\text{Ref}} \gg 1$ the large argument approximation of the Hankel function [Olv10, 10.2.6] can be used to derive

$$D(x_{\text{Ref}}, k_y, \omega) = P(\omega) \cdot \sqrt{8 \pi j \frac{\omega}{c} \cos \varphi_{\text{PW}} \cdot x_{\text{Ref}}} \cdot 2 \pi \delta(k_y - k_{y,\text{PW}}), \quad (2.168)$$

for which the inverse spatial Fourier transform yields [Ahr10d, (29)]

$$D(x_{\text{Ref}}, y_0, \omega) = P(\omega) \cdot \sqrt{8 \pi j \frac{\omega}{c} \cos \varphi_{\text{PW}} \cdot x_{\text{Ref}}} \cdot e^{-j \frac{\omega}{c} \sin \varphi_{\text{PW}} \cdot y_0}. \quad (2.169)$$

In general vector notation with a given **reference line** distance r_{Ref} to the linear SSD, the driving function can be given as

$$\boxed{D(\mathbf{x}_0, r_{\text{Ref}}, \omega) = P(\omega) \sqrt{j \frac{\omega}{c} \sqrt{8 \pi r_{\text{Ref}} \sqrt{\langle \mathbf{n}_{\text{PW}}, \mathbf{n}(\mathbf{x}_0) \rangle}}} e^{-j \frac{\omega}{c} \langle \mathbf{n}_{\text{PW}}, \mathbf{x}_0 \rangle}}, \quad (2.170)$$

where (i) the vectors \mathbf{n}_{PW} , $\mathbf{x} - \mathbf{x}_0$ and $\mathbf{n}(\mathbf{x}_0)$ must be coplanar and (ii) the plane wave propagating direction is restricted to $\cos \varphi_p > 0$. Inverse temporal Fourier transform yields the driving filter

$$d(\mathbf{x}_0, r_{\text{Ref}}, t) = \sqrt{8\pi r_{\text{Ref}}} \sqrt{\langle \mathbf{n}_{\text{PW}}, \mathbf{n}(\mathbf{x}_0) \rangle} \cdot \left(\mathcal{F}^{-1} \left(\sqrt{j \frac{\omega}{c}} \right) * p(t) * \delta \left(t - \frac{\langle \mathbf{n}_{\text{PW}}, \mathbf{x}_0 \rangle}{c} \right) \right). \quad (2.171)$$

In Fig. 2.7g and Fig. 2.7h the synthesis of a virtual plane wave with the driving function (2.170) and a linear SSD within the xy -plane is visualized.

2.5D Neumann-WFS from 3D to 2.5D (Rabenstein, Spors)

The 2.5D Neumann-WFS of a plane wave (2.26)

$$P(\mathbf{x}, \omega) = P(\omega) e^{-j \frac{\omega}{c} \langle \mathbf{n}_{\text{PW}}, \mathbf{x} \rangle} \quad (2.172)$$

can be conveniently discussed for the specialized geometry that was already used. Consider the SFS region $\mathbf{x} = (x > 0, y, 0)^T$, $\mathbf{n}(\mathbf{x}_0) = (1, 0, 0)^T$, the planar SSD $\mathbf{x}_0' = (0, y_0, z_0)^T$ and the linear SSD $\mathbf{x}_0 = (0, y_0, 0)^T$. Then again 3D SFS with the Neumann Rayleigh integral (2.52) using a planar SSD in the yz -plane can be reduced to 2.5D SFS with a linear SSD on y -axis by the stationary phase approximations [Rab06], [Spo06a, App. C.2]. These are the same stationary phase approximations that were used for 2.5D SFS of a point source.

Consider the restriction of plane wave propagating directions for the xy -plane under discussion

$$\mathbf{n}_{\text{PW}} = \begin{pmatrix} \cos \varphi_{\text{PW}} \\ \sin \varphi_{\text{PW}} \\ 0 \end{pmatrix}, \quad \mathbf{k}_{\text{PW}} = \begin{pmatrix} k_{x,\text{PW}} \\ k_{y,\text{PW}} \\ 0 \end{pmatrix} = \frac{\omega}{c} \cdot \mathbf{n}_{\text{PW}} \quad (2.173)$$

and $\cos \varphi_p > 0$ (i.e. the plane wave emanates into the target SFS plane under discussion).

The Neumann Rayleigh integral is given as [Spo06a, (5.4&5.5)]

$$P(\mathbf{x}, \omega) = \int_{-\infty}^{+\infty} \left[\int_{-\infty}^{+\infty} P(\omega) \cdot 2j \frac{\omega}{c} \cos \varphi_{\text{PW}} e^{-j \frac{\omega}{c} \sin \varphi_{\text{PW}} \cdot y_0} G_{0,3\text{D}}(\mathbf{x}, \mathbf{x}_0', \omega) dz_0 \right] dy_0 \quad (2.174)$$

after customizing the normal derivative of the plane wave (2.27) for the chosen geometry.

First stationary phase approximation

Under the assumption $|\frac{\omega}{c} |\mathbf{x} - \mathbf{x}_0'| - \frac{\omega}{c} \sin \varphi_{\text{PW}} \cdot y_0| \gg 1$ the stationary phase approximation of the inner integral yields with $\mathbf{x}_0 = (0, y_0, 0)^T$

$$P(\mathbf{x}, \omega) = \int_{-\infty}^{+\infty} P(\omega) \sqrt{8\pi |\mathbf{x} - \mathbf{x}_0|} j \frac{\omega}{c} \cos \varphi_{\text{PW}} e^{-j \frac{\omega}{c} \sin \varphi_{\text{PW}} \cdot y_0} G_{0,3\text{D}}(\mathbf{x}, \mathbf{x}_0, \omega) dy_0 \quad (2.175)$$

and hence the plane wave driving function for a linear SSD on y -axis

$$D(y_0, \mathbf{x}_{\text{Ref}}, \omega) = P(\omega) \cdot \sqrt{8\pi |\mathbf{x}_{\text{Ref}} - \mathbf{x}_0|} j \frac{\omega}{c} \cos \varphi_{\text{PW}} e^{-j \frac{\omega}{c} \sin \varphi_{\text{PW}} \cdot y_0}. \quad (2.176)$$

This driving function yields amplitude correct SFS for a **reference point** \mathbf{x}_{Ref} – or again rather along a specific parametric curve including \mathbf{x}_{Ref} [Fir16] – located within the synthesis plane. The driving function again should be more conveniently given in general vector notation [Spo08b, (27)]

$$\boxed{D(\mathbf{x}_0, \mathbf{x}_{\text{Ref}}, \omega) = P(\omega) \sqrt{j \frac{\omega}{c}} \sqrt{8\pi |\mathbf{x}_{\text{Ref}} - \mathbf{x}_0|} \langle \mathbf{n}_{\text{PW}}, \mathbf{n}(\mathbf{x}_0) \rangle e^{-j \frac{\omega}{c} \langle \mathbf{n}_{\text{PW}}, \mathbf{x}_0 \rangle}}. \quad (2.177)$$

This again requires coplanarity of $\mathbf{x} - \mathbf{x}_0$, $\mathbf{n}(\mathbf{x}_0)$, \mathbf{n}_{PW} and $\mathbf{x}_{\text{Ref}} - \mathbf{x}_0$. Inverse temporal Fourier transform yields the driving filter

$$d(\mathbf{x}_0, \mathbf{x}_{\text{Ref}}, t) = \sqrt{8\pi |\mathbf{x}_{\text{Ref}} - \mathbf{x}_0|} \langle \mathbf{n}_{\text{PW}}, \mathbf{n}(\mathbf{x}_0) \rangle \cdot \left(\mathcal{F}^{-1} \left(\sqrt{j \frac{\omega}{c}} \right) * p(t) * \delta \left(t - \frac{\langle \mathbf{n}_{\text{PW}}, \mathbf{x}_0 \rangle}{c} \right) \right). \quad (2.178)$$

In Fig. 2.7e and Fig. 2.7f at the end of the chapter the synthesis of a virtual plane wave with the driving function (2.177) and a circular SSD within the xy -plane is visualized.

Second stationary phase approximation

Applying a second stationary phase approximation on (2.175) w.r.t. y_0 yields

$$(y - y_0)^2 = (x - 0)^2 \tan^2 \varphi_{\text{PW}}. \quad (2.179)$$

This can be inserted to $|\mathbf{x}_{\text{Ref}} - \mathbf{x}_0|$ from (2.176)

$$|\mathbf{x}_{\text{Ref}} - \mathbf{x}_0| = \sqrt{(x - 0)^2 + (x - 0)^2 \tan^2 \varphi_{\text{PW}}} = x \sqrt{1 + \tan^2 \varphi_{\text{PW}}}. \quad (2.180)$$

It can be recognized that the secondary stationary point $y_{0,s}$ on the SSD is thus given where $\mathbf{x} - \mathbf{x}_0$ coincides with the plane wave propagation vector \mathbf{n}_{PW} , cf. [Fir16]. The driving function now only depends on x , which again constitutes a **reference line** correction at a chosen $x_{\text{Ref}} > x_0 = 0$. Plugging this result to (2.176) yields

$$D(x_{\text{Ref}}, y_0, \omega) = P(\omega) \cdot \sqrt{8 \pi x_{\text{Ref}} \sqrt{1 + \tan^2 \varphi_{\text{PW}}} \cos^2 \varphi_{\text{PW}}} j \frac{\omega}{c} e^{-j \frac{\omega}{c} \sin \varphi_{\text{PW}} y_0}. \quad (2.181)$$

For the allowed plane wave directions $-\frac{\pi}{2} < \varphi_{\text{PW}} < +\frac{\pi}{2}$

$$\sqrt{1 + \tan^2 \varphi_{\text{PW}}} \cos^2 \varphi_{\text{PW}} = \cos \varphi_{\text{PW}} \quad (2.182)$$

follows and thus the final driving function

$$D(x_{\text{Ref}}, y_0, \omega) = P(\omega) \cdot \sqrt{8 \pi j \frac{\omega}{c} \cos \varphi_{\text{PW}} \cdot x_{\text{Ref}}} \cdot e^{-j \frac{\omega}{c} \sin \varphi_{\text{PW}} y_0}. \quad (2.183)$$

This precisely is the same driving function that was obtained by 2.5D SDM under a farfield/high frequency approximation (2.169).

Note that the same approach using the stationary phase approximations either for a point source or a plane wave lead to the same type of driving functions: The **first** approximation results in a driving function that is valid for a **reference point** (2.137), (2.177). The **second** approximation results in

a driving function that is valid for a **reference line** parallel to the linear SSD (2.131), (2.170). In [Fir16] these two referencing schemes are special cases of a unified framework to derive WFS.

2.5D Neumann-WFS from 2D to 2.5D (Spors)

In case of a plane wave – restricted to propagation directions within the SFS plane – the derivation of 2.5D WFS from 3D \rightarrow 2.5D and from 2D \rightarrow 2.5D yields precisely the same results, which is shortly revisited here. Consider the same geometry as above and the 2D SLP (2.142)

$$P(\mathbf{x}, \omega) = \int_{-\infty}^{+\infty} \underbrace{-2 \frac{\partial P_{\text{PW}}(\mathbf{x}_0, \omega)}{\partial n}}_{D_{2\text{D}, \text{WFS}}(\mathbf{x}_0, \omega)} G_{0,2\text{D}}(\mathbf{x}, \mathbf{x}_0, \omega) dy_0. \quad (2.184)$$

The large argument approximation of the Green's function (2.143) leads to the 2.5D SLP

$$P(\mathbf{x}, \omega) = \int_{-\infty}^{+\infty} \underbrace{D_{2\text{D}, \text{WFS}}(\mathbf{x}_0, \omega) \sqrt{\frac{2\pi |\mathbf{x} - \mathbf{x}_0|}{j \frac{\omega}{c}}}}_{D_{2.5\text{D}, \text{WFS}}(\mathbf{x}, \mathbf{x}_0, \omega)} G_{0,3\text{D}}(\mathbf{x}, \mathbf{x}_0, \omega) dy_0. \quad (2.185)$$

With the 2D WFS driving function cf. (2.174) the 2.5D WFS driving function for a **reference point** \mathbf{x}_{Ref} is obtained

$$D(y_0, \mathbf{x}_{\text{Ref}}, \omega) = P(\omega) \cdot \sqrt{8\pi |\mathbf{x}_{\text{Ref}} - \mathbf{x}_0| j \frac{\omega}{c}} \cos \varphi_{\text{PW}} \cdot e^{-j \frac{\omega}{c} \sin \varphi_{\text{PW}} \cdot y_0}. \quad (2.186)$$

Eq. (2.186) is equal to (2.176). Note that this approach is not valid for a point source as discussed above. However, for the restricted 2D plane wave field this yields accurate results.

Note the misconception in [Ahr10d, Sec. IV.B], [Ahr12a, Ch. 3.9.3] when comparing the 2.5D SDM solution (2.169) with the 2.5D WFS solution (2.176), or in general vector notation (2.170) vs. (2.177). It is argued that the 2.5D WFS driving function (2.176)=(2.186) can be reformulated to a reference line correction using $\mathbf{x}_{\text{Ref}} = (x_{\text{Ref}}, y_0, 0)^T$ – which is an inaccurate stationary point

– [Ahr12a, below (3.92)] leading to

$$D_{2.5D,WFS}(x_{\text{Ref}}, y_0, \omega) = P(\omega) \cdot \sqrt{8\pi x_{\text{Ref}} j \frac{\omega}{c} \cos \varphi_{\text{PW}}} \cdot e^{-j \frac{\omega}{c} \sin \varphi_{\text{PW}} \cdot y_0}. \quad (2.187)$$

Comparing (2.187) with the 2.5D SDM driving function (2.169) reveals a supposed mismatch [Ahr10d, (30)]

$$D_{2.5D,WFS}(x_{\text{Ref}}, y_0, \omega) = D_{2.5D,SDM}(x_{\text{Ref}}, y_0, \omega) \cdot \sqrt{\cos \varphi_{\text{PW}}}. \quad (2.188)$$

This is due to the wrong assumption that the 2.5D WFS driving function obtained by the first stationary phase approximation – inherent to a **reference point** correction – is also valid for a reference line by choosing $\mathbf{x}_{\text{Ref}} = (x_{\text{Ref}}, y_0, 0)^T$. The revisited correction term originating from the second stationary phase approximation is given in (2.180). By contrast, the SDM driving function is inherently derived for a **reference line**. Therefore, the individual driving functions are correct (WFS 1× stationary phase approximation with reference point vs. SDM with reference line) and the comparison of (2.169) with an incorrectly adapted WFS driving function (2.187) is not advisable.

2.5 Prefilter FIR-Design for 2.5D SFS

As revealed above, the farfield/high-frequency approximation prefilter

$$A_{\text{Pre},2.5D}(\omega) = \sqrt{j\omega} = \sqrt{\omega} e^{+j \frac{\pi}{4}} \quad (2.189)$$

is required for driving functions of virtual spherical monopoles as well as for virtual plane waves in approximated 2.5D SDM and for 2.5D Neumann-WFS in general.

For line source array applications in sound reinforcement a similar filter is typically referred to as coupling filter or array morphing filter [LA13]. This filter then exhibits additional low- and high-shelf characteristics to compensate for finite length arrays and for spatial aliasing energy. This is also deployed in SFS applications [Spo10, Sch13].

Typically, the filter (2.189) is realized as an FIR filter with linear phase, thereby ignoring the frequency-independent, constant phase shift of $\frac{\pi}{4}$. This results in a corrupted sound field, when not only monochromatic waves are

considered, since the phase relation between temporal frequencies is not correctly synthesized, cf. [Sch13, Fig. 9-11]. It is therefore desirable to derive an FIR prefilter with correct magnitude and phase. The filter design could be started by defining an appropriate discrete-time Fourier transform (DTFT) spectrum and analytically solving towards the infinite impulse response. This can then be truncated by standard windowed FIR design. The following analytical approach is similar to Hilbert transformer FIR design [Opp10, Sec. 12.4] and could not be traced in literature for the special problem here. It is however very likely that this FIR design is well known in e.g. control engineering, when dealing with fractional order differentiators.

The DTFT spectrum's baseband of the prefilter reads

$$A_{\text{Pre},2.5\text{D}}(\Omega) = \sqrt{\Omega} e^{+j\frac{\pi}{4}} \quad 0 \leq \Omega < \pi \quad (2.190)$$

deploying the normalized digital radian frequency $\Omega = \frac{\omega}{f_s}$ and the sampling frequency f_s in Hz and ignoring a required normalization $\frac{1}{\sqrt{f_s}}$ between the domains w.r.t. Ω and ω . The derivation of time-discrete impulse responses is done via the inverse temporal DTFT [Opp10, Ch. 2.7]

$$x[n] = \frac{1}{2\pi} \int_{-\pi}^{+\pi} X(\Omega) e^{+j\Omega n} d\Omega, \quad (2.191)$$

for the chosen temporal convention of the Fourier transform (C.1). The phase properties with unit magnitude of (2.190) can be derived with

$$a_{\text{Phi}}[n] = \frac{1}{2\pi} \left(\int_{-\pi}^0 e^{-j\frac{\pi}{4}} e^{+j\Omega n} d\Omega + \int_0^{+\pi} e^{+j\frac{\pi}{4}} e^{+j\Omega n} d\Omega \right) \quad (2.192)$$

to the equivalent sequences

$$\begin{aligned} a_{\text{Phi}}[n] &= \frac{\sin(\pi n) + \cos(\pi n) - 1}{\sqrt{2}\pi n} = \frac{\sqrt{2} \cos(\pi/4 - n\pi) - 1}{\sqrt{2}\pi n} \\ &= \begin{cases} 0 & , \text{ if } n \text{ is even and } n \neq 0 \\ \frac{-\sqrt{2}}{\pi n} & , \text{ if } n \text{ is odd} \\ 1/\sqrt{2} & , \text{ } n = 0 \end{cases} . \end{aligned} \quad (2.193)$$

The magnitude properties using zero-phase of (2.190) will be derived with

$$a_{\text{Mag}}[n] = \frac{1}{2\pi} \left(\int_{-\pi}^0 \sqrt{-\Omega} e^{+j\Omega n} d\Omega + \int_0^{+\pi} \sqrt{+\Omega} e^{+j\Omega n} d\Omega \right) \quad (2.194)$$

to the axial-symmetric sequence

$$a_{\text{Mag}}[n] = \begin{cases} -\frac{S(\sqrt{2n})}{\sqrt{2\pi} n^{3/2}} & , n \neq 0 \\ \frac{2}{3} \sqrt{\pi} & , n = 0 \end{cases} \quad (2.195)$$

using [Olv10, (7.4.5/6)] and the Fresnel integral $S(\cdot)$ [Olv10, (7.28)], in Matlab given as `fresnelS(z)`

$$S(z) = \int_0^z \sin\left(\frac{1}{2}\pi t^2\right) dt. \quad (2.196)$$

The calculus succeeded with eqs. (3.381), (8.350), (8.356-1) in [Gra07] and eqs. (7.5.7), (7.5.8), (7.11.1) in [Olv10]. In Fig. 2.4 parts of the two derived infinite impulse responses (2.193) and (2.195) together with their corresponding DTFT spectra are depicted.

Considering the magnitude and phase of (2.190) together, the sequence thus consequently must be obtained by

$$a[n] = \frac{1}{2\pi} \left(\int_{-\pi}^0 e^{-j\frac{\pi}{4}} \sqrt{-\Omega} e^{+j\Omega n} d\Omega \right) + \frac{1}{2\pi} \left(\int_0^{+\pi} e^{+j\frac{\pi}{4}} \sqrt{+\Omega} e^{+j\Omega n} d\Omega \right), \quad (2.197)$$

which after substantial treatment is solved to $a[n] \in \mathbb{R}$

$$a[n] = \begin{cases} \left[\sqrt{8n} \cos(\pi n) + \text{erf}\left(e^{j\frac{3}{4}\pi} \sqrt{\pi n}\right) - \text{erf}\left(e^{j\frac{1}{4}\pi} \sqrt{\pi n}\right) \right] (4\sqrt{\pi} n^{3/2})^{-1} & \text{for } n \neq 0 \\ \sqrt{\frac{2}{9}\pi} & \text{for } n = 0 \end{cases} \quad (2.198)$$

by using the interim results from the calculus above and denoting the Error function $\text{erf}(\cdot)$ [Olv10, (7.2.1)], in Matlab given as `erf(z)`. The weight for

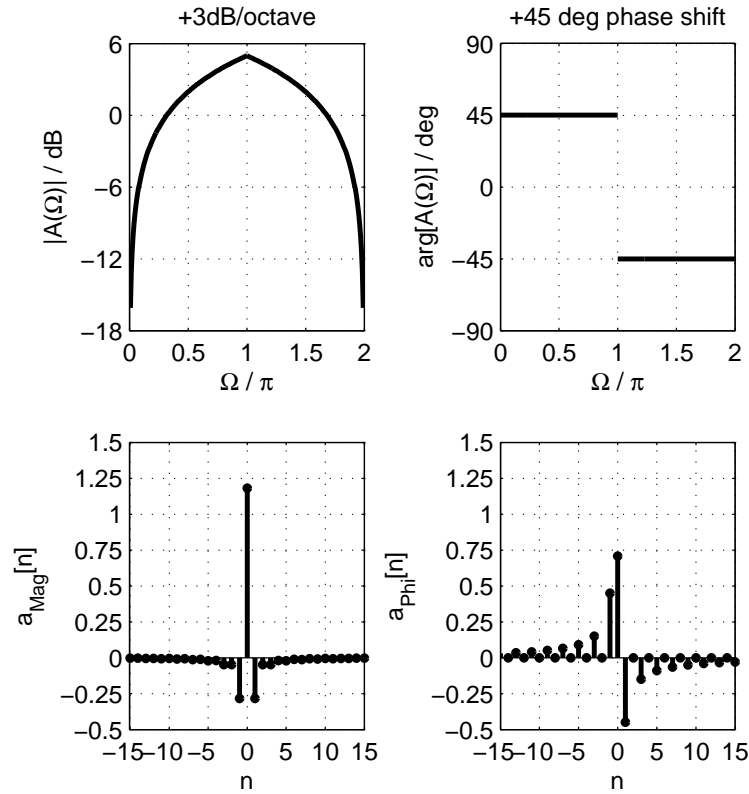


Figure 2.4: Ideal WFS prefilter impulse response according to (2.193) and (2.195).

$n = 0$ was obtained by an inverse DTFT only for $n = 0$, rather than solving the term that is valid for $n \neq 0$ in (2.198) for indeterminate expressions (which is assumed to be impossible). In Fig. 2.5 a part of the derived impulse response (2.198) and its DTFT-spectrum are depicted. The infinite sequence (2.198) can be directly used for a windowed, causal FIR design which then includes an additional constant group delay. In Fig. 2.6 an example design is given for $f_s = 48$ kHz and FIR order 2^9 , thus having $N = 2^9 + 1 = 513$ FIR coefficients. Exemplarily, a Kaiser-Bessel window [Har78], in Matlab `w=kaiser(N,beta)` with $\beta = 4$ was used. The constant group delay offset of $\frac{N-1}{2} = 256$ samples was subtracted from the phase response in order to solely indicate the $\frac{\pi}{4}$ -characteristic of the designed FIR. Due to the windowing and the FIR resolution of $\Delta f = \frac{f_s}{N} = 93.5$ Hz, the magnitude and phase will only follow the ideal spectrum for frequencies $f > 100$ Hz with negligible ripples.

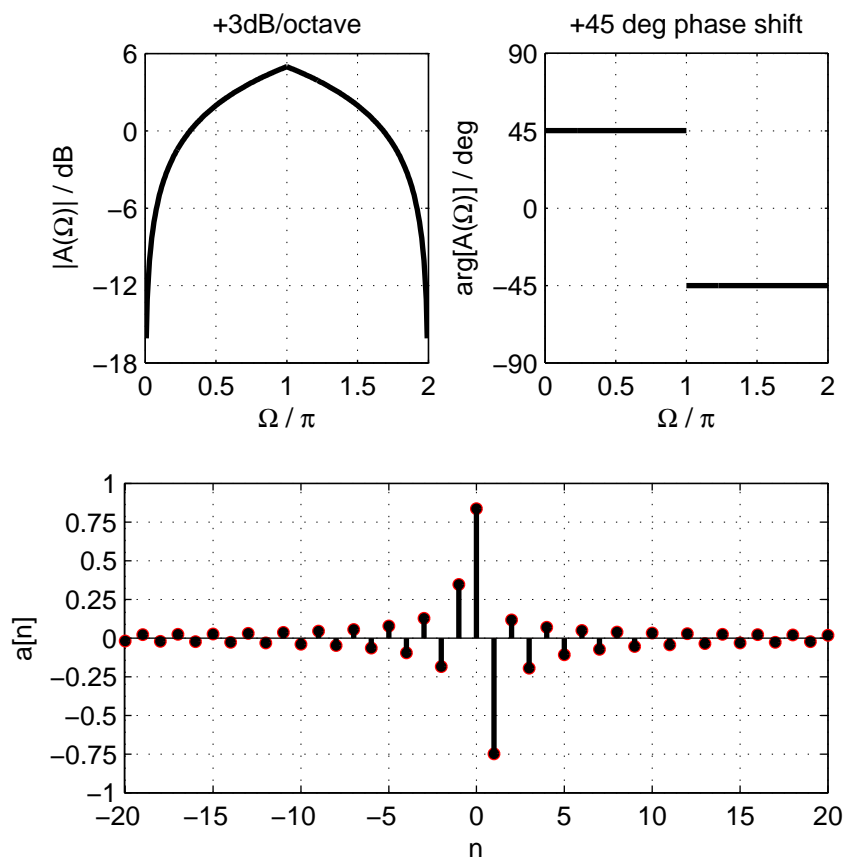


Figure 2.5: Ideal WFS prefilter impulse response according to (2.198).

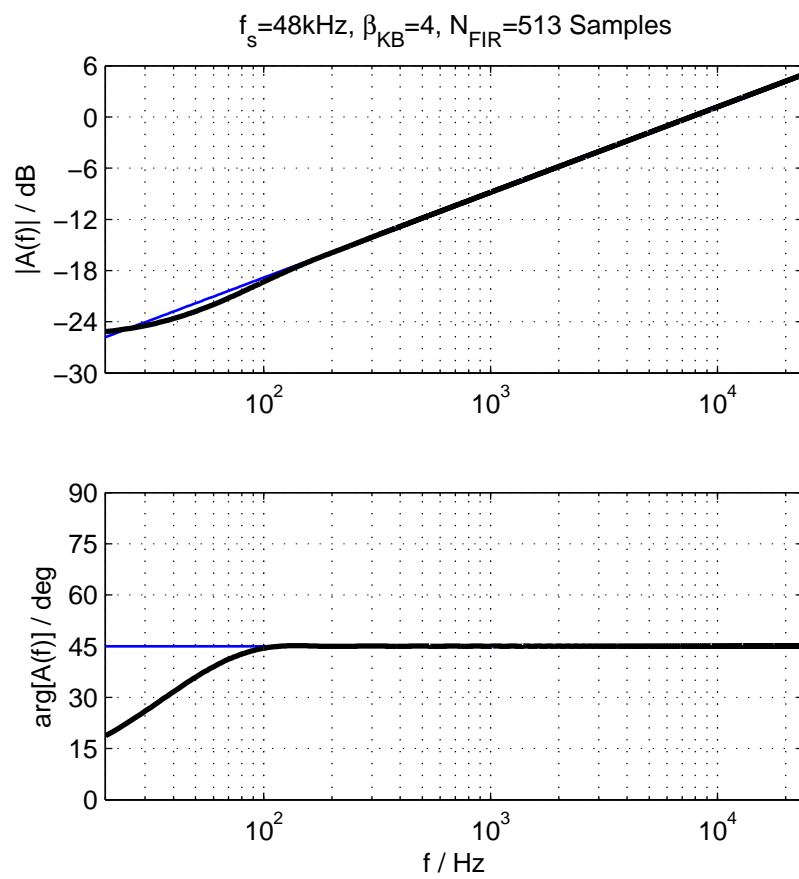


Figure 2.6: Windowed FIR-design for (2.198) using a Kaiser-Bessel window.

2.6 Summary

This chapter revisited the concepts of SFS using the SLP either as an implicit solution (WFS) or as an explicit solution (SDM). For a planar SSD realizing 3D SFS, WFS and SDM are identical approaches, which was proved with the Fourier-NAH-like approach. For a linear SSD realizing 2.5D SFS w.r.t. a reference line, SDM provides the exact solution and 2.5D Neumann-WFS with a twofold stationary phase approximation constitutes the farfield / high-frequency approximated solution, which is precisely identical with the farfield/high-frequency approximated SDM solution. This was consistently shown for a spherical and plane wave primary source. 2.5D Neumann-WFS using only the first stationary phase approximation yields driving functions for a reference point, which can be used for circular SSDs together with the secondary source selection. Reducing the Neumann Rayleigh integral from 3D towards 2.5D is valid for arbitrary primary sources, whereas 'extending' it from 2D to 2.5D works only for plane waves with propagating directions restricted to the SFS plane. In Table 2.1 the connections of SDM and WFS are arranged in terms of equivalent driving functions. It states either the WFS derivation from the 3D Neumann Rayleigh integral towards its 2.5D representation (WFS 3D \rightarrow 2.5D) or the derivation from 2D towards the 2.5D case

<p>Point source with: circular (cf. Fig. 2.7a), linear SSD, reference point, secondary source selection WFS 3D \rightarrow 2.5D 1\times Far/HF: (2.137)</p>
<p>Point source with: linear SSD (cf. Fig. 2.7c), reference line SDM 1\times Far/HF: (2.126) SDM 2\times Far/HF: (2.131), (2.128) \equiv WFS 3D \rightarrow 2.5D 2\times Far/HF (Delft): (2.141)</p>
<p>Plane wave with: circular (cf. Fig. 2.7e), linear SSD, reference point, secondary source selection WFS 3D \rightarrow 2.5D 1\times Far/HF: (2.176), (2.177) \equiv WFS 2D \rightarrow 2.5D 1\times Far/HF (2.186)</p>
<p>Plane wave with: linear SSD (cf. Fig. 2.7g), reference line SDM Exact: (2.167) SDM 1\times Far/HF: (2.169), (2.170) \equiv WFS 3D \rightarrow 2.5D 2\times Far/HF: (2.183)</p>

Table 2.1: Discussed WFS and SDM driving functions and their connections for a virtual (non-focused) spherical and plane wave.

(WFS 2D \rightarrow 2.5D), as well as the explicit SDM solutions. Additionally the required farfield/high frequency approximations (\times Far/HF) are referenced. In Fig. 2.7 some example sound fields are depicted using the discussed 2.5D WFS driving functions.

For very large distances from a point source to the origin $r_{\text{PS}} = |\mathbf{0} - \mathbf{x}_{\text{PS}}|$ a point source at position $\mathbf{x}_{\text{PS}} = -r_{\text{PS}} \mathbf{n}_{\text{PW}}$ would render a sound field that is equal to a plane wave with propagating direction \mathbf{n}_{PW} . If the primary source level $P(\omega)$ of the plane/spherical wave is equally adapted for the reference line/point, the driving functions and resulting sound fields behave equivalent.

Furthermore, in this chapter the Fresnel (2.101), Fraunhofer (2.111) approximations and HF-BEM (2.33) was revisited that are deployed in the next chapters to predict and explain the radiation characteristics of straight and curved line source arrays.

In [Fir16] a unified WFS theory will be presented. This even more formalized treatise includes a consistent framework for analytical, new referencing schemes. The above discussed referencing schemes w.r.t. a point and a parallel reference line can then be interpreted as special schemes. From the findings it will become clear that referencing to a point is in fact a referencing along a parametric curve at which amplitude correct SFS occurs, of course within the limitations of the assumed approximations. Furthermore, the inconsistencies between the different WFS derivations (3D \rightarrow 2.5D vs. 2D \rightarrow 2.5D) are solved with proper treatment of the virtual source dimension mismatch within the unified framework.

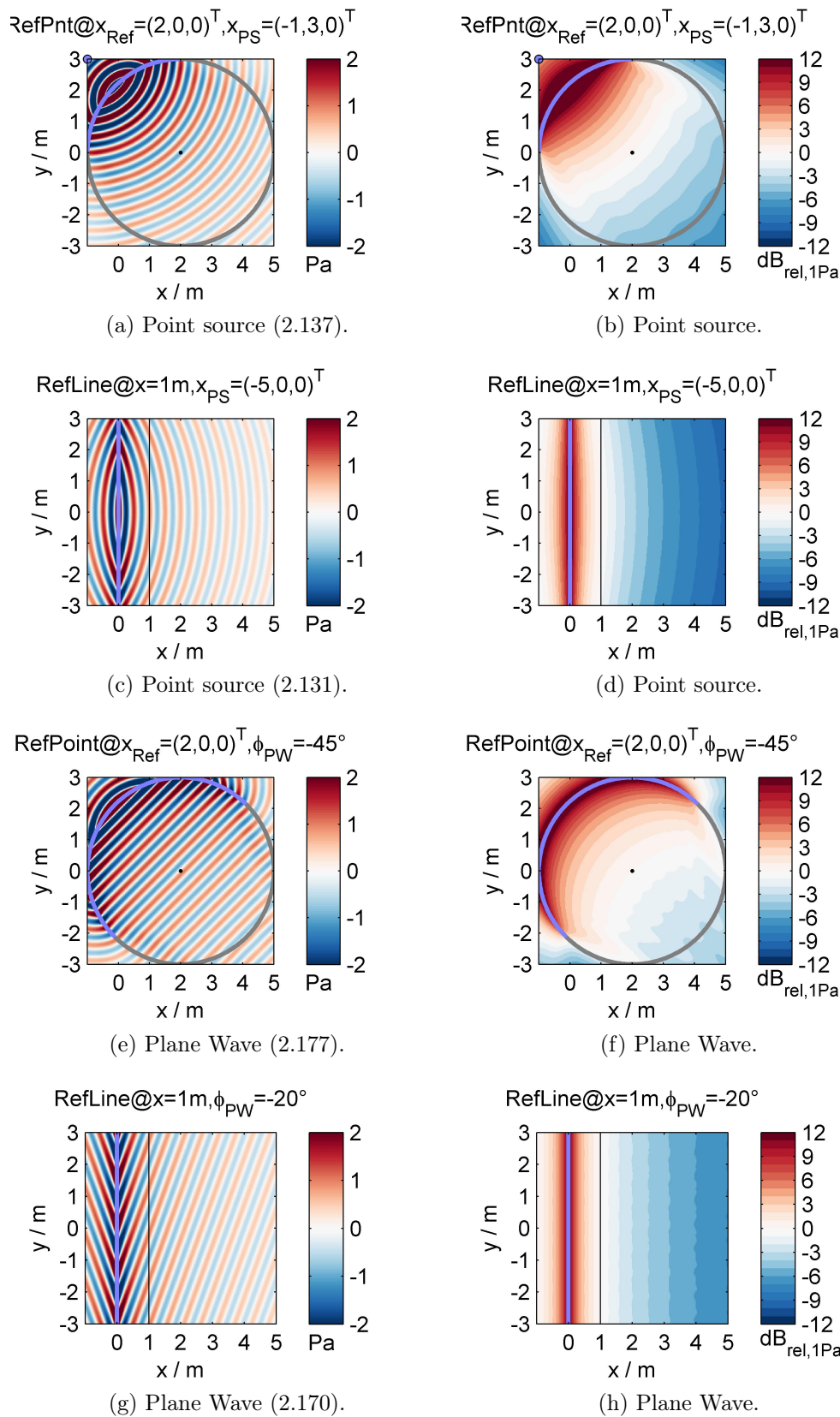


Figure 2.7: Sound fields of 2.5D WFS for a spherical or a plane wave using a circular or a linear SSD with indicated WFS driving functions, $c = 343 \text{ m/s}$, $f = 686 \text{ Hz} \rightarrow \lambda = 0.5 \text{ m}$ for 1 Pa amplitude at reference line or point.

Chapter 3

Discussion of WST

In this chapter¹ the Wavefront Sculpture Technology (WST) and its criteria [Hei92b, Urb03] for straight line source arrays are discussed. In essence, WST can be considered as a special case of sound field synthesis using a (i) rectangular windowed LSA, (ii) wave propagation perpendicular to the LSA (i.e. a broadband array) and (iii) different strategies to avoid or reduce spatial aliasing. An acoustic signal processing model that was developed for SFS [Sta97, Ver97] is utilized in this thesis in contrast to the initial formulations. Recall the synthesis integral (2.156)

$$P(\mathbf{x}, \omega) = \int_{-\infty}^{+\infty} D_{2.5D}(\mathbf{x}_0, \omega) G_{0,3D}(\mathbf{x}, \mathbf{x}_0, \omega) dy_0, \quad (3.1)$$

with the evaluation plane $\mathbf{x} = (x > 0, y, 0)^T$ and the LSA located on the y -axis, i.e. $\mathbf{x}_0 = (0, y_0, 0)^T$. This convolution integral can be conveniently discussed for discretized LSAs of finite length within the spatio-temporal spectrum domain in the same manner as the derivation of the explicit SFS solution, i.e. SDM. The acoustic signal processing framework is depicted in Fig. 3.1. It additionally includes a spatial sampling and truncation process compared to (3.1).

The discussion subsequently follows the different stages of the model in Fig. 3.1. At this point it is worth sending the implications of the physical LSA setup ahead, when exciting it with the driving functions and their spatio-temporal spectra listed in Table 3.1. The spatio-temporal spectra of the sound

¹[Sch14b],[Sch14a],[Sch15d],[Sch15c] are partly reissued herein.

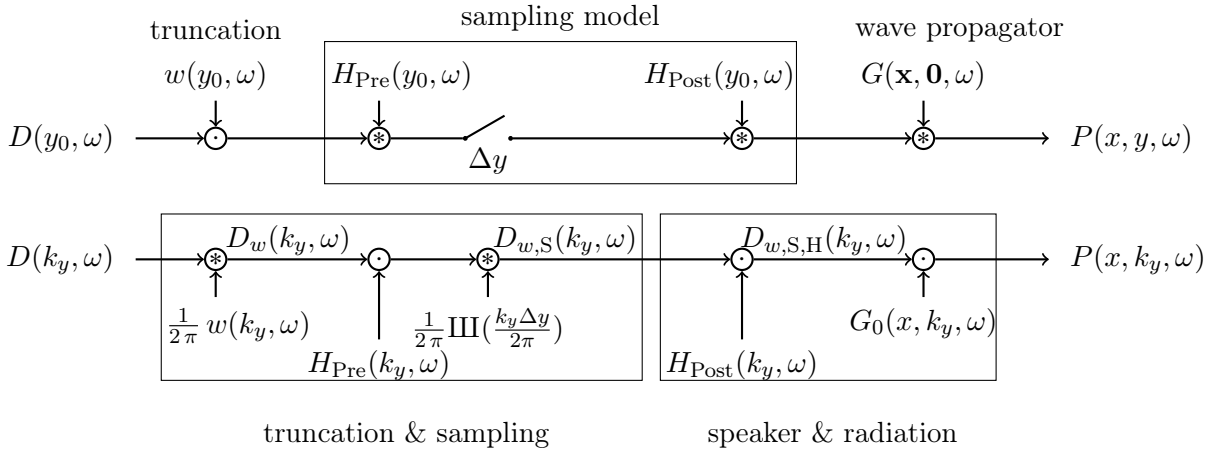


Figure 3.1: Signal processing model for SFS using a linear, spatially discretized and truncated SSD. Representation in temporal (top) and spatio-temporal spectrum domain (bottom), cf. [Sta97, Fig. 5.7], [Sta97, Fig. 5.13]. Linear convolution w.r.t. y , k_y is denoted by \otimes , multiplication w.r.t. y , k_y by \odot .

fields synthesized from the different LSA configurations are then given as

$$\begin{pmatrix} P(x, k_y, z, \omega) \\ P_S(x, k_y, z, \omega) \\ P_w(x, k_y, z, \omega) \\ P_{w,S}(x, k_y, z, \omega) \\ P_{w,S,H}(x, k_y, z, \omega) \end{pmatrix} = \begin{pmatrix} D(k_y, \omega) \\ D_S(k_y, \omega) \\ D_w(k_y, \omega) \\ D_{w,S}(k_y, \omega) \\ D_{w,S,H}(k_y, \omega) \end{pmatrix} \cdot G_0(x, k_y, z, \omega) \quad (3.2)$$

using the spectrum $G_0(x, k_y, z, \omega)$ of the 3D freefield Green's function (2.162). In case of spatial truncation, the spatio-temporal spectra $D_w(k_y, \omega)$, $D_{w,S}(k_y, \omega)$, $D_{w,S,H}(k_y, \omega)$ include the specific farfield radiation patterns of the LSA when evaluating only the *visible region* of the array (cf. p.78 for its definition).

$D(k_y, \omega)$ (3.25)	infinite, continuous LSA, driving functions for WFS & SDM
$D_S(k_y, \omega)$ (3.30)	infinite, discretized LSA built from spherical monopoles
$D_w(k_y, \omega)$ (3.38)	finite length, continuous LSA
$D_{w,S}(k_y, \omega)$ (3.68)	finite length, discretized LSA with spherical monopoles
$D_{w,S,H}(k_y, \omega)$	finite length, discretized LSA with identical non-isotropic sources

Table 3.1: Implications for the LSA setup according to Fig. 3.1 when being driven with the specified spatio-temporal spectra. References to the WST driving function equations are given.

3.1 Baseband Sampling

For the analytic description of arrays built from discrete loudspeakers, the continuous driving function is spatially sampled, here under the assumption of an equidistant sampling process. The well known critical baseband sampling of time domain signals [Uns00] is shortly revisited first to indicate the connections as well as different implications between temporal and spatial sampling.

A continuous time signal $x(t)$ is filtered with an anti-aliasing lowpass filter $h_{\text{LP,Pre}}(t)$ – creating a baseband signal – and then multiplied with an equidistantly 'spaced' Dirac comb

$$\underbrace{\sum_{\mu=-\infty}^{+\infty} \delta(t - \mu T_s)}_{=: \frac{1}{T_s} \text{III}\left(\frac{t}{T_s}\right)} \circ \bullet \underbrace{\frac{2\pi}{T_s} \sum_{\mu=-\infty}^{+\infty} \delta\left(\omega - \mu \frac{2\pi}{T_s}\right)}_{=: \text{III}\left(\frac{\omega T_s}{2\pi}\right)} \quad (3.3)$$

using the sample rate f_s , for which

$$f_s = \frac{1}{T_s} \quad \omega_s = 2\pi f_s = \frac{2\pi}{T_s} \quad (3.4)$$

holds. This yields a discrete-time signal $x_{\text{Pre,S}}(t)$. For reconstruction, the spectral repetitions in $X_{\text{Pre,S}}(\omega)$ due to (3.3) will be filtered out by the reconstruction/interpolation filter $h_{\text{LP,Post}}(t)$ yielding the continuous time signal $x_{\text{Rec}}(t)$. The sampling model is depicted in Fig. 3.2. In the temporal spectrum domain the signal processing is written as

$$X_{\text{Pre,S}}(\omega) = \frac{1}{2\pi} [X(\omega) \cdot H_{\text{LP,Pre}}(\omega)] *_\omega \text{III}\left(\frac{\omega T_s}{2\pi}\right), \quad (3.5)$$

$$X_{\text{Rec}}(\omega) = X_{\text{Pre,S}}(\omega) \cdot H_{\text{LP,Post}}(\omega). \quad (3.6)$$

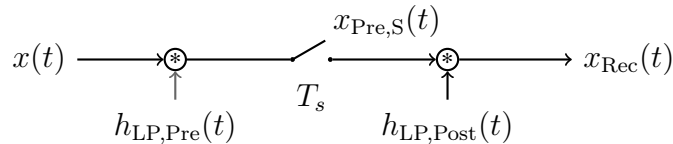


Figure 3.2: Time domain baseband sampling model.

Perfect baseband sampling and reconstruction is achieved using the cardinal sine function as the anti-aliasing and the reconstruction filter

$$h(t) = \text{si}\left(\frac{\pi t}{T_s}\right) \quad \circ \text{---} \bullet \quad H(\omega) = T_s \text{rect}\left(\frac{T_s \omega}{2\pi}\right) = T_s \text{rect}\left(\frac{\omega}{\omega_s}\right) \quad (3.7)$$

[Uns00, Fig. 2], [Opp10, Ch. 4.3], [Gir01, (11.35)] with

$$\text{si}(x) = \begin{cases} \frac{\sin x}{x} & \text{for } x \neq 0 \\ 1 & \text{for } x = 0 \end{cases} \quad \text{rect}(ax) = \begin{cases} 1 & \text{for } |x| \leq \frac{1}{2a} \\ 0 & \text{else} \end{cases}. \quad (3.8)$$

In this case of so called *critical sampling* [Gir01], the baseband $|\omega| \leq \frac{\omega_s}{2}$ of the signal $x(t)$ is perfectly reconstructed to $x_{\text{Rec}}(t)$, thus

$$X_{\text{Rec}}(|\omega| \leq \frac{\omega_s}{2}) = X(|\omega| \leq \frac{\omega_s}{2}), \quad (3.9)$$

which is well known as the Whittaker-Shannon-Kotelnikov sampling theorem [Kot33] (English reprint e.g. [Kot06]). The required cutoff frequencies for perfect critical sampling and reconstruction, i.e. the angular temporal frequency $\omega_N = \frac{\omega_s}{2}$ and temporal frequency $f_N = \frac{f_s}{2}$ are referred to as the Nyquist frequencies [Gir01, Opp10]. In case of non-ideal lowpass filters, different errors may occur, that are known as prealiasing and postaliasing:

- Ideal sampling, no pre- and postaliasing, perfect reconstruction

$$H_{\text{LP,Pre}}(\omega) = \begin{cases} T_s & \text{for } |\omega| \leq \frac{\omega_s}{2} \\ 0 & \text{else} \end{cases} \quad H_{\text{LP,Post}}(\omega) = \begin{cases} T_s & \text{for } |\omega| \leq \frac{\omega_s}{2} \\ 0 & \text{else} \end{cases} \quad (3.10)$$

- Ideal sampling, no prealiasing, but postaliasing, i.e. the baseband is not corrupted, but spectral repetitions are not perfectly suppressed, typically referred to as reconstruction error

$$H_{\text{LP,Pre}}(\omega) = \begin{cases} T_s & \text{for } |\omega| \leq \frac{\omega_s}{2} \\ 0 & \text{else} \end{cases} \quad H_{\text{LP,Post}}(\omega) = \begin{cases} T_s & \text{for } |\omega| \leq \frac{\omega_s}{2} \\ \neq 0 & \text{for } |\omega| > \frac{\omega_s}{2} \end{cases} \quad (3.11)$$

- Ideal sampling, prealiasing, but no postaliasing, i.e. spectral repetitions are perfectly suppressed but baseband is unrecoverably corrupted, due to overlapping spectral repetitions

$$H_{\text{LP,Pre}}(\omega) = \begin{cases} T_s & \text{for } |\omega| \leq \frac{\omega_s}{2} \\ \neq 0 & \text{for } |\omega| > \frac{\omega_s}{2} \end{cases} \quad H_{\text{LP,Post}}(\omega) = \begin{cases} T_s & \text{for } |\omega| \leq \frac{\omega_s}{2} \\ 0 & \text{else} \end{cases} \quad (3.12)$$

- Ideal sampling, pre- and postaliasing, i.e. the baseband is corrupted and spectral repetitions are not perfectly suppressed

$$H_{\text{LP,Pre}}(\omega) = \begin{cases} T_s & \text{for } |\omega| \leq \frac{\omega_s}{2} \\ \neq 0 & \text{for } |\omega| > \frac{\omega_s}{2} \end{cases} \quad H_{\text{LP,Post}}(\omega) = \begin{cases} T_s & \text{for } |\omega| \leq \frac{\omega_s}{2} \\ \neq 0 & \text{for } |\omega| > \frac{\omega_s}{2} \end{cases} \quad (3.13)$$

The ideal lowpass characteristic of the anti-aliasing and the reconstruction filter have to be approximated with a suitable infinite or finite impulse response by accepting a tolerated error. For time domain signal sampling, the anti-aliasing and the reconstruction filters can be designed with large degree of freedom in analog-to-digital and digital-to-analog converters. This in contrast to the sampling process for the spatial domain, to be discussed next.

Recall, that the synthesis integral (3.1) is given as, cf. (2.159)

$$P(x, k_y, z, \omega) = D(k_y, \omega) \cdot G_0(x, k_y, z, \omega) \quad (3.14)$$

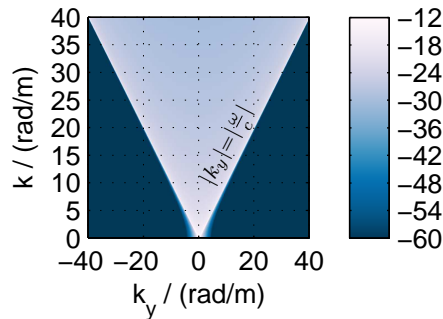


Figure 3.3: $20 \log_{10}(|G_0(x, k_y, z, \omega)|)$ in dB (2.162) for $x = 1$ m and $z = 0$ m. Levels > -12 dB clipped to white, levels < -60 dB clipped to black, $k = \frac{\omega}{c}$.

in the spatio-temporal spectrum domain. The spatio-temporal spectrum of $G_0(x = 1, k_y, z = 0, \omega)$ (2.162) is exemplarily depicted in Fig. 3.3. The spectrum $G_0(x, k_y, z, \omega)$ is not strictly spatially bandlimited. However, according to (2.162), the propagating part of $G_0(x, k_y, z, \omega)$ is bounded and thus bandlimited to the wedge where $|k_y| < |\frac{\omega}{c}|$. This is referred to as the *visible range* [IEE93], *visible region* [Van02, Ch. 2.3] or *physical region* [Hei92b] of the array. Evanescent wave radiation occurs for $|k_y| > |\frac{\omega}{c}|$, this part of the spectrum is not bandlimited. However, it is decaying rapidly for increasing x, z and ω . The spectrum of $G_0(x, k_y, z, \omega)$ exhibits a pole for $|k_y| = |\frac{\omega}{c}|$. In the remainder only the xy -plane is considered for sound reinforcement, thus setting $z = 0$ and thereby ignoring the horizontal radiation characteristics of an LSA.

A potential driving function may trigger parts of the visible region for an intended propagating wave radiation. Note that the driving function may also exhibit evanescent parts, that are also not strictly bandlimited. This is for example the case for driving functions that are used for the SFS of virtual point sources [Spo09, Spo10].

Spatial discretization of the driving function with the sampling distance Δy leads to the spatial sampling rate

$$k_{y,s} = \frac{2\pi}{\Delta y} = \Delta k_y \quad (3.15)$$

and the spatial Nyquist wave number

$$k_{y,N} = \frac{\pi}{\Delta y}. \quad (3.16)$$

Similar to time domain signal processing, the prefilter $H_{\text{Pre}}(y_0, \omega)$ and the postfilter $H_{\text{Post}}(y_0, \omega)$ in Fig. 3.1 are also understood as the anti-aliasing and the reconstruction filters respectively. For ideal critical sampling both exhibit ideal spatial lowpass characteristic

$$h(y_0) = \text{si}\left(\frac{\pi y_0}{\Delta y}\right) \quad \circ \text{---} \bullet \quad H(k_y) = \Delta y \text{rect}\left(\frac{\Delta y k_y}{2\pi}\right) = \Delta y \text{rect}\left(\frac{k_y}{k_{y,s}}\right). \quad (3.17)$$

Prior to sampling the driving function, $H_{\text{Pre}}(k_y, \omega)$ must ideally suppress all contributions for $|k_y| > \frac{\pi}{\Delta y}$ (i.e. 'above' the Nyquist wave number $k_{y,N}$)

ensuring a correctly sampled baseband. Subsequently, the ideal postfilter $H_{\text{Post}}(k_y, \omega)$ removes all spectral repetitions for baseband reconstruction.

It is important realizing, that the postfilter acts in the acoustic domain, i.e. is determined by the radiation characteristics of the loudspeaker. Once the driving function is physically sampled – modeling discrete loudspeaker positions – manipulation of the driving function is not longer possible in the electronic domain, cf. [Sta97, Ch. 5.4]. The design of appropriate postfilter characteristics is thus more demanding than for time domain signal processing, since it must be realized in the acoustic domain. The infinite impulse response (3.17) cannot be realized in practice, since it corresponds to a source of infinite extent. Hence, the approach of the anti-aliasing loudspeaker [Ahr10c] is of theoretical interest. Other suitable, however, non-ideal postfilter characteristics have to be found, that are obliged to have FIR characteristics, i.e. require finite spatial dimension of loudspeakers not larger than Δy for feasibility, cf. [Ver97, Ch. 3.3]

The signal processing in the spatio-temporal spectrum domain is similar to that for time signals in the temporal spectrum domain (3.5)

$$D_S(k_y, \omega) = \frac{1}{2\pi} \left[D(k_y, \omega) *_{k_y} \text{III}\left(\frac{k_y \Delta y}{2\pi}\right) \right] \quad \text{only sampling} \quad (3.18)$$

$$D_{\text{Rec}}(k_y, \omega) = \left[\frac{1}{2\pi} [D(k_y, \omega) \cdot H_{\text{Pre}}(k_y, \omega)] *_{k_y} \text{III}\left(\frac{k_y \Delta y}{2\pi}\right) \right] \cdot H_{\text{Post}}(k_y, \omega), \quad (3.19)$$

and will be revisited in Ch. 3.2.2ff. in detail. As for time domain signal processing, artifacts due to a non-ideal prefilter have been termed *aliasing error* or *prealiasing*, those due to the postfiltering stage *reconstruction error* or *postaliasing* [Mit88]. In SFS literature the different spatial aliasing types are typically not strictly separated in terminology and *spatial aliasing* is used to subsume all artifacts. However, according to [Spo09] spatial aliasing has (i) propagating contributions, that arise by the propagating contribution of $G_0(x, k_y, \omega)$ in conjunction with the propagating and evanescent contributions of $D_S(k_y, \omega)$ and (ii) evanescent contributions, that arise by the evanescent contribution of $G_0(x, k_y, \omega)$ in conjunction with the propagating and evanescent contributions of $D_S(k_y, \omega)$. These contributions can be additionally classified

into pre- and postaliasing contributions and are summarized in the tables 3.2 to 3.5. In the context of WFS and SDM theoretical and practical spatial pre- and postfiltering schemes were discussed in [Sta95, Ahr10c, Fir12], [Ver97, Ch. 3].

Aliasing type	Region of G	Region of D , $\mu \neq 0$
Prop. Pre \triangle $ k_y < \frac{\pi}{\Delta y}$	$ k_y < \left \frac{\omega}{c}\right $	$ k_y - \mu \frac{2\pi}{\Delta y} < \left \frac{\omega}{c}\right $
Prop. Post \blacktriangle $ k_y > \frac{\pi}{\Delta y}$	$ k_y < \left \frac{\omega}{c}\right $	$ k_y - \mu \frac{2\pi}{\Delta y} < \left \frac{\omega}{c}\right $

Table 3.2: Propagating pre- and postaliasing due to propagating D and propagating G , cf. Fig. 3.5.

Aliasing type	Region of G	Region of D , $\mu \neq 0$
Ev. Pre ∇ $ k_y < \frac{\pi}{\Delta y}$	$ k_y > \left \frac{\omega}{c}\right $	$ k_y - \mu \frac{2\pi}{\Delta y} < \left \frac{\omega}{c}\right $
Ev. Post \blacktriangledown $ k_y > \frac{\pi}{\Delta y}$	$ k_y > \left \frac{\omega}{c}\right $	$ k_y - \mu \frac{2\pi}{\Delta y} < \left \frac{\omega}{c}\right $

Table 3.3: Evanescent postaliasing due to propagating D and evanescent G , cf. Fig. 3.5. Evanescent prealiasing is not occurring due to bounded D .

Aliasing type	Region of G	Region of D , $\mu \neq 0$
Prop. Pre \triangle $ k_y < \frac{\pi}{\Delta y}$	$ k_y < \left \frac{\omega}{c}\right $	$ k_y - \mu \frac{2\pi}{\Delta y} > \left \frac{\omega}{c}\right $
Prop. Post \blacktriangle $ k_y > \frac{\pi}{\Delta y}$	$ k_y < \left \frac{\omega}{c}\right $	$ k_y - \mu \frac{2\pi}{\Delta y} > \left \frac{\omega}{c}\right $

Table 3.4: Propagating pre- and postaliasing due to evanescent D and propagating G , cf. Fig. 3.6.

Aliasing type	Region of G	Region of D , $\mu \neq 0$
Ev. Pre ∇ $ k_y < \frac{\pi}{\Delta y}$	$ k_y > \left \frac{\omega}{c}\right $	$ k_y - \mu \frac{2\pi}{\Delta y} > \left \frac{\omega}{c}\right $
Ev. Post \blacktriangledown $ k_y > \frac{\pi}{\Delta y}$	$ k_y > \left \frac{\omega}{c}\right $	$ k_y - \mu \frac{2\pi}{\Delta y} > \left \frac{\omega}{c}\right $

Table 3.5: Evanescent pre- and postaliasing due to evanescent D and evanescent G , cf. Fig. 3.6.

Following the signal processing model in Fig. 3.1, the anti-aliasing filtering, sampling and reconstruction for an infinite linear array can be qualitatively interpreted with spatio-temporal spectra that exhibit a wedge shape, considering the propagating parts, and indicating the remaining evanescent area as shown in Fig. 3.4. The schematic driving function triggers the whole visible region $|k_y| < \left|\frac{\omega}{c}\right|$ as well as the evanescent region $|k_y| > \left|\frac{\omega}{c}\right|$. It can be seen in

Fig. 3.1, that the spectra $H_{\text{Post}}(k_y, \omega)$ and $G_0(x, k_y, \omega)$ act as interpolators for the sampled driving function, whereby the Green's function is simultaneously responsible for wave radiation. Hence, the left plots in Fig. 3.4 schematically represent the anti-aliasing filtering and sampling stage of the driving function and the right plots its reconstruction and the wave propagation.

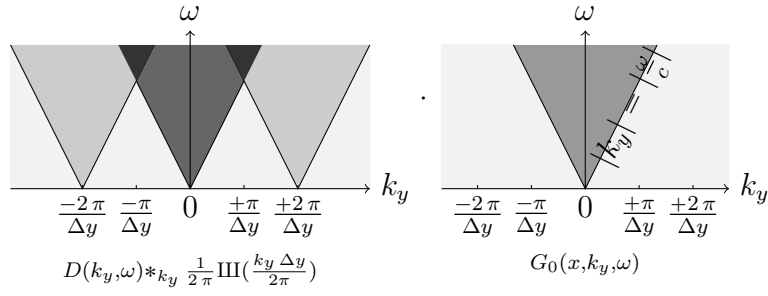
In Fig. 3.4a no pre- and postfilters are applied. The spectral repetitions overlap into the baseband of $D(k_y, \omega)$, thus corrupting it, which leads to prealiasing. Due to the spatially fullband interpolation with $G_0(k_y, \omega)$ also postaliasing occurs. This is typical for WFS applications where a spatially not bandlimited driving function controls point source-like loudspeakers.

In Fig. 3.4b the driving function is perfectly bandlimited to the Nyquist wave number, i.e. no prealiasing. No further postfilter is applied. Thus, the spectral repetitions are not perfectly suppressed by $G_0(k_y, \omega)$, i.e. postaliasing. This technique is known as modal bandlimited SFS, e.g. used for NFC-HOA [Spo08a, Ahr08a] and for WFS [Sta95].

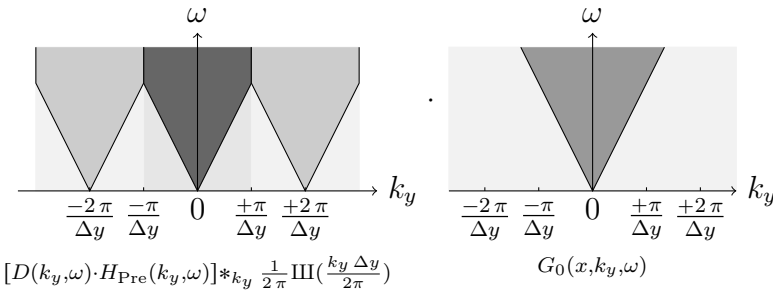
In Fig. 3.4c no prefilter is applied, leading to prealiasing. The ideal lowpass postfilter suppresses all spectral repetitions, i.e. no postaliasing. In essence this approach is used for LSA applications, however deploying non-ideal lowpass filters. The non-ideal spatial lowpass characteristic of highly directed loudspeakers (waveguides) is employed to avoid or attenuate postaliasing.

In Fig. 3.4d the ideal, critical sampling model is depicted. The spatial lowpass filters $H_{\text{Pre}}(k_y, \omega)$ and $H_{\text{Post}}(k_y, \omega)$ have ideal characteristics with the Nyquist wave number as cutoff 'frequency'. No pre- and postaliasing occurs.

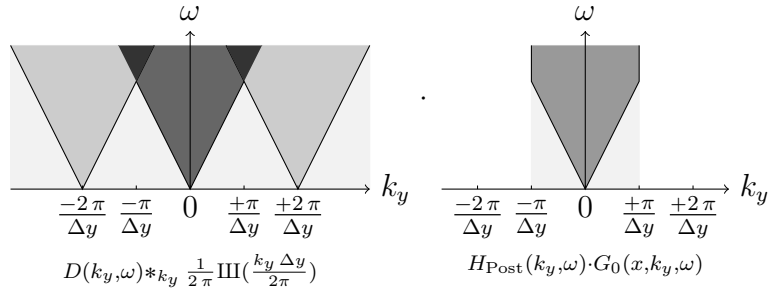
To give a further qualitative discussion of the different pre-/postaliasing artifacts according to Table 3.2 and Table 3.3, the sampling of a purely propagating driving function's spectrum is depicted in Fig. 3.5. Similarly, according to Table 3.3 and Table 3.4 a purely evanescent driving function's spectrum is considered in Fig. 3.6. These graphics indicate the possible aliasing contributions: propagating prealiasing \triangle , propagating postaliasing \blacktriangle , evanescent prealiasing ∇ and evanescent postaliasing \blacktriangledown . Note that the case *evanescent prealiasing* in Table 3.3 can never occur, due to contra-directional constraints, that cannot met with a propagating driving function's spectrum. The spectral repetitions in the schematic sketches intentionally do not overlap for convenient clarification of the specified aliasing regions.



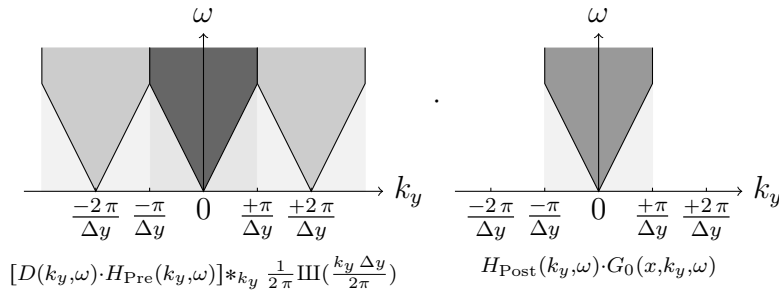
(a) Pre-/postaliasing. Fullband SFS (e.g. traditional WFS).



(b) No prealiasing, postaliasing. Bandlimited SFS (e.g. NFC-HOA).

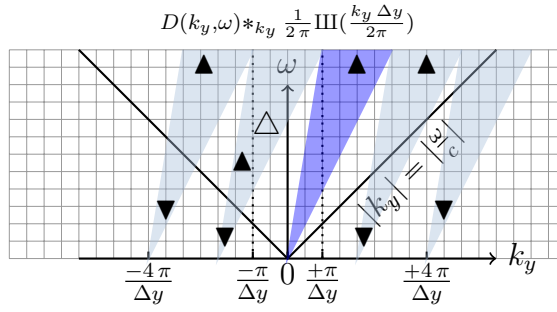


(c) Prealiasing, no postaliasing. Ideal LSA waveguide application.

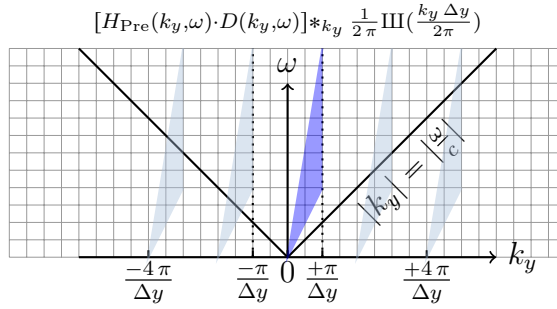


(d) No pre- and postaliasing. Ideal, critical sampling model.

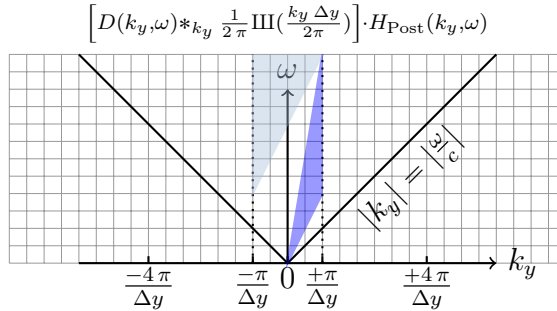
Figure 3.4: Sampling strategies for SFS applications with qualitative representations of the spatio-temporal spectra.



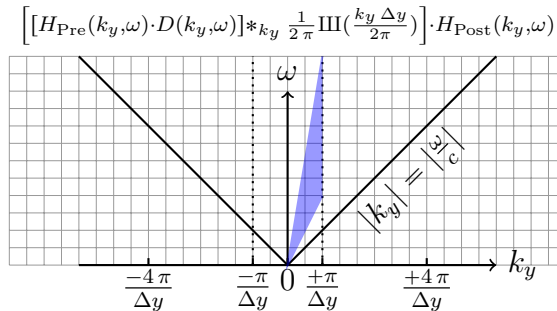
(a) Pre-/postaliasing: propagating pre Δ , propagating post \blacktriangle , evanescent post \blacktriangledown .



(b) No prealiasing, postaliasing.

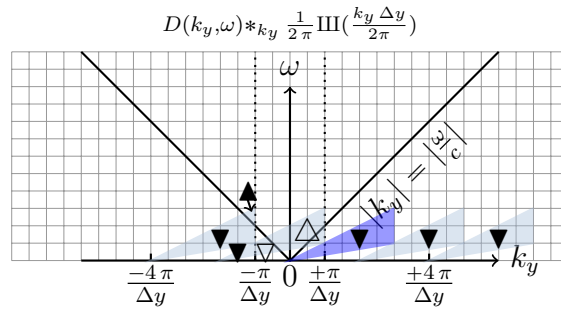


(c) Prealiasing, no postaliasing.

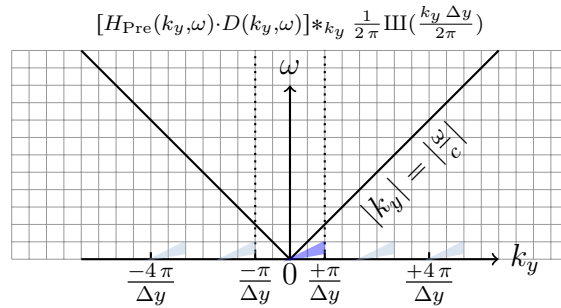


(d) No pre- and postaliasing.

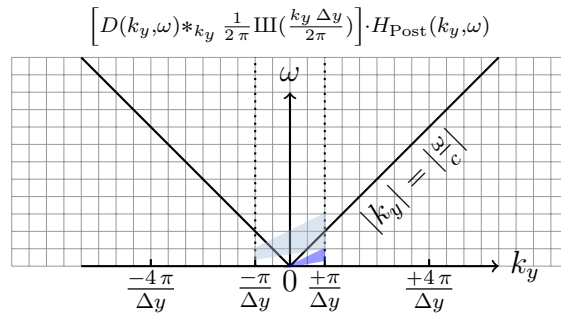
Figure 3.5: Spatial sampling of a purely propagating driving function.



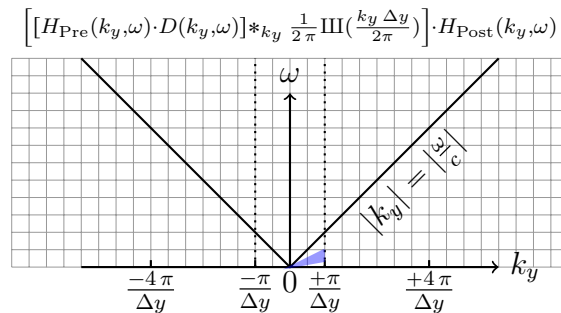
(a) Pre-/postaliasing: propagating pre Δ , propagating post \blacktriangle , evanescent pre ∇ , evanescent post \blacktriangledown .



(b) No prealiasing, postaliasing (only evanescent).



(c) Prealiasing, no postaliasing.



(d) No pre- and postaliasing.

Figure 3.6: Spatial sampling of a purely evanescent driving function.

3.2 WST Driving Functions

In essence, the first three WST criteria [Urb03] deal with the avoidance and/or attenuation of propagating postaliasing using different strategies. The WST criteria were initially derived for uniformly driven, i.e. uniformly weighted LSAs, more precisely for constant volume acceleration [Hei92b, p.2]. This results in broadband wave propagation perpendicular to the LSA in the xy -plane under discussion. The driving functions under discussion are introduced next.

The findings are well known from array processing and antenna theory [Sch43, Van02, Ell03, Bal05] and became introduced into acoustics with [Ste27, Ste29, Wol30, Ste58]. However, the existing literature on LSA radiation rarely provides a consistent link to the concepts of multidimensional signal processing and its equivalent implications [Sch15c] to sound field and radiation synthesis fundamentals. Since the discussion on LSA radiation goes beyond the characteristics of farfield radiation patterns and since the original WST literature rarely uses signal processing concepts, it is meaningful to elaborate this in-depth in this section.

3.2.1 Infinite, Continuous SSD $D(k_y, \omega)$

At first, an infinite, continuous SSD is considered, for which the signal flow of Fig. 3.7 holds. The spatio-temporal spectrum of the SDM plane wave driving function (2.166) is used and modified towards the special problem of interest: $k_{y,\text{PW}} = 0$ is chosen, i.e. $\varphi_{\text{PW}} = 0$ from which $k_{r,\text{PW}} = \frac{\omega}{c}$ follows. The adapted driving function's spatio-temporal spectrum reads

$$D(x_{\text{ref}}, k_y, \omega) = \frac{P(\omega) \cdot e^{-j \frac{\omega}{c} \cdot x_{\text{ref}}}}{-\frac{j}{4} H_0^{(2)}\left(\frac{\omega}{c} \cdot x_{\text{ref}}\right)} 2 \pi \delta(k_y) \quad (3.20)$$

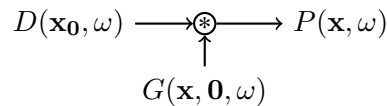


Figure 3.7: Signal flow of the single layer potential for a linear, infinite, continuous SSD located on the y -axis.

For $\frac{\omega}{c} \cdot x_{\text{ref}} \gg 1$ the large argument approximation of the Hankel function [Olv10, 10.2.6] leads to the proportionality

$$\left| \frac{1}{-\frac{j}{4} H_0^{(2)}\left(\frac{\omega}{c} \cdot x_{\text{ref}}\right)} \right| \propto \sqrt{\frac{\omega}{c} \cdot x_{\text{ref}}}. \quad (3.21)$$

Hence, the driving function (3.20) inherently includes a 3 dB/oct. temporal frequency highpass filter for the case of interest. For further discussion the compensation filter (3.21) and the phase shift $e^{-j\frac{\omega}{c} \cdot x_{\text{ref}}}$ in (3.20) is omitted for concise argumentation. The spectrum is thus restricted to

$$D(k_y, \omega) = P(\omega) \cdot 2\pi \delta(k_y), \quad (3.22)$$

which is depicted in Fig. 3.8a and yields the driving function

$$D(y_0, \omega) = P(\omega) \quad (3.23)$$

by inverse spatial Fourier transform. Inserting (3.22) into (3.14) and a subsequent spatial Fourier transform yields

$$P(x, y, \omega) = -\frac{j}{4} H_0^{(2)}\left(\frac{\omega}{c} x\right) \cdot P(\omega), \quad (3.24)$$

which is identified as the sound field of an infinite, continuous line source driven with constant volume acceleration, that produces a wavefront with a 3 dB/oct. temporal lowpass behavior and a 3 dB level loss per distance doubling in the farfield, cf. [Lip86, pg. 12]. In essence the here omitted 3 dB/oct. highpass (3.21) compensates the temporal frequency lowpass characteristic of the line source. In practical LSA applications this filter is applied with slight modifications and is referred to as the coupling filter, cf. Ch. 4, [Sch13]. Note that (2.162) represents a diverging cylindrical wave in the farfield of the source for the radial distance $r = \sqrt{x^2 + z^2}$, when driven with the 0th mode $k_y = 0$, cf. [Sku71, p.656]. For $k_y \neq 0$ (2.162) represents diverging conical wavefronts, cf. Ch. 2.4. Although the plane under discussion is the xy -plane only (i.e. $z = 0$), the term *cylindrical wave* is maintained below for the wavefronts emanated by $G_0(x, k_y, \omega)$, for simplified denotation of waves with a 3 dB level decay per distance doubling.

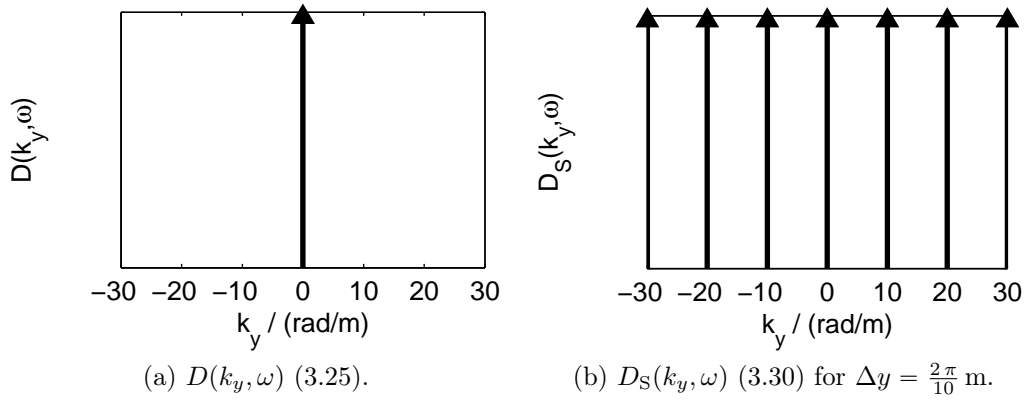


Figure 3.8: Spatio-temporal spectra of WST driving functions.

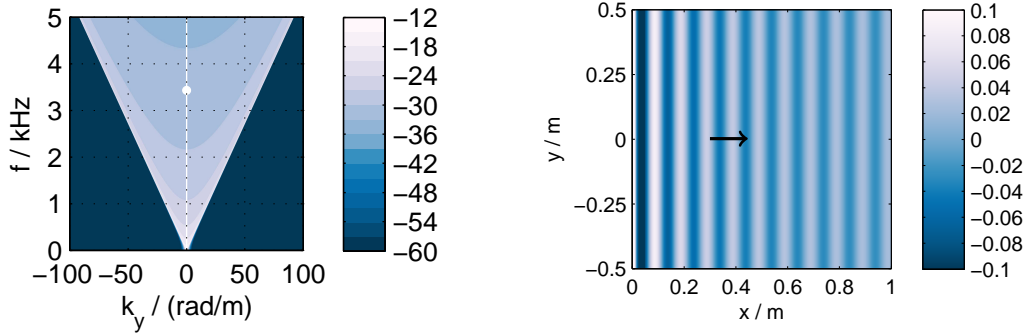


Figure 3.9: Sound field synthesis for an infinite, continuous linear array.

For a full audio-bandwidth wavefront into x -direction, $D(k_y, \omega)$ takes the shape of a vertical line as schematically depicted in Fig. 3.9a. Each 'point' of $D(k_y, \omega)$ coincident with the bounded propagating part $|k_y| < \frac{\omega}{c}$ of $G_0(k_y, \omega)$ corresponds to a propagating monochromatic cylindrical wave, as exemplarily shown for a single frequency in Fig. 3.9b. The synthesized wave exhibits a 3 dB level decay per distance doubling as expected. In Fig. 3.9a the -3 dB/oct. temporal lowpass characteristic of $G_0(x, k_y, \omega)$ along $k_y = 0$ can be observed.

In the remainder in all driving functions and their spectra $P(\omega) = 1$, thus

(3.22) is used as

$$D(k_y, \omega) = 2\pi \delta(k_y) \quad (3.25)$$

for further discussion, depicted in Fig. 3.8a. Note that (3.25) does not require a prefilter in the sampling model, since it is already perfectly bandlimited w.r.t. the spatial Nyquist wave number. Actually all WST driving functions under discussion omit the prefiltering stage in the original WST literature [Hei92b, Urb03], and hence also will be omitted here for better comparison of the derived results. A discussion on the physical implications of spatial prefiltering is found in [Sta97, Ch. 5.4].

3.2.2 Spatial Discretization $D_S(k_y, \omega)$

Obviously, a continuous SSD cannot be realized in practice and is usually implemented as a linear array of discrete loudspeakers. This constitutes the spatial discretization process of the driving function as depicted in Fig. 3.10. It models an infinite, discretized LSA built from spherical monopoles by ignoring pre- and postfiltering. Assuming identical ideal point sources, equidistantly arranged with Δy , as depicted in Fig. 3.11, ideal spatial sampling is modeled by multiplication with an accordingly spaced Dirac comb. The discretized driving function $D_S(y_0, \omega)$ then reads

$$D_S(y_0, \omega) = D(y_0, \omega) \cdot \underbrace{\sum_{\mu=-\infty}^{+\infty} \delta(y_0 - \mu \Delta y)}_{=: \frac{1}{\Delta y} \text{III}(\frac{y_0}{\Delta y})}, \quad (3.26)$$

where the shorthand notation is obtained by dilating a Dirac comb $\text{III}(y_0) := \sum_{\mu=-\infty}^{+\infty} \delta(y_0 - \mu)$ [Gir01, (11.1)] with unit spacing. The spatial Fourier trans-

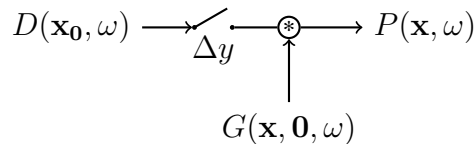


Figure 3.10: Signal flow of the single layer potential for a linear, infinite, discretized SSD located on the y -axis.

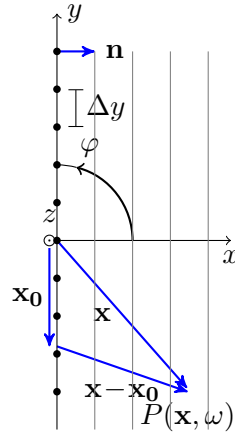


Figure 3.11: Side view of the discretized SSD setup. The infinite SSD is located on the y -axis. SFS is considered within the xy -plane ($x > 0$). The SSD becomes continuous for a secondary source spacing $\Delta y \rightarrow 0$.

form pair for the Dirac comb (3.26) is known as, cf. (3.3)

$$\underbrace{\sum_{\mu=-\infty}^{+\infty} \delta(y_0 - \mu \Delta y)}_{=: \frac{1}{\Delta y} \text{III}\left(\frac{y_0}{\Delta y}\right)} \circ \bullet \underbrace{\frac{2\pi}{\Delta y} \sum_{\mu=-\infty}^{+\infty} \delta\left(k_y - \mu \frac{2\pi}{\Delta y}\right)}_{=: \text{III}\left(\frac{k_y \Delta y}{2\pi}\right)}. \quad (3.27)$$

The multiplication/convolution duality of the Fourier transform [Gir01, (11.33)]

$$D(y_0, \omega) \cdot \frac{1}{\Delta y} \text{III}\left(\frac{y_0}{\Delta y}\right) \circ \bullet \frac{1}{2\pi} \left[D(k_y, \omega) *_{k_y} \text{III}\left(\frac{k_y \Delta y}{2\pi}\right) \right] \quad (3.28)$$

leads to the spatio-temporal spectrum of the ideally sampled driving function

$$D_S(k_y, \omega) = \frac{1}{\Delta y} \sum_{\mu=-\infty}^{+\infty} D\left(k_y - \mu \frac{2\pi}{\Delta y}, \omega\right). \quad (3.29)$$

For the problem at hand, the sampled version of (3.25)

$$D_S(k_y, \omega) = \frac{2\pi}{\Delta y} \sum_{\mu=-\infty}^{+\infty} \delta\left(k_y - \mu \frac{2\pi}{\Delta y}\right) \quad (3.30)$$

is to be discussed, exemplarily visualized in Fig. 3.8b for $\Delta y = \frac{2\pi}{10}$ m.

In Fig. 3.12 $D_S(k_y, \omega)$ (3.30) is schematically given for the spatial sampling frequency $k_{y,s} = \Delta k_y = 25$ rad/m, which yields the discretization step

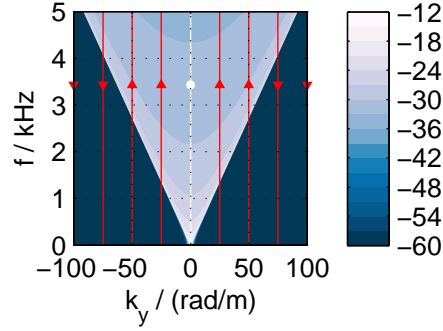


Figure 3.12: $|G_0(x, k_y, \omega)|$ in dB (2.162) for $x = 1$ m. Sampled driving function $D_S(k_y, \omega)$ (3.30) for a full-band cylindrical wave into x -direction schematically indicated with a white line. The white dot indicates the contribution for $f = 3430$ Hz. Spectral repetitions indicated with red lines. The red markers \blacktriangle indicate propagating spatial postaliasing for $f = 3430$ Hz, whereas these marked with \blacktriangledown indicate evanescent spatial postaliasing.

$\Delta y = \frac{2\pi}{25}$ m ≈ 0.25 m. Compared to Fig. 3.9a the additional repetitions in the spatio-temporal spectrum stemming from the Dirac comb are clearly indicated. Their coincidences with values of the Green's function $G_0(x, k_y, \omega)$ within the visible region $|\mu \Delta k_y| < |\frac{\omega}{c}|$, $\mu \neq 0$ indicate additional propagating contributions in the synthesized sound field, which are identified as propagating spatial postaliasing, cf. Table 3.2. The coincidences with the evanescent region of the Green's function $|\mu \Delta k_y| > |\frac{\omega}{c}|$ result in evanescent postaliasing, cf. Table 3.3. Due to the bandlimited spatio-temporal spectrum of $D(k_y, \omega)$, the sampled spectrum $D_S(k_y, \omega)$ does not contain contributions that can trigger prealiasing.

The resulting sound field can be analytically given (cf. [Ahr10d, Sec. IV.B]), when the spectrum

$$P(x, k_y, \omega) = D_S(k_y, \omega) \cdot G_0(x, k_y, \omega) \quad (3.31)$$

for the considered xy -half plane undergoes an inverse spatial Fourier transform (C.3) with subsequent simplification. This yields [Ahr10d, (37)]

$$P(x, y, \omega) = \frac{1}{\Delta y} \sum_{\mu=-\infty}^{+\infty} G_0(x, k_y = \mu \frac{2\pi}{\Delta y}, \omega) e^{-j\mu \frac{2\pi}{\Delta y} y}. \quad (3.32)$$

The exponential term in (3.32) describes the sound field component along the

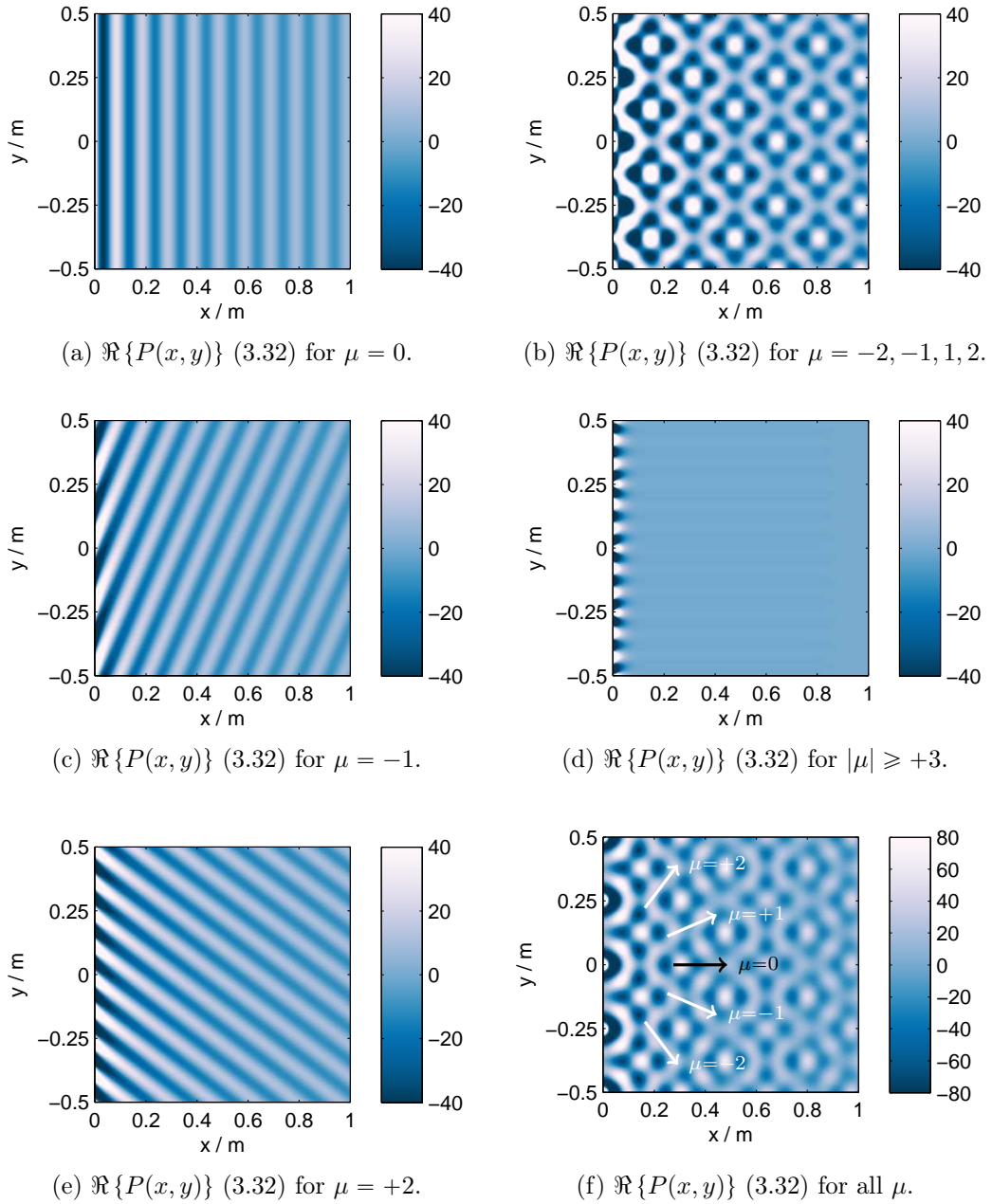


Figure 3.13: Infinite, discretized SSD with $\Delta y = \frac{2\pi}{25}$ m. Synthesized sound fields for $f = 3430$ Hz, i.e. $\lambda = 0.1$ m. Fig. 3.13a shows the intended wavefront, Fig. 3.13b all propagating spatial postaliasing contributions, Fig. 3.13d evanescent spatial postaliasing contributions, Fig. 3.13f the resulting sound field due to superposition (3.32).

y -dimension. Note the discrete set of possible wave numbers due to the discrete driving function's spatio-temporal spectrum. The Green's function's spatio-temporal spectrum describes the component into radial direction. Both compo-

nents together describe a cylindrical wave with radiation angle φ_μ for propagating waves that are given with $|\mu \Delta k_y| < |\frac{\omega}{c}|$. Then $\sin \varphi_\mu = (\mu \Delta k_y)/\frac{\omega}{c}$ holds. For $\mu = 0$ the intended cylindrical wave perpendicular to the SSD (i.e. into x -direction, $\varphi_{\mu=0} = 0$) is generated, cf. Fig. 3.13a. The radiating angles $\varphi_{\mu \neq 0}$ of the additional propagating spatial postaliasing wavefronts are strongly dependent on the temporal angular frequency ω . For the given example in Fig. 3.12 the additional cylindrical waves are derived to $\varphi_{\mu=\pm 1,2} = \pm 23.4^\circ, \pm 52.7^\circ$. Single propagating contributions for $\mu = -1$ and $\mu = +2$ are depicted in Fig. 3.13c and Fig. 3.13e, respectively. The sound field given by the superposition of propagating contributions $|\mu| \leq 2, \mu \neq 0$ is shown in Fig. 3.13b, these for the evanescent contributions $|\mu| \geq 3$ in Fig. 3.13d. The originally intended wavefront $\mu = 0$ is thus corrupted by interferences with the additional wavefronts due to superposition (3.32). The resulting sound field is shown in Fig. 3.13f. Note that Fig. 3.9b and Fig. 3.13f exhibit a level difference by $\frac{1}{\Delta y}$, which is due to the ideal sampling model. The appropriate ideal postfilter – here not applied – compensates this level difference according to the chosen sampling model normalization.

The exemplarily chosen SSD discretization does not allow the synthesis of a homogeneous wavefront for this frequency. It is important realizing that the sound field remains corrupted over the full space when performing SFS with an infinite SSD. This is in contrast to finite length, straight SSDs, where a spatial aliasing free region exists in far distances to the SSD.

In [Hei92b, II.3.a.] a similar discussion was given using the 2D freefield Green's function (2.8). Therein, a sound field that is corrupted by spatial aliasing, was named *chaotic*, which is a deterministic phenomenon due to (3.32). Referring to as *chaotic regions* in sound fields due to spatial aliasing interference should be actually avoided but will retained throughout the thesis as a simplified designation.

A criterion for avoidance of propagating postaliasing can be geometrically derived and is well known as [Kum92, (13)], [Ahr10d, (38)]

$$f < \frac{c}{\Delta y (1 + |\sin \varphi_{PW}|)}, \quad (3.33)$$

indicating the plane wave radiation angle φ_{PW} . For the WST driving function with $\varphi_{\text{PW}} = 0$, (3.33) reduces to (cf. [Hei92b, sec. II.3.a])

$$f < \frac{c}{\Delta y} \leftrightarrow \Delta y < \lambda, \quad (3.34)$$

denoting the wave length λ in m. Thus, for an infinite, discretized SSD built from monopoles (i.e. no postfilter is applied) postaliasing can only be avoided by limiting the temporal frequency bandwidth of the driving function (3.30) with an appropriate choice of $P(\omega)$.

3.2.3 Spatial Truncation $D_w(k_y, \omega)$

Practical arrays are also obviously restricted to a finite length. This is modeled by truncating the driving function with a spatial window $w(y_0, \omega) \in \mathbb{R}^+$, that might be frequency dependent. For WST a frequency independent, rectangular truncation window is considered. In Fig. 3.14 the signal processing model for a finite length, albeit continuous SSD is depicted. Hence, the complete sampling stage is omitted. This case serves as the reference LSA for derivation of the WST criteria.

With spatial truncation applied, the Rayleigh integral transforms to the Rayleigh-Sommerfeld diffraction integral as discussed above [Bor06, Ch. 8.11.2], [NV06, Ch. 6.4]. The analysis will thus only be correct if either the SSD is effectively enclosed by a rigid wall or, for SSD setups free in space: (i) the length of the SSD is much larger than the considered wave length λ and (ii) the wave length is much smaller than the evaluation distance $|\mathbf{x}|$. The driving function is truncated to

$$D_w(y_0, \omega) = w(y_0) \cdot D(y_0, \omega) \quad (3.35)$$

by deploying the rectangular window (to be comparable with [Hei92b])

$$w(y_0) = \begin{cases} 1 & \text{for } |y_0| \leq \frac{L}{2} \\ 0 & \text{else} \end{cases} \quad \circ \bullet \quad w(k_y) = \begin{cases} L \frac{\sin(k_y \frac{L}{2})}{k_y \frac{L}{2}} & \text{for } k_y \neq 0 \\ L & \text{for } k_y = 0. \end{cases} \quad (3.36)$$

The convolution of the spatial spectrum $w(k_y)$ (3.36) and the initial driving

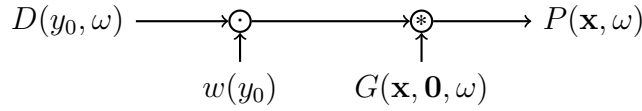
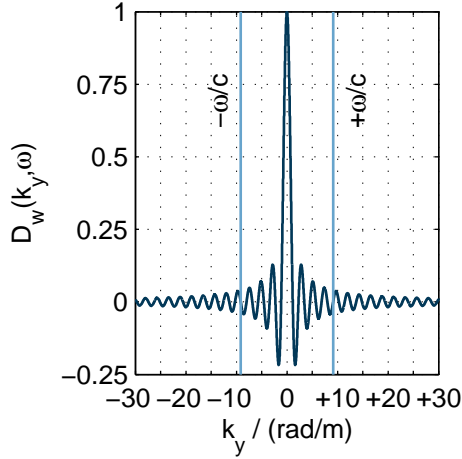
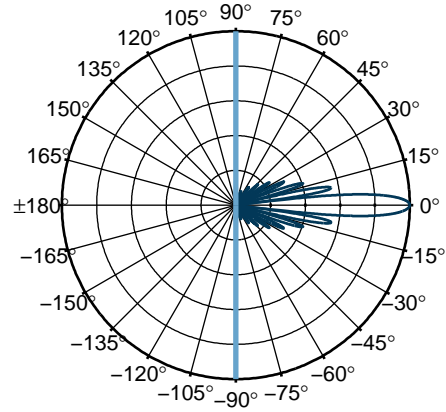


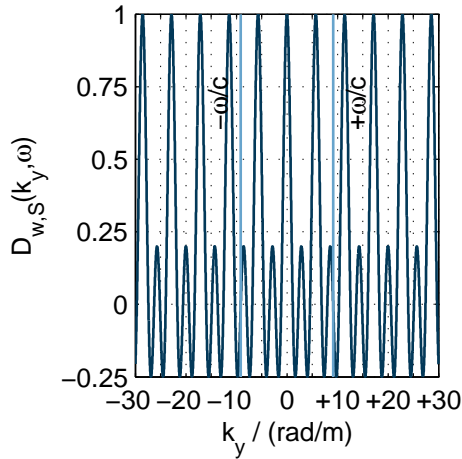
Figure 3.14: Signal flow of the single layer potential for a linear, finite length, continuous SSD located on the y -axis.



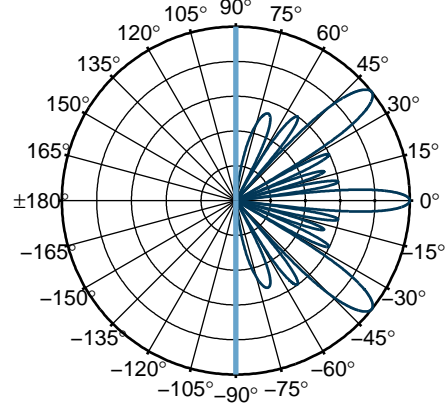
(a) Unit gain normalized $D_w(k_y, \omega)$ (3.38), $L = 5.5$ m, $\lambda = 0.6875$ m, $L/\lambda = 8$, $f \approx 500$ Hz, $\frac{\omega}{c} \approx 9.14$ rad/m.



(b) Polar plot for unit gain normalized $|D_w(\varphi)|$ in dB for $k_y = \frac{\omega}{c} \sin \varphi$, 6 dB/div.



(c) Unit gain normalized $D_{w,S}(k_y, \omega)$ (3.69), $N = 15$, $\Delta y = 1.1$ m, $L = \Delta y N = 5.5$ m, $\lambda = 0.6875$ m, $L/\lambda = 8$, $f \approx 500$ Hz, $\frac{\omega}{c} \approx 9.14$ rad/m



(d) Polar plot for unit gain normalized $|D_{w,S}(\varphi)|$ in dB for $k_y = \frac{\omega}{c} \sin \varphi$, 6 dB/div.

Figure 3.15: Relation between spatio-temporal spectra of WST driving functions with same BW_{NN} and corresponding farfield radiation patterns for a chosen temporal frequency.

function's spectrum (3.25)

$$D_w(k_y, \omega) = \frac{1}{2\pi} w(k_y) *_{k_y} D(k_y, \omega) \quad (3.37)$$

leads to the WST driving function of the finite length, continuous linear array

$$D_w(k_y, \omega) = \begin{cases} L \frac{\sin(k_y \frac{L}{2})}{k_y \frac{L}{2}} & \text{for } k_y \neq 0 \\ L & \text{for } k_y = 0. \end{cases} \quad (3.38)$$

This is the well known sinc-function (3.8) exemplarily shown in Fig. 3.15a. Similar to (3.14), the spatio-temporal spectrum of the synthesized sound field reads

$$P(x, k_y, \omega) = D_w(k_y, \omega) G_0(x, k_y, \omega). \quad (3.39)$$

The initially intended driving function of Dirac shape (3.25) is smeared by the convolution (3.37) and the driving function's spatio-temporal spectrum (3.38) is continuous w.r.t. k_y , cf. [Ahr10d, Sec. VII]. A single monochromatic wave as initially intended using a Dirac in the spatial spectrum is thus corrupted by interference with additional waves (that constitute side lobes in the farfield) with different radiation angles, which now also includes evanescent wave contributions. Hence, the treatment and the interpretation of the synthesized sound fields of the LSA becomes more demanding, particularly because the radiation characteristics are highly dependent on the array length and the temporal frequency.

Farfield Radiation Pattern

The spatially truncated single layer potential [Ahr10d, (9)]

$$P(\mathbf{x}, \omega) = \int_{-\infty}^{+\infty} w(y_0) D(y_0, \omega) \frac{e^{-j\frac{\omega}{c}|\mathbf{x}-\mathbf{x}_0|}}{4\pi|\mathbf{x}-\mathbf{x}_0|} dy_0 \quad (3.40)$$

formulates the problem of (3.39) in the temporal spectrum domain. Closed form solutions for finite length arrays are only available for special cases, cf. App. D.

Evaluating (3.40) for $|\mathbf{x}| = \text{const}$ with $|\mathbf{x}| \gg L$ and $|\mathbf{x}| \gg \lambda$, $\frac{|\mathbf{x}|}{L} \gg \frac{L}{\lambda}$ the

farfield radiation pattern (FRP) can be analytically derived [Mö09, Ch. 3.5], and the direct link to the spatio-temporal spectrum

$$P_{\text{Far}}(\mathbf{x}, \omega) \propto D_w(k_y, \omega) = \int_{-L/2}^{+L/2} D(y_0, \omega) e^{+j k_y y_0} dy_0 \quad (3.41)$$

is well known, i.e. the Fraunhofer approximation that was discussed on p. 42ff. This integral is precisely solved to (3.38) and $D_w(k_y, \omega)$ therefore includes the temporal frequency dependent FRP when taking only the visible region $|k_y| < |\frac{\omega}{c}|$ into account, cf. [Sku71, Ch. 26.2], [Kin00, Ch. 7.11], [Mö09, Ch. 3.6], [Hec77]. Thus, by restricting the spatio-temporal driving function's spectrum to the visible region $-|\frac{\omega}{c}| < k_y < +|\frac{\omega}{c}|$, the nonlinear mapping between k_y and the propagating radiation angle φ

$$k_y = \frac{\omega}{c} \sin \varphi \quad (3.42)$$

allows for the interpretation of an—what is here termed—angular spectrum synthesis, i.e. the weighted superposition of cylindrical waves with radiation angles $-\frac{\pi}{2} < \varphi < +\frac{\pi}{2}$ based on the inverse spatial Fourier transform of a spatio-temporal spectrum. The resulting polar pattern for a given temporal frequency ω is exemplarily shown in Fig. 3.15b. Note that the common term *farfield directivity* for referring to as the *farfield radiation pattern* in loudspeaker engineering should be avoided, since the term *directivity* is standardized in [IEE93] with a different meaning. For the farfield radiation pattern, usually either a normalized version in u -space with $u = \sin \varphi$ and $\frac{\omega}{c} = \frac{2\pi}{\lambda}$

$$D_w(u) = L \frac{\sin\left(\pi \frac{L}{\lambda} u\right)}{\pi \frac{L}{\lambda} u} \quad \text{for } -1 \leq u \leq +1, \quad (3.43)$$

with $D_w(u=0) = L$, or as a polar pattern in φ -space

$$D_w(\varphi) = L \frac{\sin\left(\pi \frac{L}{\lambda} \sin \varphi\right)}{\pi \frac{L}{\lambda} \sin \varphi} \quad \text{for } -\frac{\pi}{2} \leq \varphi \leq +\frac{\pi}{2} \quad (3.44)$$

with $D_w(\varphi=0) = L$ is conveniently discussed for the radiation characteristics. $|D_w(u)|$ exhibits an envelope $\frac{\lambda}{\pi L u}$ and $N_0 = 2 \cdot \lfloor \frac{L}{\lambda} \rfloor$ zeros within the visible region

($L \neq 0, \lambda \neq 0$), that are located at

$$u_0 = \frac{\lambda}{L} \mu \text{ for } -\lfloor \frac{L}{\lambda} \rfloor \leq \mu \leq +\lfloor \frac{L}{\lambda} \rfloor, \mu \neq 0, \mu \in \mathbb{Z}. \quad (3.45)$$

Besides the global maximum at $u = 0$, defined by a removable singularity i.e. the main lobe in the farfield, (3.43) additionally exhibits alternating local minima and maxima at u_m for that

$$\frac{dD_w(u)}{du} = 0 \rightarrow \cos\left(\pi \frac{L}{\lambda} u_m\right) = \frac{\sin\left(\pi \frac{L}{\lambda} u_m\right)}{\pi \frac{L}{\lambda} u_m} \rightarrow 0 = \frac{\tan\left(\pi \frac{L}{\lambda} u_m\right)}{\pi \frac{L}{\lambda} u_m} - 1 \quad (3.46)$$

must hold. For this transcendental equation the solutions [Wei]

$$u_m \approx \pm \frac{(\mu + \frac{1}{2})\pi - \frac{1}{(\mu + \frac{1}{2})\pi}}{\pi \frac{L}{\lambda}} \text{ for } \mu \geq 1, \mu \in \mathbb{Z} \quad (3.47)$$

are known as a good approximation, where odd μ indicate local minima and even μ local maxima. The number N_m of all minima and maxima located within the visible region can be roughly approximated with

$$N_m = 2 \lfloor \frac{L}{\lambda} - \frac{1}{2} \rfloor. \quad (3.48)$$

These local minima and maxima are referred to as side lobes in the farfield. The local minima at $|u_m|$ for $\mu = 1$ have a side lobe level of about -13.26 dB relative to the main lobe level of $20 \log_{10}(L)$ independently from chosen L/λ .

The so called null-to-null beamwidth BW_{NN} is the bandwidth between the first occurring zeros adjacent to the main lobe and is given as

$$BW_{NN} = \frac{4\pi}{L} \text{ in } k_y\text{-space} \quad (3.49)$$

$$BW_{NN} = \frac{2\lambda}{L} \text{ in } u\text{-space}. \quad (3.50)$$

The FRP is thus highly dependent on the ratio $\frac{L}{\lambda}$, as this determines the number of local minima and maxima, number of zeros within the visible region and the beamwidth of the main lobe. For $\frac{L}{\lambda} \ll 1$ the FRP is almost omnidirectional. For a given L this is valid for wave lengths $\lambda < L$, i.e. rather low temporal frequencies for typically chosen array lengths. For $\frac{L}{\lambda} \gg 1$ the FRP becomes

increasingly directed for increased ratios, i.e. valid for rather high temporal frequencies for typical LSA lengths. This is a special problem in acoustics engineering: dealing with radiating wave lengths that simultaneously are much larger and much smaller than the array length. This highly temporal frequency dependent behavior is not desirable in practical applications and one of the solutions that was adopted is the geometric curving of LSAs to provide a more consistent sound field over a wide frequency band, specified in the 4th WST criterion [Urb03, p.929]. Note that the listener may not be necessarily located in the farfield of the array, where the concept of farfield radiation patterns is valid.

On-Axis Radiation, Fresnel/Fraunhofer Transition

Another closed form solution of (3.40) can be derived along the main lobe axis of the finite length LSA, i.e. for positions $\mathbf{x} = (x, 0, 0)^T$. This resembles the Fresnel approximation that was discussed in Ch. 2.2.6 and App. D.2, cf. [Sku71, Ch. 26.23], [Lip86], [Hei92b, I.3.b]. The latter two papers deduced, that a continuous, finite length array with constant volume acceleration exhibits a *Fresnel* region (3 dB level decay per distance doubling with ripples, 3 dB/oct. lowpass for temporal frequencies with ripples) and a *Fraunhofer* region (6 dB level decay per distance doubling, temporal frequency independent amplitude). This is schematically depicted in Fig. 3.16. Only in the Fraunhofer region the concept of the FRP is valid and the radiation characteristics can be given with polar patterns. Note that [IEE93] distinguishes between the *Fraunhofer region* and the *farfield region*, which is here equivalently used for the problem under discussion.

The transition or border distance x_B between both regions, the Fresnel and

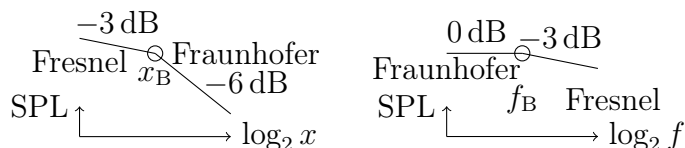


Figure 3.16: Simplified radiation characteristics on x -axis for a rectangular windowed, continuous LSA under constant volume acceleration, cf. Fig. D.8.

Fraunhofer region on the main axis is highly dependent on the frequency f and array length L . By the geometric diffraction approach, the authors of [Hei92b], [Urb03, p. 913] derived (D.79)

$$x_B = \frac{1}{2} L^2 \frac{f}{c} \sqrt{1 - \left(\frac{f}{c} L\right)^2}, \quad (3.51)$$

for which $x_B \notin \mathbb{R}$ indicates pure Fraunhofer radiation. Cylindrical wave radiation for all frequencies can therefore not be expected, contrasting to the case for the infinite line source [Lip86, p.12], cf. Fig. 3.16a.

In the following, the signal processing framework within the angular spectrum domain is utilized to derive two other, yet consistent viewpoints of Fresnel/Fraunhofer transition. The discussion is restricted to the propagating wave contributions, thus ignoring evanescent waves in the immediate vicinity of the array. The approach is valid for evaluation distances on the main axis, for which these contributions in (2.162) become negligible. The inverse spatial Fourier transform $\mathcal{F}_{|k_y| \leq \frac{\omega}{c}}^{-1}\{\cdot\}$ of only the propagating contributions within the spatio-temporal spectrum $P(x, k_y, \omega)$ is given by

$$P_{\text{prop}}(x, y, \omega) = \mathcal{F}_{|k_y| \leq \frac{\omega}{c}}^{-1}\{P(x, k_y, \omega)\} := \frac{1}{2\pi} \int_{-\frac{\omega}{c}}^{+\frac{\omega}{c}} P(x, k_y, \omega) e^{-j k_y y} dk_y \quad (3.52)$$

and specified for the problem at hand – plugging (3.38), (2.162) to (3.39) –

$$P(x, y, \omega) = \frac{-j}{8\pi} \int_{-\frac{\omega}{c}}^{+\frac{\omega}{c}} L \frac{\sin(k_y \frac{L}{2})}{k_y \frac{L}{2}} \cdot H_0^{(2)}\left(\sqrt{\left(\frac{\omega}{c}\right)^2 - k_y^2} \cdot x\right) \cdot e^{-j k_y y} dk_y. \quad (3.53)$$

Numerical evaluation (3.53) with less computational load can utilize the large argument approximation of the Hankel function for $\sqrt{\left(\frac{\omega}{c}\right)^2 - k_y^2} \cdot x \gg 1$ as

$$P(x, y, \omega) = \frac{-j}{8\pi} \int_{-\frac{\omega}{c}}^{+\frac{\omega}{c}} \left[L \frac{\sin(k_y \frac{L}{2})}{k_y \frac{L}{2}} \sqrt{\frac{2}{\pi \sqrt{\left(\frac{\omega}{c}\right)^2 - k_y^2}}} e^{-j(\sqrt{\left(\frac{\omega}{c}\right)^2 - k_y^2} \cdot x - \frac{\pi}{4})} e^{-j k_y y} \right] dk_y. \quad (3.54)$$

Angular Spectrum Synthesis of the Sound Field in the xy -Plane

An analytical solution of integrals similar to (3.53) was given in [Pee10] for the on-axis pressure of a circular and rectangular piston. The solution of a rectangular source turns out to be a infinite double sum – i.e. a discrete modal superposition – including numerical very demanding functions such as factorials, the Struve and Bessel function, the Euler beta-function and the Gamma function, cf. [Pee10, (38)]. A more general analytic solution for the whole xy -plane using the spatio-temporal spectrum domain could not be found in literature and derived so far. [Mas07] presented Fresnel integral solutions that stem from a generalized Fresnel approximation of the Rayleigh-Sommerfeld diffraction integral for rectangular sources.

Straightforward numerical evaluation of (3.54) allows for synthesizing the sound field by weighted superposition of cylindrical waves with propagating angles $-\frac{\pi}{2} < \varphi < +\frac{\pi}{2}$, which can be interpreted as angular spectrum synthesis, also referred to as *method of decomposition into wave lengths* [Mö09, Ch. 13.5.4]. Note that these waves stem from an infinite, continuous line source. The integration over k_y , i.e. over the different radiation angles, yields the radiation characteristic of a line source with finite dimension by interference phenomena. This viewpoint is in contrast to the numerical evaluation of (3.40), which can be interpreted as source synthesis by weighted spherical monopoles, also referred to as *method of source decomposition* [Mö09, Ch. 13.5.4]. Note that (3.40) inherently includes evanescent waves, which is discarded in (3.53). The discretization of k_y in (3.53) for numerical evaluation leads to spatial repetitions of the sound field along the y -axis, which must become negligible in the evaluated area under interest.

The proposed framework provides an interesting opportunity, by definition of an ideal spatial lowpass filter (cf. [Ahr12a, (4.55)], [Ahr10c, (9)])

$$H_{\text{LP}}(k_y, \omega) = \begin{cases} 1 & |k_y| < \frac{2\pi}{L} \\ 0 & \text{elsewhere,} \end{cases} \quad (3.55)$$

that might be included to the signal flow. This was discussed in [Ahr12a, Ch. 4.6.6], [Ahr10c], although with the different motivation to suppress discretization effects (spatial aliasing) instead of truncation artifacts as in the

case presented here. The cutoff wave numbers $k_y = \pm \frac{2\pi}{L}$ are the locations of the first zeros of the array's spatio-temporal spectrum (3.38), if they exist in the *visible region* $|k_y = \pm \frac{2\pi}{L}| < |\frac{\omega}{c}|$ for the chosen temporal frequency ω . The spatial lowpass is thus used to independently synthesize the sound field that corresponds to the null-to-null beam width BW_{NN} , shortly termed *main lobe sound field*,

$$P_{\text{main}}(x, y, \omega) = \mathcal{F}_{|k_y| \leq \frac{\omega}{c}}^{-1} \{H_{\text{LP}}(k_y, \omega) \cdot D_w(k_y, \omega) \cdot G_0(x, k_y, \omega)\} \quad (3.56)$$

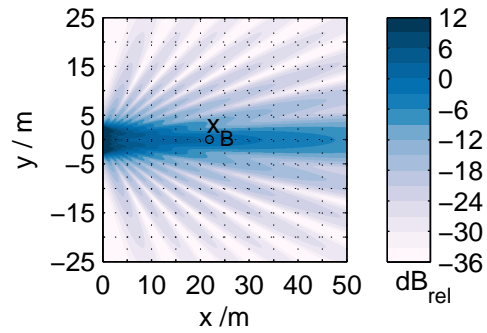
and that of the remaining propagating side lobes, the *side lobe sound field*,

$$P_{\text{side}}(x, y, \omega) = \mathcal{F}_{|k_y| \leq \frac{\omega}{c}}^{-1} \{(1 - H_{\text{LP}}(k_y, \omega)) \cdot D_w(k_y, \omega) \cdot G_0(x, k_y, \omega)\}. \quad (3.57)$$

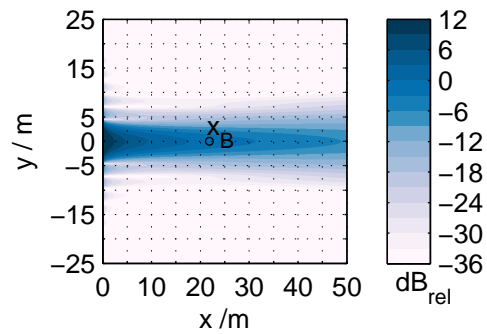
This is equivalent to splitting the integral (3.53) into three integration ranges

$$P(x, y, \omega) = \underbrace{\int_{-\frac{2\pi}{L}}^{+\frac{2\pi}{L}} \dots}_{P_{\text{main}}(x, y, \omega)} + \underbrace{\int_{-\frac{\omega}{c}}^{-\frac{2\pi}{L}} \dots + \int_{+\frac{2\pi}{L}}^{+\frac{\omega}{c}} \dots}_{P_{\text{side}}(x, y, \omega)}. \quad (3.58)$$

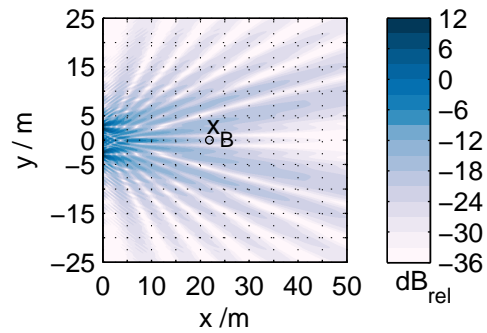
In Fig. 3.17 the introduced approach is exemplarily evaluated for the case $L = 8 \cdot \lambda = 5.5$ m. The Fresnel/Fraunhofer transition distance (3.51) for this example is given to $x_B = 21.8$ m. Fig. 3.17a shows the sound field's pressure level of the uniformly driven LSA in the xy -plane according to (3.53), (3.58). Fig. 3.17b shows the main lobe sound field's pressure level from (3.56), whereas Fig. 3.17c depicts the side lobe sound field's pressure level (3.57). The superposition of $P_{\text{main}}(x, y, \omega)$ Fig. 3.17b and $P_{\text{side}}(x, y, \omega)$ Fig. 3.17c results in the complete sound field $P(x, y, \omega)$ Fig. 3.17a by interference. Levels in the plots are equivalently normalized to $20 \log_{10}(|P(x = x_B, y = 0)|) = 0 \text{ dB}_{\text{rel}}$, i.e. to the magnitude at the Fresnel/Fraunhofer transition distance of the 'complete' sound field. The colormap is clipped for values $> 12 \text{ dB}_{\text{rel}}$ and $< -36 \text{ dB}_{\text{rel}}$. Note that in Fig. 3.17b the resulting sinc characteristic (cf. (3.17)) of the ideal spatial lowpass filter (3.55) is observable in the sound field. This ideal spatial lowpass filter is of infinite spatial dimension and thus not realizable in practice. For the intended theoretical discussion this approach is however meaningful. In Fig. 3.18 the levels along the main lobe axis were evaluated for all three



(a) $|P(x, y, \omega)| = |P_{\text{main}}(x, y, \omega) + P_{\text{side}}(x, y, \omega)|$ in dB_{rel} (3.53), (3.58)



(b) $|P_{\text{main}}(x, y, \omega)|$ in dB_{rel} (3.56) of main lobe components.



(c) $|P_{\text{side}}(x, y, \omega)|$ in dB_{rel} (3.57) of side lobe components.

Figure 3.17: Level of sound field $|P(x, y, \omega)|$ in dB_{rel} computed by numerical evaluation of (3.58). Continuous, finite length LSA driven with $D_w(k_y, \omega)$ (3.38) for $L = 5.5$ m and $L/\lambda = 8$, $\lambda = 0.6875$ m $\rightarrow f \approx 500$ Hz.

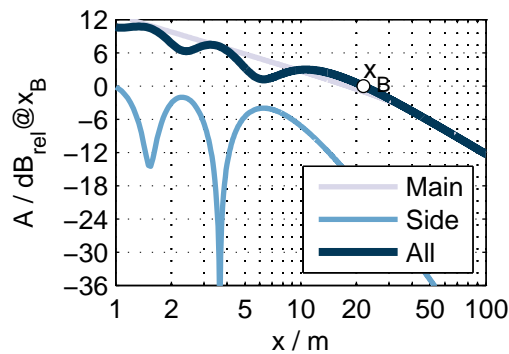


Figure 3.18: On-axis level for Fig. 3.17.

cases of Fig. 3.17. The main lobe sound field exhibits a ripple free level decay with a transition approximately at x_B (3.51) from almost ideal cylindrical (Fresnel region, -3 dB per distance doubling) to spherical (Fraunhofer region, -6 dB per distance doubling) level decay on axis. The on-axis side lobe sound field exhibits lower overall level, notches and a level attenuation, that is larger than 6 dB per distance doubling for $x > x_B$. The interference interaction of the main and side lobe sound fields for $x < x_B$ results in the rippled on-axis level that is typical for the Fresnel region of finite length linear arrays [Lip86, Hei92b, Ure04]. The total sound field in the xy -plane is corrupted by the side lobes as long as its relative overall level compared to the main lobe overall level is large enough to produce perturbing interferences. The side lobe overall level attenuation for $x > x_B$ is larger than 20 dB relative to the main lobe overall level, and thus has weak impact on the total sound field, which is expected in the Fraunhofer region.

By observing the dependence of the temporal frequency and LSA length regarding the integration limits in (3.56) for the main lobe sound field

$$|k_y = \sin \varphi \frac{\omega}{c}| = \frac{2\pi}{L}, \quad (3.59)$$

it becomes obvious that for higher frequencies and/or larger LSAs, the side lobe field is composed of smaller radiation angles φ . These waves closer to the main lobe angle $\varphi = 0^\circ$ interfere with the main lobe within a much larger spatial region. This indicates the large Fresnel/Fraunhofer transition borders in (3.51) for high frequencies and large array lengths. In other words: the more the driving function spectrum resembles a Dirac-like function within the

visible region – that is for large L and/or large frequencies – the larger is the spatial extent of the Fresnel region in which the sound field is similar to that of an infinite line monopole. The LSA radiates directly into the Fraunhofer region if the visible region exhibits less than the main lobe of (3.38) indicated also by a complex result of (3.51), i.e. $x_B \in \mathbb{C}$.

Angular Spectrum Synthesis of the On-Axis Sound Field

Another consistent viewpoint on the radiation phenomena can be given when evaluating (3.54) along the main lobe axis, i.e. $y = 0$. The integral can then be cast to

$$P(x, y = 0, \omega) = \underbrace{-\frac{j}{4} \sqrt{\frac{2}{\pi \frac{\omega}{c} x}} e^{-j \frac{\omega}{c} x} e^{+j \frac{\pi}{4}}}_{G_{0,2D,Far}(x,\omega)} \times \underbrace{\int_0^{+\pi/2} \frac{e^{-j \frac{\omega}{c} x (\cos \varphi - \sin \varphi \frac{L}{2x} - 1)} - e^{-j \frac{\omega}{c} x (\cos \varphi + \sin \varphi \frac{L}{2x} - 1)}}{j \pi \sin \varphi} \sqrt{\cos \varphi} d\varphi}_{\text{Mod}(L,x,\omega)} \quad (3.60)$$

using the variable substitution $k_y \rightarrow \varphi$. The first term in front of the integral resembles the large argument approximation of the 2D freefield Green's function (2.8), i.e. the ideal, infinite line monopole located on the y -axis, cf. (2.143). The integral represents a complex valued 'modulation' function that is dependent on L , x and ω . The ideal level decay and frequency response of the infinite line monopole thus is varied by multiplication with the modulation function which results in the on-axis radiation characteristic. A closed form solution of the integral could not be found so far. The most look alike known integral is [Gra07, (8.256/5)]. A promising way is to deploy the approach given in [Pee10, Sec. IV] for line pistons. Since the integral exhibits highly oscillating functions the stationary phase approximation may lead to a solution, which is expected to be already solved in optics when approaching the Fresnel diffraction within the angular spectrum domain. From [Vee05] it can be concluded that integrals of this kind are still an active research field in optics. This issue was not further pursued in this work. Note that the integration range includes a pole for $\varphi = 0$, similar to $|k_y| = \frac{\omega}{c}$.

When casting (3.60) towards the Fresnel approximation approach (D.59) it

can be expected that with $v_0 = \frac{\omega}{c} \frac{(L/2)^2}{2x}$ the integral

$$P(x, y = 0, \omega) = \frac{1}{4\pi} \sqrt{\frac{2}{\frac{\omega}{c}x}} e^{-j\frac{\omega}{c}x} \sqrt{2\pi} \times \quad (3.61)$$

$$\underbrace{\frac{-j}{\sqrt{2}} e^{+j\frac{\pi}{4}} \int_0^{+\pi/2} \frac{e^{-j\frac{\omega}{c}x(\cos\varphi - \sin\varphi \frac{L}{2x} - 1)} - e^{-j\frac{\omega}{c}x(\cos\varphi + \sin\varphi \frac{L}{2x} - 1)}}{j\pi \sin\varphi} \sqrt{\cos\varphi} d\varphi}_{\approx C_2(v_0) - jS_2(v_0)}$$

should resemble the Fresnel integrals. The question is under which circumstances

$$\text{Mod}_{\text{CS}}(L, \omega, x) = \frac{C_2(v_0) - jS_2(v_0)}{\frac{-j}{\sqrt{2}} e^{+j\frac{\pi}{4}}} \approx \text{Mod}(L, \omega, x) \quad (3.62)$$

holds. Since the solution (D.59) stems from the Fresnel diffraction integral (cf. Ch. 2.2.6) the condition (2.102) must be valid. Using $\mathbf{x}' = (0, 0)^T$, the most far monopole $\mathbf{x}'_0 = (L/2, 0)^T$ within the LSA and a chosen maximum angle $\frac{\pi}{32}$ for the second order exponential term, the condition

$$\frac{\omega}{c} \frac{\|\mathbf{x}' - \mathbf{x}'_0\|^4}{8x_{\text{CS}}^3} = \frac{\pi}{32} \quad (3.63)$$

leads to the on main axis border distance x_{CS}

$$\frac{\omega}{c} \frac{(L/2)^4}{8x_{\text{CS}}^3} = \frac{\pi}{32} \rightarrow x_{\text{CS}} = \left(\frac{\omega}{c} \frac{(L/2)^4}{8 \frac{\pi}{32}} \right)^{\frac{1}{3}} = \left(\frac{L^4}{2\lambda} \right)^{\frac{1}{3}}. \quad (3.64)$$

For $x > x_{\text{CS}}$ (D.59) is valid within an average error

$$20 \log \left[\left| \frac{\frac{C_2(v_0) - jS_2(v_0)}{\frac{-j}{\sqrt{2}} e^{+j\frac{\pi}{4}}}}{\text{Mod}(L, \omega, x)} \right| \right] \quad (3.65)$$

of ± 0.2 dB and a maximum error of ± 0.5 dB for large typical LSA lengths L and/or very large frequencies within the audio bandwidth. Note that for typical LSA applications also a maximum tolerated angle of $\frac{\pi}{8}$ yields a sufficiently precise prediction of the on-axis level decay with the Fresnel integral within error bound ± 0.5 dB. Hence, for $x > x_{\text{CS}}$ (3.62), (D.59) holds, whereas for

$x < x_{CS}$ only (3.60) represents the correct radiation characteristic.

In Fig. 3.19 a numerical evaluation of both approaches is depicted using the same LSA as for Fig. 3.17 and Fig. 3.18. For small x the deviation of the Fresnel integral solution (subscript 'CS') and the angular spectrum synthesis approach becomes obvious. The vertical lines represent the $\frac{\pi}{8}$ and $\frac{\pi}{32}$ boundaries. The modulation function oscillates around 0 dB with ripples that increase with larger x and exhibit a maximum of about 2.5 dB. Beyond the Fresnel/Fraunhofer transition distance (3.51) the modulation function takes the form of a straight line with 3 dB per distance doubling. Thus, in the Fresnel region the ideal level decay of the infinite line monopole is modulated with a rippled function and in the Fraunhofer region both level decays of 3 dB result in the expected spherical wave radiation. This proves consistency with the observations above. Note the different interpretation of the approaches. While for (i) the main lobe sound field with ideal 3 dB and 6 dB level decays in Fresnel and Fraunhofer is corrupted with the side lobe sound field by superposition, i.e. interference, (ii) is based on modulation of the ideal 3 dB level decay of the infinite line monopole with the Fresnel integrals.

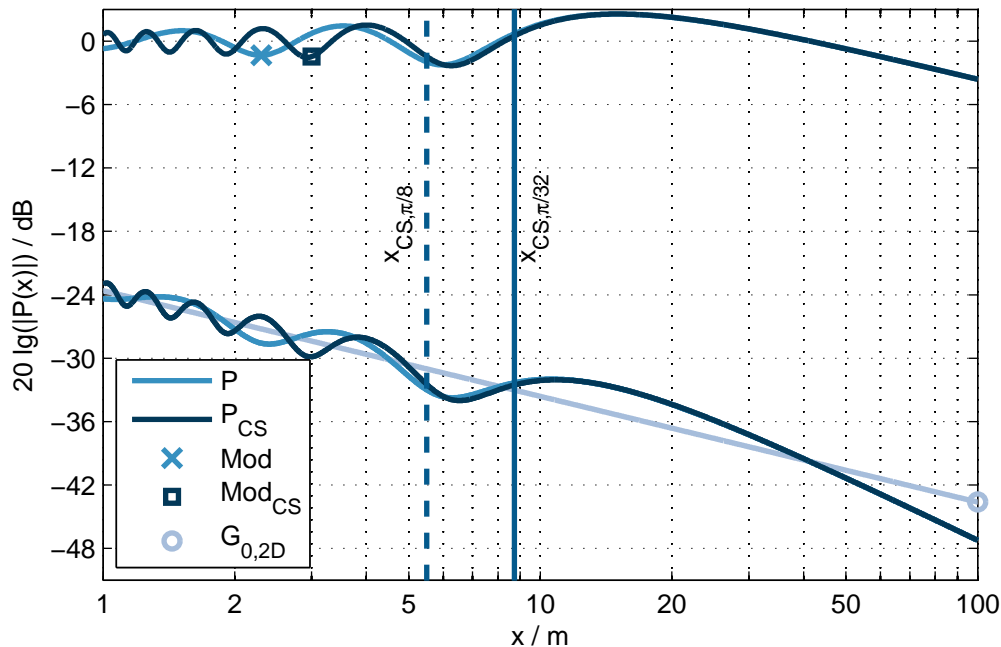


Figure 3.19: On-axis Fresnel/Fraunhofer transition: (3.60) vs. (D.59) (subscript 'CS'). $L = 5.5$ m and $L/\lambda = 8$, $\lambda = 0.6875$ m $\rightarrow f \approx 500$ Hz, cf. Fig. 3.18.

3.2.4 Spatial Truncation and Discretization $D_{w,S}(k_y, \omega)$

The driving function for a finite length, uniformly driven and discretized array built with spherical monopoles is with (3.23), (3.26) and (3.35) modeled as

$$D_{w,S}(y_0, \omega) = [w(y_0) \cdot D(y_0, \omega)] \cdot \underbrace{\sum_{\mu=-\infty}^{+\infty} \delta(y_0 - \mu \Delta y)}_{=: \frac{1}{\Delta y} \text{III}\left(\frac{y_0}{\Delta y}\right)}. \quad (3.66)$$

This includes spatial truncation by a rectangular window $w(y_0)$ and spatial sampling with step size Δy . The signal processing model is depicted in Fig. 3.20. In the following discussion, an axisymmetric LSA geometry Fig. 3.11 with regard to $y_0 = 0$ and an odd number N of spherical monopoles is considered. Hence, for the uniformly driven array follows

$$D_{w,S}(y_0, \omega) = \sum_{\mu=-\frac{N-1}{2}}^{+\frac{N-1}{2}} \delta(y_0 - \mu \Delta y). \quad (3.67)$$

The corresponding spatio-temporal spectrum is given as

$$D_{w,S}(k_y, \omega) = \sum_{\mu=-\frac{N-1}{2}}^{+\frac{N-1}{2}} e^{+j(k_y \Delta y) \mu}. \quad (3.68)$$

This geometric series has a closed form solution (cf. [Lyo11, App. B]), leading to the so called *aliased sinc-function* or *periodic sinc-function* [Van02, Ch. 2.4], [Bal05, Ch. 6.3]

$$D_{w,S}(k_y, \omega) = \frac{\sin(k_y \Delta y \frac{N}{2})}{\sin(k_y \Delta y \frac{1}{2})}. \quad (3.69)$$

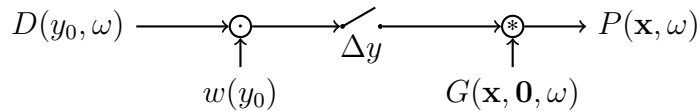


Figure 3.20: Signal flow of the single layer potential for a linear, finite length, discretized SSD located on the y -axis.

$D_{w,S}(k_y, \omega)$ in (3.69) is periodic with $\frac{2\pi}{\Delta y}$. The main maximum is at $k_y = 0$ with amplitude N , this is the main lobe or major lobe. For $k_y = \frac{2\pi}{\Delta y} \mu$ other local main maxima with the same amplitude N occur for $\mu \neq 0$, which are referred to as grating lobes. Note that for even N , the spectrum $D_{w,S}(k_y, \omega)$ is periodic with $\frac{4\pi}{\Delta y}$ and the grating lobes exhibit alternating polarities $\mp N$, i.e. local main maxima and minima at $k_y = \frac{2\pi}{\Delta y} \mu$. Thus, in general for $N \in \mathbb{N}$

$$D_{w,S}(k_y, \omega) = \begin{cases} \frac{\sin(k_y \Delta y \frac{N}{2})}{\sin(k_y \Delta y \frac{1}{2})} & \text{for } k_y \neq \frac{2\pi}{\Delta y} \mu \\ N \cdot (-1)^{\mu(N-1)} & \text{for } k_y = \frac{2\pi}{\Delta y} \mu \end{cases} \quad (3.70)$$

holds. For convenience only arrays with an odd number of N are discussed in the remainder. Between two local main maxima – i.e. between the main lobe and the first grating lobe or between two adjacent grating lobes – $(N-2)$ local minima and maxima arise – the side lobes or minor lobes – that are separated by $(N-1)$ zeros [Ste58, p.14], cf. Fig. 3.21a.

The zeros occur when the numerator of $D_{w,S}(k_y, \omega)$ (3.81) is zero and the denominator is non-zero and are located at

$$k_{y,0} = \frac{2\pi}{\Delta y N} \mu \quad \forall \mu \setminus \mu = \nu N, \quad \mu \in \mathbb{Z}, \nu \in \mathbb{Z}. \quad (3.71)$$

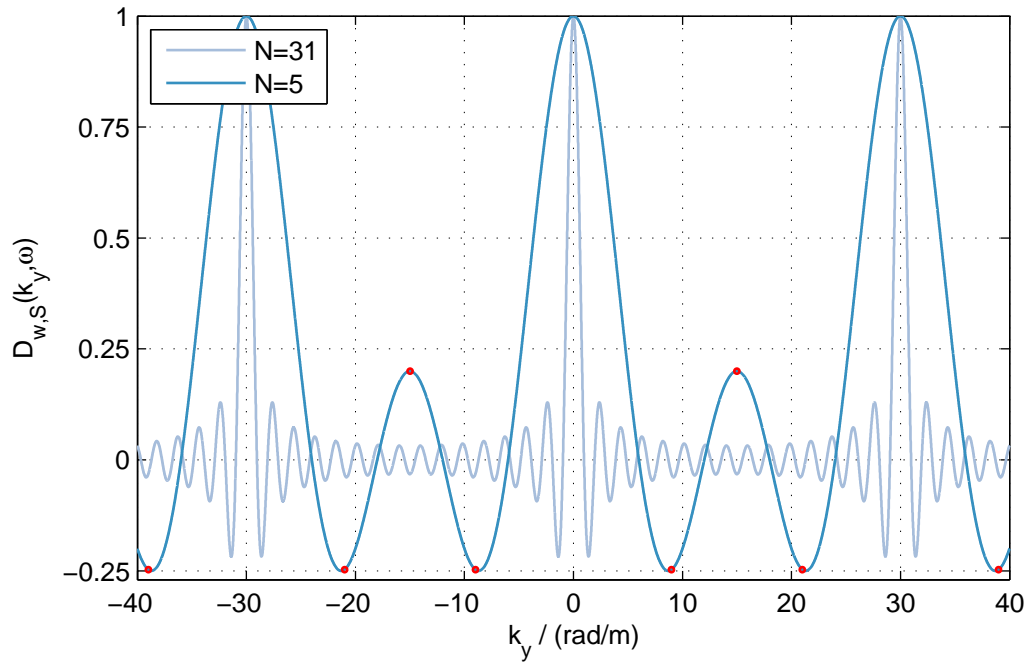
In Fig. 3.21a the depicted zeros at $k_{y,0} = \pm(6, 12, 18, 24, 36)$ rad/m are integer due to the chosen $N = 5$ and $\Delta y = \frac{2\pi}{30}$ m. The null-to-null beamwidth BW_{NN} again is the bandwidth between the first occurring zeros beside the main lobe, i.e. $\mu = -1$ and $\mu = +1$ and is given as [Van02, p.48]

$$BW_{NN} = \frac{4\pi}{\Delta y N} = \frac{4\pi}{L} \quad (3.72)$$

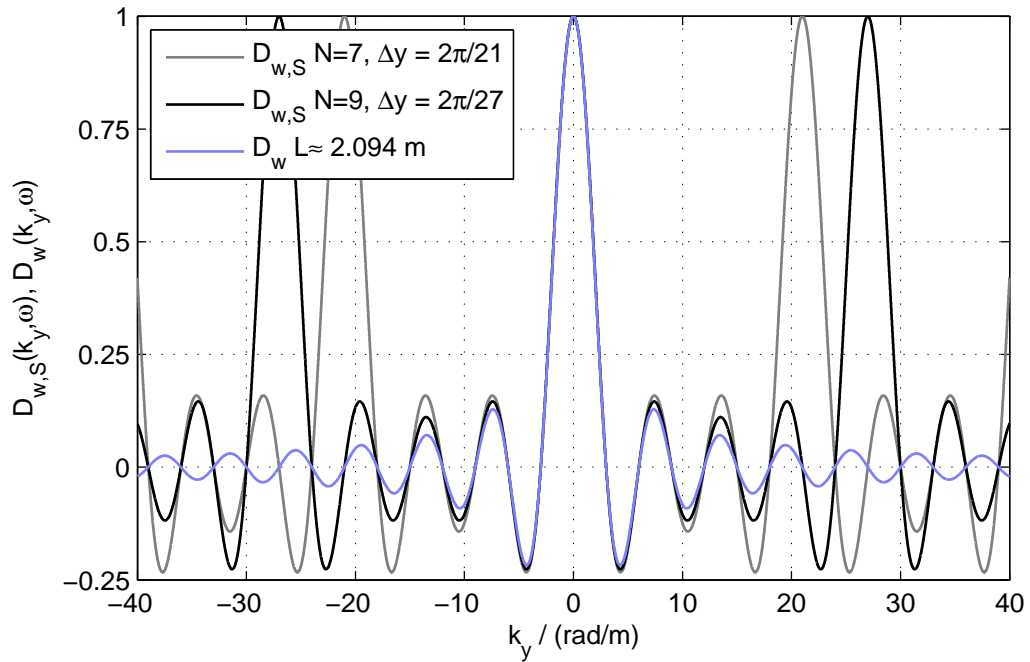
using the length $L = \Delta y N$ that would be equivalent to a continuous array. BW_{NN} decreases for increasing length, cf. Fig. 3.21a.

Similar to (3.46) the locations $k_{y,m}$ of the sidelobe minima and maxima can be derived with [Ste27, (7)], [Ste58, p.15]

$$\frac{dD_{w,S}(k_y, \omega)}{dk_y} = 0 \rightarrow \tan\left(k_{y,m} \Delta y \frac{N}{2}\right) = N \tan\left(k_{y,m} \Delta y \frac{1}{2}\right). \quad (3.73)$$



(a) Unit gain normalized $D_{w,s}(k_y, \omega)$ (3.69) for $N = 31$ and $N = 5$, both with $\Delta y = 2\pi/30$ m.



(b) Unit gain normalized $D_{w,s}(k_y, \omega)$ (3.69) for $N = 7$, $\Delta y = 2\pi/21$ m and $N = 9$, $\Delta y = 2\pi/27$ m and $D_w(k_y, \omega)$ (3.38) for $L = N \Delta y = 7 \frac{2\pi}{21}$ m = $9 \frac{2\pi}{27}$ m.

Figure 3.21: Examples of the driving functions (3.69) vs. (3.38).

This transcendental equation has to be solved numerically by iteration [Ste58, p.15]. The locations are roughly given, when the numerator of (3.69) is a maximum or minimum, i.e.

$$|\sin\left(k_{y,m} \Delta y \frac{N}{2}\right)| = 1. \quad (3.74)$$

This yields a practical approximation of the side lobe locations at

$$k_{y,m} = \pm\left(\mu + \frac{1}{2}\right) \frac{2\pi}{N \Delta y} \text{ for } N(\nu - 1) + 1 \leq \mu \leq N\nu - 2, \quad \nu \geq 1, \quad \nu \in \mathbb{N}, \quad (3.75)$$

i.e. centered between two zeros. For $\nu = \text{const}$ the $(N - 2)$ side lobe locations between two adjacent main maxima are derived. In Table 3.6 the characteristics of the side lobes maxima and minima w.r.t. their amplitude polarity are given for chosen ν and μ . In the example in Fig. 3.21a the visible side lobe max-

	ν odd	ν even
μ even	maximum	minimum
μ odd	minimum	maximum

Table 3.6: Side lobe characteristics (3.75) for odd N .

ima and minima are approximately located at $k_{y,m} = \pm(9, 15, 21, 39)$ rad/m for the chosen $N = 5$ and $\Delta y = \frac{2\pi}{30}$ m using (3.75). They are indicated with red dots in Fig. 3.21a. Numerically solving (3.73) yields more precise results $k_{y,m} = \pm(8.7064593488275, 15, 21.2935406511725, 38.7064593488275)$ rad/m for this example. Note that side lobes exist, that are exactly located centered between two grating lobes. For these side lobes the approximation (3.75) returns the exact value. This occurs when equating both tan-functions in (3.73) at their discontinuities. A strict proof of this behavior is not given here. In the example in Fig. 3.21a this holds for $k_{y,m} = \pm 15$ rad/m.

The first side lobes ($\mu = 1$) are approximately located at $k_{y,m} = \pm \frac{3}{2} \frac{2\pi}{N \Delta y}$. The level of this side lobe can be approximated by inserting $k_{y,m}$ into (3.69), obtaining

$$D_{w,S}(k_y = \pm \frac{3}{2} \frac{2\pi}{N \Delta y}, \omega) = \frac{\mp 1}{\sin(\pm \frac{3\pi}{2N})}. \quad (3.76)$$

For large N the small argument approximation $\sin(x) \approx x$ yields

$$D_{w,S}(k_y = \pm \frac{3}{2} \frac{2\pi}{N \Delta y}, \omega) = -\frac{2N}{3\pi}. \quad (3.77)$$

Relative to the main lobe amplitude $D_{w,S}(k_y = 0, \omega) = N$ the level of the first side lobe is thus

$$20 \log_{10} \left(\frac{2}{3\pi} \right) \text{ dB} \approx -13.46 \text{ dB}. \quad (3.78)$$

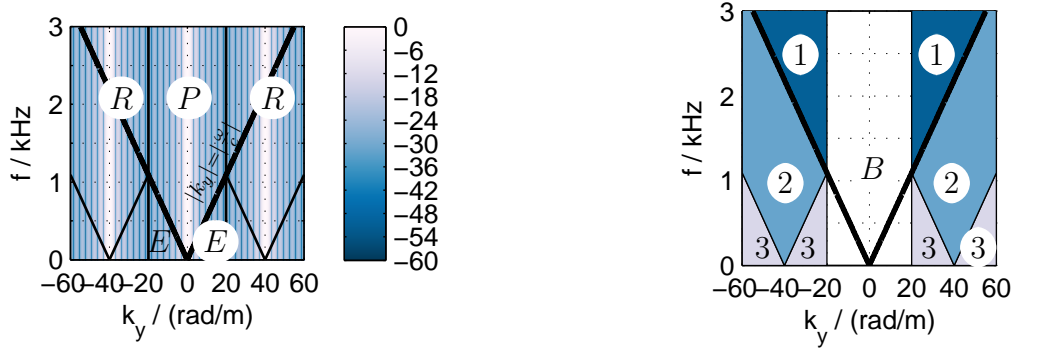
Note that the resulting level depends on N and Δy and only for very large N and very small Δy the relative side lobe level of -13.26 dB equivalent to the uniformly driven, continuous array of finite length (3.38) is obtained.

In Fig. 3.21b it is exemplarily shown that arrays with the same equivalent length $L = \Delta y N$ of a continuous array but different chosen odd $N > 1$ and Δy roughly exhibit about the same functional characteristics as $D_w(k_y, \omega)$ (3.38) for the range $|k_y| < \frac{1}{4} \frac{2\pi}{\Delta y}$ and thus also have approximately the same null-to-null beamwidth. For $L = \Delta y N$ the driving functions $D_w(k_y, \omega)$ and $D_{w,S}(k_y, \omega)$ also exhibit the same zero locations except where grating lobes occur. For smaller chosen Δy the distance $\Delta k_y = \frac{2\pi}{\Delta y}$ between the main maxima increases.

To explain the different occurring types of spatial aliasing that are generated by $D_{w,S}(k_y, \omega)$, it may be useful to consider the region $|k_y| < \frac{\pi}{\Delta y}$ of $D_{w,S}(k_y, \omega)$ as the baseband to be reconstructed. Note that this baseband is not equivalent to the baseband that stems from ideal sampling

$$D_{w,S,\text{ideal}}(k_y, \omega) = \frac{1}{2\pi} [D_w(k_y, \omega) \cdot H_{\text{Pre}}(k_y, \omega)] *_{k_y} \text{III}\left(\frac{k_y \Delta y}{2\pi}\right) \quad (3.79)$$

using $D_w(k_y, \omega)$ (3.38), $H_{\text{Pre}}(k_y, \omega)$ (3.17) and $\text{III}\left(\frac{k_y \Delta y}{2\pi}\right)$ (3.27). Since no pre-filter is considered in the WST theory, this approach is not followed and for ease of discussion the former is explained. The region $|k_y| > \frac{\pi}{\Delta y}$ of $D_{w,S}(k_y, \omega)$ exhibits spectral repetitions of the 'baseband' for each $\mu \frac{2\pi}{\Delta y}$. These repetitions have to be perfectly suppressed in the ideal sampling model in order to avoid postaliasing. The baseband of the driving function spectrum exhibits an evanescent part for $|k_y| > \frac{|\omega|}{c} \wedge |k_y| < \frac{\pi}{\Delta y}$ and a propagating part for $|k_y| < \frac{|\omega|}{c} \wedge |k_y| < \frac{\pi}{\Delta y}$, exemplarily shown in Fig. 3.22a as \textcircled{E} and \textcircled{P} respec-



(a) $|D_{w,S}(k_y, \omega)|$ in dB (3.69) for $N = 13$, $\Delta y = 2\pi/40\text{ m} \leftrightarrow \Delta k_y = 40\text{ rad/m}$. Propagating baseband indicated with \textcircled{P} , evanescent baseband indicated with \textcircled{E} , spectral repetitions of the baseband indicated with \textcircled{R} .

(b) $\textcircled{1} \rightarrow$ prop. $D\&G$, $\textcircled{2} \rightarrow$ prop. D , ev. G , $\textcircled{3} \rightarrow$ ev. $D\&G$, baseband \textcircled{B} .

Figure 3.22: Spatial postaliasing types for $D_{w,S}(k_y, \omega)$.

tively. The example uses $\Delta y = \frac{2\pi}{40}\text{ m}$ and thus the spatial Nyquist wave number is $k_{y,N} = \frac{\pi}{\Delta y} = 20\text{ rad/m}$. The spectral repetitions of $\mu = \pm 1$ are indicated with \textcircled{R} . In Fig. 3.22b the spatial postaliasing types that can occur for this example are depicted: (i) propagating postaliasing by contributions from the propagating driving function and Green's function $\textcircled{1} \rightarrow$ Table 3.2, (ii) evanescent postaliasing by contributions from the propagating driving function and the evanescent Green's function $\textcircled{2} \rightarrow$ Table 3.3 and (iii) evanescent postaliasing by contributions from the evanescent driving function and Green's function $\textcircled{3} \rightarrow$ Table 3.5. Evanescent postaliasing $\textcircled{2}$, $\textcircled{3}$ exhibits negligible contributions to the intended sound field for meaningful listener distances, cf. Fig. 3.24d. The most critical contribution is the propagating postaliasing $\textcircled{1}$ that occurs within the visible region $|k_y| < \frac{\omega}{c}$ of the array. Especially the grating lobes of same amplitude as the main lobe severely corrupt the intended sound field and thus should be strictly avoided. Usually the discussion on spatial aliasing and its avoidance is restricted to these propagating grating lobes.

Farfield Radiation Pattern

Due to the importance of avoiding grating lobes within the visible region, it is common practice in array processing to state the farfield radiation pattern for a given temporal frequency ω or wave length λ , i.e. $\frac{\omega}{c} = \frac{2\pi}{\lambda}$ and a given Δy in

different normalized spaces w.r.t. the ratio $\frac{\Delta y}{\lambda}$. The u -space definition is with $k_y = \frac{\omega}{c} \sin \varphi = \frac{2\pi}{\lambda} \sin \varphi = \frac{\omega}{c} u = \frac{2\pi}{\lambda} u$ given as [Van02, (2.96)]

$$D_{w,s}(u) = \frac{\sin(u \frac{N}{2} \frac{2\pi}{\lambda} \Delta y)}{\sin(u \frac{1}{2} \frac{2\pi}{\lambda} \Delta y)} \quad \text{for } -1 \leq u \leq +1. \quad (3.80)$$

The Ψ -space definition is highly connected to the z -transform of the array weights evaluated on the unit circle, (3.68), [Sch43]. For the visible region it is given as [Van02, (2.97)]

$$D_{w,s}(\Psi) = \frac{\sin(\frac{\Psi N}{2})}{\sin(\frac{\Psi}{2})} \quad \text{for } -\frac{2\pi \Delta y}{\lambda} \leq \Psi \leq +\frac{2\pi \Delta y}{\lambda}. \quad (3.81)$$

Thus, for the visible region (3.68) takes the form

$$D_{w,s}(\Psi) = \sum_{\mu=-\frac{N-1}{2}}^{+\frac{N-1}{2}} e^{+j\Psi\mu}, \quad (3.82)$$

from which the link to the z -transform and the discrete-space Fourier transform becomes obvious, when Ψ is not bounded to the visible region. The φ -space is used as a nonlinear mapping between $k_y \leftrightarrow \varphi$, to interpret farfield radiation patterns as polar diagrams. It is given as [Van02, (2.95)]

$$D_{w,s}(\varphi) = \frac{\sin(\sin \varphi \frac{N}{2} \frac{2\pi}{\lambda} \Delta y)}{\sin(\sin \varphi \frac{1}{2} \frac{2\pi}{\lambda} \Delta y)} \quad \text{for } -\frac{\pi}{2} \leq \varphi \leq +\frac{\pi}{2}. \quad (3.83)$$

$D_{w,s}(u)$, $D_{w,s}(\Psi)$ and $D_{w,s}(\varphi)$ therefore are the farfield radiation patterns of the array – also referred to as *array factor* [Van02, p.45], [IEE93] or *form factor* [Hei92b, II.2.a] – derived from the general function $D_{w,s}(k_y, \omega)$ for a given ω . These trigger the propagating part of the Green's function's spatio-temporal spectrum.

The number of occurring grating lobes within the visible region is given as

$$N_g = 2 \lfloor \frac{\Delta y}{\lambda} \rfloor, \quad (3.84)$$

for which $\Delta y < \lambda$ follows for its avoidance. If the complete grating lobe beams (i.e. the null-to-null beamwidth of the first grating lobes $\mu = \pm 1$) are not

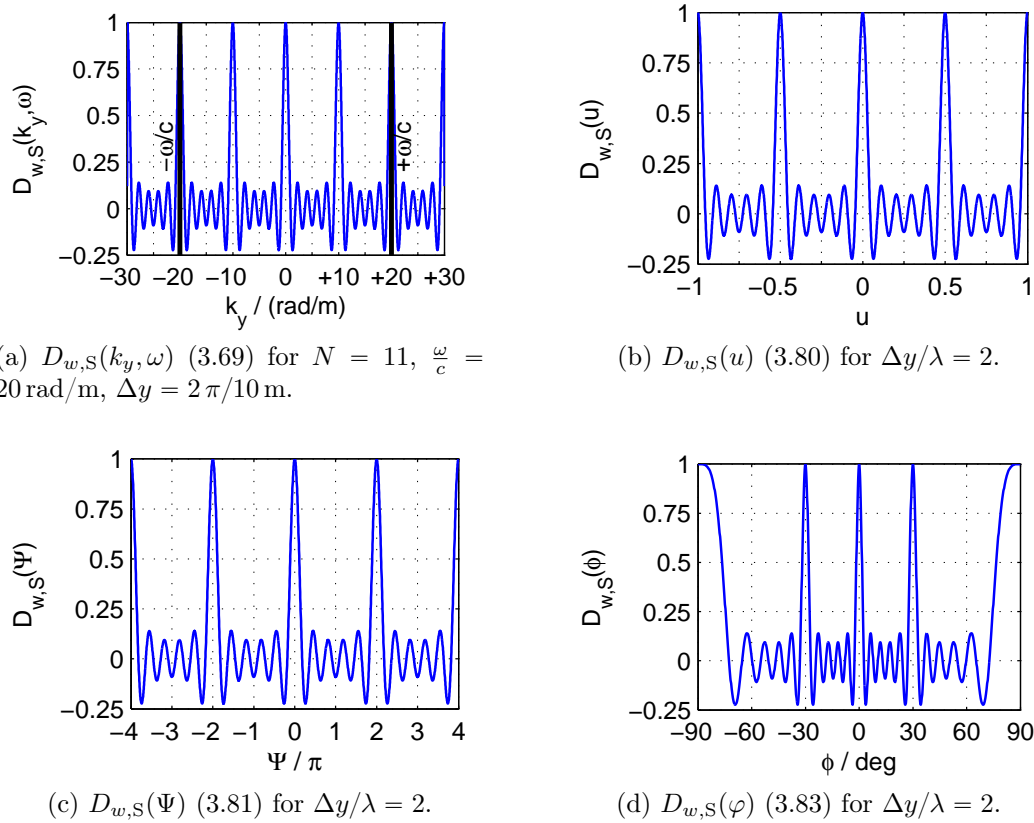


Figure 3.23: Unit gain normalized driving function (3.69) in different spaces for $N = 11$, $\frac{\omega}{c} = 20$ rad/m, $\Delta y = 2\pi/10$ m, thus $\Delta y/\lambda = 2$, cf. [Van02, Fig. 2.18].

allowed to enter the visible region, the condition reads [Ste27, (12)]

$$\Delta y \leq \lambda \frac{N-1}{N}, \quad (3.85)$$

which similar to (3.34) (i.e. the anti-aliasing condition for the infinite, discretized array) defines a criterion for avoidance of propagating spatial postaliasing by limiting the temporal frequency bandwidth of the driving function (3.69). In Fig. 3.23 $D_{w,S}(k_y, \omega)$ is exemplarily depicted in the different spaces. Four grating lobes occur within the visible region at $u = \pm 0.5, \pm 1$ that are mapped to radiation angles $\phi = \pm 30^\circ, \pm 90^\circ$ for the chosen parameters.

Another example is given in Fig. 3.15c and Fig. 3.15d that shows the mapping of the visible region of $D_{w,S}(k_y, \omega)$ to a polar diagram for a given temporal frequency. The array has a length of $L = N \Delta y$ that is equivalent to the continuous, finite length array of example Fig. 3.15a. Thus, the continuous and

discretized array exhibit the same zero-to-zero beamwidth. Also the same temporal frequency as for the continuous case is used to depict the polar pattern in Fig. 3.15d. Two grating lobes occur within the visible region at $\varphi = \pm 38.7^\circ$.

On-Axis Radiation, Fresnel/Fraunhofer Transition

(i) The same evaluation approach as for Fig. 3.17 (Angular Spectrum Synthesis of the Sound Field in the xy -Plane for the continuous LSA) using (3.58) is performed for this discretized array built from spherical monopoles. With (3.71) and (3.72) the main lobe sound field is defined for $|k_y| < \frac{2\pi}{\Delta y N} = \frac{2\pi}{L}$ with the equivalent length $L = \Delta y N$. The main lobe sound field's pressure level within the xy -plane is depicted in Fig. 3.24b. The side lobe sound field's pressure level is shown in Fig. 3.24c. Both sound fields interfere resulting in the complete sound field, for which the pressure level is depicted in Fig. 3.24a. The same observation as for the infinite, discretized array holds: non-negligible interferences yield the *chaotic region* (still a deterministic phenomenon), in which side and – here also – grating lobes corrupt the intended main lobe. The propagating postaliasing grating lobes produce beams of the same level as the main lobe.

In [Hei92b, p. 14, r_{Border}^2] the transition distance on the main lobe axis between the chaotic region and the so called collective Fraunhofer region was derived from the geometric diffraction approach to

$$x_B = \frac{1}{2} N^2 \Delta y^2 \frac{f}{c} - \frac{1}{4 \frac{f}{c}}. \quad (3.86)$$

For $x > x_B$ the interference with the side lobe sound field becomes negligible and the array radiates into the collective Fraunhofer region. For the chosen example (3.86) yields $x_B = 21.8$ m. All levels are normalized to the level of the complete sound field at this distance as before. Similar to Fig. 3.18 the on-axis level decay of the main lobe, side lobe and complete sound fields are visualized in Fig. 3.26f. The main lobe sound field exhibits a cylindrical wave level decay for $x < x_B$ and a spherical wave level decay $x > x_B$ on-axis, as expected for the Fresnel/Fraunhofer transition. In the Fresnel region the side lobe sound field has high level and the overall level of the complete sound field is highly dependent on the evaluation position due to destructive and constructive interference. It is observed that the 'rippled -3 dB per distance

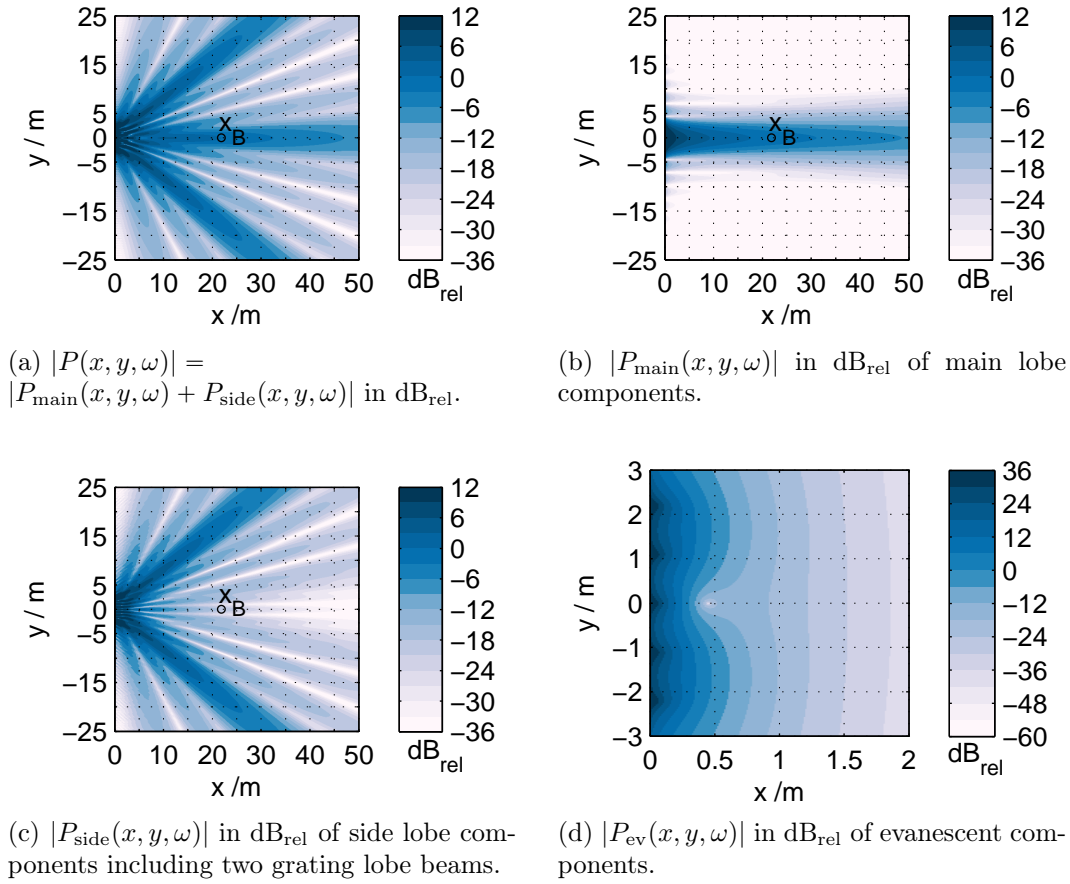


Figure 3.24: Level of sound fields with a discretized, finite length array for $L = 5.5$ m and $L/\lambda = 8$, $\lambda = 0.6875$ m $\rightarrow f \approx 500$ Hz using $D_{w,S}(k_y, \omega)$ (3.69) with $N = 5$, $\Delta y = 1.1$ m, cf. Fig. 3.15c and Fig. 3.15d that depict $D_{w,S}(k_y, \omega)$ for the same parameterization.

doubling level decay' in the Fresnel region of the continuous array not longer holds when postaliasing occurs.

The inverse spatial Fourier transform

$$\begin{aligned}
 P_{\text{ev}}(x, y, \omega) &= \frac{1}{2\pi} \int_{-\infty}^{-|\frac{\omega}{c}|} D_{w,S}(k_y, \omega) G_0(x, k_y, \omega) e^{-jk_y y} \\
 &\quad + \frac{1}{2\pi} \int_{+|\frac{\omega}{c}|}^{+\infty} D_{w,S}(k_y, \omega) G_0(x, k_y, \omega) e^{-jk_y y} \quad (3.87)
 \end{aligned}$$

constitutes the sound field that includes only the evanescent wave contributions. For that the evanescent part of the Green's function spatio-temporal spectrum (2.162) for $z = 0$ and $x > 0$

$$G_0(x, k_y, \omega) = \frac{1}{2\pi} K_0 \left(\sqrt{k_y^2 - \left(\frac{\omega}{c}\right)^2} \cdot x \right) \text{ for } k_y^2 > \left(\frac{\omega}{c}\right)^2 \quad (3.88)$$

is to be used.

For the discussed array the evanescent sound field is depicted in Fig. 3.24d. The level is also normalized w.r.t. $20 \log_{10}(|P(x = x_B, y = 0) \Delta y|) = 0 \text{ dB}_{\text{rel}}$. In the vicinity of the array, especially very near to the monopoles, very high levels exist. Besides the Fresnel and Fraunhofer region, the evanescent region is a third characteristic region. As expected, the evanescent components decay very rapidly. For $x > 1 \text{ m}$ the level is smaller $-20 \text{ dB}_{\text{rel}}$ and the evanescent contributions become insignificant compared to the propagating parts of the sound field. Thus, grating and side lobes of $D_{w,S}(k_y, \omega)$ that appear in the non-visible region of the array have minor influence on the radiation characteristics for reasonable listener positions in LS-SR and remain not further discussed in this work.

For Fig. 3.25 the array with $L = \Delta y N = 5.5 \text{ m} = \text{const}$ and $\frac{L}{\lambda} = 8$ is varied w.r.t. N and Δy . The sound field's pressure level is depicted with level normalization at x_B . Due to $\Delta y N = \text{const}$ the Fresnel/Fraunhofer region transition distance (3.86) and the zero-to-zero beamwidth are equal for all array configurations. Note that Fig. 3.25f and Fig. 3.24a show equivalent setups. In Fig. 3.26 the on-axis level decay is plotted for the side lobe sound field, the main lobe sound field and the complete sound field corresponding to the configurations used in Fig. 3.25. Starting from subfigure a), the discretization step Δy is successively increased in the following subfigures. Due to (3.85) the Fig. 3.25a to Fig. 3.25d show sound fields without spatial postaliasing, whereas Fig. 3.25e and Fig. 3.24a indicate propagating postaliasing with two grating lobes. Due to different spatial frequencies $k_y = \pm \frac{2\pi}{\Delta y} = \frac{\omega}{c} \sin \varphi$ they exhibit different radiation angles. The array configurations in Fig. 3.25a and Fig. 3.25b behave almost like the continuous array in Fig. 3.17a. The on-axis level decays in Fig. 3.26a and Fig. 3.26b support this observation, showing only very small deviations w.r.t. the side lobe level compared to the contin-

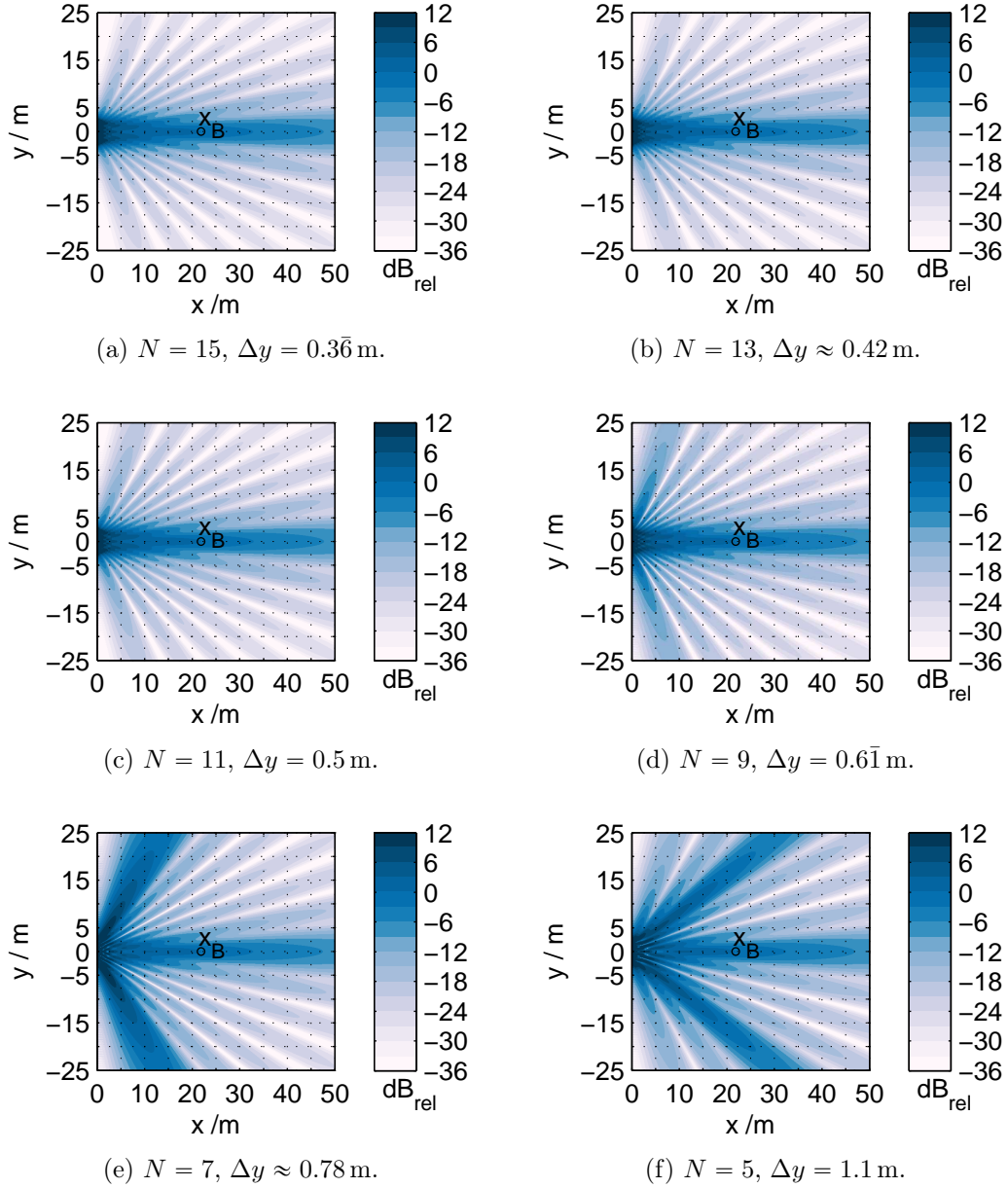


Figure 3.25: $|P(x, y, \omega) \Delta y|$ in dB_{rel} for LSA driven with $D_{w,S}(k_y, \omega)$ (3.69) using $L = \Delta y N = 5.5$ m = const for different discretization steps and $L/\lambda = 8 \rightarrow \lambda = 0.6875$ m $\rightarrow f \approx 500$ Hz.

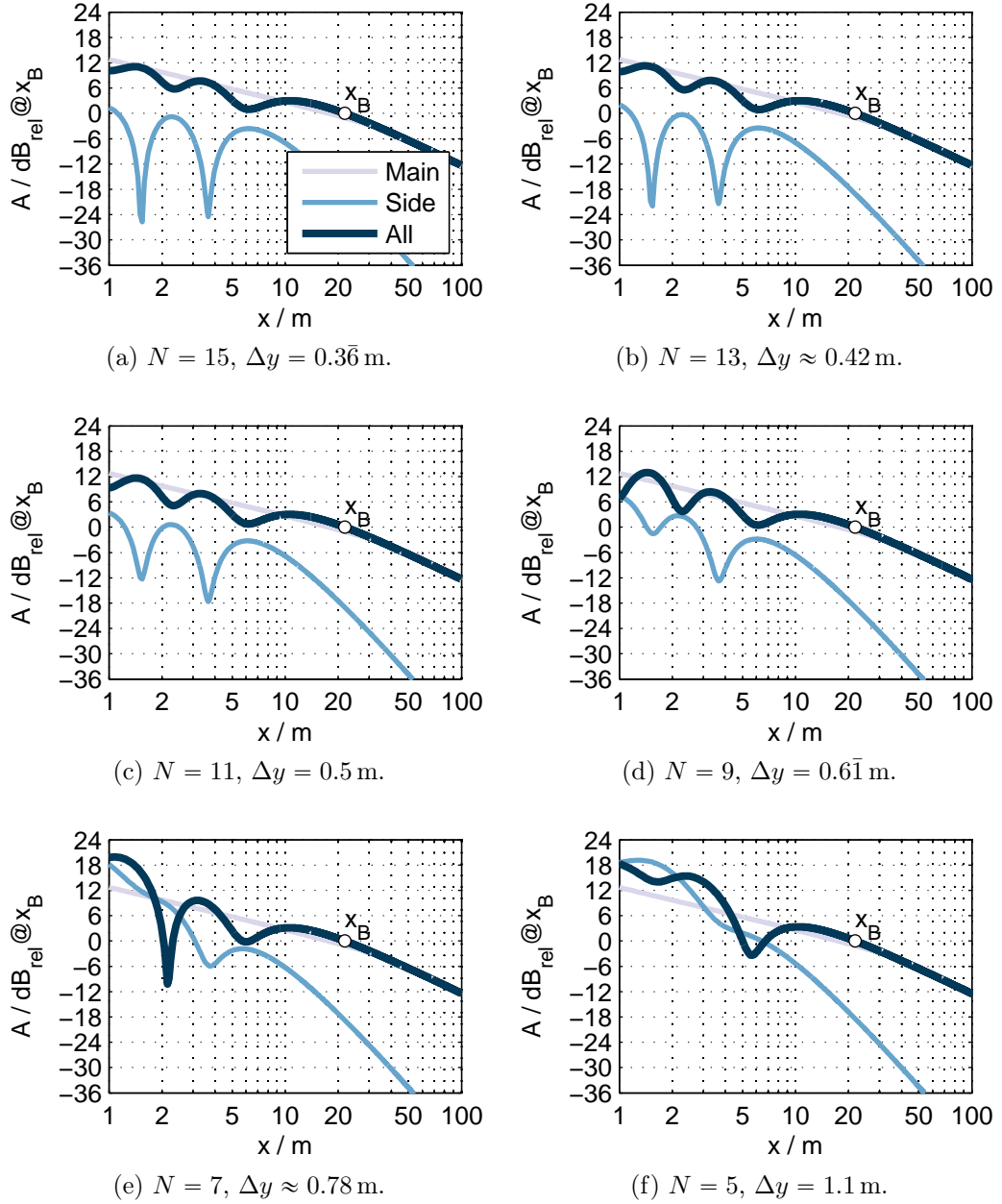


Figure 3.26: On-axis level for $|P_{\text{main}}(x, y = 0, \omega) \Delta y|$, $|P_{\text{side}}(x, y = 0, \omega) \Delta y|$ and $|P(x, y = 0, \omega) \Delta y|$ in dB_{rel} for LSA driven with $D_{w,S}(k_y, \omega)$ (3.69) using $L = \Delta y N = 5.5$ m = const for different discretization steps and $L/\lambda = 8 \rightarrow \lambda = 0.6875$ m $\rightarrow f \approx 500$ Hz.

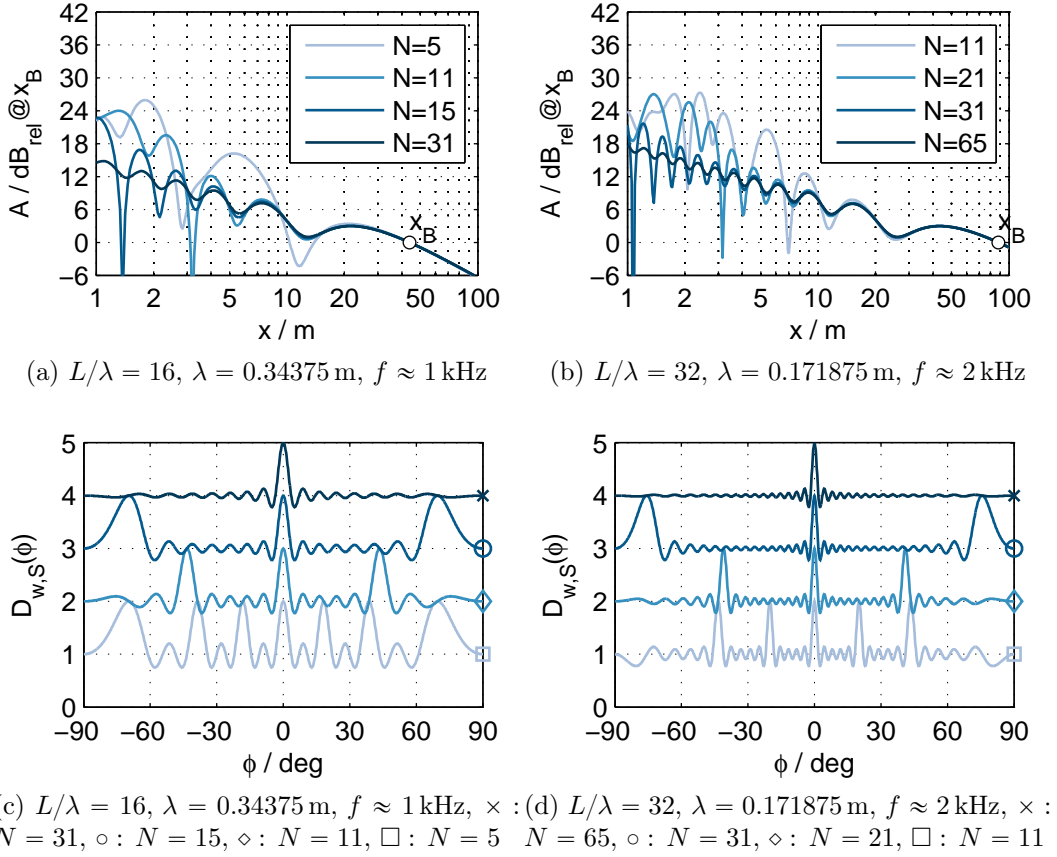


Figure 3.27: On-axis level $|P(x, y = 0, \omega) \Delta y|$ in dB_{rel} for LSA driven with $D_{w,S}(k_y, \omega)$ (3.69) using $L = \Delta y N = 5.5 \text{ m} = \text{const}$ for different discretization steps and temporal frequencies Fig. 3.27a, Fig. 3.27c: 1 kHz, Fig. 3.27b, Fig. 3.27d: 2 kHz.

uous array in Fig. 3.18. By further increasing Δy , side lobes with increased level near the first grating lobe enter the visible region. The sound field's pressure level within the xy -plane starts to deviate from that of a continuous array, cf. Fig. 3.25c and Fig. 3.25d. This is due to the altered side lobe sound fields in Fig. 3.26c and Fig. 3.26d. Their levels increase in the Fresnel region and thus the interference with the main lobe sound field has stronger impact, resulting in larger ripples in the Fresnel region. By further increasing Δy in Fig. 3.25e and Fig. 3.25f, two grating lobes enter the visible region and produce side lobe sound fields that severely corrupt the main lobe sound field in the Fresnel region. The side lobe level is partially larger than the main lobe level. The typical ripple characteristic and 3 dB level decay per distance doubling

in the Fresnel region of a continuous array is not longer observable in favor of an irregular level distribution. Although still deterministic, this characteristic is highly dependent on the chosen parameters f , N and Δy and hardly predictable without numerical evaluation. A Fresnel region that is corrupted by spatial aliasing should never be used as a listener region, when aiming at homogeneous sound reinforcement, which in essence is depicted in [Hei92b, Fig. 16, uncorrect array]. This region is not amenable for any equalization, since the behavior is highly dependent on the evaluation point and the frequency.

This phenomenon gets even worse if more grating lobes enter the visible region. For Fig. 3.27a and Fig. 3.27b the array with $L = \Delta y N = 5.5 \text{ m} = \text{const}$ is varied in frequency $\frac{L}{\lambda} = 16 \rightarrow \approx 1 \text{ kHz}$ and $\frac{L}{\lambda} = 32 \rightarrow \approx 2 \text{ kHz}$, respectively and the discretization step size as well. The on-axis level decays are depicted for the complete sound fields. In Fig. 3.27c and Fig. 3.27d the array factors $D_{w,s}(\varphi)$ (3.83) are depicted. The more grating lobes are within the visible region the more the Fresnel region is corrupted and thus becomes not very meaningfully usable for sound reinforcement. In essence, optimized LS-SR ideally requires an uncorrupted main lobe sound field free of side and grating lobe interference. In Ch. 4 it is discussed that this main lobe sound field can be interpreted as optimized wavefront shaping.

(ii) Similar to the derivation of (3.60) – i.e. the angular spectrum synthesis of the on-axis sound field – the inverse spatial Fourier transform of (3.14) using (3.69)

$$\begin{aligned}
 P(x, y, \omega) &= \frac{-j}{8\pi} \int_{-\frac{\omega}{c}}^{+\frac{\omega}{c}} \frac{\sin(k_y \Delta y \frac{N}{2})}{\sin(k_y \Delta y \frac{1}{2})} \cdot H_0^{(2)} \left(\sqrt{\left(\frac{\omega}{c}\right)^2 - k_y^2} \cdot x \right) \cdot e^{-jk_y y} dk_y \rightarrow \\
 &\quad \underbrace{G_{0,2D, \text{Far}}(x, \omega)} \\
 P(x, y = 0, \omega) &= \frac{-j}{4} \sqrt{\frac{2}{\pi \frac{\omega}{c} x}} e^{-j \frac{\omega}{c} x} e^{+j \frac{\pi}{4}} \times \\
 &\quad \underbrace{\int_0^{+\pi/2} \frac{\omega}{c} \frac{e^{-j \frac{\omega}{c} x (\cos \varphi - \sin \varphi \Delta y \frac{N}{2x} - 1)} - e^{-j \frac{\omega}{c} x (\cos \varphi + \sin \varphi \Delta y \frac{N}{2x} - 1)}}{2\pi j \sin(\frac{\omega}{c} \sin \varphi \Delta y \frac{1}{2})} \sqrt{\cos \varphi} d\varphi}_{\text{Mod}(\Delta y, N, x, \omega)}
 \end{aligned} \tag{3.89}$$

is derived for evaluation along the main lobe axis utilizing the large argument approximation of the Hankel function. This again is to be interpreted as the far- and free-field 2D Green's function that is modulated over distance x with the integral expression. With the equivalent length $L = N \Delta y$ and $\lambda \gg \Delta y$ – thus modeling a quasi-continuous, spatial aliasing free array – from (3.89) follows

$$P(x, y = 0, \omega) = \frac{-j}{4} \sqrt{\frac{2}{\pi \frac{\omega}{c} x}} e^{-j \frac{\omega}{c} x} e^{+j \frac{\pi}{4}} \times \int_0^{+\pi/2} \frac{e^{-j \frac{\omega}{c} x (\cos \varphi - \sin \varphi \frac{L}{2x} - 1)} - e^{-j \frac{\omega}{c} x (\cos \varphi + \sin \varphi \frac{L}{2x} - 1)}}{j \pi \sin \varphi \Delta y} \sqrt{\cos \varphi} d\varphi \quad (3.90)$$

with a further applied small argument approximation $\sin(x) \approx x$ in the integrand's denominator. The result is then equivalent with the continuous array (3.60) besides the weighting factor $\frac{1}{\Delta y}$ that is due to the chosen sampling scheme normalization (3.26). In Fig. 3.28 the on-axis level decay is depicted together with its generating components from (3.89). Note that $P(x, y = 0, \omega)$ and $\text{Mod}(\Delta y, N, \omega, x)$ are weighted with Δy to obtain same levels independently from the employed monopole spacing. For $x > x_B$ the same observations as for the continuous LSA hold. The modulation function takes the form of a straight line with 3 dB level decay per distance doubling. For $x < x_B$ the ripples of the modulation function highly vary in level over distance when grating lobes enter the visible region, cf. Fig. 3.28f and Fig. 3.28e. Due to the sophisticated characteristic of the modulation function (3.89) it is not expected to find an analytic closed form solution. Thus, interference phenomena have to be evaluated numerically. For that the approach (i) can be used for any desired driving function and LSA configurations including loudspeaker radiation characteristics, while (ii) is restricted to the presented case of a rectangular windowed, uniformly driven LSA using spherical monopoles.

3.2.5 Delay & Sum Beamforming $D_{w,S,\text{Steered}}(k_y, \omega)$

Up to now, only the main lobe radiation perpendicular to the array was considered with the derived WST driving functions, realizing a broadband array. For extended discussions on the possible limitations of WST it is meaningful to revisit the simplest beamforming approach, the *delay-and-sum beamformer*

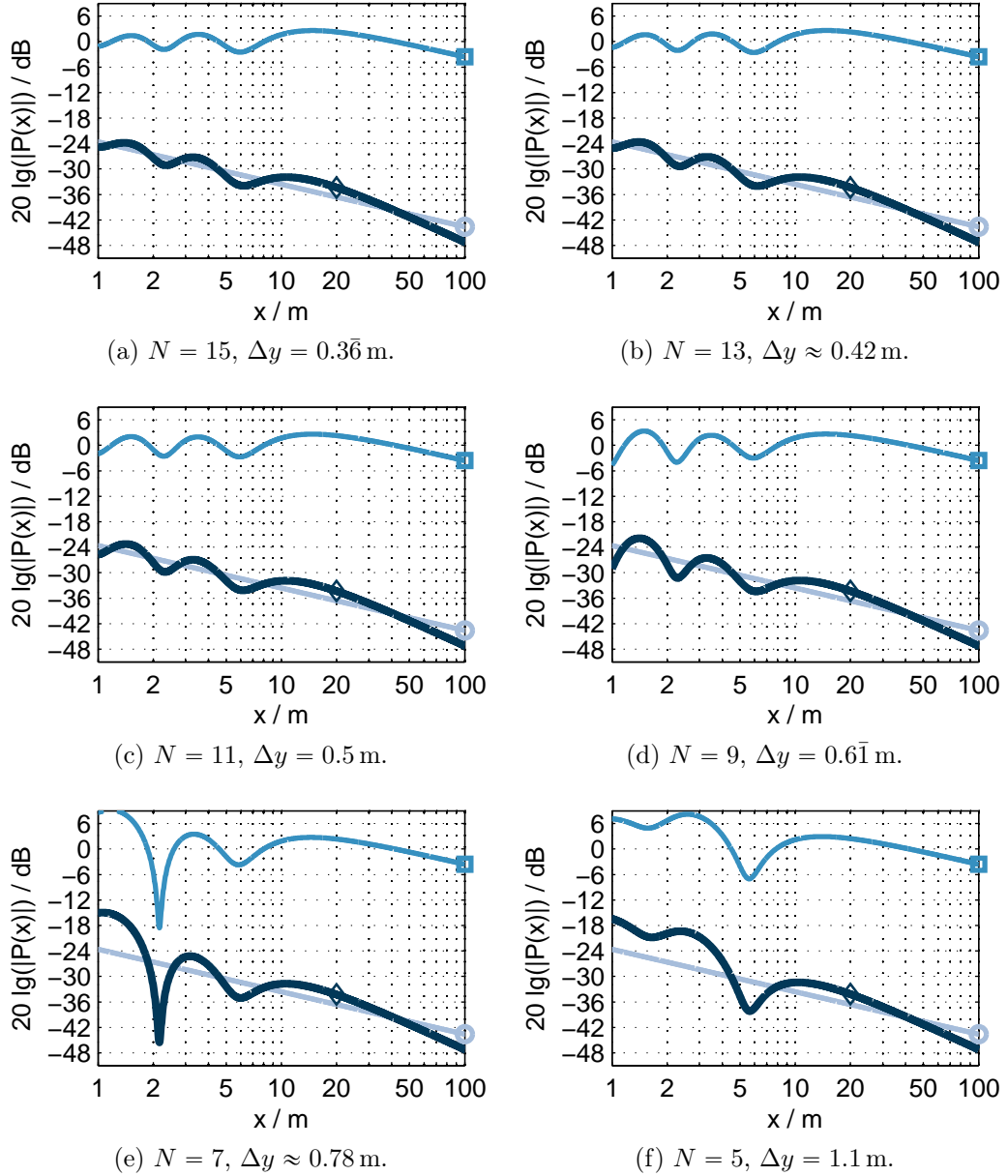


Figure 3.28: $|P(x, y = 0, \omega) \Delta y| \diamond$, $|G_{0,2D, \text{Far}}(x, \omega)| \circ$, $|\text{Mod}(\Delta y, N, x, \omega) \Delta y| \square$ (3.89) in dB_{rel} for LSA driven with $D_{w,S}(k_y, \omega)$ (3.69) using $L = \Delta y N = 5.5$ m = const and different discretization steps. $\frac{L}{\lambda} = 8$.

(DSB) [Van02, Ch. 2.5]. With the modulation theorem of the spatial Fourier transform

$$D(y_0, \omega) \circ \text{---} \bullet D(k_y, \omega), \quad (3.91)$$

$$e^{-j k_{y,\text{Steer}} y_0} \circ \text{---} \bullet 2 \pi \delta(k_y - k_{y,\text{Steer}}), \quad (3.92)$$

$$D(y_0, \omega) e^{-j k_{y,\text{Steer}} y_0} \circ \text{---} \bullet D(k_y - k_{y,\text{Steer}}, \omega) \quad (3.93)$$

the driving function's spectrum for the infinite, continuous array (3.25) can be written as (cf. (2.166) for $k_{y,\text{Steer}} = k_{y,\text{PW}}$)

$$D_{\text{Steered}}(k_y, \omega) = 2 \pi \delta(k_y - k_{y,\text{Steer}}), \quad (3.94)$$

the driving function's spectrum for the infinite, discretized array built from monopoles (3.30) as

$$D_{\text{S,Steered}}(k_y, \omega) = \frac{2 \pi}{\Delta y} \sum_{\mu=-\infty}^{+\infty} \delta(k_y - k_{y,\text{Steer}} - \mu \frac{2 \pi}{\Delta y}), \quad (3.95)$$

the driving function's spectrum for the continuous, rectangular windowed, finite length LSA (3.38) as

$$D_{w,\text{Steered}}(k_y, \omega) = L \frac{\sin\left([k_y - k_{y,\text{Steer}}] \frac{L}{2}\right)}{[k_y - k_{y,\text{Steer}}] \frac{L}{2}}, \quad (3.96)$$

and the driving function's spectrum for the discretized, rectangular windowed, finite length LSA built from monopoles (3.69) as

$$D_{w,\text{S,Steered}}(k_y, \omega) = \frac{\sin\left([k_y - k_{y,\text{Steer}}] \Delta y \frac{N}{2}\right)}{\sin\left([k_y - k_{y,\text{Steer}}] \Delta y \frac{1}{2}\right)}. \quad (3.97)$$

Considering propagating wave radiation only by using (2.165)

$$k_{x,\text{Steer}} = \frac{\omega}{c} \cos \varphi_{\text{Steer}} \quad k_{y,\text{Steer}} = \frac{\omega}{c} \sin \varphi_{\text{Steer}}, \quad (3.98)$$

the radiation direction of the main lobe within the xy -plane can be given as the unit vector

$$\mathbf{k}_{\text{Steer}} = (\cos \varphi_{\text{Steer}}, \sin \varphi_{\text{Steer}})^{\text{T}}. \quad (3.99)$$

For $0 < k_{y,\text{Steer}} < +\frac{\omega}{c}$, i.e. $0^\circ < \varphi_{\text{Steer}} < +90^\circ$ the main lobe beam is steered up into the first quadrant ($x > 0, y > 0$). For $-\frac{\omega}{c} < k_{y,\text{Steer}} < 0$, i.e. $-90^\circ < \varphi_{\text{Steer}} < 0^\circ$ the main lobe beam is steered down into the fourth quadrant ($x > 0, y < 0$). For $|k_{y,\text{Steer}}| > \frac{\omega}{c}$ the main lobe leaves the visible region, resulting in an evanescent main lobe wave radiation and thus only side and grating lobes produce propagating wave radiation.

The derivation of the DSB with the modulation theorem of the spatial Fourier transform does not reveal the practical implications on how to implement the DSB. Furthermore, the given solutions assume that positive and negative delays may be applied to the sources, which is not feasible. The implications become more obvious when applying the shift theorem of the temporal Fourier transform. Consider the practical case of a uniformly driven, finite length LSA with N spherical monopoles located on the positive y -axis, starting from the origin for convenience. With a cumulative delay time $\mu \tau$, $\tau \in \mathbb{R}_0^+$ applied to the sources and the shift theorem $x(t - \mu \tau) \circ \bullet e^{-j\omega \mu \tau} X(\omega)$ (C.12), the driving function's spatio-temporal spectrum for upward beam steering reads, cf. (3.68)

$$D_{w,S,\text{UpSteer}}(k_y, \omega) = \sum_{\mu=0}^{N-1} [e^{-j\omega \tau \mu}] e^{+j k_y \Delta y \mu} = \sum_{\mu=0}^{N-1} e^{+j(k_y \Delta y - \omega \tau) \mu}, \quad (3.100)$$

and for downward beam steering follows

$$\begin{aligned} D_{w,S,\text{DownSteer}}(k_y, \omega) &= \sum_{\mu=0}^{N-1} [e^{-j\omega \tau (N-1-\mu)}] e^{+j k_y \Delta y \mu} \\ &= e^{-j\omega \tau (N-1)} \sum_{\mu=0}^{N-1} e^{+j(k_y \Delta y + \omega \tau) \mu}. \end{aligned} \quad (3.101)$$

Similar to (3.69), both geometric series can be given in closed form

$$D_{w,S,Steered}(k_y, \omega) = e^{+j(k_y \Delta y - \omega \tau) \frac{N-1}{2}} \cdot \frac{\sin([k_y \Delta y \mp \omega \tau] \frac{N}{2})}{\sin([k_y \Delta y \mp \omega \tau] \frac{1}{2})}, \quad (3.102)$$

where the first case (−) describes upward and the second case (+) downward beam steering. With the definition of the propagation velocity $c_{\text{Steer}} \in \mathbb{R}^+$

$$c_{\text{Steer}} = \frac{\Delta y}{\tau} \quad (3.103)$$

along the array and the temporal frequency dependent source's wave number

$$k_{y,\text{Steer}} = \pm \frac{\omega}{c_{\text{Steer}}} \quad (3.104)$$

the relation

$$\omega \tau = \pm k_{y,\text{Steer}} \Delta y \quad (3.105)$$

links the temporal delay to the spatio spectrum domain, where again the first case (here with + sign) describes upward and the second case (here with − sign) downward beam steering. Introducing this into (3.102) yields

$$D_{w,S,Steered}(k_y, \omega) = e^{+j[k_y \mp k_{y,\text{Steer}}] \Delta y \frac{N-1}{2}} \cdot \frac{\sin([k_y - k_{y,\text{Steer}}] \Delta y \frac{N}{2})}{\sin([k_y - k_{y,\text{Steer}}] \Delta y \frac{1}{2})}. \quad (3.106)$$

For consistency the array is relocated symmetrical to the origin. This is conveniently done with the shift theorem of the spatial Fourier transform (C.10) and finally yields the driving functions' spatio-temporal spectrum of the DSB

$$D_{w,S,Steered}(k_y, \omega) = e^{\mp j k_{y,\text{Steer}} \Delta y \frac{N-1}{2}} \cdot \frac{\sin([k_y - k_{y,\text{Steer}}] \Delta y \frac{N}{2})}{\sin([k_y - k_{y,\text{Steer}}] \Delta y \frac{1}{2})}. \quad (3.107)$$

Note that the frequency dependent phase shift of the DSB is frequently ignored in the literature. In [Mö09, Ch. 3.5.3] the correct spatio-temporal spectrum of the DSB is given, though only for upward beam steering for convenience of the mathematical treatment.

For the supersonic case, i.e. $c_{\text{Steer}} > c$ the radiation angle φ_{Steer} of the

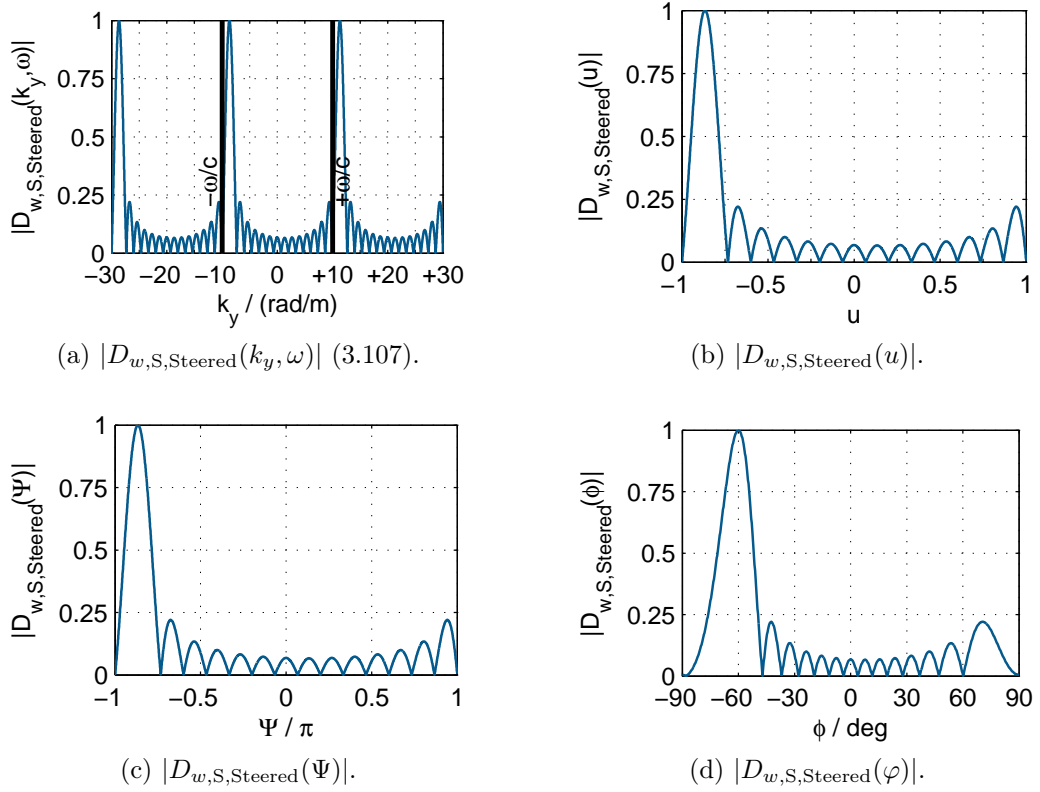


Figure 3.29: Supersonic DSB: unit gain normalized driving function (3.107) in different spaces for $N = 15$, $\frac{\omega}{c} = 10$ rad/m, $\Delta y = 2\pi/20$ m, thus $\frac{\Delta y}{\lambda} = \frac{1}{2}$ and $\varphi_{\text{Steer}} = -60^\circ$, $k_{y,\text{Steer}} = -8.66$ rad/m, $\tau = 0.7932$ ms, $c_{\text{Steer}} = 396.06$ m/s.

propagating main lobe and the propagation velocity is linked to

$$c_{\text{Steer}} = \frac{\Delta y}{\tau} = \frac{c}{|\sin \varphi_{\text{Steer}}|}. \quad (3.108)$$

The main lobe can be steered within the visible region. For the case $\varphi_{\text{Steer}} = \pm 90^\circ$ the endfired array with $c_{\text{Steer}} = c$ is obtained, whereas $\varphi_{\text{Steer}} = 0^\circ$, i.e. $c_{\text{Steer}} = \infty \rightarrow k_{y,\text{Steer}} = 0$ yields the broadband array. For the subsonic case $c_{\text{Steer}} < c$ only side and grating lobes are located in the visible region and produce propagating wave radiation. The main lobe becomes evanescent. In Fig. 3.29 an example for a supersonic DSB is depicted for an LSA that fulfills the anti-aliasing condition. The main lobe is steered to $\varphi_{\text{Steer}} = -60^\circ$. In Fig. 3.30 the subsonic DSB is visualized. The main lobe is shifted to $k_{y,\text{Steer}} = -15$ rad/m outside the visible region. In this example a grating lobe within the visible region located at $k_y = 0$ produces propagating spatial aliasing that

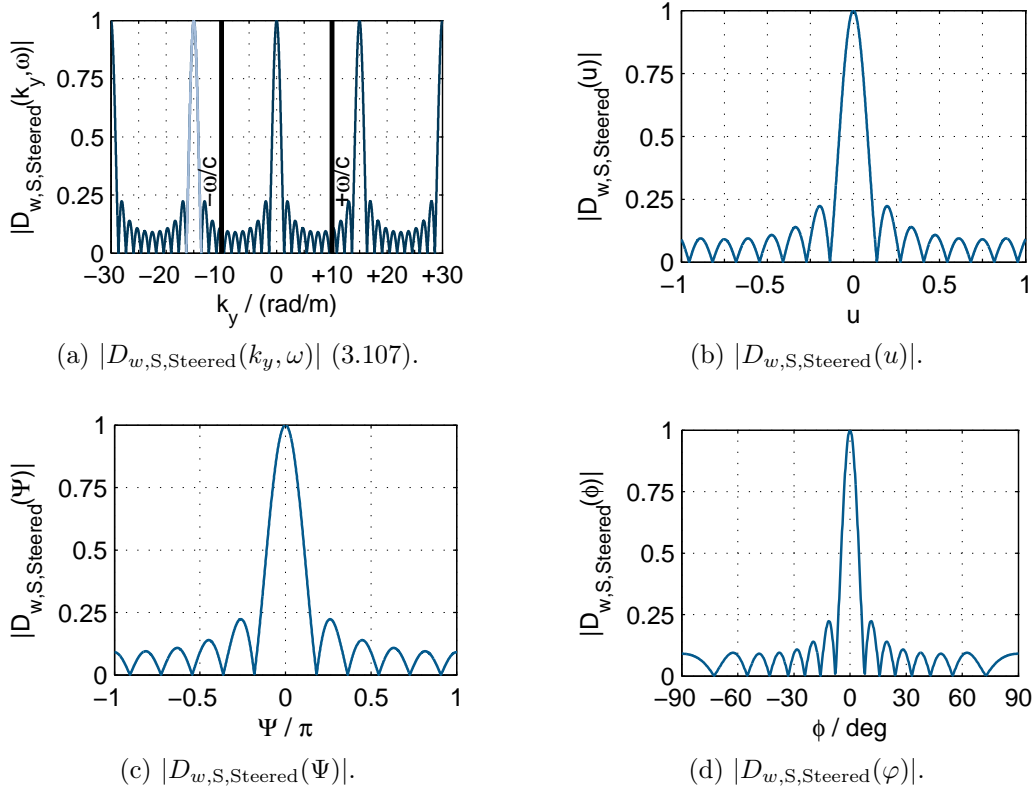


Figure 3.30: Subsonic DSB: unit gain normalized driving function (3.107) in different spaces for $N = 11$, $\frac{u}{c} = 10$ rad/m, $\Delta y = 2\pi/15$ m, thus $\frac{\Delta y}{\lambda} = \frac{2}{3}$ and $k_{y,Steer} = -15$ rad/m, $\tau = 1.8318$ ms, $c_{Steer} = 228.6$ m/s.

radiates perpendicular to the LSA with the same amplitude as the intended main lobe. Note that both LSAs exhibit about the same length, therefore their main and grating lobe beamwidth are roughly of the same size in k_y , u and Ψ -space, since these spaces are shift invariant w.r.t. the spectrum. However, in ϕ -space, due to the nonlinear mapping, for larger $|\phi|$ the main and grating lobe bandwidth increases and lobes become unsymmetrical.

Anti-Aliasing Condition

In order to avoid propagating spatial aliasing from grating lobes the anti-aliasing condition [Ste29, p.175]

$$\Delta y < \frac{\lambda_{\min}}{2} \frac{N-1}{N} \quad (3.109)$$

must hold. It ensures that no grating lobe beams enter the visible region for all possible steering angles $|\varphi_{\text{Steer}}| < 90^\circ$ of the discussed rectangular windowed LSA built from spherical monopoles. For a very large source number N (3.109) merges into – what is also stated as the WST#2 criterion –

$$\Delta y < \frac{\lambda_{\min}}{2}, \quad (3.110)$$

which is equivalent allowing only radiating wave numbers up to the spatial Nyquist wave number, cf. (3.16). Thus, instead of using the spatial lowpass characteristic of a postfilter to avoid spatial aliasing, the criterion relies on the limitation of the excitation signal's temporal frequency bandwidth to $f_{\max} = \frac{c}{\lambda_{\min}}$. Eq. (3.110) is commonly referred to as the spatial sampling condition. The condition (3.109) may be relaxed if only a limited steering angle $|\varphi_{\text{Steer}}| < |\varphi_{\text{Steer,max}}|$ is allowed. For an infinite linear array the condition [Spo06c, (10)], [Ahr10d, (38)]

$$\Delta y < \frac{\lambda_{\min}}{1 + |\sin \varphi_{\text{Steer,max}}|} \quad (3.111)$$

for SFS of a plane wave was already discussed in (3.33), which is also well known in antenna design [Kum92, (13)], [Van02, (2.129)]. For a finite length, rectangular windowed array with N spherical monopoles the condition becomes

$$\Delta y < \frac{\lambda_{\min}}{1 + |\sin \varphi_{\text{Steer,max}}|} \frac{N - 1}{N}, \quad (3.112)$$

which is consistent with the result given in [Ste27, (12)] for $\varphi_{\text{Steer,max}} = 0$.

Very small discretization steps and thus very small individual drivers are required to fulfill the condition (3.112) for the highest audio frequencies. This is visualized in Fig. 3.31 for chosen discretization steps. The LSA length is always $L \approx 5$ m. In the given example using 1"-drivers would allow grating lobe free sound fields up to 10 kHz, when restricting $|\varphi_{\text{Steer,max}}| < 20^\circ$, while the 0.45"-drivers would allow endfire beams up to 15 kHz. Such techniques (e.g. using 1.5"-drivers) have been engineered nowadays, while this was not considered feasible when initially approaching LSA designs in the early 1990s.

Therefore, WST proposed another approach to avoid or reduce propagating spatial aliasing by using a specific postfilter for uniformly driven LSAs and ini-

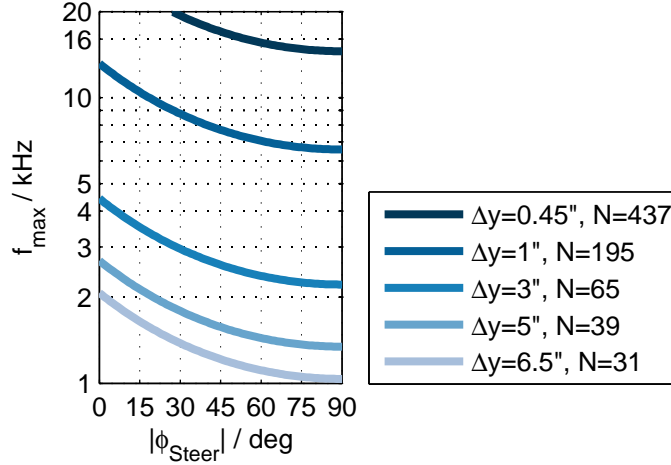


Figure 3.31: Aliasing frequency over steering angle (3.112).

tially waiving electronic beam steering approaches such as DSB for the highest audio frequencies. This technique is discussed in the next section.

3.3 Ideal WST-Postfilter

For the WST driving function (3.30) a very specific postfilter, i.e. a loudspeaker radiation characteristic acts as an ideal reconstruction filter. Consider the corresponding signal flow of an infinite, discretized SSD depicted in Fig. 3.32, for which similar to (3.32) the synthesized sound field is given as

$$P(x, y, \omega) = \frac{1}{\Delta y} \sum_{\mu=-\infty}^{+\infty} H_{\text{Post}}(k_y = \mu \frac{2\pi}{\Delta y}, \omega) G_0(x, k_y = \mu \frac{2\pi}{\Delta y}, \omega) e^{-j\mu \frac{2\pi}{\Delta y} y} \quad (3.113)$$

with an included reconstruction filter.

The ideal WST postfilter is applied for the highest audio frequencies in order to avoid the actually required very small distances between the speakers

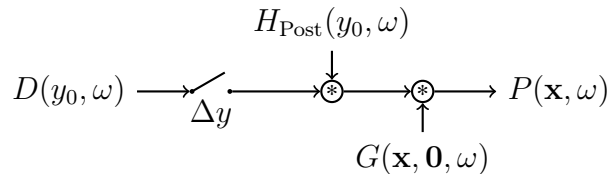


Figure 3.32: Signal flow of the single layer potential for a linear, infinite, discretized SSD located on the y -axis using a reconstruction filter.

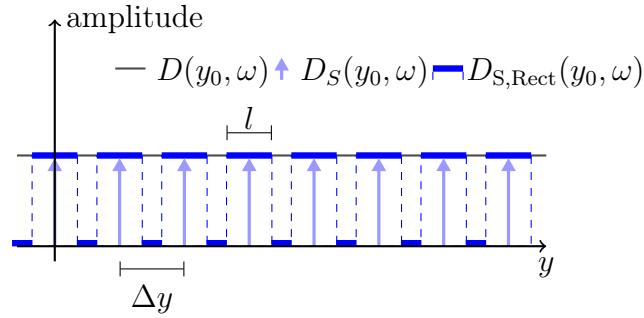


Figure 3.33: Spatial sampling and reconstruction: continuous WST driving function $D(y_0, \omega)$, sampled driving function $D_S(y_0, \omega)$ and reconstructed driving function $D_{S,Rect}(y_0, \omega)$ with the rect-function used as the postfilter.

for spatial-aliasing free SFS. This filter then allows rather large discretization steps Δy . From [Hei92b, I.3.], [Urb03, Fig. 6] it may be deduced that the employed waveguides, i.e. specially designed horns for the high frequency section can be modeled as ideal line pistons of length l (called *slot* in [Hei92b, II.2.c]). The resulting reconstructed driving function using waveguides is piecewise constant with amplitudes $D_{S,H}(y_0, \omega) = D_{S,Rect}(y_0, \omega) \in \{0, 1\}$. This is illustrated in Fig. 3.33. A similar visualization was used in [Urb03, Fig. 6] to motivate waveguide modeling. The ideal line piston can be given as a rect-function postfilter and its corresponding sinc-function in the spatial Fourier domain [Gir01, (9.19)], [Gir01, (9.24)], similar to (3.36)

$$\begin{aligned}
 H_{Rect}(y_0, \omega) &= \text{rect}\left(\frac{y_0}{l}\right) = \begin{cases} 1 & \text{for } |y_0| \leq \frac{l}{2} \\ 0 & \text{else} \end{cases} \quad \circ \bullet \\
 H_{Rect}(k_y, \omega) &= l \text{si}\left(\frac{k_y l}{2}\right) \begin{cases} l \frac{\sin\left(\frac{k_y l}{2}\right)}{\frac{k_y l}{2}} & \text{for } k_y \neq 0 \\ l & \text{for } k_y = 0. \end{cases} \quad (3.114)
 \end{aligned}$$

This constitutes a transposed correspondence of the ideal lowpass filter in temporal and spatial sampling, cf. (3.7), (3.17). The sampled driving function (3.26) is interpolated with the postfilter by convolution

$$D_{S,Rect}(y_0, \omega) = \left[D(y_0, \omega) \cdot \sum_{\mu=-\infty}^{+\infty} \delta(y_0 - \mu \Delta y) \right] *_y \text{rect}\left(\frac{y_0}{l}\right), \quad (3.115)$$

which corresponds to [Gir01, (11.49)]

$$D_{\text{S,Rect}}(k_y, \omega) = \frac{1}{2\pi} \frac{2\pi}{\Delta y} \sum_{\mu=-\infty}^{+\infty} D(k_y - \mu \frac{2\pi}{\Delta y}, \omega) \cdot l \frac{\sin\left(\frac{k_y l}{2}\right)}{\frac{k_y l}{2}} \quad (3.116)$$

in the spatio-temporal spectrum domain. Inserting the WST driving function (3.23) – Fig. 3.33, gray – into (3.115), and (3.30) into (3.116) respectively, yields

$$D_{\text{S,Rect}}(y_0, \omega) = \left[1 \cdot \sum_{\mu=-\infty}^{+\infty} \delta(y_0 - \mu \Delta y) \right] *_y \text{rect}\left(\frac{y_0}{l}\right), \quad (3.117)$$

$$D_{\text{S,Rect}}(k_y, \omega) = \frac{1}{\Delta y} \sum_{\mu=-\infty}^{+\infty} 2\pi \delta(k_y - \mu \frac{2\pi}{\Delta y}) \cdot l \frac{\sin\left(\frac{k_y l}{2}\right)}{\frac{k_y l}{2}}. \quad (3.118)$$

The Dirac comb in $D_S(y_0, \omega)$ – Fig. 3.33, light blue – is 'smeared' by the convolution with the rect-function yielding $D_{\text{S,Rect}}(y_0, \omega)$ – Fig. 3.33, dark blue.

From Fig. 3.33 can be graphically deduced that the driving function $D(y_0, \omega) = 1 = D_{\text{S,Rect}}(y_0, \omega)$ is perfectly reconstructed when $l = \Delta y$. This models a quasi-continuous LSA and is conveniently proven within the spatio-temporal spectrum domain. For $l = \Delta y$ (3.118) reads

$$D_{\text{S,Rect}}(k_y, \omega) = \sum_{\mu=-\infty}^{+\infty} 2\pi \delta(k_y - \mu \frac{2\pi}{\Delta y}) \cdot \frac{\sin\left(\frac{k_y \Delta y}{2}\right)}{\frac{k_y \Delta y}{2}}. \quad (3.119)$$

The Dirac impulses w.r.t. μ in the Dirac comb with spacing $\Delta k_y = \frac{2\pi}{\Delta y} = \frac{2\pi}{l}$ are weighted by the sinc-function. The individual contributions read

$$\begin{aligned} D_{\text{S,Rect}}(k_y, \omega)_\mu &= 2\pi \delta(k_y - \mu \frac{2\pi}{\Delta y}) \frac{\sin\left(\frac{\mu \frac{2\pi}{\Delta y} \Delta y}{2}\right)}{\frac{\mu \frac{2\pi}{\Delta y} \Delta y}{2}} \\ &= 2\pi \delta(k_y - \mu \frac{2\pi}{\Delta y}) \frac{\sin(\mu \pi)}{\mu \pi}. \end{aligned} \quad (3.120)$$

For $\mu = 0$ follows

$$D_{\text{S,Rect}}(k_y, \omega)_{\mu=0} = 2\pi \delta(k_y) = D(k_y, \omega) \quad (3.121)$$

and for $\mu \neq 0$ due to the zeros of the sinc-function

$$D_{\text{S,Rect}}(k_y, \omega)_{\mu \neq 0} = 0. \quad (3.122)$$

This proves perfect reconstruction towards (3.25)

$$D_{\text{S,Rect}}(k_y, \omega) = \begin{cases} D(k_y, \omega) = 2\pi \delta(k_y) & \text{if } \mu = 0 \\ 0 & \text{otherwise} \end{cases}. \quad (3.123)$$

Note that this perfect reconstruction holds only for the WST driving function (3.25), i.e. wave radiation perpendicular to the LSA and $\Delta y = l$. This reconstruction is then independent from the temporal frequency and from the chosen length l , as long $\Delta y = l$ holds.

The same discussion can be given for $D_{w,\text{S}}(k_y, \omega)$ (3.69), i.e. the finite length LSA using $H_{\text{Rect}}(k_y, \omega)$ (3.114) for the case $\Delta y = l$ by observing that $L = Nl = N\Delta y$. The reconstruction reads

$$\begin{aligned} D_{w,\text{S}}(k_y, \omega) \cdot H_{\text{Rect}}(k_y, \omega) &= \frac{\sin(k_y \Delta y \frac{N}{2})}{\sin(k_y \Delta y \frac{1}{2})} \cdot l \frac{\sin\left(\frac{k_y l}{2}\right)}{\frac{k_y l}{2}} \\ &= \frac{\sin(k_y l \frac{N}{2})}{\sin(k_y l \frac{1}{2})} \cdot l \frac{\sin\left(\frac{k_y l}{2}\right)}{\frac{k_y l}{2}} \cdot \frac{N}{N} = L \frac{\sin\left(k_y \frac{L}{2}\right)}{k_y \frac{L}{2}} = D_w(k_y, \omega). \end{aligned} \quad (3.124)$$

As expected this yields the driving function's spatio-temporal spectrum of the continuous, finite length LSA (3.38)

$$D_w(k_y, \omega) = D_{w,\text{S}}(k_y, \omega) \cdot H_{\text{Rect}}(k_y, \omega)|_{l=\Delta y}. \quad (3.125)$$

Designing waveguides that match the ideal line piston or using other high directed sources and LSA setups that approach $\frac{l}{\Delta y} = 1$ as close as possible can be seen as a prevailing engineering effort w.r.t. LSA design in the 1990s and 2000s, leading to various patents, e.g. [Hei92a, Leh00, Tho07, Eng09].

With the given treatment on the fundamentals of array processing derived

in the spatio-temporal spectrum domain, the WST criteria [Urb03] for straight LSAs can be conveniently revisited and reinterpreted in the following section.

3.4 WST Criteria

The initial derivations of the WST criteria consider a uniformly driven and rectangular windowed LSA of length L , a spatial discretization with equidistant source spacing Δy and an interpolation with spatial lowpass postfilters modeled from an odd number N of pistons. The signal flow of the WST is depicted in Fig. 3.34 and a geometrical sketch of the considered LSA setup is visualized in Fig. 3.35.

It appears meaningful to apply a unity gain normalization in the spatio-temporal spectra w.r.t. $k_y = 0$ in all required driving function and postfilter Fourier transform pairs. In doing so, relative grating and side lobe amplitudes can be conveniently discussed in terms of their absolute values. The corresponding spatial Fourier transform pairs for WST indicated by the $\circ\text{---}\bullet$ symbol then read, cf. (3.22), (3.38), (3.69)

$$D(y_0) = 1 \quad \circ\text{---}\bullet \quad D(k_y, \omega) = 2\pi \delta(k_y), \quad (3.126)$$

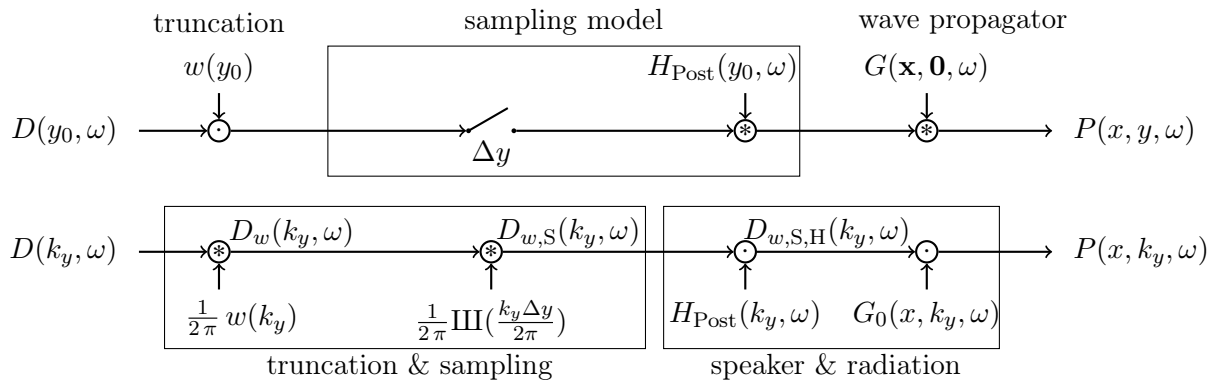


Figure 3.34: WST signal processing model in temporal (top) and spatio-temporal spectrum domain (bottom). Linear convolution w.r.t. y, k_y is denoted by \otimes , multiplication w.r.t. y, k_y by \odot . This is equivalent to Fig. 3.1 except for the omitted prefilter.

$$D_w(y_0) = \begin{cases} \frac{1}{L} & \text{for } |y_0| \leq \frac{L}{2} \\ 0 & \text{else} \end{cases} \quad \circ \text{---} \bullet \quad D_w(k_y, \omega) = \begin{cases} \frac{\sin(k_y \frac{L}{2})}{k_y \frac{L}{2}} & \text{for } k_y \neq 0 \\ 1 & \text{for } k_y = 0, \end{cases} \quad (3.127)$$

$$D_{w,S}(y_0) = \sum_{\mu=-\frac{N-1}{2}}^{+\frac{N-1}{2}} \frac{1}{N} \delta(y_0 - \mu \Delta y) \quad \circ \text{---} \bullet$$

$$D_{w,S}(k_y, \omega) = \begin{cases} \frac{\sin(k_y \Delta y \frac{N}{2})}{N \sin(k_y \Delta y \frac{1}{2})} & \text{for } k_y \neq \frac{2\pi}{\Delta y} \mu \\ 1 & \text{for } k_y = \frac{2\pi}{\Delta y} \mu. \end{cases} \quad (3.128)$$

As reconstruction filter $H_{\text{Post}}(k_y, \omega)$, the line piston on y -axis with length l

$$H_{\text{Rect}}(y_0) = \begin{cases} \frac{1}{l} & \text{for } |y_0| \leq \frac{l}{2} \\ 0 & \text{else} \end{cases} \quad \circ \text{---} \bullet$$

$$H_{\text{Post}}(k_y, \omega) = H_{\text{Rect}}(k_y, \omega) = \begin{cases} \frac{\sin(k_y \frac{l}{2})}{k_y \frac{l}{2}} & \text{for } k_y \neq 0 \\ 1 & \text{for } k_y = 0, \end{cases} \quad (3.129)$$

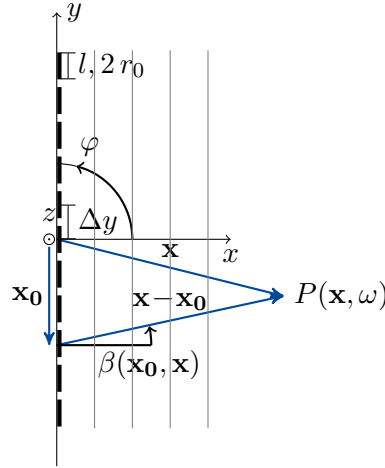


Figure 3.35: Side view of the discussed setup with LSA length L . The LSA is either built from line pistons of length l on the y -axis or circular pistons of diameter $2r_0$ located within the yz -plane and centered on y -axis. The distance between the centers of two adjacent pistons is indicated as the spatial discretization step Δy . Wave propagation within the xy -plane for $\mathbf{x} = (x > 0, y, z = 0)^T$ is considered. The wave propagation angle $-\frac{\pi}{2} \leq \varphi \leq +\frac{\pi}{2}$ holds.

and the circular piston within the yz -plane with radius r_0

$$H_{\text{Circ}}(y_0, z_0) = \begin{cases} \frac{1}{\pi r_0^2} & \text{for } y_0^2 + z_0^2 \leq r_0^2 \\ 0 & \text{else} \end{cases} \quad \circ \text{---} \bullet$$

$$H_{\text{Post}}(k_y, \omega) = H_{\text{Circ}}(k_y, \omega) = \begin{cases} \frac{2 J_1(k_y r_0)}{k_y r_0} & \text{for } k_y \neq 0 \\ 1 & \text{for } k_y = 0 \end{cases} \quad (3.130)$$

were considered for the derivation of the first WST criterion, denoting the cylindrical Bessel function of 1st kind of 1st order [Olv10, §10.2] with $J_1(\cdot)$. The derivations of these postfilter characteristics are revisited in App. D. Note that [Hei92b] introduced the rectangular piston at first, by applying the second product theorem [Ste27], [Van02, Ch. 2.8] and reducing the rectangular to a line piston by assuming the piston's width to be much smaller than the radiated wave length λ , cf. [Hei92b, p.8]. In case of using ideal spherical monopoles the postfilter reads

$$H_{\text{Sph}}(y_0) = \delta(y_0) \quad \circ \text{---} \bullet \quad H_{\text{Sph}}(k_y) = 1. \quad (3.131)$$

Another advantage of the introduced Fourier pair normalization now becomes obvious. If the piston dimension is decreased to zero in the limit, i.e. $l \rightarrow 0$, $r_0 \rightarrow 0$ the signal processing allows for the interpretation of using monopoles.

Under the assumption that the LSA is built from identical individual sources, the reconstructed driving function's spatio-temporal spectrum

$$D_{w,S,H}(y_0, \omega) = D_{w,S}(y_0) * H_{\text{Post}}(y_0, \omega) \quad \circ \text{---} \bullet$$

$$D_{w,S,H}(k_y, \omega) = D_{w,S}(k_y, \omega) \cdot H_{\text{Post}}(k_y, \omega) \quad (3.132)$$

follows as a consequence of the *product or pattern multiplication theorem* [Ste29, p.174], [Van02, Ch. 2.8]. This was already deployed in Ch. 3.3 to derive the special WST case of perfect reconstruction. In the visible region this product is composed of the *array factor* $D_{w,S}(\varphi, \omega)$ and the farfield radiation pattern of the utilized sources $H_{\text{Post}}(\varphi, \omega)$ (referred to as *form factor* [Hei92b, II.2.a]). This yields the *final array factor* $D_{w,S,H}(\varphi, \omega)$, i.e. the farfield radiation pattern of the LSA that holds in the Fraunhofer region. A very related problem

discussion in antenna design using subarrays is given in [Bro12]. When using ideal spherical monopoles, the final array factor is identical to the array factor.

The propagating contributions of the sound field can be again computed by the angular spectrum synthesis, cf. (3.2)

$$P(x, y, \omega) = \frac{1}{2\pi} \int_{-\frac{\omega}{c}}^{+\frac{\omega}{c}} D_{w,S,H}(k_y, \omega) G_0(x, k_y, \omega) e^{-j k_y y} dk_y. \quad (3.133)$$

This correctly synthesizes the sound field of the LSA's Fresnel (nearfield) and Fraunhofer (farfield) region, when being in the farfield of the individual pistons. The synthesis is equivalent to

$$P(\mathbf{x}, \omega) = \sum_{n=1}^N D(\mathbf{x}_0[n], \omega) H_{\text{Post}}(\beta(\mathbf{x}_0[n], \mathbf{x}), \omega) \frac{1}{4\pi} \frac{e^{-j \frac{\omega}{c} |\mathbf{x} - \mathbf{x}_0[n]|}}{|\mathbf{x} - \mathbf{x}_0[n]|}. \quad (3.134)$$

This equation, already introduced as (1.3) forms the basis for numerical LSA prediction software that use measured farfield radiation patterns of loudspeakers. Note that (3.134) allows for the usage of individual postfilters, whereas the proposed sampling/reconstruction model leading to $D_{w,S,H}(k_y, \omega)$ by the product theorem in (3.133) relies on the fact that the postfilter characteristic is identical for all sources.

It is worth reiterating that the term $G_0(x, k_y, \omega) e^{-j k_y y}$ in (3.133) describes sound fields generated by an infinite, pulsating line monopole with different radial wave propagation directions due to (2.157), cf. [Sku71, Ch. 21.12]. These will be triggered and weighted by the spatio-temporal spectrum $D_{w,S,H}(k_y, \omega)$ and the superposition of all waves (i.e. the integral operation) yields the sound field of the finite length LSA by interference. Grating lobes within the array factor that become insufficiently suppressed in the final array factor are the most critical contributions to spatial aliasing since they trigger propagating waves. Their interference with the intended main lobe beam yields a corrupted Fresnel region. Furthermore, these grating lobes may undesirably radiate into space where a low sound pressure level is required by application. In general it is observed, that a 'smoother' function $D_{w,S,H}(k_y, \omega)$ (smooth spatial truncation window, no or well suppressed grating lobes) will produce a more homogeneous sound field in both, the Fresnel and Fraunhofer region of the

LSA.

The first three WST criteria are aimed at different approaches for straight and uniformly driven LSAs (i) to completely avoid grating lobes within the visible region (WST #2) and (ii) to attenuate them, if entering into the visible region cannot be avoided (WST #1, WST #3).

3.4.1 WST#1 Criterion

The WST#1 criterion, also referred to as the *active radiating factor* (ARF) theorem

$$\text{WST \#1 for line piston:} \quad \text{ARF} = \frac{l}{\Delta y} \geq 0.82 \quad (3.135)$$

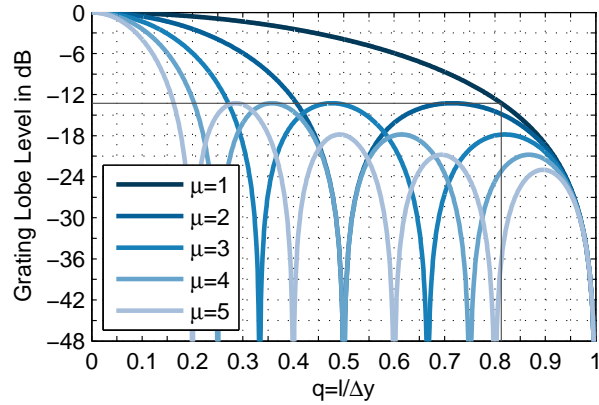
relates the discretization step size Δy between adjacent, identical line pistons of length l and a tolerated grating lobe level. The criterion ensures, that the maximum grating lobe level in the farfield does not exceed -13.5 dB relative to the intended main lobe level and holds for a large number N of line pistons. The physical length of a line piston LSA is

$$L = (N - 1) \Delta y + l. \quad (3.136)$$

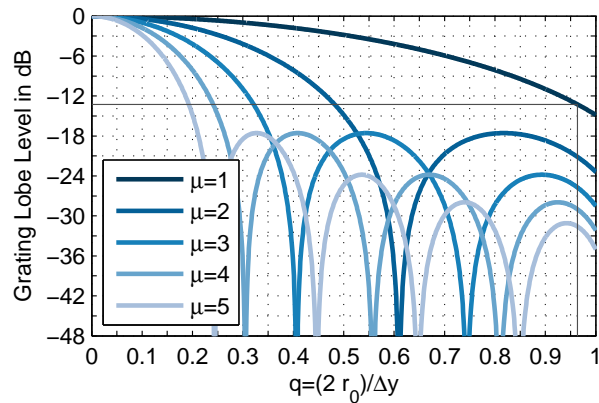
By utilizing the spatial lowpass characteristics of highly directed sources, i.e. waveguides for the high audio frequency band, spatial aliasing is aimed to be reduced or even avoided by means of this criterion. It follows from an enhanced discussion of the perfect reconstruction given in Ch. 3.3 by henceforth allowing gaps between the waveguides. The maximum tolerated grating lobe level of -13.5 dB relative to the intended main lobe can be understood as the essence of the 1st WST criterion (3.135). In [Hei92b, Urb01, Urb03] it is concluded that this is only realizable with line pistons, i.e. waveguides. A discussion for both, the line and the circular piston is given in the present work.

The ARF Theorem for a Line Piston LSA

The initial derivation of the ARF-theorem [Hei92b, (8)], [Urb03, Sec. 3.2] was performed by defining a continuous, uniformly driven, finite length line source and a polarity-inverted so called *disruption grid* (cf. [Urb03, Fig. 6]). This inherently models a line piston LSA. Another, yet consistent derivation



(a) Line piston LSA, $\text{ARF} = q$, the ratio $q = 0.812797$ with a resulting 1st grating lobe attenuation of 13.26 dB is indicated with lines.



(b) Circular piston LSA, $\text{ARF} = \frac{\pi}{4} q^2$, the ratio $q = 0.9635792$ with a resulting 1st grating lobe attenuation of 13.26 dB is indicated with lines.

Figure 3.36: Grating lobe level vs. q for (a) a line piston LSA and (b) a circular piston LSA. Relative grating lobe levels for $k_y = \mu \frac{2\pi}{\Delta y}$, $1 \leq \mu \leq 5$ are given. Only for a large number N of pistons this level corresponds to the actual local maxima/minima of (3.137) and (3.143).

directly using the product theorem (3.132) with (3.128) and (3.129)

$$D_{w,S,H}(k_y, \omega) = \frac{1}{N} \frac{\sin(k_y \Delta y \frac{N}{2})}{\sin(k_y \Delta y \frac{1}{2})} \cdot \frac{\sin(k_y \frac{l}{2})}{k_y \frac{l}{2}} \quad (3.137)$$

is given here. This is similar to discussing Fraunhofer diffraction of gratings, i.e. multiple slits, cf. [Ots90], [Bor06, Ch. 8.6]. Finding the local minima and maxima using

$$\frac{dD_{w,S,H}(k_y, \omega)}{dk_y} = 0, \quad (3.138)$$

– especially these of grating lobes in order to control their largest occurring level by the ratio $\frac{l}{\Delta y}$ – does not lead to a general closed form solution, rather again to a transcendental equation. However, for large N the grating lobe maxima are approximately located at $k_y = \mu \frac{2\pi}{\Delta y}$, $\mu \in \mathbb{Z}, \neq 0$ in (3.137). The grating lobes decrease in level – except for the case $l = 0$ – for increasing $|k_y|$ due to the spatial lowpass characteristic of (3.129). Hence, the first grating lobes at $\mu = \pm 1$ determine the maximum occurring, tolerated level of grating lobes. With the initial definition of the active radiating factor [Urb03, p.917]

$$\text{ARF} = q = \frac{l}{\Delta y} \quad 0 \leq q \leq 1, \quad (3.139)$$

(3.137) is evaluated at $k_y = \Delta k_y = \frac{2\pi}{\Delta y}$ to

$$A(q) = D_{w,S,H}(k_y = \Delta k_y, \omega) = \frac{\sin(\pi q)}{\pi q}, \quad (3.140)$$

for which $A(q) \in \mathbb{R}^+$ is valid within the given range of q . For $q = 0$ a linear array built from point sources is modeled. In this case all grating lobes will not be suppressed – $D_{w,S,H}(k_y = \mu \Delta k_y, \omega) = 1$ – due to the missing spatial lowpass characteristic of the spherical monopole. In the limit of $q = 1$ all grating lobes are perfectly attenuated due to $D_{w,S,H}(k_y = \mu \Delta k_y, \omega) = 0$ for $\mu \neq 0$. This yields the already discussed perfect reconstruction (3.125)

$$D_w(k_y, \omega) = D_{w,S}(k_y, \omega) \cdot H_{\text{Rect}}(k_y, \omega)|_{l=\Delta y} \quad (3.141)$$

towards the driving function's spectrum of the continuous, finite length LSA (3.127).

The maximum tolerated grating lobe level thus can be controlled within the range 0 dB to $-\infty$ dB by setting $0 \leq q \leq 1$. This is depicted in Fig. 3.36a.

In [Hei92b, Urb03] the maximum tolerated level of grating lobes is set to -13.26 dB, i.e. the largest occurring side lobe level of a uniformly driven, continuous linear array. To be precise, -12 dB in [Hei92b] and -13.5 dB in [Urb03] were actually used. Numerically solving (3.140) for $A(q) = 10^{-\frac{13.26}{20}}$, the ARF is given as

$$\text{ARF} = q \approx 0.812797. \quad (3.142)$$

This is in accordance with (3.135) [Urb03, p.917], where the approximation $\text{ARF} \geq 0.82$ for large N is given. Note that (3.140) is independent of N in first instance. As discussed above, the largest local maxima of (3.137) except for $k_y = 0$ are located at $k_y = \pm \Delta k_y$ for large N .

The ARF seems to be a temporal frequency independent measure since the derivation was performed in the k_y -domain. The occurrence of (attenuated) grating lobes however depends on the visible region $-\frac{\omega}{c} < k_y < +\frac{\omega}{c}$. This indicates that if (3.110) can be fulfilled, the ARF criterion is of secondary importance and conversely, if (3.110) cannot be met, the grating lobe suppression is largely dependent on the characteristics of the spatial reconstruction filter. An LSA with smaller Δy and smaller ARF may produce less spatial aliasing for an intended frequency range, than an LSA with larger Δy and larger ARF. This becomes especially important when aiming for electronic beam steering. A discussion on this issue is presented in Ch. 3.4.2.

The ARF Theorem for a Circular Piston LSA

A similar treatment for the ARF theorem is given for the circular piston LSA. Applying the circular piston's postfilter characteristic (3.130) and the driving function (3.128) to the product theorem (3.132) yields

$$D_{w,S,H}(k_y, \omega) = \frac{1}{N} \frac{\sin(k_y \Delta y \frac{N}{2})}{\sin(k_y \Delta y \frac{1}{2})} \cdot \frac{2 J_1(k_y r_0)}{k_y r_0}. \quad (3.143)$$

With the piston's diameter $d_0 = 2r_0$ a ratio of lengths

$$q = \frac{d_0}{\Delta y} \quad 0 \leq q \leq 1 \quad (3.144)$$

is defined. The ARF can be deduced to

$$\text{ARF} = \frac{\pi r_0^2}{\Delta y^2} = \frac{\pi \left(\frac{q}{2} \Delta y\right)^2}{\Delta y^2} = \frac{\pi}{4} q^2, \quad (3.145)$$

by modeling a quadratic enclosure of side length Δy , cf. [Urb03, p.918]. The physical length of a circular piston LSA is

$$L = (N - 1) \Delta y + d_0. \quad (3.146)$$

The ARF here is effectively a ratio of surface areas ($\text{ARF} \neq q$), whereas for the line piston a ratio of line lengths is defined ($\text{ARF} = q$). Therefore, care must be taken when comparing the definitions of the ARF and q and its implications for different pistons.

Evaluating (3.143) at $k_y = \Delta k_y = \frac{2\pi}{\Delta y}$ yields the relative level of the first grating lobe

$$A(q) = D_{w,s,h}(k_y = \Delta k_y, \omega) = \frac{2 J_1(\pi q)}{\pi q}. \quad (3.147)$$

The levels of the first five grating lobes over q are depicted in Fig. 3.36b. The maximum possible $\text{ARF} = \frac{\pi}{4}$ holds for $q = 1$ using directly adjacent pistons $\Delta y = d_0$, cf. [Urb03, p.918]. This yields the maximum possible attenuation of grating lobes. The level of the first grating lobe is then evaluated to

$$20 \log_{10} \left(A(q = 1) = \frac{2 J_1(\pi)}{\pi} \right) \approx -14.84 \text{ dB}. \quad (3.148)$$

This is in contrast to the line piston, for which perfect suppression ($-\infty$ dB) of the first grating lobe (and all others) results if $q = 1$, cf. Fig. 3.36a vs. Fig. 3.36b. This is due to the fact that the first zero of the Bessel function cannot be coincidentally located at $k_y = \Delta k_y$ without overlapping pistons, which is not feasible, cf. Fig. 3.37b.

Following the initial intention of the 1st WST criterion, numerically solving

(3.147) for $A(q) = 10^{-\frac{13.26}{20}}$ yields

$$q = 0.9635792 \quad \text{ARF} = \frac{\pi}{4} q^2 = 0.72923. \quad (3.149)$$

Hence, the circular piston postfilter is able to attenuate the first grating lobe by 13.26 dB and could be stated WST #1 compliant if

$$\text{WST \#1 for circular piston:} \quad \text{ARF} = \frac{\pi}{4} \left(\frac{2r_0}{\Delta y} \right)^2 \geq 0.72923. \quad (3.150)$$

This deduction is in contrast to that given in [Hei92b, Urb03]. In fact, the postfilter of the ideal circular piston has a better spatial lowpass characteristic than the line piston since the jinc-function $\frac{2J_1(x)}{x}$ exhibits a larger envelope decay for increasing arguments than the sinc-function $\frac{\sin(x)}{x}$. This can also be graphically deduced in Fig. 3.36. Only for $q \approx 1$ the grating lobe suppression for a line piston LSA is superior to a circular one. However, only very small gaps between adjacent circular pistons are allowed to fulfill its WST#1 (3.150), which might be a demanding requirement.

In Fig. 3.37 an example with 3" line and circular pistons is given. It visualizes the farfield radiation patterns of the pistons over k_y and the temporal frequency f . The grating lobe maxima positions w.r.t. k_y of the aliased sinc-function $D_{w,s}(k_y, \omega)$ are indicated with red lines according to different spatial discretizations. The upper graphics indicate directly adjacent pistons with no gaps between them, yielding perfect reconstruction for the line piston. The grating lobe maxima here coincide with the zeros of $D_{w,s}(k_y, \omega)$. The circular piston exhibits better spatial lowpass characteristics, although grating lobes cannot be perfectly suppressed. Note that the zeros of $H_{\text{Rect}}(k_y, \omega)$ (3.129) are equidistantly spaced w.r.t. k_y -space, which is not the case for the circular piston $H_{\text{Circ}}(k_y, \omega)$ (3.130). The lower graphics represent the case of WST#1-compliance using the minimum required ARFs (3.142), (3.149) for both pistons. Holding the piston dimensions constant changes the discretization step Δy . For the circular piston only small changes compared to the upper case are observed due to almost the same spatial sampling. For the line piston the spatial sampling step size is more increased and the grating lobe maxima not longer coincide with the zeros of the driving function $D_{w,s}(k_y, \omega)$. The

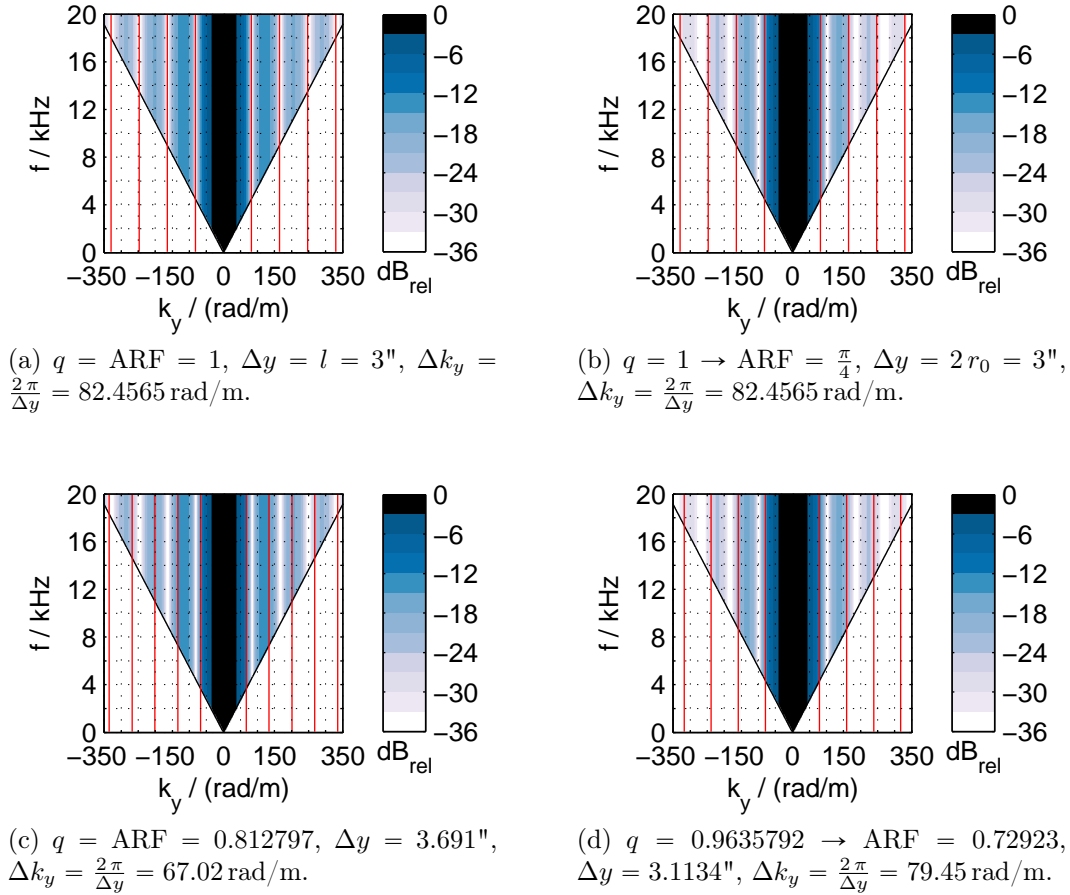


Figure 3.37: Comparison of $l = 3''$ line piston (left) and $2r_0 = 3''$ circular piston (right) postfilter characteristics. Top: $q = 1$ (no gaps between adjacent pistons), bottom: WST#1 compliant according to (3.142), (3.149)

first grating lobes at $k_y = \pm 67.02 \text{ rad/m}$, $k_y = \pm 79.45 \text{ rad/m}$ respectively are attenuated by 13.26 dB as intended for WST#1 compliance. The outermost grating lobes experience a stronger attenuation using the circular piston post-filter characteristic as already observed in Fig. 3.36.

Another valuable information can be derived from the wedges in Fig. 3.37. For temporal frequencies where the visible region does not include a zero in the postfilter characteristic, the piston does not exhibit a Fresnel region and radiates almost omnidirectional and directly into the Fraunhofer region, i.e. the farfield. For the line piston this holds approximately for $f < 4.5 \text{ kHz}$, whereas for the circular piston $f < 5.5 \text{ kHz}$ can be stated for the given piston dimension.

While this discussion provides the whole picture of the ARF theorem from a theoretical viewpoint, LSAs may preferably be designed with waveguides for high audio frequencies due to the following reasons: (i) the circular piston model assumes a constant velocity over the diaphragm's surface which is in practice much more demanding than designing an appropriate waveguide with an intended wavefront curvature and (ii) LSAs aim at a frequency independent horizontal coverage. This is much easier to control with the design of an appropriate waveguide than using circular pistons, i.e. electrodynamic loudspeakers. Nevertheless, using very small circular electrodynamic drivers (e.g. 1") for the high frequency section of an LSA by simultaneously controlling the horizontal coverage with a horn-like mouth was already successfully engineered.

On-Axis Radiation, Fresnel/Fraunhofer Transition

Using (3.133), a $L \approx 5$ m-LSA modeled with line pistons is numerically evaluated according to the strategy in (3.58) for the main lobe, side lobe and complete sound field. This is similar to Fig. 3.24. The LSA parameters in Fig. 3.46 are used. The evaluation is only valid in the farfield of the line pistons. The sound field's pressure levels are visualized in Fig. 3.38. The farfield directivity exhibits two grating lobes at $k_y = \pm 15.987$ rad/m, $\varphi \approx \pm 33^\circ$, that are attenuated by 6 dB due to the line piston postfilter, cf. Fig. 3.46c. The resulting spatial aliasing is observable in Fig. 3.38a, showing the level of the complete sound field $P_{\text{All}}(x, y, \omega)$. The level of the main lobe sound field $P_{\text{Main}}(x, y, \omega)$ is depicted in Fig. 3.38b. This sound field is corrupted by interference with the side lobe sound field $P_{\text{Side}}(x, y, \omega)$ that is shown in Fig. 3.38c, resulting in the chaotic region in Fig. 3.38, Fig. 3.46f close to the array. The Fresnel/Fraunhofer transition distance (3.86) between the chaotic region and the collective Fraunhofer region is calculated to $x_B = 60.83$ m. For $x > x_B$ the side lobe level becomes negligible, which is confirmed by the on-axis level decay depicted in Fig. 3.46b. All levels are again normalized to the level of the complete sound field at x_B on the main axis, i.e. $20 \log_{10}(|P_{\text{All}}(x_B, 0)|) = 0$ dB_{rel}.

LSA Radiation Characteristics for varied ARF

Further properties and special cases for uniformly driven, discretized, finite length LSAs should be discussed in the following examples Fig. 3.40 to Fig. 3.46. The frequencies and LSA configurations for the synthesized sound fields were

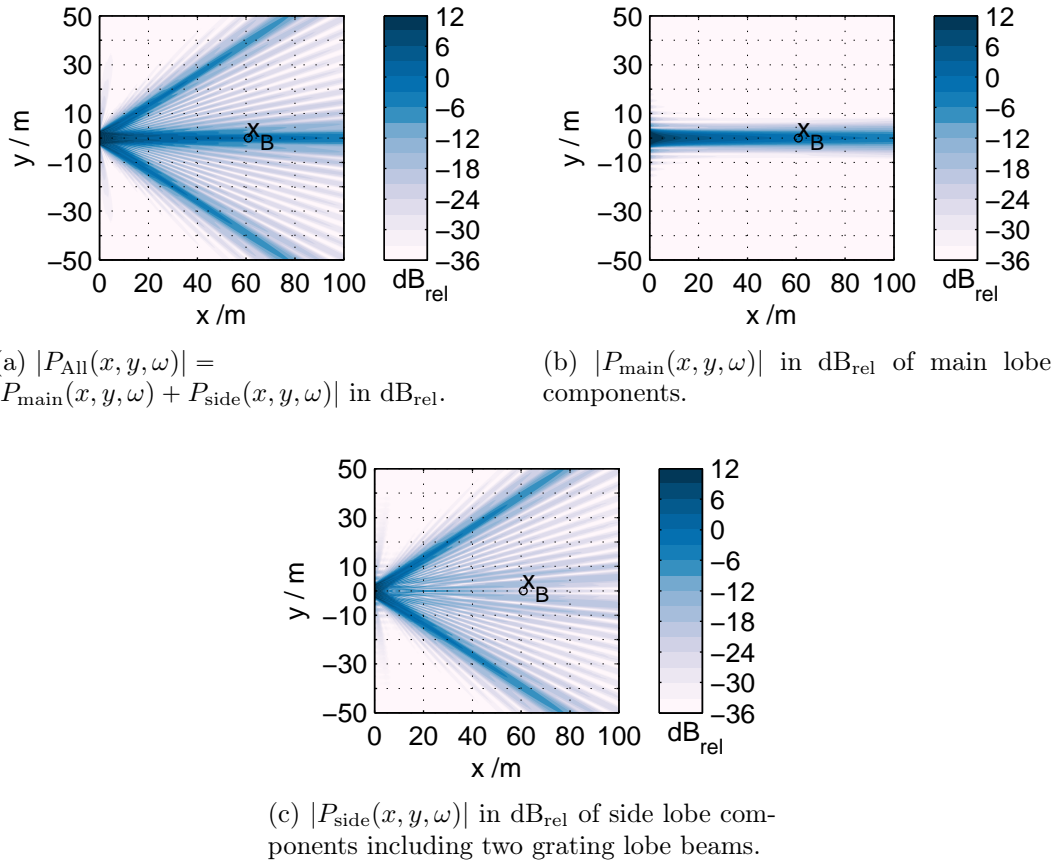


Figure 3.38: LSA with line piston using (3.132), (3.128), (3.129), (3.133), (3.58) and $f = 1.6$ kHz, $\lambda = 0.214$ m, $L = 4.953$ m, $L/\lambda = 23.1044$, $N = 13$, $\Delta y = 0.3930179$ m, $\Delta k_y = 15.9870214$ rad/m, $q = 0.6024800$, $l = 0.2367854$ m.

chosen to highlight a particular phenomenon under discussion. All examples are visualized with the same subfigure structure. Subplot (a) depicts the final array factor as $|D_{w,S,H}(k_y, \omega)|$ in dB normalized to the main lobe. Levels < -36 dB are clipped to white, levels > 0 dB to black (which however not occurs). Subplot (c) represents one slice of $|D_{w,S,H}(k_y, \omega)|$ for the specific frequency under discussion. Subplot (d) visualizes the final array factor as a polar diagram. Subplot (b) depicts the main lobe, side lobe and complete sound field's on-axis level decays. The subplots (e) and (f) depict the sound field's level over the xy -plane with equal normalization to $20 \log_{10}(|P_{\text{All}}(x = 10 \text{ m}, 0)|) = 0 \text{ dB}_{\text{rel}}$, which also holds for (b). Subplot (e) represents the numerical evaluation of (2.85) using $-2 \frac{\partial P(\mathbf{x}_0, \omega)}{\partial n} = \text{const}$, i.e. the WST driving function with appropriately discretized pistons located on

the y -axis (line pistons) or within the yz -plane (circular pistons). For subplot (f) the angular spectrum synthesis (3.133) is utilized. Both approaches yield identical results, except for evanescent wave propagation as discussed above. Grey contour lines for the levels ± 3 dB, ± 9 dB, ± 15 dB are additionally given in (f). Note that similar examples were given in [Sch14a, Fig. 13-15], however with a differently chosen definition $\text{ARF} = \frac{N \cdot l}{L}$ [Sch14a, (42)] and thereby with slightly different LSA configurations. As for the whole thesis, $c = 343$ m/s is assumed.

Example I: Circular vs. Line Piston LSA, $\text{ARF} = \pi/4$

In Fig. 3.40 an LSA with $\text{ARF} = \frac{\pi}{4}$, $L \approx 5$ m modeled with circular pistons and in Fig. 3.41 an LSA with same $\text{ARF} = \frac{\pi}{4}$, $L \approx 5$ m modeled with line pistons are compared according to the original WST derivation and discussion. The circular piston LSA – although violating both, the WST#1 and #2 criterion – has better spatial lowpass characteristics, the two observable grating lobes in Fig. 3.40c for 1.6 kHz are attenuated by ≈ 15 dB in the far field. For $20 < |k_y| < 30$ rad/m side lobe suppression of more than 36 dB is observed. This results in small sound pressure level in the proximity above and below the LSA. The line piston LSA on the other hand violates the WST#1 criterion (3.135): four prominent grating lobes in Fig. 3.41c can be observed, a postfilter attenuation of minimum 13.26 dB is not achieved for the first pair. The outermost grating lobes produce a high sound pressure level in the proximity above and below the LSA. A more corrupted Fresnel region than that produced by the circular piston LSA is observable. For the discussed case the circular piston LSA exhibits less spatial aliasing, as already shown in Fig. 3.36. The result with the chosen parameters is of theoretical interest, since a circular piston with $d_0 = 15''$ is (i) typically not used for the chosen frequency and is (ii) not able to radiate uniformly at this frequency in practice and thus the farfield piston model is not valid. However, when scaling the wave length and the piston dimensions to more appropriate values the same conclusions can be drawn.

Example II: LSAs with Different Line Piston Length, $\text{ARF} = 0.812797$

The ARF criterion (3.135) alone only states a minimum ratio for piston size and source spacing, which can be obviously met by different setups. In Fig. 3.42 and Fig. 3.43 two LSAs with an ARF according to (3.142) and $L \approx 5$ m

modeled with $N = 11$ and $N = 21$ line pistons are visualized. The $\text{LSA}_{N=11}$ exhibits four grating lobes within the visible region for $f = 1.6$ kHz due to the larger discretization step Δy , concurrently with high suppression in the range of $k_y \approx 20$ rad/m. The $\text{LSA}_{N=21}$ exhibits only two grating lobes within the visible region that have about the same farfield radiation angles as the two outermost grating lobes of $\text{LSA}_{N=11}$. This is due to $\Delta y_{N=11} \approx 2 \Delta y_{N=21}$. In both cases all side and grating lobes are attenuated by at least 13.26 dB in the farfield, due to intentionally fulfilling the ARF criterion. Again, the Fresnel region of the LSA with smaller Δy ($N = 21$) is more homogeneous. Note that the maximum line piston size was only defined in [Urb03, Sec. 6.2] by linking it with a maximum allowed splaying angle of adjacent pistons for curved arrays.

Example III: LSA with Spatial Aliasing at $\varphi = \pm 90^\circ$

For Fig. 3.44 the same LSA setup as for Fig. 3.42 is deployed, although at a different frequency. Evaluating at $f = 1.4635$ kHz illustrates the phenomenon of propagating waves along the array axis, depicted in Fig. 3.44e. Here the spectral repetitions with $\mu = \pm 2$ occur at wave numbers $k_y = \pm 26.808$ rad/m, close to the pole of $G_0(x, k_y, \omega)$ at $\frac{\omega}{c} = 26.808$ rad/m. This results in wave propagation along the array ($\varphi \approx \pm 90^\circ$). The level of the sound field close to the array is not predicted by the final array factor $D_{w,S,H}(\varphi, \omega)$. In Fig. 3.39 the sound pressure level along the x - and the y -axis is evaluated. It indicates that the wave propagation along the array (grating lobe on positive y -axis) decays with 6 dB per distance doubling and therefore faster than the main lobe (on

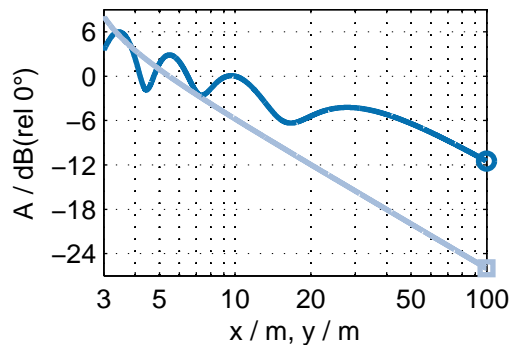


Figure 3.39: Example III: \circ : main lobe level decay on x -axis ($\varphi = 0^\circ$), \square : grating lobe level decay on y -axis ($\varphi = +90^\circ$)

x -axis) that exhibits a typical spatial-aliasing corrupted Fresnel/Fraunhofer level decay. However, very close to the array ($x, y < 7$ m) both sound pressure levels exhibit the same order of magnitude. In the collective Fraunhofer region (c.f. $x = y = 100$ m in Fig. 3.39) $|D_{w,s,H}(k_y, \omega)|$ predicts the grating lobe suppression of about 15 dB as expected in Fig. 3.44c. Wave propagation along the array with high SPL, that results from spatial aliasing, occurs for all LSA designs that violate the WST#2 criterion and $\text{ARF} < 1$. The phenomenon is observable at particular frequencies, where the grating lobes trigger the Green's function's spatio-temporal spectrum very close to its pole. It holds for $|\nu \frac{2\pi}{\Delta y}| = |\frac{\omega}{c}|$, i.e. $\Delta y = \nu \lambda$, $\nu \in \mathbb{Z}$, in the example here $\nu = \pm 2$. This behavior cannot be avoided when spatial aliasing is tolerated.

Example IV: Spatial-Aliasing-Free LSA with ARF=1

In Fig. 3.45 for completeness a continuous LSA is simulated corresponding to Sec. 3.2.3. Due to (3.125) this also models a discretized LSA using line pistons with $\text{ARF} = 1$. No grating lobes occur and only the sinc-function of the spatial truncation window (3.38) is observable. The well known sound field of a continuous, uniformly driven line source, cf. [Ure04, Fig. 13] and the typical main lobe level decay, cf. [Lip86] is visualized.

Example V: High-Spatial-Aliasing LSA with ARF=0.6

In Fig. 3.46 an LSA with rather large gaps between line pistons is simulated. The ARF is chosen for a grating lobe suppression of only 6 dB. This results in a severely corrupted Fresnel region. Hence, rather small ARFs should be clearly avoided for homogeneous sound reinforcement.

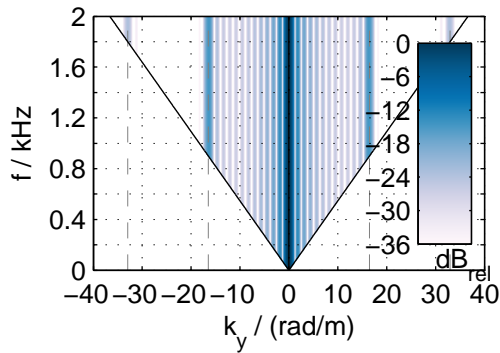
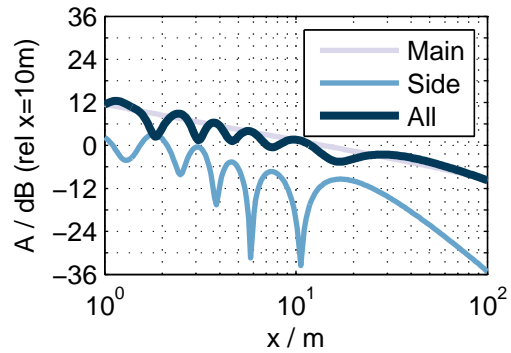
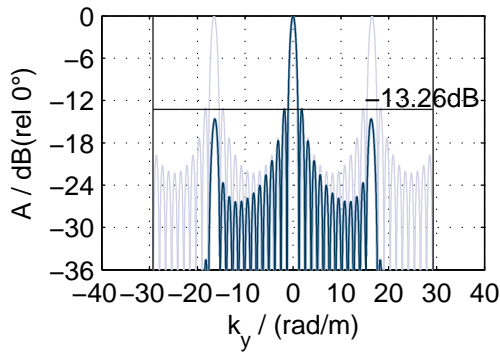
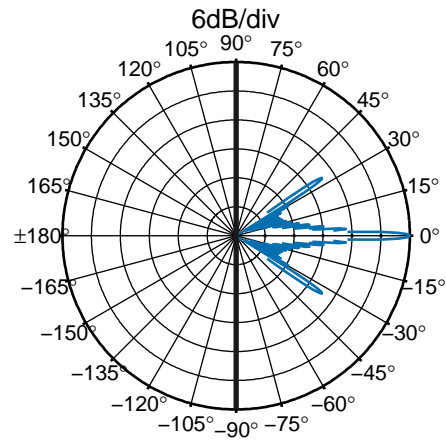
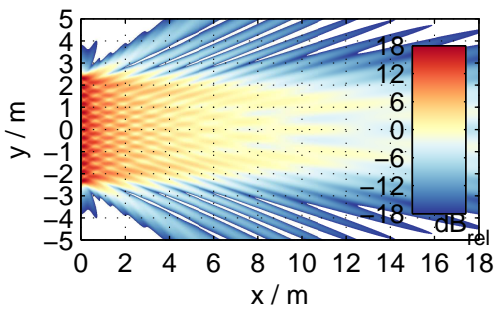
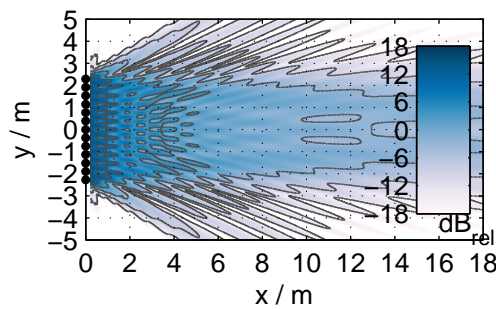
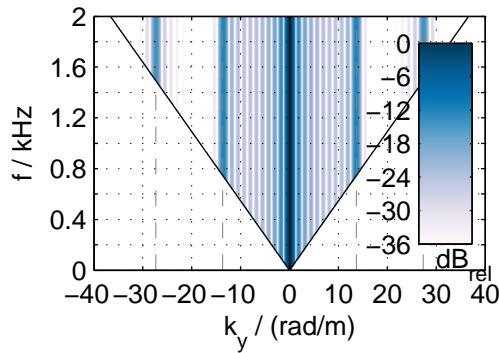
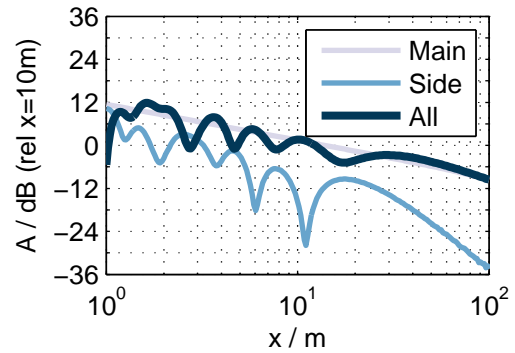
(a) $|D_{w,S}(k_y, \omega) \cdot H_{\text{Circ}}(k_y, \omega)|$.(b) $P_{\text{Main}}, P_{\text{Side}}, P_{\text{All}}$ along x -axis.(c) visible region of $|D_{w,S,H}(k_y, \omega)|$ for $f = 1.6$ kHz, underlay: $|D_{w,S}(k_y, \omega)|$ (d) farfield radiation pattern, i.e. final array factor $|D_{w,S,H}(\varphi, \omega)|$ for $f = 1.6$ kHz.(e) SPL in xy -plane.(f) SPL in xy -plane.

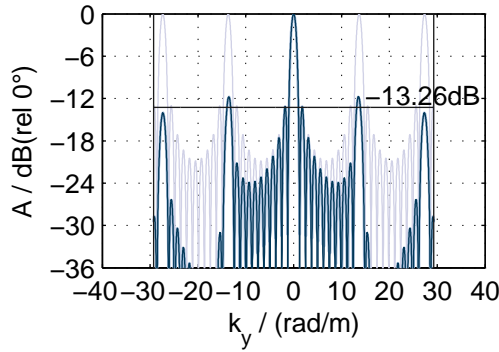
Figure 3.40: Example I: $f = 1.600$ kHz, $\lambda = 0.214$ m, $L = 4.9530000$ m, $N = 13$, $\Delta y = 0.3810000$ m, $\Delta k_y = 16.4913000$ rad/m, $q = 1.0000000$, $r_0 = 0.1905000$ m .



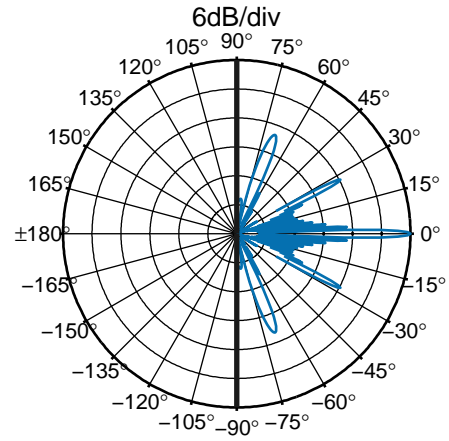
(a) $|D_{w,S}(k_y, \omega) \cdot H_{\text{Rect}}(k_y, \omega)|$.



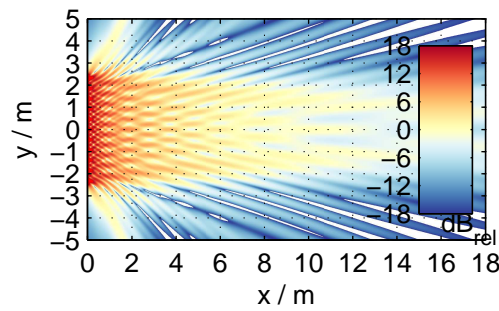
(b) $P_{\text{Main}}, P_{\text{Side}}, P_{\text{All}}$ along x -axis.



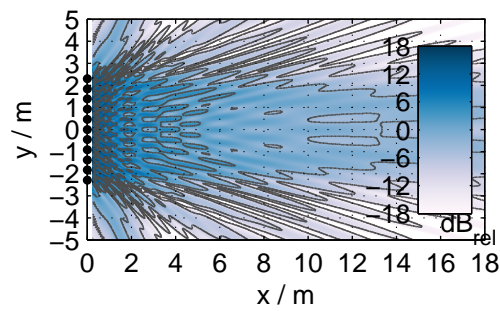
(c) visible region of $|D_{w,S,H}(k_y, \omega)|$ for $f = 1.6\text{ kHz}$, underlay: $|D_{w,S}(k_y, \omega)|$



(d) farfield radiation pattern, i.e. final array factor $|D_{w,S,H}(\varphi, \omega)|$ for $f = 1.6\text{ kHz}$.



(e) SPL in xy -plane.



(f) SPL in xy -plane.

Figure 3.41: Example I: $f = 1.600\text{ kHz}$, $\lambda = 0.214\text{ m}$, $L = 4.9530000\text{ m}$, $N = 11$, $\Delta y = 0.4592320\text{ m}$, $\Delta k_y = 13.6819413\text{ rad/m}$, $q = 0.7853982$, $l = 0.3606800\text{ m}$.

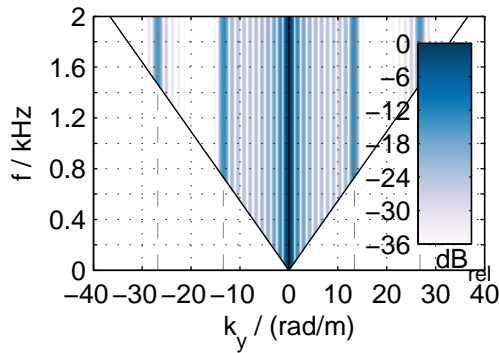
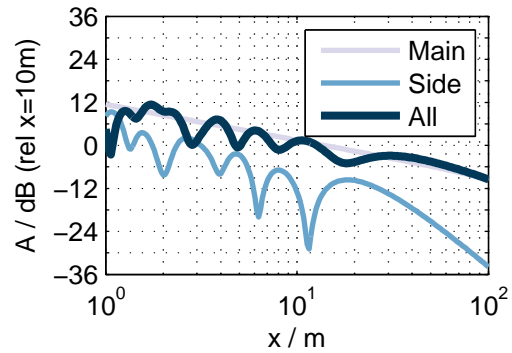
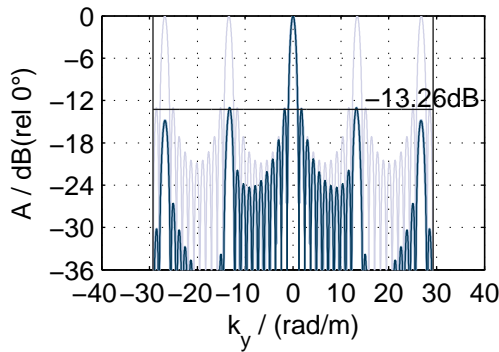
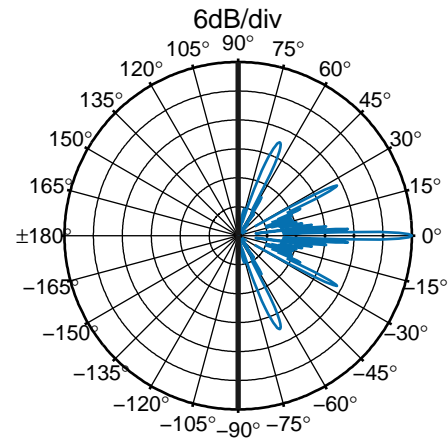
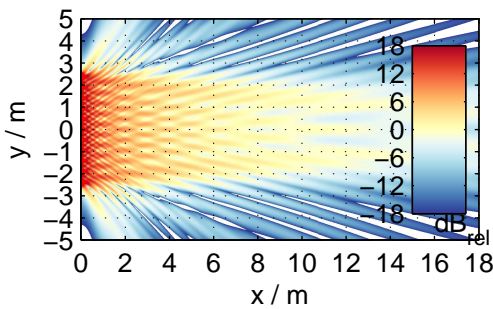
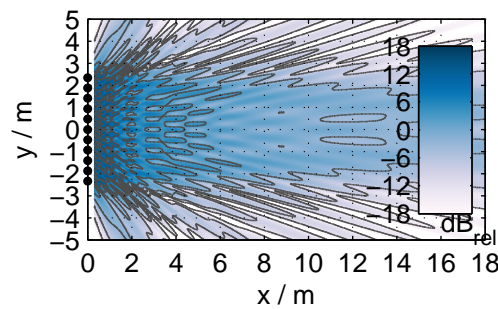
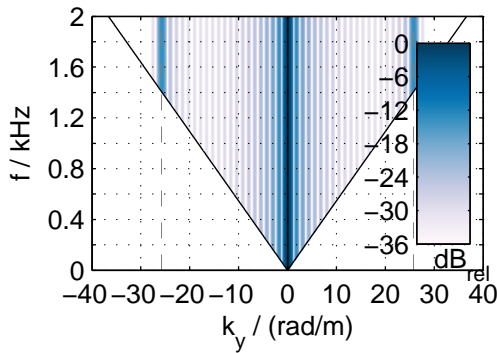
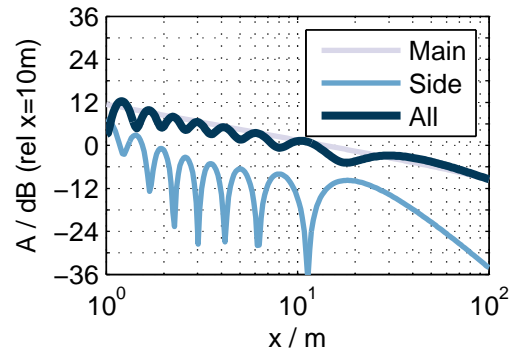
(a) $|D_{w,S}(k_y, \omega) \cdot H_{\text{Rect}}(k_y, \omega)|$.(b) $P_{\text{Main}}, P_{\text{Side}}, P_{\text{All}}$ along x -axis.(c) visible region of $|D_{w,S,H}(k_y, \omega)|$ for $f = 1.6$ kHz, underlay: $|D_{w,S}(k_y, \omega)|$ (d) farfield radiation pattern, i.e. final array factor $|D_{w,S,H}(\varphi, \omega)|$ for $f = 1.6$ kHz.(e) SPL in xy -plane.(f) SPL in xy -plane.

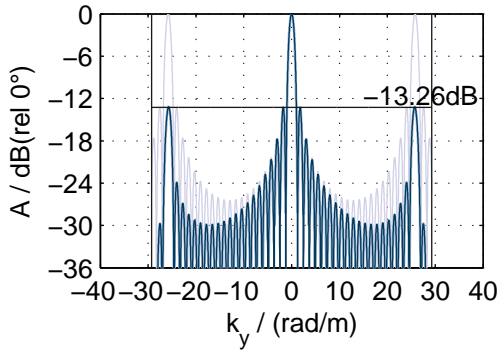
Figure 3.42: Example II: $f = 1.600$ kHz, $\lambda = 0.214$ m, $L = 5.0685173$ m, $N = 11$, $\Delta y = 0.4687517$ m, $\Delta k_y = 13.4040792$ rad/m, $q = 0.8127970$, $l = 0.3810000$ m .



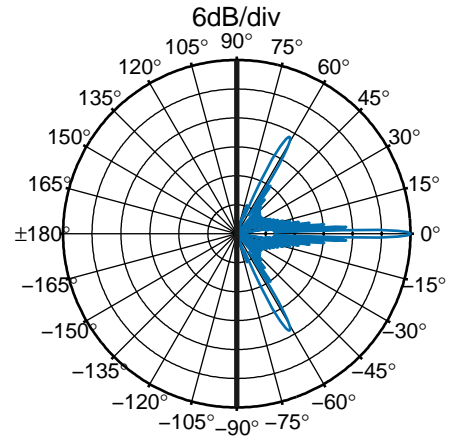
(a) $|D_{w,S}(k_y, \omega) \cdot H_{\text{Rect}}(k_y, \omega)|$.



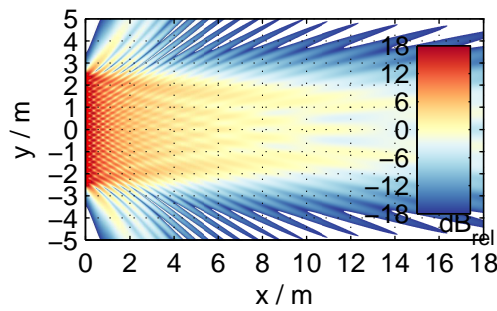
(b) $P_{\text{Main}}, P_{\text{Side}}, P_{\text{All}}$ along x -axis.



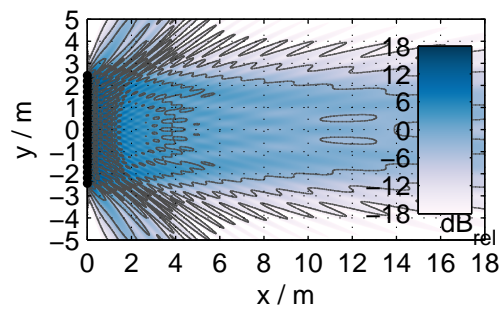
(c) visible region of $|D_{w,S,H}(k_y, \omega)|$ for $f = 1.6$ kHz, underlay: $|D_{w,S}(k_y, \omega)|$



(d) farfield radiation pattern, i.e. final array factor $|D_{w,S,H}(\varphi, \omega)|$ for $f = 1.6$ kHz.



(e) SPL in xy -plane.



(f) SPL in xy -plane.

Figure 3.43: Example II: $f = 1.600$ kHz, $\lambda = 0.214$ m, $L = 5.0685173$ m, $N = 21$, $\Delta y = 0.2435289$ m, $\Delta k_y = 25.8005749$ rad/m, $q = 0.8127970$, $l = 0.1979395$ m .

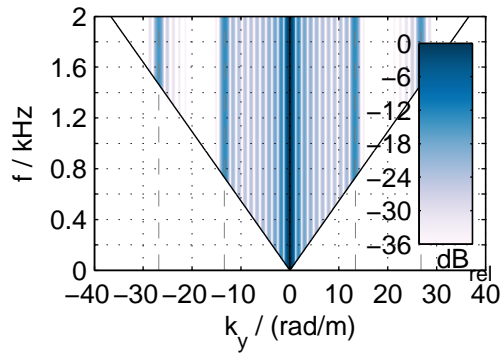
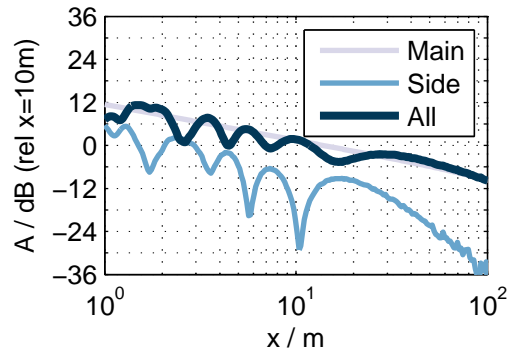
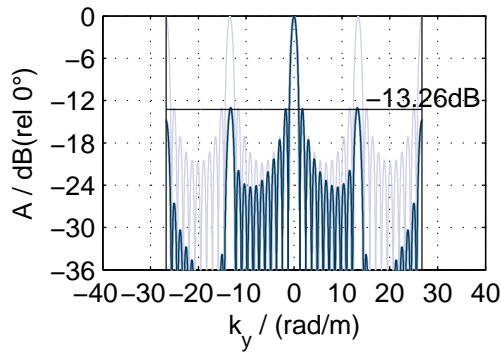
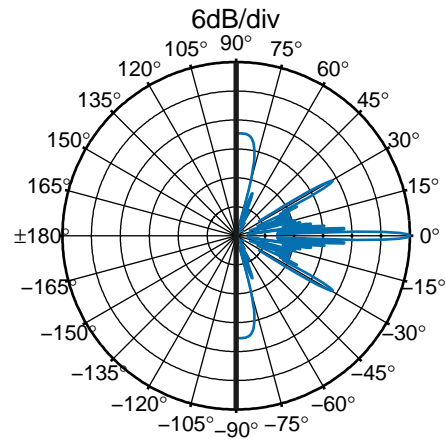
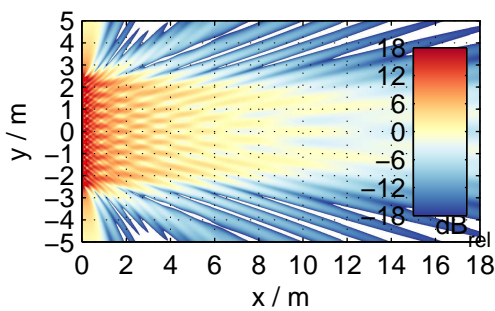
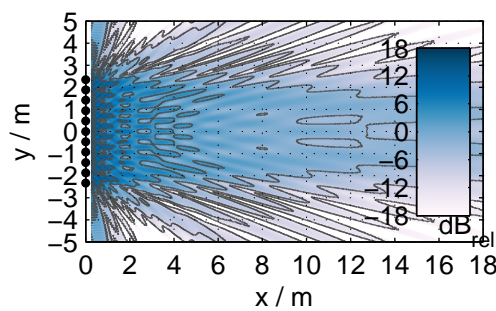
(a) $|D_{w,S}(k_y, \omega) \cdot H_{\text{Rect}}(k_y, \omega)|$.(b) $P_{\text{Main}}, P_{\text{Side}}, P_{\text{All}}$ along x -axis.(c) visible region of $|D_{w,S,H}(k_y, \omega)|$ for $f = 1.463$ kHz, underlay: $|D_{w,S}(k_y, \omega)|$ (d) farfield radiation pattern, i.e. final array factor $|D_{w,S,H}(\varphi, \omega)|$ for $f = 1.463$ kHz.(e) SPL in xy -plane.(f) SPL in xy -plane.

Figure 3.44: Example III: $f = 1.463$ kHz, $\lambda = 0.234$ m, $L = 5.0685173$ m, $N = 11$, $\Delta y = 0.4687517$ m, $\Delta k_y = 13.4040792$ rad/m, $q = 0.8127970$, $l = 0.3810000$ m .

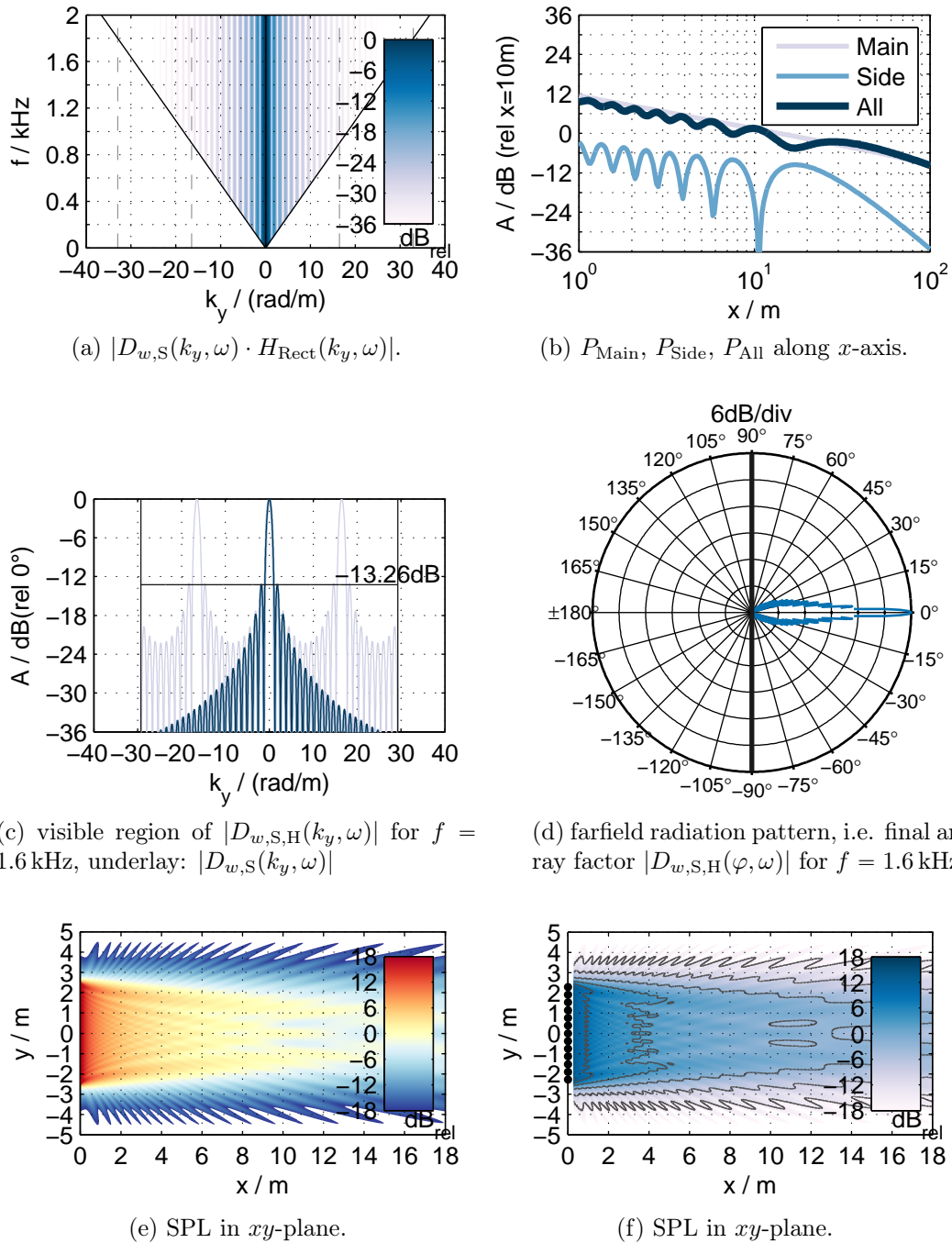


Figure 3.45: Example IV: $f = 1.600$ kHz, $\lambda = 0.214$ m, $L = 4.9530000$ m, $N = 13$, $\Delta y = 0.3810000$ m, $\Delta k_y = 16.4913000$ rad/m, $q = 1.0000000$, $l = 0.3810000$ m .

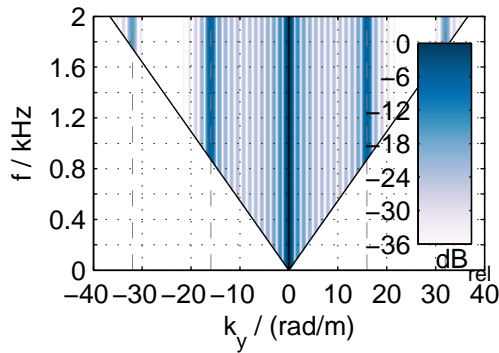
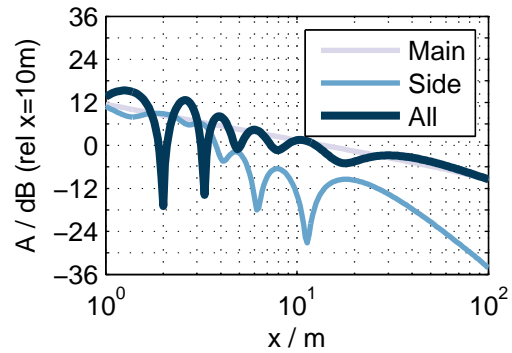
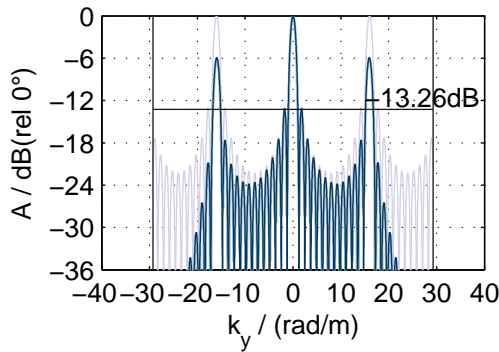
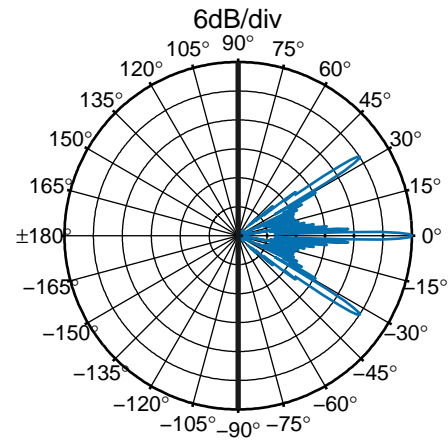
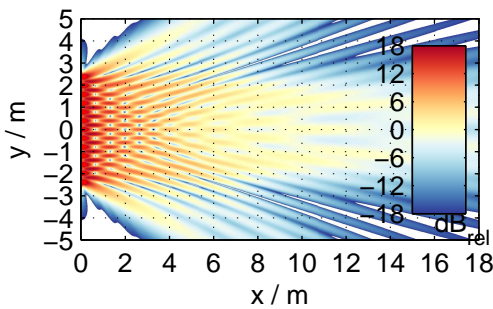
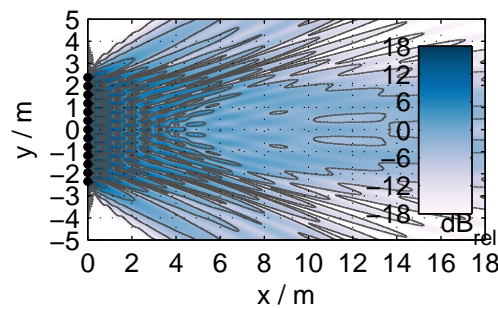
(a) $|D_{w,S}(k_y, \omega) \cdot H_{\text{Rect}}(k_y, \omega)|$.(b) $P_{\text{Main}}, P_{\text{Side}}, P_{\text{All}}$ along x -axis.(c) visible region of $|D_{w,S,H}(k_y, \omega)|$ for $f = 1.6$ kHz, underlay: $|D_{w,S}(k_y, \omega)|$ (d) farfield radiation pattern, i.e. final array factor $|D_{w,S,H}(\varphi, \omega)|$ for $f = 1.6$ kHz.(e) SPL in xy -plane.(f) SPL in xy -plane.

Figure 3.46: Example V: $f = 1.600$ kHz, $\lambda = 0.214$ m, $L = 4.9530000$ m, $N = 13$, $\Delta y = 0.3930179$ m, $\Delta k_y = 15.9870214$ rad/m, $q = 0.6024800$, $l = 0.2367854$ m .

3.4.2 WST#2 Criterion

The WST#2 criterion considers a finite length, spatially discretized LSA built from ideal spherical monopoles. According to the sampling theorem for baseband signals, perfect reconstruction² requires an ideal spatial lowpass with Nyquist bandwidth (cf. p.78, (3.17))

$$H_{\text{LP,Post}}(k_y) = \begin{cases} 1 & \text{for } |k_y| < \frac{\Delta k_y}{2} = \frac{\pi}{\Delta y} \\ 0 & \text{else.} \end{cases} \quad (3.151)$$

For WST it was considered to reconstruct the baseband $|k_y| < \frac{\pi}{\Delta y}$ of $D_{w,s}(k_y, \omega)$ (3.128), cf. [Urb03, p.917]. As discussed earlier, (3.151) would require individual sources of infinite spatial extent, with a sinc-shaped velocity along the piston's axis. This is obviously not feasible. Thus, the temporal bandwidth of the driving function must be limited

$$|k_y| = \frac{\omega}{c} < \frac{\Delta k_y}{2}, \quad (3.152)$$

which after rearranging with $c = \lambda f$ yields

$$\text{WST \#2:} \quad f_{\text{max}} < \frac{c}{2 \Delta y} \leftrightarrow \Delta y < \frac{\lambda_{\text{min}}}{2}. \quad (3.153)$$

This is the general spatial anti-aliasing condition – already discussed in Ch. 3.2.5 – of arrays built of ideal point sources. It ensures a grating lobe free visible region for arbitrarily chosen driving function's spatio-temporal spectra, thus completely avoiding propagating spatial aliasing.

For the WST driving function the condition can be easily fulfilled for low and mid audio frequencies using the typical bandwidths and dimensions of electrodynamic loudspeakers. This can be seen in Fig. 3.47 for $\varphi_{\text{max}} = 0^\circ$, when referring to 12" and 15" drivers for the low frequencies (typically driven up to 200 - 400 Hz) and 5" and 6.5" drivers for the mid frequencies (typically driven between 200-400 Hz and 1.5-2kHz). For the high audio frequencies (typically >1.5-2 kHz) the required source spacing is more demanding and by the time WST was initially invented this was not yet considered feasible. Thus,

²cf. Fig. 3.22 and its corresponding discussion for the definition of perfect reconstruction when no prefilter is applied in the sampling scheme.

the WST#1 and WST#3 – holding for uniformly driven arrays without using beam steering – were introduced to reduce propagating spatial aliasing, when WST#2 cannot be met for the high audio frequencies.

Implications for Electronic Beam Steering

Some recent LSA designs exhibit a very small source spacing Δy – of about 1" – for the high frequency audio band to shift spatial aliasing to very high audio frequencies and to relax the ARF requirements. Some of these LSA designs can even be fixed straightly and are exclusively aimed at electronic beam steering [But14], instead of controlling the LSA radiation characteristics with geometric curving. Combined approaches of electronic and geometrically curved beam-forming are also realized [Dur07, Tho08, Tho09, Tho11, Tho13, Fei13]. Thus, it is worth to revisit the spatial anti-aliasing condition for typical spatial discretization of LSAs.

The implications for electronic beam steering using the delay-and-sum beam-former Ch. 3.2.5 for a straight LSA are discussed next. For typical source spacings in LSA designs the maximum allowed frequency f_{\max} for grating lobe free beam steering over the steering angle φ_{Steer} is depicted in Fig. 3.47, assuming $q = 1$. The LSA length is always $L \approx 5$ m. Note that the required gain to compensate the loss of the driver's farfield polar pattern (assuming ideal circular or line piston characteristics) is not more than ≈ 4 dB within the tolerated values given in Fig. 3.47.

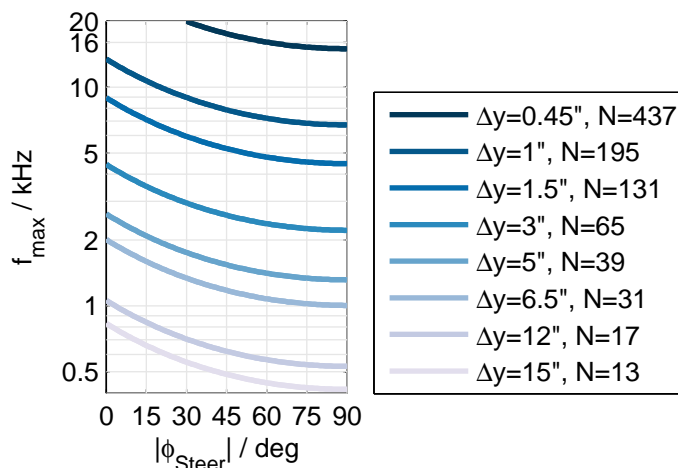
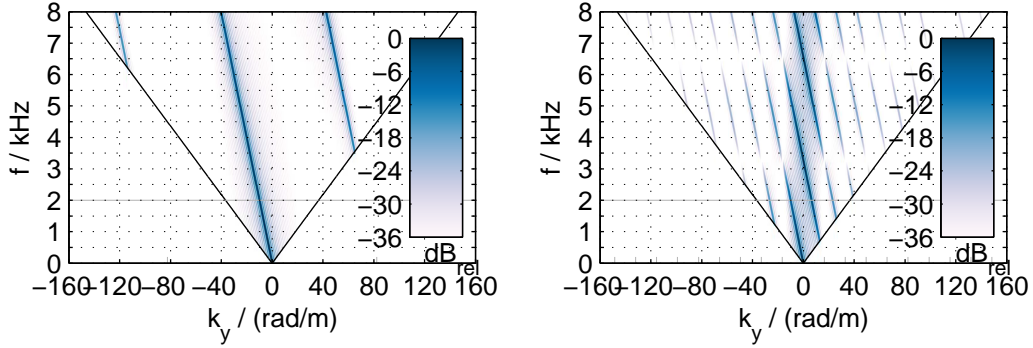
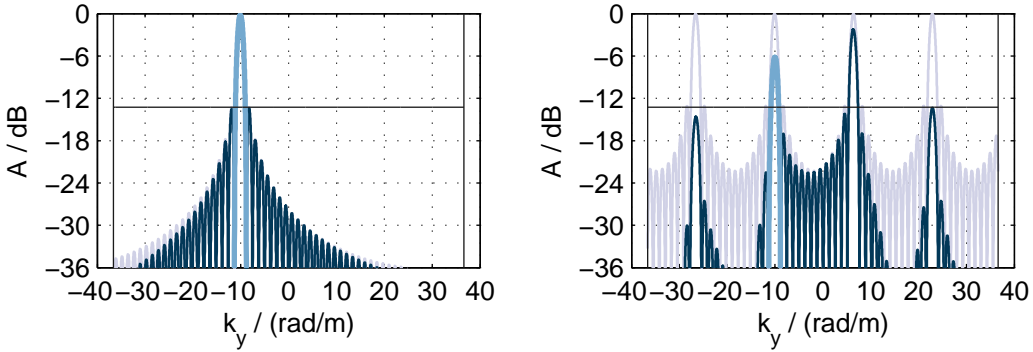


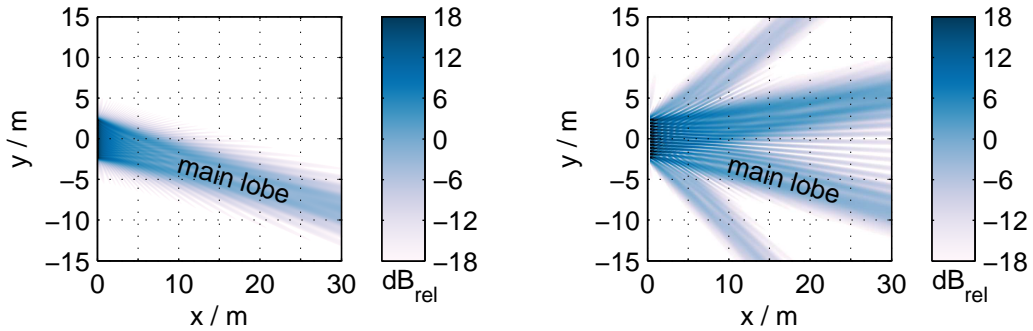
Figure 3.47: Aliasing frequency $f_{\max} = \frac{c}{\lambda_{\min}}$ over steering angle (3.112).



(a) $|D_{w,S,Steered}(k_y, \omega) \cdot H_{\text{Rect}}(k_y, \omega)|$, $\Delta y = l = 3''$, $N = 65$, $\Delta k_y = \frac{2\pi}{\Delta y} = 82.4565 \text{ rad/m}$. (b) $|D_{w,S,Steered}(k_y, \omega) \cdot H_{\text{Rect}}(k_y, \omega)|$, $\Delta y = l = 15''$, $N = 13$, $\Delta k_y = \frac{2\pi}{\Delta y} = 16.49 \text{ rad/m}$.



(c) $|D_{w,S,Steered}(k_y, \omega) \cdot H_{\text{Rect}}(k_y, \omega)|$ for $f = 2 \text{ kHz}$, $k_{y,Steer} \approx -10 \text{ rad/m}$. (d) $|D_{w,S,Steered}(k_y, \omega) \cdot H_{\text{Rect}}(k_y, \omega)|$ for $f = 2 \text{ kHz}$, $k_{y,Steer} \approx -10 \text{ rad/m}$.



(e) Level in xy -plane normalized to $x = 20 \text{ m}$, $y = -5 \text{ m}$. (f) Level in xy -plane normalized to $x = 20 \text{ m}$, $y = -5 \text{ m}$.

Figure 3.48: DSB with $D_{w,S,Steered}(k_y, \omega)$ (3.107) for $\varphi_{\text{Steer}} = -16^\circ$. Line piston LSAs with $q = \text{ARF} = 1$, $L = 4.953 \text{ m}$ (3.136). Left: $l = 3''$, right: $l = 15''$.

For the lowest audio frequencies the range is approximately given as e.g. $400 \text{ Hz} < f_{\max} < 800 \text{ Hz}$ for $90^\circ \geq \varphi_{\text{Steer}} \geq 0^\circ$ ($N = 13$, $\Delta y = 15''$) and $500 \text{ Hz} < f_{\max} < 1000 \text{ Hz}$ for $90^\circ \geq \varphi_{\text{Steer}} \geq 0^\circ$ ($N = 17$, $\Delta y = 12''$). The low frequency band is thus uncritical for grating lobe free beam steering. The limiting factor here is rather the chosen LSA length that determines the possible beam width resolution, i.e. the null-to-null beamwidth, cf. (3.72).

For the mid-band of audio frequencies an appropriate trade-off between the crossover lowpass cutoff frequency and the allowed maximum steering angle has to be defined. The high-band of audio frequencies is the most critical w.r.t. spatial aliasing and requires very small distances between drivers to avoid it. In the given example the 1"-piston would allow grating lobe free sound fields up to 10 kHz, when restricting $|\varphi_{\text{Steer,max}}| < 20^\circ$, while the 0.45"-design would allow endfire beams up to 15 kHz.

Large waveguides of about the same dimension as the low frequency drivers implicate $f_{\max} \ll f_{\text{HF}}$. Thus, for these LSAs it is not meaningful to apply electronic beam steering for high frequencies unless generating much spatial aliasing [Mey02, Sch14a]. Therefore, such LSAs have to be curved geometrically, beam steering should be avoided for these frequencies and beamforming should only be realized by applying real valued gains to the sources. In Fig. 3.48 an example of DSB using a $l = 3''$ (left column) and $l = 15''$ (right column) is given for line piston LSAs of the same physical length $L = 4.953 \text{ m}$ and an $\text{ARF} = 1$. The farfield radiation patterns, i.e. the final array factor $|D_{w,S,H}(k_y, \omega)|$ for electronically steering to $\varphi_{\text{Steer}} = -16^\circ$ is depicted over k_y and f in Fig. 3.48a and Fig. 3.48b. For the considered frequency of 2 kHz the final array factor is given in detail in Fig. 3.48c and Fig. 3.48d. The sound pressure level over the xy -plane for this frequency is depicted in Fig. 3.48e and Fig. 3.48f.

For the chosen steering angle, the 3" line piston LSA is grating lobe free up to 3.5 kHz, cf. Fig. 3.47. Two grating lobes are observed within the plotted range. The intended main lobe is maintained within the plotted frequency range, due to the less directed farfield radiation pattern of the 3" postfilter. The final array factor for 2 kHz resembles the spatio-temporal spectrum of (3.96) producing the intended main ($k_{y,\text{Steer}} \approx -10 \text{ rad/m}$) and side lobe pattern in the xy -plane.

The 15" line piston LSA cannot be used for beam steering in the high frequency range $f > (1.5...2)$ kHz without grating lobes entering the visible region. The intended main lobe level becomes attenuated due to the sinc-function postfilter, which is highly temporal frequency dependent. Between (3...3.5) kHz and at about 6.5 kHz the main lobe even vanishes due the coincidence with the sinc-function's zeros of the postfilter. A prominent grating lobe enters the visible region at about 750 Hz and can be traced towards $k_y \approx -25$ rad/m at 8 kHz. Between 2.8 kHz and 3.8 kHz this grating lobe exhibits the level of 0 dB and radiates approximately perpendicular to the LSA axis. For 2 kHz three grating lobes are located within the visible region at about $k_y = -27, 7, 23$ rad/m exhibiting different levels that are even larger than the main lobe level at $k_{y,Steer} \approx -10$ rad/m. The resulting sound field is thus severely corrupted in the Fresnel region and by high level beams towards undesired propagation directions, cf. [Mey02, Fig. 4].

A spatial-aliasing-free control of the visible region up to 16 kHz would require a sampling distance $\Delta y = \frac{c/16 \text{ kHz}}{2} = 1.07$ cm according to the sampling theorem (3.153). Such an LSA could be termed 'purely WST#2-compliant'. In array processing such an array is termed *standard linear array* [Van02, p.51].

3.4.3 WST#3 Criterion

The WST#3 criterion was derived for an LSA with directly adjacent, identical horns with no gaps between them. It relates an occurring wavefront curvature (WFC) emanated by these horns, i.e. the arc in Fig. 3.49 and a tolerated grating lobe level. For the so called sagitta S

$$\text{WST \#3:} \quad S < \frac{\lambda_{\min}}{4}, \quad (3.154)$$

must hold in order that the LSA exhibits a grating lobe attenuation larger than 10 dB relative to the intended main lobe, cf. [Urb03, Fig. 9,10], [Ure01b, Fig. 19]. This criterion also aims at reducing spatial aliasing by utilizing the spatial lowpass characteristic of the sources that construct the LSA. By discussing the WST#1 (3.135) and WST#3 (3.154) criteria separately in [Urb03, Ure04], one may erroneously assume that they are not interrelated. However, both criteria interact and determine the quality of grating lobe avoidance and suppression, which should be discussed next.

Line Piston with Wavefront Curvature

Since a line piston with WFC exhibits a specific postfilter characteristic $H_{\text{Post}}(k_y, \omega)$, the discussion remains consistent within the signal processing model in Fig. 3.34 by interpreting the resulting spatio-temporal spectrum $D_{w,S,H}(k_y, \omega)$ and the final array factor $D_{w,S,H}(\varphi, \omega)$ respectively. The discussion – based on the product theorem – is given in [Ure01b, Ure04], however the FRP of a physically arc-shaped, uniformly driven source is utilized, i.e. the Huygens' principle is applied. Here it is proposed to use Rayleigh-Sommerfeld diffraction [Bor06, Ch. 8.11.2] of a baffled, infinitesimally narrow slit of finite length that is 'illuminated' by a point source. In [Hec77] analytic spatial Fourier transforms of line piston velocity distributions are given, where the case 3 in Table I – although not parameterizable – is most likely comparable to the phenomenon observed here.

The WFC can be controlled by the point source position behind the slit on negative x -axis with the distance x_{PS} in Fig. 3.49. The vector $\mathbf{x}_{\text{PS}} = (-x_{\text{PS}}, 0, 0)^T$ holds. With the line piston length l and a desired WFC in terms of a wave length fraction $S = \alpha \lambda$ – the so called sagitta [Urb03, p.918] –, the geometric length and angle relations

$$x_{\text{PS}} = \frac{l^2}{8S} - \frac{S}{2} = \frac{l^2}{8\alpha\lambda} - \frac{\alpha\lambda}{2}, \quad (3.155)$$

$$r = \frac{l^2}{8S} + \frac{S}{2} = \frac{l^2}{8\alpha\lambda} + \frac{\alpha\lambda}{2}, \quad (3.156)$$

$$\tan \theta = \frac{\frac{l}{2}}{\frac{l^2}{8S} - \frac{S}{2}} = \frac{\frac{l}{2}}{\frac{l^2}{8\alpha\lambda} - \frac{\alpha\lambda}{2}} \quad (3.157)$$

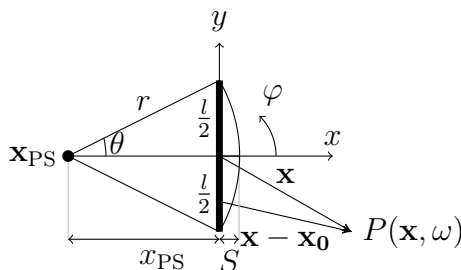


Figure 3.49: Geometry for WFC model, cf. [Urb03, Fig. 8], [Ure04, Fig. 38].

are derived according to Fig. 3.49. A distance $x_{\text{PS}} > 0$ is required, which is valid if $\frac{l^2}{4} > (\alpha \lambda)^2$.

SFS of a virtual point source using a linear, finite length, continuous secondary source distribution that models the slit is deployed. The diffracted sound field is synthesized with the Neumann Rayleigh-Sommerfeld integral

$$P(\mathbf{x}, \omega) = \int_{-l/2}^{+l/2} D_{\text{WFC}}(y_0, \omega) G_N(\mathbf{x}, \mathbf{x}_0, \omega) dy_0, \quad (3.158)$$

describing the slit $\mathbf{x}_0 = (0, y_0, 0)^T$ on the y -axis, the evaluation points $\mathbf{x} = (x > 0, y, 0)^T$ and the 3D Neumann Green's function $G_N(\mathbf{x}, \mathbf{x}_0, \omega) = 2G(\mathbf{x}, \mathbf{x}_0, \omega)$. With (3.155) the SDM driving function of a virtual point source reads (2.126), [Spo10, (24)]

$$D_{\text{WFC}}(y_0, \omega) = \frac{1}{4} \sqrt{\frac{x_{\text{ref}}}{x_{\text{ref}} + x_{\text{PS}}}} j \frac{\omega}{c} (-x_{\text{PS}}) \frac{1}{|\mathbf{x}_0 - \mathbf{x}_{\text{PS}}|} H_1^{(2)}\left(\frac{\omega}{c} |\mathbf{x}_0 - \mathbf{x}_{\text{PS}}|\right), \quad (3.159)$$

denoting the Hankel function of second kind of order one as $H_1^{(2)}(\cdot)$ [Olv10, §10.2]. In contrast to WFS driving functions, (3.159) is also valid for point sources close to the slit, when the reference line at x_{ref} – at which the sound field is to be synthesized correctly in amplitude and phase – is far away from the piston. This is in accordance for the quested farfield radiation pattern.

In Fig. 3.50 an example of the diffracted sound field for a WFC of $\alpha = \frac{1}{2}$ is given. The drawn circles exhibit a radius increment of $\frac{\lambda}{2}$. One circle intersects the line piston in the origin and the subsequent circle intersects the line piston at its edges, which defines the sagitta $S = \alpha \lambda$.

Since the driving function $D_{\text{WFC}}(y_0, \omega)$ is proportional to the normal source velocity's temporal spectrum, its spatio-temporal spectrum

$$H_{\text{WFC}}(k_y, \omega) = \int_{-l/2}^{+l/2} D_{\text{WFC}}(y_0, \omega) e^{+j k_y y_0} dy_0, \quad (3.160)$$

– normalized to unity gain at $k_y = 0$ for consistency – includes the farfield radiation pattern of the line piston with WFC [Mö09, Ch. 3.6], [Hec77]. The in-

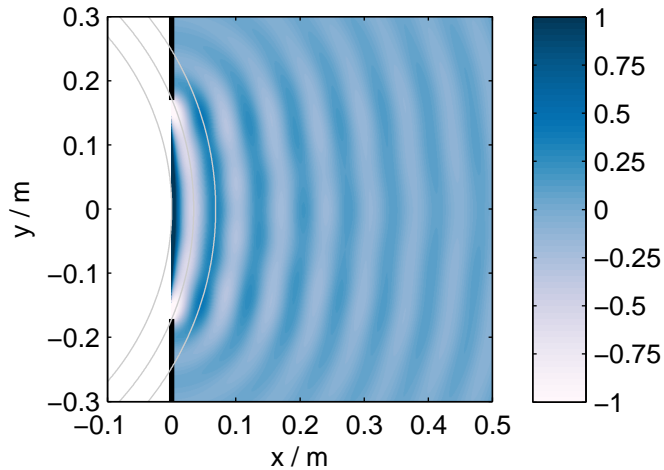


Figure 3.50: Diffracted sound field $\Re \{P(\mathbf{x}, \omega)\}$ of a virtual point source synthesized by a baffled line piston with $l = 0.343$ m for $f = 5$ kHz using a WFC $\alpha = 1/2$, i.e. $x_{\text{PS}} = 0.4116$ m, $\theta = 22.62^\circ$, $x_{\text{ref}} = 100$ m, $c = 343$ m/s. Normalized to $\Re \{P(\mathbf{x} = (\frac{\lambda}{2}, 0, 0)^T, \omega)\} = -1/2$.

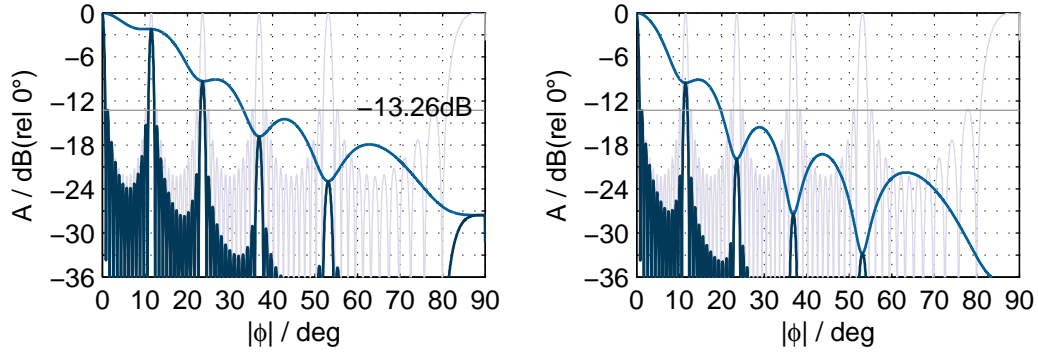
tegral is presumably not treatable for an analytic closed form solution. Hence, numerical evaluation with a zero-padded, spatial FFT of a properly discretized version (3.159) is deployed. In the following subsections the influence of the WFC w.r.t. grating lobe suppression is discussed for exemplarily chosen LSA setups and frequencies.

Single Waveguide Per LSA Cabinet

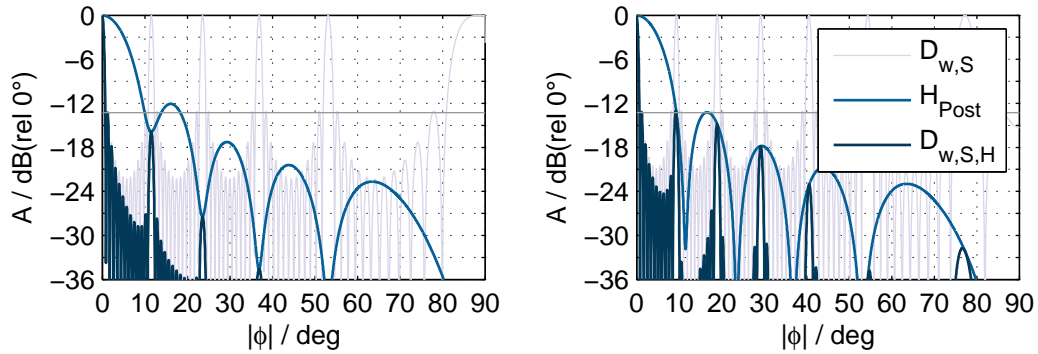
Different LSA setups of the same physical length $L = (N - 1) \Delta y + l \approx 4.5$ m are modeled with N identical line pistons of length $l = 0.343$ m that exhibit different WFCs and ARFs. The specific array factors, postfilter FRPs and the resulting LSA FRPs (final array factors) over radiation angle φ are depicted for $f = 5$ kHz in Fig. 3.51.

The line piston with a WFC of $\alpha = \frac{1}{2}$ (cf. Fig. 3.50) is used to model an ARF = 1, $N = 13$ LSA in Fig. 3.51a. The first two grating lobes, with radiation angles $\approx \pm 10^\circ$, are attenuated by ≈ 2 dB (cf. [Ure01b, Fig. 20]), the second two by about 9 dB. For Fig. 3.51b the WFC is decreased choosing $\alpha = \frac{1}{4}$. The maximum grating lobe level is about -10 dB relative to the main lobe level (cf. [Ure01b, Fig. 19], [Urb03, p.919]). According to the 3rd WST criterion (3.154), $\alpha = \frac{1}{4}$ holds as the maximum tolerated WFC, which however violates the 1st WST criterion (3.135), even for ARF = 1.

An ARF = 1, $N = 13$ LSA with WFC of $\alpha = \frac{1}{8}$ is depicted in Fig. 3.51c (cf. [Ure01b, Fig. 18]). The maximum grating lobe level does not exceed approx. -16 dB. An ARF = 0.82, $N = 11$ LSA yields a maximum grating lobe level of about -11.5 dB (not depicted) and thereby this WFC violates the 1st WST criterion also for ARF = 0.82. In compliance with a tolerated maximum grating lobe level of -13.26 dB a WFC of $\alpha = \frac{1}{6}$ is required, which however holds only for ARF ≈ 1 (not depicted). If ARF = 0.82 is allowed, thus fulfilling the 1st WST criterion, the WFC of $\alpha > \frac{1}{50}$ ensures the maximum allowed grating lobe level of -13.26 dB, as shown in Fig. 3.51d. For $\alpha > \frac{1}{50}$, i.e. $x_{\text{PS}} \gg \lambda_0$ the WFC postfilter exhibits almost the same characteristic as the ideal line piston without WFC (3.129).



(a) $\alpha = 1/2$, ARF = $q = 1$, $N = 13$, $\Delta y = 0.343$ m (b) $\alpha = 1/4$, ARF = $q = 1$, $N = 13$, $\Delta y = 0.343$ m



(c) $\alpha = 1/8$, ARF = $q = 1$, $N = 13$, $\Delta y = 0.343$ m (d) $\alpha = 1/50$, ARF = $q = 0.812797$, $N = 11$, $\Delta y = 0.422$ m

Figure 3.51: Uniformly driven LSA with line pistons that exhibit a specified WFC. The array factor $D_{w,S}(\varphi)$ (3.82), the postfilter $H_{\text{Post}}(\varphi) = H_{\text{WFC}}(\varphi)$ (3.160) and the resulting final array factor $D_{w,S,H}(\varphi) = D_{w,S}(\varphi) \cdot H_{\text{Post}}(\varphi)$ for $f = 5$ kHz, $l = 0.343$ m, $c = 343$ m/s are visualized.

Multiple Waveguides Per LSA Cabinet

The discussion above holds for a single waveguide per single LSA cabinet. In practical designs an LSA cabinet is often built from multiple and smaller waveguides each coupled to an individual compression driver [But02]. From Fig. 3.52 the geometrical relations w.r.t. the individual ARFs and physical lengths are derived to

$$q_l = \frac{l}{\Delta y_l} \quad L_B = (N_l - 1) \Delta y_l + l, \quad (3.161)$$

$$q_B = \frac{L_B}{\Delta y_B} \quad L_{\text{LSA}} = (N_B - 1) \Delta y_B + L_B. \quad (3.162)$$

Ideally the waveguides should be driven individually, since this enhances the capability for electronic beam steering, cf. Ch. 3.4.2.

For a uniformly driven, straight LSA with identical waveguides the product theorem for nested arrays – also referred to as subarrays [Bro12] – yields the spatio-temporal spectrum

$$D_{w,S,H}(k_y, \omega) = \underbrace{\frac{1}{N_l} \frac{\sin(k_y \Delta y_l \frac{N_l}{2})}{\sin(k_y \Delta y_l \frac{1}{2})}}_{D_{w,S,l}(k_y, \omega)} \cdot H_{\text{Post}}(k_y, \omega) \cdot \underbrace{\frac{1}{N_B} \frac{\sin(k_y \Delta y_B \frac{N_B}{2})}{\sin(k_y \Delta y_B \frac{1}{2})}}_{D_{w,S,B}(k_y, \omega)}, \quad (3.163)$$

for which the first product models the farfield radiation pattern of a single LSA cabinet built from N_l pistons, each featuring the spatial postfilter characteristics $H_{\text{WFC}}(k_y, \omega)$ (3.160). The subsequent product models the complete farfield radiation pattern (final array factor) of the LSA built from N_B cabinets.

Due to the interaction of three spatial spectra, the discussion becomes more demanding and for line pistons with WFC no closed form solution exists

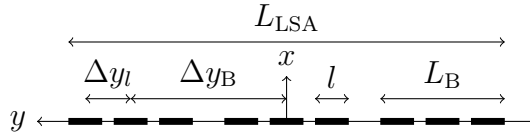


Figure 3.52: Schematic sketch of an LSA built from $N_B = 3$ cabinets of physical length L_B spaced by Δy_B . Each cabinet has $N_l = 3$ line pistons of length l spaced by Δy_l . The total physical length of the LSA is L_{LSA} . N_B and N_l are assumed to be odd-numbered.

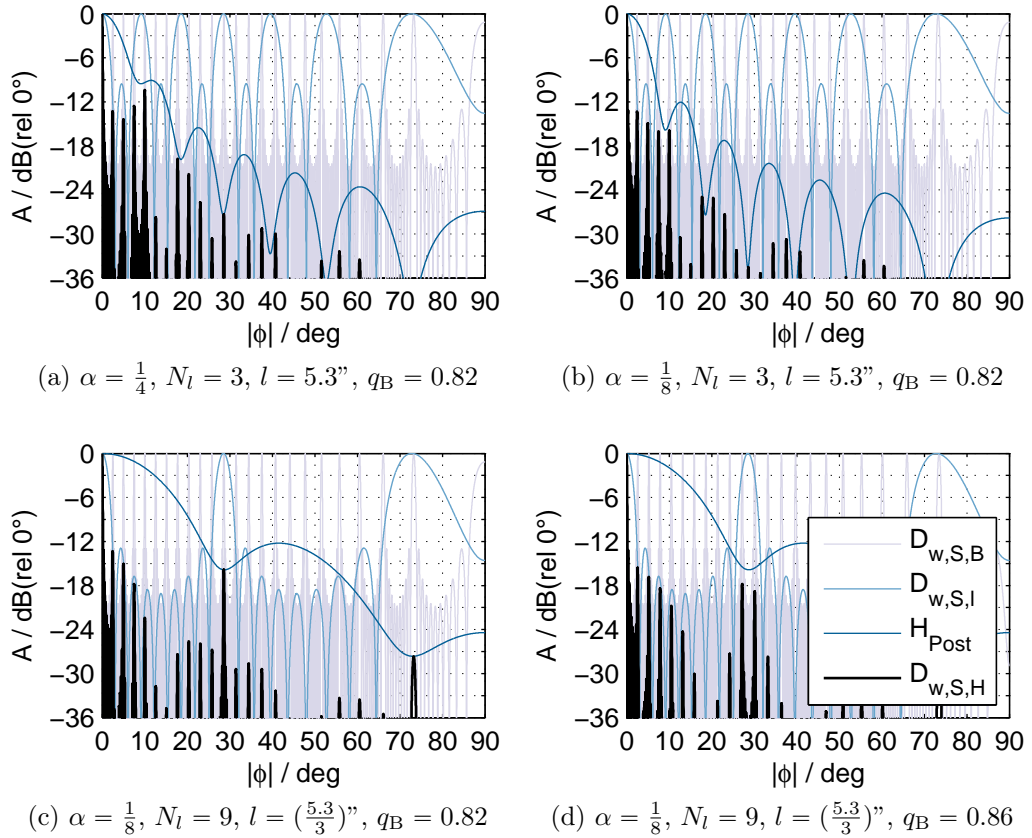


Figure 3.53: Array factors $D_{w,S,B}(\phi)$, $D_{w,S,l}(\phi)$ and the final array factor $D_{w,S,H}(\phi)$ (3.163) using $H_{WFC}(\phi)$ for $f = 16$ kHz, $c = 343$ m/s are visualized. Fig. a) and b): 3x 5.3" waveguides per LSA cabinet, α is varied. Fig. c) and d): 9x 1.76" waveguides per LSA cabinet, q_B is varied. $q_l=1$, $N_C = 11$ for all cases.

so far. In Fig. 3.53 examples of the (final) array factors for the frequency $f = 16$ kHz for a 'multiple waveguides per cabinet'-LSA design are presented. For Fig. 3.53a and Fig. 3.53b three rather large waveguides per LSA cabinet are used and the WFC is varied. The chosen parameters closely match typical LSA designs, i.e. $q_l = 1$ and $\text{ARF} = q_B = 0.82$, cf. [But02]. For Fig. 3.53c and Fig. 3.53d the waveguides are three times smaller, thus more of them fit into an LSA cabinet. For this case q_B is varied, while $q_l = 1$ and a WFC of $\alpha = \frac{1}{8}$ holds.

For the chosen source spacing and frequency no LSA is grating lobe free, due to non-compliance with WST#2. The rather large WFC in Fig. 3.53a results in grating lobes larger than -12 dB at small radiation angles, which can

be reduced when decreasing the WFC in Fig. 3.53b. By comparing Fig. 3.53b (large waveguides) and Fig. 3.53c (small waveguides) with otherwise the same parameters, it is observed that the grating lobes at small angles φ are more attenuated for the latter LSA, due to the larger decay of $D_{w,S,1}(k_y, \omega)$. This advantage, however comes along with a comparably larger grating lobe level at $|\phi| \approx 30^\circ$ since the smaller waveguide exhibits a less directed FRP. It is worth reminding that grating lobes at small angles corrupt the intended audience sound field in a much larger spatial region than these emanated with large radiation angles. This consequently has large influence on the homogeneity of the Fresnel region. Due to the almost perfect coincidence of the aliased-sinc function grating lobe maxima of $D_{w,S,1}(k_y, \omega)$ (1st maximum) and $D_{w,S,B}(k_y, \omega)$ (11th maximum) only the postfilter determines the attenuation level, which yields over 30 dB in Fig. 3.53b and about 16 dB in Fig. 3.53c. The coincidence of common maxima from $D_{w,S,1}(k_y, \omega)$ and $D_{w,S,B}(k_y, \omega)$ can be controlled by

$$q_B = \frac{q_l \cdot L_B}{\sigma \cdot l} \quad \sigma \geq N_l, \sigma \in \mathbb{N}. \quad (3.164)$$

Herein $\sigma = N_l$ generally models $q_B = 1$ if $q_l = 1$. This then constitutes an ARF=1 LSA, for which the grating lobe suppression depends only on the spatial postfilter characteristic. The chosen example in Fig. 3.53c closely matches $\sigma = N_l + 2 = 9 + 2 \rightarrow q_B = 0.\overline{81}$. By increasing the ARF in Fig. 3.53d compared to Fig. 3.53c the grating lobes are generally more attenuated. Grating lobes at $|\varphi| \approx 30^\circ$ differ significantly due to different interaction of the involved functions.

In contrast to the 'Single Waveguide Per LSA Cabinet'-approach, here larger WFC (in the example $\alpha \leq \frac{1}{8}$) can be tolerated to fulfill the WST#1 criterion when using multiple smaller waveguides per LSA cabinet. This is due to the additional spatial lowpass filter characteristic of $D_{w,S,1}(k_y, \omega)$, that compensates the insufficient lowpass characteristic of a waveguide with large WFC.

Despite the comparably large grating lobe level at about 30° , the LSAs in Fig. 3.53c, Fig. 3.53d might be preferable, due to the smaller discretization step (leaving more frequency bandwidth uncorrupted from aliasing, improved capability for electronic beam steering) and due to the larger decay of grating

lobe levels for small radiation angles, yielding a larger spatial region without spatial aliasing and a more homogeneous Fresnel region. Naturally, these phenomena are highly dependent on temporal frequency .

3.5 Summary

Wavefront Sculpture Technology (WST) introduced line source arrays (LSAs) for large scale sound reinforcement (LS-SR). It aims at sound fields for full audio bandwidth with less spatial-aliasing than using conventional loudspeaker cluster arrays. WST is based on array processing fundamentals.

In contrast to the initial WST derivation, the radiation characteristics of straight arrays are consistently explained within the spatio-temporal Fourier spectrum domain in this thesis. Thus, in contrast to the Rayleigh integral formulation sound fields are generated with the angular spectrum synthesis. This allows for a more convenient interpretation of the occurring interference and diffraction phenomena in the near and farfield of line source arrays. The LS-SR problem is treated as a sound field synthesis (SFS) problem rather than a radiation synthesis problem: optimum LS-SR ideally aims at the synthesis of a desired homogeneous wavefront for audience coverage that constitutes the main lobe of the array in the farfield. This is only possible when additional wavefronts originating from spatial truncation and spatial sampling are sufficiently suppressed. These additional wavefronts corrupt the intended wavefront by interference, yielding a severely corrupted Fresnel region (nearfield) and cause side and grating lobes in the Fraunhofer region (farfield). Obviously, this should be avoided as best as possible.

In essence, the first three WST criteria deal with the avoidance or attenuation of grating lobes in the farfield radiation pattern (FRP) of straight, uniformly driven LSAs, which consequently avoids or reduces spatial aliasing in the LSA's Fresnel and Fraunhofer region. For their full avoidance the spatial sampling theorem (i.e. WST#2) has to be fulfilled. This requires a very small spacing Δy between drivers for the highest audio frequencies and was not considered feasible when initially introducing WST in the early 1990s.

When WST#2 cannot be met, the WST#1 criterion deploys the spatial low-pass filter characteristics of line and circular pistons to reduce spatial aliasing. The gap size between adjacent pistons determines the grating lobe attenuation

which for the ARF theorems were given for tolerated spatial aliasing. The usage of ideal line pistons for a special WST case (uniformly driven array and no gaps between the pistons) is superior compared to a circular piston driven LSA: in this ideal case all spatial aliasing is suppressed. This is not achievable with circular pistons. However, for $\Delta y > l$ or $\Delta y > 2r_0$ of line and circular pistons with same dimension (length l and radius r_0) reveals an improved spatial lowpass characteristic of the ideal circular piston.

The WST#3 criterion discusses the influence of a tolerated deviation from the ideal line piston characteristic in terms of a wavefront curvature and tolerated spatial aliasing energy. The WST#1 and WST#3 interact for which an in-depth discussion is firstly given.

The requirements for avoiding propagating spatial aliasing is conveniently discussed within the spatio-temporal spectrum domain. It is obviously preferable using rather small source spacings (i.e. rather large distance Δk_y of the spectral repetitions in the driving function's spatio-temporal spectrum) and thereby small pistons, ideally fulfilling the spatial sampling theorem for all audio frequencies. In the ideal case no grating lobes would enter the visible region of the array. This allows for synthesizing the desired wavefront using electronic beamforming and beam steering methods with a high degree of freedom. This is especially interesting for an homogeneous Fresnel region that becomes less corrupted with less occurring spatial aliasing. A severely corrupted Fresnel region should be avoided as audience region, since this region cannot be optimized. The frequency response there is heavily dependent on the actual listening position and is far away from being linear.

For very small source spacing, and thus very small piston dimensions, the postfilter characteristics of the circular and line piston consequently are less directive. This implies that ideally no additional postfilter would be required and only the Green's functions (i.e. the ideal spherical monopole) acts as the reconstruction postfilter of the sampled driving function. The ARF theorem consequently becomes less important.

The first generation of LSAs – following the initial WST with rather large waveguides – cannot be meaningfully utilized with electronic beam steering due to the occurring spatial aliasing. The desired wavefront for optimum audience must therefore realized by means of geometrical array curving and

additional electronic beamforming that only uses frequency dependent, real valued gain weights but no delays. In practice arc-shaped, J-shaped and spirally shaped arrays are appropriate for typical venues. Ideally, the wavefront shaping then yields a frequency independent FRP, Fresnel/Fraunhofer transition and smooth sound pressure level decay over the audience. Both cannot be achieved with the uniformly driven, straight LSA as was revisited throughout this chapter. However, for array curving it is also preferable to not allow gaps between the drivers to avoid spatial aliasing. The implications of uniformly driven, curved arrays for an intended audience coverage are defined with the WST#4 and WST#5 criterion.

The WST#5 states a maximum tilt angle between adjacent LSA cabinets, such that their individual farfield sound fields don't produce discontinuities in the audience coverage [Urb03, p.929]. The initial WST#4 criterion defines the LSA's curvature for roughly a -3 dB SPL loss per distance doubling along the audience with a constant product αd of the tilt angle α between adjacent LSA cabinets and their throw distance towards d the audience [Urb03, p.929]. This is known as progressive curvature leading to a spirally curved LSA. Other curvature schemes that are typically used for typical audience coverages are: arc LSA with $\alpha = \text{const}$ yielding -6 dB SPL loss per distance doubling along the audience, J-shaped LSA with $\alpha d^2 = \text{const}$ yielding no SPL loss along the audience. It is common practice to combine all of them designing an intended composite SPL target curve along the audience [LA16, Ch. 2].

Optimum, audience adapted wavefront shaping is discussed in the next chapter, showing that WST can be interpreted as a special case of WFS.

Chapter 4

Wavefront Shaping

After recollecting the fundamentals of SFS in Ch. 2 and the detailed treatment on the WST criteria for straight LSAs using the angular spectrum synthesis in Ch. 3, the thesis proceeds¹ with the discussion on suitable LSA control techniques for LS-SR. In Ch. 3 it was shown that the uniformly driven, finite length, straight LSA exhibits a highly frequency dependent near-/farfield transition and an increasing directivity for increasing frequencies. Homogeneous LS-SR is thus not feasible using this LSA type.

The goal for optimized LS-SR using LSAs is the synthesis of an appropriate, homogeneous wavefront – here called wavefront shaping – which realizes any desired (within the limits of physics), ideally frequency independent SPL loss over the audience area. To this end, three different major trends for designing, setting up and controlling LSAs can be observed these days:

1. LSAs with rather large waveguides (ca. 1-3 per LSA cabinet) with geometric curving and electronically controlled wavefront shaping by either (i) manually adjusted broadband and frequency dependent gain shading (cf. designs such as *Electro Voice X-Line Advance*, *JBL VTX*, *L-ACOUSTICS K1*, *Meyer Sound LEO-M*) or (ii) numerically optimized frequency dependent gain shading (i.e. frequency dependent spatially windowing, cf. designs such as *d&B audiotechnik J&Y series*).
2. LSAs with large to medium sized waveguides (ca. 2-6 per LSA cabinet) with geometric curving and electronically controlled wavefront shaping

¹[Sch13, Sch14d, Str15b, Str15a, Str16] are partly reissued or reconsidered herein.

by numerically optimized beam steering and -forming (cf. designs such as *d&b audiotechnik J&Y series*, *Martin Audio MLA & OmniLine*, *AFMG's FIRmaker*).

3. straight LSAs with very small waveguides (≥ 8 per LSA cabinet) with electronically controlled wavefront shaping solely by optimized beam steering and -forming (cf. designs such as *EAW Anya & Anna*).

Most of the deployed LSA control algorithms are not fully documented in research preserving intellectual property. This chapter discusses the usage of WFS for optimized wavefront shaping as a forward problem solution. This reveals that WST can be understood as a special application of WFS, which in its initial formulation is achieved by LSA curving.

The chapter is organized as follows: in Ch. 4.1 the implications of curving an LSA w.r.t. grating lobes and the farfield radiation pattern are discussed by means of the so called arc array. In Ch. 4.2 a specially developed simulation toolbox is introduced that simulates the radiation characteristic of model-based LSAs. A suitable WFS based LSA control technique is proposed. In Ch. 4.3 visualization methods and quality measures are proposed that allow an in-depth interpretation of the performance. In Ch. 4.4 several LSA design studies are simulated and discussed. The chapter concludes in Ch. 4.5.

4.1 Arc Array vs. Straight Array

First of all, this section shall discuss the effect of curving an LSA towards an arc w.r.t. the near-/farfield transition, the farfield radiation pattern and side/grating lobes characteristics compared to a straight LSA. This enhances the discussions given in [Urb03, Ure04, Kee10]. Note that dissipation is not considered for the sound field prediction.

The HF-BEM kernel (2.33) is used for predicting the sound field of a continuous source in the first instance. A line integral along the line C

$$P(\mathbf{x}, \omega) = \int_C D(\mathbf{x}_0, \omega) \frac{1 + \cos(\beta(\mathbf{x}, \mathbf{x}_0))}{2} H_{\text{Post}}(\beta(\mathbf{x}, \mathbf{x}_0), \omega) \frac{e^{-j\frac{\omega}{c}|\mathbf{x}-\mathbf{x}_0|}}{4\pi|\mathbf{x}-\mathbf{x}_0|} dC \quad (4.1)$$

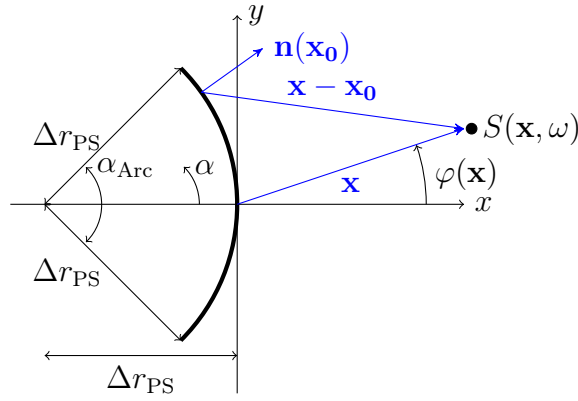


Figure 4.1: Geometry for an arc array with arc length L , cf. [Ure04, Fig. 14], [Ure04, Fig. 16].

with $H_{\text{Post}}(\beta(\mathbf{x}, \mathbf{x}_0), \omega) = 1$ of the spherical monopole is to be deployed. For

$$\cos(\beta(\mathbf{x}, \mathbf{x}_0)) = \frac{\langle \mathbf{x} - \mathbf{x}_0, \mathbf{n}(\mathbf{x}_0) \rangle}{|\mathbf{x} - \mathbf{x}_0|} \quad (4.2)$$

is used, which is identical to $\cos \varphi_r$, cf. Ch. 2, (2.20).

The curve parametrization of a straight array of length L – as already used above – is for $-\frac{L}{2} \leq y_0 \leq +\frac{L}{2}$ given as

$$C_{\text{Straight}} : \quad \mathbf{x}_0 = (0, y_0, 0)^T \quad \mathbf{n}_{\mathbf{x}_0} = (1, 0, 0)^T. \quad (4.3)$$

The arc source depicted in Fig. 4.1 with an arc length L and a definable central angle $\alpha_{\text{Arc}} \neq 0$ is given with the curve parametrization

$$C_{\text{Arc}} : \quad \mathbf{x}_0(\alpha) = \begin{pmatrix} \Delta r_{\text{PS}} \cos(\alpha) - \Delta r_{\text{PS}} \\ \Delta r_{\text{PS}} \sin(\alpha) \\ 0 \end{pmatrix} \quad \mathbf{n}_{\mathbf{x}_0}(\alpha) = \begin{pmatrix} \cos(\alpha) \\ \sin(\alpha) \\ 0 \end{pmatrix} \quad (4.4)$$

for $-\frac{\alpha_{\text{Arc}}}{2} \leq \alpha \leq +\frac{\alpha_{\text{Arc}}}{2}$. According to Fig. 4.1 the radius of the circle that set the arc up is given as

$$\Delta r_{\text{PS}} = \frac{L}{\alpha_{\text{Arc}}}, \quad (4.5)$$

hence yielding the circle's origin at $(-\Delta r_{\text{PS}}, 0, 0)^T$ for the chosen geometry. Doing so, the middle of the arc intersects the coordinate system's origin.

A discrete source distribution is modeled with the Riemann sum along the curve, here choosing an odd number N of individual sources. For the arc array the discrete angles are given as

$$\alpha_\mu = -\frac{\alpha_{\text{Arc}}}{2} + \mu \frac{\alpha_{\text{Arc}}}{N-1} \quad \text{for } 0 \leq \mu \leq N-1, \quad \Delta C = \frac{\alpha_{\text{Arc}}}{N-1} \Delta r_{\text{PS}} \quad (4.6)$$

for the curve parametrization. The straight source is defined with

$$y_0 = -L/2 + \mu \frac{L}{N-1} \quad \text{for } 0 \leq \mu \leq N-1, \quad \Delta C = \Delta y = \frac{L}{N-1}. \quad (4.7)$$

The discrete model can use different postfilters $H_{\text{Post}}(\beta(\mathbf{x}, \mathbf{x}_0), \omega)$ of the discrete sources that build the array. In the following simulations the line piston postfilter (4.27) with line piston length l is deployed for all frequencies with a definable factor $q = \frac{l}{\Delta C}$, cf. (3.139).

The SFS driving function of a plane wave (2.170) for $\varphi_{\text{PW}} = 0$

$$D(\mathbf{x}_0, \omega) = w(\mathbf{x}_0) \sqrt{j \frac{\omega}{c} \sqrt{8\pi x_{\text{Ref}}}} \quad (4.8)$$

with an additional spatial window $w(\mathbf{x}_0)$ realizes a broadside array. From [Spo10, Sch13, LA13] it can be deduced that finite length arrays require additional prefiltering in order that a flat frequency response is obtained at the reference evaluation point, here on-axis at x_{Ref} . In LSA applications this is achieved by so called U-shaping, array morphing or array contour filtering that is realized with different FIR/IIR filter design strategies. Here, applying the additional preshelling filter $H_{\text{LS,HalfInt}}(\omega)$ (4.13) to the driving function yields

$$D(\mathbf{x}_0, \omega) = w(\mathbf{x}_0) \sqrt{j \frac{\omega}{c} \sqrt{8\pi x_{\text{Ref}}}} \cdot H_{\text{LS,HalfInt}}(\omega). \quad (4.9)$$

A suitable design of $H_{\text{LS,HalfInt}}(\omega)$ is discussed next, providing a proposed half integrator and half differentiator design method.

Half Differentiator and Half Integrator from 2nd Order Lowshelving Filters

The Laplace transfer function of a 2nd order low-shelf is given as

$$H_{\text{LS}}(s) = \frac{\frac{s^2}{\omega_c^2} + \frac{s}{\omega_c} \frac{n_1}{Q} + n_2}{\frac{s^2}{\omega_c^2} + \frac{s}{\omega_c} \frac{d_1}{Q} + d_2}, \quad (4.10)$$

denoting the zero/pole quality Q . With the gain G in dB a symmetrical low-shelf with $g = 10^{\frac{|G|}{20}}$ and a so called *one-half pad loss* characteristic [Kim38], where the magnitude is $\frac{G}{2}$ at the cutoff frequency ω_c , is realized with the coefficients

$$\begin{aligned} G > 0: \quad n_1 &= g^{+\frac{1}{4}} & n_2 &= g^{+\frac{1}{2}} & d_1 &= g^{-\frac{1}{4}} & d_2 &= g^{-\frac{1}{2}} \\ G \leq 0: \quad n_1 &= g^{-\frac{1}{4}} & n_2 &= g^{-\frac{1}{2}} & d_1 &= g^{+\frac{1}{4}} & d_2 &= g^{+\frac{1}{2}}. \end{aligned} \quad (4.11)$$

For the pole/zero quality $Q = \frac{1}{\sqrt{2}}$ and $G = \pm 10 \log_{10}(2) \approx \pm 3.01$ dB $\rightarrow g = 2^{\frac{1}{2}}$, $H_{\text{LS}}(s)$ simplifies to

$$H_{\text{LS},+3\text{dB}}(s) = \frac{\frac{s^2}{\omega_c^2} + \frac{s}{\omega_c} 2^{\frac{+5}{8}} + 2^{\frac{+1}{4}}}{\frac{s^2}{\omega_c^2} + \frac{s}{\omega_c} 2^{\frac{+3}{8}} + 2^{\frac{-1}{4}}} \quad H_{\text{LS},-3\text{dB}}(s) = \frac{\frac{s^2}{\omega_c^2} + \frac{s}{\omega_c} 2^{\frac{+3}{8}} + 2^{\frac{-1}{4}}}{\frac{s^2}{\omega_c^2} + \frac{s}{\omega_c} 2^{\frac{+5}{8}} + 2^{\frac{+1}{4}}}, \quad (4.12)$$

due to the symmetrical characteristic $H_{\text{LS},+3\text{dB}}(s) = H_{\text{LS},-3\text{dB}}(s)^{-1}$. A cascade connection with subsequent reduction of the biquad's individual cutoff frequency each time by one octave

$$H_{\text{LS},\text{HalfInt}}(s) = \prod_{\mu=0}^{+\infty} H_{\mu,\text{LS},+3\text{dB}}(s) = \prod_{\mu=0}^{+\infty} \frac{\frac{s^2}{(2^{-\mu}\omega_c)^2} + \frac{s}{(2^{-\mu}\omega_c)} 2^{\frac{+5}{8}} + 2^{\frac{+1}{4}}}{\frac{s^2}{(2^{-\mu}\omega_c)^2} + \frac{s}{(2^{-\mu}\omega_c)} 2^{\frac{+3}{8}} + 2^{\frac{-1}{4}}} \quad (4.13)$$

$$H_{\text{LS},\text{HalfDiff}}(s) = \prod_{\mu=0}^{+\infty} H_{\mu,\text{LS},-3\text{dB}}(s) = \prod_{\mu=0}^{+\infty} \frac{\frac{s^2}{(2^{-\mu}\omega_c)^2} + \frac{s}{(2^{-\mu}\omega_c)} 2^{\frac{+3}{8}} + 2^{\frac{-1}{4}}}{\frac{s^2}{(2^{-\mu}\omega_c)^2} + \frac{s}{(2^{-\mu}\omega_c)} 2^{\frac{+5}{8}} + 2^{\frac{+1}{4}}} \quad (4.14)$$

yields either the half integrator $H_{\text{LS},\text{HalfInt}}(s) \propto \frac{1}{\sqrt{s}}$ or the half differentiator $H_{\text{LS},\text{HalfDiff}}(s) \propto \sqrt{s}$ for $\omega \ll \omega_c$ and linear characteristic $H_{\text{LS},\text{HalfInt}}(s) \rightarrow 1$ and $H_{\text{LS},\text{HalfDiff}}(s) \rightarrow 1$ when $\omega \gg \omega_c$.

With $H_{\text{LS},\text{HalfDiff}}(s)$ adapted prefilters for WFS can be designed similar to [Sch13] by defining the aliasing frequency $\omega_c = \omega_{\text{Aliasing}}$ and the lower cut-

off frequency $\omega_{\text{Low}} = \omega_c 2^{-\mu}$. Note that the approach here does not allow an independent choice of ω_{Aliasing} and ω_{Low} (here they are linked by a definable octave distance) and the interpolation bandwidth (here this is predefined by $Q = \frac{1}{\sqrt{2}}$). However, the numerical optimization scheme used in [Sch13] precisely yields the same result of the analytical exact minimum phase shelving filter $H_{\text{LS,HalfDiff}}(s)$ when these parameters match.

Half Differentiator and Half Integrator from 2nd Order Highshelving Filters

The Laplace transfer function of a 2nd order half-pad loss, symmetrical high-shelf is given as

$$H_{\text{HS}}(s) = \frac{\frac{s^2}{\omega_c^2} n_2 + \frac{s}{\omega_c} \frac{n_1}{Q} + 1}{\frac{s^2}{\omega_c^2} d_2 + \frac{s}{\omega_c} \frac{d_1}{Q} + 1}, \quad (4.15)$$

using the same parameters and coefficients from (4.11). Again, for the pole/zero quality $Q = \frac{1}{\sqrt{2}}$ and $G = \pm 10 \log_{10}(2) \approx \pm 3.01 \text{ dB} \rightarrow g = 2^{\frac{1}{2}}$, $H_{\text{HS}}(s)$ simplifies to

$$H_{\text{HS,+3dB}}(s) = \frac{\frac{s^2}{\omega_c^2} 2^{\frac{+1}{4}} + \frac{s}{\omega_c} 2^{\frac{+5}{8}} + 1}{\frac{s^2}{\omega_c^2} 2^{\frac{-1}{4}} + \frac{s}{\omega_c} 2^{\frac{+3}{8}} + 1} \quad H_{\text{HS,-3dB}}(s) = \frac{\frac{s^2}{\omega_c^2} 2^{\frac{-1}{4}} + \frac{s}{\omega_c} 2^{\frac{+3}{8}} + 1}{\frac{s^2}{\omega_c^2} 2^{\frac{+1}{4}} + \frac{s}{\omega_c} 2^{\frac{+5}{8}} + 1}. \quad (4.16)$$

The same cascade connection as above

$$H_{\text{HS,HalfDiff}}(s) = \prod_{\mu=0}^{+\infty} H_{\mu,\text{HS,+3dB}}(s) = \prod_{\mu=0}^{+\infty} \frac{\frac{s^2}{(2^{-\mu} \omega_c)^2} 2^{\frac{+1}{4}} + \frac{s}{(2^{-\mu} \omega_c)} 2^{\frac{+5}{8}} + 1}{\frac{s^2}{(2^{-\mu} \omega_c)^2} 2^{\frac{-1}{4}} + \frac{s}{(2^{-\mu} \omega_c)} 2^{\frac{+3}{8}} + 1} \quad (4.17)$$

$$H_{\text{HS,HalfInt}}(s) = \prod_{\mu=0}^{+\infty} H_{\mu,\text{HS,-3dB}}(s) = \prod_{\mu=0}^{+\infty} \frac{\frac{s^2}{(2^{-\mu} \omega_c)^2} 2^{\frac{-1}{4}} + \frac{s}{(2^{-\mu} \omega_c)} 2^{\frac{+3}{8}} + 1}{\frac{s^2}{(2^{-\mu} \omega_c)^2} 2^{\frac{+1}{4}} + \frac{s}{(2^{-\mu} \omega_c)} 2^{\frac{+5}{8}} + 1} \quad (4.18)$$

yields either the half integrator $H_{\text{HS,HalfInt}}(s) \propto \frac{1}{\sqrt{s}}$ or the half differentiator $H_{\text{HS,HalfDiff}}(s) \propto \sqrt{s}$ for $\omega \ll \omega_c$. This time the gain is $|H_{\text{HS,FracInt}}(s \rightarrow 0)| = 1$ and $|H_{\text{HS,FracDiff}}(s \rightarrow 0)| = 1$. For $\omega \gg \omega_c$ constant magnitude is observed, which theoretically for $\mu \rightarrow \infty$ tends to zero (integrator) or infinity (differentiator). In practice, only a limited range μ (finite number of biquads) would be realized depending on the frequency range for which half integration/dif-

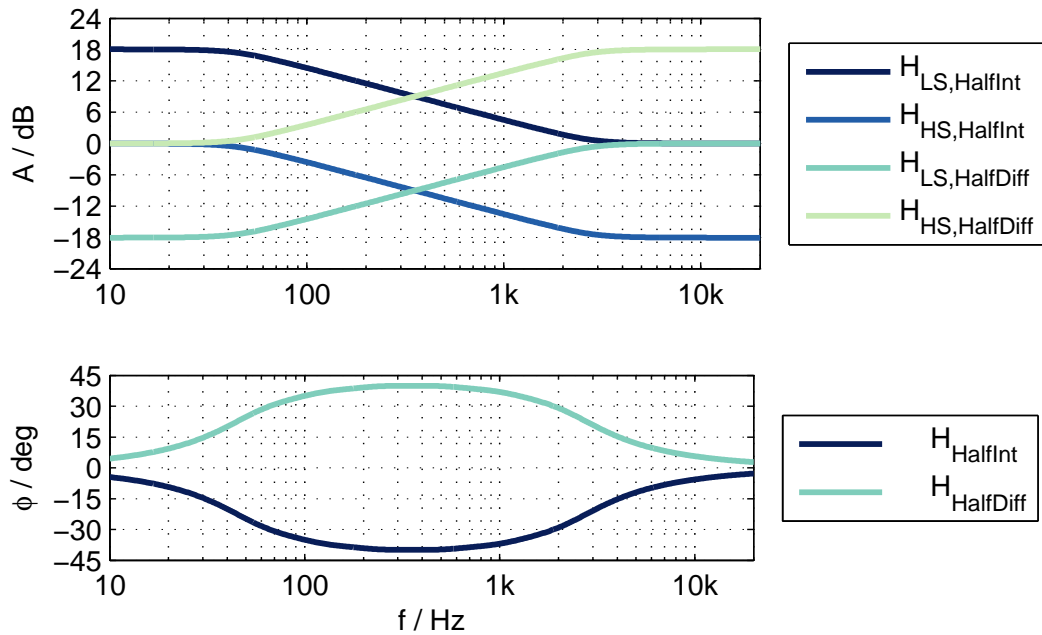


Figure 4.2: Fractional order differentiators/integrators (4.13), (4.14), (4.18) and (4.17) using $\omega_c = 2\pi 2000 \text{ rad/s}$ evaluated for $0 \leq \mu \leq 5$.

differentiation is desired as exemplarily shown in Fig. 4.2. The upper shelving frequency is set to 2 kHz and 6 second order filter structures ($0 \leq \mu \leq 5$) are realized leading to the cutoff frequency of 62.5 Hz for the last biquad. Within the range $100 \text{ Hz} < f < 1 \text{ kHz}$ the $\pm 3 \text{ dB/oct.}$ slope is well matched, the phase approximately reaches almost $\pm \frac{\pi}{4}$ as desired. Note that the $\pm 3 \text{ dB}$ slopes of all derived filters exhibit a negligible peak to peak deviation of $< 0.05 \text{ dB}$ (ripples) compared to the ideal slope.

4.1.1 Array Morphing

In the white paper [LA13] it is discussed that the three types of variation i) increasing/decreasing the size of an LSA, ii) increasing/decreasing the curvature of an LSA and iii) increasing/decreasing the listening distance to an LSA induce similar effects on the ATF, cf. [LA13, Fig. 2&3] and thus can be equally addressed by the same prefiltering. This is referred to as array morphing therein. Since the schematically given figures [LA13, Fig. 2&3] are oversimplifications it is worth providing a detailed simulation for these three types of variation.

Consider a line array with length $L = 4 \text{ m}$ ($L = 8 \text{ m}$) built from $N = 801$

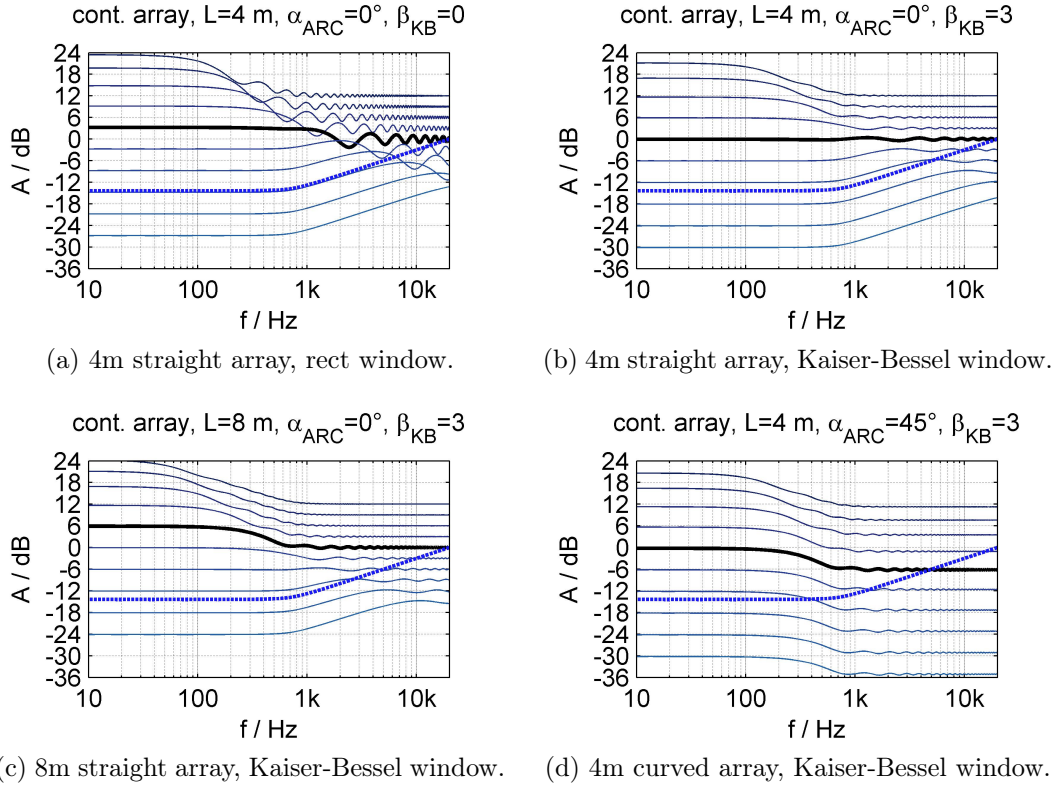


Figure 4.3: On-axis frequency responses for variations of array size, windowing, curving and distance doubling. Array driven with (4.9) and synthesized with (4.1), $x_{\text{Ref}} = 16$ m, $f_c = 515$ Hz = const.

($N = 1601$) spherical monopoles (i.e. modeling a quasi continuous array with $\Delta C = 5$ mm for frequencies $f < 20$ kHz). The driving function (4.9) is used, setting $x_{\text{Ref}} = 16$ m. Either a rectangular or a Kaiser-Bessel window with $\beta = 3$ is used. The cutoff frequency for $H_{\text{LS,HalfInt}}(\omega)$ (4.13) is set to $f_c = 515$ Hz and the cascade connection of biquads is performed until the last biquad's cutoff frequency is smaller than 1 Hz. The array is either straight or an arc with arc angle $\alpha_{\text{Arc}} = 45^\circ$, cf. Fig. 4.1. The on-axis frequency responses for distance doublings $x/m = (1, 2, 4, 8, 16, 32, 64, 128, 256, 512)$ are evaluated. The results of evaluating the synthesis integral (4.1) are depicted in Fig. 4.3. The thick black line indicates the frequency response for $x_{\text{Ref}} = 16$ m, the curves above indicate a subsequent distance halving $x/m = (8, 4, 2, 1)$, the curves below subsequent distance doublings, i.e. $x/m = (32, 64, 128, 256, 512)$. The dotted blue curve shows the applied prefilter $\sqrt{j \frac{\omega}{c}} \sqrt{8 \pi x_{\text{Ref}}} \cdot H_{\text{LS,HalfInt}}(\omega)$ (cf. (4.8)) normalized by -51.7 dB corresponding to the level at 20 kHz for $c = 343$ m/s.

Let's assume that the resulting 0 dB_{rel} at 20 kHz is the highest possible normalized driving level for the drivers.

The chosen prefiltering realizes a fairly flat frequency response at $x_{\text{Ref}} = 16\text{ m}$ for the straight array setup of $L = 4\text{ m}$ and Kaiser-Bessel windowing with $\beta = 3$ depicted in Fig. 4.3b. Applying the same prefilter for the other array setups leads to deviations in the $x_{\text{Ref}} = 16\text{ m}$ frequency responses. The rectangularly windowed array in Fig. 4.3a shows the previously discussed diffraction ripples in the frequency responses. In Fig. 4.3a, Fig. 4.3b and Fig. 4.3c the highly frequency dependent Fresnel/Fraunhofer transition becomes obvious. When moving towards the array from the reference distance, lower frequencies increase in level by 6 dB per distance doubling (for these frequencies the listener is located in the Fraunhofer region), whereas higher frequencies increase in level by 3 dB per distance doubling (indicating the Fresnel region). Only very near to the array the Fresnel region becomes significant at the very lowest frequencies. Vice versa, when moving away from the array, the level decay for lower frequencies exhibits Fraunhofer region characteristic and for the higher frequencies Fresnel region characteristic holds. Only for the very highest frequencies at a large distance a Fraunhofer characteristic can be observed for the 4 m array. Due to the smooth transition between the Fresnel and Fraunhofer region the frequency responses over distance vary with shelving filter characteristic. This is also described with [LA13, Fig. 2b]. It can be seen that the 8 m array exhibits a more extended Fresnel region for a larger frequency range than the 4 m array. This yields the low-shelf behavior with 6 dB gain at low frequencies at $x_{\text{Ref}} = 16\text{ m}$ for the 8 m array in Fig. 4.3c compared to the flat frequency response of the 4 m array in Fig. 4.3b. This is also described with [LA13, Fig. 3a]. With the arc array a smooth and frequency independent Fresnel/Fraunhofer transition is achieved, depicted in Fig. 4.3d. Compared to the straight arrays an almost perfect Fraunhofer characteristic with 6 dB level decay per distance doubling is observed. Distance doublings and halvings lead to virtually the same shelving shaped frequency responses, however with loosing level at the high frequencies (here about 6 dB, cf. [Urb03, Fig. 18]). This frequency responses can be flattened by setting $f_c = 130\text{ Hz}$ in (4.13) and thus reducing also the level at low frequencies. This is described with [LA13, Fig. 3c], however the figure ignores the fact that by curving the -3 dB

per distance doubling merges to a -6 dB per distance doubling for the high frequencies and thus obtaining homogeneous 6 dB loss per distance doubling for all frequencies. In fact, curving an array reduces the extent of the Fresnel region in general, since the array gets less directed by increased curving. In the limit, an arc array with $\alpha_{\text{ARC}} = 180^\circ$ synthesizes a virtual point source located in the arc's origin. This is consistent with the Huygens principle. Therefore, the deduction made in [Urb03, p.923]:

"It will be shown in the following that this [Fresnel/Fraunhofer] border distance depends on the radius of curvature and is always further away for a convex line source than for a flat line source of equivalent length. ... Thus the far field of a curved array begins farther away than the corresponding one for a flat array."

by applying Fresnel analysis to arc arrays cannot be confirmed. In fact, any smooth wavefront shaping that significantly differs from the uniformly driven LSA reduces the extent of the nearfield.

The constant beamwidth transducer (CBT) [Rog78, Van83, Kee00, Kee10, Kee15] constitutes an arc array with special windowing. [Rog78] derived the connection of the source velocity

$$v(\alpha) \propto \begin{cases} P_n(\cos \alpha) & \text{for } \alpha \leq \frac{\alpha_{\text{Arc}}}{2} \\ 0 & \text{else} \end{cases} \quad (4.19)$$

of an arc array with its farfield radiation pattern

$$p(\varphi = \alpha) \propto \begin{cases} P_n(\cos \alpha) & \text{for } \alpha \leq \frac{\alpha_{\text{Arc}}}{2} \\ 0 & \text{else} \end{cases}, \quad (4.20)$$

which is valid for a certain cutoff frequency and for which the order n of the involved Legendre polynomial $P_n(\cdot)$ is to be chosen for a specific α_{Arc} . By curving and windowing, a very homogeneous FRP with opening angle α_{Arc} can be achieved that is equivalent with the applied spatial window. However, it is worth realizing that the largest impact on producing more frequency independent FRPs than that of a straight LSA is the curving of a straight array. Additional windowing then even improves the smoothness of the FRP since side lobes become suppressed.

To conclude this section, the simulations confirm that increasing the array

size, moving towards the array and array curving lead to similar positive gain low-shelf characteristic referenced to the flat frequency response initial setup. Vice versa, decreasing the array size, moving away from the array and applying less curving lead to a similar, but negative gain low-shelf characteristic referenced to the initial flat frequency response.

4.1.2 Beamwidth and Grating Lobes for Arc Arrays

In literature, FRPs of curved LSAs, such as of the arc array, the J-shaped array and the spirally shaped array are discussed for continuous radiators [Ure01a, Ure02, Ure04, Kee10] only. It is however important to discuss the impact of grating lobes as well. Since FRPs of discretized, curved arrays cannot be easily given in closed form solutions – such as it was the case for the linear array in Ch. 3 – simulations are given next for the arc array. The knowledge of grating lobes characteristics for linear LSAs is however very helpful interpreting the obtained results. In [Str15b] FRPs of differently discretized, spirally curved LSAs were given.

Simulation parameters

The same simulation strategy as for Sec. 4.1.1 is utilized, here varying several parameters. In Fig. 4.4 and Fig. 4.5 a quasi continuous array with length $L = 4$ m (801 spherical monopoles) with a rectangular and a Kaiser-Bessel ($\beta = 3$) window respectively is simulated. Different arc angles

- 0° for subfigures a), b)
- 10° for subfigures c), d)
- 30° for subfigures e), f)
- 50° for subfigures g), h)

are realized for the following figures. The left column of such a figure shows the on-axis frequency responses for distance doublings similar as above for the different curvings. The thick black line again indicates the frequency response for $x_{\text{Ref}} = 16$ m that is always made flat by using an appropriate cutoff frequency f_c for $H_{\text{LS,HalfInt}}(\omega)$ (4.13). The resulting prefilter is indicated with the blue line with a squared marker. The right column visualizes the corresponding FRPs evaluated at a radius $r = |\mathbf{x}| = 2^{17}$ m (cf. Fig. 4.1), for which the prefilter is adapted to exhibit a flat on-axis frequency response at this distance. No further normalization of the FRP level is applied and by doing so

the level loss due to curving can be evaluated. The FRP's specific prefilter is indicated with the dotted, blue line with a circled marker in the left column. Using this huge, rather theoretical value for the FRP's radius—assuming no air absorption—the on-axis level for lowest frequencies for the straight arrays is about -60 dB, which was an intentionally chosen level for convenient visualization.

In Fig. 4.6 to Fig. 4.11 discretized LSAs using $N = 11$ line pistons with $\Delta C = 0.4$ m for the whole frequency range are simulated either with a rectangular or a Kaiser-Bessel ($\beta = 3$) window respectively and varying the ARF factor $q = \frac{l}{\Delta C}$ (3.139), i.e. the ratio of the line piston length l and the discretization step ΔC . Hence, the following simulation results are presented

- $q = 1$, rectangular window ($\beta = 0$) in Fig. 4.6
- $q = 1$, Kaiser-Bessel window ($\beta = 3$) in Fig. 4.7
- $q = 0.82$, rectangular window in Fig. 4.8
- $q = 0.82$, Kaiser-Bessel window ($\beta = 3$) in Fig. 4.9
- $q = 0.67$, rectangular window in Fig. 4.10
- $q = 0.67$, Kaiser-Bessel window ($\beta = 3$) in Fig. 4.11

for the arc angles $\alpha_{\text{ARC}} = 0^\circ, 10^\circ, 30^\circ, 50^\circ$. The on-axis frequency response for $x_{\text{Ref}} = 16$ m and the FRP are again made flat with prefilters that were obtained for a continuous array in the first instance. Hence, the on-axis responses and the FRPs for the discretized LSAs show the impact of spatial aliasing and the interaction of the directed line pistons.

Continuous LSA

The quasi-continuous arrays in Fig. 4.4 and Fig. 4.5 show decreased diffraction ripples when applying the Kaiser-Bessel window compared to the rectangular window. This also leads to reduced side lobe levels in the FRPs as expected. An increased curving leads to a more homogeneous on-axis level decay for distance doubling in both cases as discussed above in Sec. 4.1.1. The FRPs indicate a growing broadening of the main lobe and all side lobes with increased curving, for which the Kaiser-Bessel window (similar to the CBT) provides more homogenous main beam widths. This is due to the reduced side lobes that smear into the main lobe. The directivity is only developed for wave lengths that are larger than the array length. For larger wave lengths (lower frequencies) the array acts like a spherical monopole. For the rectangular win-

dowed, curved array the applied curvature leads to '6 dB main lobe beam widths' that are directly connected to the arc angle α_{Arc} . For the straight array the main lobe width of the Kaiser-Bessel windowed array is broadened compared to the rectangular window as expected. However, when curving the array the main lobe width of the Kaiser-Bessel windowed array is smaller than for the rectangular windowed array. This behavior is heavily dependent on the chosen β and in general from the chosen window type.

It is worth realizing that even a small curving angle significantly improves the radiation characteristic of the LSA making it more suitable for homogeneous LS-SR instead of using a straight array.

LSA with ARF=1

In Fig. 4.6 and Fig. 4.7 a discretized line piston LSA with $q = 1$ is simulated. It can be observed that by modeling an LSA without gaps between adjacent cabinets – which was favored to avoid grating lobes when concluding Ch. 3 – the FRP exhibits a 'tooth spaces'-like structure at the highest frequencies when too much curving is applied. The case $\alpha_{\text{Arc}} = 50^\circ$ is equivalent to a 5° splaying angle between adjacent cabinets. This indicates that the line pistons not longer interact in the farfield – more precisely the interference of the line pistons becomes negligible – and rather 'illuminate' a specific coverage angle isolated from each other. Too much curving should be avoided which was also concluded in [Urb03, Sec. 6.2] by stating the fifth WST criterion. However, note that the optimum coverage of the audience is of importance and for this spatial region the line pistons may produce not negligible interference.

A further important characteristic for discrete arrays is observed in the on-axis responses. The frequency responses exhibit the general trend of a more homogeneous level decay per distance doubling for increased curving. However, the responses have a larger deviation from the intended flat response. This is due to the fact that the ATF is built from discrete sources here introducing smoothed out comb filter characteristics.

When moving very near towards the array the ATF follows the applied prefilter at high frequencies. This indicates that only one specific LSA cabinet (here the one in the middle of the LSA) is accountable for the resulting sound pressure, since all other cabinets radiate into another spatial region due to their directivity. This can be observed in practice as well, when being located

very near to the bottom-most LSA cabinet on its main axis. Therefore, LSA cabinets for long and near throw should be processed with different prefilters or with suitable adapted wavefront shaping.

LSA with ARF=0.82

In Fig. 4.8 and Fig. 4.9 a discretized line piston LSA with $q = 0.82$ is simulated. This corresponds to a relative grating lobe level of -13.5 dB for a linear LSA as discussed in Ch. 3, cf. (3.135). The first grating lobe enters the FRP at $\pm 90^\circ$ for $f = 857.5$ Hz, cf. Fig. 4.8b. The FRPs reveal an effect that – although also observable for side lobes – heavily affects the quality of the main lobe. By increasing the curvature all lobes are broadened by approximately maintaining their relative levels as for the non-curved array. Therefore, the knowledge of grating lobe locations and relative levels is helpful for studying curved arrays. When the array is being curved too much, broadened grating lobes smear into the broadened main lobe, which is naturally heavily frequency dependent, cf. Fig. 4.9f, Fig. 4.9h. This is of course undesirable since the main lobe not longer provides a homogeneous beam. It can be concluded that also for curved arrays the gap size between adjacent LSA cabinets should be as small as possible, making so called *front hinge splaying* of the LSA cabinets the preferred choice compared to *rear hinge splaying* [Mar03]. Furthermore, it may be deduced that the sinc-function postfilter characteristic of a line piston is not the optimum choice for curved arrays. Reduced side lobes along with a broader main lobe beam as a postfilter characteristic would allow a larger array curvature and could eliminate the discussed tooth spacing. This is currently subject to research and development and is not further elaborated here.

The on-axis frequency responses for the straight arrays reveal the already discussed effect of vanishing spatial aliasing when being very far away from the array on main axis, cf. Fig. 4.8a, Fig. 4.9a that are similar to Fig. 4.6a, Fig. 4.7a for listening distances larger than 16 m. Array curving still leads to a more homogeneous level decay per distance doubling. Furthermore, the corruption from spatial aliasing becomes more independent w.r.t. distance doubling.

LSA with ARF=0.67

In Fig. 4.10 and Fig. 4.11 a discretized line piston LSA with $q = 0.67$ is simulated. This corresponds to a relative grating lobe level of about -8 dB for a straight LSA. Since $\Delta C = 0.4$ m is held constant for all line piston LSAs the grating lobes occur at the same locations within the FRP but here with more level. Thus, the main lobe beam is even more corrupted when grating lobes smear into it. Furthermore, the on-axis frequency responses exhibit larger level variations in these regions where aliasing corrupts the intended flat frequency responses, cf. Fig. 4.11g ($q = 0.67$) vs. Fig. 4.9g ($q = 0.82$). This should be avoided by approaching $q \rightarrow 1$ as close as possible.

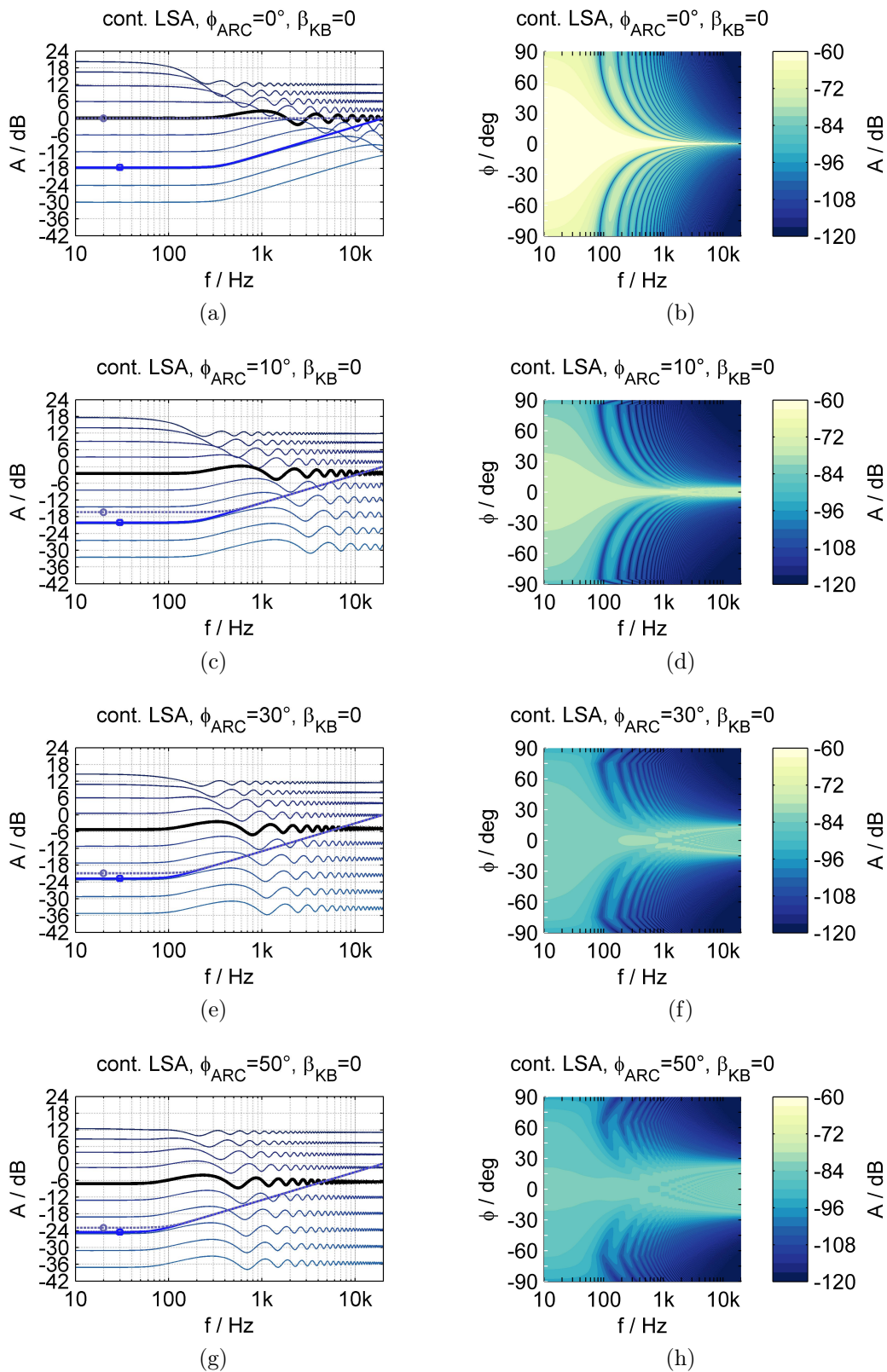


Figure 4.4: Continuous arc array, rectangular window. Left: on-axis pressure for distance doublings starting from $x = 1$ m. Right: FRP for $r = 2^{17}$ m.

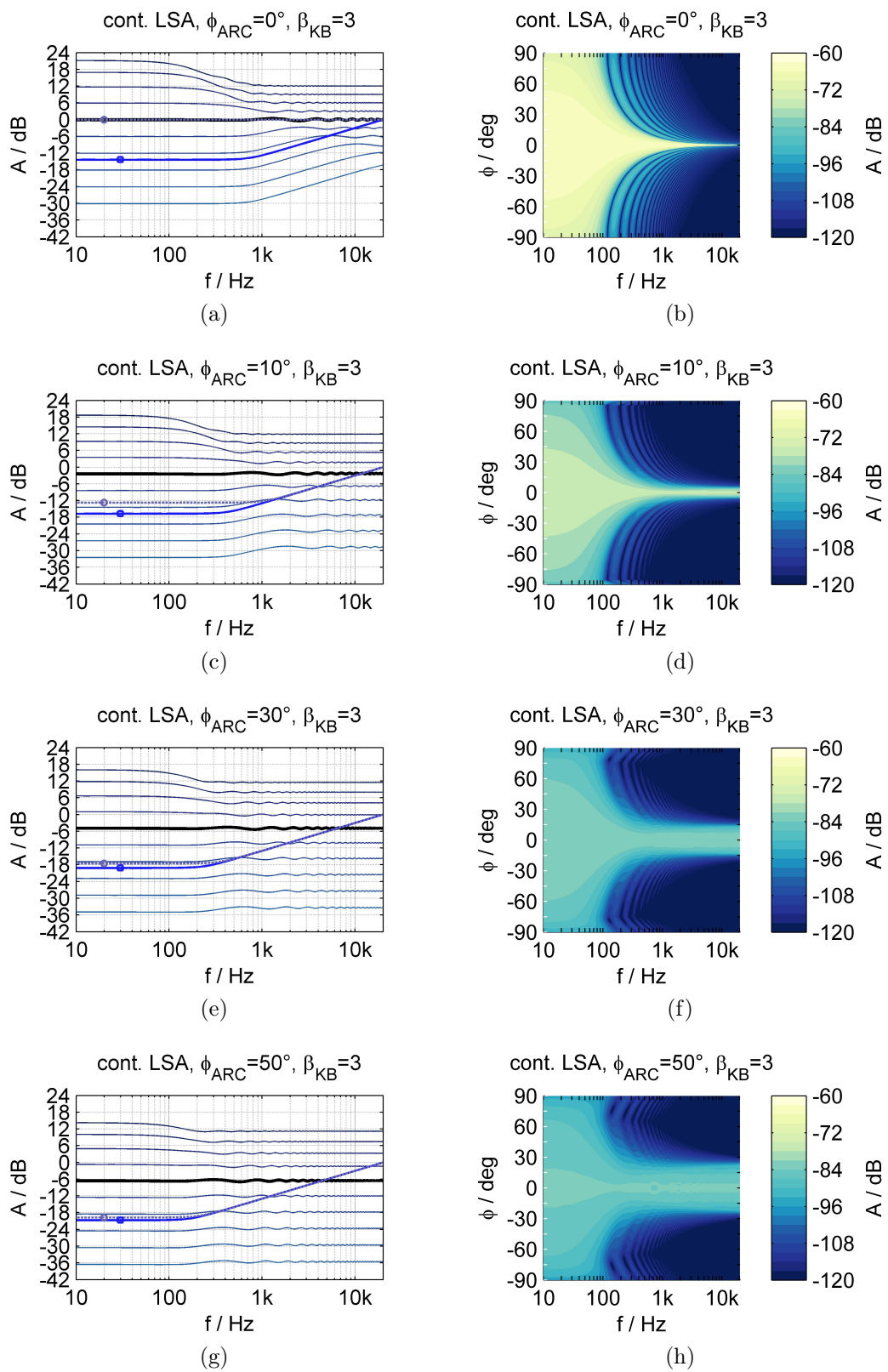


Figure 4.5: Continuous arc array, Kaiser-Bessel window. Left: on-axis pressure for distance doublings starting from $x = 1$ m. Right: FRP for $r = 2^{17}$ m.

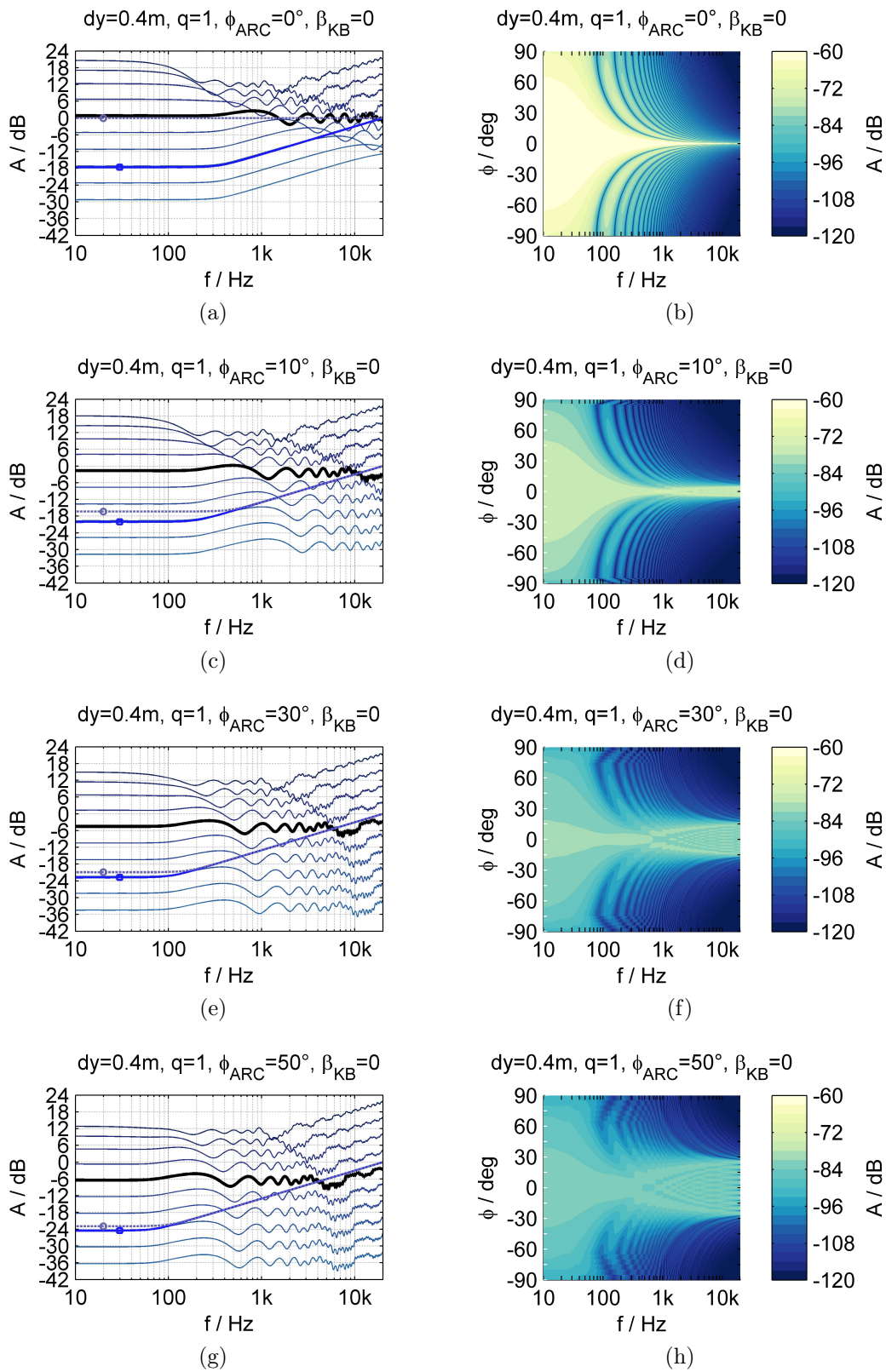


Figure 4.6: Discrete arc array, rectangular window. Left: on-axis pressure for distance doublings starting from $x = 1\text{m}$. Right: FRP for $r = 2^{17}\text{m}$.

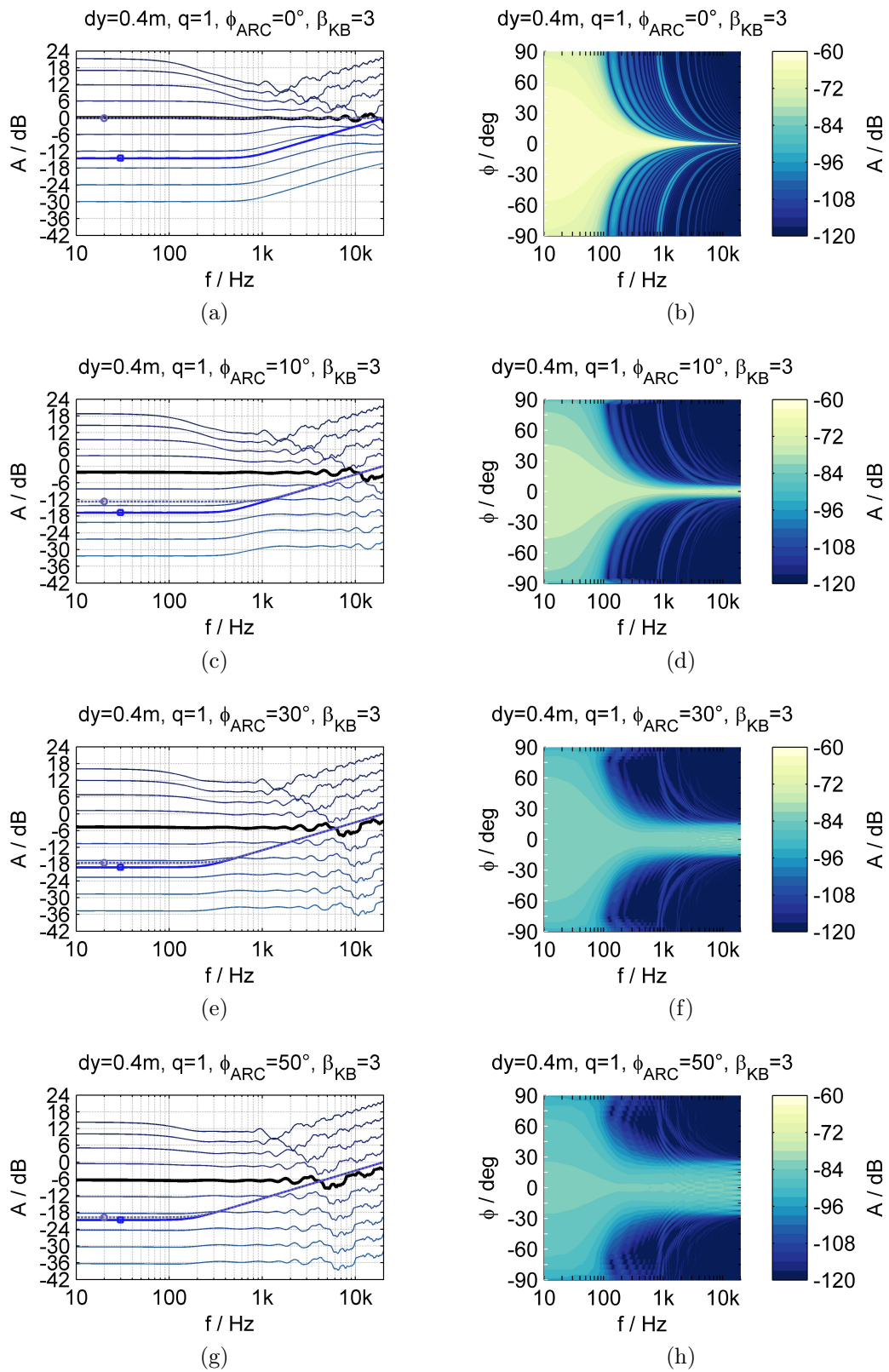


Figure 4.7: Discrete arc array, Kaiser-Bessel window. Left: on-axis pressure for distance doublings starting from $x = 1\text{m}$. Right: FRP for $r = 2^{17}\text{m}$.

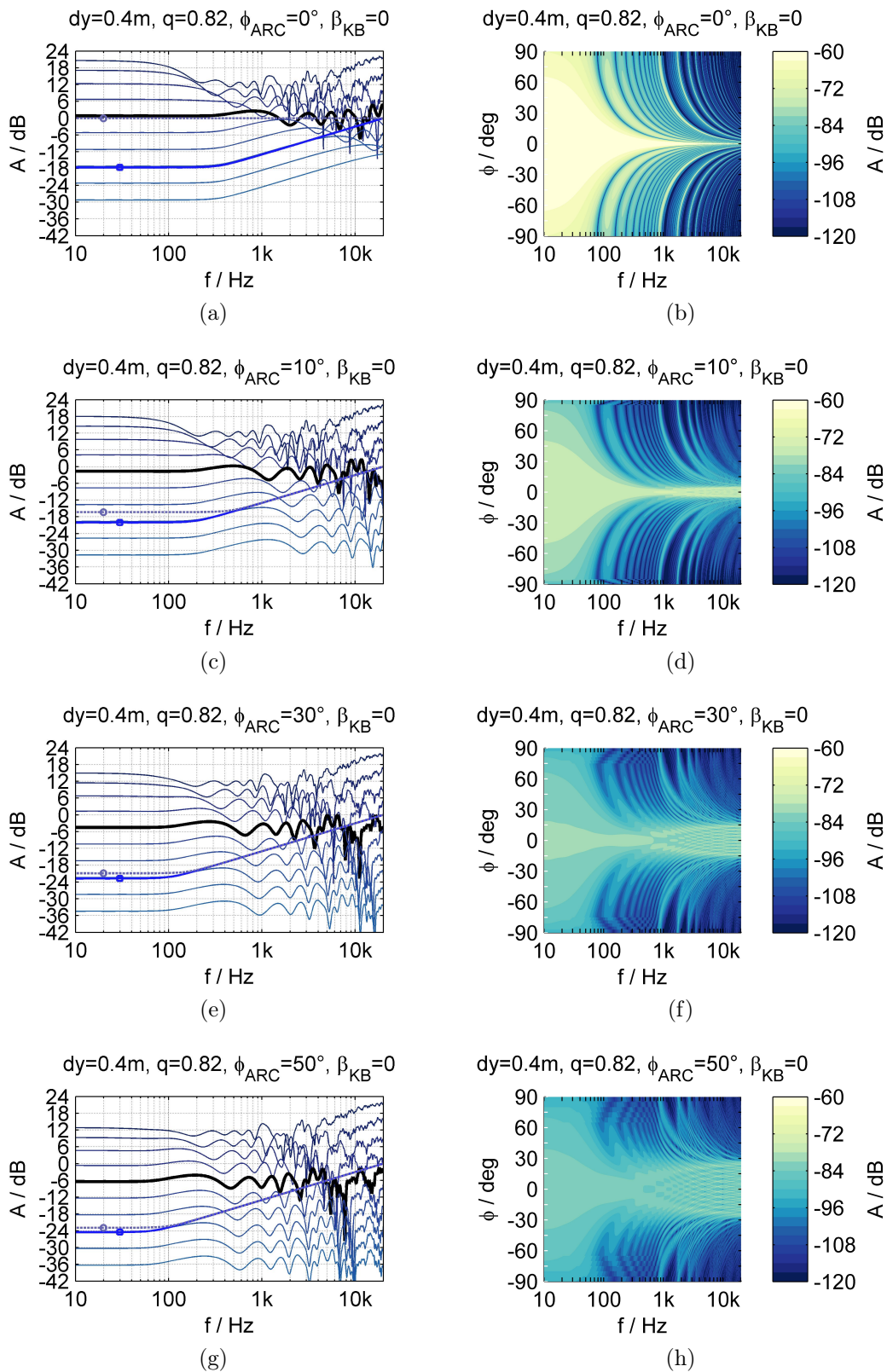


Figure 4.8: Discrete arc array, rectangular window. Left: on-axis pressure for distance doublings starting from $x = 1\text{m}$. Right: FRP for $r = 2^{17}\text{m}$.

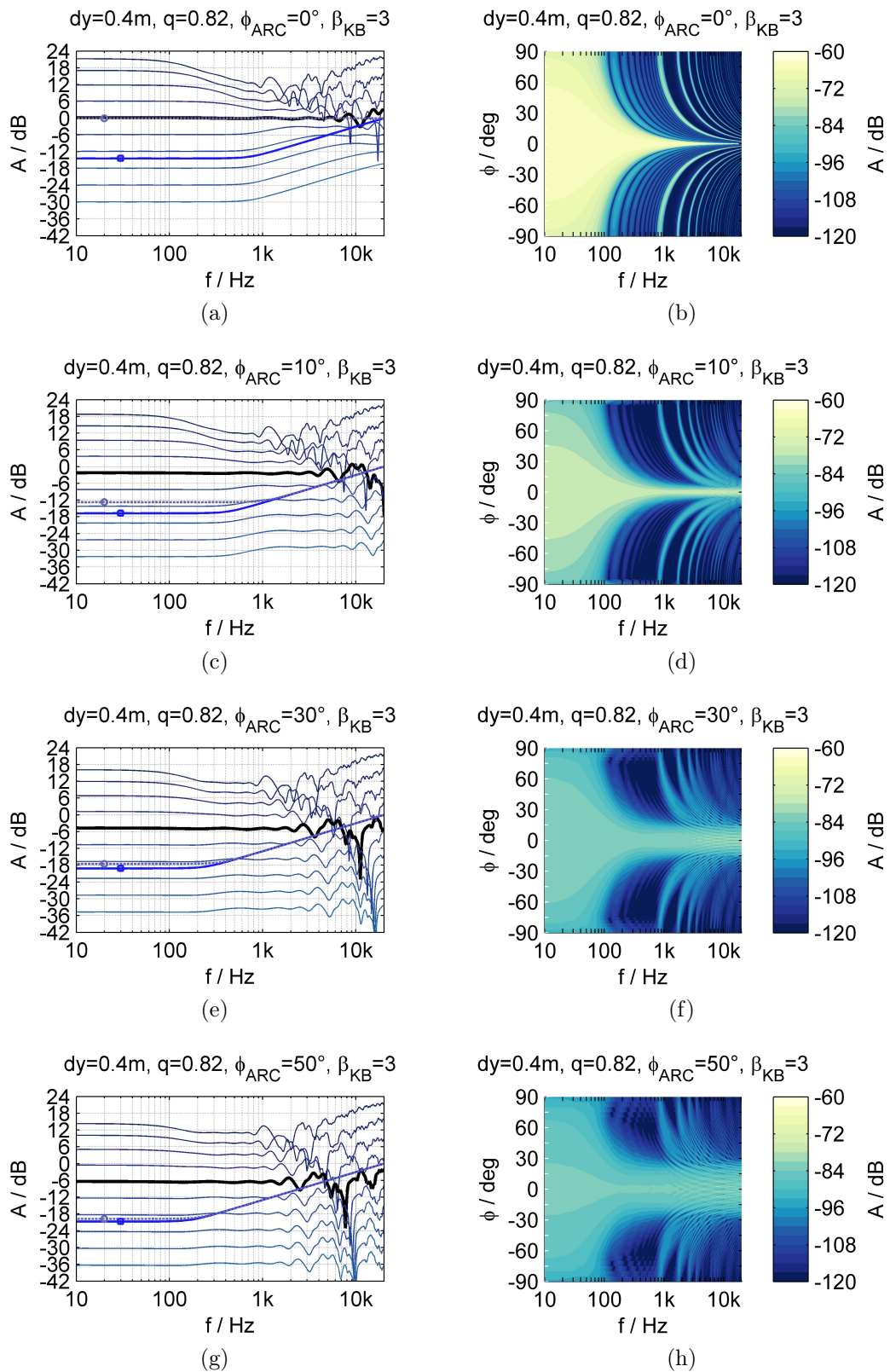


Figure 4.9: Discrete arc array, Kaiser-Bessel window. Left: on-axis pressure for distance doublings starting from $x = 1\text{m}$. Right: FRP for $r = 2^{17}\text{m}$.

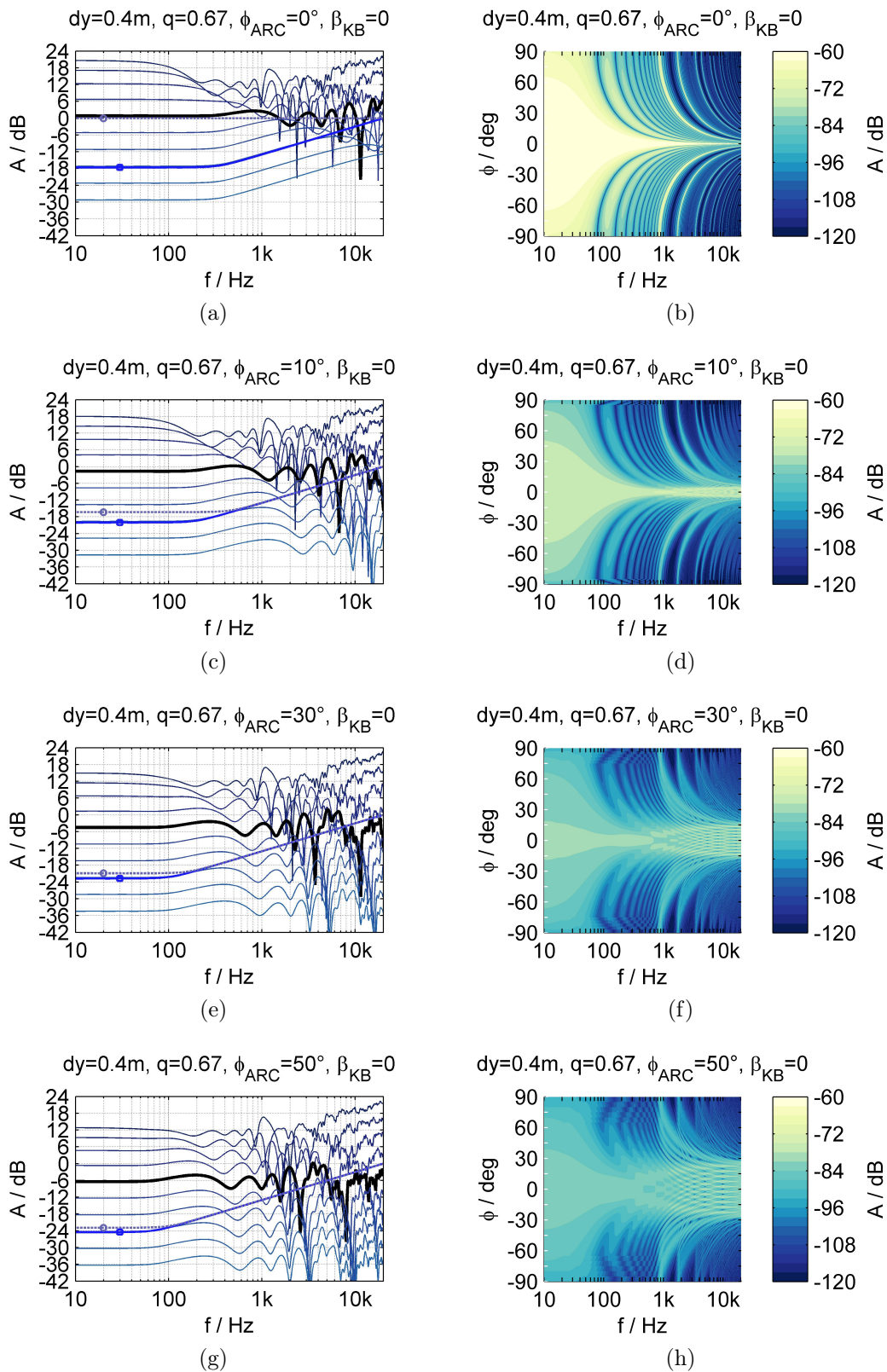


Figure 4.10: Discrete arc array, rectangular window. Left: on-axis pressure for distance doublings starting from $x = 1\text{ m}$. Right: FRP for $r = 2^{17}\text{ m}$.

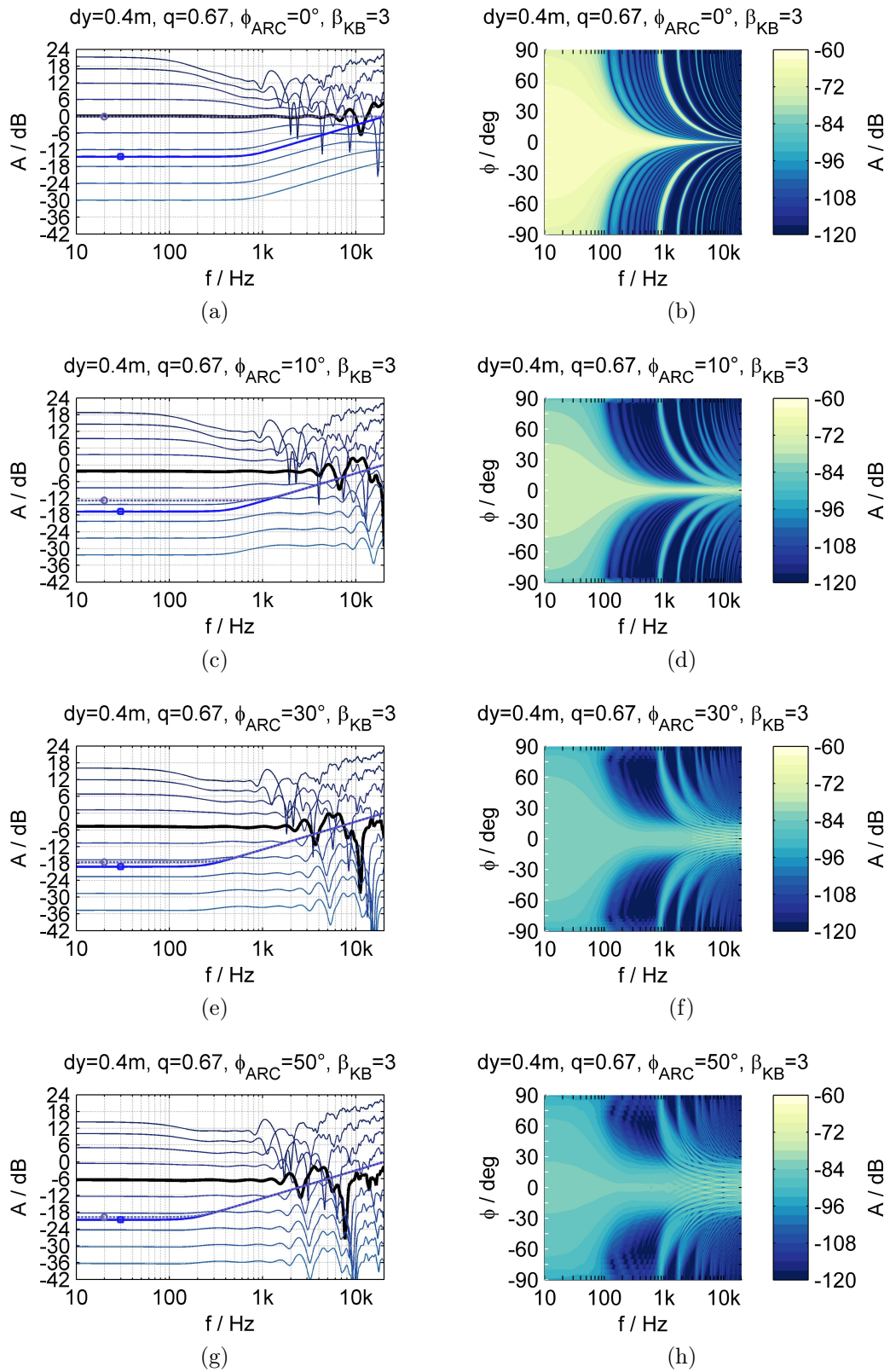


Figure 4.11: Discrete arc array, Kaiser-Bessel window. Left: on-axis pressure for distance doublings starting from $x = 1\text{m}$. Right: FRP for $r = 2^{17}\text{m}$.

4.2 Line Source Array Control and Prediction

Practical LSA setup and control is supervised with sound field prediction software. This is often tied to a specific LSA manufacturer or exhibits manufacturer limited/-specific control possibilities. To further investigate appropriate LSA control techniques within a consistent framework an open-source toolbox for the 2D prediction of sound fields was developed for research purposes. This is termed *Line Source Array Prediction Toolbox* (LSAPT)²

4.2.1 LSA Prediction Kernel

For ease of discussion sound fields in a plane (here again in the xy -plane) are predicted by a complex-directivity point source model using the Kirchhoff diffraction, i.e. the HF-BEM kernel (2.33). As already stated above, this model holds (i) in the farfield of an individual source within an LSA, i.e. a single LSA cabinet, (ii) for $\frac{\omega}{c} r \gg 1$ and (iii) wave lengths that are small compared to the LSA length, (iv) when ignoring diffraction effects between adjacent drivers, (v) not for rearward prediction. However, by deploying baffled piston models for the individual sources in favor of convenient parametrization of LSA setups, this model could be used for LSA control algorithm's prototyping.

The considered geometry is depicted in Fig. 4.12. All used variables are collected in the tables 4.1 and 4.2. For ease of discussion the individual transducers that build an LSA are located in $z = 0$ w.r.t. the piston centers. Typical

²<https://bitbucket.org/fs446/lsapt>, Matlab

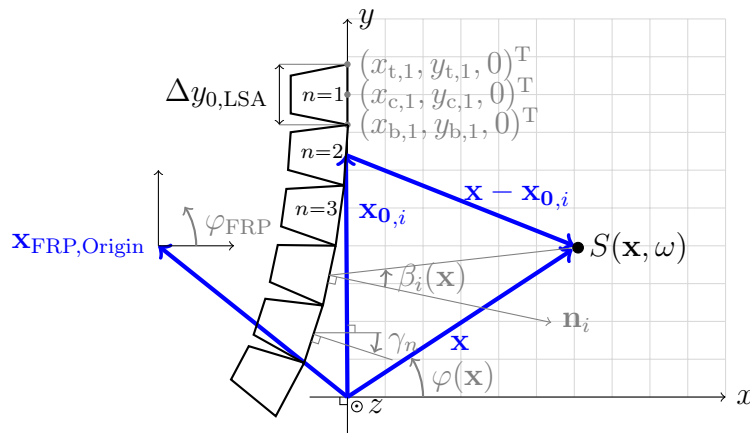


Figure 4.12: Geometry and variables for the LSA setup, cf. [Str15a, Fig. 1].

cabinet designs with z -symmetrical low and mid frequency band transducer setups are not considered. Due to consistent usage of vector algebra the LSAPT could be easily enhanced towards this feature.

Top and bottom front grille position vectors – modeling so called front hinge splaying of the LSA cabinets [Mar03] – are given as [Str15b, (3,4)], [Str15a, (1,2)]

$$\mathbf{x}_{t,n} = \begin{pmatrix} x_{t,n} \\ y_{t,n} \\ 0 \end{pmatrix} = \begin{pmatrix} x_H \\ y_H \\ 0 \end{pmatrix} - \sum_{\mu=1}^{\mu=n-1} \Delta y_{0,\text{LSA}} \begin{pmatrix} \sin \gamma_\mu \\ \cos \gamma_\mu \\ 0 \end{pmatrix}, \quad (4.21)$$

$$\mathbf{x}_{b,n} = \begin{pmatrix} x_{b,n} \\ y_{b,n} \\ 0 \end{pmatrix} = \begin{pmatrix} x_H \\ y_H \\ 0 \end{pmatrix} - \sum_{\mu=1}^{\mu=n} \Delta y_{0,\text{LSA}} \begin{pmatrix} \sin \gamma_\mu \\ \cos \gamma_\mu \\ 0 \end{pmatrix}. \quad (4.22)$$

For all possible $i = (n - 1) \cdot L + l$ using $n = 1, 2, \dots, N$ and $l = 1, 2, \dots, L$ the piston center position of the i -th source is given as [Str15b, (7)], [Str15a, (3)]

$$\mathbf{x}_{0,i} = \begin{pmatrix} x_{0,i} \\ y_{0,i} \\ 0 \end{pmatrix} = \begin{pmatrix} x_{t,n} \\ y_{t,n} \\ 0 \end{pmatrix} + \frac{l - 0.5}{L} \begin{pmatrix} x_{b,n} - x_{t,n} \\ y_{b,n} - y_{t,n} \\ 0 \end{pmatrix} \quad (4.23)$$

and the unit vector of the i -th piston surface as

$$\mathbf{n}_i = \begin{pmatrix} +\cos(-\gamma_n) & -\sin(-\gamma_n) & 0 \\ +\sin(-\gamma_n) & +\cos(-\gamma_n) & 0 \\ 0 & 0 & 1 \end{pmatrix} \cdot \begin{pmatrix} 1 \\ 0 \\ 0 \end{pmatrix}. \quad (4.24)$$

For $L = 1$ follows $\mathbf{x}_{c,n} = \mathbf{x}_{0,i}$ and $\mathbf{n}_n = \mathbf{n}_i$, i.e. the center front grille position of the n -th LSA cabinet and its corresponding unit normal, i.e. its on-axis 'shooting direction' vector. With $\mathbf{x} - \mathbf{x}_{0,i}$ and \mathbf{n}_i the angle

$$\beta_i(\mathbf{x}) = \text{acos} \left(\frac{\langle \mathbf{x} - \mathbf{x}_{0,i}, \mathbf{n}_i \rangle}{|\mathbf{x} - \mathbf{x}_{0,i}|} \right) \quad (4.25)$$

can be calculated based on the scalar product.

The farfield radiation pattern of the circular piston with radius r_0 (D.37)

$$H_{\text{Post,Circ}}(\beta_i(\mathbf{x}), \omega) = \frac{2 J_1\left(\frac{\omega}{c} r_0 \sin(\beta_i(\mathbf{x}))\right)}{\frac{\omega}{c} r_0 \sin(\beta_i(\mathbf{x}))} \quad (4.26)$$

and the farfield radiation pattern of the line piston with length l_0 (D.75)

$$H_{\text{Post,Line}}(\beta_i(\mathbf{x}), \omega) = \frac{\sin\left(\frac{\omega}{c} \frac{l_0}{2} \sin(\beta_i(\mathbf{x}))\right)}{\frac{\omega}{c} \frac{l_0}{2} \sin(\beta_i(\mathbf{x}))} \quad (4.27)$$

are used to model LSA designs with circular pistons in the low frequency (LF) and mid frequency (MF) band and with line pistons in the high frequency band (HF).

The temporal Fourier spectrum of the i -th driving function is given as

$$D_i(\omega) = w_i 4 \pi p_0 x_{\text{ref}} 10^{\left(\frac{\text{Sens}_i}{20}\right)} g_{i,\text{comp}} \frac{\sqrt{P_{i,\text{max}}}}{\sqrt{P_{\text{ref}}}} H(\omega) H_i(\omega) D_{i,\text{LSA}}(\omega). \quad (4.28)$$

The driver sensitivity Sens_i is modeled as a constant per frequency band LF, MF, HF equally for all pistons. Also the applicable power $P_{i,\text{max}}$ is modeled as a frequency independent measure per frequency band LF, MF, HF for all pistons for convenience. The factor $g_{i,\text{comp}}$ (also constant within one frequency band) is used to compensate the different sensitivities of the LF, MF and HF band and adapts the final driving gain in order to achieve the maximum applicable power for a specific LSA control technique. $H(\omega)$ – individually applicable to a certain frequency band – realizes the low/highpass, cross-over filters as well as the shelving prefilter. The application of an individual filter $H_i(\omega)$ for an individual source is not considered here. Typically, air absorption compensation filters can be applied with this filter. The LSAPT ignores air absorption so far, which can however easily be deployed considering the ISO 9613-1/2 and a suitable filter design such as [Pet13]. $D_{i,\text{LSA}}(\omega)$ is the source dependent driving function corresponding to a specific LSA control technique. Additionally, a frequency independent spatial window function w_i can be applied.

With all introduced variables the sound field is predicted by the adapted

HF-BEM kernel (2.33)

$$S(\mathbf{x}, \omega) = \sum_{i=1}^{LN} D_i(\omega) \frac{1 + \cos(\beta_i(\mathbf{x}))}{2} H_{\text{Post}}(\beta_i(\mathbf{x}), \omega) \frac{e^{-j \frac{\omega}{c} |\mathbf{x} - \mathbf{x}_{0,i}|}}{4\pi |\mathbf{x} - \mathbf{x}_{0,i}|}, \quad (4.29)$$

where it is worth realizing that the control variable i might differ for the different frequency bands LF, MF and HF due to a potentially different count of the considered pistons.

j	imaginary unit $j^2 = -1$
c	speed of sound in m/s
f	frequency in Hz
t	time in s
ω	temporal angular frequency in rad/s, $\omega = 2\pi f$
$\Delta y_{0,\text{LSA}}$	front grille's height in m of a single LSA cabinet, constant for all cabinets
$\mathbf{x}_H = (x_H, y_H, 0)^T$	initial front grille top position of LSA cabinet $n = 1$
N	number of LSA cabinets
n	index for n -th LSA cabinet, $1 \leq n \leq N$, top $n = 1$, bottom $n = N$
L	number of individual pistons per LSA cabinet, constant for all cabinets
i	index for i -th piston within LSA, $1 \leq i \leq NL$, top $i = 1$, bottom $i = NL$
$\mathbf{x}_{t,n} = (x_{t,n}, y_{t,n}, 0)^T$	resulting front grille top position of n -th LSA cabinet
$\mathbf{x}_{c,n} = (x_{c,n}, y_{c,n}, 0)^T$	resulting front grille mid position of n -th LSA cabinet
$\mathbf{x}_{b,n} = (x_{b,n}, y_{b,n}, 0)^T$	resulting front grille bottom position of n -th LSA cabinet
γ_n	tilting angle of n -th LSA cabinet w.r.t. the normal vector $(1, 0, 0)^T$, - for upward tilting, + for downward tilting
$\mathbf{x}_{0,i} = (x_{0,i}, y_{0,i}, 0)^T$	position of the i -th piston center, i.e. i -th source origin
$\mathbf{n}_i = (e_{x,i}, e_{y,i}, 0)^T$	normal unit vector to the i -th piston surface
$\beta_i(\mathbf{x})$	angle between normal unit vector \mathbf{n}_i of the i -th piston surface and the vector $\mathbf{x} - \mathbf{x}_{0,i}$ from i -th piston center to evaluation position
$\mathbf{x} = (x, y, 0)^T$	sound field evaluation position

Table 4.1: Geometric and acoustic parameters for the LSA setup in Fig. 4.12.

$D_i(\omega)$	temporal Fourier spectrum of the i -th piston's driving function
$H_{\text{Post}}(\beta_i(\mathbf{x}), \omega)$	spatial lowpass characteristic of the i -th piston, i.e. its farfield radiation pattern over radiation angle and temporal angular frequency
r_0	radius in m of the circular piston
l_0	height in m of the line piston
p_0	reference sound pressure, $20 \mu\text{Pa}$
P_{ref}	1 W
x_{ref}	1 m
$\text{Sens}_i(\omega)$	temporal Fourier spectrum of the i -th piston's sensitivity in $\text{dB}_{\text{SPL}}@1\text{W}, 1\text{m}$
$P_{i,\text{max}}(\omega)$	maximum applicable electric power in W for the i -th source
$H_i(\omega)$	temporal transfer function of an equalization filter for i -th source, not used in the present simulations
$H(\omega)$	temporal transfer function of an equalization filter equally applied to all sources of the LSA in a specific frequency band, i.e. here lowpass $H_{\text{LP}}(\omega)$, highpass $H_{\text{HP}}(\omega)$, cross-over filters $H_{\text{LP,XO}}(\omega)$ and $H_{\text{HP,XO}}(\omega)$, SFS shelving prefilter $H_{\text{LS,FracInt}}(\omega)$
$D_{i,\text{LSA}}(\omega)$	driving function for a specific LSA control method
$S(\mathbf{x}, \omega)$	temporal Fourier spectrum of the sound field at evaluation position \mathbf{x}

Table 4.2: Electro-acoustic parameters for the LSA setup in Fig. 4.12.

$c = 343 \text{ m/s}$
$\Delta y_{0,\text{LSA}} = 0.45 \text{ m}$
$\mathbf{x}_H = (0, 13.5, 0)^T \cdot \text{m}$
$N = 18$
$L_{\text{LF}} = 1, \text{ circular piston}$
$L_{\text{MF}} = 2, \text{ circular piston}$
$r_{0,\text{LF}} = 15/2'' \rightarrow q_{\text{LF}} = \frac{2r_{0,\text{LF}}}{\Delta y_{0,\text{LSA}}/L_{\text{LF}}} = 0.8467$
$r_{0,\text{MF}} = 6.5/2'' \rightarrow q_{\text{MF}} = \frac{2r_{0,\text{MF}}}{\Delta y_{0,\text{LSA}}/L_{\text{MF}}} = 0.7338$
$p_0 = 2 \cdot 10^{-5} \text{ Pa}$
$\text{Sens}_{\text{LF}}(\omega) = 104 \text{ dB}_{\text{SPL}}@1\text{W}, 1\text{m} = \text{const}$ (equivalent to a 2x98 dB design)
$\text{Sens}_{\text{MF}}(\omega) = 104 \text{ dB}_{\text{SPL}}@1\text{W}, 1\text{m} = \text{const}$ (equivalent to a 2x98 dB design)
$\text{Sens}_{\text{HF}}(\omega) = 113 \text{ dB}_{\text{SPL}}@1\text{W}, 1\text{m} = \text{const}$
$P_{\text{LF,max}}(\omega) = 1200 \text{ W} = \text{const}$ (equivalent to a 2x600 W 15" design)
$P_{\text{MF,max}}(\omega) = 300 \text{ W} = \text{const}$ (equivalent to a 2x150 W 6.5" design)
$P_{\text{HF,max}}(\omega) = 75 \text{ W} = \text{const}$
cross-over frequency between LF and MF $f_{\text{XO,LM}} = 350 \text{ Hz}$
cross-over frequency between MF and HF $f_{\text{XO,MH}} = 1.3 \text{ kHz}$
Linkwitz-Riley cross-over $H_{\text{LP,XO}}(\omega)/H_{\text{HP,XO}}(\omega)$ with 120dB/oct. slope [Lin76]
highpass: $H_{\text{HP}}(\omega)$ Butterworth order 6, $f_{\text{HP}} = 68 \text{ Hz}$
lowpass: $H_{\text{LP}}(\omega)$ Butterworth order 6, $f_{\text{LP}} = 13 \text{ kHz}$
equalizing filter for individual sources, constant for all sources $H_i(\omega) = 1$

Table 4.3: Parameters that are held constant for the given simulations of different LSA design studies.

4.2.2 Venue Model

For the simulations a typical open-air amphitheater is considered (resembling the Waldbühne in Berlin that takes up to 23000 attendees³). This venue is modeled by a vertical sectional drawing. It exhibits 4 audience zones, the floor and three stands that can be defined by the lines $\mathbf{x}_{\text{Aud}} = (10, 0, 0)^{\text{T}}$ $\xrightarrow{\text{Floor}}$ $(30, 1.5, 0)^{\text{T}}$ $\xrightarrow{1^{\text{st}}\text{St}}$ $(60, 10, 0)^{\text{T}}$ $\xrightarrow{2^{\text{nd}}\text{St}}$ $(85, 20, 0)^{\text{T}}$ $\xrightarrow{3^{\text{rd}}\text{St}}$ $(110, 30, 0)^{\text{T}}$, setting the stage edge at $x = 0$, cf. Fig. 4.14. Thus, $\mathbf{x}_{m=1} = (10, 0, 0)^{\text{T}}$ and $\mathbf{x}_{m=M} = (110, 30, 0)^{\text{T}}$ is defined. The venue features some demanding characteristics. With an assumed maximum possible rigging height of the top most LSA cabinet of 13.5 m the tilting angle must be about $\gamma_1 = -9^\circ$ ($+9^\circ$ into positive y -axis direction) for WST-like audience coverage yielding a demanding mechanical burden of the rigging hardware. Furthermore, audience distances from 10 m to about 115 m have to be covered.

4.2.3 LSA Model

The LSA is modeled with a typical LF=15"/MF=6.5" three-way cabinet design, cf. Table 4.3. The chosen sensitivities and maximum applicable power ratings are similar to real LSA designs using typical ratings of electro-dynamic loudspeakers and waveguides. The LF and MF band parameters are held constant throughout the simulations. An array with $N = 18$ LSA cabinets is chosen yielding an LSA length of 8.1 m. Note that the resulting mechanical load of about 1.5 – 2 t may not be feasible in the real venue. However, the length was chosen in order that the diffraction model still holds for lower audio frequencies and to better demonstrate the performance of wavefront shaping at the low frequencies. For the HF band either 3 or 15 waveguides per LSA cabinet are deployed resulting in different frequency bandwidths not corrupted by spatial aliasing for electronic beam steering. It is assumed that each individual piston is driven with an individual amplifier and can be individually controlled with an FIR filter. The cross-over, low/highpass filters and the shelving prefilter are realized as linear-phase FIRs in the given simulations, precisely as zero-phase filters, which in practical realizations then can be made linear-phase with an appropriately chosen group delay.

³Special thanks to Thorsten Schulze for sharing details on practical LS-SR applications in this venue.

4.2.4 LSA Control

For (4.28) the required filters are collected for different LSA control techniques. With $H_{\text{LS,HalfInt}}(\omega)$ from (4.13) the zero-phase filters

$$H(\omega) = \begin{cases} |H_{\text{HP}}(\omega) H_{\text{LS,HalfInt}}(\omega) H_{\text{LP}}(\omega) H_{\text{LP,XO}}(\omega)| & \text{for LF band} \\ |H_{\text{HP}}(\omega) H_{\text{LS,HalfInt}}(\omega) H_{\text{LP}}(\omega) H_{\text{LP,XO}}(\omega) H_{\text{HP,XO}}(\omega)| & \text{for MF band} \\ |H_{\text{HP}}(\omega) H_{\text{LS,HalfInt}}(\omega) H_{\text{LP}}(\omega) H_{\text{HP,XO}}(\omega)| & \text{for HF band} \end{cases} \quad (4.30)$$

are applied to realize the lowpass/highpass, the cross-over and the preshelving characteristics for the different frequency bands.

LSA Control with WST

For the uniformly driven LSA, the driver independent prefilter

$$D_{\text{LSA}}(\mathbf{x}_{0,i}, \omega) = \sqrt{\frac{j \frac{\omega}{c}}{2 \pi}} \quad (4.31)$$

is used. For practical realization the FIR design proposed in Ch. 2.5 might be used. The filter

$$H_{\text{coupling}}(\omega) = \sqrt{\frac{j \frac{\omega}{c}}{2 \pi}} H_{\text{LS,HalfInt}}(\omega) \quad (4.32)$$

then realizes the complete prefilter for this LSA control technique, that is typically referred to as the coupling filter in LSA applications. With the above discussed array morphing this coupling filter can be adapted to the length and curvature of the LSA.

LSA Control with WFS

At the beginning of this chapter it was proposed to use WFS as a straightforward control method for wavefront shaping. Among other things, this can be realized with a non-focused point source with additional directivity, that was already introduced in literature, e.g. [Jac05, Cor07, Fra12, Rom15]. The WFS driving function (2.137) of a non-focused, directed point source for a reference

point reads [Cor07, (10)], [Rom15, (4)]

$$D_{\text{LSA}}(\mathbf{x}_{0,i}, \mathbf{x}_{\text{Ref}}, \omega) = \sqrt{\frac{j\omega}{2\pi c}} \sqrt{\frac{|\mathbf{x}_{\text{Ref}} - \mathbf{x}_{0,i}|}{|\mathbf{x}_{0,i} - \mathbf{x}_{\text{PS}}| + |\mathbf{x}_{\text{Ref}} - \mathbf{x}_{0,i}|}} \times \frac{\langle \mathbf{x}_{0,i} - \mathbf{x}_{\text{PS}}, \mathbf{n}(\mathbf{x}_{0,i}) \rangle}{|\mathbf{x}_{0,i} - \mathbf{x}_{\text{PS}}|} \frac{e^{-j\frac{\omega}{c}|\mathbf{x}_{0,i} - \mathbf{x}_{\text{PS}}|}}{\sqrt{|\mathbf{x}_{0,i} - \mathbf{x}_{\text{PS}}|}} \cdot g(\mathbf{x}_{0,i}), \quad (4.33)$$

with the gain factor $g(\mathbf{x}_{0,i})$ realizing the farfield directivity of the virtual point source. While recent literature discussed simple model-based directivities (such as from spherical harmonics modes [Jac05, Cor07] or baffled piston FRPs [Rom08, Rom15]) homogeneous LS-SR requires a specially adapted FRP for the virtual point source to obtain the desired wavefront shaping, which was not yet considered in the literature and is introduced here.

Herein, it is proposed to calculate a reference FRP pattern w.r.t. a chosen reference point \mathbf{x}_{Ref} . The distance ratio between $|\mathbf{x}_{\text{Ref}} - \mathbf{x}_{\text{PS}}|$ and any other audience location $|\mathbf{x} - \mathbf{x}_{\text{PS}}|$ can be expressed in terms of a dB gain/attenuation term

$$H_{\text{PS,FRP}}(\varphi_{\mathbf{x}}) = DD_{\text{dB}} \cdot \log_{10} \left(\frac{|\mathbf{x}_{\text{Ref}} - \mathbf{x}_{\text{PS}}|}{|\mathbf{x} - \mathbf{x}_{\text{PS}}|} \right), \quad (4.34)$$

where the factor DD_{dB} controls the effective SPL loss over the audience if \mathbf{x}_{Ref} is an audience position. For $DD_{\text{dB}} = -20$ no SPL loss over the whole audience is obtained, $DD_{\text{dB}} = -10$ realizes a -3 dB SPL loss w.r.t. the considered distance ratio, whereas $DD_{\text{dB}} = 0$ defines an omnidirectional pattern within the given spatial region. Any other suitable 'distance ratio to dB mapping' can be easily adapted (cf. the *array processing* tool of *déjà audiotchnik's ArrayCalc* prediction software). The corresponding radiation angle $\varphi_{\mathbf{x}}$ is given as

$$\varphi_{\mathbf{x}} = \arccos \left(\left\langle \frac{\mathbf{x} - \mathbf{x}_{\text{PS}}}{|\mathbf{x} - \mathbf{x}_{\text{PS}}|}, (1, 0, 0)^{\text{T}} \right\rangle \right) \cdot \begin{cases} (-1) & \text{if } \langle (0, 0, 1)^{\text{T}}, \frac{\mathbf{x} - \mathbf{x}_{\text{PS}}}{|\mathbf{x} - \mathbf{x}_{\text{PS}}|} \times (1, 0, 0)^{\text{T}} \rangle > 0 \\ (+1) & \text{else} \end{cases}, \quad (4.35)$$

w.r.t. the reference direction into x -axis. For typical LSA/venue setups $\varphi_{\mathbf{x}}$ exhibits a certain range, very roughly within $|\varphi_{\mathbf{x}}| < 30^\circ$.

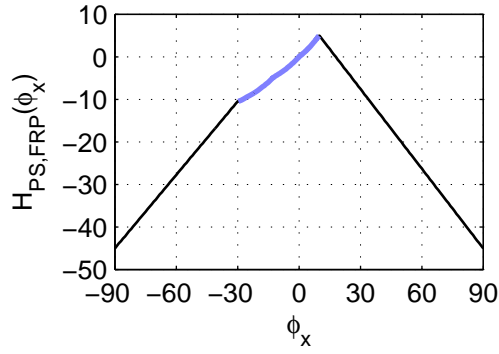


Figure 4.13: Example of a farfield radiation pattern for a virtual, directed non-focused point source, cf. [Gun03c, Fig. 15].

The FRP $H_{PS,FRP}(\varphi_{\mathbf{x}})$ and the angles $\varphi_{\mathbf{x}}$ are then expanded to a $-90^\circ < \varphi_{\mathbf{x}} < +90^\circ$ representation. For that the FRP is simply continued with a linear level loss (dB over degree) from the maximum $\varphi_{\mathbf{x}}$ towards $\varphi_{\mathbf{x}} = +90^\circ$ and from the minimum $\varphi_{\mathbf{x}}$ towards $\varphi_{\mathbf{x}} = -90^\circ$ respectively. The maximum attenuation of the FRP is defined at $H_{PS,FRP,\min}(\varphi_{\mathbf{x}} = \pm 90^\circ) = H_{PS,FRP,\max}(\varphi_{\mathbf{x}}) + A_{\min,\text{dB}}$; in the simulations $A_{\min,\text{dB}} = -100$ was chosen. In Fig. 4.13 an example is given originating from the later discussed LSA design study #7. For convenient visualization only the parameter $A_{\min,\text{dB}} = -50$ is changed here. No SPL loss over the audience is setup with $DD_{\text{dB}} = -20$ leading to a required high level for very far audience positions ($H_{PS,FRP}(\varphi_{\mathbf{x}} = +10^\circ) = 5$ dB) and required low level near the array ($H_{PS,FRP}(\varphi_{\mathbf{x}} = -30^\circ) = -10$ dB) for the chosen \mathbf{x}_{PS} and \mathbf{x}_{Ref} , cf. the blue line. The FRP is then completed with the lines towards $H_{PS,FRP}(\varphi_{\mathbf{x}} = \pm 90^\circ) \approx -45$ dB, cf. the black lines. Note that a dense sampling of the audience region is required to obtain a valid series for $H_{PS,FRP}(\varphi_{\mathbf{x}})$ and $\varphi_{\mathbf{x}}$.

The gain factor $g(\mathbf{x}_{0,i})$ within the WFS driving function requires the knowledge of the FRP's gain w.r.t. the secondary source position's angle

$$\varphi_{\mathbf{x}_{0,i}} = \text{acos} \left(\left\langle \frac{\mathbf{x}_{0,i} - \mathbf{x}_{\text{PS}}}{|\mathbf{x}_{0,i} - \mathbf{x}_{\text{PS}}|}, (1, 0, 0)^T \right\rangle \right).$$

$$\begin{cases} (-1) & \text{if } \langle (0, 0, 1)^T, \frac{\mathbf{x}_{0,i} - \mathbf{x}_{\text{PS}}}{|\mathbf{x}_{0,i} - \mathbf{x}_{\text{PS}}|} \times (1, 0, 0)^T \rangle > 0 \\ (+1) & \text{else} \end{cases}. \quad (4.36)$$

Since, $\varphi_{\mathbf{x}_{0,i}}$ and $\varphi_{\mathbf{x}}$ typically not coincide, a interpolation is performed. Using $H_{\text{PS,FRP}}(\varphi_{\mathbf{x}})$ in dB and $\varphi_{\mathbf{x}}/\varphi_{\mathbf{x}_{0,i}}$ in degrees a cubic spline interpolation yields $H_{\text{PS,FRP}}(\varphi_{\mathbf{x}_{0,i}})$. The corresponding linear gain factor

$$g(\mathbf{x}_{0,i}) = 10^{\left(\frac{H_{\text{PS,FRP}}(\varphi_{\mathbf{x}_{0,i}})}{20}\right)} \quad (4.37)$$

is then applied in $D_{\text{WFS}}(\mathbf{x}_{0,i}, \mathbf{x}_{\text{Ref}}, \omega)$ (4.33) to realize the directed point source.

An appropriate virtual point source location has to be defined for this approach. For SFS of a virtual point source using finite length linear arrays, the limited listener region can be roughly estimated by means of a geometric approximation [Spo09, Sec. 4.2], [Rom15, Sec. 2.1], which holds for smaller wave lengths than the array dimension. In simulations it turned out that the theoretical point source position \mathbf{x}_{PS} defined by the intersection of the two lines (cf. Fig. 4.12)

$$\mathbf{x}_{m=1} - \mathbf{x}_{0,i=L N} \quad \mathbf{x}_{m=M} - \mathbf{x}_{0,i=1}, \quad (4.38)$$

(i.e. from a vector that starts from the nearest audience point to the bottom-most LSA source and from a vector that starts from the farthest audience point to the topmost LSA source) is not the optimum choice for the application under discussion. So far, no analytical solution for the optimum location could be derived. However, the simulations revealed that an appropriate point source position is located within the area that is spanned by the LSA and the theoretical point source position behind the LSA. The point source on the one hand should not be too far away from the LSA to avoid a plane wave like wavefront curvature and on the other hand not too close to the LSA to avoid a point source like wavefront curvature. In both cases a proper wavefront shaping with the desired FRP of the virtual source is not possible. The position of \mathbf{x}_{PS} was eventually determined by trial and error for the intended performance of the LSA design study #5 and then held constant throughout other design studies.

4.3 Visualization and Quality Measures

In [Str15a] we proposed visualization methods and quality measures for convenient and in-depth interpretation of the sound fields synthesized by LSAs. Some of them are deployed as well in this thesis. Note that no avoid zone is defined here for the open-air situation under discussion. The simulations are evaluated by the following visualizations:

- **PIP**, position index plot, SPL over frequency f and audience positions m
- **FAP**, frequency responses (magnitude) of all audience positions, SPL over frequency f
- **IAP**, impulse responses of all audience positions, normalized peak level over time t
- **FRP**, farfield radiation pattern, SPL over frequency f and radiation angle φ_{FRP}
- **SPL_{xy}**, SPL over xy -plane for individual frequencies f
- **DFIP**, driving function index plot, magnitude/group delay of the driving functions $D_i(\omega)$ over frequency f and driver index i

The FAP and IAP constitute the ATF and AIR for the audience positions. Since WFS applies constant group delays, i.e. pure delays to the individual drivers, the DFIP is given as a single delay plot over driver index i . Note that in this plot the travel time of the virtual point source towards the LSA is compensated (minimum delay is thus 0 s, just like one would implement the FIRs in practical realizations), whereas in the IAP it is preserved for convenient interpretation. The frequency resolution is set to 1 Hz. The audience positions are equally discretized such that two adjacent positions exhibit a distance of 1 m, in total 107 audience positions are evaluated. The FRP is evaluated with 1° resolution using the origin point in the middle of and behind the array

$$\mathbf{x}_{\text{FRP,Origin}} = \mathbf{x}_{0,i=1} - \frac{\mathbf{x}_{0,i=1} - \mathbf{x}_{0,i=LN}}{2} \quad (4.39)$$

for \mathbf{x}_0 of the HF band and again a huge radius of 2^{14} m. Its visualization is then performed with no normalization, but rather adapting the SPL to a distance of 16 m by the $\frac{1}{r}$ -law, which of course only holds if the farfield condition holds. The IAP is given only for 11 positions throughout the venue for convenient visualization, depicted blue in Fig. 4.14 and normalized to the highest occurring peak of all 11 impulse responses. They are chosen such that by starting at $\mathbf{x} = (10, 0, 0)^T$ each subsequent AIR exhibits exactly a 30 ms offset, when the LSA is controlled with the virtual point source. Additionally the last AIR is evaluated at the last audience position $\mathbf{x} = (110, 30, 0)^T$. Note that for uniformly driven arrays the AIRs arrive earlier since no delay is used and the AIR offsets may differ (but only very slightly) due to the different time alignment of this LSA control technique.

Furthermore, some distribution measures should help for a convenient interpretation of the simulations. The first two of them are defined as, cf. [Str15a, (20&21)]

$$LB1(\omega) = \mathcal{Q}_q \underset{i}{[20 \log_{10}(|D_i(\omega)|)]} \quad (4.40)$$

$$LB2_i = \mathcal{Q}_q \underset{\omega}{[20 \log_{10}(|D_i(\omega)|)]} \quad (4.41)$$

using the operator $\mathcal{Q}_q[\cdot]$ to calculate the $q = \{0.05, 0.25, 0.50, 0.75, 0.95, 1\}$ quantiles either over an individual driver i in case of $LB1(\omega)$ or over the frequency ω (considering the pass band of the specific driver) in case of $LB2_i$. These measures provide a convenient overview of the load balancing of the drivers either w.r.t. to frequency or w.r.t. an individual driver. A further quality measure for the obtained SPL distribution per audience position m is calculated as

$$L_{p,\text{aud},m} = \mathcal{Q}_q \underset{\omega}{\left[20 \log_{10} \left(\frac{S(\mathbf{x}_m, \omega)}{p_0} \right) \right]}. \quad (4.42)$$

For the given simulations the frequency range $200 \text{ Hz} < f < 5 \text{ kHz}$ is used considering this as the most important frequency bandwidth for LS-SR, precluding the highest audio frequencies where potential spatial aliasing would have severe impact on this measure. This then provides a very convenient overview for the SPL loss over the audience as well as the frequency response

variation over the audience in terms of the considered quantiles.

4.4 Simulations

Since the degree of freedom for changing variables in the LSAPT is numerous, eight LSA design studies are chosen that should highlight the most important aspects for discussing and linking WST and WFS control techniques.

The presented graphics are rendered with LSAPT Tag 'v0.06' and 'v0.07'⁴. Besides variables that are held constant in general being listed in Table 4.3, the following parameters do not change for certain design cases:

- $L_{\text{HF}} = 3$ for LSA designs 1-4, $L_{\text{HF}} = 15$ for LSA designs 5-8
- $q_{\text{HF}} = 0.847$ for LSA designs 1 & 4-8, $q_{\text{HF}} = 1$ for LSA designs 2 & 3
- tilt angle & splaying angles are held constant for LSA designs 3-7 realizing a progressively curved LSA [Ure04], tilt angle & splaying angles are equal for LSA designs 1 & 8 realizing a straight LSA
- $\mathbf{x}_{\text{PS}} = \text{const}$ for LSA designs 5-8
- $A_{\text{min,dB}} = \text{const}$ for LSA designs 5-8

All design cases are visualized with the same figure style. The first figure shows the LSA and venue setup and – additionally for WFS controlled LSAs – the FRP of the virtual point source as well as the applied delays. Below this figure the varied parameters used for the specific design study are given. The second figure is related to the driving functions giving the DFIPs and distribution measures $LB1(\omega)$ and $LB2_i$, additionally indicating the maximum applicable as well as the actually required maximum power load of the drivers. The third figure shows the FRP, the PIP, the FAP and the IAP as well as the SPL distribution measure $L_{p,\text{aud},m}$. The fourth and last figure per LSA design study shows the SPL within the xy -plane for individual frequencies.

While the first four LSA designs are controlled merely by gain shading (windowing) and curving, the LSA designs 5-8 are controlled with the proposed WFS approach.

⁴<https://bitbucket.org/fs446/lsapt/commits/tag/v0.06>

LSA Design 1

The LSA is fixed straightly using an $\text{ARF}_{\text{HF}} = q_{\text{HF}} = 0.847$ with 3 line pistons per LSA cabinet and a rectangular window. The radiation characteristic can thus be directly interpreted with the results of Ch. 3. The HF band exhibits the maximum power load. $LB1(\omega)$ exhibits no distribution at all, indicating that all drivers are equally driven. From $LB1(\omega)$ the prefilter and crossover characteristics as well the sensitivity difference of the different frequency bands can be easily determined. All quantiles of $LB2_i$ are lines due to the equally driven pistons indicating a distribution due to the applied low/highpass, pre- and crossover filters only. The FRP indicates the highly directed main lobe beam for $f > 500$ Hz, as well as the expected side lobes (due to the rectangular window) and grating lobes in the HF band (due to the ARF as discussed in Ch. 3). The main lobe covers only the audience positions 40-60 for $f > 500$ Hz with very high SPL about 120 dB, whereas the positions 1-40 and 60-107 are mostly covered from down-/upward beaming grating lobes. This can be seen in the PIP and is affirmed by the IAP and $L_{p,\text{aud},m}$. The IAPs at the first four evaluation positions are severely corrupted from spatial aliasing, whereas the IAPs at positions 5 and 6 within the main lobe beam exhibit the best impulsiveness and thus the most flat frequency responses with highest SPL. The $L_{p,\text{aud},m}$ exhibits a large variation of the quantiles for the audience positions that are covered by the main lobe beam due to the highly frequency dependent near-/farfield transition of this straight LSA. Even more variation is observed for audience position very near and very far to the array where mostly spatial aliasing contributes to the achieved FAP. In the SPL plot the frequency dependent near-/farfield transition as well as the side and grating lobes can be studied for individual frequencies. Obviously, this LSA design and control method does not lead to a desired, homogeneous LS-SR of the audience.

LSA Design 2

The arc array with 2.5° splaying angles between the LSA cabinets exhibits an $\text{ARF}_{\text{HF}} = q_{\text{HF}} = 1$ with 3 line pistons per LSA cabinet and a Kaiser-Bessel windowing with $\beta = 3$. Thus, an arc angle $\alpha_{\text{Arc}} = 17 \cdot 2.5^\circ = 42.5^\circ$ is realized. The arc curving together with windowing resembles a CBT array.

The HF band exhibits the maximum power load. $LB1(\omega)$ indicates that gain shading occurs since the quantiles are just offset to each other showing again the prefilter and crossover characteristics as well the sensitivity difference of the different frequency bands. In comparison to design study 1, the lower cutoff frequency f_c of the preshelling filter is clearly visible. From $LB2_i$ the applied window can be extracted. The FRP shows the broadened main lobe beam that approximately matches the arc angle for $f > 300$ Hz. Side lobe levels are reduced by windowing. Due to rather small splaying angles and no gaps between waveguides no significant grating lobes occur. The PIP and $L_{p,aud,m}$ indicate a very homogeneous audience coverage with little frequency response variation and a rather large SPL loss rate throughout the audience. This is confirmed with the IAP showing very similar impulse response characteristics except that one very near to the array. The homogeneous PIP and IAP is a result of the windowed arc array. Similar results were reported recently for the exact CBT array in [Kee15]. The SPL plot within the xy -plane shows almost frequency independent main lobe beams. For the frequencies in the HF band some rippling in the beams is observed due to the waveguides' directivity. Thus, even for a waveguide spacing without gaps realized here, the splaying of ideal line pistons introduces artifacts that might be overcome by another postfilter characteristic.

The homogeneous audience coverage comes with the price of a high SPL loss for very far audience positions which might be undesired. Thus, other curving and control methods could be more suitable.

LSA Design 3

The curving of the LSA is adapted to the venue with progressively increased splaying angles between the LSA cabinets realizing a so called progressive source with terminal angle of 38° [Ure04]. As for study 2 an $ARF_{HF} = q_{HF} = 1$ with 3 line pistons per LSA cabinet holds here using a Kaiser-Bessel windowing with $\beta = 2$. The DFIPs and $LB1(\omega)$ and $LB2_i$ look similar to case 2, however more electric power is used due to less windowing. The FRP indicates the adapted wavefront shaping producing high SPLs for far throw and comparable low SPL for near throw to compensate the propagating distances. By doing so, the first 20 audience positions are covered with SPL loss smaller than 3 dB with ripples not more than 3 dB in the frequency response variation. The

positions 20-60 are covered with almost no SPL loss and very small frequency response variation. From position 60 to the last audience position a SPL loss of 9 dB occurs with rather high frequency response variations. This is the price of windowing the LSA and thereby reducing side lobes to provide a more homogeneous coverage in the middle audience positions. The PIP reveals the typical problem of homogeneous coverage of the lowest audio frequencies: for very near audience positions the SPL is too high whereas for very far audience positions the SPL is too low compared to higher frequencies. The SPL over xy -plane shows similar beams for frequencies $f > 500$ Hz that are adapted such that an isobar curve approximately coincides with the audience from positions 1 to 80.

LSA Design 4

The design 4 is identical to the third design except changing the $\text{ARF}_{\text{HF}} = q_{\text{HF}} = 0.847$, i.e. allowing gaps between the line pistons. This introduces grating lobes into the FRP that smear into the main lobe for frequencies $f > 3$ kHz. The frequency responses are then corrupted by spatial aliasing, clearly seen in the FAP, IAP and the PIP. This also yields a larger distribution of the frequency responses in $L_{p,\text{aud},m}$ for very near audience positions. It is worth reminding that $L_{p,\text{aud},m}$ is evaluated only within the frequency range $200 \text{ Hz} < f < 5 \text{ kHz}$ and thus not considers spatial aliasing above 5 kHz. The grating lobe beams are visible in the SPL_{xy} plots that affect the smoothness of the isobars w.r.t. the desired main beam. The audience coverage is thus less homogeneous as for the LSA design study 3.

LSA Design 5

The curving of the LSA is identical to the designs 3 and 4. Now the LSA is controlled with WFS and thus uses more HF drivers per LSA cabinet to shift spatial aliasing to high frequencies. The size of one HF waveguide is 1", similar to some commercially available LSA designs. For all WFS controlled LSAs the maximum power load is now observed in the MF band. The virtual point source directivity (4.34) is defined with $DD_{\text{dB}} = -10$ yielding a -3 dB SPL loss per doubling the distance $|\mathbf{x}_m - \mathbf{x}_{\text{PS}}|$. The theoretical SPL range from the first to the last audience position amounts to 7.8 dB that can be observed in the virtual point source's FRP Fig. 4.30b. The applied delay ranges from 0

ms to about 1.25 ms. The shape of the virtual point source's FRP is mapped to the DFIPs. The FRP shows a grating lobe beginning at 10 kHz that smears into the main lobe. A second grating lobe starts to evolve in the end of the MF band due to the chosen 6.5" drivers and the cross-over frequency of 1.3 kHz, which however not smears into the main lobe. The PIP and $L_{p,aud,m}$ show the intended -3 dB SPL loss per $|\mathbf{x}_m - \mathbf{x}_{PS}|$ doubling and a very homogeneous audience coverage. Only the frequency responses and impulse responses of very near audience positions are corrupted with spatial aliasing, seen in the FAP and IAP. The main lobe beams shown in the SPL_{xy} plot are similar for frequencies $f > 500$ kHz and comparable to the design case 3, here with more homogeneity. However, for very low frequencies, cf. 125 Hz the beam control is not able to reduce the coverage only to the audience, but rather high SPL is radiated into air.

LSA Design 6

For this LSA design study the same progressive curving as for studies 3-5 is used. The waveguide size is again 1". With $DD_{dB} = 0$ a virtual point source FRP of constant directivity over a certain spatial region is realized, cf. Fig. 4.34b. This yields CBT-like radiation characteristic, with an approximately constant main lobe beamwidth of about 45° for frequencies $f > 500$ Hz. In the HF band, one grating lobe smears into the main lobe at the highest audio frequencies. The PIP and FAP indicate homogeneous audience coverage. From $L_{p,aud,m}$ the SPL loss of about 15 dB over the audience with very few frequency response variation can be extracted. Except for the very near audience positions the IAP shows very similar impulse responses over the audience only varying in their peaks due to the SPL loss. For the very near audience positions spatial aliasing corrupts the impulse responses. Again, as for design study 2 the high SPL loss over audience might not be a suitable choice in this large venue.

LSA Design 7

The same LSA setup as for study 5 is used, here with $DD_{dB} = -20$ intending no SPL loss for the audience coverage. This implies 5 dB more level and 10 dB less level for the very far and very near audience positions, respectively w.r.t. to the reference position \mathbf{x}_{Ref} in the virtual point source's FRP Fig. 4.38b,

cf. also Fig. 4.13. This is also observable in the resulting FRP that indicates the adapted beam for the intended wavefront shaping. The PIP and FAP are homogeneous and show the intended audience coverage without any SPL loss. Only for the very low frequencies larger variations occur. Here, the array is too short to realize this demanding wavefront shaping. The very near audience positions suffer from spatial aliasing, here more than for the LSA design studies 5 and 6, cf. the IAP. This is due to the fact that the required high levels for the far throw are mapped (and not strictly postfiltered) as spectral repetitions into the array's visible near throw region with comparable larger level than for the other two designs. The SPL_{xy} plots show almost frequency independent beams again for $f > 500$ Hz, where the 106 dB_{SPL} contour line exactly coincides for most audience positions yielding the constant SPL coverage. For the very far audience positions a 3 dB SPL loss is obtained using this setup. Note that this approach produces a slight overshoot over the venue, which could be optimized with an improved virtual source's FRP design and interpolation method.

LSA Design 8

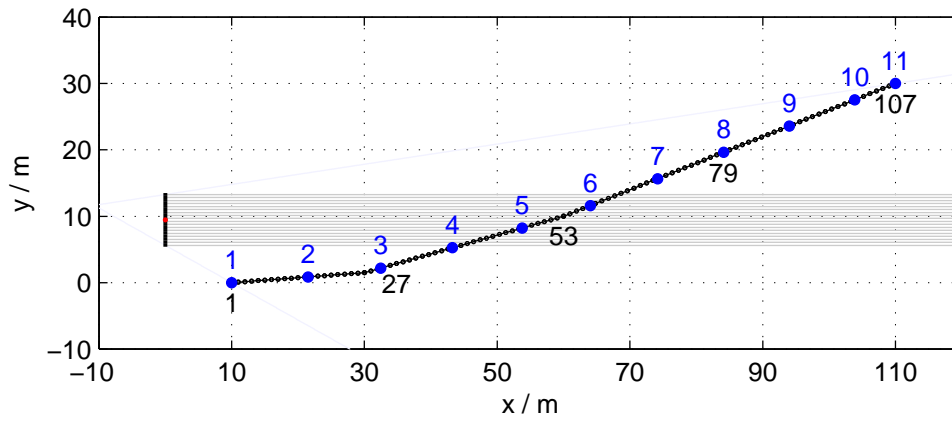
To demonstrate that the wavefront shaping with WFS is – within the limits of the LSA's radiation capabilities (grating lobe occurrence, spatial coverage of the waveguides) – rather a result of synthesizing the virtual source, than of curving the array the last LSA design study uses exactly the same parameters as study 7 only changing the LSA's geometric shape to a straight one. This yields a different $D_{\text{LSA}}(\mathbf{x}_{0,i}, \mathbf{x}_{\text{Ref}}, \omega)$. As a result, the intended main beam in the FRP is equal to the curved array design, however an MF band grating lobe evolves and the HF grating lobe is shifted towards lower frequencies producing slightly more spatial aliasing, cf. the right, bottom border of the PIP and the AIRs of the first audience positions. Besides that the PIP, FAP, IAP and $L_{p,\text{aud},m}$ are similar to the curved array design 7. At 8 kHz and 10 kHz the occurring grating lobes are clearly visible in the SPL_{xy} plot. The down-steered grating lobes corrupt the frequency responses of the very near audience positions. Note that the up-steered grating lobe would be reflected by the ceiling when considering indoor venues.

For this straight array the interpretation of the spatio-temporal Fourier spectra of the driving functions $D_{w,S}(k_y, \omega)$ and $D_{w,S,H}(k_y, \omega)$ can be performed as discussed in Ch. 3, providing the link to the WST criteria for straight ar-

rays. In Fig. 4.46 – visualizing $D_{w,S}(k_y, \omega)$ for the different frequency bands – the base band and the spectral repetitions for the discretized array are shown. It can be seen that spectral repetitions enter the visible region in the MF and HF band. In the HF band the already discussed 'far throw to near throw' aliasing mapping as well as the 'near throw to far throw' aliasing mapping can be observed starting at about 8 kHz. Furthermore, the smearing of the spectral repetitions into the baseband starting at about 13 kHz is revealed. The postfilter characteristic of the circular piston for the MF band and of the line piston for the HF band reduce the level of the spectral repetitions, cf. Fig. 4.47 visualizing the FRP $D_{w,S,H}(k_y, \omega)$.

Note that changing the $\text{ARF}_{\text{HF}} = q_{\text{HF}} = 1$ slightly improves this, but cannot completely suppress all repetitions, since the sinc postfilter of the line piston only perfectly reconstructs the broadband plane wave using a rectangular windowed array, cf. Ch. 3.3. To suppress all propagating spatial aliasing in the case of arbitrary wavefront shaping with full audio bandwidth the spatial sampling condition should hold.

The comparison of design study 7 and 8 confirms the observations of [Sch92, Sta96]: using directed sources and array curving towards the audience that is to be covered, slightly increases the spatial aliasing cutoff frequency compared to a straight array.



(a) LSA and venue setup.

Figure 4.14: LSA_K1_Design1: Setup.

LSA_K1_Design1: Uniformly driven, $L_{\text{HF}} = 3$, $q_{\text{HF}} = 0.847$, $l_{0,\text{HF}} = 5.000''$, tilt angle & splay angles: $+0.00^\circ$, $\beta_{\text{KB}} = 0.0$, $f_c = 250$ Hz, $\mathbf{x}_{\text{FRP,Origin}} = (0.000, 9.450, 0)^\text{T}$,

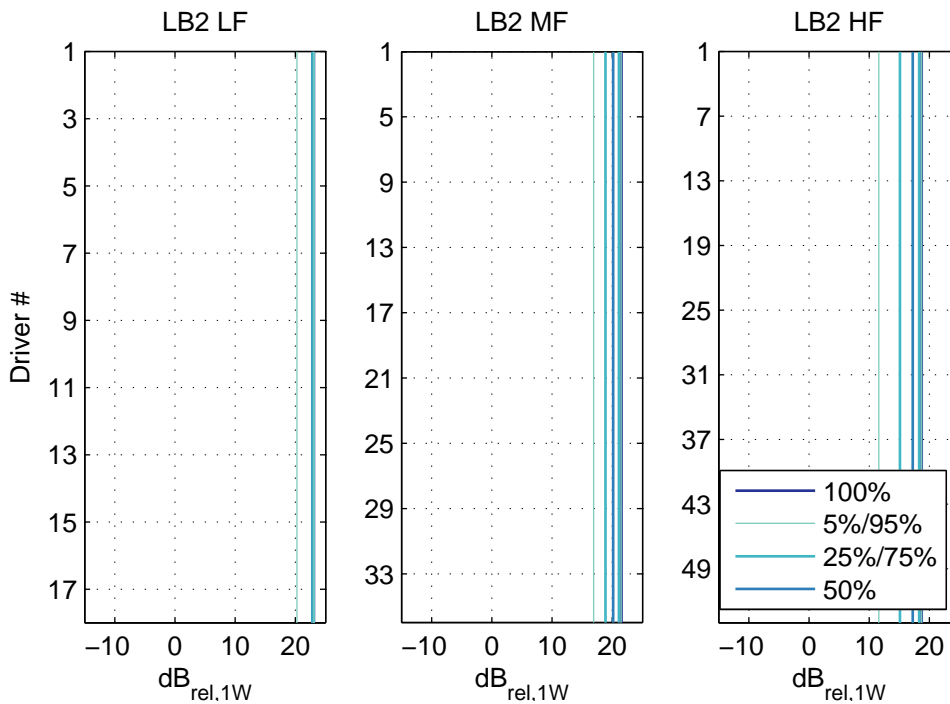
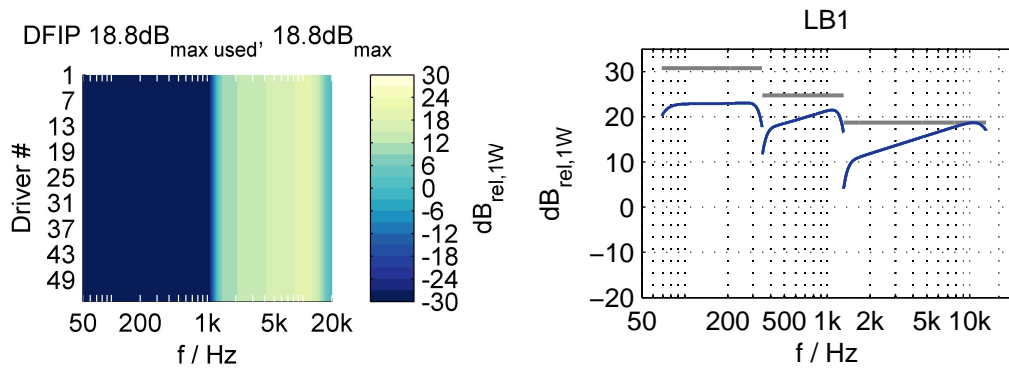
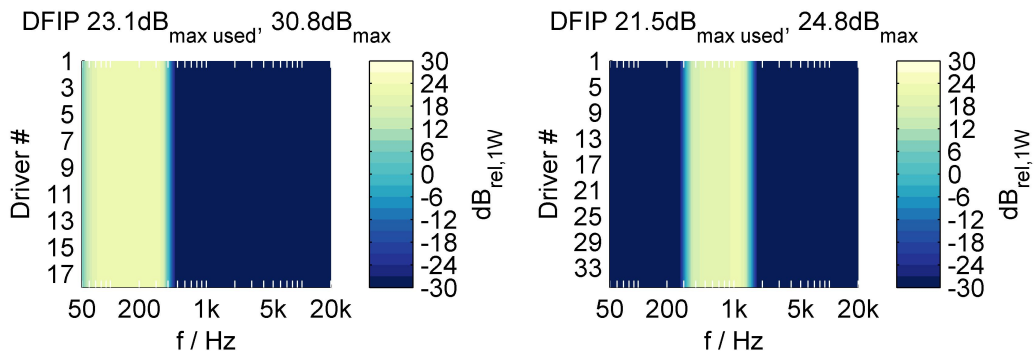


Figure 4.15: LSA_K1_Design1: Driving functions.

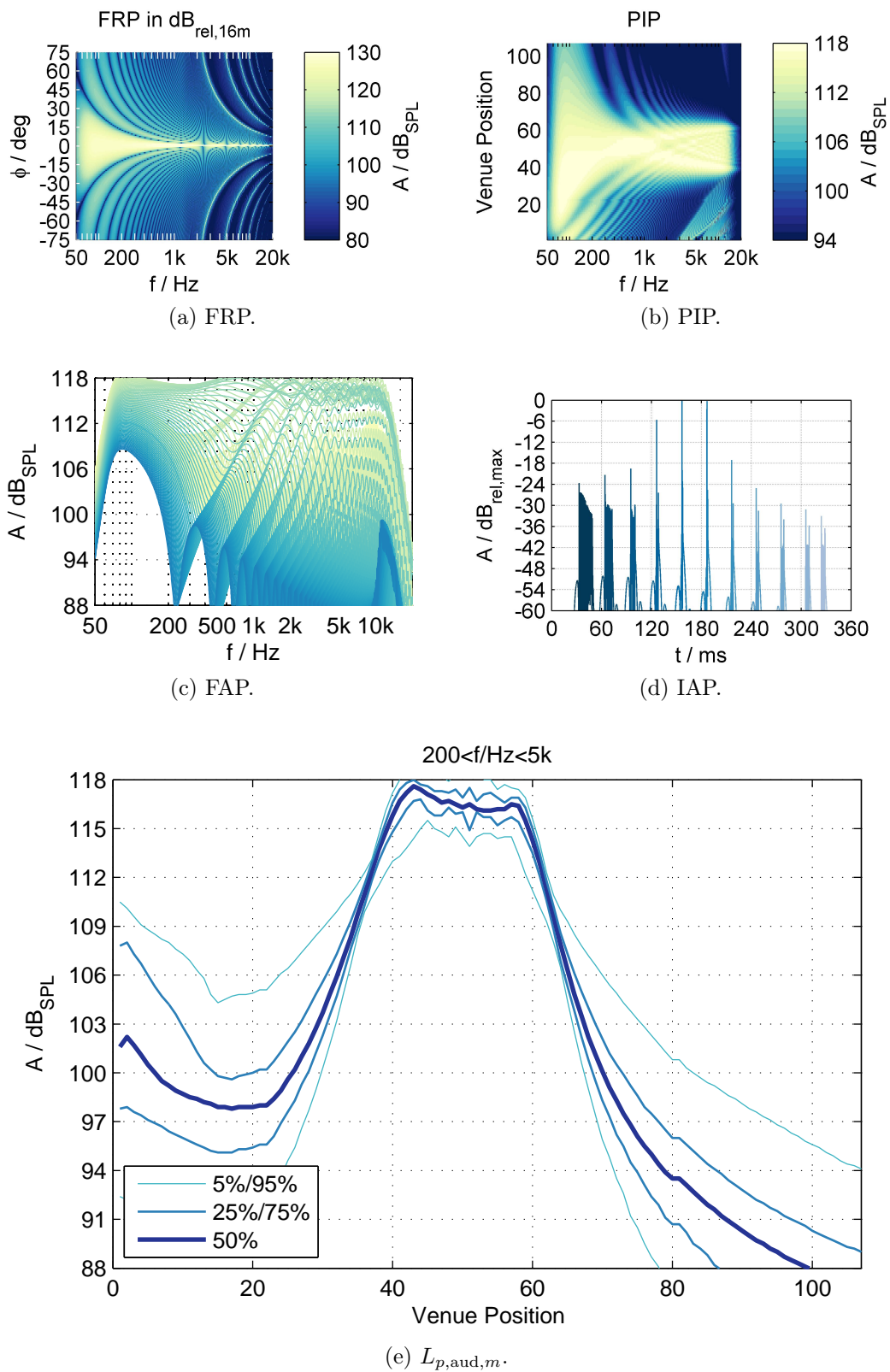


Figure 4.16: LSA_K1_Design1: Frequency response.

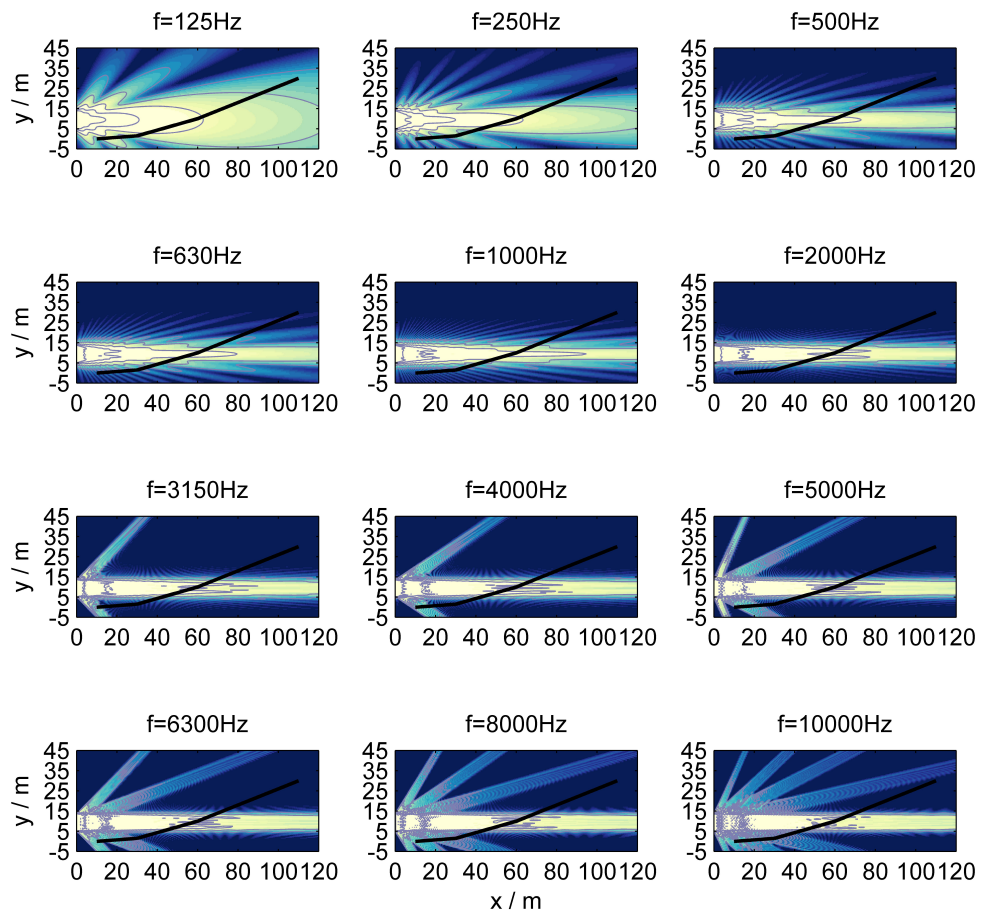
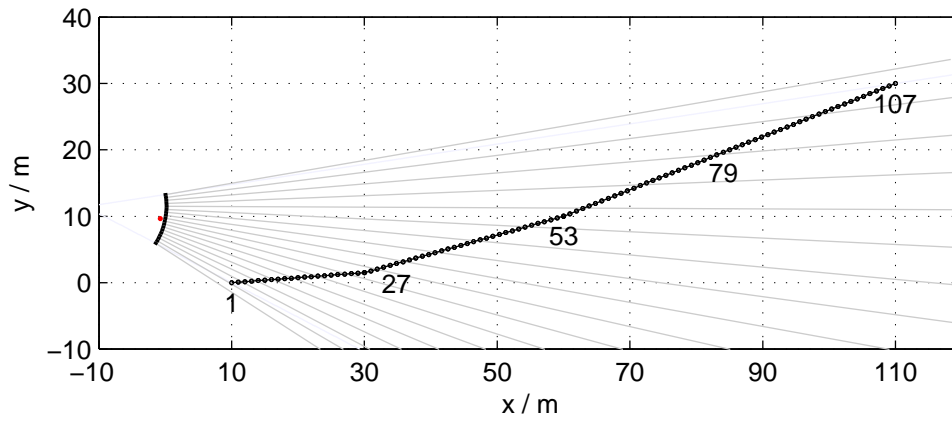


Figure 4.17: LSA_K1_Design1: SPL distribution in xy -plane with the same colormap as Fig. 4.16b and 6 dB isobars w.r.t. $116 \text{ dB}_{\text{SPL}}$.



(a) LSA and venue setup.

Figure 4.18: LSA_K1_Design2: Setup.

LSA_K1_Design2: Uniformly driven, $L_{\text{HF}} = 3$, $q_{\text{HF}} = 1.000$, $l_{0,\text{HF}} = 5.906''$, tilt angle & splay angles: $+9.75^\circ$, -2.50° , $\beta_{\text{KB}} = 3.0$, $f_c = 50$ Hz, $\mathbf{x}_{\text{FRP,Origin}} = (-0.760, 9.627, 0)^T$,

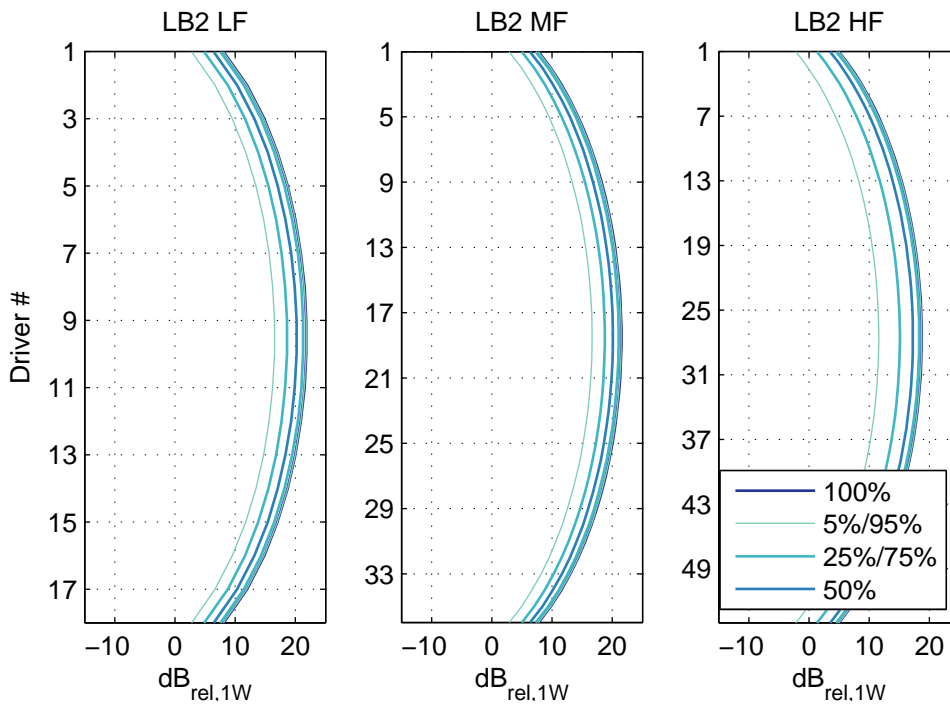
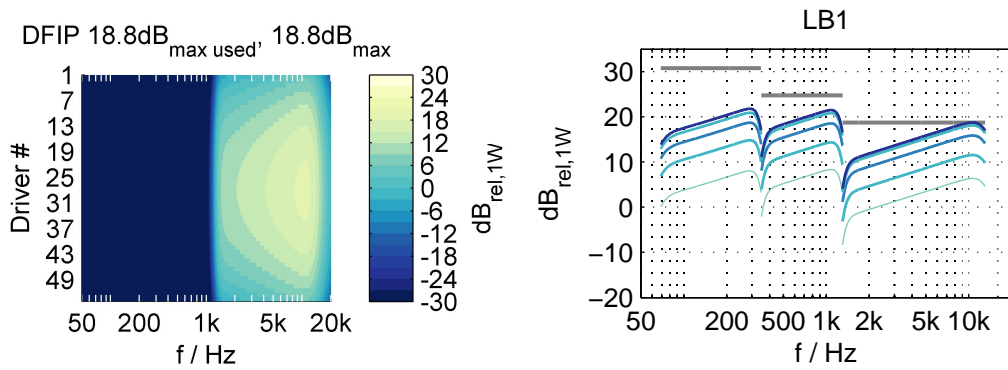
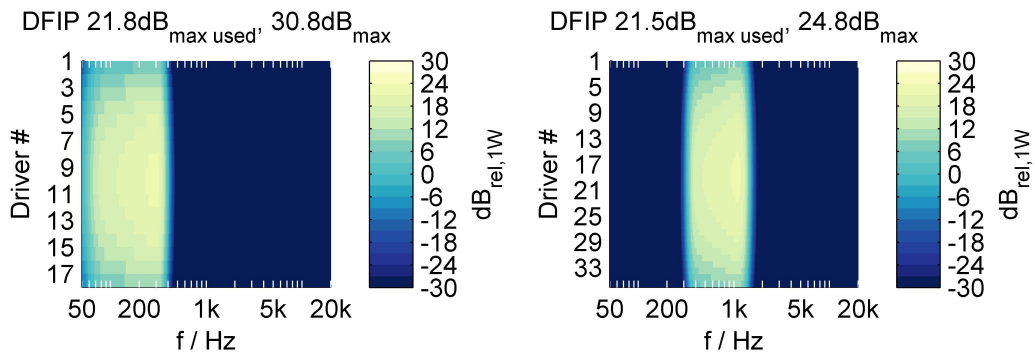


Figure 4.19: LSA_K1_Design2: Driving functions.

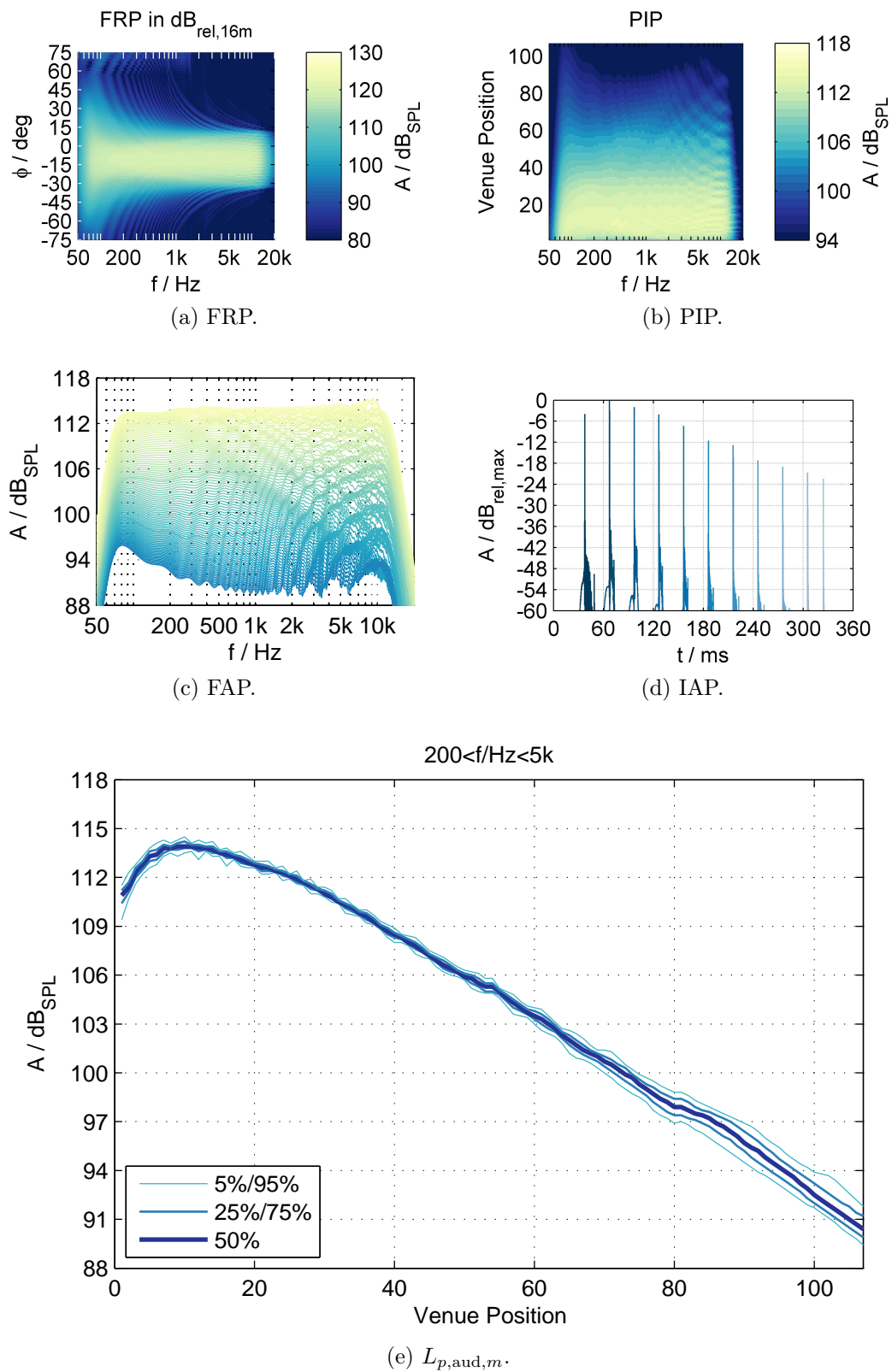


Figure 4.20: LSA_K1_Design2: Frequency response.

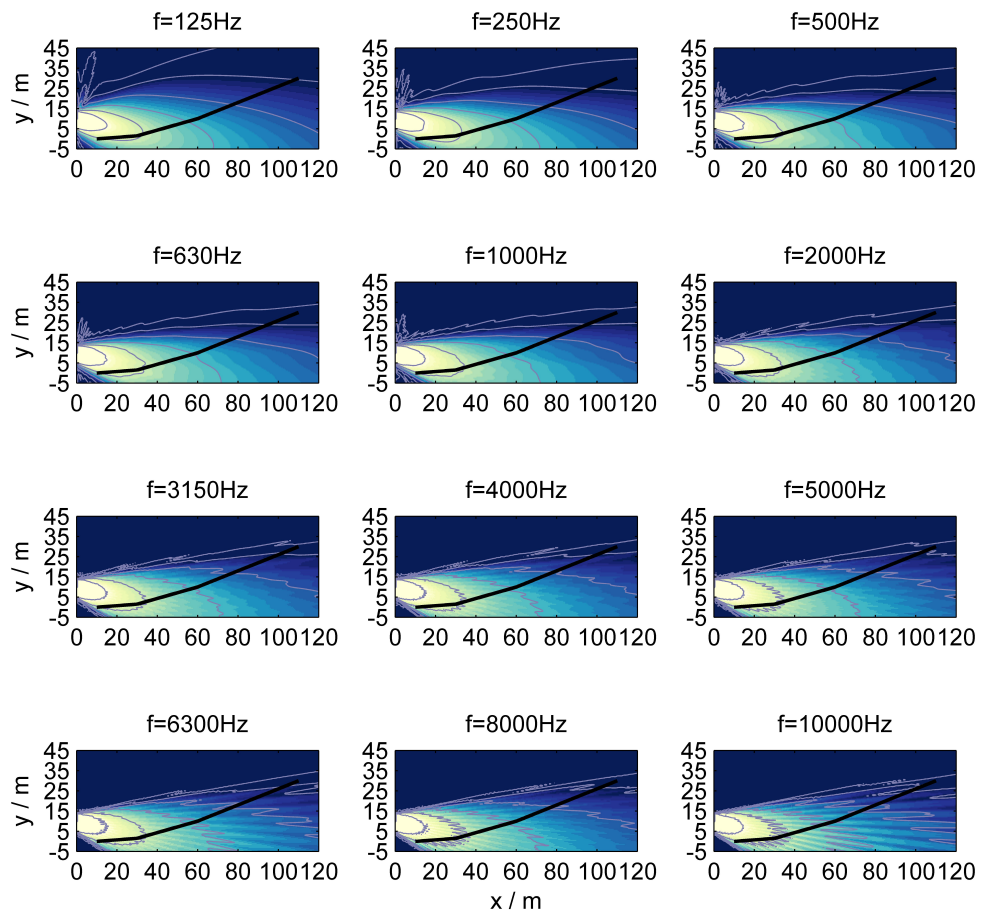
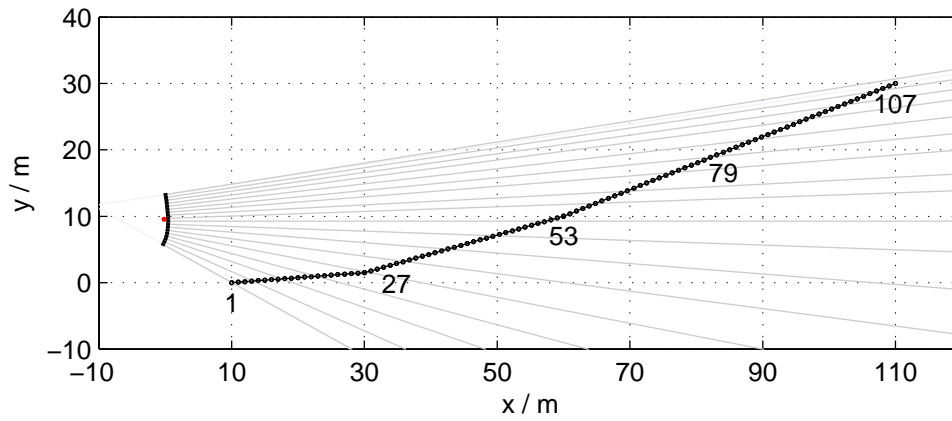


Figure 4.21: LSA_K1_Design2: SPL distribution in xy -plane with the same colormap as Fig. 4.20b and 6 dB isobars w.r.t. $106\text{ dB}_{\text{SPL}}$.



(a) LSA and venue setup.

Figure 4.22: LSA_K1_Design3: Setup.

LSA_K1_Design3: Uniformly driven, $L_{\text{HF}} = 3$, $q_{\text{HF}} = 1.000$, $l_{0,\text{HF}} = 5.906''$, tilt angle & splay angles: $+9.00^\circ$, -0.50° , -0.50° , -0.50° , -1.00° , -1.00° , -1.00° , -1.50° , -1.00° , -2.00° , -2.00° , -2.50° , -3.00° , -3.50° , -4.00° , -4.00° , -5.00° , -5.00° , $\beta_{\text{KB}} = 2.0$, $f_c = 80$ Hz, $\mathbf{x}_{\text{FRP,Origin}} = (-0.192, 9.533, 0)^\text{T}$,

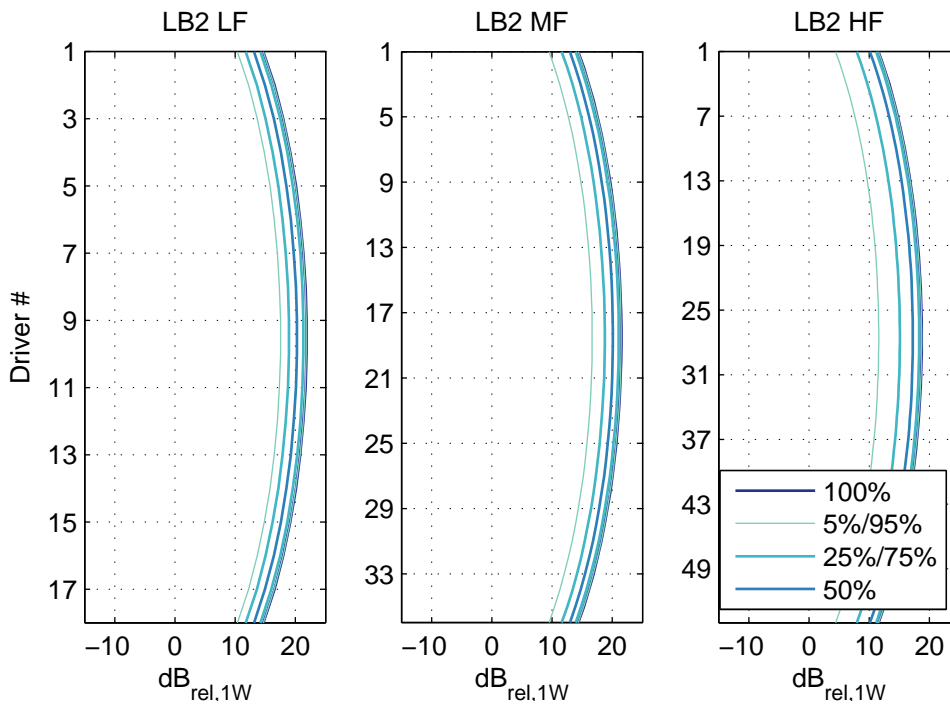
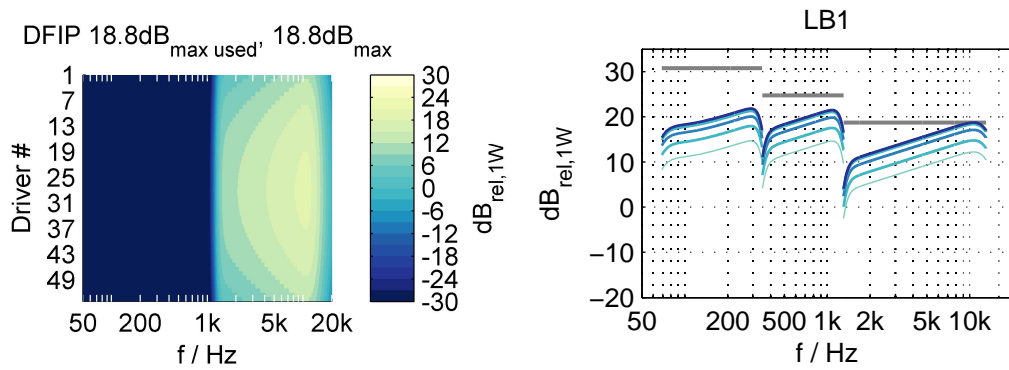
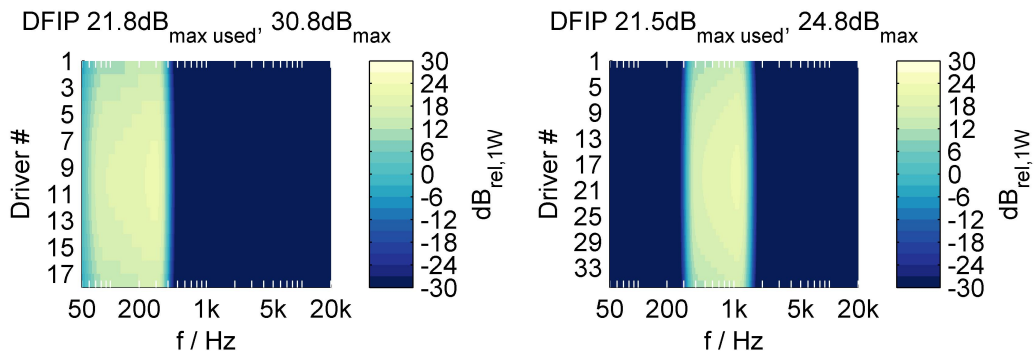


Figure 4.23: LSA_K1_Design3: Driving functions.

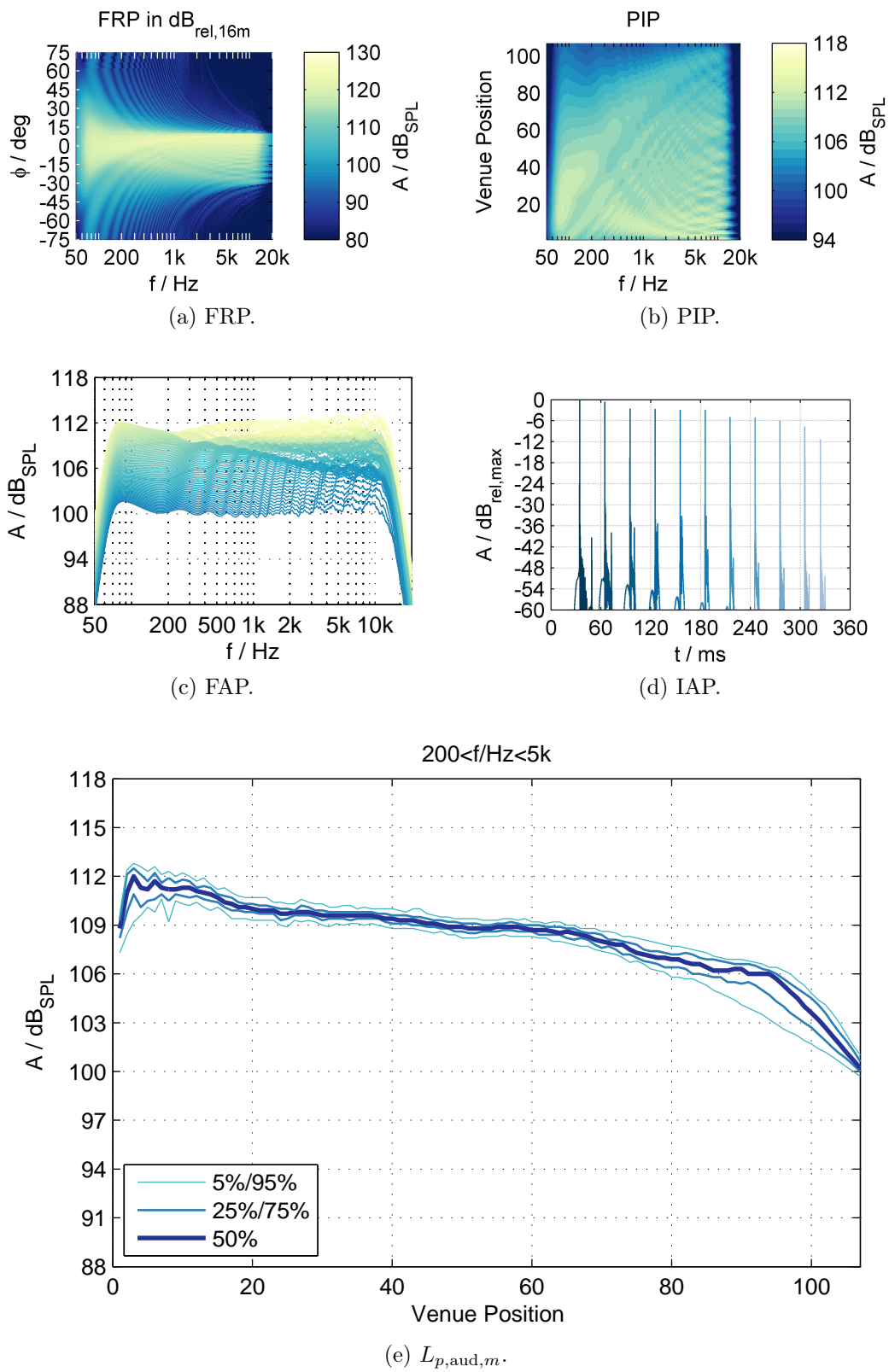


Figure 4.24: LSA_K1_Design3: Frequency response.

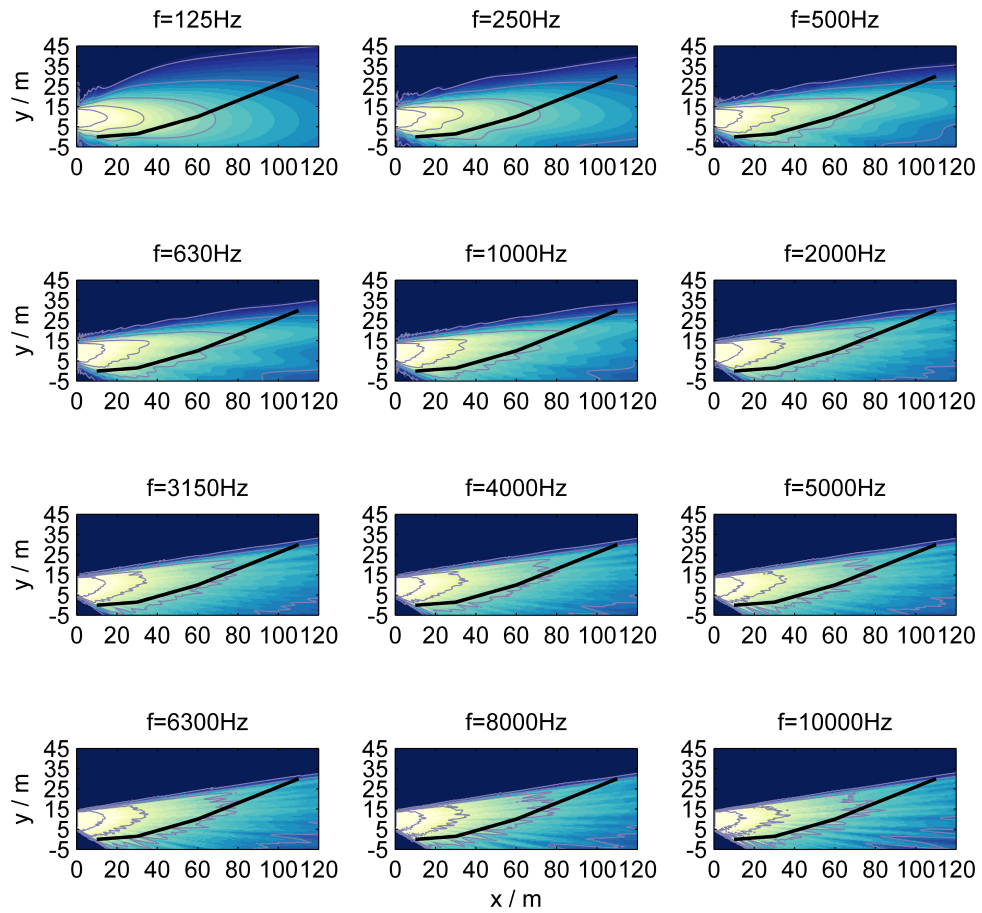
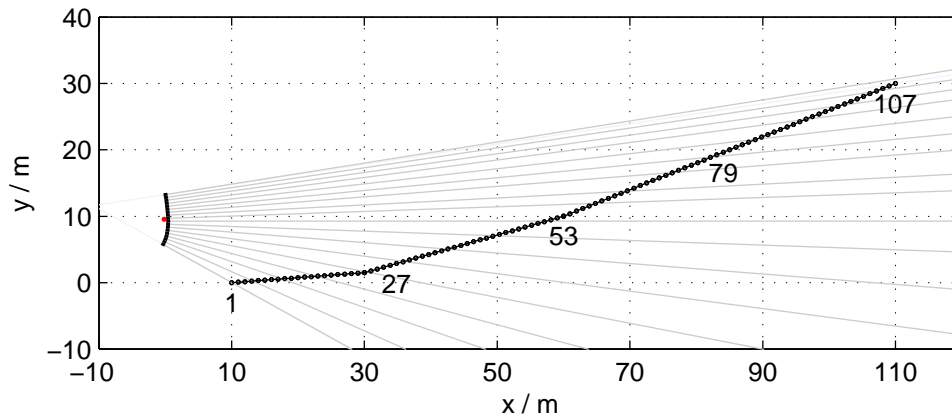


Figure 4.25: LSA_K1_Design3: SPL distribution in xy -plane with the same colormap as Fig. 4.24b and 6 dB isobars w.r.t. 108 dB_{SPL}.



(a) LSA and venue setup.

Figure 4.26: LSA_K1_Design4: Setup.

LSA_K1_Design4: Uniformly driven, $L_{\text{HF}} = 3$, $q_{\text{HF}} = 0.847$, $l_{0,\text{HF}} = 5.000''$, tilt angle & splay angles: $+9.00^\circ$, -0.50° , -0.50° , -0.50° , -1.00° , -1.00° , -1.00° , -1.50° , -1.00° , -2.00° , -2.00° , -2.50° , -3.00° , -3.50° , -4.00° , -4.00° , -5.00° , -5.00° , $\beta_{\text{KB}} = 2.0$, $f_c = 80 \text{ Hz}$, $\mathbf{x}_{\text{FRP,Origin}} = (-0.192, 9.533, 0)^\text{T}$,

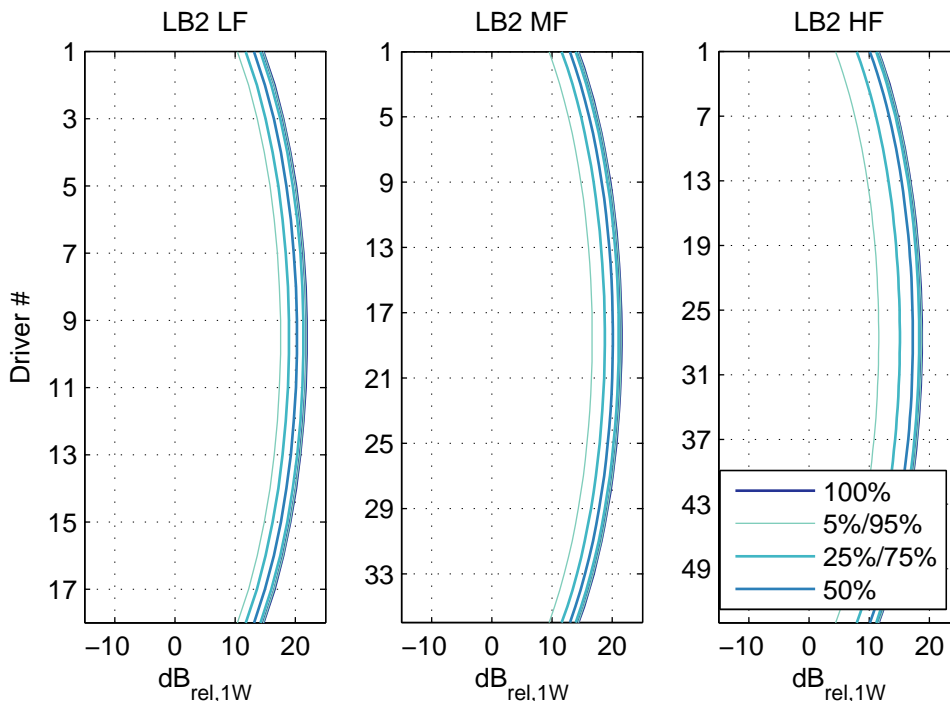
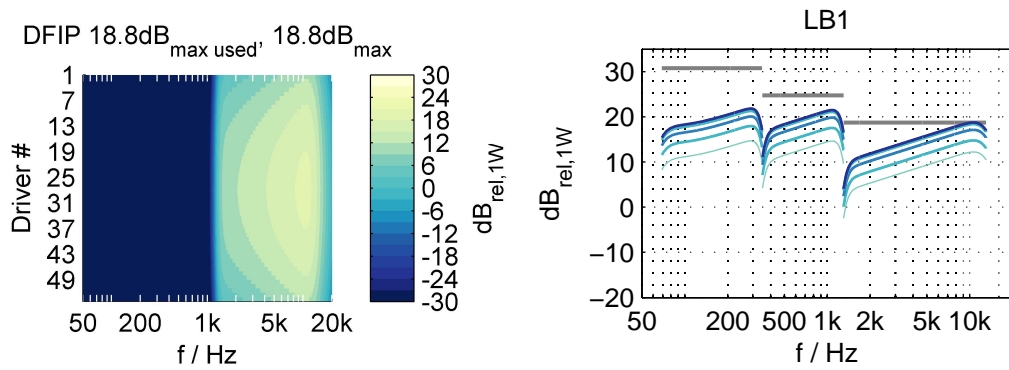
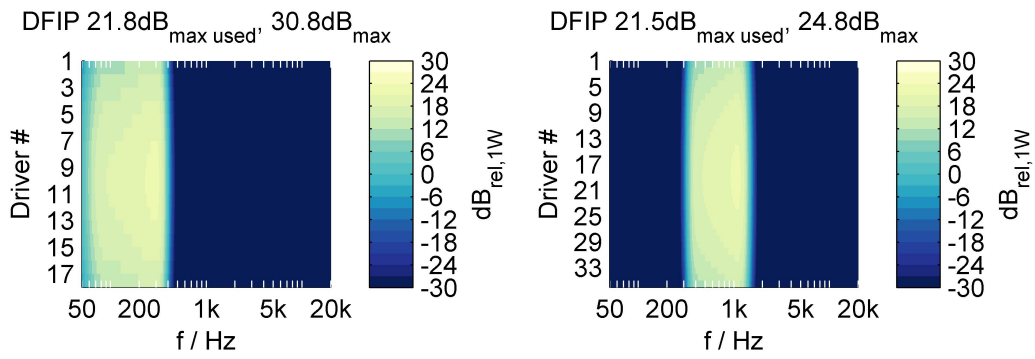


Figure 4.27: LSA_K1_Design4: Driving functions.

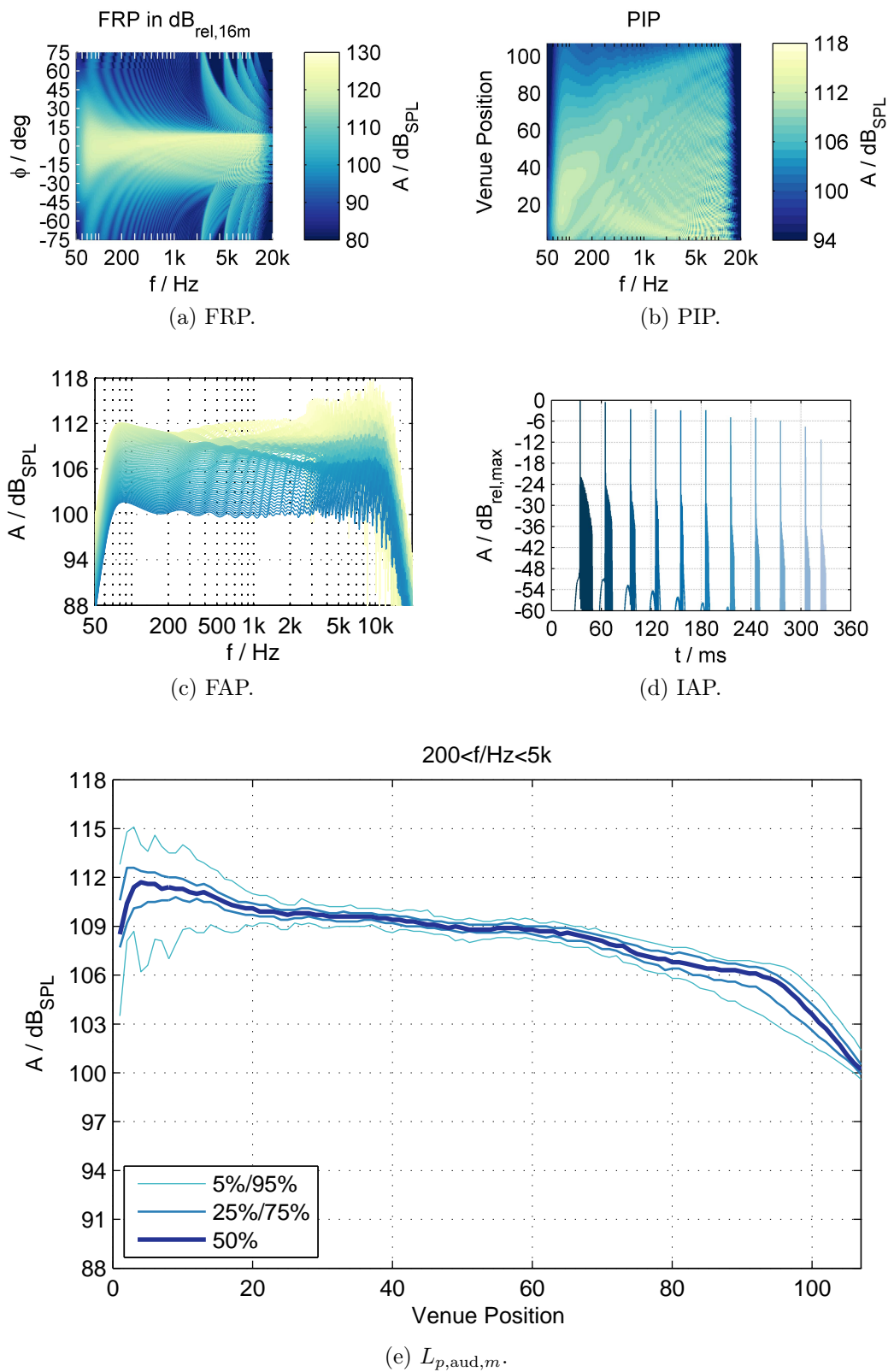


Figure 4.28: LSA_K1_Design4: Frequency response.

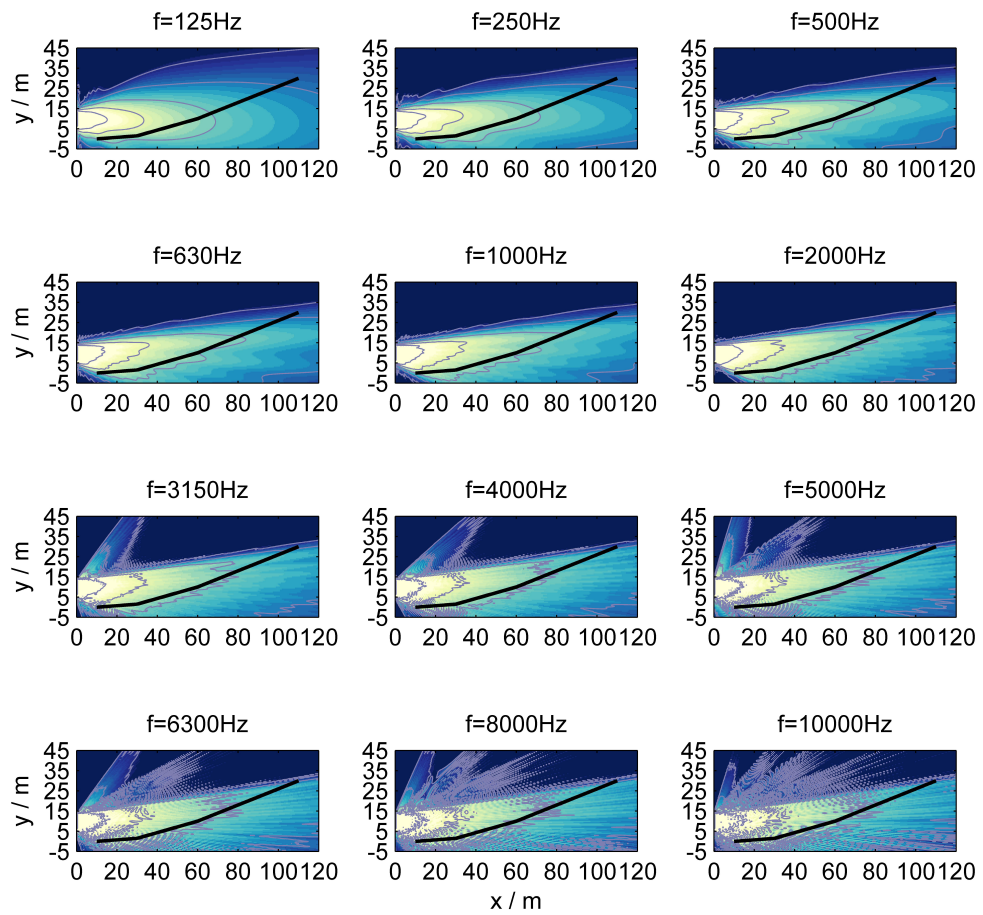
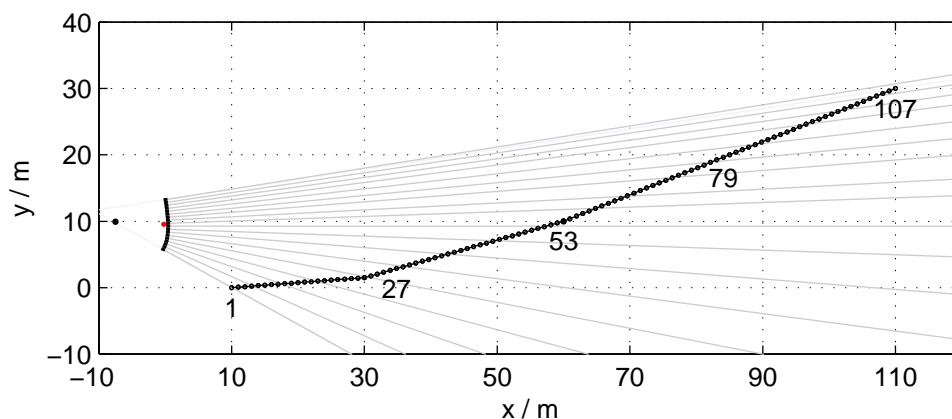
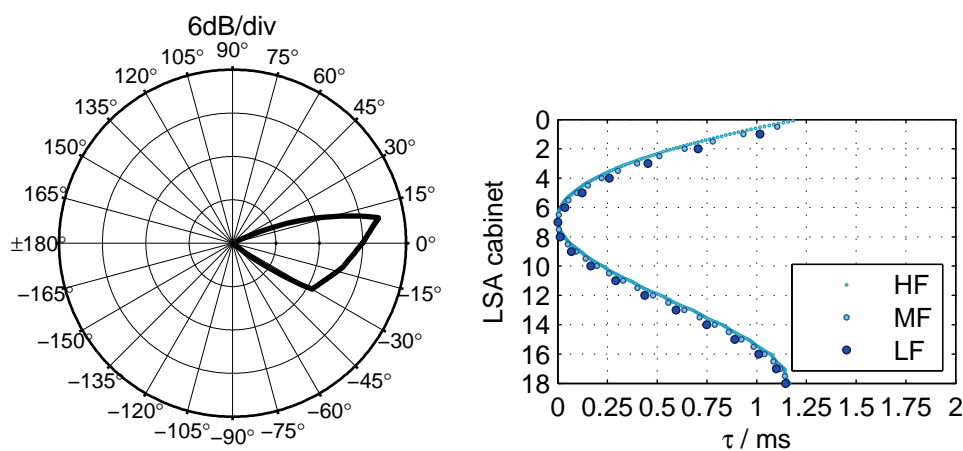


Figure 4.29: LSA_K1_Design4: SPL distribution in xy -plane with the same colormap as Fig. 4.28b and 6 dB isobars w.r.t. $108\text{ dB}_{\text{SPL}}$.



(a) LSA and venue setup.



(b) Polar plot of virtual source's FRP.

(c) DFIP: Driving function delays.

Figure 4.30: LSA_K1_Design5: Setup and virtual source.

LSA_K1_Design5: WFS of a virtual source, $\mathbf{x}_{PS} = (-7.500, 9.925, 0)^T$, $\mathbf{x}_{Ref} = (60.0, 10.0, 0)^T$, $A_{\min, \text{dB}} = -100$, $DD_{\text{dB}} = -10$, $L_{\text{HF}} = 15$, $q_{\text{HF}} = 0.847$, $l_{0, \text{HF}} = 1.000''$, tilt angle & splay angles: $+9.00^\circ$, -0.50° , -0.50° , -0.50° , -1.00° , -1.00° , -1.00° , -1.50° , -1.00° , -2.00° , -2.00° , -2.50° , -3.00° , -3.50° , -4.00° , -4.00° , -5.00° , -5.00° , $\beta_{\text{KB}} = 1.0$, $f_c = 100 \text{ Hz}$, $\mathbf{x}_{\text{FRP, Origin}} = (-0.212, 9.537, 0)^T$,

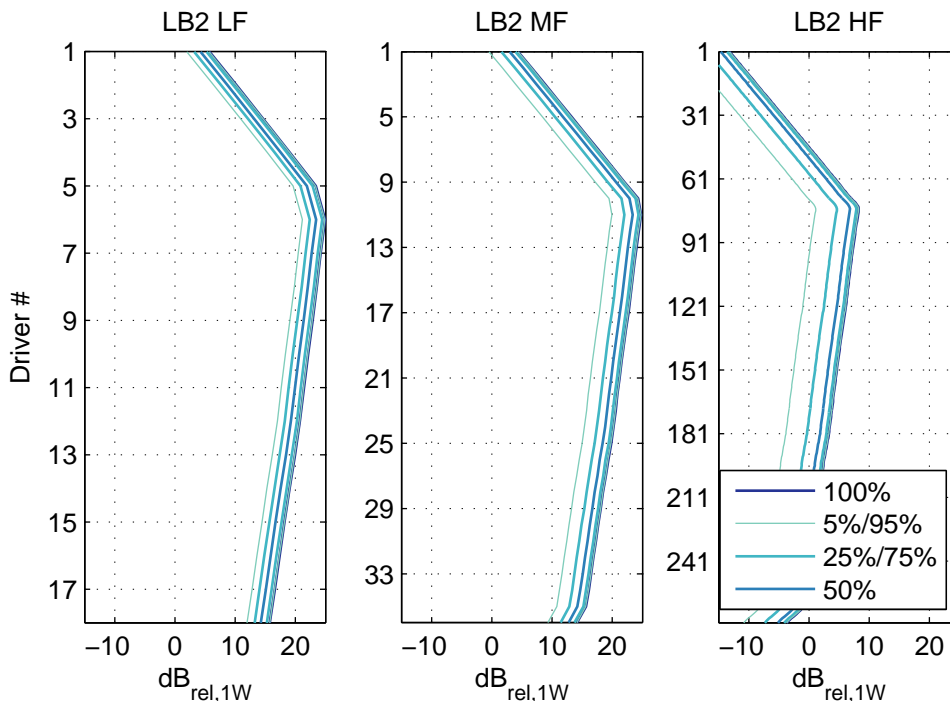
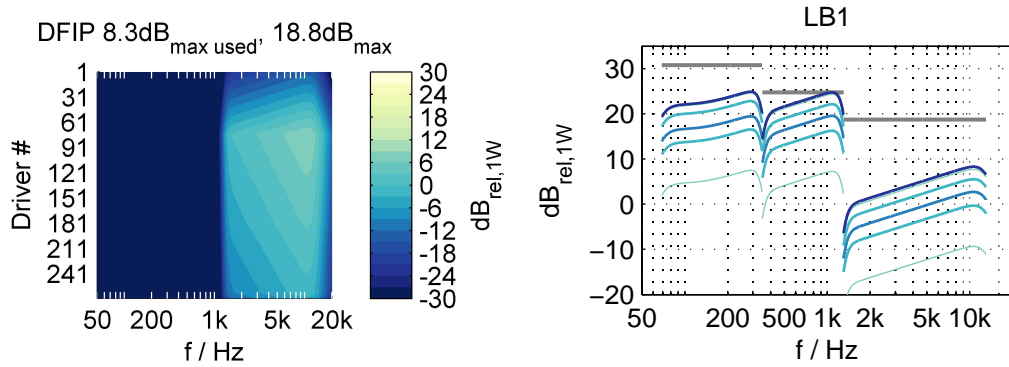
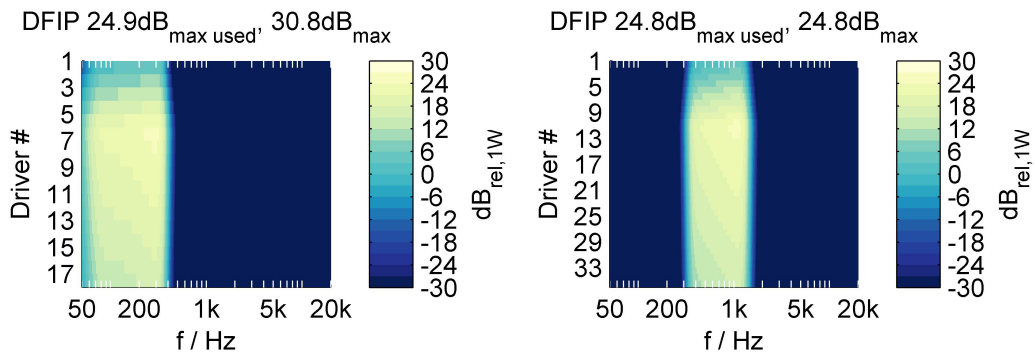


Figure 4.31: LSA_K1_Design5: Driving functions.

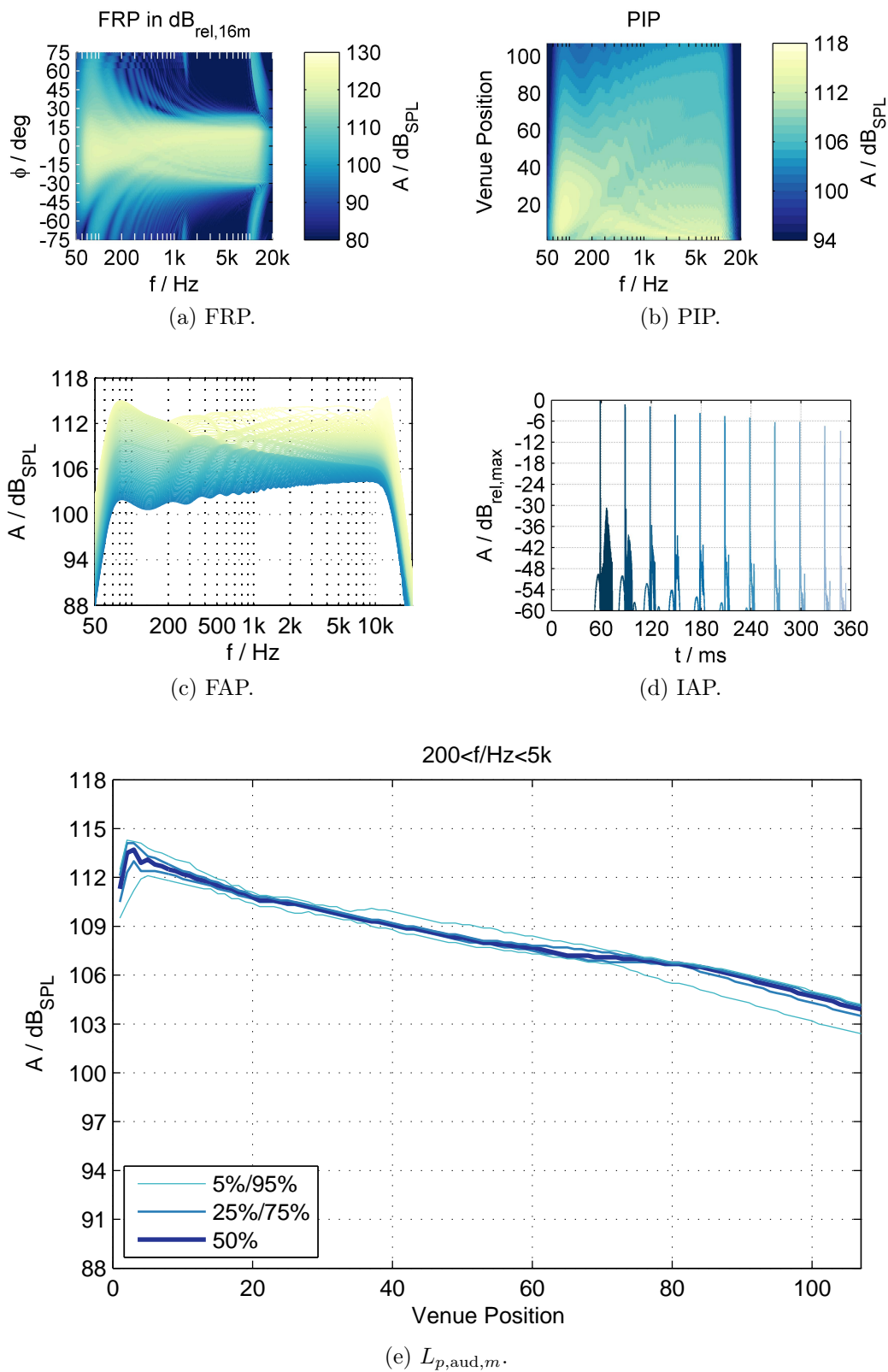


Figure 4.32: LSA_K1_Design5: Frequency response.

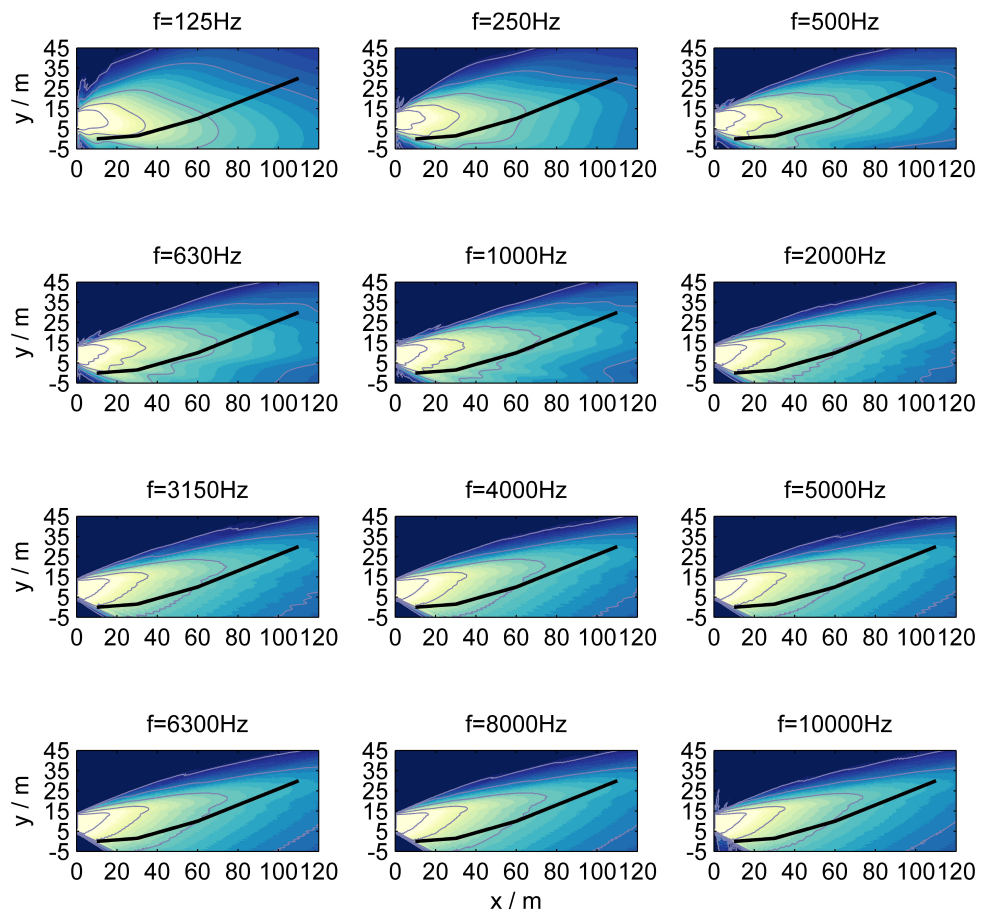
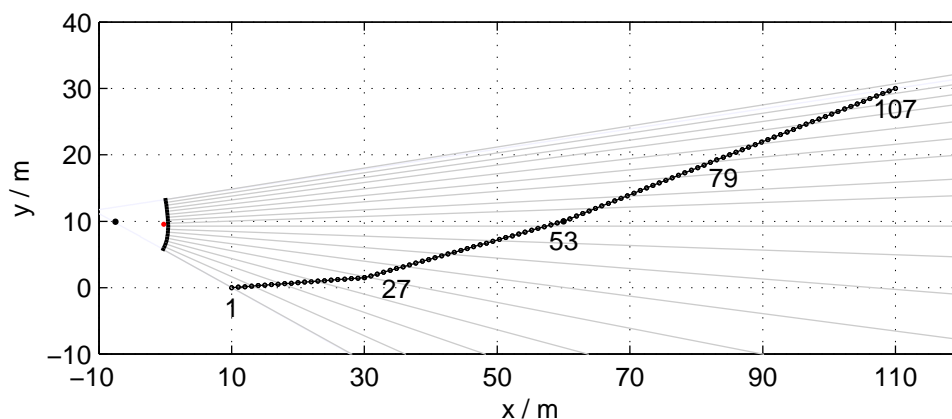
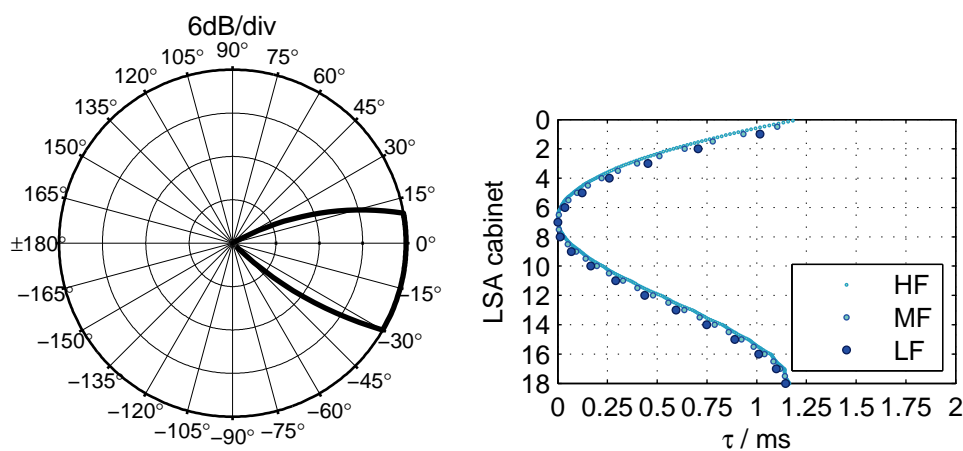


Figure 4.33: LSA_K1_Design5: SPL distribution in xy -plane with the same colormap as Fig. 4.32b and 6 dB isobars w.r.t. 108 dB_{SPL}.



(a) LSA and venue setup.



(b) Polar plot of virtual source's FRP.

(c) DFIP: Driving function delays.

Figure 4.34: LSA_K1_Design6: Setup and virtual source.

LSA_K1_Design6: WFS of a virtual source, $\mathbf{x}_{PS} = (-7.500, 9.925, 0)^T$, $\mathbf{x}_{Ref} = (60.0, 10.0, 0)^T$, $A_{min,dB} = -100$, $DD_{dB} = 0$, $L_{HF} = 15$, $q_{HF} = 0.847$, $l_{0,HF} = 1.000''$, tilt angle & splay angles: $+9.00^\circ$, -0.50° , -0.50° , -0.50° , -1.00° , -1.00° , -1.00° , -1.50° , -1.00° , -2.00° , -2.00° , -2.50° , -3.00° , -3.50° , -4.00° , -4.00° , -5.00° , -5.00° , $\beta_{KB} = 2.0$, $f_c = 100$ Hz, $\mathbf{x}_{FRP,Origin} = (-0.212, 9.537, 0)^T$,

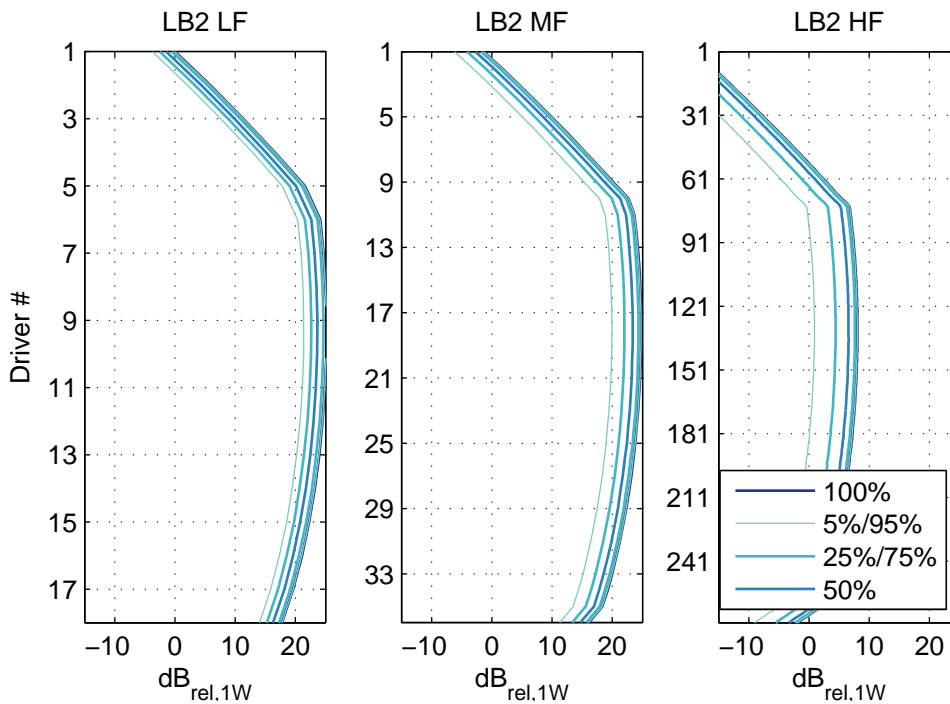
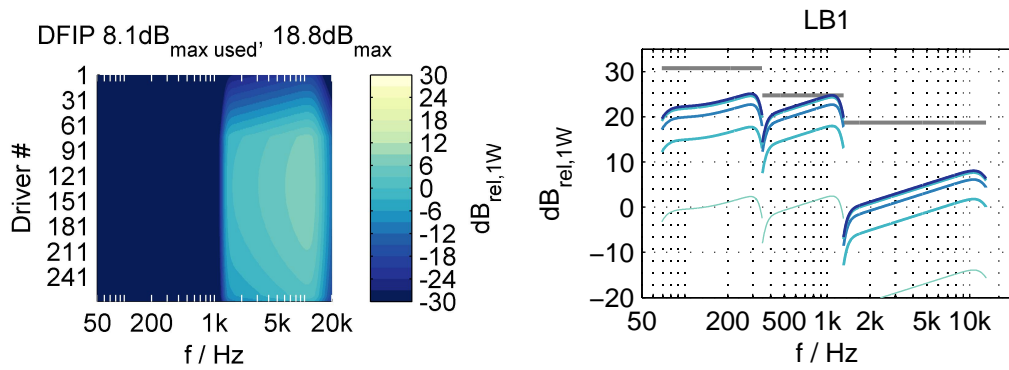
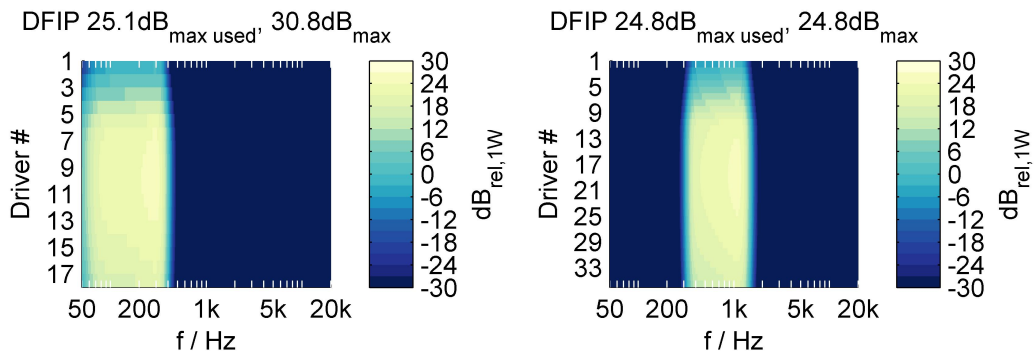


Figure 4.35: LSA_K1_Design6: Driving functions.

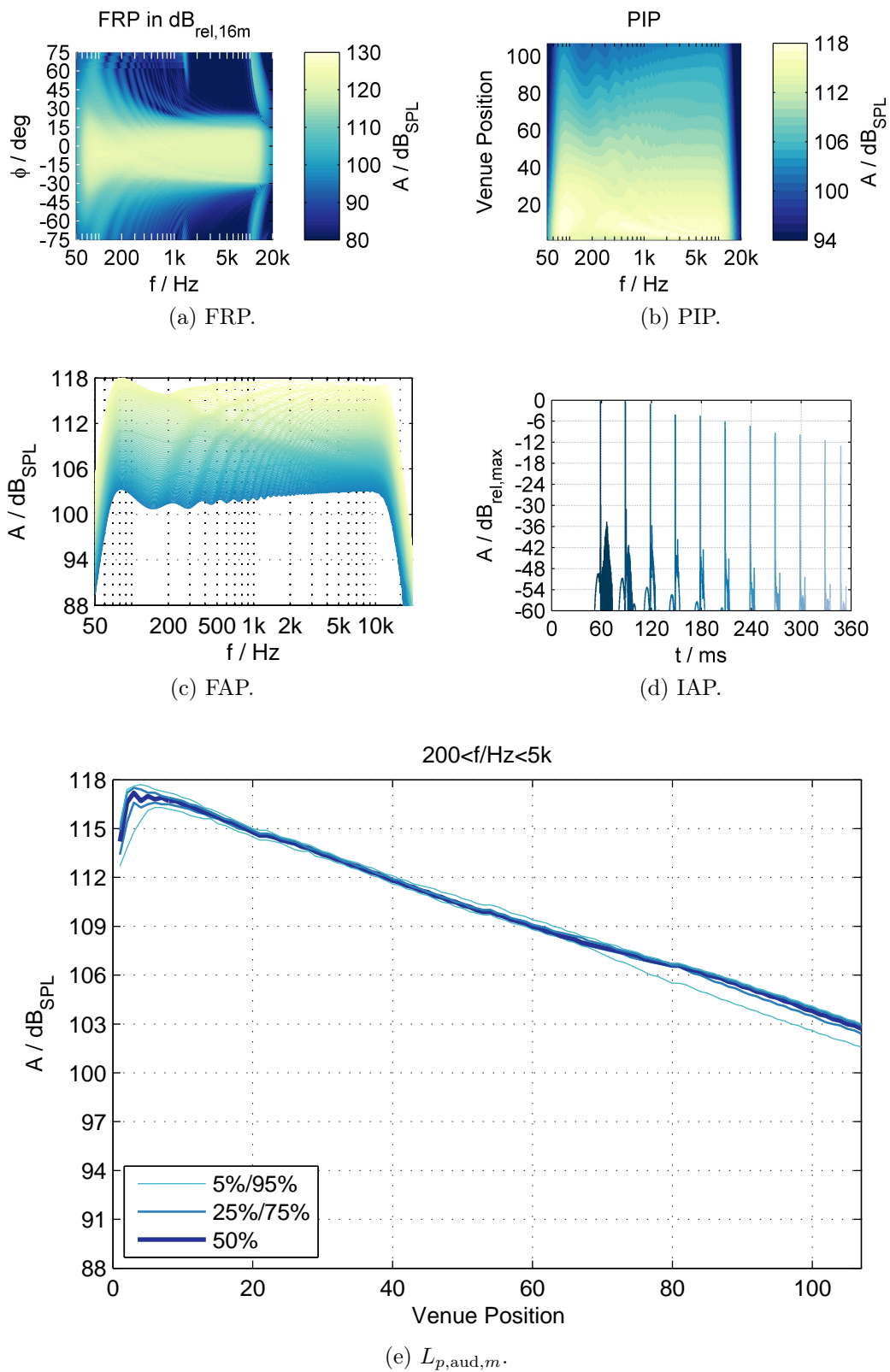


Figure 4.36: LSA_K1_Design6: Frequency response.

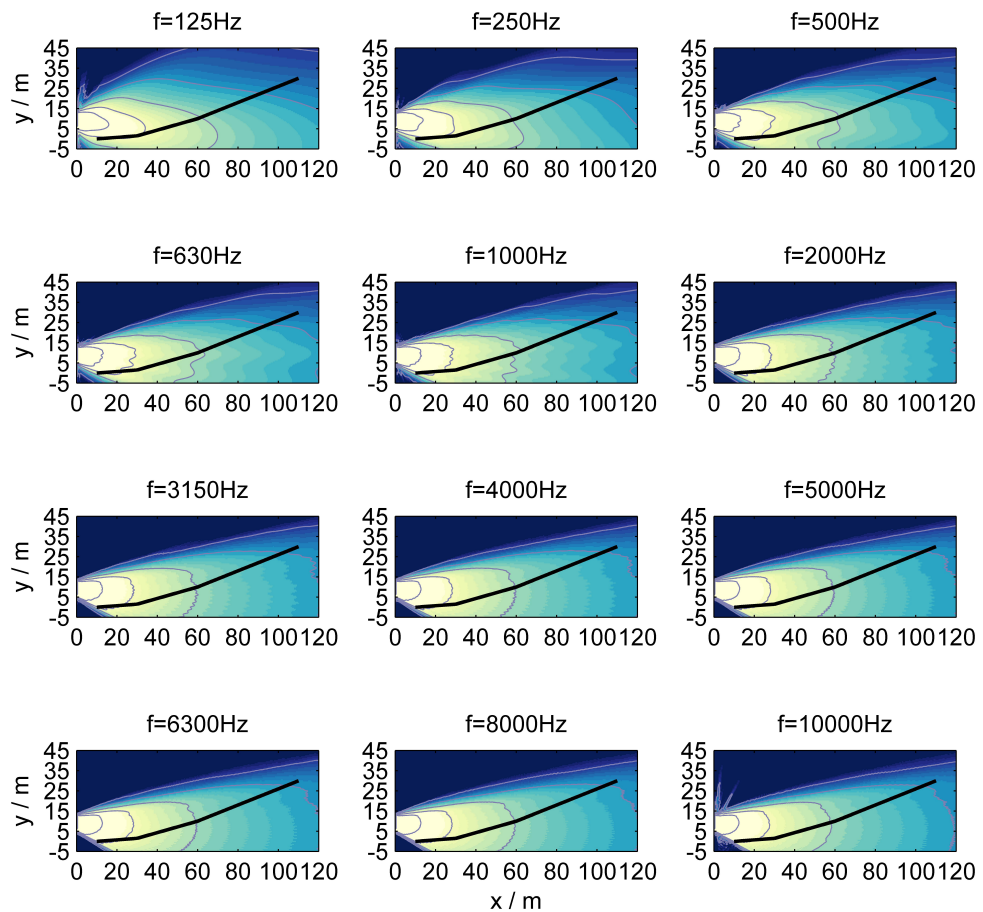
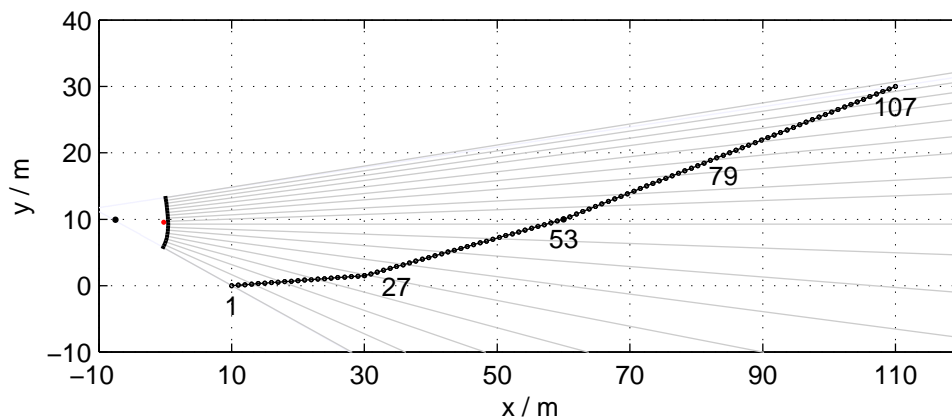
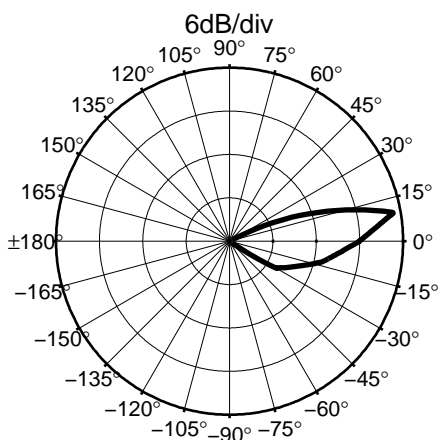


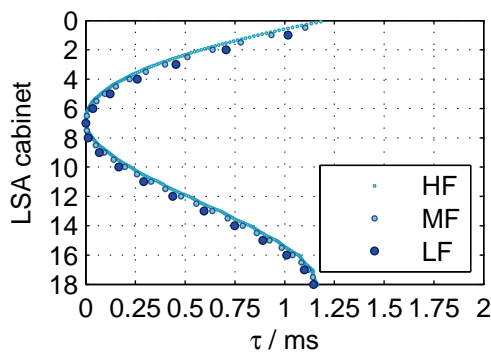
Figure 4.37: LSA_K1_Design6: SPL distribution in xy -plane with the same colormap as Fig. 4.36b and 6 dB isobars w.r.t. 110 dB_{SPL}.



(a) LSA and venue setup.



(b) Polar plot of virtual source's FRP.



(c) DFIP: Driving function delays.

Figure 4.38: LSA_K1_Design7: Setup and virtual source.

LSA_K1_Design7: WFS of a virtual source, $\mathbf{x}_{PS} = (-7.500, 9.925, 0)^T$, $\mathbf{x}_{Ref} = (60.0, 10.0, 0)^T$, $A_{min,dB} = -100$, $DD_{dB} = -20$, $L_{HF} = 15$, $q_{HF} = 0.847$, $l_{0,HF} = 1.000''$, tilt angle & splay angles: $+9.00^\circ$, -0.50° , -0.50° , -0.50° , -1.00° , -1.00° , -1.00° , -1.50° , -1.00° , -2.00° , -2.00° , -2.50° , -3.00° , -3.50° , -4.00° , -4.00° , -5.00° , -5.00° , $\beta_{KB} = 1.0$, $f_c = 100$ Hz, $\mathbf{x}_{FRP,Origin} = (-0.212, 9.537, 0)^T$,

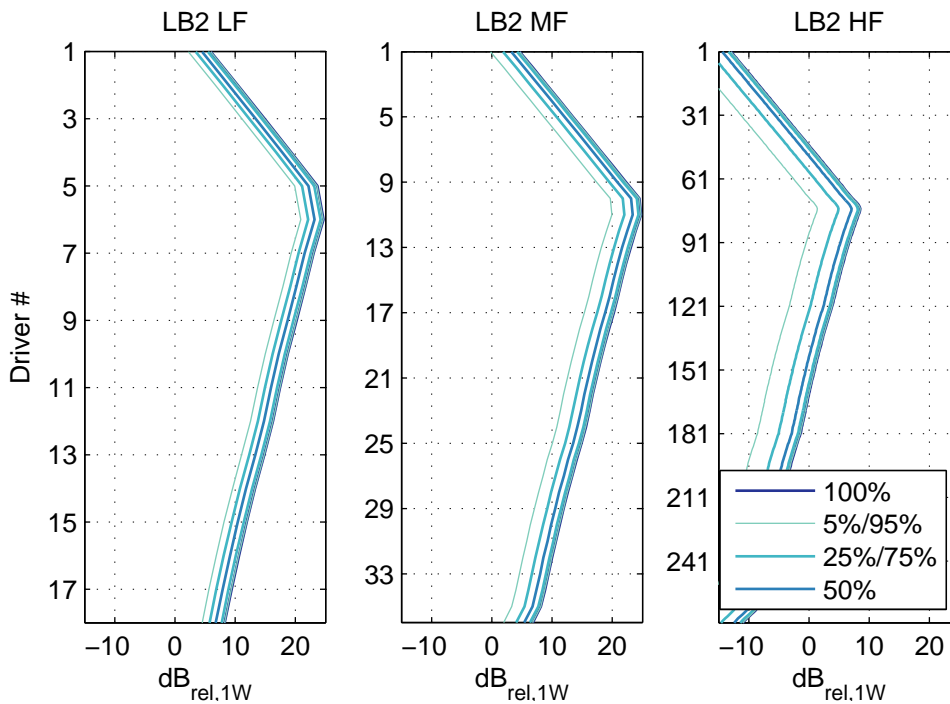
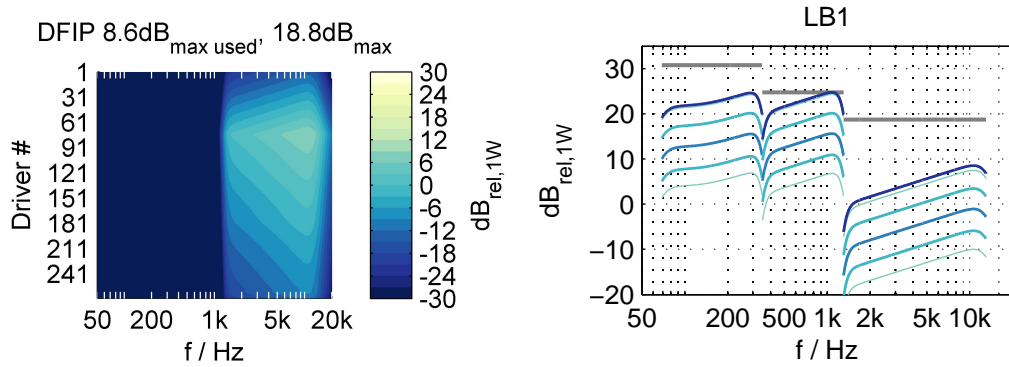
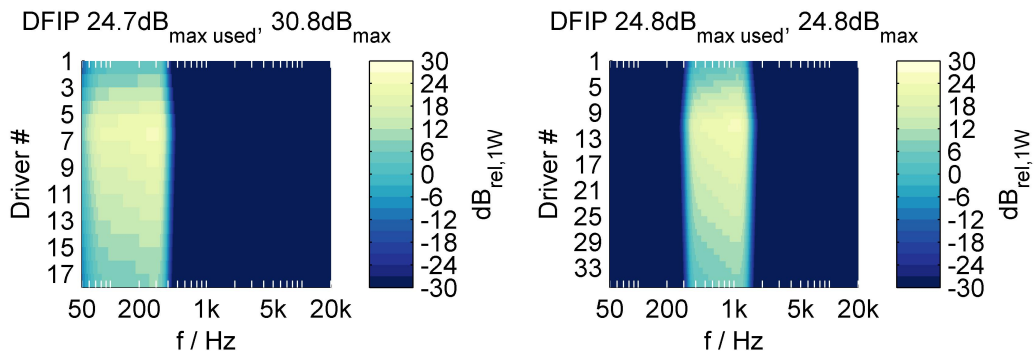


Figure 4.39: LSA_K1_Design7: Driving functions.

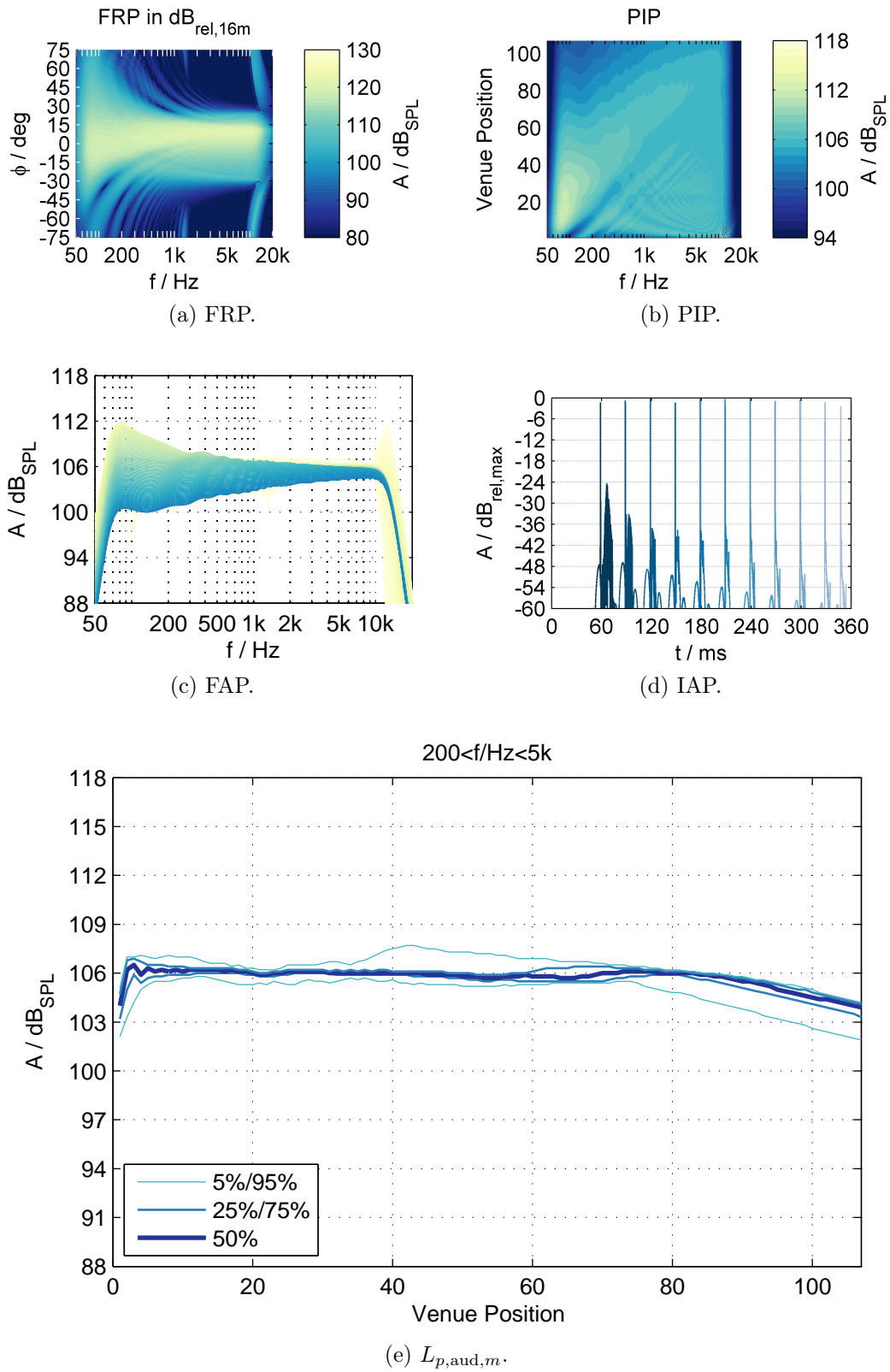


Figure 4.40: LSA_K1_Design7: Frequency response.

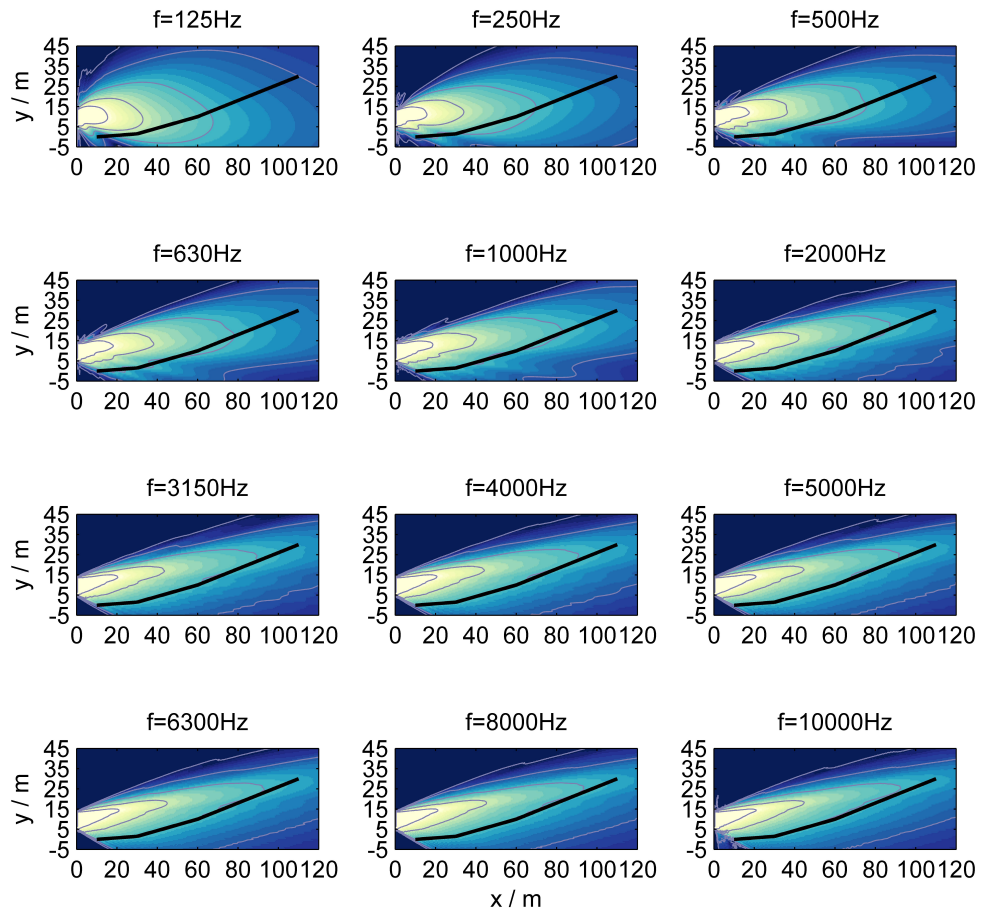
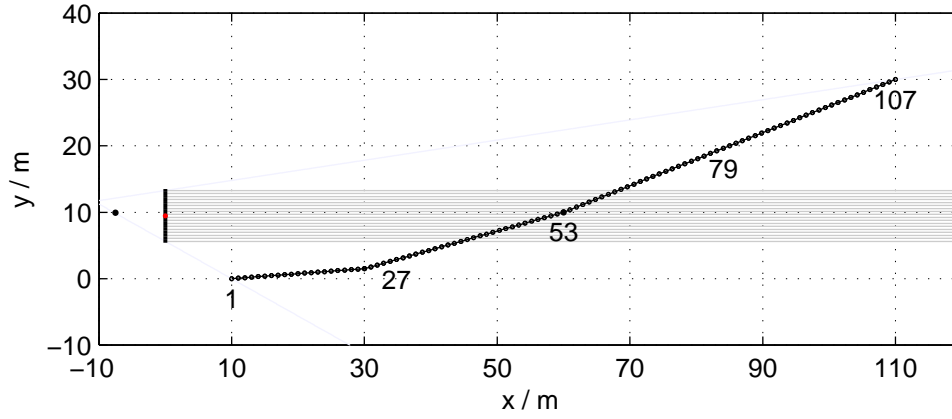
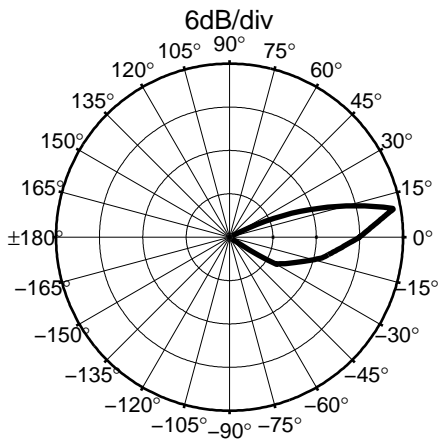


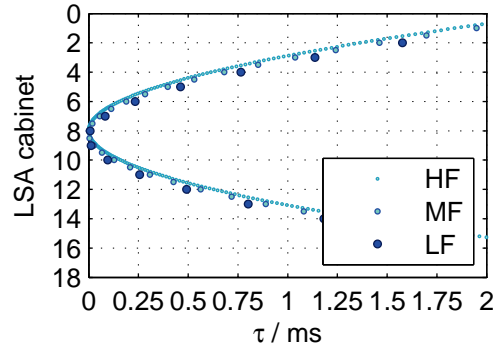
Figure 4.41: LSA_K1_Design7: SPL distribution in xy -plane with the same colormap as Fig. 4.40b and 6 dB isobars w.r.t. 106 dB_{SPL}.



(a) LSA and venue setup.



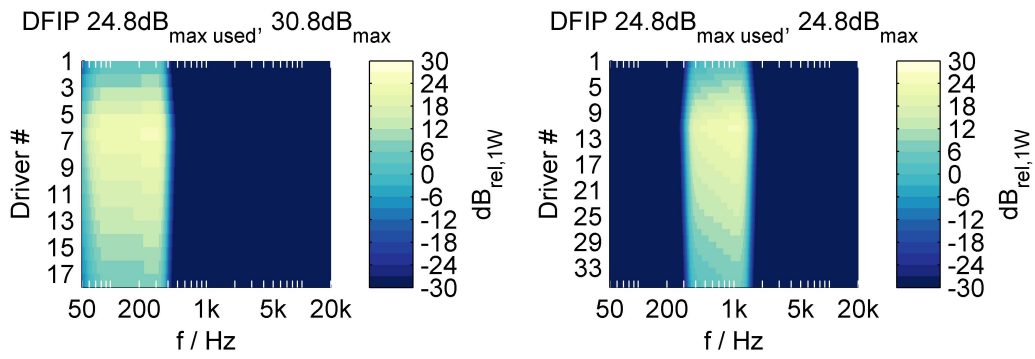
(b) Polar plot of virtual source's FRP.



(c) DFIP: Driving function delays.

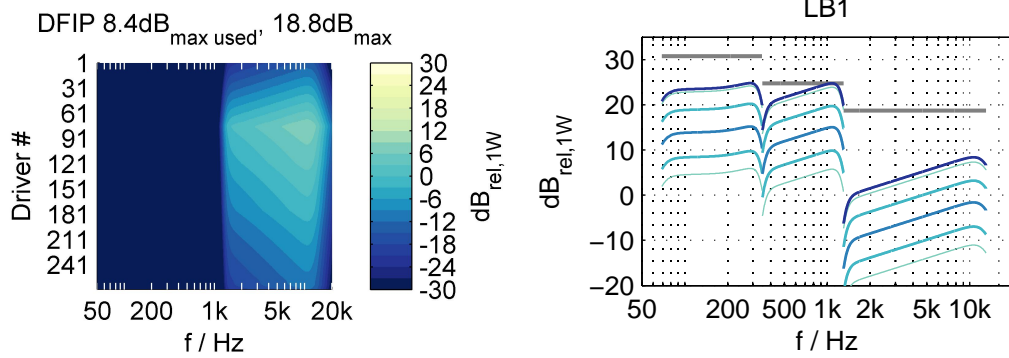
Figure 4.42: LSA_K1_Design8: Setup and virtual source.

LSA_K1_Design8: WFS of a virtual source, $\mathbf{x}_{PS} = (-7.500, 9.925, 0)^T$, $\mathbf{x}_{Ref} = (60.0, 10.0, 0)^T$, $A_{min,dB} = -100$, $DD_{dB} = -20$, $L_{HF} = 15$, $q_{HF} = 0.847$, $l_{0,HF} = 1.000''$, tilt angle & splay angles: $+0.00^\circ$, $\beta_{KB} = 1.0$, $f_c = 150 \text{ Hz}$, $\mathbf{x}_{FRP,Origin} = (0.000, 9.450, 0)^T$,



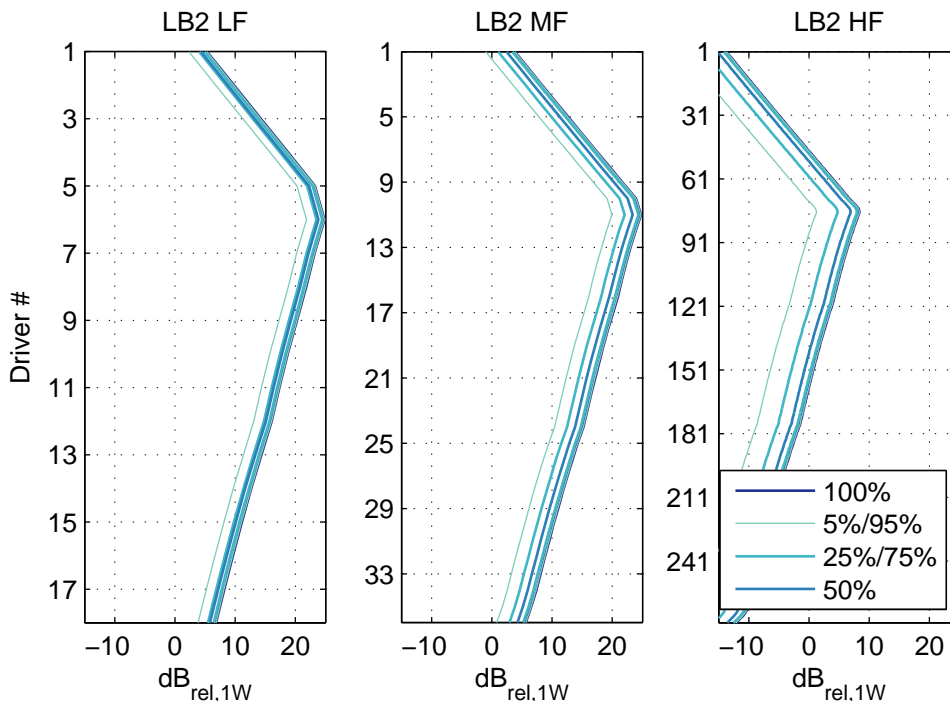
(a) Driving functions: LF band.

(b) Driving functions: MF band.



(c) Driving functions: HF band.

(d) $LB1(\omega)$.



(e) $LB2_i$.

Figure 4.43: LSA_K1_Design8: Driving functions.

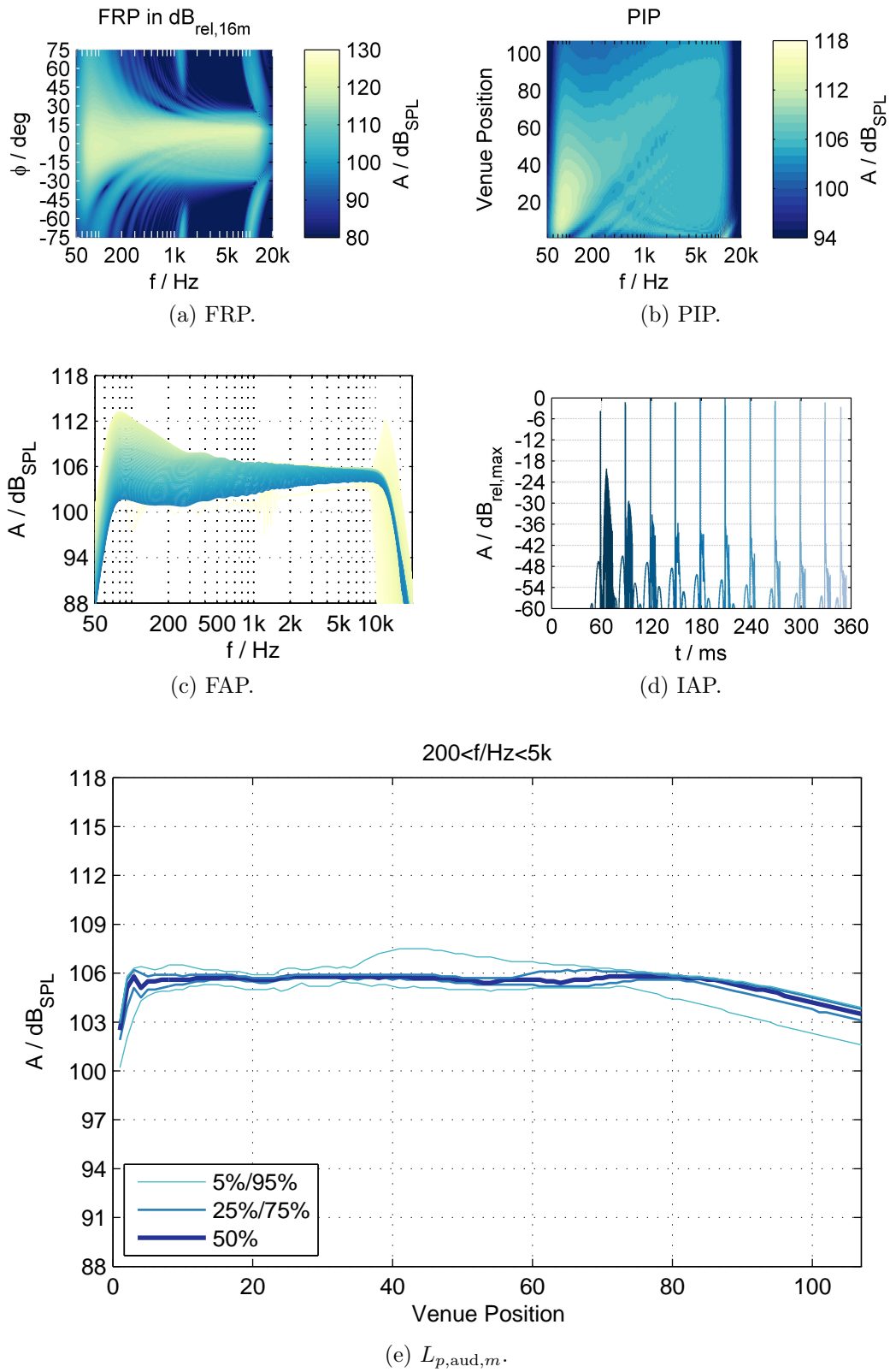


Figure 4.44: LSA_K1_Design8: Frequency response.

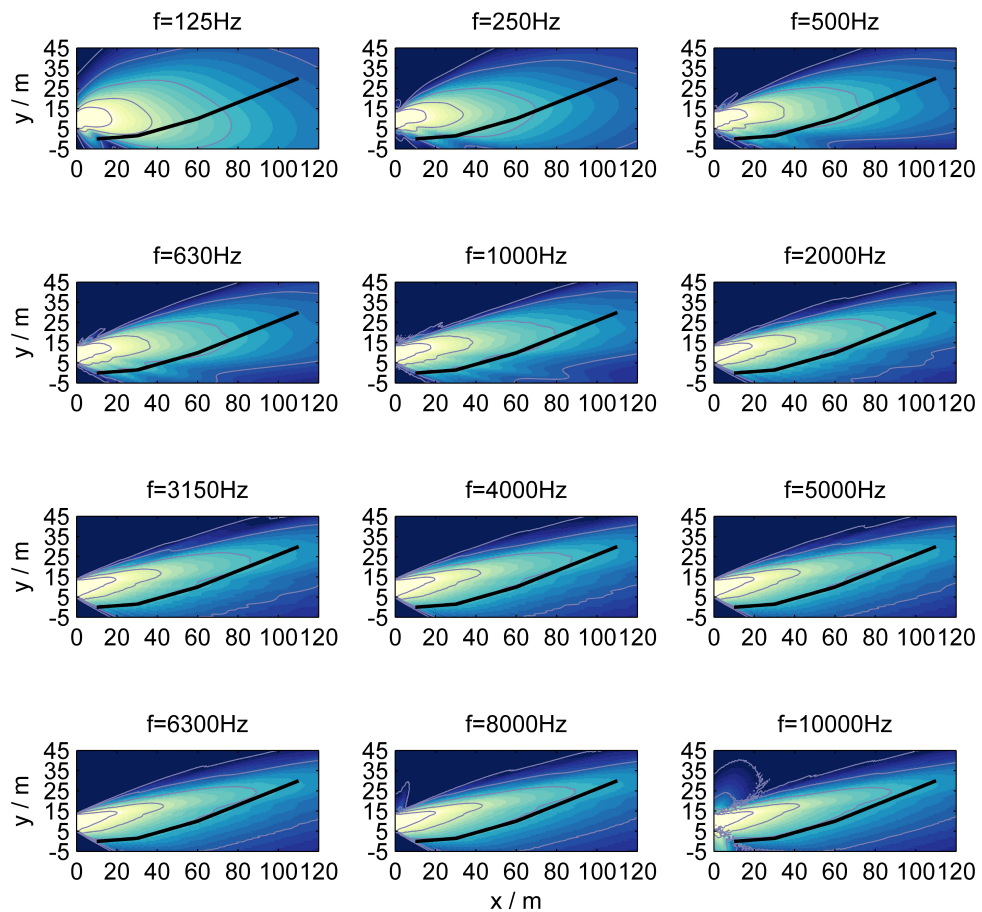


Figure 4.45: LSA_K1_Design8: SPL distribution in xy -plane with the same colormap as Fig. 4.44b and 6 dB isobars w.r.t. 106 dB_{SPL}.

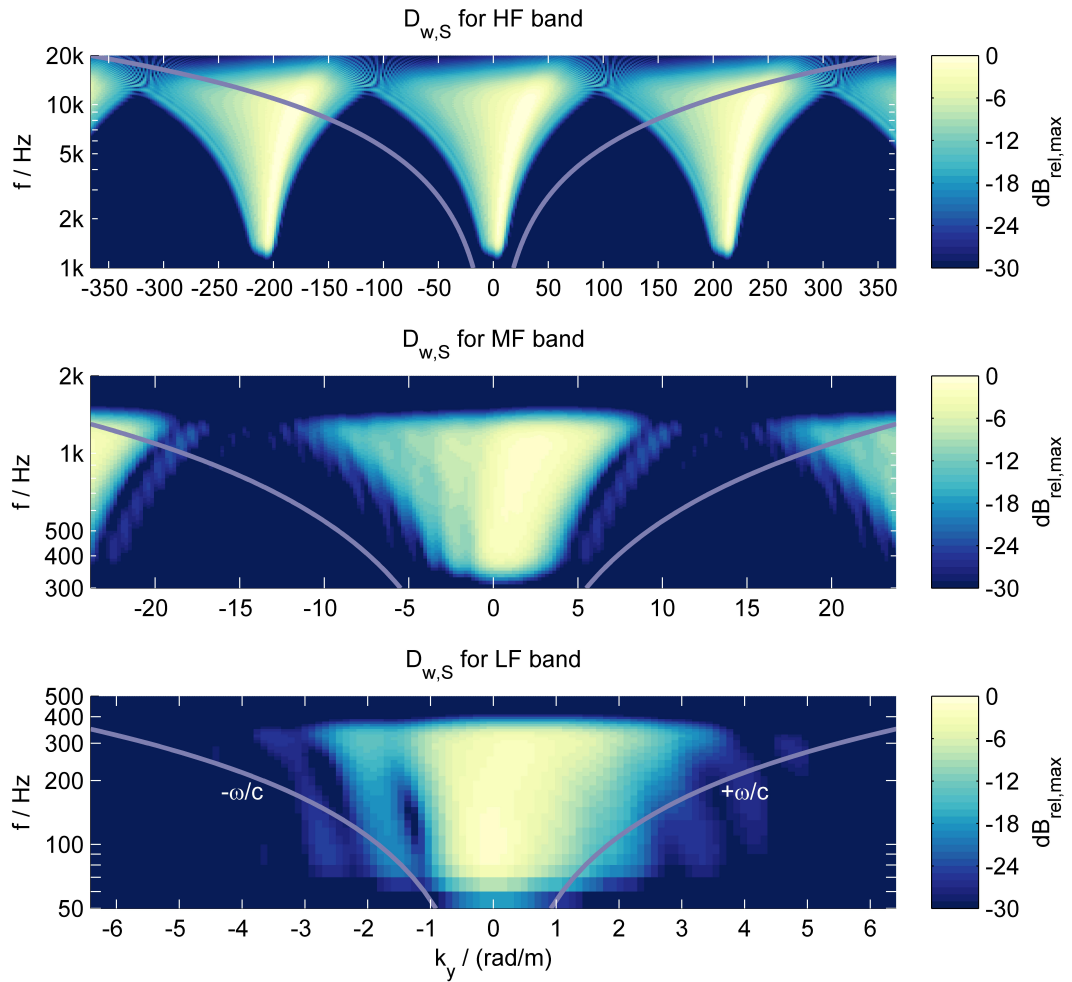


Figure 4.46: LSA_K1_Design8: $D_{w,S}(k_y, \omega)$, cf. Table 3.1.

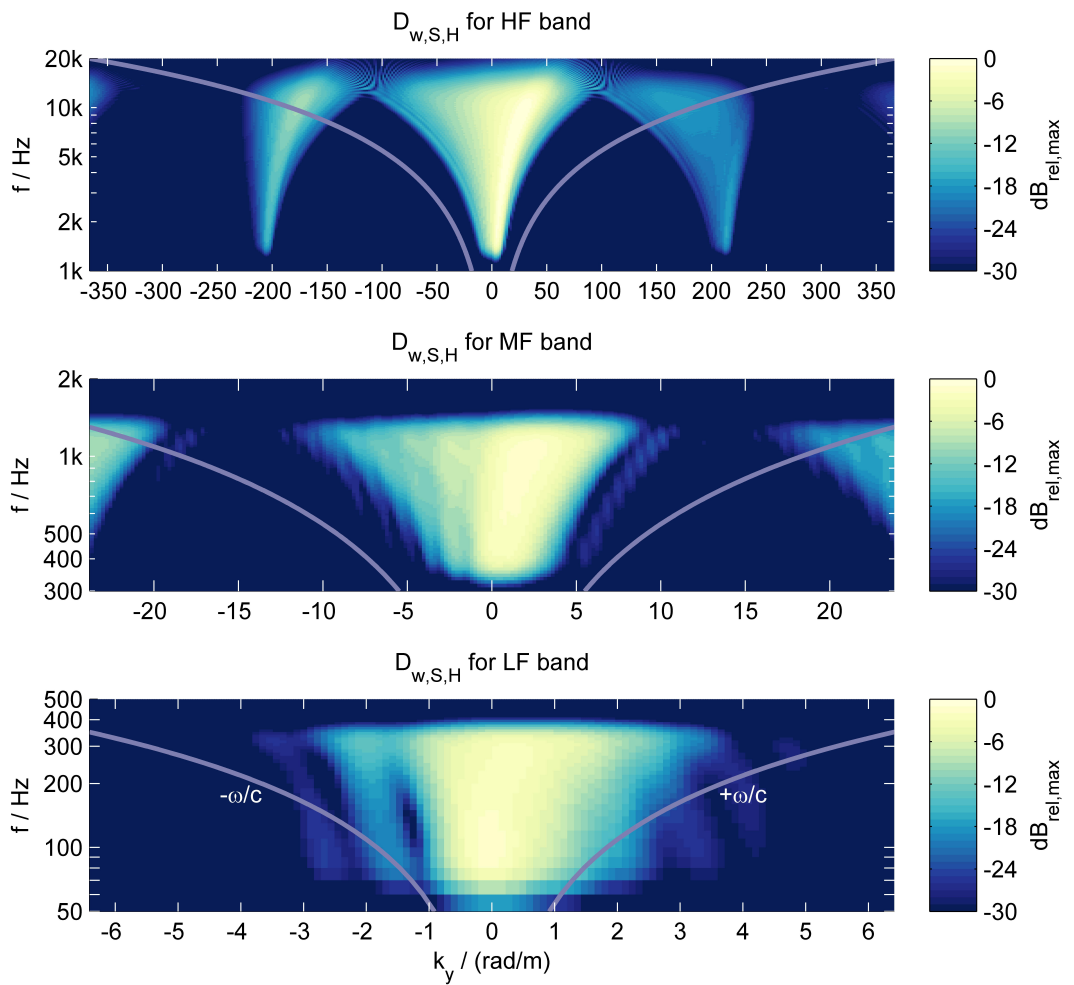


Figure 4.47: LSA_K1_Design8: $D_{w,S,H}(k_y, \omega)$, cf. Table 3.1.

4.5 Summary

This chapter discussed different control methods for optimized LS-SR using LSAs. It was shown that the LS-SR problem could also be interpreted as an SFS problem, rather than a radiation synthesis problem. While radiation synthesis is concerned with optimized FRPs, SFS of a virtual source allows for adapting the radiation characteristic of an LSA for a given venue geometry. This was shown by means of a straightforward WFS driving method using a virtual point source with a farfield directivity pattern. It can be concluded that approaching the LS-SR with WST can be interpreted as a special case of SFS using curving and gain shading of the array in its initial formulation.

Regardless of the specific LSA curving and electronic control the main goal of optimized LS-SR is an appropriate wavefront shaping in order that the main lobe beam covering the audience becomes frequency independent with a desired homogeneous SPL loss over the audience. For that it is very important realizing that a 'smoother' driving function (e.g. $D_{w,S,H}(k_y, \omega)$ in case of a straight array) inherently results in a 'smoother', more homogenous pressure field. This implies that if the desired wavefront starts to radiate from the array without any artifacts (introduced by spatial aliasing and windowing) the sound field remains uncorrupted within space. To achieve these objectives with electronic control by delays – such as with the proposed WFS approach – a small spatial discretization of the LSA's HF band is required.

With WFS of a virtual point source's FRP any physical meaningful sound field distribution over the audience can be achieved, once a suitable point source position is determined for a given LSA/venue setup. It is shown, that the virtual point source's sound field can be synthesized independently from the actual array curving within the limits of aliasing free beam steering. This was also reported in [Tho11]. If spatial aliasing cannot be avoided, optimal array curving helps to increase the spatial aliasing cutoff frequency or more precisely to enhance the postfiltering of grating lobes and thus to improve the homogeneity of the sound field. Hence, an optimal LSA design would utilize highest feasible spatial sampling of the HF and MF band drivers and would additionally allow curving.

Chapter 5

Conclusion

Large-scale sound reinforcement (LS-SR) for large audiences in large venues is nowadays mostly realized with line source arrays (LSAs). LSAs were introduced with the Wavefront Sculpture Technology (WST) in the early 1990s aiming at sound fields with less spatial aliasing in the full audio bandwidth than using conventional clustered loudspeaker arrays.

In this thesis the LS-SR problem is treated as a sound field synthesis (SFS) problem aiming at creating a homogeneous wavefront as best as possible that is adapted for the required audience coverage. For that it is meaningful to introduce a virtual point source with a complex farfield radiation pattern which is to be synthesized with an LSA. This can be realized with Wave Field Synthesis (WFS) also introduced in the early 1990s, which is the implicit solution of the SFS problem. WFS is strongly linked to diffraction theories and the high frequency boundary element method and constitutes the farfield/high frequency approximation of the explicit SFS solution.

How well the homogeneous wavefront can be synthesized with an LSA is one of the key questions of the WST and herein. In this thesis WST is reconsidered with a consistent treatment of the SFS problem within an acoustic signal processing model, that includes spatial truncation and sampling and pre- as well as postfiltering of the LSA's driving function. For straight arrays this model can be conveniently interpreted within the spatio-temporal Fourier spectrum domain. This reveals that the introduced WST criteria for straight arrays essentially originate from array processing fundamentals. With the involved spatio-temporal Fourier spectra of the 3D freefield Green's function and

the LSA's driving function, angular spectrum synthesis of sound fields rather than Rayleigh integral synthesis is feasible. This allows for a more convenient interpretation and classification of occurring diffraction and interference phenomena. Furthermore, WST can be interpreted as a special case of SFS.

The homogeneous wavefront for optimum LS-SR constitutes the main lobe of the LSA in the farfield. This wavefront can be corrupted by interference with additional wavefronts that originate from spatial truncation and spatial sampling. These then constitute the side and grating lobes in the farfield. Obviously these wavefronts/lobes should be avoided as much as possible. If full electronic control without spatial aliasing within the array's visible region is aimed at, the spatial sampling theorem must be fulfilled. This then allows beamforming and steering towards the desired wavefront shaping with a high degree of freedom within the physical limits of the array size. If the spatial sampling theorem cannot be met, the postfilter characteristics of highly directed loudspeakers suppress spatial aliasing. This is frequently realized with waveguides for the high audio frequencies in LSA designs. The desired wavefront shaping must then be realized with geometric array curving and beamforming with indeed frequency dependent, but real gain values.

Further specific conclusions are given in the summary sections of the individual chapters, treating WFS, WST and wavefront shaping in detail.

5.1 Novelty Aspects

The discussed array processing on line source arrays is in principle well understood, essentially dealing with interferences of waves. Naturally, in this thesis no new physics is created, but rather illuminating details are examined that were not given in the context of line source array research so far. For that it appeared meaningful to embed these details in the fundamentals on line array theory and sound field synthesis by providing a comprehensive manuscript. It is worth summarizing the discussed aspects that can be considered novel in this thesis. In particular the following results could not be traced in other literature or remained uncompleted:

- The directional derivative of the Green's function in the Helmholtz integral equation is performed w.r.t. \mathbf{x}_0 (2.17), not w.r.t. \mathbf{x} , which is often misinterpreted in literature and then corrected with an inverted normal

vector. The correct treatment yields a consistent derivation of diffraction theory and sound field synthesis.

- The identity of 3D SDM (explicit SFS solution by deconvolution, inverse diffraction) and 3D WFS (implicit solution, forward diffraction) is more precisely derived with the Fourier-Like NAH approach, p.34f. .
- The stationary phase approximations to obtain the 2.5D Neumann Rayleigh integral from its 3D version are consistently connected for the WFS driving functions of a virtual point source (p.51, p.52) and a virtual plane wave (p.61, p.62).
- WFS as the implicit SFS solution constitutes the high/farfield approximation of SDM as the explicit SFS solution. This is consistently shown for the virtual point source and the virtual plane wave, Table 2.1.
- The derivation of WFS from the 2D Neumann Rayleigh integral towards the 2.5D version is only correct for a virtual plane wave (2.186). For all other 3D source types this yields considerable deviations from the correct solution, as shown for the virtual point source (2.146).
- The analytic impulse response of the WFS prefilter interpreted as a half-derivative filter is derived that is suitable for an FIR design Ch. 2.5. Furthermore, analytic IIR approximations of the half-derivative and half-integral filters are given, p.177ff. .
- A complete itemization of propagating and evanescent pre- and postaliasing using linear, discretized arrays is given, Table 3.5.
- The so called Wavefront Sculpture Technology for straight arrays is consistently treated within the spatio-temporal spectrum domain. It turns out that this approach reconsiders the fundamentals of array processing, Table 3.1.
- The treatment within the spatio-temporal spectrum domain allows for so called angular spectrum synthesis of sound fields using a straight array. The given examples for on-axis sound field synthesis and the separate main lobe and side lobes synthesis allows for convenient interpretation of the interference and diffraction phenomena, p.99ff., p.115ff. .

- The on-axis sound field synthesis with the angular spectrum is compared to the Fresnel diffraction approach for uniformly driven, straight arrays allowing for different interpretations of the interference phenomena, p.105f. .
- The line piston acts as an ideal reconstruction filter for a uniformly driven array that exhibits no gaps between the piston, modeling a quasi-continuous array, Ch. 3.3.
- The connection of the gaps between adjacent line or circular pistons and the resulting grating lobe level (known as the ARF theorem) is consistently derived within the angular spectrum domain, Ch. 3.4.1.
- The characteristics of a line piston that exhibits a certain wavefront curvature is discussed as a sound field synthesis problem treated in the angular spectrum domain. Furthermore, the interaction of multiple waveguides per loudspeaker cabinet is discussed by application of the product theorem for nested arrays, Ch. 3.4.3.
- The characteristics and impact of grating and side lobes in the farfield radiation pattern and in the on-axis sound field is compared for the straight array and arc shaped array, Ch. 4.1.2
- Additional included electro-acoustic parameters allows for the prediction of sound fields synthesized from loudspeaker arrays w.r.t. the actually achieved sound pressure levels, Ch. 4.2.
- A WFS driving function for a virtual point source with a directivity adapted to the audience is derived, p.203ff. With that optimized LS-SR is achieved with a wavefront that ideally exhibits no grating and side lobes. This allows for interpreting the LS-SR problem as a sound field synthesis problem, where a virtual source adapted for optimum audience coverage is to be synthesized with a line source array.
- The Matlab-based *Line Source Array Prediction Toolbox* for the prediction of 2D sound fields generated by line source arrays is provided as open-source software for research on optimal LSA control methods.

5.2 Outlook

WST for straight arrays and WFS are well understood nowadays. However, for curved, discretized arrays the evolvement of grating lobes could be more conveniently interpreted, when the proposed acoustic signal processing model can be derived within a coordinate system, for which an eigenmode expansion of the wave equation is possible and where the curved array matches an inherent axis, such as the prolate spheroidal or elliptic cylindrical coordinate system. This would allow for interpreting the spatio-temporal spectra of the (reconstructed) driving function and consequently also an explicit SFS solution for optimized LS-SR could be derived. Furthermore, the role of the postfilter could be better specified and its optimum characteristics for curved arrays could be derived. This is not yet undertaken in SFS and LSA research and should be checked for feasibility.

Since most LSA manufacturers use proprietary control methods a technical and perceptual comparison of suitable methods within a consistent framework should be provided. For that the presented open-source toolbox could be extended with numerical optimization schemes for different beamforming and -steering, as well as gain shading control methods. Currently, this is being pursued by Florian Straube at TU Berlin under the author's supervision.

The WST driving function for a virtual point source with directivity that realizes the audience adapted wavefront shaping could be further improved. An appropriate position for optimized LS-SR was found by trial and error within the thesis. It is desirable to calculate an optimum position by considering the occurring diffraction and wavefront shaping limitations. Furthermore, the spatial window characteristics of the virtual point source directivity and its interpolation could be further optimized for improved non-audience non-coverage and reduced side lobes.

Commercially available sound field prediction software still requires too much time to render results, that provide the full picture of the LS-SR performance. For optimum LS-SR, the user/software interaction should be ideally real-time capable. This allows for faster reiterating adjustments and thus for a more convenient interpretation of occurring phenomena when changing parameters. Potentially faster rendering kernels and rendering hardware could

be initially evaluated in research. This becomes even more significant when not only freefield conditions but also room acoustics is to be simulated.

Appendix A

Abbreviations and Acronyms

AES	Audio Engineering Society
AIR	acoustic impulse response
ARF	active radiating factor
ASCII	American Standard Code for Information Interchange
ATF	acoustic transfer function
BW	beamwidth
CBT	constant beamwidth transducer
CDPS	complex-directivity point source (model)
DDC	digital directivity control
DDS	digital directivity synthesis
DFIP	driving function index plot
DFT	discrete Fourier transform
DSB	delay-and-sum beamformer / delay-and-sum beamforming
DSP	digital signal processor / digital signal processing
DGRC	digital and geometric radiation controlled (array)
DTFT	discrete-time Fourier transform
FAP	frequency responses of all audience positions
FFT	fast Fourier transform
FIR	finite impulse response
Fourier-NAH	Fourier transform-based near-field acoustical holography
FRP	farfield radiation pattern
GLL	generic loudspeaker library
HF	high frequency (band for audio signals)

HF-BEM	high frequency boundary element method
HIE	Helmholtz-Integral equation
IAP	impulse responses of all audience positions
IIR	infinite impulse response
IR	impulse response
KHI	Kirchhoff-Helmholtz Integral
LA	line array
LF	low frequency (band for audio signals)
LSA	line source array
LSAPT	Line Source Array Prediction Toolbox
LS-SR	large-scale sound reinforcement
MF	mid frequency (band for audio signals)
NAH	nearfield acoustic holography
NFC-HOA	Nearfield Compensated Higher Order Ambisonics
PA	public address
PIP	position index plot
PPST	Phased Point Source Technology
PS	point source
PW	plane wave
SDM	Spectral Division Method
SFS	sound field synthesis
SLP	single layer potential
SPL	sound pressure level
SSD	secondary source distribution
ULA	uniformly driven line array
WFC	wavefront curvature
WFR	wave field reconstruction
WFS	Wave Field Synthesis
WST	Wavefront Sculpture Technology

Appendix B

Coordinate Systems

This section defines general conventions that are used throughout this thesis. A constant speed of sound $c = 343$ m/s, free-field conditions and a dissipationless medium are assumed. The imaginary number is denoted by j ($j^2 = -1$). The complex conjugate notation $(e^{-j\omega t})^* = e^{+j\omega t}$ is used. The temporal angular frequency $\omega = 2\pi f$ in rad/s is linked to the temporal frequency f in Hz. A position vector in space is given by

$$\mathbf{x} = \begin{pmatrix} x \\ y \\ z \end{pmatrix} = |\mathbf{x}| \cdot \begin{pmatrix} \cos \varphi & \sin \vartheta \\ \sin \varphi & \sin \vartheta \\ & \cos \vartheta \end{pmatrix} \quad (\text{B.1})$$

using the vector norm $|\mathbf{x}| = r = \sqrt{x^2 + y^2 + z^2}$, the azimuth $\varphi \in [0, 2\pi)$ and colatitude $\vartheta \in [0, \pi]$. The wave number vector is given by

$$\mathbf{k} = \begin{pmatrix} k_x \\ k_y \\ k_z \end{pmatrix} = \frac{\omega}{c} \cdot \begin{pmatrix} \cos \varphi & \sin \vartheta \\ \sin \varphi & \sin \vartheta \\ & \cos \vartheta \end{pmatrix}, \quad (\text{B.2})$$

with $\frac{\omega}{c} = \sqrt{\langle \mathbf{k}, \mathbf{k} \rangle}$, denoting the scalar product with $\langle \cdot, \cdot \rangle$. The dispersion relation of linear acoustics

$$\left(\frac{\omega}{c}\right)^2 = k_x^2 + k_y^2 + k_z^2 \quad (\text{B.3})$$

holds.

Appendix C

Fourier Transform Conventions

Multidimensional acoustic signal processing w.r.t. space \mathbf{x} and time t can be performed with different conventions, cf. [Tou15]. The used conventions are shortly summarized here. Functions in space and/or time are denoted with small letters. If a Fourier transform is performed the corresponding spectrum is denoted with an uppercase letter specifying the transformation domain in the argument. The Fourier transform convention with respect to time

$$p(\mathbf{x}, t) = \mathcal{F}_t^{-1} \{P(\mathbf{x}, \omega)\} = \frac{1}{2\pi} \int_{-\infty}^{+\infty} P(\mathbf{x}, \omega) e^{+j\omega t} d\omega, \quad (\text{C.1})$$

$$P(\mathbf{x}, \omega) = \mathcal{F}_t \{p(\mathbf{x}, t)\} = \int_{-\infty}^{+\infty} p(\mathbf{x}, t) e^{-j\omega t} dt \quad (\text{C.2})$$

is used for the relationship of the sound pressure $p(\mathbf{x}, t)$ and its temporal spectrum $P(\mathbf{x}, \omega)$ using the temporal angular frequency ω . The Fourier transform convention with respect to space, here exemplarily given for the spatial coordinate $y \circ \bullet k_y$

$$p(y, t) = \mathcal{F}_y^{-1} \{P(k_y, t)\} = \frac{1}{2\pi} \int_{-\infty}^{+\infty} P(k_y, t) e^{-jk_y y} dk_y, \quad (\text{C.3})$$

$$P(k_y, t) = \mathcal{F}_y \{p(y, t)\} = \int_{-\infty}^{+\infty} p(y, t) e^{+jk_y y} dy \quad (\text{C.4})$$

is used for the relationship of the sound pressure $p(y, t)$ and its spatial spectrum $P(k_y, t)$ using the spatial angular frequency (wave number) k_y .

A double Fourier transform pair

$$p(y, t) = \frac{1}{4\pi^2} \iint_{-\infty}^{+\infty} P(k_y, \omega) e^{-jk_y y} e^{+j\omega t} d\omega dk_y, \quad (\text{C.5})$$

$$P(k_y, \omega) = \iint_{-\infty}^{+\infty} p(y, t) e^{+jk_y y} e^{-j\omega t} dt dy \quad (\text{C.6})$$

yields the relationship between the sound pressure $p(y, t)$ and its spatio-temporal spectrum $P(k_y, \omega)$. The thesis frequently uses

$$P(x, k_y, k_z, \omega) = \mathcal{F}_y \{ \mathcal{F}_z \{ \mathcal{F}_t \{ p(\mathbf{x}, t) \} \} \} \quad (\text{C.7})$$

for the description of the spatio-temporal spectrum w.r.t. ω , k_y and k_z in 3D problems and

$$P(x, k_y, z, \omega) = \mathcal{F}_y \{ \mathcal{F}_t \{ p(\mathbf{x}, t) \} \} \quad (\text{C.8})$$

for the description of the spatio-temporal spectrum w.r.t ω and k_y in 2D and 2.5D problems.

The used conventions imply that the wave number vector $\mathbf{k} = (k_x, k_y, k_z)^T$ denotes the propagation direction of a plane wave. The dispersion relation $(\frac{\omega}{c})^2 = k_x^2 + k_y^2 + k_z^2$ and the scalar product notation $\langle \mathbf{k}, \mathbf{x} \rangle = k_x x + k_y y + k_z z$ are used for the description of plane waves in cartesian coordinates. Therefore,

$$p(\mathbf{x}, t) = \Re \{ e^{-j\langle \mathbf{k}_{PW}, \mathbf{x} \rangle} e^{+j\omega_{PW} t} \} \quad (\text{C.9})$$

describes a monochromatic, unit amplitude plane wave that propagates into direction of \mathbf{k}_{PW} and oscillates with ω_{PW} .

The used convention implicates the properties w.r.t. the shift and modulation theorem for the Fourier transform pairs

$$x(t) \circ \text{---} \bullet X(\omega) \quad \text{and} \quad d(y) \circ \text{---} \bullet D(k_y) :$$

Temporal Delay / Spatial Shift

$$\delta(y - y_0) \circ \bullet e^{+j k_y y_0} \quad (\text{C.10})$$

$$d(y - y_0) \circ \bullet e^{+j k_y y_0} \cdot D(k_y) \quad (\text{C.11})$$

$$\delta(t - \tau) \circ \bullet e^{-j \omega \tau} \quad (\text{C.12})$$

$$x(t - \tau) \circ \bullet e^{-j \omega \tau} \cdot X(\omega) \quad (\text{C.13})$$

Modulation

$$e^{-j k_0 y} \circ \bullet 2 \pi \delta(k_y - k_0) \quad (\text{C.14})$$

$$e^{-j k_0 y} D(y) \circ \bullet D(k_y - k_0) \quad (\text{C.15})$$

$$e^{j \omega_0 t} \circ \bullet 2 \pi \delta(\omega - \omega_0) \quad (\text{C.16})$$

$$e^{j \omega_0 t} \cdot x(t) \circ \bullet X(\omega - \omega_0) \quad (\text{C.17})$$

Appendix D

Piston Diffraction Theory

In [Hei92b] a detailed treatment on diffraction characteristics for the simple piston types, the circular and the line piston is provided. This was given as a prerequisite to explain spatial aliasing artifacts of straight, linear arrays built from these pistons. It appears meaningful to revisit the most important results of the diffraction theory, since these models are used in this thesis as well.

D.1 Circular Piston

The baffled circular piston with radius r_0 or diameter $d_0 = 2r_0$, respectively under constant volume acceleration or constant velocity over the piston's diaphragm is considered as a very simple model of loudspeakers. The subsections deal with the description of the on-axis pressure characteristics, the farfield radiation pattern and its Fresnel/Fraunhofer (near-/farfield) transition.

D.1.1 On-Axis Pressure

Consider the baffled circular piston symmetrical to the origin within the yz -plane – as also used in Ch. 3 – denoting positions within the plane as $\mathbf{x}_0 = (0, y_0, z_0)^T$ with a velocity spectrum

$$V_n(r, \omega) = \begin{cases} \frac{1}{j \varrho_0 \omega \pi r_0^2} & \text{for } r = \sqrt{y_0^2 + z_0^2} \leq r_0 \\ 0 & \text{for } r = \sqrt{y_0^2 + z_0^2} > r_0. \end{cases} \quad (\text{D.1})$$

This models a piston under constant volume acceleration (cf. [Hei92b, (2)]) using an energy spread of the spatial dirac impulse over the piston's surface [Ste29, Hec77]. The on-axis sound pressure (on x -axis, $x > 0$) can be de-

rived analytically from the Neumann Rayleigh integral (2.69) or the Neumann Rayleigh-Sommerfeld diffraction integral (2.85) to (cf. [Mö09, (3.65)])

$$P(x, \omega) = \frac{1}{\pi r_0^2} \frac{1}{j \frac{\omega}{c}} e^{-j \frac{\omega}{c} x} \left(1 - e^{-j \frac{\omega}{c} (\sqrt{r_0^2 + x^2} - x)} \right), \quad (\text{D.2})$$

or rewritten as (cf. [Kin00, (7.4.5)], [Ler09, (6.104)], [Bla00, (13.C-4)])

$$P(x, \omega) = \frac{1}{\pi r_0^2} \frac{2}{\frac{\omega}{c}} \sin \left(\frac{\omega}{2c} (\sqrt{r_0^2 + x^2} - x) \right) \cdot e^{-j \frac{\omega}{2c} (\sqrt{r_0^2 + x^2} + x)}, \quad (\text{D.3})$$

respectively, cf. [Hei92b, Sec. I.2.b].

Fresnel region

Since (D.2) and (D.3) are exact solutions, a Fresnel approximation as simplification of the Neumann Rayleigh integral is not required and the on-axis characteristics of the Fresnel region can be discussed directly.

In the Fresnel region of the piston – if existing – the sound pressure level may fluctuate between $-\infty$ dB (nodes) and +6 dB (antinodes), when the $\frac{1}{\pi r_0^2} \frac{1}{\frac{\omega}{c}}$ dependency of (D.2) and (D.3) is omitted in the discussion.

Nodes occur at x_Z , if the bracket term of (D.2) or the sin-function of (D.3), respectively becomes zero. That is for (cf. [Mö09, p.107], [Hei92b, (3)])

$$m 2 \pi = \frac{\omega}{c} (\sqrt{r_0^2 + x_Z^2} - x_Z) \quad m \in \mathbb{N}, \neq 0, \quad (\text{D.4})$$

leading to (cf. [Mö09, (3.66)])

$$\frac{x_Z}{\lambda} = \frac{\frac{r_0^2}{\lambda^2} - m^2}{2m} \quad \text{for all } m \text{ that lead to } \frac{x_Z}{\lambda} \geq 0 \quad (\text{D.5})$$

or rewritten as (cf. [Ler09, (6.106)])

$$x_Z = \frac{1}{4\pi} \frac{\left(\frac{\omega}{c} r_0\right)^2 - (2\pi m)^2}{\frac{\omega}{c} m} \quad \text{for all } m \text{ that lead to } x_Z \geq 0. \quad (\text{D.6})$$

The farthest node away from the piston– if existing – results for $m = 1$ (cf. [Kin00, (7.4.11)], [Mö09, (3.67)], [Hei92b, (4)])

$$\frac{x_{Z,\max}}{\lambda} = \frac{r_0^2}{\lambda^2} - 1 \qquad x_{Z,\max} = \frac{1}{4\pi} \frac{\left(\frac{\omega}{c} r_0\right)^2 - 4\pi^2}{\frac{\omega}{c}}. \quad (\text{D.7})$$

No nodes occur for $\lambda > r_0$, indicating the absence of a typical Fresnel region.

The farthest antinode at x_P away from the piston– if existing – is obtained when

$$\frac{\pi}{2} = \frac{\omega}{2c} \left(\sqrt{r_0^2 + x_{P,\max}^2} - x_{P,\max} \right) \quad (\text{D.8})$$

yielding (cf. [Kin00, (7.4.10)])

$$\frac{x_{P,\max}}{\lambda} = \frac{r_0^2}{\lambda^2} - \frac{1}{4} \qquad x_{P,\max} = \frac{1}{2\pi} \frac{\left(\frac{\omega}{c} r_0\right)^2 - \pi^2}{\frac{\omega}{c}}, \quad (\text{D.9})$$

which is valid for cases $\frac{r_0}{\lambda} > \frac{1}{2}$ only. This is equivalent to one possible Fresnel/Fraunhofer transition border definition

$$x_{B,\text{Fresnel}} = \frac{r_0^2}{\lambda} - \frac{\lambda}{4}, \quad \text{no Fresnel region for } d_0 < \lambda \quad (\text{D.10})$$

$$= \frac{1}{4} \frac{f d_0^2}{c} \left(1 - \frac{1}{\left(\frac{f d_0}{c}\right)^2} \right), \quad \text{no Fresnel region for } \frac{f}{c} < \frac{1}{d_0} \quad (\text{D.11})$$

derived from the Fresnel zones approach in [Hei92b, I.2.c].

For $\frac{r_0}{\lambda} < \frac{1}{2}$ and $x \ll r_0$ the sound pressure can be approximated from (D.3) to

$$P(x, \omega) = \frac{1}{\pi^2 r_0^2} \lambda \sin\left(\frac{\pi}{\lambda} r_0\right) e^{-j \frac{\omega}{2c} (\sqrt{r_0^2 + x^2} + x)}, \quad (\text{D.12})$$

indicating a constant pressure level for $x \ll r_0$ dependent on the weighting factor that includes λ and r_0 . Note that this weighting factor does not follow a simple rule due to the sin-function.

Another common Fresnel/Fraunhofer transition distance definition and thereby farfield condition can be derived from the second equation in (D.9). For reasonable large temporal frequencies the term $\pi^2/(2\pi \frac{\omega}{c})$ is negligible compared

to the remainder and the farfield condition reads (cf. [Mö09, (3.68)])

$$x_{\text{B,Far}} > \frac{1}{2\pi} \frac{(\frac{\omega}{c} r_0)^2}{\frac{\omega}{c}} \rightarrow x_{\text{B,Far}} > \frac{r_0^2}{\lambda} \quad (\text{D.13})$$

if $\frac{r_0}{\lambda} > \frac{1}{2}$ is fulfilled. Note that this is similar to the Fraunhofer validity condition (2.106), which can be linked to the Fresnel number [Bor06, Ch. 8.2 (18)]

$$N_F = \frac{r_0^2}{\lambda x_B} = 1 \quad (\text{D.14})$$

The Fresnel number indicates Fraunhofer diffraction for $N_F \ll 1$ and Fresnel diffraction for $N_F \gg 1$. In Fig. D.1 the level decay and frequency response of a circular piston with $d_0 = 0.5$ m exemplarily indicates the discussed characteristics of the Fresnel region.

Fraunhofer region

For

$$\begin{cases} x > x_{\text{B,Fresnel}}, x > x_{\text{B,Far}} & \text{if } \frac{r_0}{\lambda} > \frac{1}{2} \\ x > r_0 & \text{if } \frac{r_0}{\lambda} \leq \frac{1}{2} \end{cases} \quad (\text{D.15})$$

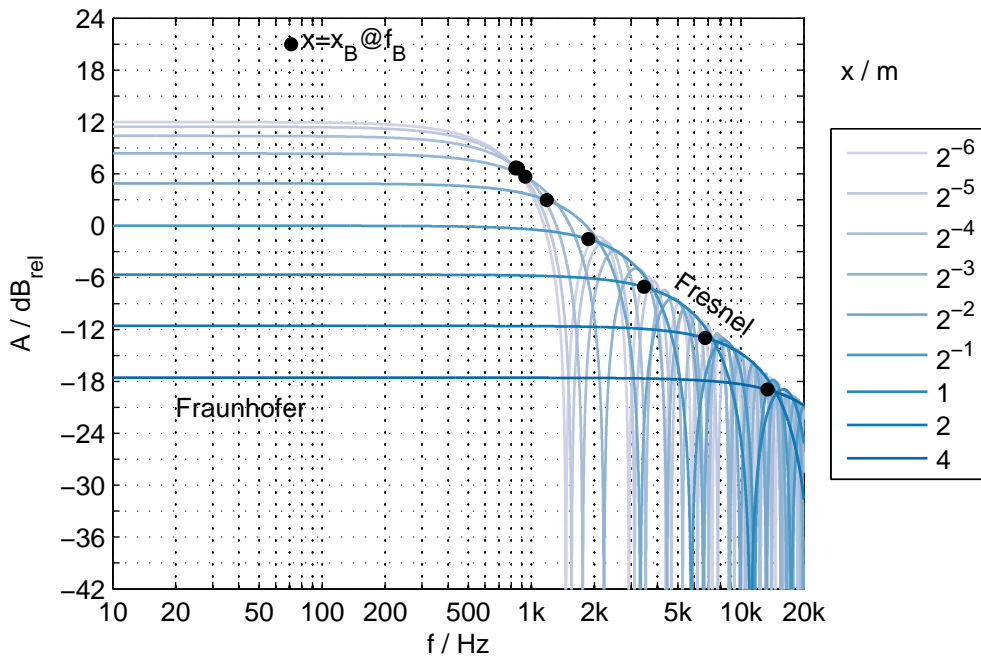
the sound pressure exhibits the typical asymptotic characteristics of a 6 dB level decay per distance doubling. This indicates the Fraunhofer region where no pressure nodes and antinodes are observed anymore.

Applying the first condition for Fraunhofer region validity $x \gg r_0$ (cf. (2.104)) on (D.2) using the Taylor series expansion $\sqrt{x^2 + r_0^2} \approx x + \frac{r_0^2}{2x}$ leads to

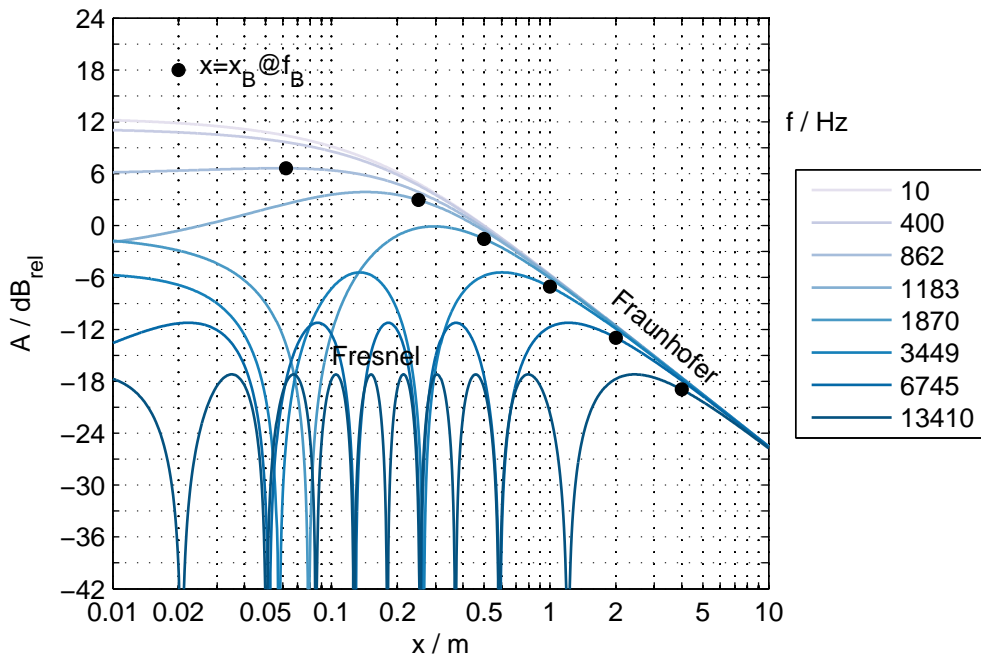
$$P(x, \omega) = \frac{1}{\pi r_0^2} \frac{1}{j \frac{\omega}{c}} e^{-j \frac{\omega}{c} x} \left(1 - e^{-j \frac{\pi r_0^2}{\lambda} \frac{1}{x}} \right). \quad (\text{D.16})$$

Setting the term $\frac{\pi r_0^2}{\lambda} \frac{1}{x} = 1$ in the exp-function of (D.16) reveals the so called Rayleigh distance or Rayleigh length of a circular piston (cf. [Kin00, p.180], [Bla00, p.448])

$$x_{\text{B,Rayleigh}} = \frac{\pi r_0^2}{\lambda} \rightarrow N_F = \frac{1}{\pi} \quad (\text{D.17})$$



(a) Relative frequency responses indicating the Fresnel-/Fraunhofer transition distance x_B (D.44). 0 dB normalization to $x = 0.5 \text{ m}$ and $f = 10 \text{ Hz}$.



(b) Relative pressure level for Fig. D.1a. Some chosen temporal frequencies correspond to $x_B | f_B$ pairs of Fig. D.1a. 0 dB normalization to $x = 0.5 \text{ m}$ and $f = 10 \text{ Hz}$.

Figure D.1: Baffled circular piston with constant volume acceleration on main axis (D.2). Diameter $d_0 = 0.5 \text{ m}$, $c = 343 \text{ m/s}$.

as a further possible definition of the Fresnel/Fraunhofer transition border. Using this or $r_0^2 \ll \lambda x$ from (D.13) and the Taylor series expansion $e^{-j\alpha} \approx 1 - j\alpha$ yields

$$P(x, \omega) = \frac{e^{-j\frac{\omega}{c}x}}{2\pi x}, \quad (\text{D.18})$$

which is identified as the on-axis sound pressure characteristic of the Neumann Green's function, i.e. a baffled spherical monopole with temporal frequency independent 6 dB level decay per distance doubling. In Fig. D.1 the level decay and frequency response of a circular piston with $d_0 = 0.5$ m exemplarily indicates the discussed characteristics of the Fraunhofer region.

A further possible Fresnel/Fraunhofer transition border can be defined by usage of the so called geometric diffraction approach. Since for that the farfield radiation pattern (Fraunhofer approximation) is required, this will be later discussed in Ch. D.1.3.

D.1.2 Fraunhofer Approximation

The diffraction characteristics and farfield radiation pattern of an ideally baffled circular piston with constant velocity over the diaphragm's surface with radius r_0 is derived by (2.110), which is well documented, e.g. [Ste27], [Ste58, p.7ff.], [Sku71, Ch. 26.9], [Zio95, Ch. 6.5], [Wil99, Ch. 2.11.5], [Bla00, Ch. 13], [Kin00, Ch. 7.4], [Goo05a, Ch. 2.1.5f], [Bor06, Ch. 8.5.2]. It is shortly revisited here following [Hec77, Wil99] using the Fourier-Bessel transform [Bad09] approach.

The position vector $\mathbf{x}_0 = (x_0, y_0, z_0)^T = r(\cos\alpha \sin\beta, \sin\alpha \sin\beta, \cos\beta)^T$ within the SSD generally holds using $0 \leq \alpha < 2\pi$, $0 \leq \beta \leq \pi$. For the moment consider the SSD – and thus the circular piston symmetrical to the origin – within the xy -plane for convenient notation of functions with radial dependence. Then with $\beta = \frac{\pi}{2}$ the positions within the SSD in polar coordinates are denoted as

$$x_0 = r \cos\alpha, \quad y_0 = r \sin\alpha, \quad z_0 = 0, \quad r = \sqrt{x_0^2 + y_0^2}, \quad \tan\alpha = \frac{y_0}{x_0}. \quad (\text{D.19})$$

The dispersion relation of linear acoustics

$$\left(\frac{\omega}{c}\right)^2 = (k_x^2 + k_y^2) + k_z^2 = k_r^2 + k_z^2 \quad (\text{D.20})$$

holds, and a radiation into the half-space w.r.t. the positive z -axis is considered by the possible wave numbers

$$k_z = \begin{cases} +\sqrt{\left(\frac{\omega}{c}\right)^2 - k_r^2} & \text{for } \left(\frac{\omega}{c}\right)^2 > k_r^2 \\ -j\sqrt{k_r^2 - \left(\frac{\omega}{c}\right)^2} & \text{for } k_r^2 > \left(\frac{\omega}{c}\right)^2. \end{cases} \quad (\text{D.21})$$

The spatio-temporal spectrum of the source's normal velocity temporal spectrum is obtained by, cf. p. 43

$$H(k_x, k_y, \omega) = \iint_{-\infty}^{+\infty} V_n(x_0, y_0, \omega) e^{+j k_x x_0} e^{+j k_y y_0} dx_0 dy_0 \quad (\text{D.22})$$

in cartesian coordinates. The spatial Fourier transform is performed over $k_x, k_y \in \mathbb{R}$. Thus, a $k_r \in \mathbb{R}^+$ using $0 \leq \varphi < 2\pi$

$$k_r = \sqrt{k_x^2 + k_y^2}, \quad k_x = k_r \cos \varphi, \quad k_y = k_r \sin \varphi, \quad \tan \varphi = \frac{k_y}{k_x} \quad (\text{D.23})$$

can be defined in general, cf. Fig. D.2. Note that some textbooks here already impose a restriction on k_r for propagating wave radiation only, which at this stage of the discussion is not necessarily required to obtain the spatial Fourier transform (D.22) or equivalently perform the Fourier-Bessel transform in the first instance. Moreover, the spatio-temporal Fourier spectrum over k_x, k_y includes the evanescent part of the diffracted wave field as well [Har79]. The interpretation for propagating waves only yields the farfield radiation pattern then, that most textbooks are interested in.

Inserting (D.19) and (D.23) into (D.22) and changing the integration to

polar coordinates yields

$$H(k_r, \varphi, \omega) = \int_0^{+\infty} \int_0^{+2\pi} V_n(r, \alpha, \omega) e^{+j k_r r \cos(\alpha - \varphi)} r \, d\alpha \, dr. \quad (\text{D.24})$$

With an assumed constant normal velocity over the piston's surface and an ideal sound-hard boundary baffle

$$V_n(r, \alpha, \omega) = \begin{cases} \frac{1}{\pi r_0^2} & \text{for } r \leq r_0 \\ 0 & \text{for } r > r_0, \end{cases} \quad (\text{D.25})$$

(D.24) can be simplified for this radially symmetric function by deploying the integral definition [Gra07, (3.915)] of the Bessel function $J_0(\cdot)$ of first kind of zeroth order [Olv10, §10.2(ii)], yielding

$$H(k_r, \omega) = 2\pi \underbrace{\int_0^{+\infty} V_n(r, \omega) J_0(k_r r) r \, dr}_{\mathbb{H}_0\{f(r)\}}, \quad (\text{D.26})$$

for which the result is equivalent to a 2π -weighted zeroth order Hankel transform, also termed Fourier-Bessel transform $F(k_r) \circ\text{---}\bullet \mathbb{H}_0\{f(r)\}$ [Wil99, Ch. 1.4], [Bad09]. For $V_n(r, \omega) = 1 \circ\text{---}\bullet H(k_x, k_y, \omega) = (2\pi)^2 \delta(k_x) \delta(k_y)$ is obtained as expected, cf. [Bad09, p.1770]. The finite integral of (D.26) for the piston's surface is with (D.25) solved to [Hec77, Table II(1)]

$$H(k_r, \omega) = \frac{2}{r_0^2} \int_0^{+r_0} J_0(k_r r) r \, dr = 2 \frac{J_1(k_r r_0)}{k_r r_0} \quad (\text{D.27})$$

$$(\text{D.28})$$

using derivative theorems on Bessel functions [Olv10, Ch. 10.6(ii)] and the Bessel function $J_1(\cdot)$ of first kind of first order [Olv10, §10.2(ii)].

The wave number vector $\mathbf{k} = (k_x, k_y, k_z)^T = \frac{\omega}{c} (\cos \varphi \sin \vartheta, \sin \varphi \sin \vartheta, \cos \vartheta)^T$ for propagating waves with the general angle definition $0 \leq \varphi < 2\pi$, $0 \leq \vartheta \leq \pi$

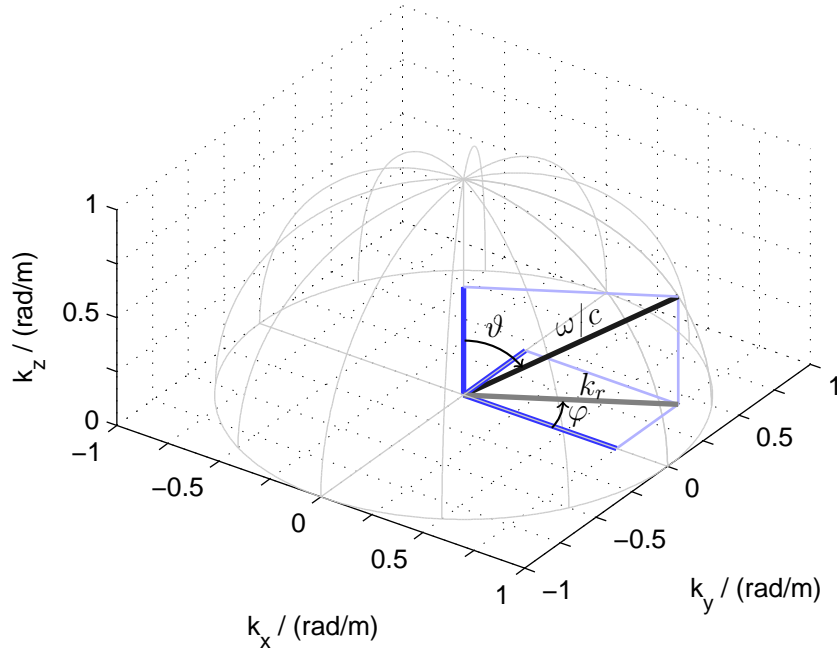


Figure D.2: Dispersion relation for propagating waves using Ewald sphere, $k_r = \sqrt{k_x^2 + k_y^2}$, $k_x = k_r \cos \varphi$, $k_y = k_r \sin \varphi$, $k_z = \frac{\omega}{c} \cos \vartheta$, $k_r = \frac{\omega}{c} \sin \vartheta$, $\frac{\omega}{c} = \sqrt{k_r^2 + k_z^2}$. Example for: $\varphi = 30^\circ$, $\vartheta = 60^\circ$, $\frac{\omega}{c} = 1 \text{ rad/m}$.

leads to

$$k_r = \frac{\omega}{c} \sqrt{\cos^2 \varphi \sin^2 \vartheta + \sin^2 \varphi \sin^2 \vartheta} = \frac{\omega}{c} \sin \vartheta, \quad (\text{D.29})$$

canceling out the φ -dependency. Since only wave radiation into the positive z -axis is considered by (D.21), the radiation angle $0 \leq \vartheta \leq \pi/2$ w.r.t. to the piston's normal axis z is allowed that exclusively defines the radiation direction within the $z > 0$ half space of interest, cf. Fig. D.2. The farfield radiation pattern – rotationally symmetric w.r.t. the z -axis, cf. [Wil99, Fig. 2.19] – is thus given as

$$H(\vartheta, \omega) = 2 \frac{J_1\left(\frac{\omega}{c} \sin \vartheta r_0\right)}{\frac{\omega}{c} \sin \vartheta r_0} \quad 0 \leq \vartheta \leq \pi/2. \quad (\text{D.30})$$

It is common practice to evaluate the FRP in terms of normalized variables

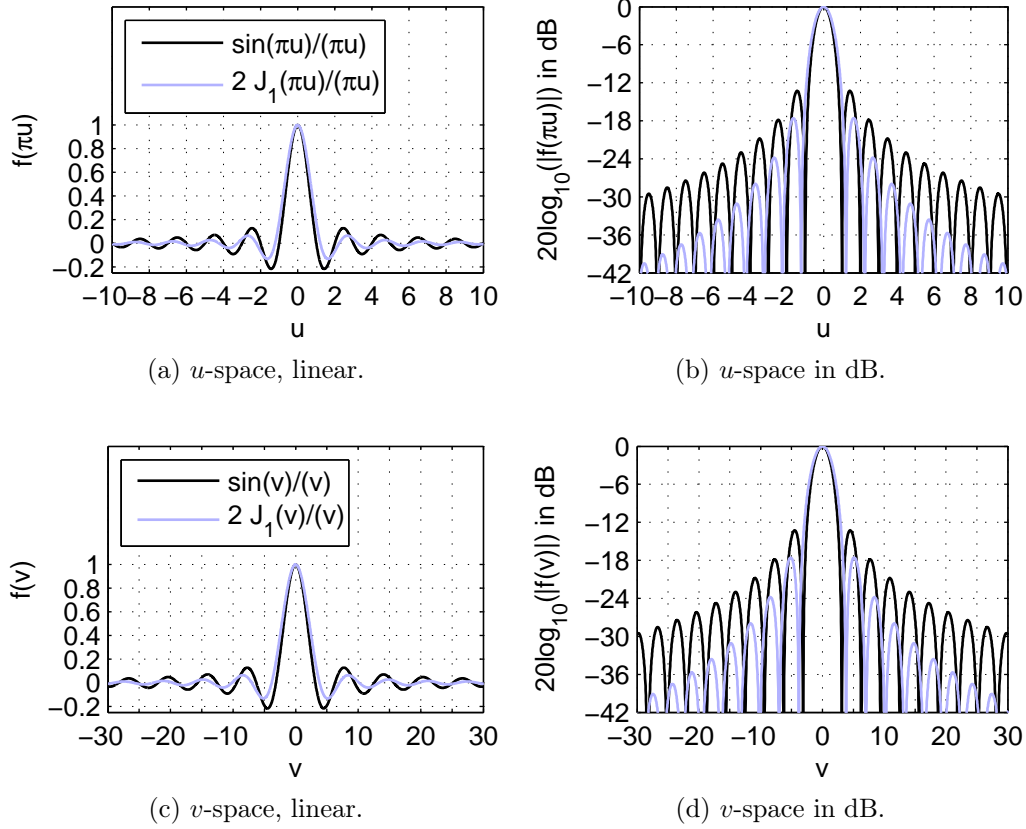


Figure D.3: Jinc function for circular piston, sinc function for line piston.

u or v , leading to the functions, cf. Fig. D.3

$$H(u) = 2 \frac{J_1(\pi u)}{\pi u} \qquad H(v) = 2 \frac{J_1(v)}{v}, \qquad (\text{D.31})$$

that are known as *sombrero function*, *besinc function* or *jinc function* [Goo05a, p.15]. The u -space version is termed *universal function* in [Hei92b, p.4] where the factor 2 was omitted. Note that similar to the sinc function there is no unique terminology if the argument normalized to πu or just to v is deployed. The variable substitution is given as

$$\frac{\omega}{c} r_0 \sin \vartheta = \pi \left(\frac{2 r_0}{\lambda} \sin \vartheta \right) = \pi u \qquad (\text{D.32})$$

$$\frac{\omega}{c} r_0 \sin \vartheta = \frac{2 \pi}{\lambda} r_0 \sin \vartheta = v. \qquad (\text{D.33})$$

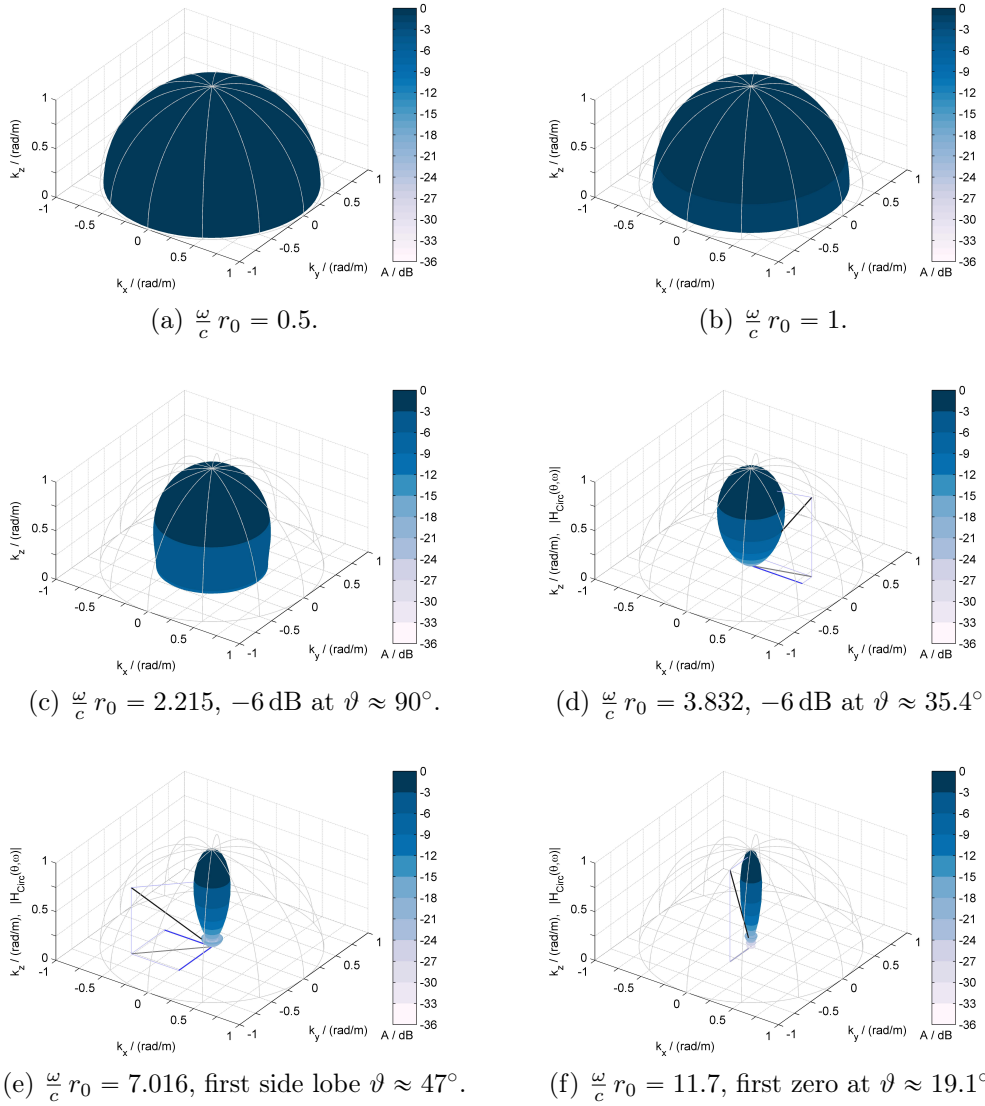


Figure D.4: Farfield radiation pattern of circular pistons with $\frac{\omega}{c} = 1$ rad/m (for convenient Ewald sphere visualization, cf. Fig. D.2) and different radii, $c = 343$ m/s, cf. [Kin00, Fig. 7.4.5], [Bor06, Tbl. 8.2].

Since $0 \leq \vartheta \leq \pi/2 \rightarrow 0 \leq \sin \vartheta \leq 1$ the ranges

$$0 \leq u \leq \frac{2r_0}{\lambda} = \frac{d_0}{\lambda} \quad (\text{D.34})$$

$$0 \leq v \leq \frac{2\pi}{\lambda} r_0 = \pi \frac{d_0}{\lambda} = \frac{\omega}{c} r_0 \quad (\text{D.35})$$

determine radiation wave propagation over angle ϑ . For $\frac{\omega}{c} r_0 \ll 1$ or $\frac{d_0}{\lambda} \ll \frac{1}{3}$ resp. the FRP is half-space omnidirectional, whereas for $\frac{\omega}{c} r_0 \gg 1$ or $\frac{d_0}{\lambda} \gg \frac{1}{3}$ resp. (e.g. increasing the temporal frequency while holding r_0 constant) an increasing amount of side lobes and zeros of the jinc function are mapped to the radiation angles, yielding a more directed FRP, cf. Fig. D.3. For exemplarily chosen $\frac{\omega}{c} r_0$ -values this is depicted in Fig. D.4. To use the Ewald sphere construction as in Fig. D.2, $\frac{\omega}{c} = 1$ rad/m was chosen by varying the piston radius. The beams are plotted linearly as $|H(\vartheta, \omega)|$ (D.30), from which the values on k_z -axis also indicate the attenuation of $|H(\vartheta, \omega)|$. This however holds only values $\frac{\omega}{c} r_0 > 3.8317$, i.e. when at least one zero entered the visible region. The beam color indicates the level $20 \log_{10}(|H(\vartheta, \omega)|)$ in dB over the radiating angle. The Fig. D.4a and Fig. D.4b show undirected, almost half-space omnidirectional FRPs due to rather small $\frac{\omega}{c} r_0$. For Fig. D.4c $\frac{\omega}{c} r_0$ was chosen in order to obtain -6 dB level at $\vartheta = 90^\circ$, while Fig. D.4d shows an FRP where the first zero of the jinc function just entered the visible region at $\vartheta \approx 90^\circ$. Here the -6 dB level is obtained at $\vartheta = 35.4^\circ$, indicated by the Ewald sphere construction of vector \mathbf{k} for an arbitrary chosen φ . By further increasing the piston radius in Fig. D.4e two zeros of the jinc function map into the FRP and one first side lobe with level -17.57 dB appears at about $\vartheta = 47^\circ$. In Fig. D.4f the $\frac{\omega}{c} r_0$ was chosen to have three side lobes ($\vartheta \approx 26, 46, 90^\circ$) and three zeros ($\vartheta \approx 19, 37, 60^\circ$) within the visible region creating the FRP.

When considering a circular piston within the yz -plane and only the xy -plane with $x > 0$ as sound reinforcement region – as later on used here and in Ch. 3 – one may rewrite (D.27) and (D.30) to

$$H(k_y, \omega) = 2 \frac{J_1(k_y r_0)}{k_y r_0} \quad (\text{D.36})$$

and (cf. (2.165))

$$H(\varphi, \omega) = 2 \frac{J_1\left(\frac{\omega}{c} \sin \varphi r_0\right)}{\frac{\omega}{c} \sin \varphi r_0} \quad -\pi/2 \leq \varphi \leq \pi/2, \quad (\text{D.37})$$

respectively, using the fact that with [Olv10, (10.11.1)]

$$\frac{J_1(-\arg)}{-\arg} = \frac{-J_1(\arg)}{-\arg} = \frac{J_1(\arg)}{\arg}. \quad (\text{D.38})$$

D.1.3 Fresnel-/Fraunhofer Transition Distance

With $d_0 = 2r_0$ the FRP of the circular piston is written as

$$H(\varphi, \omega) = 2 \frac{J_1\left(\frac{2\pi}{\lambda} \sin \varphi \frac{d_0}{2}\right)}{\frac{2\pi}{\lambda} \sin \varphi \frac{d_0}{2}} = 2 \frac{J_1\left(\pi \frac{d_0}{\lambda} \sin \varphi\right)}{\pi \frac{d_0}{\lambda} \sin \varphi}. \quad (\text{D.39})$$

If for a chosen wave length λ and radius r_0 at least the first zero¹ of the Bessel function $J_1(\pi \alpha_0) = 0$ is located within the visible region – that is for

$$\alpha_0 \approx 3.8317059702075 \cdot \pi^{-1} = 1.2196698912665, \quad (\text{D.40})$$

[Hei92b] uses $\alpha_0 = 1.24$ – one may find the radiation angle φ_N of that FRP's zero (notch) by

$$\pi \frac{d_0}{\lambda} \sin \varphi_N = \pi \alpha_0 \rightarrow \sin \varphi_N = \alpha_0 \frac{\lambda}{d_0}. \quad (\text{D.41})$$

According to Fig. D.5 the Fresnel-/Fraunhofer distance x_B may be defined

¹<http://keisan.casio.com/exec/system/1180573472>

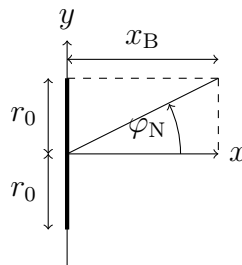


Figure D.5: Fresnel-/Fraunhofer distance x_B of a circular piston within yz -plane with radius r_0 using the half angle opening φ_N , cf. [Hei92b, Fig. 6].

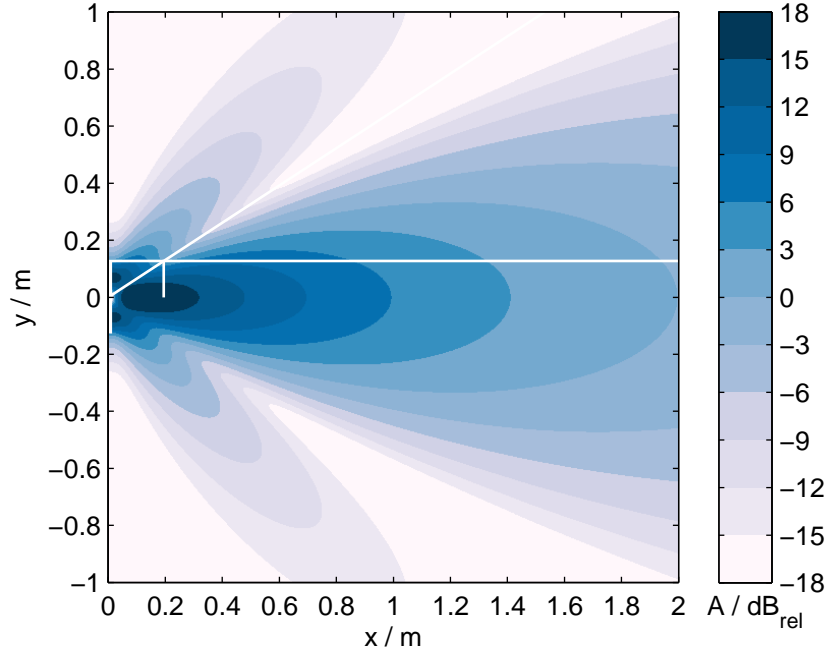


Figure D.6: Radiation of a baffled circular piston within yz -plane with (2.85), $\frac{\omega}{c} r_0 = 7$, $d_0 = 10''$, $c = 343 \text{ m/s}$, $\varphi_N = 33.2^\circ$, $x_B = 0.194 \text{ m}$, 0 dB at $\mathbf{x} = (2, 0, 0)^T$.

with the geometric diffraction approach as (cf. Fig. D.6)

$$\tan \varphi_N = \frac{d_0}{2x_B}. \quad (\text{D.42})$$

Using $\tan \varphi = \frac{\sin \varphi}{\cos \varphi}$ and $\cos \varphi = \sqrt{1 - \sin^2 \varphi}$ yields

$$x_B = \frac{d_0}{2} \frac{\sqrt{1 - \sin^2 \varphi_N}}{\sin \varphi_N} \quad (\text{D.43})$$

and furthermore introducing $\sin \varphi_N$ from (D.41) with $c = \lambda f$

$$x_B = \frac{d_0}{2} \frac{\sqrt{1 - \left(\alpha_0 \frac{\lambda}{d_0}\right)^2}}{\alpha_0 \frac{\lambda}{d_0}} = \frac{1}{2} \frac{d_0^2}{\alpha_0} \frac{f}{c} \sqrt{1 - \frac{\alpha_0^2}{\left(d_0 \frac{f}{c}\right)^2}} \quad (\text{D.44})$$

If $\alpha_0 \frac{\lambda}{d_0} > 1$, $x_B \in \mathbb{C}$ respectively, no Fresnel region exists and the circular piston only radiates a Fraunhofer field for the chosen λ and d_0 . In other words, no zeros exist within the visible region of the FRP. Note that in [Hei92b,

I.2.e] the transition border in meters was given with frequency F in kHz and $c = 333.\bar{3}$ m/s to

$$x_B = \frac{3}{2} \frac{d_0^2}{\alpha_0} F \sqrt{1 - \frac{\alpha_0^2}{9 (d_0 F)^2}} \approx 1.23 d_0^2 F \sqrt{1 - \frac{1}{6.05 (d_0 F)^2}}. \quad (\text{D.45})$$

With [Hei92b, Fig. 13] a schematic sketch of the circular piston's Fresnel/Fraunhofer characteristics was given over frequency and on-axis distance. For typically deployed loudspeaker sizes this is shown in Fig. D.10 by evaluating (D.2) and indicating x_B (D.44). From that it can be concluded that typical listener distances in front of an LSA rarely are in the Fresnel region of a single loudspeaker, but rather in its Fraunhofer region. Hence, the Fresnel region of a circular piston can be, but must not necessarily be considered for prediction of audience sound fields produced by line arrays.

D.2 Line Piston

The so called baffled line piston with length l under constant volume acceleration or constant velocity over the piston's diaphragm is considered as a very simple model of waveguides that are deployed in LSA designs for high audio frequencies $> (1\dots 2)$ kHz. The subsections again deal with the description of the on-axis pressure, the farfield radiation pattern and its Fresnel/Fraunhofer (near-/farfield) transition.

D.2.1 On-Axis Pressure

Consider a finite length, continuous and baffled line source with the length l on the y -axis symmetrical to the origin, denoting positions within the source with y_0 . The Neumann Rayleigh integral for the on-axis sound pressure is given as

$$P(x, \omega) = 2j \varrho_0 \omega \iint_{-\infty}^{+\infty} V_n(\mathbf{x}_0, \omega) \frac{e^{-j \frac{\omega}{c} |\mathbf{x} - \mathbf{x}_0|}}{4 \pi |\mathbf{x} - \mathbf{x}_0|} dy_0 dz_0 \quad (\text{D.46})$$

in general with $\mathbf{x} = (x, 0, 0)^T$ and $\mathbf{x}_0 = (0, y_0, z_0)^T$. The velocity spectrum

$$V_n(\mathbf{x}_0) = \begin{cases} \frac{1}{j \varrho_0 \omega l} & \text{for } |y_0| \leq \frac{l}{2} \\ 0 & \text{elsewhere in } yz\text{-plane} \end{cases} \quad (\text{D.47})$$

describes the ideal, finite length line piston on y -axis under consideration within an otherwise rigid yz -plane. This models the line piston under constant volume acceleration (cf. [Hei92b, (2)]) using an energy spread of the spatial dirac impulse over the piston's surface [Ste29, Hec77]. With resulting $|\mathbf{x} - \mathbf{x}_0| = r = \sqrt{x^2 + y_0^2}$ and axial symmetry, the integral (D.46) can be rewritten

$$P(x, \omega) = \frac{4}{l} \int_0^{+\frac{l}{2}} \frac{e^{-j \frac{\omega}{c} r}}{4 \pi r} dy_0. \quad (\text{D.48})$$

This simple looking integral is not generally solvable for a closed form solution and further approximations must be deployed. The calculus in [Hei92b, p.9] is revisited in detail for consistent treatment. From the problem's geometry one obtains

$$r \approx x + \frac{y_0^2}{2x} \quad (\text{D.49})$$

with a Taylor series expansion including the linear and quadratic term, cf. [Pri04, (3)]. Inserting (D.49) into the argument of the exp-function and only $r \approx x$ into the denominator of (D.48) yields

$$P(x, \omega) = \frac{4}{l} \frac{1}{4 \pi} \frac{e^{-j \frac{\omega}{c} x}}{x} \int_0^{+\frac{l}{2}} e^{-j \frac{\omega}{c} \frac{y_0^2}{2x}} dy_0, \quad (\text{D.50})$$

which is precisely identified as the Fresnel approximation for a diffracted plane wave (2.101) for the special case of on-axis evaluation, cf. [Pri04, (4)]. The Fresnel approximation is valid under the condition (2.102). Using $\mathbf{x}' = (0, 0)^T$ and the farthest spherical monopole $\mathbf{x}'_0 = (\frac{l}{2}, 0)^T$ within the line piston as well as an arbitrarily chosen allowed maximum angle of $\frac{\pi}{32}$ for the third order

exponential term, the condition (2.102)

$$\frac{\omega}{c} \frac{|\mathbf{x}' - \mathbf{x}_0'|^4}{8 x_{\text{CS}}^3} = \frac{\pi}{32} = \frac{\omega}{c} \frac{\left(\frac{l}{2}\right)^4}{8 x_{\text{CS}}^3} \quad (\text{D.51})$$

leads to model validity distances on axis $x > x_{\text{CS}}$ with

$$x_{\text{CS}} = \left(\frac{l^4}{2\lambda} \right)^{\frac{1}{3}}. \quad (\text{D.52})$$

Eq. (D.50) can be reshaped into a Fresnel integral by the variable substitution (the variable v is chosen similar to [Hei92b, p. 9], not to be confused with the piston velocity)

$$v = \frac{\omega}{c} \frac{y_0^2}{2x} \rightarrow \frac{dv}{dy_0} = 2 \frac{\omega}{c} \frac{y_0}{2x} \rightarrow dy_0 = \frac{dv}{2 \frac{\omega}{c} \frac{y_0}{2x}} \quad (\text{D.53})$$

and the new integration limits

$$v_0 = v(y_0 = \frac{l}{2}) = \frac{\omega}{c} \frac{\left(\frac{l}{2}\right)^2}{2x}, \quad v(y_0 = 0) = 0. \quad (\text{D.54})$$

With (D.52) the corresponding

$$v_0(x_{\text{CS}}) = \frac{\omega}{c} \frac{\left(\frac{l}{2}\right)^2}{2x_{\text{CS}}} = \frac{\pi}{32^{\frac{1}{3}}} \left(\frac{l}{\lambda} \right)^{\frac{2}{3}} \quad (\text{D.55})$$

indicates a valid Fresnel approximation for $v_0 < v_0(x_{\text{CS}})$ only. Applying the substitution yields

$$P(x, \omega) = \frac{2}{l} \frac{1}{4\pi} \frac{e^{-j\frac{\omega}{c}x}}{x} \int_0^{v_0} e^{-jv} \frac{dv}{\frac{\omega}{c} \frac{y_0}{2x}}, \quad (\text{D.56})$$

that now can be casted to a Fresnel integral representation, cf. [Sku71, Ch. 26.23] for a possible solution. The appropriate Fresnel integrals [Gra07, p. xxxvii], [Abr72, p.321] – using the subscript convention from [Gra07] – are

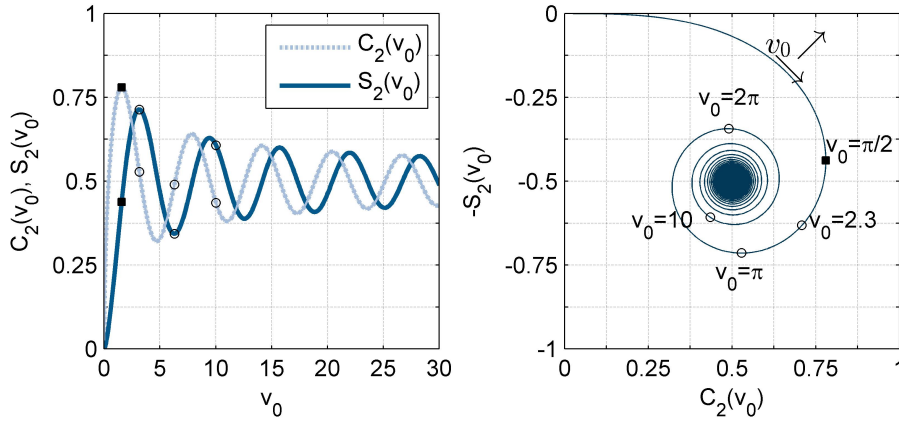


Figure D.7: left: Fresnel integrals (D.57), right: Cornu's spiral in complex plane

given as

$$\begin{aligned}
 C_2(v_0) &= \frac{1}{\sqrt{2\pi}} \int_0^{v_0} \frac{\cos v}{\sqrt{v}} dv = C_1\left(\sqrt{\frac{2v_0}{\pi}}\right) \\
 S_2(v_0) &= \frac{1}{\sqrt{2\pi}} \int_0^{v_0} \frac{\sin v}{\sqrt{v}} dv = S_1\left(\sqrt{\frac{2v_0}{\pi}}\right)
 \end{aligned} \tag{D.57}$$

for which $C_1(\cdot)$ and $S_1(\cdot)$ are implemented in Matlab and Mathematica as `FresnelC(.)` and `FresnelS(.)`, respectively. The Fresnel integrals are depicted in Fig. D.7. The visualization in the complex plane shows the so called Cornu spiral, cf. [Sku71, Fig. 5.5], [Bor06, Ch. 8.7.2]. Introducing \sqrt{v} into (D.56) yields

$$P(x, \omega) = \frac{2}{l} \frac{1}{4\pi} \sqrt{\frac{2}{\frac{\omega}{c}x}} e^{-j\frac{\omega}{c}x} \int_0^{v_0} \frac{e^{-jv}}{\sqrt{v}} dv \tag{D.58}$$

and by applying the short notations $C_2(v_0)$ and $S_2(v_0)$ follows

$$P(x, \omega) = \frac{2}{l} \frac{1}{4\pi} \sqrt{\frac{2}{\frac{\omega}{c}x}} e^{-j\frac{\omega}{c}x} \sqrt{2\pi} [C_2(v_0) - jS_2(v_0)], \tag{D.59}$$

which is the result in [Hei92b, p. 9] except for the negative signs due to the different spatio-temporal Fourier conventions $e^{-j\frac{\omega}{c}x} e^{+j\omega t}$ (here) vs. $e^{+j\frac{\omega}{c}x} e^{+j\omega t}$ ([Hei92b, p.2]) and another chosen normalization scheme. Therefore, an analytic expression for the sound pressure on axis for a baffled line piston and wave propagation perpendicular to the piston is available under the given assumptions. Note again that only certain parameter sets $v_0(l, x, \omega)$ yield a valid prediction due to (D.52) and (D.55), i.e. $x > x_{CS} \leftrightarrow v_0 < v_0(x_{CS})$.

Fresnel region

The asymptotic representations for $v_0 \rightarrow \infty$ [Gra07, (8.255)]

$$C_2(v_0) \approx \frac{1}{2} + \frac{1}{\sqrt{2\pi}v_0} \sin(v_0) \quad S_2(v_0) \approx \frac{1}{2} - \frac{1}{\sqrt{2\pi}v_0} \cos(v_0) \quad (\text{D.60})$$

hold and correspond to the highly oscillating region of the Cornu spiral, cf. Fig. D.7. Eq. (D.55) allows very large, valid v_0 only for large piston lengths and/or very small wave lengths. The Fresnel integrals approach the same limit [Olv10, (7.29)]

$$\lim_{v_0 \rightarrow \infty} C_2(v_0) = \frac{1}{2} \quad \lim_{v_0 \rightarrow \infty} S_2(v_0) = \frac{1}{2}. \quad (\text{D.61})$$

The Fresnel integrals $C_2(v_0), S_2(v_0)$ oscillate around the limit $1/2$ and the term $|C_2(v_0) - jS_2(v_0)|$ oscillates around the limit $1/\sqrt{2}$ for $v_0 \rightarrow \infty$. The envelope is therefore given by

$$C_{2,\text{env}}(v_0) = \frac{1}{2} + \frac{1}{\sqrt{2\pi}v_0} \quad S_{2,\text{env}}(v_0) = \frac{1}{2} - \frac{1}{\sqrt{2\pi}v_0}. \quad (\text{D.62})$$

For a rough estimation of the frequency and distance dependence in the Fresnel region, the oscillatory behaviour is shortly ignored for convenience. Thus, using (D.61) for (D.59) leads to

$$P(x, \omega) \approx \frac{1}{l} \cdot \left(-\frac{j}{2} \sqrt{\frac{2}{\pi \frac{\omega}{c} x}} e^{-j(\frac{\omega}{c} x - \frac{\pi}{4})} \right). \quad (\text{D.63})$$

The result resembles the large argument approximation of the 2D Neumann Green's function weighted by $\frac{1}{l}$, i.e. the ideal, baffled, infinite line monopole located on y -axis, cf. (2.143) including only on-axis distance x . The magnitude

of the sound pressure

$$|P(x, \omega)| \propto \frac{1}{\sqrt{\frac{\omega}{c} x}} \quad (\text{D.64})$$

has -3 dB/oct. lowpass characteristics with ripples due to (D.62) and a 3 dB level decay per distance doubling with ripples also due to (D.62). This corresponds to the Fresnel region of the finite line source. Note that – in contrast to the Fresnel region of the circular piston – the sound pressure will never reach zero due to the Cornu's spiral characteristic.

Fraunhofer region

Under the assumption $v_0 \ll 1$, which holds for very low frequencies, very small line pistons or very far distances, (D.58) can with $e^{-jv} \approx 1$ be simplified to

$$P(x, \omega) = \frac{2}{l} \frac{1}{4\pi} \sqrt{\frac{2}{\frac{\omega}{c} x}} e^{-j\frac{\omega}{c} x} \int_0^{v_0} \frac{1}{\sqrt{v}} dv. \quad (\text{D.65})$$

Evaluation of the integral yields

$$P(x, \omega) = \frac{e^{-j\frac{\omega}{c} x}}{2\pi x}, \quad (\text{D.66})$$

which – similar to the circular piston – is identified as the on-axis sound pressure characteristic of the 3D Neumann Green's function, i.e. a baffled spherical monopole. The sound pressure is frequency independent and exhibits a 6 dB level decay per distance doubling, cf. p.270. This characterizes the Fraunhofer region of the finite line source. Note that this only considers the very first part (starting from the origin) of the Cornu spiral, which excludes all oscillations.

As for the circular piston a Fresnel/Fraunhofer transition distance may be defined as the last local sound pressure maximum – if existing – away from the line piston before the asymptotic 6 dB level decay per distance doubling holds. Therefore, from (D.59)

$$|P(x, \omega)_{\text{loc,max}}| \propto \max \left\{ \left| \frac{C_2(v_0) - j S_2(v_0)}{\sqrt{x}} \right| \right\} \quad (\text{D.67})$$

has to be found. No general closed solution can be given, since the numerator with the Fresnel integrals depends on x (due to $v_0(x)$) as well as the denomi-

nator on \sqrt{x} . A rough approximation can be derived if only the numerator is considered. The maximum modulus of $|C_2(v_0) - j S_2(v_0)|$ is numerically found for

$$v_0 \approx 2.29744, \quad (\text{D.68})$$

cf. Fig. D.7, which for a chosen line piston length and temporal frequency should indicate the Fresnel/Fraunhofer transition distance $x_{\text{B,CS}}$. Note that this distance is in general further away from the piston than the actual location of the last local pressure maximum. For increasing distances $x > x_{\text{B,CS}}$, and thus decreasing v_0 (following the not oscillating part of the Cornu's spiral towards the origin) the Fresnel integrals $|C_2(v_0) - j S_2(v_0)|$ exhibits a 3 dB level decay per distance doubling. Together with the 3 dB level decay stemming from $\sqrt{\frac{1}{x}}$ in (D.59) this indicates an overall 6 dB level decay per distance doubling, i.e. Fraunhofer behavior. The Fresnel/Fraunhofer transition border can be defined with (D.54) for

$$2.29744 \approx v_0 = \frac{\omega}{c} \frac{\left(\frac{l}{2}\right)^2}{2 x_{\text{B,CS}}} \quad (\text{D.69})$$

yielding

$$x_{\text{B,CS}} \approx \frac{1}{3} \frac{l^2}{\lambda} \quad \text{valid only if } x_{\text{B,CS}} \geq x_{\text{CS}}. \quad (\text{D.70})$$

It turns out that if $x_{\text{B,CS}} > x_{\text{CS}}$ does not hold – i.e. the Fresnel approximation is not valid – a reasonable good approximation for the transition border is $x_{\text{B,CS}} = x_{\text{CS}}$ from (D.52), thus

$$x_{\text{B,CS}} \approx \max \left\{ \frac{1}{3} \frac{l^2}{\lambda}, \left(\frac{l^4}{2\lambda} \right)^{\frac{1}{3}} \right\}. \quad (\text{D.71})$$

Note that in [Hei92b, p.10] the same calculus using $v_0 = 1.5$ is performed, referring to the global maximum of $C_2(v_0)$, which is actually exactly the case for $v_0 = \frac{\pi}{2}$. For their common normalization $c = 333.3 \text{ m/s}$ and the frequency

F in kHz they give

$$x_{\text{B,CS,Heil1992}} \approx \frac{\pi}{2} l^2 F, \quad (\text{D.72})$$

compared to a normalization of (D.70)

$$x_{\text{B,CS}} \approx l^2 F. \quad (\text{D.73})$$

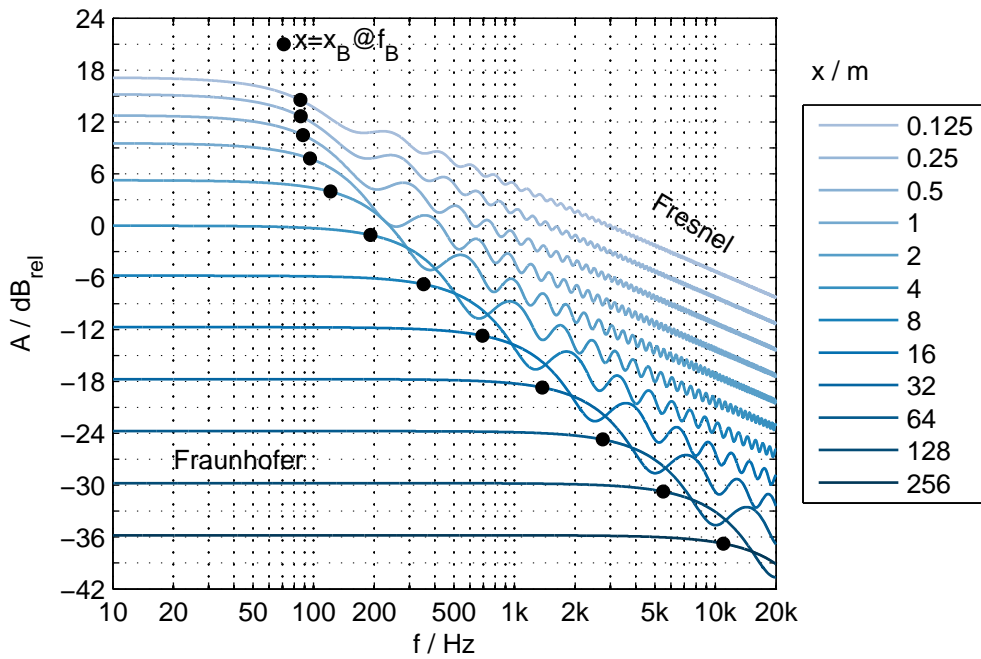
Thus, the solution from [Hei92b] indicates the Fresnel/Fraunhofer transition at a larger distance. However, both approaches correctly consider the l^2 -dependency, which is frequently ignored in other literature.

There is a smooth transition between Fresnel and Fraunhofer region. Let's assume that the listener is located exactly at x_{B} . By changing only one of the parameters of v_0 leaving the others constant the variation (increase/decrease) of the parameter reveals into which region the radiation characteristic merges. This is summarized as follows:

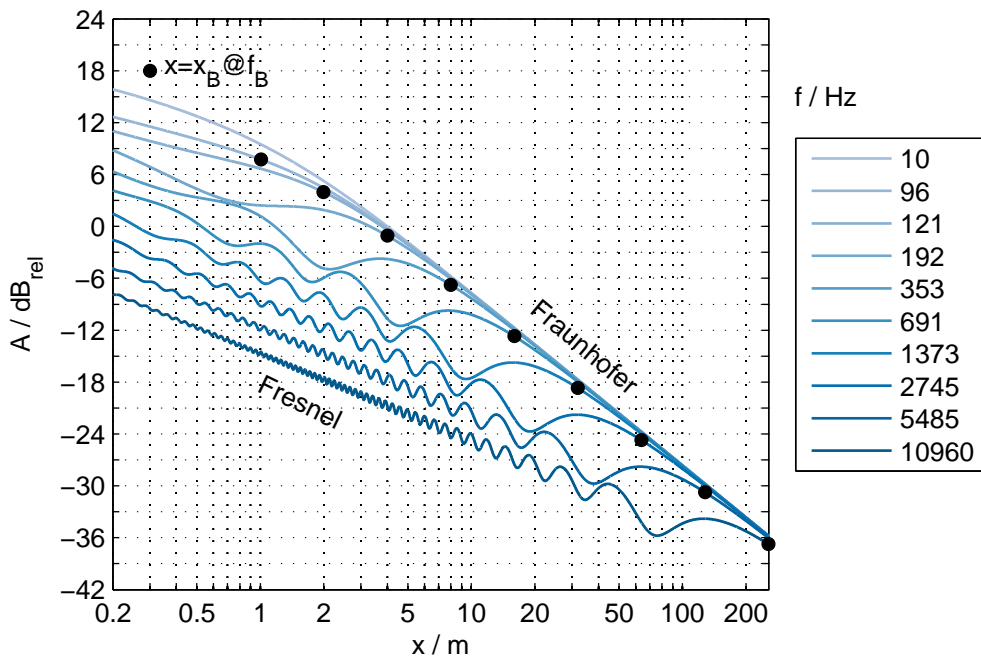
- $l = \text{const}, f = \text{const}$: Fresnel for $x \searrow, v_0 \nearrow$; Fraunhofer for $x \nearrow, v_0 \searrow$
- $l = \text{const}, x = \text{const}$: Fraunhofer for $f \searrow, v_0 \searrow$; Fresnel for $f \nearrow, v_0 \nearrow$
- $f = \text{const}, x = \text{const}$: Fraunhofer for $l \searrow, v_0 \searrow$; Fresnel for $l \nearrow, v_0 \nearrow$

This characteristics can be tracked in Fig. D.8. The plots also indicate the general -3 dB/oct. lowpass characteristics and -3 dB level decay per distance doubling in the Fresnel region, both exhibiting ripples due to the diffraction. The Fraunhofer region is characterized by a flat amplitude spectrum and -6 dB level decay per distance doubling.

Note that the length of the array enters the Fresnel/Fraunhofer transition border with quadratic dependence. This strong dependence on L, f, x is of course not meaningful for homogeneous sound reinforcement. The uniformly driven, straight LSA is however the basic concept for the derivation of Wavefront Sculpture Technology (WST, [Hei92b, Urb03]) and was therefore discussed in detail.



(a) Frequency response of a baffled line piston with constant volume acceleration on main axis indicating the Fresnel-/Fraunhofer transition distance x_B (D.79). Numerical evaluation of (D.48), air absorption not considered. Length $l = 4$ m, $c = 343$ m/s. 0 dB normalization to $x = 4$ m and $f = 10$ Hz.



(b) Sound pressure level decay over on-axis distance for Fig. D.8a. Some chosen temporal frequencies correspond to the $x_B|f_B$ of Fig. D.8a using the same dB-normalization.

Figure D.8: Line piston on-axis characteristics, cf. [Lip86], [Ure02], [Ure04]

D.2.2 Fraunhofer Approximation

The Fraunhofer approximation of a line piston with normalized, constant normal velocity is straightforward and reads [Hec77]

$$H(k_y, \omega) = \int_{-\frac{l}{2}}^{+\frac{l}{2}} \frac{1}{l} e^{+j k_y y_0} dy_0 = \frac{\sin\left(\frac{k_y l}{2}\right)}{\frac{k_y l}{2}}, \quad (\text{D.74})$$

$$H(\varphi, \omega) = \frac{\sin\left(\frac{\omega}{c} \sin \varphi \frac{l}{2}\right)}{\frac{\omega}{c} \sin \varphi \frac{l}{2}}, \quad (\text{D.75})$$

for which an equivalent v and u -space definitions of the resulting sinc-function is deployed, cf. Fig. D.3. It becomes obvious that the jinc and sinc exhibit about the same characteristics for small v/u . For large v/u the jinc function however exhibits a larger envelope decay than the sinc function.

D.2.3 Fresnel-/Fraunhofer Transition Distance

The FRP of the line piston is written as

$$H(\varphi, \omega) = \frac{\sin\left(\frac{2\pi}{\lambda} \sin \varphi \frac{l}{2}\right)}{\frac{2\pi}{\lambda} \sin \varphi \frac{l}{2}} = \frac{\sin\left(\pi \frac{l}{\lambda} \sin \varphi\right)}{\pi \frac{l}{\lambda} \sin \varphi}. \quad (\text{D.76})$$

If for a chosen λ and l at least the first zero of the sine function $\sin(\pi \alpha_0) = 0$ – that is for $\alpha_0 = 1$ – is located within the visible region, one may find the radiation angle φ_N of that FRP's zero (notch) by

$$\pi \frac{l}{\lambda} \sin \varphi_N = \pi \rightarrow \sin \varphi_N = \frac{\lambda}{l} \quad (\text{D.77})$$

According to Fig. D.9 the Fresnel-/Fraunhofer distance x_B again (cf. p.278) may be defined by the geometric diffraction approach as

$$x_B = \frac{l}{2} \frac{\sqrt{1 - \sin^2 \varphi_N}}{\sin \varphi_N} \quad (\text{D.78})$$

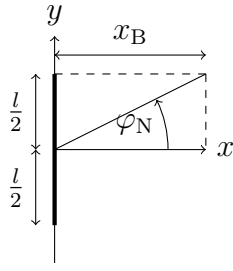


Figure D.9: Fresnel-/Fraunhofer distance x_B of a line piston with length l using the half angle opening φ_N , cf. [Hei92b, Fig. 12].

and furthermore introducing $\sin \varphi_N$ from (D.77) with $c = \lambda f$

$$x_B = \frac{1}{2} l^2 \frac{f}{c} \sqrt{1 - \frac{1}{(l \frac{f}{c})^2}} \quad (\text{D.79})$$

If $\frac{\lambda}{l} > 1$, $x_B \in \mathbb{C}$ respectively, no Fresnel region exists and the line piston immediately radiates a Fraunhofer field for the chosen λ and l . In other words, no zeros exist within the visible region of the FRP. Note that in [Hei92b, I.3.e], [Urb03, p.913] the transition border in meters was given with frequency F in kHz and $c = 333.3 \bar{3} \text{ m/s}$ to

$$x_B = \frac{3}{2} l^2 F \sqrt{1 - \frac{1}{9 (l F)^2}}. \quad (\text{D.80})$$

Note that a further possible Fresnel/Fraunhofer transition was given as $r_B = L^2 \frac{f}{c}$ [Lip86, (25)], that is precisely the condition for the Fraunhofer approximation validity (2.106). In [Lip86] this was found by the intersection of the flat, low frequency Fraunhofer spectrum with the asymptotic Fresnel spectrum for high frequencies.

[Hei92b, Fig. 13] contains also a schematic sketch of the line piston's Fresnel/Fraunhofer characteristics over frequency and on-axis distance. For typically deployed waveguide sizes this is shown in Fig. D.11 by numerical evaluation of the integral (D.48) and indicating x_B (D.79). From that it again can be concluded that typical listener distances in front of an LSA rarely are in the Fresnel region of a single waveguide, but rather in its Fraunhofer region. However, when considering linear arrays built from line pistons listeners may be situated in the Fresnel region of the whole array.

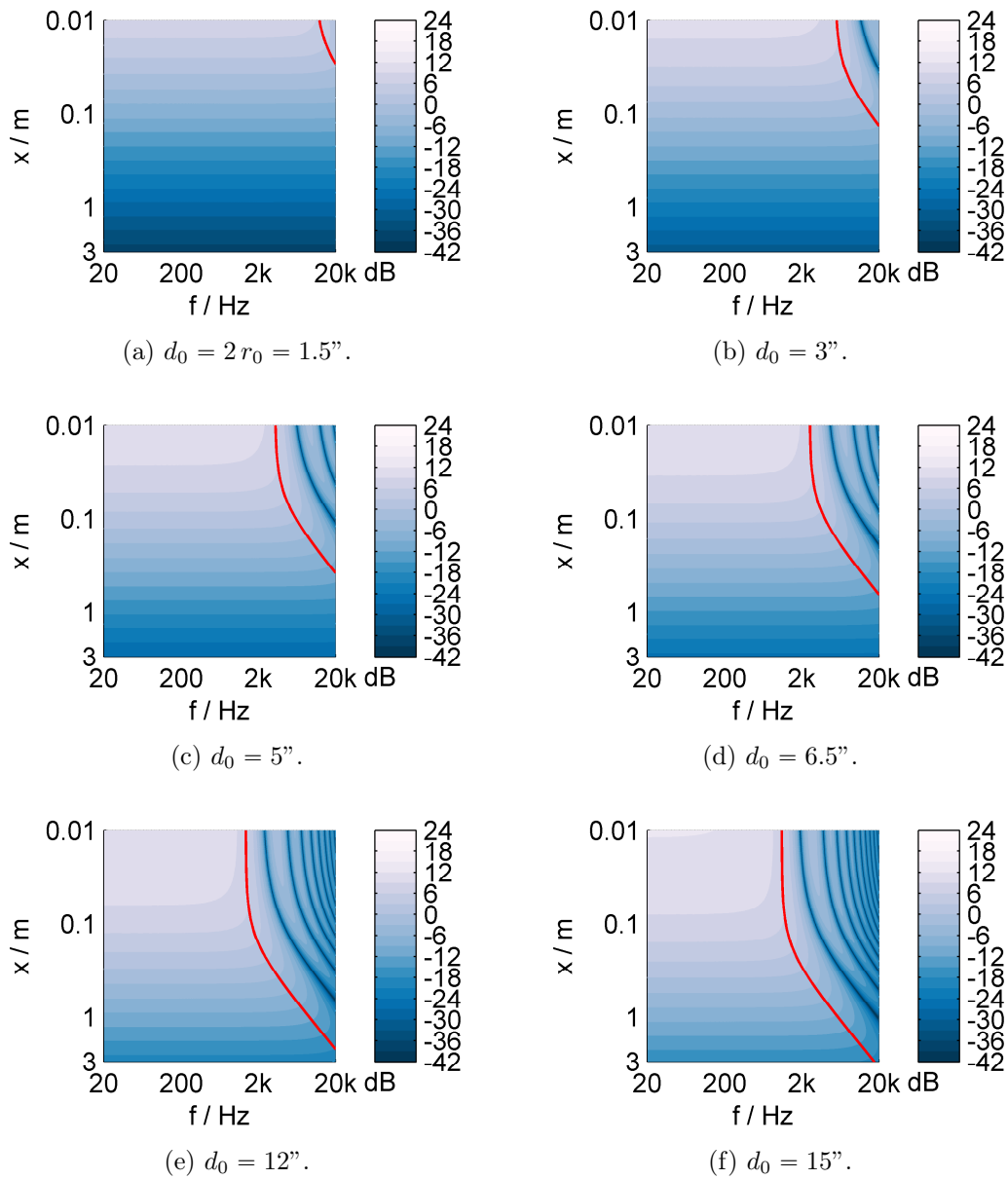


Figure D.10: Circular piston on axis, cf. [Hei92b, Fig. 13]. Evaluation of (D.2) normalized to 0 dB at $x = 2r_0$ and $f = 20$ Hz. Fresnel/Fraunhofer transition distance x_B (D.44) indicated as line.

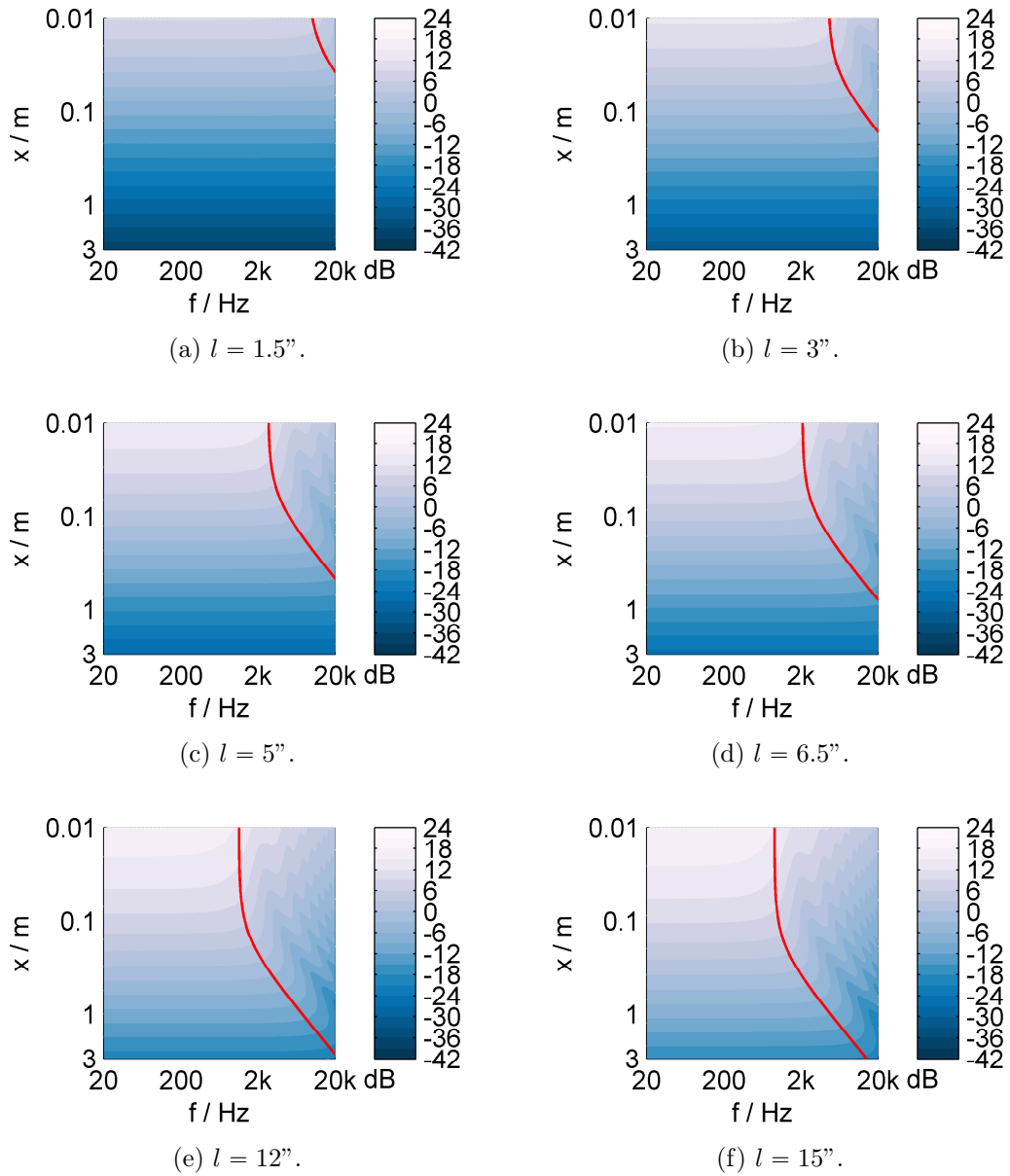


Figure D.11: Line piston on axis, cf. [Hei92b, Fig. 13]. Numerical evaluation of the integral (D.48) normalized to 0 dB at $x = l$ and $f = 20$ Hz. Fresnel/Fraunhofer transition distance x_B (D.79) indicated as line.

Bibliography

- [Aar00] Aarts, R.M.; Jansen, A.J.E.M. (2000): “On analytic design of loudspeaker arrays with uniform radiation characteristics.” In: *J. Acoust. Soc. Am.*, **107**(1):287–292.
- [Abr72] Abramowitz, M.; Stegun, I.A. (1972): *Handbook of Mathematical Functions with Formulas, Graphs, and Mathematical Tables*. New York: Dover, 9. ed.
- [Ahn96] Ahnert, W.; Feistel, R. (1996): “Prediction of wave fields synthesized by speaker cluster – Needs and limitations.” In: *Proc. of 100th Audio Eng. Soc. Convention, Copenhagen, #4146*.
- [Ahn00] Ahnert, W.; Baird, J.; Feistel, S.; Meyer, P. (2000): “Accurate electroacoustic prediction utilizing the complex frequency response of far-field polar measurements.” In: *Proc. of 108th Audio Eng. Soc. Convention, Paris, #5129*.
- [Ahr08a] Ahrens, J.; Spors, S. (2008): “An analytical approach to sound field reproduction using circular and spherical loudspeaker distributions.” In: *Acta Acust United Ac*, **94**(6):988–999.
- [Ahr08b] Ahrens, J.; Spors, S. (2008): “Analytical driving functions for higher order Ambisonics.” In: *Proc. of 33rd Intl. Conference on Acoustics, Speech and Signal Processing (IEEE 33rd ICASSP), Las Vegas*, 373–376.
- [Ahr08c] Ahrens, J.; Spors, S. (2008): “Reproduction of a plane-wave sound field using planar and linear arrays of loudspeakers.” In: *Proc. of 3rd Intl. Symposium on Communications, Control and Signal Processing (IEEE 3rd ISCCSP), Malta*, 1486–1491.
- [Ahr09] Ahrens, J.; Spors, S. (2009): “Alterations of the temporal spectrum in high-resolution sound field reproduction of different spatial bandwidths.” In: *Proc. of 126th Audio Eng. Soc. Convention, Munich, #7742*.
- [Ahr10a] Ahrens, J. (2010): *The Single-layer Potential Approach Applied to Sound Field Synthesis Including Cases of Non-enclosing Distributions of Secondary Sources*. doctoral thesis, TU Berlin.

- [Ahr10b] Ahrens, J.; Spors, S. (2010): “Applying the Ambisonics approach on planar and linear arrays of loudspeakers.” In: *Proc. of the 2nd Intl. Symposium on Ambisonics and Spherical Acoustics, Paris*.
- [Ahr10c] Ahrens, J.; Spors, S. (2010): “On the anti-aliasing loudspeaker for sound field synthesis employing linear and circular distributions of secondary sources.” In: *Proc. of 129th Audio Eng. Soc. Convention, San Francisco, #8246*.
- [Ahr10d] Ahrens, J.; Spors, S. (2010): “Sound field reproduction using planar and linear arrays of loudspeakers.” In: *IEEE Trans. Audio Speech Language Process.*, **18**(8):2038–2050.
- [Ahr10e] Ahrens, J.; Wierstorf, H.; Spors, S. (2010): “Comparison of Higher Order Ambisonics and Wave Field Synthesis with respect to spatial discretization artifacts in time domain.” In: *Proc. of 40th Audio Eng. Soc. Intl. Conference on Spatial Audio, Tokyo, #6-1*.
- [Ahr12a] Ahrens, J. (2012): *Analytic Methods of Sound Field Synthesis*. Heidelberg: Springer, 1. ed.
- [Ahr12b] Ahrens, J.; Spors, S. (2012): “Applying the Ambisonics approach to planar and linear distributions of secondary sources and combinations thereof.” In: *Acta Acust United Ac*, **98**(1):28–36.
- [An09] An, K.; Shen, Y.; Zhang, A. (2009): “Increasing active radiating factor of high-frequency horns by using staggered arrangement in loudspeaker line array.” In: *Proc. of 126th Audio Eng. Soc. Convention, Munich, #7720*.
- [Ang98] Angus, J.A.; Evans, M.J. (1998): “Loudspeaker polar pattern measurement and representation with surface spherical harmonics.” In: *Proc. of 104th Audio Eng. Soc. Convention, Amsterdam, #4717*.
- [Ape04] Apel, A.; Röder, T.; Brix, S. (2004): “Equalization of Wave Field Synthesis systems.” In: *Proc. of 116th Audio Eng. Soc. Convention, Berlin, #6121*.
- [Arf05] Arfken, G.B.; Weber, H.J. (2005): *Mathematical Methods for Physicists*. Burlington, San Diego, London: Elsevier, 6. ed.
- [Aug70] Augspurger, G.L. (1970): “The colinear array - A two-way loudspeaker system for sound reinforcement.” In: *Proc. of 39th Audio Eng. Soc. Convention, New York, #762*.
- [Baa08] Baalman, M.A. (2008): *On wave field synthesis and electro-acoustic music, with a particular focus on the reproduction of arbitrarily shaped sound sources*. doctoral thesis, TU Berlin.
- [Bad09] Baddour, N. (2009): “Operational and convolution properties of two-dimensional Fourier transforms in polar coordinates.” In: *J. Opt. Soc. Am. A*, **26**(8):1767–1777.

- [Bai01] Baird, J.; Meyer, P.; Meyer, J. (2001): “Far-field loudspeaker interaction: Accuracy in theory and practice.” In: *Proc. of 110th Audio Eng. Soc. Convention, Amsterdam*, #5309.
- [Bai03] Bailey, M. (2003): “Experiences with line arrays.” In: *Proc. of 19th Audio Eng. Soc. UK Conference: Live Sound, Westminster*, #17.
- [Bai13a] Bai, M.R.; Chen, C.C. (2013): “Application of convex optimization to acoustical array signal processing.” In: *J. of Snd. Vibr.*, **332**(25):6596–6616.
- [Bai13b] Bai, M.R.; Ih, J.G.; Benesty, J. (2013): *Acoustic Array Systems: Theory, Implementation, and Application*. Singapore: Wiley.
- [Bai14] Bai, M.R.; Wen, J.C.; Hsu, H.; Hua, Y.H.; Hsieh, Y.H. (2014): “Investigation on the reproduction performance versus acoustic contrast control in sound field synthesis.” In: *J. Acoust. Soc. Am.*, **136**(4):1591–1600.
- [Bak50] Baker, B.B.; Copson, E.T. (1950): *The mathematical theory of Huygens’ Principle*. Oxford: Clarendo Press, 2. ed.
- [Bal05] Balanis, C.A. (2005): *Antenna Theory - Analysis and Design*. Hoboken: Wiley, 3. ed.
- [Bei02] Beigelbeck, R.; Paschke, F.; Pichler, H. (2002): “Near field analysis and optimization of linear loudspeaker arrays.” In: *Proc. of 112th Audio Eng. Soc. Convention, Munich*, #5608.
- [Bel15] Bellmann, C.; Klippel, W.; Knobloch, D. (2015): “Holographic loudspeaker measurement based on near field scanning.” In: *Fortschritte der Akustik: Tagungsband d. 41. DAGA, Nürnberg*, 75–76.
- [Ber54] Beranek, L.L. (1954): *Acoustics*. New York: McGraw Hill, 1. ed.
- [Ber88] Berkhout, A.J. (1988): “A holographic approach to acoustic control.” In: *J. Audio Eng. Soc.*, **36**(12):977–995.
- [Ber92a] Berkhout, A.J.; de Vries, D.; Vogel, P. (1992): “Wave Front Synthesis: A new direction in electroacoustics.” In: *Proc. of 93rd Audio Eng. Soc. Convention, San Francisco*, #3379.
- [Ber92b] Berkhout, A.J.; Vogel, P.; de Vries, D. (1992): “Use of wave field synthesis for natural reinforced sound.” In: *Proc. of 92nd Audio Eng. Soc. Convention, Vienna*, #3299.
- [Ber93] Berkhout, A.J.; de Vries, D.; Vogel, P. (1993): “Acoustic control by Wave Field Synthesis.” In: *J. Acoust. Soc. Am.*, **93**(5):2764–2778.
- [Bet12] Betlehem, T.; Withers, C. (2012): “Sound field reproduction with energy constraint on loudspeaker weights.” In: *IEEE Trans. Audio Speech Language Process.*, **20**(8):2388–2392.
- [Bla00] Blackstock, D.T. (2000): *Fundamentals of Physical Acoustics*. New York: Wiley, 1. ed.

- [Ble71] Blessener, B.; Lee, F.F. (1971): “An audio delay system using digital technology.” In: *Proc. of 40th Audio Eng. Soc. Convention, Los Angeles*, #793.
- [Boo95] Boone, M.M.; Verheijen, E.N.G.; van Tol, P.F. (1995): “Spatial sound-field reproduction by wave-field synthesis.” In: *J. Audio Eng. Soc.*, **43**(12):1003–1012.
- [Bor72] Born, M. (1972): *Optik - Ein Lehrbuch der elektromagnetischen Lichttheorie*. Berlin: Springer, 3. ed.
- [Bor06] Born, M.; Wolf, E. (2006): *Principles of optics*. Cambridge: Cambridge University Press, 7th (expanded), 4th printing ed.
- [Bro12] Brockett, T.J.; Rahmat-Samii, Y. (2012): “Subarray design diagnostics for the suppression of undesirable grating lobes.” In: *IEEE Trans. Antennas and Propagation*, **60**(3):1373–1380.
- [But02] Button, D. (2002): “High frequency components for high output articulated line arrays.” In: *Proc. of 113th Audio Eng. Soc. Convention, Los Angeles*, #5684.
- [But14] Butler, N. (2014): “Anya™ designer’s notebook.” Tech. rep., Eastern Acoustic Works, <http://eaw.com/anya-designers-notebook/>, last seen on 2016-06-02.
- [Cai14] Cai, Y.; Wu, M.; Yang, J. (2014): “Sound reproduction in personal audio systems using the least-squares approach with acoustic contrast control constraint.” In: *J. Acoust. Soc. Am.*, **135**(2):734–741.
- [Cho02] Choi, J.W.; Kim, Y.H. (2002): “Generation of an acoustically bright zone with an illuminated region using multiple sources.” In: *J. Acoust. Soc. Am.*, **111**(4):1695–1700.
- [Col01] Cola, M.D.; Doldi, D.; Saronni, D. (2001): “Analysis of directivity anomalies in mid and high frequency horn loudspeakers.” In: *Proc. of 111th Audio Eng. Soc. Convention, New York*, #5432.
- [Col09] Cola, M.D.; Cinanni, D.; Manzini, A.; Nizzoli, T.; Ponteggia, D. (2009): “Design and optimization of high directivity waveguide for vertical array.” In: *Proc. of 127th Audio Eng. Soc. Convention, New York*, #7955.
- [Col13] Colton, D.; Kress, R. (2013): *Inverse Acoustic and Electromagnetic Scattering Theory*. New York: Springer, 3. ed.
- [Col14a] Coleman, P.; Jackson, P.J.B.; Olik, M. (2014): “Personal audio with a planar bright zone.” In: *J. Acoust. Soc. Am.*, **136**(4):1725–1735.
- [Col14b] Coleman, P.; Jackson, P.J.B.; Olik, M.; Møller, M.; Olsen, M.; Pedersen, J.A. (2014): “Acoustic contrast, planarity and robustness of sound zone methods using a circular loudspeaker array.” In: *J. Acoust. Soc. Am.*, **135**(4):1929–1940.

- [Col15] Cola, M.D.; Tatini, A. (2015): “A novel approach to large-scale sound reinforcement systems.” In: *Proc. of 139th Audio Eng. Soc. Convention, New York*, #9479.
- [Cor06] Corteel, E. (2006): “Equalization in an extended area using multichannel inversion and Wave Field Synthesis.” In: *J. Audio Eng. Soc.*, **54**(12):1140–1161.
- [Cor07] Corteel, E. (2007): “Synthesis of directional sources using Wave Field Synthesis, possibilities, and limitations.” In: *EURASIP J. on Adv. in Sig. Proc.*, (90509).
- [Dan03] Daniel, J. (2003): “Spatial sound encoding including near field effect: Introducing distance coding filters and a viable, new Ambisonic format.” In: *Proc. of 23rd Audio Eng. Soc. Intl. Conference on Signal Processing in Audio Recording and Reproduction, Helsingør*, #16.
- [Dav52] Davids, N.; Thurston, E.G.; Mueser, R.E. (1952): “The design of optimum directional acoustic arrays.” In: *J. Acoust. Soc. Am.*, **24**(1):50–56.
- [Dav75] Davis, D.; Wickersham, R. (1975): “Experiments in the enhancement of the artist’s ability to control his interface with the acoustic environment in large halls.” In: *Proc. of 51st Audio Eng. Soc. Convention, Los Angeles*, #1033.
- [DeS92] DeSanto, J.A. (1992): *Scalar wave theory, Green’s functions and applications*. Berlin: Springer, 1. ed.
- [Dub99] Dubra, A.; Ferrari, J.A. (1999): “Diffracted field by an aperture.” In: *J. Am. Phys.*, **67**(1):87–92.
- [Dur07] Duran Audio BV (2007): “The AXYS® Target System.” Tech. rep., http://www.duran-audio.com/pdfs/downloads/brochures/AXYS_Target_brochure.pdf, last seen on 2016-06-02.
- [dV94a] de Vries, D.; Start, E.W.; Valstar, V.G. (1994): “The Wave Field Synthesis concept applied to sound reinforcement: Restrictions and solutions.” In: *Proc. of 96th Audio Eng. Soc. Convention, Amsterdam*, #3812.
- [dV94b] de Vries, G.; van Beuningen, G. (1994): “A digital control unit for loudspeaker arrays.” In: *Proc. of 96th Audio Eng. Soc. Convention, Amsterdam*, #3836.
- [dV96] de Vries, D. (1996): “Sound reinforcement by wavefield synthesis: Adaptation of the synthesis operator to the loudspeaker directivity characteristics.” In: *J. Audio Eng. Soc.*, **44**(12):1120–1131.
- [dV09] de Vries, D. (2009): *Wave Field Synthesis – AES Monograph*. New York: Audio Engineering Society.

- [Ear04] Eargle, J.M.; Gander, M. (2004): "Historical perspectives and technology overview of loudspeakers for sound reinforcement." In: *J. Audio Eng. Soc.*, **52**(4):412–432.
- [EAW98] EAW (1998): "Phased point source technology and the resultant KF900 series." Tech. rep., white paper, http://eaw.com/docs/6_Technical_Information/White_Papers/PPSTWhitepaper.pdf, last seen on 2016-06-02.
- [Ell03] Elliott, R.S. (2003): *Antenna Theory and Design*. Hoboken: Wiley.
- [Ell10] Elliott, S.J.; Cheer, J.; Murfet, H.; Holland, K.R. (2010): "Minimally radiating sources for personal audio." In: *J. Acoust. Soc. Am.*, **128**(4):1721–1728.
- [Ell12] Elliott, S.J.; Cheer, J.; Choi, J.W.; Kim, Y. (2012): "Robustness and regularization of personal audio systems." In: *IEEE Trans. Audio Speech Language Process.*, **20**(7):2123–2133.
- [Eng01] Engebretson, M.E. (2001): "Directional radiation characteristics of articulating line-array loudspeaker systems." In: *Proc. of 111th Audio Eng. Soc. Convention, New York*, Abstract only, white paper available online.
- [Eng09] Engebretson, M.E. (2009): "Curved line array loudspeaker." Tech. rep., U.S. Patent #7,606,383, 2009-10-20.
- [Esk86] Eskow, D.; Hodges, R. (1986): "The heart of Rock 'n' Roll." In: *Popular Mechanics*, **163**(3):99–101, 138, PA for Bruce Springsteen's "Born in the U.S.A." tour.
- [Faz07a] Fazi, F.M.; Nelson, P.A. (2007): "Application of functional analysis to the sound field reconstruction." In: *Proc. of 23rd Conference on Reproduced Sound: Hall of Sound - Audio for Live Events, Institute of Acoustics, Gateshead, GB, 29 - 30 Nov 2007*.
- [Faz07b] Fazi, F.M.; Nelson, P.A. (2007): "The ill-conditioning problem in sound field reconstruction." In: *Proc. of 123rd Audio Eng. Soc. Convention, New York*, #7244.
- [Faz07c] Fazi, F.M.; Nelson, P.A. (2007): "A theoretical study of sound field reconstruction techniques." In: *Proc. of the 19th Intl. Congress on Acoustics, Madrid, ES, 02 - 07 Sep 2007*.
- [Faz08] Fazi, F.M.; Brunel, V.; Nelson, P.A.; Hörchens, L.; Seo, J. (2008): "Measurement and Fourier-Bessel analysis of loudspeakers radiation patterns using a spherical array of microphones." In: *Proc. of 124th Audio Eng. Soc. Convention, Amsterdam*, #7354.
- [Faz09] Fazi, F.M.; Nelson, P.A.; Potthast, R. (2009): "Analogies and differences between three methods for sound field reproduction." In: *Proc. of 1st Ambisonics Symposium, Graz*.

- [Faz10a] Fazi, F.M. (2010): *Sound Field Reproduction*. doctoral thesis, University of Southampton, Institute of Sound and Vibration Research.
- [Faz10b] Fazi, F.M.; Nelson, P.A. (2010): “The relationship between sound field reproduction and near-field acoustical holography.” In: *Proc. of 129th Audio Eng. Soc. Convention, San Francisco*, #8247.
- [Faz12] Fazi, F.M.; Nelson, P.A. (2012): “Nonuniqueness of the solution of the sound field reproduction problem with boundary pressure control.” In: *Acta Acust United Ac*, **98**(1):1–14.
- [Faz13] Fazi, F.M.; Nelson, P.A. (2013): “Sound field reproduction as an equivalent acoustical scattering problem.” In: *J. Acoust. Soc. Am.*, **134**(5):3721–3729.
- [Fei05a] Feistel, S.; Ahnert, W. (2005): “The significance of phase data for the acoustic prediction of combinations of sound sources.” In: *Proc. of 119th Audio Eng. Soc. Convention, New York*, #6632.
- [Fei05b] Feistel, S.; Ahnert, W.; Bock, S. (2005): “New data format to describe complex sound sources.” In: *Proc. of 119th Audio Eng. Soc. Convention, New York*, #6631.
- [Fei07a] Feistel, S.; Ahnert, W. (2007): “Modeling of loudspeaker systems using high-resolution data.” In: *J. Audio Eng. Soc.*, **55**(7/8):571–597.
- [Fei07b] Feistel, S.; Ahnert, W.; Hughes, C.; Olson, B. (2007): “Simulating the directivity behavior of loudspeakers with crossover filters.” In: *Proc. of 123rd Audio Eng. Soc. Convention, New York*, #7254.
- [Fei09a] Feistel, S.; Ahnert, W. (2009): “The effect of sample variation among cabinets of a line array on simulation accuracy.” In: *Proc. of 127th Audio Eng. Soc. Convention, New York*, #7842.
- [Fei09b] Feistel, S.; Thompson, A.; Ahnert, W. (2009): “Methods and limitations of line source simulation.” In: *J. Audio Eng. Soc.*, **57**(6):379–402.
- [Fei13] Feistel, S.; Sempf, M.; Köhler, K.; Schmalle, H. (2013): “Adapting loudspeaker array radiation to the venue using numerical optimization of FIR filters.” In: *Proc. of 135th Audio Eng. Soc. Convention, New York*, #8937.
- [Fei14] Feistel, S. (2014): *Modeling the Radiation of Modern Sound Reinforcement Systems in High Resolution*. doctoral thesis, RWTH Aachen.
- [Fen14] Feng, X.; Shen, Y.; Chen, S.; Zhao, Y. (2014): “Analysis of sound field generated by line arrays with waveguides.” In: *Proc. of 137th Audio Eng. Soc. Convention, Los Angeles*, e-Brief 156.

- [Fen15] Feng, X.; Shen, Y.; Keele, Jr., D.B.; Xia, J. (2015): “Directivity-customizable loudspeaker arrays using constant-beamwidth transducer (CBT) overlapped shading.” In: *Proc. of 139th Audio Eng. Soc. Convention, New York, #9478*.
- [Fid89] Fidlin, P.F.; Carlson, D.E. (1989): “The basic concepts and problems associated with large scale concert-sound loudspeaker arrays.” In: *Proc. of 86th Audio Eng. Soc. Convention, Hamburg, #2802*.
- [Fin08] Fincham, L.; Brown, P. (2008): “Line arrays with controllable directional characteristics - theory and practice.” In: *Proc. of 125th Audio Eng. Soc. Convention, San Francisco, #7535*.
- [Fir12] Firtha, G.; Fiala, P. (2012): “Prefiltering the wave field synthesis operators - anti-aliasing and source directivity.” In: *Intl. Conference on Noise and Vibration Engineering (ISMA 2012), Leuven, Belgium, 3121 – 3136*.
- [Fir16] Firtha, G.; Fiala, P.; Schultz, F.; Spors, S. (2016): “Referencing schemes for wave field synthesis driving functions—A unified theory.” In: *IEEE/ACM Trans. Audio Speech Language Process.*, (submitted).
- [Fos26] Foster, R.M. (1926): “Directive diagrams of antenna arrays.” In: *Bell System Tech. J.*, **5**(2):292–307.
- [Fra83] Franssen, N.V. (1983): “Direction and frequency independent column of electro-acoustic transducers.” Tech. rep., U.S. Patent #4,399,328, 1983-08-16.
- [Fra12] Franck, A.; Rath, M.; Sladeczek, C.; Brix, S. (2012): “Efficient rendering of directional sound sources in wave field synthesis.” In: *Proc. of 40th Audio Eng. Soc. Intl. Conference on Applications of Time-Frequency Processing in Audio, Helsinki*.
- [G14] Gálvez, M.F.S. (2014): *Design of an Array-Based Aid for the Hearing Impaired*. doctoral thesis, University of Southampton.
- [G15] Gálvez, M.F.S.; Elliott, S.J.; Cheer, J. (2015): “Time domain optimization of filters used in a loudspeaker array for personal audio.” In: *IEEE/ACM Trans. Audio Speech Language Process.*, **23**(11):1869–1878.
- [Gan90] Gander, M.R.; Eargle, J.M. (1990): “Measurement and estimation of large loudspeaker array performance.” In: *J. Audio Eng. Soc.*, **38**(4):204–220.
- [Gir01] Girod, B.; Rabenstein, R.; Stenger, A. (2001): *Signals and Systems*. Chichester: Wiley, 1. ed.
- [Glo02] Gloukhov, A. (2002): “Loudspeaker array simulator with coordinated positioning of elements.” In: *Proc. of 21st Audio Eng. Soc.*

- Intl. Conference: Architectural Acoustics and Sound Reinforcement, St. Petersburg, #111.*
- [Glo03] Gloukhov, A. (2003): “A method of loudspeaker directivity prediction based on Huygens-Fresnel principle.” In: *Proc. of 115th Audio Eng. Soc. Convention, New York, #5985.*
- [Goe10] Goertz, A.; Makarski, M.; Feistel, S. (2010): “Welche Lautsprecherdaten werden für eine aussagekräftige Simulation benötigt?” In: *Proc. of 26. Tonmeistertagung, Leipzig.*
- [Goo93] Goodwin, M.M.; Elko, G.W. (1993): “Constant beamwidth beamforming.” In: *Proc. of 18th Intl. Conference on Acoustics, Speech and Signal Processing (IEEE 18th ICASSP), Minneapolis.*
- [Goo05a] Goodman, J.W. (2005): *Introduction to Fourier Optics.* Greenwood Village: Roberts & Co Publ, 3. ed.
- [Goo05b] Goodwin, M.M. (2005): “Cost-constrained broadband array design based on optimal spacing.” In: *Proc. of IEEE Workshop on Applications of Signal Processing to Audio and Acoustics (WASPAA), New Paltz, 98–101.*
- [Goo06] Goodwin, M.M. (2006): “Efficient designs for broadband linear arrays.” In: *Proc. of 31st Intl. Conference on Acoustics, Speech and Signal Processing (IEEE 31st ICASSP), Toulouse, 113–116.*
- [Goo08] Goodwin, M.M. (2008): “All-pass linear arrays.” In: *J. Audio Eng. Soc., 56(12):1090–1101.*
- [Gra07] Gradshteyn, I.S.; Ryzhik, I.M.; Jeffrey, A.; Zwillinger, D. (2007): *Table of Integrals, Series, and Products.* Academic Press, 7. ed.
- [Gre23] Green, I.W.; Maxfield, J.P. (1923): “Public address systems.” In: *Bell System Tech. J., 2(2):113–142.*
- [Gun90] Gunness, D.W. (1990): “Loudspeaker directional response measurement.” In: *Proc. of 89th Audio Eng. Soc. Convention, Los Angeles, #2987.*
- [Gun98] Gunness, D.W.; Siegel, S. (1998): “A technique for improved performance of multi-driver loudspeaker arrays using new measurement, modeling and optimization processes.” In: *Proc. of 13th Audio Eng. Soc. UK Conference: Microphones & Loudspeakers, #MAL-16.*
- [Gun99] Gunness, D.W.; Hoy, W.R. (1999): “Improved loudspeaker array modeling.” In: *Proc. of 107th Audio Eng. Soc. Convention, New York, #5020.*
- [Gun00a] Gunness, D.W. (2000): “Touring line array technical issues.” Tech. rep., EAW Research Brief, http://eaw.com/docs/6_Technical_Information/White_Papers/KF760_whitepapers.pdf, last seen 2016-06-02.

- [Gun00b] Gunness, D.W.; Hoy, W.R. (2000): “Improved loudspeaker array modeling-Part 2.” In: *Proc. of 109th Audio Eng. Soc. Convention, Los Angeles*, #5211.
- [Gun00c] Gunness, D.W.; Mihelich, R.J. (2000): “Loudspeaker acoustical field calculations with application to directional response measurement.” In: *Proc. of 109th Audio Eng. Soc. Convention, Los Angeles*, #5210.
- [Gun03a] Gunness, D.W. (2003): “The design and implementation of line arrays using digital signal processing.” In: *Proc. of 19th Reproduced Sound*, Abstract only, white paper available online.
- [Gun03b] Gunness, D.W.; Butler, N.D. (2003): “Implementation of a wide-bandwidth, digitally steered loudspeaker array.” In: *Proc. of 115th Audio Eng. Soc. Convention, New York*, Abstract only, white paper available online.
- [Gun03c] Gunness, D.W.; Hoy, W.R. (2003): “Practical benefits and limitations of digitally steered arrays.” In: *Proc. of 115th Audio Eng. Soc. Convention, New York*, Abstract only, white paper available online.
- [Har75] Hartman, W.H. (1975): “Directional characteristics of phased audio reproducers.” In: *Proc. of 51st Audio Eng. Soc. Convention, Los Angeles*, #1026 (D-7).
- [Har78] Harris, F.J. (1978): “On the use of windows for harmonic analysis with the discrete fourier transform.” In: *Proc. of the IEEE*, **66**(1):51–83.
- [Har79] Harvey, J.E. (1979): “Fourier treatment of near-field scalar diffraction theory.” In: *Am. J. Phys.*, **47**(11):974–980.
- [Hay12] Hayashi, S.; Mochimaru, A.; Fidlin, P.F. (2012): “The radiation characteristics of a horizontally asymmetrical waveguide that utilizes a continuous arc diffraction slot.” In: *Proc. of 133rd Audio Eng. Soc. Convention, San Francisco*, #8709.
- [Hay13] Hayashi, S.; Mochimaru, A.; Fidlin, P.F. (2013): “The radiation characteristics of an array of horizontally asymmetrical waveguides that utilize continuous arc diffraction slots.” In: *Proc. of 134th Audio Eng. Soc. Convention, Rome*, #8865.
- [Hec77] Heckl, M. (1977): “Abstrahlung von ebenen Schallquellen (Radiation from plane sound sources).” In: *Acta Acust United Ac*, **37**(3):155–166.
- [Hei92a] Heil, C. (1992): “Sound wave guide.” Tech. rep., U.S. Patent #5,163,157 1992-11-10.
- [Hei92b] Heil, C.; Urban, M. (1992): “Sound fields radiated by multiple sound sources arrays.” In: *Proc. of 92nd Audio Eng. Soc. Convention, Vienna*, #3269.

- [Her03] Herrin, D.W.; Martinus, F.; Wu, T.; Seybert, A. (2003): “A new look at the high frequency boundary element and Rayleigh integral approximations.” In: *Proc. of Soc. of Autom. Eng. Noise & Vibration Conference, Traverse City, #2003-01-1451*.
- [Hil51] Hills, Jr., R. (1951): *Synthesis of Directivity Patterns of Acoustic Line Sources*. doctoral thesis, Harvard University.
- [Hix70] Hixson, E.L.; Au, K.T. (1970): “Wide-bandwidth constant-beamwidth acoustic array.” In: *J. Acoust. Soc. Am. (Abstract of the paper for 79th Meeting of the A.S.A.)*, **48**(1A):117.
- [Hug15] Hughes, C. (2015): “Progressive degenerate ellipsoidal phase plug.” In: *Proc. of 139th Audio Eng. Soc. Convention, New York, #9388*.
- [Hul04] Hulsebos, E. (2004): *Auralization using Wave Field Synthesis*. doctoral thesis, Delft University of Technology.
- [IEE93] IEEE (1993): “IEEE Standard definitions of terms for antennas: IEEE Std 145-1993.” Tech. rep.
- [Jac90] Jacob, K.D.; Birkle, T.K. (1990): “Prediction of the full-space directivity characteristics of loudspeaker arrays.” In: *J. Audio Eng. Soc.*, **38**(4):250–259.
- [Jac05] Jacques, R.; Albrecht, B.; Melchior, F.; de Vries, D. (2005): “An approach for multichannel recording and reproduction of sound source directivity.” In: *Proc. of 119th Audio Eng. Soc. Convention, New York, #6554*.
- [Jia04] Jiang, C.; Zou, J.; Shen, Y. (2004): “Impulse response and frequency response of a line loudspeaker array.” In: *Proc. of 117th Audio Eng. Soc. Convention, San Francisco, #6248*.
- [Kü15] Küster, J. (2015): “Helene Fischer Stadion-Tour.” In: *Production Partner*, **7-8/2015**:24–37.
- [Kam10] Kamado, N.; Hokari, H.; Shimada, S.; Saruwatari, H.; Shikano, K. (2010): “Sound field reproduction by wavefront synthesis using directly aligned multi point control.” In: *Proc. of 40th Intl. Audio Eng. Soc. Conference on Spatial Audio, Tokyo, #6-8*.
- [Kee90] Keele, Jr., D.B. (1990): “Effective performance of Bessel arrays.” In: *J. Audio Eng. Soc.*, **38**(10):723–748.
- [Kee00] Keele, Jr., D.B. (2000): “The application of broadband constant beamwidth transducer (CBT) theory to loudspeaker arrays.” In: *Proc. of 109th Audio Eng. Soc. Convention, Los Angeles, #5216*.
- [Kee02] Keele, Jr., D.B. (2002): “Implementation of straight-line and flat-panel constant beamwidth transducer (CBT) loudspeaker arrays using signal delays.” In: *Proc. of 113th Audio Eng. Soc. Convention, Los Angeles, #5653*.

- [Kee03] Keele, Jr., D.B. (2003): “Full-sphere sound field of constant-beamwidth transducer (CBT) loudspeaker line arrays.” In: *J. Audio Eng. Soc.*, **51**(7/8):611–624.
- [Kee10] Keele, Jr., D.B. (2010): “A performance ranking of seven different types of loudspeaker line arrays.” In: *Proc. of 129th Audio Eng. Soc. Convention, San Francisco*, #8155.
- [Kee15] Keele, Jr., D.B. (2015): “Time/phase behavior of constant beamwidth transducer (CBT) circular-arc loudspeaker line arrays.” In: *Proc. of 139th Audio Eng. Soc. Convention, New York*, #9387.
- [Kid79] Kido, K.; Abe, M.; Ishigame, M. (1979): “Linear loudspeaker array for sound reinforcement system using delay device.” In: *Proc. of 64th Audio Eng. Soc. Convention, New York*, #1522 (F-5).
- [Kim38] Kimball, H. (1938): *Motion Picture Sound Engineering*, Ch. XVI: Attenuation Equalizers, 228–272. New York: D. Van Nostrand, 3rd print ed.
- [Kim04] Kim, Y.; Nelson, P. (2004): “Optimal regularisation for acoustic source reconstruction by inverse methods.” In: *J. of Snd. Vibr.*, **275**(3):463–487.
- [Kin00] Kinsler, L.E.; Frey, A.R.; Coppens, A.B.; Sanders, J.V. (2000): *Fundamentals of Acoustics*. Hoboken: Wiley, 4. ed.
- [Kir93] Kirkeby, O.; Nelson, P.A. (1993): “Reproduction of plane wave sound fields.” In: *J. Acoust. Soc. Am.*, **94**(5):2992–3000.
- [Kir96] Kirkeby, O.; Nelson, P.A.; Orduna-Bustamante, F.; Hamada, H. (1996): “Local sound field reproduction using digital signal processing.” In: *J. Acoust. Soc. Am.*, **100**(3):1584–1593.
- [Kit83] Kitzen, W.J. (1983): “Multiple loudspeaker arrays using Bessel coefficients.” In: *Philips Electronic Components & Applications*, **5**(200–205).
- [Kle63] Klepper, D.L.; Steele, D.W. (1963): “Constant directional characteristics from a line source array.” In: *J. Audio Eng. Soc.*, **11**(3):198–202.
- [Kol09] Kolundzija, M.; Faller, C.; Vetterli, M. (2009): “Designing practical filters for sound field reconstruction.” In: *Proc. of 127th Audio Eng. Soc. Convention, New York*, #7851.
- [Kot33] Kotelnikov, V.A. (1933): “On the transmission capacity of ‘ether’ and wire in electric communications.” In: *Proc. 1st All-Union Conf. Technological Reconstruction of the Commun. Sector and Low-Current Eng., Moscow*.
- [Kot06] Kotelnikov, V.A. (2006): “On the transmission capacity of ‘ether’ and wire in electric communications.” In: *Phys. Usp. (Advances in Physical Sciences)*, **49**(7):736–744.

- [Koy13] Koyama, S. (2013): *Boundary Integral Approach to Sound Field Transform and Reproduction*. doctoral thesis, University of Tokyo.
- [Kum92] Kummer, W.H. (1992): “Basic array theory.” In: *Proc. of the IEEE*, **80**(1):127–140.
- [Kut78] Kuttruff, H.; Quadt, H.P. (1978): “Elektroakustische Schallquellen mit ungebündelter Schallabstrahlung.” In: *Acustica*, **41**(1):1–10.
- [Kut82] Kuttruff, H.; Quadt, H.P. (1982): “Ebene Schallstrahlergruppen mit ungebündelter Abstrahlung.” In: *Acustica*, **50**(4):273–279.
- [LA01] L-Acoustics (2001): “Line arrays versus line source arrays.” Tech. rep., white paper.
- [LA13] L-Acoustics (2013): “Array morphing, V2.1.” Tech. rep., <http://www.l-acoustics.com/23-bulletins.html>, last seen on 2016-06-02.
- [LA16] L-Acoustics (2016): “Variable Curvature Line Source–Behavior & Optimization.” Tech. rep., customer’s support training module v1.1.
- [Lal68a] Lator, E. (1968): “Conditions for the validity of the angular spectrum of plane waves.” In: *J. Opt. Soc. Am.*, **58**(9):1235–1237.
- [Lal68b] Lator, E. (1968): “Inverse wave propagator.” In: *J. Math. Phys.*, **9**(12):2001–2006.
- [Lec13] Leckschat, D.; Muscheites, A.; Epe, C. (2013): “High-frequency loudspeakers using air motion transformer technology in high-power sound reinforcement systems.” In: *Proc. of International Conference on Acoustics AIA-DAGA 2013 including the 40th Italian (AIA) Annual Conference on Acoustics and the 39th German Annual Conference on Acoustics (DAGA), Merano, Italy*, 192–193.
- [Lec15] Leckschat, D.; Muscheites, A.; Epe, C. (2015): “Suitability of folded-ribbon high-frequency drivers for high-power sound reinforcement systems.” In: *Proc. of 59th Intl. Audio Eng. Soc. Conference, Montreal, #2-3*.
- [Lee94] Lee, C.; Benkeser, P.J. (1994): “A computationally efficient method for the calculation of the transient field of acoustic radiators.” In: *J. Acoust. Soc. Am.*, **96**(1):545–551.
- [Lee98] Leembruggen, G.; Packer, N.; Goldberg, B.; Backstrom, D. (1998): “Development of a shaded, beam steered line array loudspeaker with integral amplification and DSP processing.” In: *Proc. of 105th Audio Eng. Soc. Convention, San Francisco, #4835*.
- [Lee12] Lee, J.M.; Choi, J.W.; Kang, D.S.; Kim, Y.H. (2012): “Reproduction of proximity virtual sources using a line array of loudspeakers.” In: *Proc. of 132nd Audio Eng. Soc. Convention, Budapest, #8618*.

- [Lee13] Lee, J.M.; Choi, J.W.; Kim, Y.H. (2013): “Wave field synthesis of a virtual source located in proximity to a loudspeaker array.” In: *J. Acoust. Soc. Am.*, **134**(3):2106–2117.
- [Leh00] Lehman, R.W. (2000): “Loudspeaker with differentiated energy distribution in vertical and horizontal planes.” Tech. rep., U.S. Patent #6.112.847, 2000-09-05.
- [Ler09] Lerch, R.; Sessler, G.M.; Wolf, D. (2009): *Technische Akustik*. Berlin: Springer.
- [Lil10] Lilis, G.N.; Angelosante, D.; Giannakis, G.B. (2010): “Sound field reproduction using the Lasso.” In: *IEEE Trans. Audio Speech Language Process.*, **18**(8):1902–1912.
- [Lin76] Linkwitz, S.H. (1976): “Active crossover networks for noncoincident drivers.” In: *J. Audio Eng. Soc.*, **24**(1):2–8.
- [Lip86] Lipshitz, S.P.; Vanderkooy, J. (1986): “The acoustic radiation of line sources of finite length.” In: *Proc. of 81st Audio Eng. Soc. Convention, Los Angeles, #2417*.
- [Lip90] Lipshitz, S.P.; Scott, T.C.; Salvy, B. (1990): “On the acoustic impedance of strip radiators.” In: *Proc. of 89th Audio Eng. Soc. Convention, Los Angeles, #2977*.
- [Lip95] Lipshitz, S.P.; Scott, T.C.; Salvy, B. (1995): “On the acoustic impedance of baffled strip radiators.” In: *J. Audio Eng. Soc.*, **43**(7/8):573–580.
- [Lyo11] Lyons, R.G. (2011): *Understanding Digital Signal Processing*. Upper Saddle River: Prentice Hall, 3. ed.
- [Mö88] Möser, M. (1988): *Analyse und Synthese akustischer Spektren*. Berlin: Springer, 1. ed.
- [Mö09] Möser, M. (2009): *Engineering Acoustics, An Introduction to Noise Control*. Dordrecht, Berlin, Heidelberg, New York: Springer, 2. ed.
- [Mar03] Martin Audio (2003): “W8L Line Array White Paper.” Tech. rep.
- [Mas07] Mast, T.D. (2007): “Fresnel approximations for acoustic fields of rectangularly symmetric sources.” In: *J. Acoust. Soc. Am.*, **121**(6):3311–3322.
- [McC10] McCarthy, B. (2010): *Sound Systems: Design and Optimization*. Oxford: Focal Press, 2. ed.
- [Mel08] Melchior, F.; Sladeczek, C.; de Vries, D.; Fröhlich, B. (2008): “User-dependent optimization of Wave Field Synthesis reproduction for directive sound fields.” In: *Proc. of 124th Audio Eng. Soc. Convention, Amsterdam, #7376*.

- [Mey82] Meyer, D.G. (1982): “Development of a model for loudspeaker dispersion simulation.” In: *Proc. of 72nd Audio Eng. Soc. Convention, Anaheim*, #1912.
- [Mey83] Meyer, D.G. (1983): “Digital control of loudspeaker array directivity.” In: *Proc. of 74th Audio Eng. Soc. Convention, New York*, #2014.
- [Mey84a] Meyer, D.G. (1984): “Computer simulation of loudspeaker directivity.” In: *J. Audio Eng. Soc.*, **32**(5):294–315.
- [Mey84b] Meyer, D.G. (1984): “Digital control of loudspeaker array directivity.” In: *J. Audio Eng. Soc.*, **32**(10):747–754.
- [Mey85a] Meyer, D.G. (1985): “Signal processing architecture for loudspeaker array directivity control.” In: *Proc. of 10th Intl. Conference on Acoustics, Speech and Signal Processing (IEEE 10th ICASSP), Tampa*, 600–603.
- [Mey85b] Meyer, D.G. (1985): “Toward VLSI implementation of loudspeaker array directivity control signal processing electronics.” In: *Proc. of 78th Audio Eng. Soc. Convention, Anaheim*, #2225.
- [Mey89] Meyer, D.G. (1989): “Multiple beam, electronically steered line source arrays for sound reinforcement applications.” In: *Proc. of 87th Audio Eng. Soc. Convention, New York*, #2826.
- [Mey90a] Meyer, D.G. (1990): “Multiple-beam, electronically steered line-source arrays for sound-reinforcement applications.” In: *J. Audio Eng. Soc.*, **38**(4):237–249.
- [Mey90b] Meyer, J.; Seidel, F. (1990): “Large arrays: Measured free-field polar patterns compared to a theoretical model of a curved surface source.” In: *J. Audio Eng. Soc.*, **38**(4):260–270.
- [Mey02] Meyer Sound Laboratories Inc. (2002): “DSP beam steering with modern line arrays.” Tech. rep., https://www.meyersound.com/pdf/support/papers/beam_steering.pdf, last seen on 2016-06-02.
- [Mey03] Meyer, P.; Schwenke, R. (2003): “Comparison of the directional point source model and BEM model for arrayed loudspeakers.” In: *Proc. of the Institute of Acoustics*, 25(4).
- [Mey06] Meynial, X. (2006): “DGRC arrays : A synthesis of geometric and electronic loudspeaker arrays.” In: *Proc. of 120th Audio Eng. Soc. Convention, Paris*, #6786.
- [Mit88] Mitchell, D.P.; Netravali, A.N. (1988): “Reconstruction filters in computer graphics.” In: *Computer Graphics*, **22**(4):221–228.
- [Mor86] Morse, P.M.; Ingard, K.U. (1986): *Theoretical Acoustics*. Princeton: Princeton University Press, 1. ed.

- [Mus16] Muscheites, A.; Leckschat, D.; Epe, C. (2016): “Line Array Sound Reinforcement Systems using Air Motion Transformer.” In: *Acta Acust United Ac*, **102**(3):592–599.
- [Nel01] Nelson, P.A. (2001): “A review of some inverse problems in acoustics.” In: *J. Acoust. and Vibr.*, **6**(3):118–134.
- [Nic99] Nicol, R.; Emerit, M. (1999): “3D-sound reproduction over an extensive listening area: A hybrid method derived from holophony and ambisonic.” In: *Proc. of 16th Audio Eng. Soc. Conference on Spatial Sound Reproduction, Rovaniemi*, #16-039.
- [Niz13] Nizzoli, T.; Prati, S. (2013): “Boundary element simulation of an arrayable loudspeaker horn.” In: *Proc. of 134th Audio Eng. Soc. Convention, Rome*, #8846.
- [NV06] Nieto-Vesperinas, M. (2006): *Scattering And Diffraction in Physical Optics*. Singapore: World Scientific, 2. ed.
- [Och89] Ocheltree, K.B.; Frizzell, L.A. (1989): “Sound field calculation for rectangular sources.” In: *IEEE Trans. on Ultrasonics, Ferroelectrics and Frequency Control*, **36**(2):242–248.
- [Oka14] Okamoto, T. (2014): “Generation of multiple sound zones by spatial filtering in wavenumber domain using a linear array of loudspeakers.” In: *Proc. of 39th Intl. Conference on Acoustics, Speech and Signal Processing (IEEE 39th ICASSP), Florence*, 4733–4737.
- [Ols36] Olson, H.F. (1936): “Sound reenforcing systems.” In: *J. Acoust. Soc. Am. (Abstract of the paper for 14th Meeting of the A.S.A.)*, **7**(3):239.
- [Ols40] Olson, H.F. (1940): *Elements of acoustical engineering*. New York: D. Van Nostrand Company, Inc.
- [Olv10] Olver, F.W.J.; Lozier, D.W.; Boisvert, R.F.; Clark, C.W. (2010): *NIST Handbook of Mathematical Functions*. Cambridge University Press, 1. ed.
- [Opp10] Oppenheim, A.V.; Schafer, R.W. (2010): *Discrete-Time Signal Processing*. Upper Saddle River: Pearson, 3. ed.
- [Ots90] Otsuki, T. (1990): “Diffraction by multiple slits.” In: *J. Opt. Soc. Am A*, **7**(4):646–652.
- [Paw61] Pawlowski, R.J. (1961): “The line radiator.” In: *Audio*, **45**(7):19–21.
- [Pee10] Pees, E.H. (2010): “A relationship between the far field diffraction pattern and the axial pressure radiating from a two-dimensional aperture.” In: *J. Acoust. Soc. Am.*, **127**(3):1381–1390.
- [Per08] Peretti, P.; Romoli, L.; Palestini, L.; Cecchi, S.; Piazza, F. (2008): “Wave field synthesis: Practical implementation and application to sound beam digital pointing.” In: *Proc. of 125th Audio Eng. Soc. Convention, San Francisco*, #7618.

- [Per10a] Peretti, P.; Cecchi, S.; Piazza, F.; Secondini, M.; Fusco, A. (2010): “A mixed mechanical/digital approach for sound beam pointing with loudspeakers line array.” In: *Proc. of 129th Audio Eng. Soc. Convention, San Francisco*, 8210.
- [Per10b] Peretti, P.; Romoli, L.; Cecchi, S.; Palestini, L.; Piazza, F. (2010): “Phase approximation of linear geometry driving functions for sound field synthesis.” In: *Proc. of 18th European Signal Processing Conference (EUSIPCO), Aalborg*, 1939–1943.
- [Pet13] Petruzzellis, C.; Zanghieri, U. (2013): “Digital filter for modeling air absorption in real time.” In: *Proc. of 134th Audio Eng. Soc. Convention, Rome*, #8888.
- [Pol05] Poletti, M.A. (2005): “Three-dimensional surround sound systems based on spherical harmonics.” In: *J. Audio Eng. Soc.*, **53**(11):1004–1025.
- [Pri53] Pritchard, R.L. (1953): “Optimum directivity patterns for linear point arrays.” In: *J. Acoust. Soc. Am.*, **25**(5):879–891.
- [Pri04] Pritchett, T.M.; Trubatch, A.D. (2004): “A differential formulation of diffraction theory for the undergraduate optics course.” In: *Am. J. Phys.*, **72**(8):1026–1034.
- [Rab06] Rabenstein, R.; Spors, S.; Steffen, P. (2006): *Topics in Acoustic Echo and Noise Control*, Ch. 13: Wave Field Synthesis Techniques for Spatial Sound Reproduction, 517–545. Berlin: Springer.
- [Rab08] Rabenstein, R.; Spors, S. (2008): *Handbook of Speech Processing*, Ch. 53. Sound Field Reproduction, 1095–1114. Berlin: Springer.
- [Rad13] Radmanesh, N.; Burnett, I.S. (2013): “Generation of isolated wide-band sound fields using a combined two-stage Lasso-LS algorithm.” In: *IEEE Trans. Audio Speech Language Process.*, **21**(2):378–387.
- [rBR96] 3rd Baron Rayleigh, J.W.S. (1896): *The Theory of Sound, Vol. II*. New York: Macmillan & Co., 2. ed.
- [Rob13] Robin, O.; Berry, A.; Moreau, S. (2013): “Reproduction of random pressure fields based on planar nearfield acoustic holography.” In: *J. Acoust. Soc. Am.*, **133**(6):3885–3899.
- [Rog78] Rogers, P.H.; Van Buren, A.L. (1978): “New approach to a constant beamwidth transducer.” In: *J. Acoust. Soc. Am.*, **64**(1):38–43.
- [Rom08] Romoli, L.; Peretti, P.; Palestini, L.; Cecchi, S.; Piazza, F. (2008): “A new approach to digital directivity control of loudspeakers line arrays using wave field synthesis theory.” In: *Proc. of the Intl. Workshop on Acoustic Signal Enhancement (IWAENC), Seattle*, #9022.
- [Rom15] Romoli, L.; Cecchi, S.; Peretti, P.; Piazza, F. (2015): “Real-time implementation and performance evaluation of digital control for loudspeakers line arrays.” In: *Applied Acoustics*, **97**:121–132.

- [Sal72] Salava, T. (1972): “Arrays of discrete sound sources and/or continuous line radiators.” In: *Proc. of 2nd Central Europe Audio Eng. Soc. Convention, Munich*, #C05.
- [Sal10] Salvador, C.D. (2010): “Wave field synthesis using fractional order systems and fractional delays.” In: *Proc. of 128th Audio Eng. Soc. Convention, London*, #8122.
- [Sch43] Schelkunoff, S.A. (1943): “A mathematical theory of linear arrays.” In: *Bell System Tech. J.*, **22**(1):80–107.
- [Sch50] Schneider, A.W. (1950): “Sound reinforcing systems.” In: *Audio Engineering Magazine (referred to as J. Audio Eng. Soc. Vol. 0)*, **34**(11):27,28,53–55.
- [Sch68] Schenck, H.A. (1968): “Improved integral formulation for acoustic radiation problems.” In: *J. Acoust. Soc. Am.*, **44**(1):41–58.
- [Sch92] Schmidmaier, R.; Meyer, D.G. (1992): “Dynamic amplitude shading of electronically steered line source arrays.” In: *Proc. of 92nd Audio Eng. Soc. Convention, Vienna*, #3272.
- [Sch02] Scheirman, D.W. (2002): “Practical considerations for field deployment of modular line array systems.” In: *Proc. of 21st Audio Eng. Soc. Intl. Conference: Architectural Acoustics and Sound Reinforcement, St. Petersburg*, #56.
- [Sch06a] Schröder, N.B.; Schwalbe, T.; Mores, R. (2006): “Methods to improve the horizontal pattern of a line array module in the midrange band.” In: *Proc. of 120th Audio Eng. Soc. Convention, Paris*, #6776.
- [Sch06b] Schröder, N.B.; Schwalbe, T.; Mores, R. (2006): “The performance and restrictions of high frequency waveguides in line arrays.” In: *Proc. of 120th Audio Eng. Soc. Convention, Paris*, #6777.
- [Sch13] Schultz, F. et al. (2013): “Derivation of IIR prefilters for soundfield synthesis using linear secondary source distributions.” In: *Proc. of AIA-DAGA 2013, Merano, Italy*, 2372–2375.
- [Sch14a] Schultz, F.; Rettberg, T.; Spors, S. (2014): “On spatial-aliasing-free sound field reproduction using finite length line source arrays.” In: *Proc. of 137th Audio Eng. Soc. Convention, Los Angeles*, #9098.
- [Sch14b] Schultz, F.; Rettberg, T.; Spors, S. (2014): “On spatial-aliasing-free sound field reproduction using infinite line source arrays.” In: *Proc. of 136th Audio Eng. Soc. Convention, Berlin*, #9078.
- [Sch14c] Schultz, F.; Spors, S. (2014): “Comparing approaches to the spherical and planar single layer potentials for interior sound field synthesis.” In: *Acta Acust United Ac*, **100**(5):900–911.

- [Sch14d] Schultz, F.; Spors, S. (2014): “On the frequency response variation of sound field synthesis using linear arrays.” In: *Fortschritte der Akustik: Tagungsband d. 40. DAGA, Oldenburg*, 592–593.
- [Sch15a] Scheirman, D. (2015): “Large-scale loudspeaker arrays: Past, present, and future – Part One: Control, user interface, and audio transport.” In: *Proc. of 59th Intl. Audio Eng. Soc. Conference, Montreal*, #1-2.
- [Sch15b] Scheirman, D. (2015): “Large-scale loudspeaker arrays: Past, present, and future – Part Two: Electroacoustic considerations.” In: *Proc. of 59th Intl. Audio Eng. Soc. Conference, Montreal*, #1-3.
- [Sch15c] Schultz, F.; Spors, S. (2015): “On the connections between radiation synthesis and sound field synthesis using linear arrays.” In: *Fortschritte der Akustik: Tagungsband d. 41. DAGA, Nürnberg*, 498–501.
- [Sch15d] Schultz, F.; Straube, F.; Spors, S. (2015): “Discussion of the Wavefront Sculpture Technology criteria for straight line arrays.” In: *Proc. of 138th Audio Eng. Soc. Convention, Warsaw*, #9323.
- [Sch16] Schultz, F.; Spors, S. (2016): “On the Connections of Wave Field Synthesis and Spectral Division Method Plane Wave Driving Functions.” In: *Fortschritte der Akustik: Tagungsband d. 42. DAGA, Aachen*, 1027–1029.
- [Sei96] Seidel, F.; Staffeldt, H. (1996): “Frequency and angular resolution for measuring, presenting, and predicting loudspeaker polar data.” In: *Proc. of 100th Audio Eng. Soc. Convention, Copenhagen*, #4209.
- [She67a] Sherman, G.C. (1967): “Application of the convolution theorem to Rayleigh’s integral formulas.” In: *J. Opt. Soc. Am.*, **57**(4):546–547.
- [She67b] Sherman, G.C. (1967): “Integral-transform formulation of diffraction theory.” In: *J. Opt. Soc. Am.*, **57**(12):1490–1498.
- [She07a] Shen, Y.; An, K.; Ou, D. (2007): “The relation between active radiating factor and frequency responses of loudspeaker line arrays – Part 2.” In: *Proc. of 123rd Audio Eng. Soc. Convention, New York*, #7191.
- [She07b] Shen, Y.; Ou, D.; An, K. (2007): “The relation between active radiating factor and frequency responses of loudspeaker line arrays.” In: *Proc. of 122nd Audio Eng. Soc. Convention, Vienna*, #7058.
- [Shi10] Shin, M.; Lee, S.Q.; Fazi, F.M.; Nelson, P.A.; Kim, D.; Wang, S.; Park, K.H.; Seo, J. (2010): “Maximization of acoustic energy difference between two spaces.” In: *J. Acoust. Soc. Am.*, **128**(1):121–131.
- [Sin78] Sinclair, R. (1978): “Stacked and splayed acoustical sources.” In: *Proc. of 61st Audio Eng. Soc. Convention, New York*, #1389.

- [Sku54] Skudrzyk, E. (1954): *Die Grundlagen der Akustik*. Wien: Springer.
- [Sku71] Skudrzyk, E. (1971): *The Foundations of Acoustics*. New York, Wien: Springer.
- [Smi71] Smith, A.P. (1971): “A three-way columnar loudspeaker for reinforcement of the performing arts.” In: *J. Audio Eng. Soc.*, **19**(3):213–219.
- [Smi95] Smith, D.L. (1995): “Discrete element line arrays (everything there is to know about...)” In: *Proc. of 99th Audio Eng. Soc. Convention, New York*, #4060.
- [Smi97] Smith, D.L. (1997): “Discrete-element line arrays – their modeling and optimization.” In: *J. Audio Eng. Soc.*, **45**(11):949–964.
- [Som54] Sommerfeld, A. (1954): *Lectures on Theoretical Physics, Vol. IV: Optics*. New York: Academic Press.
- [Son00] Sonke, J.J. (2000): *Variable Acoustics by Wave Field Synthesis*. doctoral thesis, Delft University of Technology.
- [Spo06a] Spors, S. (2006): *Active Listening Room Compensation for Spatial Sound Reproduction Systems*. doctoral thesis, Friedrich-Alexander-Universität Erlangen-Nürnberg.
- [Spo06b] Spors, S. (2006): “Spatial aliasing artifacts produced by linear loudspeaker arrays used for wave field synthesis.” In: *Proc. of the 2nd Intl. Symposium on Control, Communications and Signal Processing (EURASIP 2nd ISCCSP), Marrakech*.
- [Spo06c] Spors, S.; Rabenstein, R. (2006): “Spatial aliasing artifacts produced by linear and circular loudspeaker arrays used for wave field synthesis.” In: *Proc. of 120th Audio Eng. Soc. Convention, Paris*, #6711.
- [Spo07a] Spors, S. (2007): “Extension of an analytic secondary source selection criterion for Wave Field Synthesis.” In: *Proc. of 123rd Audio Eng. Soc. Convention, New York*, #7299.
- [Spo07b] Spors, S.; Ahrens, J. (2007): “Analysis of near-field effects of wave field synthesis using linear loudspeaker arrays.” In: *Proc. of 30th Intl. Audio Eng. Soc. Conference: Intelligent Audio Environments, Saariselkä*, #29.
- [Spo08a] Spors, S.; Ahrens, J. (2008): “A comparison of Wave Field Synthesis and Higher-Order Ambisonics with respect to physical properties and spatial sampling.” In: *Proc. of 125th Audio Eng. Soc. Convention, San Francisco*, #7556.
- [Spo08b] Spors, S.; Rabenstein, R.; Ahrens, J. (2008): “The theory of Wave Field Synthesis revisited.” In: *Proc. of 124th Audio Eng. Soc. Convention, Amsterdam*, #7358.

- [Spo08c] Spors, S.; Rath, M.; Ahrens, J. (2008): “Towards a theory for arbitrarily shaped sound field reproduction systems.” In: *Abstract and Talk for Acoustics’08, Paris*, #2991.
- [Spo09] Spors, S.; Ahrens, J. (2009): “Spatial sampling artifacts of Wave Field Synthesis for the reproduction of virtual point sources.” In: *Proc. of 126th Audio Eng. Soc. Convention, Munich*, #7744.
- [Spo10] Spors, S.; Ahrens, J. (2010): “Analysis and improvement of pre-equalization in 2.5-dimensional Wave Field Synthesis.” In: *Proc. of 128th Audio Eng. Soc. Convention, London*, #8121.
- [Spo11] Spors, S. (2011): “Schallfeldsynthese: Stand der Technik und Perspektiven.” In: *Fortschritte der Akustik: Tagungsband d. 37. DAGA, Düsseldorf*.
- [Spo13] Spors, S.; Wierstorf, H.; Raake, A.; Melchior, F.; Frank, M.; Zotter, F. (2013): “Spatial sound with loudspeakers and its perception: A review of the current state.” In: *Proceedings of the IEEE*, **101**(9):1920–1938.
- [Sta95] Start, E.W.; Valstar, V.G.; de Vries, D. (1995): “Application of spatial bandwidth reduction in Wave Field Synthesis.” In: *Proc. of 98th Audio Eng. Soc. Convention, Paris*, #3972.
- [Sta96] Start, E.W. (1996): “Application of curved arrays in Wave Field Synthesis.” In: *Proc. of 100th Audio Eng. Soc. Convention, Copenhagen*, #4143.
- [Sta97] Start, E.W. (1997): *Direct Sound Enhancement by Wave Field Synthesis*. doctoral thesis, Delft University of Technology.
- [Sta01] Start, E.; van Beuningen, G. (2001): “Analysis of DDS-controlled loudspeaker arrays by near field acoustic holography.” In: *Proc. of 17th Reproduced Sound Conference*, #17.14.
- [Sta04] Staffeldt, H.; Thompson, A. (2004): “Line array performance at mid and high frequencies.” In: *Proc. of 117th Audio Eng. Soc. Convention, San Francisco*, #6274.
- [Ste27] Stenzel, H. (1927): “Über die Richtwirkung von Schallstrahlern.” In: *Elektrische Nachrichtentechnik*, **4**(6):239–253.
- [Ste29] Stenzel, H. (1929): “Über die Richtcharakteristik von in einer Ebene angeordneten Strahlern.” In: *Elektrische Nachrichtentechnik*, **6**(5):165–181.
- [Ste58] Stenzel, H.; Brosze, O. (1958): *Leitfaden zur Berechnung von Schallvorgängen*. Berlin: Springer, 2. ed.
- [Ste71] Stepanishen, P.R. (1971): “Transient radiation from pistons in an infinite planar baffle.” In: *J. Acoust. Soc. Am.*, **49**(5B):1629–1638.

- [Ste82] Stephanishen, P.R.; Benjamin, K.C. (1982): “Forward and backward projection of acoustic fields using FFT methods.” In: *J. Acoust. Soc. Am.*, **71**(4):803–812.
- [Str15a] Straube, F.; Schultz, F.; Weinzierl, S. (2015): “Evaluation strategies for the optimization of line source arrays.” In: *Proc. of the 59th Intl. Audio Eng. Soc. Conference, Montreal*, #P.2-1.
- [Str15b] Straube, F.; Schultz, F.; Weinzierl, S. (2015): “On the effect of spatial discretization of curved line source arrays.” In: *Fortschritte der Akustik: Tagungsband d. 41. DAGA, Nürnberg*, 459–462.
- [Str16] Straube, F.; Schultz, F.; Markarski, M.; Weinzierl, S. (2016): “Optimized driving functions for curved line source arrays using modeled and measured loudspeaker data.” In: *Fortschritte der Akustik: Tagungsband d. 42. DAGA, Aachen*, 1136–1139.
- [Tay64] Taylor, P.H. (1964): “The line-source loudspeaker and its applications.” In: *British Kinematography*, **44**(3):64–83.
- [Ter10] Terrell, M.; Sandler, M. (2010): “Optimising the controls of a homogeneous loudspeaker array.” In: *Proc. of 129th Audio Eng. Soc. Convention, San Francisco*, #8159.
- [Tho06] Thompson, A. (2006): “Line array splay angle optimization.” In: *Proc. of the Institute of Acoustics*, 28(8).
- [Tho07] Thompson, A. (2007): “Acoustic horn waveguides.” Tech. rep., Intl. Patent WO 2007/054709 A2.
- [Tho08] Thompson, A. (2008): “Real world line array optimisation.” In: *Proc. of the Institute of Acoustics*, 30(6).
- [Tho09] Thompson, A. (2009): “Improved methods for controlling touring loudspeaker arrays.” In: *Proc. of 127th Audio Eng. Soc. Convention, New York*, #7828.
- [Tho11] Thompson, A.; Baird, J.; Webb, B. (2011): “Numerically optimised touring loudspeaker arrays - Practical applications.” In: *Proc. of 131st Audio Eng. Soc. Convention, New York*, #8511.
- [Tho13] Thompson, A.; Luzarraga, J. (2013): “Drive granularity for straight and curved loudspeaker arrays.” In: *Proc. of the Institute of Acoustics*, 35(2).
- [Tou15] Tourbabin, V.; Rafaely, B. (2015): “On the consistent use of space and time conventions in array processing.” In: *Acta Acust United Ac*, **101**(3):470–473.
- [Uns00] Unser, M. (2000): “Sampling - 50 years after Shannon.” In: *Proc. of the IEEE*, **88**(4):569–587.

- [Urb01] Urban, M.; Heil, C.; Baumann, P. (2001): “Wavefront Sculpture Technology.” In: *Proc. of 111th Audio Eng. Soc. Convention, New York*, #5488.
- [Urb03] Urban, M.; Heil, C.; Baumann, P. (2003): “Wavefront Sculpture Technology.” In: *J. Audio Eng. Soc.*, **51**(10):912–932.
- [Ure94] Ureda, M.S. (1994): “The convolution method for horn array directivity prediction.” In: *Proc. of 96th Audio Eng. Soc. Convention, Amsterdam*, #3790.
- [Ure95a] Ureda, M.S. (1995): “Amplitude and signal delay shading of vertical horn arrays.” In: *Proc. of 99th Audio Eng. Soc. Convention, New York*, #4061 (E-4).
- [Ure95b] Ureda, M.S. (1995): “Directivity response of horn arrays.” In: *Proc. of 98th Audio Eng. Soc. Convention, Paris*, #3963.
- [Ure96] Ureda, M.S. (1996): “Wave field synthesis with horn arrays.” In: *Proc. of 100th Audio Eng. Soc. Convention, Copenhagen*, #4144.
- [Ure01a] Ureda, M.S. (2001): “J and Spiral line arrays.” In: *Proc. of 111th Audio Eng. Soc. Convention, New York*, #5485.
- [Ure01b] Ureda, M.S. (2001): “Line arrays: Theory and applications.” In: *Proc. of 110th Audio Eng. Soc. Convention, Amsterdam*, #5304.
- [Ure02] Ureda, M.S. (2002): “Pressure response of line sources.” In: *Proc. of 113th Audio Eng. Soc. Convention, Los Angeles*, #5649.
- [Ure04] Ureda, M.S. (2004): “Analysis of loudspeaker line arrays.” In: *J. Audio Eng. Soc.*, **52**(5):467–495.
- [Vö11] Völk, F.; Lindner, F.; Fastl, H. (2011): “Primary source correction (PSC) in wave field synthesis.” In: *Proc. of the 1st Intl. Conference on Spatial Audio (1st ICSA), Detmold*.
- [Vö12] Völk, F.; Fastl, H. (2012): “Wave Field Synthesis with primary source correction: Theory, simulation results, and comparison to earlier approaches.” In: *Proc. of 133rd Audio Eng. Soc. Convention, San Francisco*, #8717.
- [Van83] Van Buren, A.L.; Luker, L.D.; Jevnager, M.D.; Tims, A.C. (1983): “Experimental constant beamwidth transducer.” In: *J. Acoust. Soc. Am.*, **73**(6):2200–2209.
- [Van02] Van Trees, H.L. (2002): *Optimum Array Processing. Part IV of Detection, Estimation, and Modulation Theory*. New York: Wiley.
- [vB00] van Beuningen, G.W.J.; Start, E.W. (2000): “Optimizing directivity properties of DSP controlled loudspeaker arrays.” In: *Proc. of the Institute of Acoustics*, 22(6).

- [vB01] van Beuningen, G.W.J.; Start, E.W. (2001): “Digital directivity synthesis of DSP-controlled loudspeaker arrays – A new concept.” In: *Proc. of 27. Jahrestagung der Deutschen Gesellschaft für Akustik (DAGA), Hamburg-Harburg*, only abstract.
- [vdW94] van der Werff, J. (1994): “Design and implementation of a sound column with exceptional properties.” In: *Proc. of 96th Audio Eng. Soc. Convention, Amsterdam, #3835*.
- [vdW96] van der Wal, M.; W.Start, E.; de Vries, D. (1996): “Design of logarithmically spaced constant-directivity transducer arrays.” In: *J. Audio Eng. Soc.*, **44**(6):497–507.
- [Vee05] Veerman, J.A.C.; Rusch, J.J.; Urbach, H.P. (2005): “Calculation of the Rayleigh-Sommerfeld diffraction integral by exact integration of the fast oscillating factor.” In: *J. Opt. Soc. Am. A*, **22**(4):636–646.
- [Ver97] Verheijen, E. (1997): *Sound Reproduction by Wave Field Synthesis*. doctoral thesis, Delft University of Technology.
- [Vog93] Vogel, P. (1993): *Application of Wave Field Synthesis*. doctoral thesis, Delft University of Technology.
- [War01] Ward, D.B.; Abhayapala, T.D. (2001): “Reproduction of a plane-wave sound field using an array of loudspeakers.” In: *IEEE Trans. Audio Speech Language Process.*, **9**(6):697–707.
- [Wat15] Watanabe, K. (2015): *Integral Transform Techniques for Green’s Function*. Cham: Springer, 2. ed.
- [Web03] Webb, B.; Baird, J. (2003): “Advances in line array technology for live sound.” In: *Proc. of 19th Audio Eng. Soc. UK Conference: Live Sound, Westminster*.
- [Wei] Weisstein, E.W.: “Tanc function.” Tech. rep., MathWorld—A Wolfram Web Resource <http://mathworld.wolfram.com/TancFunction.html>.
- [Wie14] Wierstorf, H. (2014): *Perceptual assessment of sound field synthesis*. doctoral thesis, TU Berlin.
- [Wil99] Williams, E.G. (1999): *Fourier Acoustics, Sound Radiation and Nearfield Acoustic Holography*. London, San Diego: Academic Press, 1. ed.
- [Wol30] Wolff, I.; Malter, L. (1930): “Directional radiation of sound.” In: *J. Acoust. Soc. Am.*, **2**(2):201–241.
- [Wol36] Wolf, S.K.; Stanton, G.T. (1936): “Sound reenforcement—An acoustic problem.” In: *J. Acoust. Soc. Am. (Abstract of the paper for 14th Meeting of the A.S.A.)*, **7**(3):239.

- [Wol64] Wolf, E.; Marchand, E.W. (1964): “Comparison of the Kirchhoff and the Rayleigh-Sommerfeld theories of diffraction at an aperture.” In: *J. Opt. Soc. Am.*, **54**(5):587–594.
- [Wor77] Worsley, K. (1977): “A multi source digital delayed sound reinforcement system for a large gothic cathedral.” In: *Proc. of 57th Audio Eng. Soc. Convention, Los Angeles*, #1258.
- [Wu08] Wu, S.F. (2008): “Methods for reconstructing acoustic quantities based on acoustic pressure measurements.” In: *J. Acoust. Soc. Am.*, **124**(5):2680–2697.
- [Wu09] Wu, Y.J.; Abhayapala, T.D. (2009): “Theory and design of sound-field reproduction using continuous loudspeaker concept.” In: *IEEE Trans. Audio Speech Language Process.*, **17**(1):107–116.
- [Wun96] Wunsch, G.; Schulz, H.G. (1996): *Elektromagnetische Felder*. Berlin: Verlag Technik, 2. ed.
- [Zha13] Zhang, W.; Abhayapala, T.D.; Fazi, F.M. (2013): “Functional analysis guided approach for sound field reproduction with flexible loudspeaker layouts.” In: *Proc. of IEEE Workshop on Applications of Signal Processing to Audio and Acoustics (WASPAA), New Paltz*.
- [Zio95] Ziomek, L.J. (1995): *Fundamentals of Acoustic Field Theory and Space-Time Signal Processing*. Boca Raton: CRC Press, 1. ed.
- [Zot09] Zotter, F.; Pomberger, H.; Frank, M. (2009): “An alternative ambisonics formulation: Modal source strength matching and the effect of spatial aliasing.” In: *Proc. of 126th Audio Eng. Soc. Convention, Munich*, #7740.
- [Zot13] Zotter, F.; Spors, S. (2013): “Is sound field control determined at all frequencies? How is it related to numerical acoustics?” In: *Proc. of 52nd Audio Eng. Soc. Intl. Conference on Sound Field Control, Guildford*, #1-3.

Curriculum Vitae

Frank Schultz, M.Sc.

Birth: 17th of May 1979 in Leipzig, Germany

Nationality: German

Web: https://www.researchgate.net/profile/Frank_Schultz
<https://spatialaudio.net/author/frank-schultz/>
<https://orcid.org/0000-0002-3010-0294>

University Education

2013-2015 research assistant with Prof. Sascha Spors at research group *Signal Processing and Virtual Acoustics*, Institute of Communications Engineering, University of Rostock

2009–2012 research assistant with Prof. Stefan Weinzierl at *Audio Communication Group*, TU Berlin

2007-2011 M.Sc. in audio communication and technology, TU Berlin

1999-2003 Dipl.-Ing. (FH) in communications engineering (B.Eng. equivalent), HTWK Leipzig

Professional Work Experience

2003-2007 Audio-DSP R&D engineer (hard- & software) at EVI Audio GmbH/Bosch Communications Systems, Straubing

High School Education

1992-1997 secondary high school with school-leaving examination (gymnasiales Abitur), Leipzig

Publications by Frank Schultz

The following publications – given in chronological publishing order – originated from research directly related to the present thesis. Revisited parts of these proceedings and articles are reissued in this dissertation.

- [Sch13] Schultz, F. et. al (2013): "Derivation of IIR prefilters for soundfield synthesis using linear secondary source distributions." In: *Proc. of AIA-DAGA 2013, Merano*, 2372-2375. (abstract reviewed, talk)
- [Sch14d] Schultz, F.; Spors, S. (2014): "On the frequency response variation of sound field synthesis using linear arrays." In: *Proc. of 40th DAGA, Oldenburg*, 592-593. (abstract reviewed, talk)
- [Sch14b] Schultz, F.; Rettberg, T.; Spors, S. (2014): "On spatial-aliasing-free sound field reproduction using infinite line source arrays." In: *Proc. of 136th Audio Eng. Soc. Conv., Berlin, #9078*. (peer reviewed, talk)
- [Sch14c] Schultz, F.; Spors, S. (2014): "Comparing Approaches to the Spherical and Planar Single Layer Potentials for Interior Sound Field Synthesis." In: *Acta Acust United Ac*, **100**(5):900-911. DOI 10.3813/AAA.918769 (peer reviewed), originally submitted, peer reviewed and accepted for the *EAA Joint Symposium on Auralization and Ambisonics 2014, Berlin* (talk).
- [Sch14a] Schultz, F.; Rettberg, T.; Spors, S. (2014): "On spatial-aliasing-free sound field reproduction using finite length line source arrays." In: *Proc. of 137th Audio Eng. Soc. Conv., Los Angeles, #9098*. (précis reviewed, talk)
- [Sch15c] Schultz, F.; Spors, S. (2015): "On the Connections between Radiation Synthesis and Sound Field Synthesis using Linear Arrays." In: *Proc. of 41st DAGA, Nürnberg*, 498-501. (abstract reviewed, talk)
- [Str15b] Straube, F.; Schultz, F.; Weinzierl, S. (2015): "On the Effect of Spatial Discretization of Curved Line Source Arrays." In: *Proc. of 41st DAGA, Nürnberg*, 459-462. (abstract reviewed, poster)
- [Sch15d] Schultz, F.; Straube, F.; Spors, S. (2015): "Discussion of the Wavefront Sculpture Technology Criteria for Straight Line Arrays." In: *Proc. of 138th Audio Eng. Soc. Conv., Warsaw, #9323*. (peer reviewed, talk, best peer-reviewed paper award).
- [Str15a] Straube, F.; Schultz, F.; Makarski, M; Spors, S.; Weinzierl, S. (2015): "Evaluation Strategies for the Optimization of Line Source Arrays." In: *Proc. of 59th Audio Eng. Soc. Intl. Conf., Montreal, #P2-8*. (peer reviewed, talk)
- Schultz, F.; Straube, F; Spors, S. (2015): "Discussion of the Wavefront Sculp-

ture Technology Criteria for Straight Line Arrays." submitted to *J. Audio Eng. Soc.* (peer reviewed, then withdrawn by the author in order to provide a concise, extended, open source white paper to the community), originally submitted, peer reviewed and released as preprint [Sch15d] for the *138th Audio Eng. Soc. Conv., Warsaw*

–[Sch16] Schultz, F.; Spors, S. (2016): "On the Connections of Wave Field Synthesis and Spectral Division Method Plane Wave Driving Functions." In: *Proc. of 42nd DAGA, Aachen*, 1027-1029. (abstract reviewed, talk)

–[Str16] Straube, F.; Schultz, F.; Makarski, M.; Weinzierl, S. (2016): "Optimized Driving Functions for Curved Line Source Arrays Using Modelled and Measured Loudspeaker Data." In: *Proc. of 42nd DAGA, Aachen*, 1136-1139. (abstract reviewed, talk)

–[Fir16] Firtha, G.; Fiala, P.; Schultz, F.; Spors, S. (2016): "Referencing Schemes for Wave Field Synthesis Driving Functions—A Unified Theory." In: *IEEE/ACM Trans. Audio Speech Language Process.* (submitted).

Further university related work by the author that is not directly linked to the present thesis in chronological order:

–Schultz, F. (2003): *DSP-Algorithmen zum thermischen Überlastschutz von Lautsprechern*. Bachelor thesis, Institut für Nachrichtentechnik, HTWK Leipzig (FH).

–Schultz, F.; Cholakov, V.; Maempel, H.J. (2009): "Zur Hörbarkeit von digitalen Clipping-Verzerrungen." In: *Bericht der 25. Tonmeistertagung 2008, Leipzig*, 479-486. (abstract reviewed, talk)

–Schultz, F.; Maempel, H.J. (2009): "Hörbarkeit von digitalen Clippingverzerrungen." In: *FKT - Die Fachzeitschrift für Fernsehen, Film und elektronische Medien*, **63**(3):62-65. (editor reviewed)

–Schultz, F.; Lindau, A.; Weinzierl, S. (2009): "Just noticeable BRIR grid resolution for lateral head movements." In: *Proc. of NAG/DAGA 2009, Rotterdam*, 200-201. (abstract reviewed, talk)

–Pollow, M.; Behler, G.K.; Schultz, F. (2010): "Musical instrument recording for building a directivity database." In: *Proc. of 36th DAGA, Berlin*, 703-704. (abstract reviewed, talk)

–Krämer, J.; Schultz, F.; Pollow, M.; Weinzierl, S. (2010): "Zur Schalleistung von modernen und historischen Orchesterinstrumenten I: Streichinstrumente." In: *Proc. of 36th DAGA, Berlin*, 889-890. (abstract reviewed, talk)

- Detzner, E.; Schultz, F.; Pollow, M.; Weinzierl, S. (2010): "Zur Schalleistung von modernen und historischen Orchesterinstrumenten II: Holz- und Blechblasinstrumente." In: *Proc. of 36th DAGA, Berlin*, 891-892. (abstract reviewed, talk)
- Weinzierl, S.; Schultz, F.; Sanvito, P. (2011): "Die Akustik des Teatro Olimpico in Vicenza." In: *Proc. of 37th DAGA, Düsseldorf*, 163-164. (abstract reviewed, talk)
- Schultz, F.; Lindau, A.; Markarski, M.; Weinzierl, S. (2011): "An extraaural headphone for optimized binaural reproduction." In: *Bericht der 26. Tonmeistertagung 2010, Leipzig*, 702-714. (abstract reviewed, talk)
- Schultz, F. (2011): *Elektroakustisch optimierte Wiedergabe binauraler Signale*. Master thesis, Fachgebiet Audiokommunikation, TU Berlin.
- Schultz, F.; Spors, S. (2013): "Data-based binaural synthesis including rotational and translatory head-movements." In: *Proc. of 52nd Audio Eng. Soc. Intl. Conf., Guildford*, P-7. (précis reviewed, poster)
- Büttner, C; Schultz, F; Weinzierl, S. (2014): "Room acoustical measurements and simulations of Italian Renaissance theatres." Electronic resource accompanying *Acta Acust United Ac*, **101**(3), <http://dx.doi.org/10.14279/depositonce-32>. (poster at <http://goo.gl/6WRF7Q>)
- Winter, F.; Schultz, F.; Spors, S. (2014): "Localization properties of data-based binaural synthesis including translatory head-movements." In: *Proc. of 7th EAA Forum Acusticum, Krakow*, #SS16/3. (précis reviewed, talk)
- Weinzierl, S.; Sanvito, P.; Schultz, F.; Büttner, C. (2015): "The Acoustics of Renaissance Theatres in Italy." In: *Acta Acust United Ac*, **101**(3):632-641. DOI 10.3813/AAA.918858. (peer reviewed)
- Spors, S.; Schultz, F.; Wierstorf H. (2015): "Non-smooth secondary source distributions in Wave Field Synthesis." In: *Proc. of 41st DAGA, Nürnberg*, 1591-1594. (abstract reviewed, talk)
- Spors, S.; Schultz, F.; Rettberg, T. (2016): "Improved Driving Functions for Rectangular Loudspeaker Arrays Driven by Wave Field Synthesis." In: *Proc. of 42nd DAGA, Aachen*, 1030-1033. (abstract reviewed, talk)

Selbständigkeitserklärung

Ich, Frank Schultz, stelle fest und versichere, dass (i) diese der Universität Rostock—erstmalig einer akademischen Institution zur Prüfung—vorgelegte Dissertation mit dem Titel „*Sound Field Synthesis for Line Source Array Applications in Large-Scale Sound Reinforcement*“ von mir selbständig und ohne fremde Hilfe verfasst wurde, ich (ii) andere als die von mir angegebenen Quellen und Hilfsmittel nicht benutzt habe und ich (iii) die den benutzten Quellen wörtlich oder inhaltlich entnommene Stellen als solche kenntlich gemacht habe.

Frank Schultz

Rostock, 13.12.2015 & Wien, 13.06.2016

Zusammenfassung

Diese Dissertation beschäftigt sich mit der Beschallung großer Zuhörerflächen mit sogenannten Line Source Arrays. Eine optimale Beschallung erfordert lineare Frequenzgänge an allen Zuhörerpunkten und einen gewünschten Schalldruckpegelverlauf. Anstatt als Richtcharakteristiksynthese wird das Problem hier als Schallfeldsynthese beschrieben. Die Synthese einer virtuellen Quelle mit einem Line Source Array erlaubt das Beschallungsproblem als Formung einer geeigneten und für den Zuhörerbereich angepassten Wellenfront zu interpretieren. Dies wird entweder durch geometrische Krümmung des Arrays, durch geeignete elektronische Ansteuerung der Lautsprecher oder idealerweise durch beides gleichzeitig erreicht. Offensichtlich hängt das Ergebnis davon ab, wie akkurat ein Array die gewünschte Wellenfront abstrahlen kann. In der Praxis wird dies beeinflusst von den verwendeten Lautsprechern und ihrer Anordnung, ihrer elektronischen Ansteuerung und potentiell auftretendem räumlichen Aliasing. Der Einfluss dieser Parameter wird mit Hilfe von Array-Signalverarbeitung diskutiert, wofür die sogenannte Wavefront Sculpture Technology aufgegriffen und Wellenfeldsynthese als mögliche Ansteuerungsmethode vorgeschlagen wird.

Abstract

This thesis deals with optimized large-scale sound reinforcement for large audiences in large venues using line source arrays. Homogeneous audience coverage requires flat frequency responses for all listeners and an appropriate sound pressure level distribution. This is treated as a sound field synthesis problem rather than a directivity synthesis problem. For that the synthesis of a virtual source via the line source array allows for interpreting the problem as audience adapted wavefront shaping. This is either achieved by geometrical array curving, by electronic control of the loudspeakers or by ideally combining both approaches. Obviously the obtained results depend on how accurately an array can emanate the desired wavefront. For practical array designs and setups this is affected by the deployed loudspeakers and their arrangement, its electronic control and potential spatial aliasing occurrence. The influence of these parameters is discussed with the aid of array signal processing revisiting the so called wavefront sculpture technology and proposing so called wave field synthesis as a suitable control method.

Theses

1. Optimized large-scale sound reinforcement can be interpreted as a sound field synthesis problem rather than a directivity synthesis problem.
2. Wave Field Synthesis of a directed virtual source allows for an audience adapted wavefront shaping. This is another interpretation of synthesizing frequency independent, homogeneous beam patterns adapted to the audience.
3. The quality of wavefront shaping using a line source array depends on the array's geometry, its spatial discretization, its electronic control and the deployed loudspeaker characteristics.
4. Wavefront shaping by concurrently avoiding/suppressing side and grating lobes is realizable either with full electronic control when the spatial sampling condition holds, or if not with frequency dependent gain shading and additional geometric array curving using highly directed loudspeakers.
5. Wavefront Sculpture Technology essentially constitutes fundamental array processing and can be consistently discussed with an acoustic signal processing model for sound field synthesis.
6. Rayleigh integral sound field synthesis is identically equal to the angular spectrum synthesis. The latter allows for a more convenient interpretation of occurring interference and diffraction phenomena of line array radiation.
7. The side and grating lobe characteristic in the farfield radiation pattern of a straight array built from non-isotropic pistons is directly linked to the shape of these pistons, to the gaps between them and the control method. This can be conveniently discussed with the angular spectrum synthesis.
8. The discrete-time impulse response of the half-derivative filter can be analytically given. The half-derivative and half-integral discrete-time filters can be approximated with a cascade connection of analytically given discrete-time 2nd order low-/high-shelf IIR filters.